

**Absolute Photoabsorption and Photoionization Studies  
of Halogen Containing Molecules by Dipole Electron  
Impact Methods**

by

Terry N. Olney

B.Sc. (Chemistry) University of Victoria, 1991

A THESIS SUBMITTED IN PARTIAL FULFILLMENT OF  
THE REQUIREMENTS FOR THE DEGREE OF  
DOCTOR OF PHILOSOPHY

in

THE FACULTY OF GRADUATE STUDIES  
DEPARTMENT OF CHEMISTRY

We accept this thesis as conforming  
to the required standard

THE UNIVERSITY OF BRITISH COLUMBIA

August 1996

© Terry N. Olney, 1996

In presenting this thesis in partial fulfilment of the requirements for an advanced degree at the University of British Columbia, I agree that the Library shall make it freely available for reference and study. I further agree that permission for extensive copying of this thesis for scholarly purposes may be granted by the head of my department or by his or her representatives. It is understood that copying or publication of this thesis for financial gain shall not be allowed without my written permission.

Department of Chemistry

The University of British Columbia  
Vancouver, Canada

Date Sept 27/96

## Abstract

Dipole (e,e) spectroscopy has been used to determine absolute photoabsorption oscillator strengths (cross-sections) for the discrete and continuum electronic transitions of  $\text{CH}_3\text{F}$ ,  $\text{CH}_3\text{Cl}$ ,  $\text{CH}_3\text{Br}$ ,  $\text{CH}_3\text{I}$ , and  $\text{BrCN}$ . These data have been obtained at low resolution (1 eV fwhm), spanning the visible to soft X-ray equivalent photon energy regions (4.5 to 450 eV), and at high resolution (0.05 to 0.15 eV fwhm), in the valence and inner shell (Br 3d; I 4d; C 1s (BrCN); N 1s) regions. The absolute photoabsorption oscillator strength scales were established using either the Thomas-Reiche-Kuhn sum-rule ( $S(0)$ ) or an  $S(-2)$ -based sum-rule normalization technique.

To confirm the global accuracy of the dipole (e,e) photoabsorption oscillator strength data, an assessment of the absolute scales of previously published dipole (e,e) photoabsorption spectra 51 atoms and small molecules is made by deriving static dipole polarizabilities using the  $S(-2)$  sum-rule. Alternative methods of absolute scale determination for photoabsorption spectra using  $S(-2)$ -based normalization with dipole polarizabilities are also considered. Various dipole oscillator strength sums  $S(u)$  ( $u=-1$  to  $-10$ ) and  $L(u)$  ( $u=-1$  to  $-6$ ) are evaluated using the previously published, and presently reported, dipole (e,e) measurements. It is also shown that normal Verdet constants and values of the rotationally averaged  $C_6(A, B)$  dispersion coefficients can be reliably obtained either directly from the measured oscillator strength spectra or from approximations which require only values of the dipole sums  $S(u)$  and  $L(u)$  reported here.

Quantitative aspects of the molecular and dissociative photoionization are reported in the valence shells of  $\text{CH}_3\text{F}$  and  $\text{CH}_3\text{Cl}$ , and the valence shells and low energy inner shells (Br 3d and I 4d) of  $\text{CH}_3\text{Br}$ ,  $\text{CH}_3\text{I}$  and  $\text{BrCN}$ , have been studied using dipole (e,e+ion) spectroscopy. Time-of-flight mass spectroscopy was used to determine the absolute partial oscillator str-

engths for the molecular and dissociative photoionization channels of the methyl halides and BrCN. In other work synchrotron radiation photoelectron spectroscopy measurements made by Dr. Cooper, Dr. Chan and Dr. Tan were used to determine the absolute partial photoionization oscillator strengths for the production of the electronic states of  $\text{CH}_3\text{F}^+$ ,  $\text{CH}_3\text{Cl}^+$  and  $\text{CH}_3\text{Br}^+$ . These measurements together were used to provide detailed quantitative information on the dipole-induced breakdown pathways of the methyl halides and BrCN under the influence of VUV and soft X-ray radiation.

# Table of Contents

Abstract	ii
List of Tables	vii
List of Figures	ix
Abbreviations	xii
Acknowledgements	xiv
<b>1 Introduction</b>	<b>1</b>
<b>2 Theoretical Background</b>	<b>11</b>
2.1 Photoabsorption and Photoionization Processes . . . . .	12
2.2 Photoabsorption Oscillator Strengths by Electron Impact . . . . .	16
2.3 Beer-Lambert Law Photoabsorption . . . . .	19
2.4 Photoionization Cross-sections <i>via</i> Photoelectron Spectroscopy . . . . .	20
2.5 Spectral Analysis . . . . .	23
2.5.1 Discrete photoabsorption spectrum . . . . .	26
2.5.2 Continuum photoabsorption spectrum . . . . .	30
2.5.3 Photoionization <i>via</i> Auger and autoionization processes . . . . .	32
2.5.4 Photoelectron spectrum . . . . .	33
2.6 Sum-rule Moments and the Photoabsorption Spectrum . . . . .	39
<b>3 Experimental Methods</b>	<b>40</b>
3.1 Low Resolution Dipole (e,e+ion) Spectrometer . . . . .	40
3.2 Absolute Oscillator Strengths <i>via</i> Dipole Sum-rules . . . . .	45
3.3 High Resolution Dipole (e,e) Spectrometer . . . . .	49
3.4 Photoelectron Spectrometer . . . . .	52
3.5 PIPICO Spectrometer . . . . .	55
3.6 Sample Handling . . . . .	56
<b>4 Dipole Sum-Rules</b>	<b>58</b>
4.1 Introduction . . . . .	58
4.2 Experimental Background . . . . .	62
4.3 Results and Discussion . . . . .	63
4.3.1 Static dipole polarizabilities, the S(-2) sum-rule and the evaluation of VTRK sum-rule normalization . . . . .	63
4.3.2 Normalization of photoabsorption spectra using the S(-2) sum-rule and dipole polarizabilities . . . . .	74

4.3.3	Dipole sum-rules and molecular properties . . . . .	79
4.3.4	Verdet constants . . . . .	95
4.3.5	$C_6$ interaction coefficients . . . . .	96
<b>5</b>	<b>Absolute Photoabsorption Studies of the Methyl Halides</b>	<b>107</b>
5.1	Introduction . . . . .	107
5.2	Electronic Structure of the Methyl Halides . . . . .	111
5.3	Methyl Fluoride Results and Discussion . . . . .	114
5.3.1	Low resolution photoabsorption (7 to 250 eV) . . . . .	114
5.3.2	High resolution photoabsorption (7.5 to 50 eV) . . . . .	119
5.4	Methyl Chloride Results and Discussion . . . . .	122
5.4.1	Low resolution photoabsorption (6 to 350 eV) . . . . .	122
5.4.2	High resolution photoabsorption (5 to 50 eV) . . . . .	127
5.5	Methyl Bromide Results and Discussion . . . . .	130
5.5.1	Low resolution photoabsorption (6 to 350 eV) . . . . .	130
5.5.2	High resolution valence shell photoabsorption (5 to 26 eV) . . . . .	136
5.5.3	High resolution Br 3d photoabsorption . . . . .	139
5.6	Methyl Iodide Results and Discussion . . . . .	142
5.6.1	Low resolution photoabsorption (4.5 to 350 eV) . . . . .	142
5.6.2	High resolution valence shell photoabsorption (4 to 26 eV) . . . . .	149
5.6.3	High resolution I 4d photoabsorption . . . . .	153
5.7	Dipole Sum-rules of the Methyl Halides . . . . .	156
<b>6</b>	<b>Photoionization Studies of the Methyl Halides</b>	<b>158</b>
6.1	Introduction . . . . .	158
6.2	Methyl Fluoride Results and Discussion . . . . .	160
6.2.1	Binding energy spectrum . . . . .	160
6.2.2	Molecular and dissociative photoionization . . . . .	164
6.2.3	Dipole-induced breakdown . . . . .	176
6.2.4	Photoelectron spectroscopy . . . . .	183
6.3	Methyl Chloride Results and Discussion . . . . .	189
6.3.1	Binding energy spectrum . . . . .	189
6.3.2	Molecular and dissociative photoionization . . . . .	192
6.3.3	Dipole-induced breakdown . . . . .	204
6.3.4	Photoelectron spectroscopy . . . . .	210
6.4	Methyl Bromide Results and Discussion . . . . .	213
6.4.1	Binding energy spectrum . . . . .	213
6.4.2	Molecular and dissociative photoionization . . . . .	216
6.4.3	Dipole-induced breakdown . . . . .	229
6.4.4	Photoelectron spectroscopy . . . . .	237
6.5	Methyl Iodide Results and Discussion . . . . .	239
6.5.1	Binding energy spectrum . . . . .	239
6.5.2	Molecular and dissociative photoionization . . . . .	242
6.5.3	Dipole-induced breakdown . . . . .	254

<b>7</b>	<b>Photoabsorption and Photoionization of Cyanogen Bromide</b>	<b>263</b>
7.1	Introduction . . . . .	263
7.2	Electronic Structure . . . . .	266
7.3	Results and Discussion . . . . .	267
7.3.1	Low resolution photoabsorption (5 to 451 eV) . . . . .	267
7.3.2	High resolution valence shell photoabsorption (4 to 50 eV) . . . . .	274
7.3.3	Low and high resolution inner shell photoabsorption . . . . .	278
7.3.3.1	C 1s and N 1s spectra . . . . .	278
7.3.3.2	Br 3d spectrum . . . . .	286
7.3.4	Dipole sum-rules of cyanogen bromide . . . . .	293
7.3.5	Molecular and dissociative photoionization . . . . .	294
7.3.6	PIPICO spectra and the decomposition of multiply charged ions. . .	305
7.3.7	Dipole-induced breakdown . . . . .	314
<b>8</b>	<b>Concluding Remarks</b>	<b>316</b>
	<b>Bibliography</b>	<b>318</b>

## List of Tables

3.1	Sample purity . . . . .	57
4.1	Static dipole polarizability values derived from dipole (e,e) absolute photoabsorption spectra, compared with experiment and theory . . . . .	70
4.2	Static dipole polarizability values used to determined absolute oscillator strength scales by $S(-2)$ -based normalization . . . . .	80
4.3	Dipole sums $S(u)$ obtained from dipole (e,e) absolute photoabsorption spectra compared to sums from other sources . . . . .	87
4.4	Logarithmic dipole sums $L(u)$ obtained from dipole (e,e) absolute photoabsorption spectra compared to sums from other sources . . . . .	91
4.5	$C_6(A, B)$ coefficients derived from dipole (e,e) spectroscopy compared with values from theory and experiment . . . . .	100
4.6	$C_6(A, B)$ coefficients derived from dipole (e,e) oscillator strength spectra . . . . .	105
5.1	Valence shell ionization potentials of the methyl halides . . . . .	112
5.2	Absolute photoabsorption differential oscillator strengths of methyl fluoride . . . . .	117
5.3	Absolute photoabsorption differential oscillator strengths of methyl chloride . . . . .	125
5.4	Absolute oscillator strengths for selected valence shell regions of the photoabsorption spectrum of methyl chloride . . . . .	130
5.5	Absolute photoabsorption differential oscillator strengths of methyl bromide . . . . .	134
5.6	Absolute oscillator strengths for selected regions of the valence shell photoabsorption spectrum of methyl bromide . . . . .	139
5.7	Energies, term values, oscillator strengths, and assignment of the Br 3d spectrum of methyl bromide . . . . .	142
5.8	Absolute photoabsorption differential oscillator strengths of methyl iodide . . . . .	147
5.9	Absolute oscillator strengths for selected regions of the valence shell photoabsorption spectrum of methyl iodide . . . . .	152
5.10	Energies, term values, oscillator strengths, and assignment of the I 4d spectrum of methyl iodide . . . . .	155
5.11	Dipole sums $S(u)$ and logarithmic dipole sums $L(u)$ obtained from the absolute photoabsorption spectra of the methyl halides . . . . .	157
6.1	Absolute partial differential oscillator strengths for the molecular and dissociative photoionization of methyl fluoride . . . . .	170
6.2	Calculated and measured appearance potentials for the production of positive ions from methyl fluoride . . . . .	174
6.3	Absolute partial differential oscillator strengths for production of electronic ion states of methyl fluoride . . . . .	182
6.4	Absolute partial differential oscillator strengths for the molecular and dissociative photoionization of methyl chloride . . . . .	198

6.5	Calculated and measured appearance potentials for the production of positive ions from methyl chloride . . . . .	202
6.6	Absolute partial differential oscillator strengths for production of electronic ion states of methyl chloride . . . . .	209
6.7	Absolute partial differential oscillator strengths for the molecular and dissociative photoionization of methyl bromide . . . . .	223
6.8	Calculated and measured appearance potentials for the production of positive ions from methyl bromide . . . . .	227
6.9	Absolute partial differential oscillator strengths for production of electronic ion states of methyl bromide . . . . .	236
6.10	Absolute differential oscillator strengths for the molecular and dissociative photoionization of methyl iodide . . . . .	249
6.11	Calculated and measured appearance potentials for the production of positive ions from methyl iodide . . . . .	252
6.12	Absolute electronic ion state partial photoionization differential oscillator strengths for methyl iodide . . . . .	261
6.13	Single and double photoionization branching ratios and partial differential oscillator strengths for methyl iodide at 41 eV . . . . .	262
7.1	Absolute photoabsorption differential oscillator strengths of cyanogen bromide	271
7.2	Absolute oscillator strengths for selected regions of the valence shell photoabsorption spectrum of cyanogen bromide . . . . .	277
7.3	Energies, term values, oscillator strengths, and assignments of the C 1s and N 1s spectra of cyanogen bromide . . . . .	284
7.4	Energies, term values, oscillator strengths, and assignment of the Br 3d spectrum of cyanogen bromide . . . . .	291
7.5	Dipole sums $S(u)$ and logarithmic dipole sums $L(u)$ obtained from the absolute photoabsorption spectrum of cyanogen bromide . . . . .	293
7.6	Absolute partial differential oscillator strengths for the molecular and dissociative photoionization of cyanogen bromide . . . . .	301
7.7	Calculated and measured appearance potentials for the production of positive ions from cyanogen bromide . . . . .	304
7.8	PIPICO branching ratios for double and triple dissociative photoionization of cyanogen bromide . . . . .	312

## List of Figures

2.1	Molecular orbital scheme and various transition processes . . . . .	25
3.1	Low resolution dipole (e,e+ion) spectrometer. . . . .	41
3.2	High resolution dipole (e,e) spectrometer. . . . .	49
3.3	Photoelectron spectrometer electron analyser transmission calibration curve. . . . .	54
4.1	Absolute photoabsorption (df/dE) and the S(-2) (df/dE)/E <sup>2</sup> spectra of water . . . . .	65
4.2	Absolute photoabsorption (df/dE) and the S(-2) (df/dE)/E <sup>2</sup> spectra of silane . . . . .	67
4.3	Absolute photoabsorption (df/dE) and the S(-2) (df/dE)/E <sup>2</sup> spectra of molecular chlorine . . . . .	76
4.4	Absolute photoabsorption (df/dE) and S(-2) (df/dE)/E <sup>2</sup> spectra of silicon tetrafluoride . . . . .	78
4.5	The energy weighted absolute photoabsorption spectra (df/dE)/E <sup>u</sup> of molecular iodine for u=0, -1, -2, -4 and -6 . . . . .	83
5.1	Absolute photoabsorption spectrum (6–251 eV) of methyl fluoride . . . . .	115
5.2	Absolute valence shell photoabsorption spectrum (7 to 51 eV) of methyl fluoride . . . . .	120
5.3	Absolute photoabsorption spectrum (6–350 eV) of methyl chloride . . . . .	124
5.4	Absolute valence shell photoabsorption spectrum (6–25 eV) of methyl chloride . . . . .	128
5.5	Absolute photoabsorption spectrum (5–352 eV) of methyl bromide . . . . .	131
5.6	Absolute valence shell photoabsorption spectrum (5–26 eV) of methyl bromide . . . . .	136
5.7	Expanded view of the valence shell photoabsorption spectrum (5–12.5 eV) of methyl bromide . . . . .	138
5.8	Photoabsorption spectrum of methyl bromide in the Br 3d region . . . . .	140
5.9	Absolute photoabsorption spectrum (4–352 eV) of methyl iodide . . . . .	143
5.10	Absolute valence shell photoabsorption spectrum (4–26 eV) of methyl iodide . . . . .	149
5.11	Expanded view of the absolute photoabsorption spectrum (4–11.5 eV) of methyl iodide . . . . .	151
5.12	Photoabsorption spectrum of methyl iodide in the I 4d region . . . . .	153
6.1	Photoelectron spectrum of methyl fluoride at 72 eV . . . . .	162
6.2	TOF mass spectrum and photoionization efficiency curve of methyl fluoride . . . . .	165
6.3	Branching ratios for the molecular and dissociative photoionization of methyl fluoride . . . . .	166
6.4	Absolute partial photoionization oscillator strengths for the molecular and dissociative photoionization of methyl fluoride . . . . .	168
6.5	Absolute partial photoionization oscillator strengths for production of electronic ion states of methyl fluoride . . . . .	180
6.6	Proposed dipole-induced breakdown scheme of methyl fluoride . . . . .	181
6.7	Photoelectron spectra of methyl fluoride at 44, 50, 56, and 72 eV . . . . .	185

6.8	Photoelectron spectrum of methyl chloride at 72 eV . . . . .	190
6.9	TOF mass spectrum and photoionization efficiency curve of methyl chloride .	193
6.10	Branching ratios for the molecular and dissociative photoionization of methyl chloride . . . . .	194
6.11	Absolute partial photoionization oscillator strengths for the molecular and dissociative photoionization of methyl chloride . . . . .	196
6.12	Absolute partial photoionization oscillator strengths for production of electronic states of $\text{CH}_3\text{Cl}^+$ . . . . .	207
6.13	Proposed dipole-induced breakdown scheme for the ionic photofragmentation of methyl chloride . . . . .	208
6.14	Photoelectron spectrum of methyl bromide at 70 eV . . . . .	214
6.15	TOF mass spectrum and photoionization efficiency curve of methyl bromide	217
6.16	Branching ratios for the molecular and dissociative photoionization of methyl bromide . . . . .	218
6.17	Absolute partial photoionization oscillator strengths for the molecular and dissociative photoionization of methyl bromide . . . . .	221
6.18	Absolute partial photoionization oscillator strengths for production of electronic ion states of methyl bromide . . . . .	233
6.19	Proposed dipole-induced breakdown scheme of methyl bromide . . . . .	235
6.20	The HeII photoelectron spectrum of methyl iodide . . . . .	241
6.21	TOF mass spectrum and photoionization efficiency curve of methyl iodide . .	243
6.22	Branching ratios for the molecular and dissociative photoionization of methyl iodide . . . . .	245
6.23	Absolute partial photoionization oscillator strengths for the molecular and dissociative photoionization of methyl iodide . . . . .	247
6.24	Absolute partial photoionization oscillator strengths for production of electronic ion states of methyl iodide . . . . .	257
6.25	Proposed dipole-induced breakdown scheme of methyl iodide . . . . .	258
7.1	Absolute photoabsorption spectrum (5–451 eV) of cyanogen bromide . . . . .	268
7.2	Absolute valence shell photoabsorption spectrum (4–41 eV) of cyanogen bromide	275
7.3	Expanded view of the valence shell photoabsorption spectrum (7.5–17 eV) of cyanogen bromide . . . . .	276
7.4	Absolute valence shell subtracted photoabsorption spectrum (65–451 eV) of cyanogen bromide . . . . .	279
7.5	Absolute C 1s and N 1s photoabsorption spectra (low resolution) of cyanogen bromide . . . . .	280
7.6	Absolute C 1s and N 1s photoabsorption spectra (high resolution) of cyanogen bromide . . . . .	282
7.7	Absolute Br 3d photoabsorption spectrum of cyanogen bromide . . . . .	287
7.8	TOF mass spectrum and photoionization efficiency curve of cyanogen bromide	295
7.9	Branching ratios for the molecular and dissociative photoionization of cyanogen bromide . . . . .	296
7.10	Absolute partial photoionization oscillator strengths for the molecular and dissociative photoionization of cyanogen bromide . . . . .	299

7.11	PIPICO spectra for double and triple dissociative photoionization of cyanogen bromide . . . . .	306
7.12	PIPICO branching ratios for dissociative double photoionization of cyanogen bromide . . . . .	308
7.13	PIPICO branching ratios for dissociative triple photoionization of cyanogen bromide . . . . .	310
7.14	Proposed dipole induced breakdown pathways of cyanogen bromide . . . . .	315

## Abbreviations

**AP** appearance potential

**BE** binding energy

**CI** configuration interaction

**DOSD** dipole oscillator strength distribution

**DPI** double photoionization

**E** energy loss or equivalent photon energy

**EELS** electron energy-loss spectroscopy

**Emp** Empirical methods

**EMS** electron momentum spectroscopy

**ESCA** electron spectroscopy for chemical analysis

**FWHM** full width at half maximum

**GOS** generalized oscillator strength

**HR** high resolution

**IP** ionization potential

**ISEELS** inner-shell electron energy-loss spectroscopy

**LR** low resolution

**LUMO** lowest unoccupied molecular orbital

**MO** molecular orbital

**OVGF** outer valence Green's function

**PE** photoelectron

**PEPICO** photoelectron-photoion coincidence

**PEPIPICO** photoelectron-photoion-photoion coincidence

**PES** photoelectron spectroscopy

**PIMS** photoionization mass spectroscopy

**PIPICO** photoion-photoion coincidence

**POS** partial differential oscillator strength

**SCF** self-consistent field

**T** term value

**TAC** time-to-amplitude converter

**TOF** time-of-flight

**TOFMS** time-of-flight mass spectroscopy

**TRK** Thomas-Reiche-Kuhn

**UV** ultraviolet

**VIP** vertical ionization potential

**VTRK** valence shell Thomas-Reiche-Kuhn

**VUV** vacuum ultraviolet

**XPS** X-ray photoelectron spectroscopy

## Acknowledgements

I would sincerely like to thank my supervisor, Dr. C. E. Brion, for his support, expertise, and encouragement throughout the entire course of my graduate studies. I am greatly indebted to Dr. G. Cooper, Dr. W. F. Chan and Dr. G. R. Burton who taught me the art and science of dipole (e,e) spectroscopy. I would like to thank Dr. N. Cann for her guidance through various calculations that were undertaken in this work, for discussions and contributions regarding the dipole sum-rule work and for proof-reading portions of this thesis. I would also like to acknowledge others from whom I have learned a great deal through many enlightening discussions: Dr. B. Hollebhone, Dr. T. Ibuki, Dr. N. Lermer, J. Neville, and Dr. B. Todd. I would like to add a special thanks to Dr. G. Cooper for his invaluable comments and suggestions while proof-reading this thesis.

The photoelectron spectra of  $\text{CH}_3\text{F}$ ,  $\text{CH}_3\text{Cl}$  and  $\text{CH}_3\text{Br}$  were recorded by Dr. G. Cooper, Dr. W. F. Chan and Dr. K. H. Tan. The PIPICO data of  $\text{BrCN}$  were supplied by Dr. T. Ibuki and Dr. A. Hiraya.

I would also like to thank the staff of the electronics and mechanical engineering shops at UBC for their assistance in maintaining the spectrometers, in particular Mr. B. Greene and Mr. E. Gomm.

Funding for this research was provided by the Natural Sciences and Engineering Research Council (NSERC) of Canada and by the Canadian National Networks of Centres of Excellence (Centres of Excellence in Molecular and Interfacial Dynamics).

Finally, I wish to thank my parents, Harry and Doreen Olney, and my wife, Gigi, for their continual support, infinite patience and unlimited encouragement. This thesis is dedicated to them and Thumper.

# Chapter 1

## Introduction

Many properties that are of importance to experimental and theoretical aspects of physics, chemistry, astronomy, biology and environmental sciences [1] can be obtained from the wide range absolute photoabsorption spectrum of a molecule. Transition energies and absolute oscillator strengths (cross-sections) obtained from absolute photoabsorption spectra are required to both qualitatively and quantitatively identify molecules that are present in an astrophysical environment [2–5] or in the terrestrial atmosphere [3, 5–7]. Absolute oscillator strengths are also used in other fields such as laser development, radiation protection, lithography, radiation biology, dosimetry and health physics [1]. In addition, many molecular properties can be obtained from a long range absolute photoabsorption spectrum using dipole sum-rules. These molecular properties, such as dipole polarizability, refractive index, normal Verdet constant and  $C_6$  long-range dispersion coefficient, are used in physics and chemistry because they describe molecular response to a field, effects on circularly polarized light and the long range interaction of molecules.

In general, oscillator strength spectra (i.e. photoabsorption spectra) are not available from direct optical photoabsorption experiments over a wide enough energy range to evaluate dipole sum-rules because the spectral region required must extend from the first electronic excitation threshold (visible or UV region) to high energies, into the VUV/soft X-ray region and beyond. In contrast, accurate wide range absolute photoabsorption spectra can readily be obtained using dipole (e,e) spectroscopy. This method has been shown to produce very

reliable absolute photoabsorption oscillator strengths [1, 8, 9] and molecular properties [10–12].

The ongoing problem of the detrimental effects of atmospheric pollutants, specifically the freons and other halogenated compounds, on the ozone layer and the upper atmosphere, has received much attention [13–18]. The most abundant halohydrocarbon species in the upper atmosphere is methyl chloride [13, 14, 19]. A large amount, estimated to be  $1 \times 10^6$  tonnes of  $\text{CH}_3\text{Cl}$ , is emitted annually into the atmosphere, mainly from biological synthesis [13, 19]. The other methyl halides are also released into the atmosphere in large quantities both by natural and man-made sources [16–18, 20–26]. In order to provide insight into the interaction of energetic UV, VUV and soft X-ray radiation with halogen-containing species, studies of the absolute photoabsorption and photoionization of the methyl halides and BrCN are presented in this thesis.

The photoabsorption spectra of the methyl halides and cyanogen bromide have been measured using dipole (e,e) spectroscopy over a wide range of equivalent photon energies in order to provide accurate oscillator strength and dipole sum-rule values. Furthermore, where possible, interpretation and assignment of both valence and inner shell features in these spectra have been made. Both qualitative and quantitative information about the molecular and dissociative photoionization pathways for the methyl halides and BrCN have been obtained using dipole (e,e+ion) spectroscopy. In addition, binding energy spectra, recorded by Dr. G. Cooper, Dr. W. F. Chan and Dr. K. H. Tan using photoelectron spectroscopy (PES) over a wide range of photon energies with synchrotron radiation, have been used to determine the absolute partial oscillator strengths for the production of the electronic states of  $\text{CH}_3\text{F}^+$ ,  $\text{CH}_3\text{Cl}^+$  and  $\text{CH}_3\text{Br}^+$ . Finally, using the available photoionization data, along with photoion-photoion coincidence (PIPICO) data for BrCN provided by Dr. T. Ibuki and Dr. A. Hiraya, the major ionic dipole-induced breakdown pathways are predicted for each of the

molecules.

Until comparatively recently most of the molecular photoabsorption data available in the literature have emphasized the determination of accurate transition energies for discrete bands rather than the measurements of absolute photoabsorption cross-sections. The number of absolute cross-section (oscillator strength) measurements reported using conventional (optical) methods has been small because of limitations in the spectral range and intensity of light sources and in the efficient monochromation of short wavelength radiation. There are several inherent difficulties associated with making absolute measurements by optical methods. First, absolute photoabsorption measurements using optical methods required accurate particle or number density (i.e. pressure) measurements. Second, errors from line-saturation (bandwidth-linewidth interaction) effects can often occur in absolute cross-section measurements obtained for discrete transitions using the Beer-Lambert law. This is because the profile of a measured photoabsorption band, a convolution of the instrumental bandwidth (resolution) with the natural linewidth of the discrete transition, can be seriously distorted by the logarithmic transformation of the  $I/I_0$  ratio required by the Beer-Lambert law method. These errors, which occur when the natural linewidth is of comparable magnitude to, or smaller than, the instrumental bandwidth, can result in serious underestimation of the cross-section, particularly for transitions with higher cross-sections and narrower natural linewidths [6, 27, 28]. Chan *et al.* [28-30] have illustrated this fact for some of the oscillator strengths of transitions in the VUV electronic spectra of  $H_2$  [29], CO [30] and  $N_2$  [28], which were underestimated by optical cross-section measurements when compared with theoretical calculations and dipole (e,e) spectroscopy measurements. Errors from line-saturation effects cannot occur in dipole (e,e) measurements because no logarithmic transformation is involved.

Many practical applications, including the determination of molecular properties from absolute dipole oscillator strengths, require very wide range photoabsorption spectra extending from the electronic excitation threshold up to a few hundred electron volts (eV). However, restrictions were encountered in earlier photoabsorption studies because of an upper limit of  $\sim 21$  eV in the photon energy range of gas discharge continuum light sources [31]. Furthermore, the LiF cut-off prevents measurements from being made above 11.9 eV (below 124 nm) unless a windowless vacuum spectrometer is used [31]. This situation confined photoabsorption studies to the valence shell discrete region. In the past 10 to 20 years wider energy range measurements have become possible with the increasing availability of synchrotron radiation facilities that provide a continuous photon energy source from the infra-red to the X-ray region. However, despite the much larger range of photon energies available, this approach is still subject to limitations imposed by the individual synchrotron designs and by the low and high energy cut-offs of the monochromators, windows and filters. Furthermore, photoabsorption spectra recorded in the discrete region using synchrotron radiation are still subject to the errors associated with the Beer-Lambert method, as mentioned above.

Serious problems can also occur in the VUV and soft X-ray regions because of the presence of higher order radiation transmitted by the monochromator. Specifically, distortion of the measured cross-section will occur from any contamination by higher order radiation. Higher order radiation will always be present because of the continuum nature of the photon beam available from a synchrotron radiation source and the resulting need for monochromatization. While selecting the desired wavelength, the monochromator also transmits wavelengths of higher order (energy) because of the Bragg diffraction condition, which results in a multi-energy photon beam. Accurate assessment of the contributions from higher orders is difficult and their presence varies with time and the surface condition of the grating. Another problem is stray light, which is always present when using synchrotron radiation and must be corrected for in absolute photoabsorption measurements. As a result of these considerations

most synchrotron radiation work has focused on photoelectron and Auger spectroscopy or solid state photoemission rather than absolute photoabsorption measurements. Nevertheless, there are some synchrotron radiation absolute photoabsorption measurements in the literature. In general, however, these spectra do not cover a very wide energy range because of the limitations imposed by the apparatus used. These limitations have typically restricted the photon energy ranges of absolute photoabsorption spectra to either the discrete valence shell and near edge continuum ( $\leq 30$  eV) or to various inner shell regions.

In contrast to conventional optical spectroscopy, the method of dipole *electron* scattering [1, 8, 9, 27, 32] offers a relatively inexpensive and versatile technique for recording absolute photoabsorption spectra of free atoms and molecules covering a wide energy range, from the first electronic excitation threshold up to high energy, typically to several hundred eV. Furthermore, the dipole (e,e) method, which is used for a large portion of this thesis and is described below, is not subject to many of the limitations and errors that affect measurements by conventional (optical) photoabsorption spectroscopy.

The dipole electron scattering method combines fast electron impact with electron energy-loss analysis of the forward scattered electrons [1, 8, 9, 27, 32–35]. Under suitable conditions, namely in the limit of zero momentum transfer, such scattering events induce electronic transitions in the target which are governed by dipole (i.e. optical) selection rules, as in conventional optical photoabsorption spectroscopy. The energy transferred from the fast electron to the target (the energy loss) is equivalent to the photon energy in optical spectroscopy. The main advantages of the dipole electron scattering techniques are: 1) a continuous and wide range of ‘photon’ energies is available, typically from  $\sim 2$  eV up to 500 eV energy loss (from 6200 to 25 Å); 2) no accurate pressure measurements (or any absolute particle density determinations) are required to obtain absolute spectra; 3) there is no contamination by higher order radiation or stray light; 4) the measurements are not subject to errors from line saturation effects. In addition a single dipole (e,e) spectrometer covers the entire energy

range whereas in optical photoabsorption studies several different types of monochromators would be required to cover the same range. Several dipole electron scattering techniques have been developed which simulate optical photoabsorption, photoionization, photoelectron and photoionization mass spectroscopies [1, 8, 9]. The main disadvantages of the dipole electron scattering methods are that at present the techniques are limited to gaseous targets and that the effective energy-loss (equivalent photon energy) range is limited to below  $\sim 1000$  eV by the electron scattering cross-section.

The theory of dipole electron scattering and its relationship to optical photoabsorption spectroscopy was developed by Bethe [33] in 1930 and has more recently been reviewed [34, 35] and discussed with respect to experimental considerations by Lassette [36] and by Brion *et al.* [8, 9, 37]. Using the Born approximation, Bethe [33] showed that, when electrons are scattered off a target under conditions of negligible momentum transfer, these scattering events give rise to electronic transitions in the target that are governed by dipole selection rules. The transition probability is not the same as in optical spectroscopy. However, Bethe showed that the two transition probabilities were related by the so called Bethe-Born factor. The Bethe-Born factor is independent of the electronic structure of the target and depends only on the geometry and kinematics of the scattering event.

Lassette [38–40] pioneered the study of discrete electronic transitions of atoms and molecules using intermediate impact energy electron scattering techniques. Unfortunately, Lassette's method involved the tedious and uncertain procedure of extrapolating a series of measurements made over a range of scattering angles (i.e. momentum transfers) to zero momentum transfer. Van der Wiel *et al.* [41, 42] achieved a major advance in 1970 by developing the dipole (e,e) method. Use of a high impact energy (typically 8 keV) and zero degree scattering angle results in negligible momentum transfer (i.e. optical) conditions. Similarly, coincident detection of mass analysed ions and energy-loss electrons led to development of the dipole (e,e+ion) method [43–45], which simulates photoionization mass spectroscopy

(PIMS). These two techniques, along with dipole (e,2e) spectroscopy, which simulates PES, have since been further developed and applied at UBC [1, 8, 9].

It has been shown [1, 27, 46] that absolute photoabsorption spectra measured using dipole (e,e) spectroscopy are entirely equivalent to results obtained using direct optical methods or highly accurate quantum mechanical calculations in simple cases such as He [27] and H<sub>2</sub> [29] where such theoretical procedures are possible. In the dipole electron scattering techniques the transit of a fast electron induces an electric field in the target that approximates a delta function in the time domain [8, 9, 47]. Fourier transformed into the frequency domain this gives a virtual photon field that, within the Bethe-Born theory, appears to the target as a flat continuum electromagnetic field which induces electronic transitions that are dominated by dipole (optical) selection rules. In so doing an incident electron with a high velocity (kinetic energy) undergoes an inelastic collision with the target, imparting a small quantity of its energy to the target. The energy imparted to the target, which is the energy-loss of the incident electron, excites an electronic transition. This energy-loss, which is equivalent to the photon energy required for the same process in an optical experiment, is continuous and is analogous to a tunable photon source while avoiding the problems associated with the monochromation of photons. Thus, using dipole (e,e) spectroscopy, a long-range photoabsorption spectrum of correct relative shape can be recorded. The absolute scale of these photoabsorption oscillator strength spectra normally have been obtained using the S(0) sum-rule (also known as the Thomas-Reiche-Kuhn (TRK) sum-rule) [8, 9]. This method, which requires a long range relative photoabsorption spectrum covering the energies from the electronic absorption threshold up to high energy, typically 200 eV or higher, removes the need to make the absolute pressure and pathlength measurements that are a major source of error in direct optical experiments. The long range photoabsorption spectra that are required to obtain molecular properties using dipole sum-rules are readily available from dipole (e,e) spectroscopy results.

To study the molecular and dissociative photoionization pathways of a molecule, dipole (e,e+ion) spectroscopy has been shown [1] to provide a very effective quantitative simulation of photoionization mass spectroscopy (PIMS). In PIMS, where mass spectra are recorded at regular photon energy intervals over a specific energy range, information is obtained about the variation of molecular and dissociative photoionization products (i.e. the ionic photofragmentation) as a function of the ionizing photon energy. The dipole (e,e+ion) experiment [9, 43, 44, 48, 49] involves coincident detection of forward scattered electrons of a given energy-loss (photon energy) with the time-of-flight (TOF) mass analysed ions formed from those scattering events. It is important to note that the dipole (e,e+ion) apparatus used in the present work [9, 43, 44, 48, 49] collects all fragment ions with equal efficiency for ions with up to 20 eV kinetic energy of fragmentation. This is essential for quantitative work involving dissociative photoionization. The dipole (e,e+ion) technique has been used successfully to determine the products of molecular and dissociative photoionization for many molecules [1, 50, 51] from the first ionization potential up to  $\sim 80$  eV or higher in the valence shell. Dipole (e,e+ion) spectroscopy has also been used to obtain photoionization mass spectra and absolute oscillator strengths for ionic photofragmentation in selected inner shell regions. A recent example of such inner shell work is in the Cl 2p (200 eV) region of  $\text{CCl}_4$  [51].

The high resolution available in PES using line sources and synchrotron radiation has permitted the determination of ionization potentials (IPs) in both the valence and inner shells of many free atoms and molecules [52–55]. However, relatively few measurements of the absolute partial photoionization cross-sections (oscillator strengths) for production of the electronic states of molecular ions as a function of photon energy have been made [1], because of the difficulties associated with quantitative PES measurements and because the absolute total photoabsorption cross-section is also required in most cases. Tunable energy quantitative PES has been effectively simulated using the electron scattering technique of

dipole (e,2e) spectroscopy, and partial oscillator strength measurements have been reported for a number of diatomic and small polyatomic molecules [1]. In dipole (e,2e) spectroscopy coincident detection of the forward scattered electrons with “photoelectrons” ejected at the magic angle ( $54.7^\circ$ ) produces a “photoelectron spectrum” at a photon energy equivalent to the energy-loss of the forward scattered electrons. This technique can be used to obtain photoelectron (PE) spectra at varying photon energies just as if one were using a continuously tunable photon source. While the dipole (e,2e) method has been applied to several systems [1, 8, 37, 56–60], wider application has been restricted by its limited energy resolution (1.3 eV fwhm) and the low (e,2e) cross-sections involved. Meanwhile, tunable energy PES using synchrotron radiation has been developed into a method that can measure moderately high resolution PE spectra. However, accurate quantitative electronic ion state branching ratios can be obtained only if the photoelectron spectra are corrected for electron analyser transmission efficiency as a function of electron kinetic energy [1]. The absolute partial photoionization cross-sections for production of electronic ion states can be determined from the product of the quantitative PES branching ratios, the absolute photoabsorption oscillator strengths and the photoionization efficiencies for the molecule. Such procedures have been adopted in the present work by combining synchrotron radiation PES measurements with dipole (e,e) photoabsorption data for the methyl halides ( $\text{CH}_3\text{X}$ ;  $\text{X} = \text{F}, \text{Cl}, \text{Br}$ ).

The remainder of this thesis has been organized as follows. In chapter 2 the theory behind the use of dipole electron scattering techniques to produce absolute photoabsorption oscillator strengths is presented. Furthermore, a brief discussion of photoabsorption spectra and their common spectral features and interpretation is also given. Finally, the relationship between dipole sum-rules and long-range absolute photoabsorption oscillator strength spectra is demonstrated. The experimental apparatus and procedures used to obtain the ab-

solute photoabsorption and photoionization oscillator strength data reported in this thesis are outlined in chapter 3.

The roles that dipole sum-rules play in considerations of photoabsorption spectra, absolute scale calibration and the determination of molecular properties are discussed in chapter 4. Briefly, several sum-rules, including the TRK sum-rule, can be used to place a relative photoabsorption spectrum onto an absolute scale or, conversely, can be used to ascertain the accuracy of absolute photoabsorption oscillator strength scales. Sum-rules can also be used to determine molecular properties from sufficiently wide range absolute spectra. In chapter 4 static dipole polarizabilities and the  $S(-2)$  dipole sum-rule are used to evaluate the accuracy of a large data bank of previously published absolute photoabsorption oscillator strength spectra (as well as those obtained in the present work) that have been measured using dipole (e,e) spectroscopy and in many cases normalized using the TRK ( $S(0)$ ) sum-rule. An alternative normalization procedure, which uses experimental dipole polarizabilities and the  $S(-2)$  sum-rule, is evaluated for use with the photoabsorption spectra of atoms and molecules where spectral features prevent the application of the TRK sum-rule. Various moments of the dipole sum-rules are evaluated from the previously published and presently measured wide range absolute photoabsorption spectra. The values obtained for the molecular properties in the present work from photoabsorption spectra via the dipole sum-rules are more accurate than the relatively few values available from other sources. In many cases the present photoabsorption sum-rule data are the only such information available. The molecular properties resulting from these sums are presented and discussed in chapter 4.

The presently measured experimental results are given in chapters 5 to 7. For the methyl halides the photoabsorption spectra are presented in chapter 5 and the ionic photofragmentation and photoelectron results are reported in chapter 6. The photoabsorption, photoionization and PIPICO results for BrCN are presented in chapter 7. A brief summary and concluding remarks are given in chapter 8.

## Chapter 2

### Theoretical Background

The UV/VUV photoabsorption spectrum, composed of many individual photoabsorption and photoionization events, can be interpreted in several different ways to yield much information about the target being studied. The photoabsorption differential oscillator strength (cross-section) spectrum can be measured using either optical or dipole electron scattering methods. These techniques are both subject to dipole selection rules. The intensities in the recorded spectra are related by an energy-dependent scaling factor that is defined by the experimental conditions of the dipole electron scattering instrument. The photoionization process can be investigated in terms of molecular and dissociative positive ion formation or in terms of electronic ion states formed by ejection of a photoelectron. These ionization processes give rise to the many local and global features observed in the photoion differential oscillator strength or PE spectra. The local and global features of photoabsorption, photoionization and PE spectra can reveal much information about the electronic structure of the target. Furthermore, the total photoabsorption spectrum, using dipole sum-rules, can be used to calculate many molecular properties that are not commonly associated with photoabsorption spectroscopy.

The electron impact techniques used to obtain absolute differential oscillator strength data all rely on the Bethe theory of electron scattering and are discussed in section 2.2. A brief note on the relationship between the differential oscillator strength and the photoabsorption cross-section is given in section 2.3. A general discussion of photoionization cross-sections and pole strengths is presented in section 2.4. Many of the various features of

the electronic spectrum which are most pertinent to the photoabsorption, photoionization and PE spectra presented in this thesis are described in section 2.5. Section 2.5.4 gives a general description, both experimentally and conceptually, of photoelectron spectroscopy. Finally, section 2.6 gives an overview of the dipole sum-rules and their relationship with the photoabsorption spectra.

## 2.1 Photoabsorption and Photoionization Processes

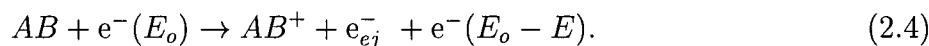
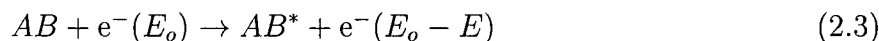
The basic photoabsorption process, where the target  $AB$  absorbs a photon (of energy  $E = h\nu$ ) and is excited into some higher energy electronic state  $AB^*$ , is depicted by



The typical photoionization process, where the absorbed photon excites an electron into some continuum state leaving the target in a ground ion state  $AB^+$ , is depicted as



where  $e_{ej}^-$  is the ejected photoelectron. The equivalent electron impact processes which simulate the optical photoabsorption and photoionization are



In these processes a molecule  $AB$  is either excited or ionized by a scattering event with a fast moving electron having an initial kinetic energy of  $E_o$  and a final kinetic energy of  $E_o - E$ . The energy-loss,  $E$ , of the scattered electron is the energy transferred to the excited target  $AB^*$  or to the ionized target  $AB^+$  plus the ejected electron. The energy analysis of scattered electrons to determine the number of electrons with a particular energy-loss,  $E$ , is analogous to measuring the attenuation of a photon beam with an energy  $E = h\nu$ . The

collision is carried out under conditions of near zero momentum transfer such that the induced excitation or ionization process is governed by dipole selection rules and is equivalent to the photoabsorption process. Several other processes can result from photon absorption, each having an equivalent electron impact process. These have been summarized elsewhere [1]. The photoabsorption process can be studied by a variety of optical techniques (described elsewhere [6, 27, 31, 35]) or by the electron impact technique of dipole (e,e) spectroscopy, which has been used to collect much of the experimental data presented in this thesis.

At a given energy the cross-section (differential oscillator strength) for neutral processes ( $\sigma_n$ ) plus the cross-section for all ionization processes ( $\sigma_t^{ion}$ ) is equal to the total photoabsorption cross-section,

$$\sigma_t^{abs} = \sigma_n + \sigma_t^{ion}. \quad (2.5)$$

The photoionization efficiency,  $\eta_i$ , gives a measure, as a function of energy, of the degree of ionization per photon absorbed and is defined as

$$\eta_i = \frac{\text{number of ionization events/second}}{\text{number of photons absorbed/second}}. \quad (2.6)$$

The total photoabsorption and photoionization cross-sections are related by

$$\sigma_t^{ion} = \eta_i \sigma_t^{abs}, \quad (2.7)$$

where  $\eta_i \leq 1$ . A measurement of the photoionization efficiency is important to determine the photoionization cross-section and, indirectly from equation (2.5), the cross-section for the production of neutral excited state species, at a given photon energy. Dipole (e,e) and (e,e+ion) spectroscopies are the electron impact techniques used to measure the relative photoionization efficiency in this thesis (see section 3.1).

The photoionization cross-section of a molecule,  $\sigma_t^{ion}$ , can be partitioned in two different, but complementary ways. The partial cross-sections for molecular and dissociative photoionization are quantitative measurements of all positive molecular and fragment ions formed

from ionization at a particular energy. Using PIMS, or equivalently dipole (e,e+ion) spectroscopy, mass spectra are recorded as a function of photoionization energy. The peak area for each ion formed in the mass spectrum represents the relative proportion of that ion formed at that photoionization energy. For a given ion  $f$ , the branching ratio,  $Br_f^{ion}$ , is equal to the number of  $f$  ions formed,  $N_f^{ion}$ , divided by the total number of all ions formed,  $N_t^{ion}$ , at that energy

$$Br_f^{ion} = \frac{N_f^{ion}}{N_t^{ion}}. \quad (2.8)$$

The partial cross-section for the formation of ion  $f$  is obtained from the triple product of the branching ratio, the absolute photoabsorption cross-section and the photoionization efficiency

$$\sigma_f^{ion} = Br_f^{ion} \eta_i \sigma_t^{abs}. \quad (2.9)$$

The sum of the molecular and dissociative partial photoionization cross-sections is equal to the total photoionization cross-section.

Alternatively the total photoionization cross-section can be partitioned into electronic state partial cross-sections which are quantitative measurements of the various electronic ion states that result from photoionization at a particular energy. The area of the PE band for each electronic ion state in a spectrum represents the relative number of photoelectrons produced from ionization to that electronic ion state. The branching ratio for a given electronic state,  $Br_s^{PE}$ , is equal to the number of photoelectrons produced for that electronic state,  $N_s^{PE}$ , divided by the total number of photoelectrons produced,  $N_t^{PE}$ , at that energy

$$Br_s^{PE} = N_s^{PE} / N_t^{PE}. \quad (2.10)$$

The cross-section for the formation of that electronic ion state is given by

$$\sigma_s^{ion} = Br_s^{PE} \eta_i \sigma_t^{abs}. \quad (2.11)$$

Similarly, the sum of the electronic state partial cross-sections is equal to the total photoionization cross-section.

The inter-relationship of all of these quantities is illustrated in the following example. Consider a target, AB, being studied at a particular photon energy  $E = h\nu$ . It is found that the total photoabsorption cross-section of AB is  $\sigma_t^{abs}=10$  and that 80 ionization events are produced for every 100 photons absorbed. It is determined from the TOF mass spectrum obtained using PIMS that the ionization products are  $AB^+$ ,  $A^+$  and  $B^+$ , with relative peak areas of 1.0, 0.6 and 0.4, respectively. From PES it is shown that only two ion states are formed,  $\tilde{X}$  and  $\tilde{A}$ , and their relative peak areas in the PE spectrum are 30 and 10, respectively. It can be determined from these data that the photoionization efficiency, using equation (2.6), is  $\eta_i=80/100=0.8$  and the photoionization cross-section is  $\sigma_t^{ion} = 10 \times 0.8 = 8.0$  (equation (2.7)). The branching ratios for molecular and dissociative photoionization, using equation (2.8), are 0.5, 0.3 and 0.2 for  $AB^+$ ,  $A^+$  and  $B^+$ , respectively, and their corresponding partial cross-sections (equation (2.9)) are 4.0, 2.4 and 1.6. The electronic ion state branching ratios (equation (2.10)) are found to be 0.75 and 0.25 for  $\tilde{X}$  and  $\tilde{A}$ , respectively, and their corresponding partial cross-sections (equation (2.11)) are 6.0 and 2.0. Note that the sum of the partial cross-sections, for either all ions formed or all of the electronic states formed, is equal to the total photoionization cross-section.

In the present work branching ratios for molecular and dissociative photoionization are obtained using dipole (e,e+ion) spectroscopy and electronic ion state branching ratios are obtained from PES using synchrotron radiation as the tunable photon source. Each of these sets of branching ratios are combined with absolute differential oscillator strength and photoionization efficiency data, obtained using dipole (e,e) and dipole (e,e+ion) spectroscopies, to produce their respective absolute partial oscillator strengths (POSs).

## 2.2 Photoabsorption Oscillator Strengths by Electron Impact

The description of the scattering of fast charged particles off matter was proposed by Hans Bethe [33] in 1930 using the first Born approximation. The transition probability, defined as the unitless oscillator strength  $f$ , for an *optical* transition from some ground electronic state,  $|0\rangle$ , to an excited electronic state,  $|n\rangle$ , that has an energy of transition  $E_n$ , is given (in atomic units<sup>1</sup>) by

$$f_{on}^o(E) = 2E_n |M_{on}|^2. \quad (2.12)$$

The square of the dipole matrix element,  $|M_{on}|^2$ , for the electronic transition is given by

$$M_{on} = \left\langle n \left| \sum_{j=1}^N \mathbf{r}_j \right| 0 \right\rangle \quad (2.13)$$

where  $\mathbf{r}_j$  is the position operator of the  $j^{\text{th}}$  electron in the  $N$  electron species. For a *scattering* event [33–35] between an incident fast moving electron, with initial energy  $E_o$ , and a target atom or molecule, the scattered electron induces a transition in the target from the ground electronic state,  $|0\rangle$ , to an excited electronic state,  $|n\rangle$ , with an associated energy of transition (energy loss),  $E_n$ , being lost by the scattered electron and transferred to the target. The fast electron has incident and final momenta,  $\mathbf{k}_i$  and  $\mathbf{k}_f$ , and thus the momentum transferred is  $\mathbf{K} = (\mathbf{k}_i - \mathbf{k}_f)$ . The transition probability, described by the generalized oscillator strength (GOS), for this process was shown by Bethe [33] to be

$$f_{on}(\mathbf{K}, E) = \frac{2E_n}{|\mathbf{K}|^2} |\epsilon_{0n}(\mathbf{K})|^2 \quad (2.14)$$

where

$$\epsilon_{0n}(\mathbf{K}) = \left\langle n \left| \sum_{j=1}^N e^{i\mathbf{K}\cdot\mathbf{r}_j} \right| 0 \right\rangle \quad (2.15)$$

---

<sup>1</sup>All equations are given in atomic units unless otherwise noted. Atomic units are used for both convenience and clarity because the relationship between the electron scattering cross-section and the photoabsorption oscillator strength is one of proportionality. The absolute scales of the oscillator strength spectra in the present work are derived *via* dipole sum-rules and not by the equations above. Thus any proportionality constants are unimportant in the present work.

and  $\hat{\mathbf{K}}$  is the unit vector in the direction  $\mathbf{K}$ . The electron scattering differential cross-section for electrons having initial energies  $E_o$ , describes the probability of electrons being scattered into a cone of solid angle  $d\Omega$  with a transfer of energy  $E$  to the target and is given by

$$\frac{d\sigma_e(E)}{d\Omega} = \frac{2}{E} \frac{|\mathbf{k}_f|}{|\mathbf{k}_i|} \frac{f_{on}(\mathbf{K}, E)}{|\mathbf{K}|^2} \quad (2.16)$$

which relates the electron scattering cross-section to the GOS. For transitions between two discrete bound states, the generalized oscillator strength is a dimensionless quantity. For transitions to unbound states in the continuum (ionization) the oscillator strength is given in terms of the differential oscillator strength with respect to energy,  $df(\mathbf{K}, E)/dE$ , then the GOS, equation (2.14), can be written as [35]

$$\frac{df_{on}(\mathbf{K}, E)}{dE} = \sum_n \frac{2E_n}{|\mathbf{K}|^2} |\epsilon_{0n}(\mathbf{K})|^2 \delta(E_n - E) \quad (2.17)$$

and the differential electron scattering cross-section becomes

$$\frac{d^2\sigma_e(E)}{dEd\Omega} = \frac{2}{E} \frac{|\mathbf{k}_f|}{|\mathbf{k}_i|} \frac{1}{|\mathbf{K}|^2} \frac{df_{on}(\mathbf{K}, E)}{dE}. \quad (2.18)$$

As discussed by Inokuti [35], there has been some disagreement as to the representation of the optical cross-section ( $\sigma_t^{abs}$ ) with respect to energy. For consistency with the literature the cross-section will be designated here as  $\sigma$ , not as the more correct [35] differential cross-section,  $d\sigma/dE$ .

The momentum transfer is related to the polar scattering angle,  $\theta$ , through the cosine rule. The various momenta are related by the equations

$$|\mathbf{K}|^2 = |\mathbf{k}_i|^2 + |\mathbf{k}_f|^2 - 2|\mathbf{k}_i||\mathbf{k}_f|\cos\theta, \quad (2.19)$$

from momentum conservation, and

$$|\mathbf{k}_i|^2 - |\mathbf{k}_f|^2 = 2E_n \quad (2.20)$$

$$|\mathbf{k}_i|^2 = 2E_o, \quad (2.21)$$

from energy conservation. The expression given in equation (2.14) can be expanded in terms of a power series in the momentum transfer [33–35],  $|\mathbf{K}|^2$

$$\frac{df_{on}(\mathbf{K}, E)}{dE} = E_n \left[ \epsilon_1^2 + (\epsilon_2^2 - 2\epsilon_1\epsilon_3)\mathbf{K}^2 + (\epsilon_3^2 + 2\epsilon_1\epsilon_5 - 2\epsilon_2\epsilon_4)\mathbf{K}^4 + O(\mathbf{K}^6) + \dots \right] \quad (2.22)$$

$$= \frac{df_{on}^o(E)}{dE} + A\mathbf{K}^2 + B\mathbf{K}^4 + O(\mathbf{K}^6) + \dots \quad (2.23)$$

where  $\epsilon_t$  is the  $t$ -th order multipole matrix element given by

$$\epsilon_t = \frac{1}{t!} \langle n | \sum_{j=1}^N (\mathbf{r}_j)^t | 0 \rangle, \quad (2.24)$$

and  $O(\mathbf{K}^6)$  represents terms of the order  $\mathbf{K}^6$ . The higher order terms in the momentum transfer involve the higher multipole moments (quadrupole, octupole). The first term in equation (2.23) is the dipole term and thus at the limit of zero momentum transfer the GOS approaches the dipole (optical) oscillator strength.

$$\frac{df_{on}^o(E)}{dE} = \left[ \frac{E}{2} \frac{|\mathbf{k}_i|}{|\mathbf{k}_f|} |\mathbf{K}|^2 \right] \frac{d^3\sigma_e(E)}{dE d\Omega}. \quad (2.25)$$

The conditions that are required to obtain the vanishingly small momentum transfer can be seen by combining equations 2.19 to 2.21, to obtain

$$|\mathbf{K}|^2 = 2E_o + (2E_o - 2E_n) - 2\sqrt{2E_o} \cdot \sqrt{2E_o - 2E_n} \cdot \cos\theta \quad (2.26)$$

which becomes

$$|\mathbf{K}|^2 = 2E_o \left( 2 - \frac{E_n}{E_o} - 2\sqrt{1 - \frac{E_n}{E_o}} \cos\theta \right). \quad (2.27)$$

By inspection, to approach the  $\mathbf{K} \rightarrow 0$  limit, the scattering angle  $\theta$  must be close to zero and small energy losses must be used such that  $E_n/E_o \sim 0$ . In practice [35], when integrating over the small acceptance angle,  $\Omega$ , equation (2.25) becomes

$$\frac{df_{on}^o(E)}{dE} = B(E) \frac{d\sigma_e(E)}{dE}. \quad (2.28)$$

The quantity  $B(E)$  is the Bethe-Born factor, which is determined solely by the collision kinematics (i.e. only on the scattering conditions of the individual spectrometer) and is a function of the energy loss,  $E$ . The Bethe-Born factor can be derived for a particular spectrometer from its scattering geometry. For the low resolution dipole (e,e) spectrometer used in the present work the Bethe-Born factor was determined from the experimental scattering geometry [27, 43, 44, 61]. For the high resolution dipole (e,e) spectrometer used in the present work the Bethe-Born factor was determined experimentally by Chan *et al.* [27, 46] by fitting the measured high resolution dipole electron energy-loss spectra for He and Ne to the optical oscillator strength spectra obtained using the low resolution spectrometer.

It is worthwhile noting that the electron scattering cross-section decreases more rapidly with increasing energy than does the optical oscillator strength. The relationship for scattering in the forward direction, for energy losses,  $E$ , which are small compared with the kinetic energy of the incident electron,  $E_o$ , is given by [35]

$$\left. \frac{d^2\sigma}{d\Omega dE} \right|_{\theta=0} = 4E_o E^{-3} \frac{df^o}{dE}. \quad (2.29)$$

The fact that the electron scattering cross-section decreases by a factor of  $E^3$  faster than the optical oscillator strength requires that a good signal-to-noise ratio be maintained throughout the entire energy-loss range of the electron scattering experiment.

### 2.3 Beer-Lambert Law Photoabsorption

The photoabsorption cross-section of a species can be obtained experimentally by measuring the attenuation of a light beam passing through a sample in a gas cell. The attenuation from an initial intensity,  $I_o$ , to a final intensity,  $I$ , will depend on the number density ( $n$ ) of the sample gas, the length ( $l$ ) of the sample cell and the photoabsorption cross-section ( $\sigma_t^{abs}$ ) of the sample. The result is given in terms of the Beer-Lambert law

$$\ln \frac{I_o}{I} = \sigma_t^{abs} n l. \quad (2.30)$$

The cross-section is a function of wavelength (energy) and its magnitude is dependent on the absorbance of the target sample gas giving an indication of the transition strength(s) at that wavelength.

The cross-section is commonly expressed in units of megabarns ( $1 \text{ Mb} = 1 \times 10^{-18} \text{ cm}^2$ ) and is related to the differential oscillator strength by

$$\sigma_t^{abs} = \frac{e^2 \pi h}{mc} \frac{df}{dE}, \quad (2.31)$$

where the terms of differential oscillator strength and cross-section are equivalent within a constant factor given by

$$\sigma_t^{abs} (\text{Mb}) = 109.75 \frac{df}{dE} (\text{eV}^{-1}), \quad (2.32)$$

which explicitly shows the relationship for the units used in the present work. Experimental determination of absolute cross-sections using the Beer-Lambert Law, equation (2.30), requires an accurate measurement of four quantities: two photon intensities, the particle density and the pathlength. For reasons outlined in chapter 1 and elsewhere [6, 27, 31, 35], the accurate measurement of an absolute optical cross-section is difficult and thus much of the absolute oscillator strength data available today have been recorded using dipole (e,e) spectroscopy [1, 27, 46].

## 2.4 Photoionization Cross-sections *via* Photoelectron Spectroscopy

Photoelectron spectroscopy uses a mono-energetic photon beam ( $E = h\nu$ ) to ionize a target. The PE spectrum is produced by analysing the kinetic energy distribution of the photoelectrons ejected from the target. The peaks in the photoelectron kinetic energy spectrum correspond to photoelectrons having kinetic energy  $\epsilon_k$ . In an independent particle model, Koopmans' theorem [62] states that the ionization energy  $I_k$ , which is the difference between the exciting photon energy and the kinetic energy of the ejected electron

$$I_k = h\nu - \epsilon_k, \quad (2.33)$$

is equal to the negative orbital energy from which the electron was ejected. Photoelectron spectra are most often published using an energy scale giving the ionization energy  $I_k$ , which is more commonly referred to as the IP or the binding energy (BE), rather than the electron kinetic energy.

The cross-section,  $\sigma_{0N}$ , for the photoionization of a system from an initial state  $|0\rangle$ , by a photon beam of energy  $E$ , leaving the system in a multitude of final ion states  $|n\rangle$ , each consisting of a photoelectron of energy,  $\epsilon_n$  (in all possible  $\ell$  states where  $\ell$  is the angular momentum), and an ion in state,  $\Psi_n$ , is given [63, 64] by

$$\sigma_{0N}(E) = E|M_{0N}|^2. \quad (2.34)$$

Note the ionization energy,  $I_n$ , and the photoelectron energy,  $\epsilon_n$ , must satisfy the relationship  $E = \epsilon_n + I_n$ .  $|M_{0N}|^2$  is the square of the dipole matrix element for photoionization to all of the possible final states,  $|n\rangle$ . For incident photon energies less than several keV,  $|M_{0N}|^2$  is given in the dipole approximation as [65, 66]

$$|M_{0N}|^2 = \sum_n \left| \left\langle n \left| \sum_j \mathbf{r}_j \right| 0 \right\rangle \right|^2 = \sum_n |M_{0n}|^2 \quad (2.35)$$

where  $\mathbf{r}_j$  is the position operator for the  $j^{\text{th}}$  electron, and

$$M_{0n} = \left\langle n \left| \sum_j \mathbf{r}_j \right| 0 \right\rangle \quad (2.36)$$

is the dipole matrix element for photoionization, expressed in its dipole length form. Note that  $|0\rangle$  and  $|n\rangle$  refer to specific initial and final states respectively, so that the summation shown in equation (2.35) is necessary to arrive at a total cross-section for processes occurring with  $E = \epsilon_n + I_n$ . To calculate the total cross-section for the production of an ion in a given electronic state, one must sum all the  $|M_{0n}|^2$  values that lead to production of an ion in that state, so that  $|M_{0k}|^2$  is a summation is taken over all final states which contain the ion in the ion state  $\psi_k$ . For example, for ionization of a neon 2p electron to give a  $2p^5$  final ion

state, a summation must be taken over final state channels containing the photoelectron in the different ( $\epsilon\ell$ ,  $\ell=0$  (s) and  $\ell=2$  (d)) angular momentum states.

For photoionization processes within the independent particle approximation (i.e. as in outer valence photoionization), there will be only a single ion state,  $\psi_k$ , resulting from the removal of the  $j^{\text{th}}$  electron from the initial state,  $|0\rangle$ . If there are significant final state correlation and relaxation effects (e.g. as in inner valence photoionization) then the removal of a given electron,  $j$ , will result in a manifold of final ion states,  $\psi_k$ , each having its characteristic ionization energy,  $I_k$ . In this situation,  $\sigma^j$ , the total photoionization cross-section over this manifold of states (i.e. the cross-section for removal of the  $j^{\text{th}}$  electron) will involve a summation over the final ion states,  $\psi_k$ ,

$$\sigma^j(E) = \sum_k \sigma_{0k}(E_k) = \sum_k (\epsilon_k + I_k) |M_{ok}|^2. \quad (2.37)$$

The relative peak intensities corresponding to each of the different final states in the manifold of the positive ion in the PE spectrum will therefore be proportional to the respective values of the sums of the squares of the dipole matrix elements  $\sum_k |M_{ok}|^2$ , corresponding to the removal of electron  $j$  from the initial state. Many-body Green's function [67, 68] or configuration interaction calculations give the relative intensities as pole strengths according to the simple overlap

$$P_k^j = |\langle \psi_k | 0 \rangle|^2. \quad (2.38)$$

The quantity  $P_k^j$ , the pole strength, is the probability that ionization of the  $j^{\text{th}}$  electron from  $|0\rangle$  results in the final ion state,  $\psi_k$  (i.e. the probability that the  $j^{\text{th}}$  hole state appears in the final ion state,  $\psi_k$ ). If the independent particle description applies then there is a single final ion state,  $\psi_k$ , for ionization of an electron from each orbital in the neutral molecule, and the pole strength,  $P_k^j$ , is unity. In contrast, where final state correlation and relaxation effects occur, there will be multiple final ion states and the pole strengths for removal of a given electron will be partitioned accordingly. In this case the pole strength corresponding

to ionization of the  $j^{\text{th}}$  electron will be spread out over a number of lines, each corresponding to a different final ion state,  $\psi_k$ , such that

$$\sum_k P_k^j = 1. \quad (2.39)$$

The calculated pole strength spectrum (equation (2.38)) and the PE spectrum (given *via* equation (2.34)) will exhibit different relative intensities for the different electronic states, as a result of the (photon energy dependent) dipole matrix element terms in equation (2.34) compared with the simple overlap term in equation (2.38). Also, the PES intensities include the effects of orbital degeneracy whereas pole strength calculations sum to unity for ionization of the  $j^{\text{th}}$  electron regardless of initial state degeneracy. For many-body final ion states, within a given manifold of states (corresponding to ionization of the same initial state electron,  $j$ , in the neutral molecule), the relative intensities of the peaks in the PE spectrum will closely approximate the relative strengths of the calculated poles if the ionizing photon energy is large compared with the ionization energies. Under these conditions the continuum parts of the wavefunctions (i.e. those which describe the state of the photoelectron) will be approximately the same for all final states within a given manifold. Note, however, that relative intensities of peaks in different manifolds in the PE spectra resulting from ionization of different initial state electrons,  $j$ , will not be the same as the corresponding calculated pole strengths, regardless of the ionizing photon energy or other experimental conditions. These intensity differences arise because of the quite different  $M_{0k}$  values for each final ion state manifold.

## 2.5 Spectral Analysis

Using molecular orbital (MO) theory the state of an electron in a molecule is described by a one electron wavefunction. For the present discussion consider four types of orbitals: inner shell (core), occupied valence, unoccupied (virtual) valence and unoccupied Rydberg

orbitals. These various molecular orbitals are shown in figure 2.1a arising from the combination of atomic orbitals. The inner shell MOs are considered to remain essentially atomic in character because they are located so close to their respective atomic centers that they have very little spatial overlap with inner shell MOs of similar energies on other atoms. Thus, in photoabsorption spectra the inner shell orbitals of a molecule often retain their atomic designation (for example in figure 2.1a the  $1\sigma$  and  $2\sigma$  orbitals would be continued to be labeled as the  $1s$  orbitals of their respective atoms.) The valence orbitals, which can be bonding, anti-bonding or non-bonding in character, extend over the entire molecule and are responsible for the molecule's structure, bonding and reactivity. Rydberg orbitals are larger, diffuse orbitals of considerable spatial extent.

Differentiation between unoccupied virtual valence and Rydberg orbitals is made by considering the effect that a hole state has on those orbitals. A hole state is created by an excitation or ionization process that leaves a vacancy or hole in a valence or inner shell orbital which would normally be occupied in the neutral ground state. The field created by a hole state will cause varying degrees of relaxation and possibly energy re-ordering of all the molecular orbitals in the molecule. When a hole state is created, the new field causes a degree of relaxation in a virtual valence orbital which depends on the relative energy and location of the orbital in which the hole state is formed. On the other hand, a Rydberg orbital, because it is so large and diffuse, 'sees' the hole state as just a  $+1$  point charge on the molecular center and experiences the same degree of relaxation regardless of which orbital the hole is in. Rydberg orbitals are given atomic designations because they 'see' the molecule as if it were an atomic point charge.

Three basic types of electronic transition are considered here; excitation to a virtual-valence orbital (lowest energy processes), to a Rydberg orbital (medium energy processes) and to a continuum state (the highest energy processes). These transitions, which are shown schematically in figure 2.1a originating from both valence and core orbitals, along with

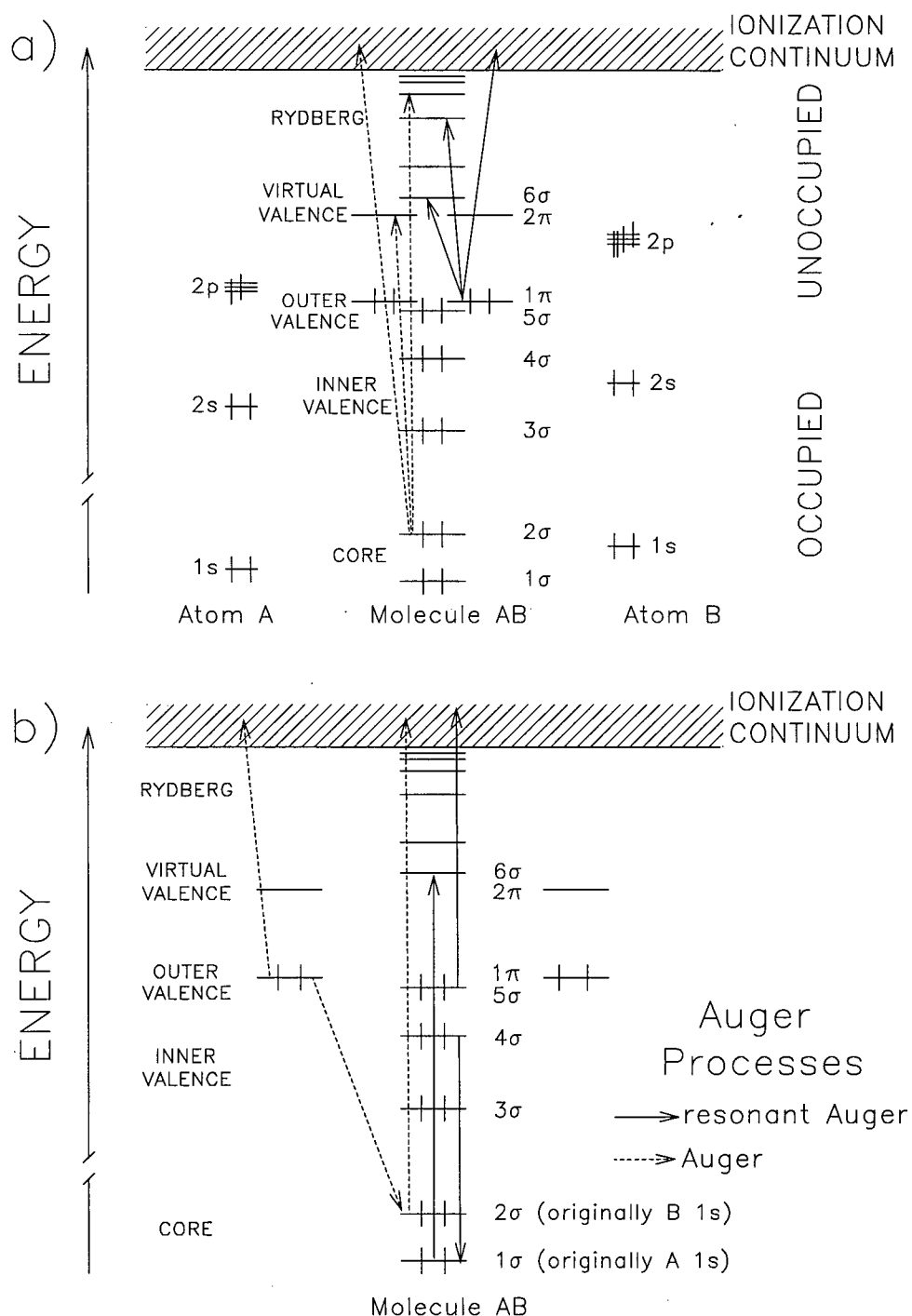


Figure 2.1: A schematic of the molecular orbitals of a molecule. a) Construction of the molecular orbitals of AB from the atomic orbitals of A and B. The horizontal lines represent orbitals, some of which are filled with electrons being represented by vertical lines. The three basic transition processes, each originating from a valence and from a core orbital, are shown by the solid and dashed lines. b) The Auger process (dashed lines) and resonant Auger process (solid lines), both shown as KLL or KVV processes. Note the breaks in the energy axes because the core orbitals are at a much lower (more negative) energy than the valence orbitals.

other spectral features relevant to the interpretation and assignment of the photoabsorption, photoionization and PE spectra presented in this thesis, are discussed in sections 2.5.1 to 2.5.4 below.

### 2.5.1 Discrete photoabsorption spectrum

The photoabsorption spectrum represents a set of transition energies resulting from excitations of electrons from occupied valence and inner shell orbitals to unoccupied virtual valence and Rydberg orbitals (excitation) as well as to unbound continuum states (ionization). These transitions can leave the molecule in an excited or ionized state which may also be vibrationally excited. In the various valence and inner shell discrete spectra of a molecule many features such as term values, vibrational progressions, peak profiles and intensities can be used to interpret and assign each individual spectrum. Often there are common features amongst the valence and inner-shell discrete spectra of a molecule and these can further aid in spectral interpretation.

The transition energy ( $E = h\nu$ ) for a discrete transition is the difference between the energies of the initial and final states. Each transition can be given a term value,  $T$ , defined by [69]

$$T = E_{IP} - E \quad (2.40)$$

where  $E_{IP}$  is the ground (initial) state IP of the electron involved in the transition. The term value can be viewed as the ionization potential of the electron in the excited (final) state. As described above the formation of a hole state will cause a virtual valence orbital to relax, more or less, depending of the characteristics of the hole state. Thus transitions to the same virtual valence state, but from different initial states, will result in different term values because of varying degrees of relaxation. The term values of transitions to virtual valence orbitals are considered to be non-transferable because the magnitude of the term

value is dependent on the initial orbital. In contrast, the uniform relaxation of a Rydberg orbital in the presence of any hole state results in a relatively constant term value for all transitions to that Rydberg state. Thus, term values for Rydberg transitions are considered transferable [70, 71] because the magnitude of the term value is independent of the initial orbital. The transferability of Rydberg term values often simplifies the assignment of valence and inner shell photoabsorption spectra and, in many cases, is essential for interpretation of complicated discrete spectra [70, 71]. For example, the term values from an identifiable Rydberg series in an inner shell spectrum may be used to assign absorption bands, involving the same final Rydberg orbitals, in the valence shell spectrum which is often complicated by many overlapping Rydberg series involving several different initial orbitals.

The atomic character of the Rydberg orbital allows its term value to be represented by the Rydberg formula [69] (borrowed from atomic spectroscopy). The energy of a transition to a Rydberg orbital is given by

$$E = E_{IP} - T = E_{IP} - \frac{R}{(n - \delta)^2}. \quad (2.41)$$

where  $R$  is the Rydberg energy (13.606 eV), the constant  $\delta$  is the quantum defect and  $n$  is the principal quantum number of the Rydberg orbital. The IP of the initial orbital, normally obtained from PES, could also be determined using the Rydberg formula providing a sufficiently long Rydberg series was identifiable in the photoabsorption spectrum to allow for a reliable extrapolation to the limit  $n \rightarrow \infty$ . The quantum defect accounts for shielding of the positively charged molecular core by intervening filled molecular orbitals which (partially) screen the Rydberg orbital from the full effect of the atom-like +1 point charge of the molecule. In other words,  $\delta$  allows for some deviation from the Rydberg model because of screening. The degree of screening is dependent on the angular momentum of the Rydberg orbital. For transitions to s, p and d-Rydberg orbitals values for  $\delta$  are commonly found to be 0.8–1.3, 0.5–0.9 and 0–0.3, respectively. In the present work, for continuity with the

principal quantum numbers of the atomic species that make up a molecule, the designation of the first Rydberg orbitals will be governed by the highest principal quantum number of the largest atomic species in the molecule. This convention can result in a change in the value of  $\delta$  by an integral number. For example, in a simple hydrocarbon (C 2s and 2p) the first Rydberg orbitals are labeled 3s, 3p, and 3d, and have  $\delta$  values of 0.8–1.3, 0.5–0.9 and 0–0.3, respectively. For methyl bromide (Br 4s, 4p, 3d), where the first Rydberg orbitals are labeled 5s, 5p, and 4d,  $\delta$  values of 2.8–3.3, 2.5–2.9 and 0.8–1.3, respectively, are used.

In some molecular systems there is no clear distinction between the higher energy virtual valence orbitals and the lowest energy Rydberg orbitals. Rydberg-virtual-valence mixing can result when the lowest energy Rydberg orbitals are of approximately the same energy as the higher energy virtual valence orbitals. The transferability of term values for a mixed orbital is unreliable because of the valence character of the orbital.

Vibrational excitation often accompanies a valence shell transition because of the inherent bonding or anti-bonding nature of the valence and virtual valence orbitals. Transitions involving these orbitals can give rise to an excited state with an appreciably different equilibrium bond-length than the ground state and a long vibrational progression would then be associated with this excitation. However, a transition from an inner shell orbital, which is inherently non-bonding, would have vibrational structure only if the final orbital has bonding or anti-bonding character. Therefore an inner shell transition to a Rydberg orbital will not be accompanied by vibrational excitation, whereas a transition to a virtual valence orbital may have an associated vibrational progression.

Inner shell discrete spectra can often be divided into two regions. The first region is at the lower excitation energies and is characterized by broad, often featureless bands which are associated with virtual valence transitions. The second region is at higher excitation energies and contains sharp bands which arise from Rydberg transitions. The band profile of an inner shell transition is dependent on any vibrational progression associated with the

transition, the lifetime of the upper state and on the overlap of the initial and final states involved. The broad profile associated with excitation to virtual valence states can arise from the vibrational progressions that often accompany these transitions or the fact that virtual valence states are frequently short lived. An excited state with a short lifetime has a large uncertainty in its transition energy which gives rise to a broad band in the photoabsorption spectrum. The combination of a vibrational progression and short lifetime of the excited state often results in the broad featureless bands commonly observed in inner shell spectra for virtual valence transitions. However, in some cases the lifetime of the virtual valence excited state is sufficiently long to observe individual vibronic states [72, 73] (for example, the carbon and nitrogen K-shell photoabsorption spectra of BrCN in section 7.3). The sharp band profile of a Rydberg transition is a result of the longer lifetime of the Rydberg state and the absence of any vibrational structure associated with the transition.

The intensity of a transition depends upon the square of the dipole matrix element as shown in equation (2.13). A condition for appreciable transition probability is significant spatial overlap of the initial and final state wavefunctions. The spatial overlap of inner shell orbitals with virtual valence orbitals is greater than it is for overlap with the spatially diffuse Rydberg orbitals. Therefore, in the absence of perturbing features such as potential barrier effects, inner shell spectra are characterized by having broad, intense virtual valence transitions and sharp, lower intensity Rydberg transitions. Furthermore, as the quantum number  $n$  of the Rydberg orbital increases, there is less spatial overlap with the initial state orbital and the transition intensity has been shown to decrease as  $n^3$  [74, 75] for some atomic systems.

An inner shell spectrum may undergo a redistribution of spectral intensity causing an enhancement of one or more virtual valence transitions as well as localized transitions in the continuum region with a corresponding decrease or even elimination of Rydberg transitions close to the ionization threshold. This was first observed and considered to be particular

to molecules with a central atom surrounded by a “cage” of electronegative ligands such as  $\text{BF}_3$  [76],  $\text{SiF}_4$  [77],  $\text{SF}_6$  [78–80] and  $\text{IF}_5$  [81], but this effect has also been observed in diatomic and triatomic molecules such as  $\text{CO}$ ,  $\text{N}_2$  [82],  $\text{BrCN}$  (see chapter 7) and  $\text{ICN}$  [73]. For a general discussion of this phenomenon see refs. [80, 81].

### 2.5.2 Continuum photoabsorption spectrum

Discrete transitions comprise only a small portion of the entire photoabsorption oscillator strength of an atom or molecule. The bulk of the oscillator strength is made up from transitions to ionization continua. The photoionization differential oscillator strength profile in a many-electron system does not, in general, have a hydrogenic profile [34], i.e. a maximum near the ionization threshold and a monotonic decrease at higher energies. There are several circumstances which lead to non-hydrogenic behavior. A Cooper minimum and a delayed maximum (shape resonance) are two such continuum features that are prominent in photoabsorption spectra of systems containing larger atomic species.

In some photoabsorption spectra a local minimum, called a Cooper minimum, occurs in the cross-section at several tens of eV above the ionization threshold [34, 74, 83]. In atomic spectroscopy Cooper minima are observed in the ionization continua of subshells that have radial nodes, e.g. 3p, 4p, 4d, 5f, etc. If one considers the square of the dipole matrix element as being represented by the overlap of the radial portions of the initial and final state wavefunctions [74] (e.g. equation (2.38)) then at some energy the node in the initial state wavefunction will result in a zero net overlap of the initial and final state wavefunctions. The intensity from that channel will be zero which may give rise to a minimum in the overall cross-section. A prominent Cooper minimum is observed in the valence shell ionization continuum of Ar [84] from 3p ionization. The above description for atomic systems can be extended to molecular systems, particularly when the molecular orbital has a primary

contribution from one atomic orbital, as in the case of  $\text{Cl}_2$  (see figure 4.3 in section 4.3.2) where the valence shell ionization continuum is dominated by  $2\pi_g$  and  $2\pi_u$  ionization which are largely Cl 3p in character.

The inner shell ionization continua of atoms and molecules containing the heavier p-block (or d-block) elements, in some cases, undergo a redistribution of oscillator strength intensity such that there is a shift of the differential oscillator strength maximum 20 to 100 eV above the ionization threshold. This is termed a delayed maximum or delayed onset. This redistribution arises from a potential barrier formed by the interaction between coulombic attraction of the electron to the positive nucleus and centrifugal repulsion [34, 74]. Near the nucleus the coulombic attraction term creates an inner well potential. At larger distances the screening of the nucleus by intervening electrons allows the centrifugal repulsion term to dominate, forming a barrier outside which there is an outer well. The formation of the barrier causes states with total energies below the barrier maximum to be eigenfunctions of either the inner well or the outer well [85]. Transitions to states of the outer well (e.g.  $nd \rightarrow \epsilon f$  transitions in Br or I systems) cause the delayed onsets observed in the heavier noble gases [84],  $\text{CH}_3\text{Br}$ ,  $\text{CH}_3\text{I}$  (chapter 5) and  $\text{BrCN}$  (chapter 7). This delay arises from the potential barrier which causes the radial function of the  $\epsilon f$  wavefunction at threshold energies to be diffuse such that the overlap of the  $nd$  and  $\epsilon f$  wavefunctions is near zero. At energies above threshold the radial part of the  $\epsilon f$  wavefunction has significant intensity at smaller distances, which leads to larger overlap of the two wavefunctions. Thus the maximum intensity of the  $nd \rightarrow \epsilon f$  transitions will occur at energies significantly above threshold.

Both the Cooper minimum and delayed onset phenomena are dominated by  $\ell \rightarrow (\ell + 1)$  transitions because, in general, the transition probability to  $(\ell + 1)$  waves is greater than to  $(\ell - 1)$  waves [65]. For example the  $\text{Cl}_2$  valence shell ionization continuum is dominated by  $2\pi_g$  and  $2\pi_u$  (largely Cl 3p in character) transitions to the  $\epsilon d$  orbitals rather than to the  $\epsilon s$  orbitals, giving rise to an observable Cooper minimum.

### 2.5.3 Photoionization *via* Auger and autoionization processes

Most photoionization events arise from a direct non-resonant ionization channel, but in some cases indirect processes such as Auger and autoionization occur. These processes play important roles in the photoionization studies carried out by dipole (e,e+ion) spectroscopy and variable photon energy PES because they are often responsible for discrete structure observed in partial photoionization oscillator strength spectra and for multiple ionization which, upon decomposition by a dissociative pathway, can be readily studied using photoion-photoion coincidence (PIPICO) spectroscopy.

Autoionization is a resonant process that arises from a transition to a bound (neutral) state having a potential energy curve which lies at a higher energy than the potential energy curve of some ion state. The initial excitation in the autoionization process usually involves transition from an inner valence or inner shell orbital, but it may also involve a double excitation process. The neutral excited state then decays into the lower energy ion state continuum, resulting in an ion in the lower energy electronic state configuration as if direct photoionization had occurred. While these autoionization resonances can be observed in photoabsorption spectra [27, 46, 84] they are more readily observed as resonant enhancement in partial photoionization oscillator strength spectra from both variable photon energy PES and PIMS. Resonant enhancement is observed as an increase in the yield of the photoelectron or photoion products resulting from the autoionization process. Furthermore, this enhancement only occurs in those particular channels involved with the autoionization process and only when the photon energy matches the resonance energy.

The Auger and resonant Auger processes, shown schematically in figure 2.1, are two step processes involving three electrons and result in a multiply ionized or an excited ion state, respectively. The first step of the Auger process is the ionization of some inner valence or core electron to form a hole state. The second step involves simultaneous relaxation of

an outer (less tightly bound) electron, filling the newly formed hole, and ionization of a second outer electron. The second step is governed by a quasi energy balance where the energy obtained from the electron relaxing into the hole state is “transferred” to the ionized electron in the form of binding energy plus kinetic energy. There are several types of Auger processes involving different shells and subshells of electrons. Commonly, the Auger process begins with the ionization of a K-shell electron (or other core electron) and the subsequent relaxation plus ionization of two valence electrons. A process of this type is labeled KVV (i.e. K shell ionization, valence shell relaxation, valence shell ionization). A KLV process is a K-shell hole followed by filling of the hole with an L-shell electron and the ionization of a valence shell electron. The VVV Auger process begins with the formation of an inner valence hole and the subsequent relaxation and ionization of two outer valence electrons. These Auger processes all result in the formation of a doubly ionized species. The Auger process can also give rise to triply and higher ionized species. In these cases the second step involves a relaxation of an outer electron plus the ionization of two or more electrons. An example is the KLVV process where a K-shell hole is followed by filling of the hole with an L-shell electron and the ionization of two valence shell electrons. Resonance Auger, which is less common than normal Auger, occurs as a result of the formation of a hole state created by **excitation** of an inner shell electron. This process is followed by relaxation plus ionization of two valence (or outer shell) electrons to form an excited ion.

#### 2.5.4 Photoelectron spectrum

Much of the understanding that we have today of molecular electronic structure has been gained as a result of a close comparison of theoretical predictions with experimental observations made using a range of different experimental techniques. A simple picture of PES is provided by Koopmans’ theorem which states that the ionization energy  $I_j$  is equal to

the negative of the orbital energy of the ionized electron. Also, in the independent particle model, each band in the PE spectrum will correspond to ionization from a single MO and each MO will give rise to only one PE band. These ideas are approximately valid only for outer valence ionization processes [55]. Koopmans' theorem would be true only if orbital energies remained the same in both the neutral ground and final ion states, which is also termed the "frozen orbital" approximation. However, the molecular orbital energies of the final ion state do differ from the energies in the neutral ground state because of rearrangement (relaxation, correlation and re-ordering) of the MOs caused by changes in the molecular geometry and by changes in the molecular field of the newly formed hole state.

Experimentally, all PE spectra contain more PE bands than there are valence orbitals because of vibrational excitation in the final ion state, removal of orbital degeneracy in the final ion state and electron correlation. The removal of an electron from a bonding or anti-bonding outer valence orbital is accompanied by a change in internuclear distance which results in the formation of a vibrationally excited final ion state and can lead to a vibrational manifold in the PE spectrum. Vibrational progressions observed in PE spectra often have vibrational spacings similar to those observed in bound transitions involving excitation from the same initial state orbitals to Rydberg states. This correspondence can aid in the assignment of either the photoabsorption or photoelectron spectrum. Furthermore, a long vibrational progression (large number of vibrational bands) can indicate that the electron was ionized from either a strongly bonding or an anti-bonding orbital. Ionization of a predominantly non-bonding electron causes either a short progression or no vibrational structure at all to be observed in the PE spectrum. Apart from vibrational excitation, multiple PE band structures can also arise from the removal of ground state orbital degeneracy by spin-orbit/ligand-field splitting or Jahn-Teller distortion in the final ion state. For example, ionization of the HOMO of  $\text{CH}_3\text{Cl}$  produces a  $(2e)^{-1}$  hole and a  ${}^2\text{E}$  final ion state whose degeneracy is lifted because of spin-orbit coupling which leads to two bands in the PE

spectrum corresponding to the of  ${}^2E_{3/2}$  and  ${}^2E_{1/2}$  final ion state configurations. The effects of both vibrational excitation and the removal of ground state orbital degeneracy are most prominent in the photoionization of outer valence orbitals and inner shell orbitals. While the outer valence orbitals are particularly important from the standpoint of chemical reactivity [86], inner valence IPs, PE branching ratios, and partial photoionization cross-sections are of key importance in processes such as dissociative photoionization [87] and also for the evaluation of electron correlation (many-body) theories of photoionization [88, 89].

Electron correlation effects encompass the notion that electrons “see” each other and that during the ionization process the outgoing electron can interact with other electrons. This interaction can lead to events occurring in tandem with the ionization event such as the simultaneous excitation or ionization of one or more electrons as well as orbital relaxation or re-ordering. The PE spectrum of an electronic ion state that is split into several different ionization processes of varying intensity by electron correlation effects can have a highly irregular PE band profile. The ionization process may be split into just two or three moderately intense transitions or into many low intensity processes covering several electron volts. Significant electron correlation effects are most often observed in the region of the PE spectrum involving inner valence ionization, but can occur to a lesser extent in the outer valence region. Extensive electron correlation effects in the inner valence region of the PE spectrum make it the most difficult region to interpret.

Early PES experiments were restricted to investigations of the outer valence orbitals, at binding energies below  $\sim 21$  eV, since He I or other noble gas resonance lines were used as ionizing light sources. The subsequent development of He II resonance line sources (40.8 eV) in principle permits access to the inner valence region, but the spectra are, in almost all cases, restricted to binding energies below  $\sim 25$  eV because of the presence of an overlapping outer valence spectrum arising from the large amount of He I radiation also present in such undispersed sources. While the He I and II resonance lines could be separated

using a VUV monochromator, this would result in an unacceptable reduction in the photon flux and a broadening of the line width. Meanwhile, the parallel development of X-ray photoelectron spectroscopy (XPS)<sup>2</sup> by Siegbahn *et al.* [52, 90] using X-ray lines such as Mg K $\alpha$  (1253.6 eV) and Al K $\alpha$  (1486.6 eV) provided access to the complete valence shell and also a wide range of core (inner shell) ionization processes. However, the X-ray resonance lines have a relatively broad line-width (typically  $\geq 1$  eV) and the resulting low resolution spectra limit the information which can be obtained in the valence shell region. In addition, the cross-sections for valence shell processes are rather low at X-ray energies since these are far above the valence shell ionization thresholds. Although other sources at lower X-ray energies, such as the Y M $\xi$  (132.3 eV) and Zr M $\xi$  (151.4 eV) lines, have somewhat narrower line widths, the photon fluxes are extremely low. Similarly, other possible low energy X-ray sources using low Z targets such as carbon are not viable, since in such cases non-radiative decay (autoionization or Auger processes) is the dominant decay mechanism rather than X-ray fluorescence.

The growing availability of monochromated synchrotron radiation has enabled a wide range of core and valence shell binding energy spectra to be obtained at any desired photon energy below  $\sim 10000$  eV, provided that suitable VUV or X-ray monochromators are available. In addition, photoelectron branching ratios and partial cross-sections can be obtained as a function of photon energy if the measurements are made at the magic angle. A further consideration in all types of PES studies is the need to correct measured intensities for the changing analyser transmission efficiency as a function of electron kinetic energy if quantitative spectra are to be obtained (see section 3.4). This correction can often be quite large at lower kinetic energies and is thus much more important for PES studies than in XPS. Care must also be exercised in the use of synchrotron radiation because higher order radiation or stray light may also be present [91]. Furthermore, large non-spectral backgrounds, rising

---

<sup>2</sup>XPS has also been referred to as ESCA, i.e. Electron Spectroscopy for Chemical Analysis.

with decreasing electron kinetic energy, are usually found in photoelectron spectra at lower kinetic energies, and this background can complicate the assessment of spectral intensities at higher binding energies. This situation is particularly serious for inner valence spectra where broad spectral structures of low intensity are often found.

An alternative technique for measuring binding energy spectra is electron momentum spectroscopy (EMS) [92, 93], which often provides the only experimental spectra covering the complete valence shell binding energy range. However, the signal to noise ratio of this coincidence technique is usually quite limited and the energy resolution is only  $\sim 1.5$  eV fwhm. On the other hand, electron momentum spectra do not suffer from the rising non-spectral backgrounds which plague the PE spectra, particularly at lower kinetic energies. Additionally, EMS has the powerful capability of being able to record binding energy spectra as a function of the azimuthal angle (and thus of the initial electron momentum in the neutral molecule) and the resulting momentum distributions provide much more direct information on the symmetry of the ionized orbital than is available from photoelectron angular distribution measurements. Thus a joint consideration of photoelectron and EMS binding energy spectra can provide more detailed information on molecular electronic structure and ionization processes than can be gained by the use of either technique alone.

In the realm of theory, good quality self-consistent field (SCF) and  $\Delta$ SCF calculations of orbital energies often yield reasonable values for outer valence IPs, while somewhat improved values usually result from models such as configuration interaction (CI) and the outer valence, many body Green's function (OVGF) methods [88, 89], which consider electron correlation and relaxation effects. Both methods of calculation predict that, in almost all cases, the photoelectron intensity for each outer valence ion state is concentrated in a single peak (outside of spin-orbit, Jahn-Teller, and vibrational effects) of essentially unit pole strength, which is consistent with the spectra observed in PES experiments. This situation contrasts markedly with that in the inner valence region of the binding energy spectrum

of most molecules, where many more peaks than the number of inner valence orbitals are usually observed. It is found that the inner valence ionization intensity is split into many poles of varying intensity spread out over an extensive range of binding energies. Many-body Green's function [88, 89] and CI calculations have predicted this phenomenon in the inner valence region of many atoms and molecules and have shown that the ionization intensity corresponding to the removal of a given electron is, in many cases, severely split by predominantly final state correlation effects into many poles (or quasi particles) belonging to the same symmetry manifold.

The pole strengths predicted in CI or Green's function calculations may be compared directly with the relative intensities observed in EMS binding energy spectra within a given symmetry manifold and also approximately with PE spectra recorded at sufficiently high photon energies (see section 2.4). However, in order to compare the complete binding energy spectrum with pole strength calculations the EMS spectra must be integrated over all momenta, or alternatively the calculated pole strengths can be corrected for the momentum dependencies of the initial orbitals using the measured or calculated momentum distributions [94, 95]. Comparison of the complete binding energy spectrum with theory is more complicated in the case of PE spectra because the dipole matrix element for photoionization depends on photon energy in a different fashion for each orbital ionization process (i.e. for each symmetry manifold). It should also be noted that, at present, the calculation of intensities (i.e. photoionization cross-sections) for the different partial channels is at best semi-quantitative [1] because of the difficulties in modeling the final state wavefunctions which must include the continuum photoelectron. The various preceding considerations and limitations must therefore be taken into account when comparing calculated pole strengths with the relative intensities obtained from EMS and magic angle PES binding energy spectra. The quantitative aspects of these different intensity relationships have been discussed in section 2.4.

## 2.6 Sum-rule Moments and the Photoabsorption Spectrum

The success of the dipole (e,e) method has relied upon the accurate determination of an absolute oscillator strength scale, which has normally been obtained using the  $S(0)$  dipole (TRK) sum-rule. Dipole sum-rules are important not only because they are used to obtain the absolute oscillator strength scale for long range photoabsorption spectra, but also because they can be used to determine several important molecular properties. These can be obtained from the sum-rules which result from the integration of excitation-energy-weighted dipole differential oscillator strength spectra over all discrete and continuum electronic states. The general forms of the sum-rules presently considered are

$$S(u) = \int_{E_o}^{\infty} \left( \frac{E}{E_H} \right)^u \left( \frac{df}{dE} \right) dE \quad (2.42)$$

and

$$L(u) = \int_{E_o}^{\infty} \left( \frac{E}{E_H} \right)^u \left( \frac{df}{dE} \right) \ln \left( \frac{E}{E_H} \right) dE \quad (2.43)$$

where  $E_o$  is the threshold for electronic absorption, the photoabsorption spectrum is given by the differential oscillator strength ( $df/dE$ ) as a function of excitation-energy,  $E$ , and  $E_H$  is the Hartree energy unit. Many of these sums correspond to particular target properties [34, 35]; for instance  $S(0)$  is the total number of electrons in the target (the TRK sum-rule);  $S(-1)$  and  $L(-1)$  are associated with the cross-section for inelastic scattering;  $S(-2)$  is the static dipole polarizability;  $S(-3)$  is related to the non-adiabatic interaction of a charged particle with an atom; the even-ordered moments ( $S(-4)$ ,  $S(-6)$ , ...) are related to the light scattering and refracting properties (e.g. frequency dependence of refractive index and normal Verdet constant); and the dipole-dipole dispersion energy coefficient is reproduced very well by combinations of  $S(-2)$  and  $L(-2)$ .

## Chapter 3

### Experimental Methods

The photoabsorption, photoionization and photofragmentation data presented in this thesis were recorded on three spectrometers. The wide range absolute photoabsorption differential oscillator strength spectra were recorded using a low resolution (1 eV fwhm) dipole (e,e+ion) spectrometer (section 3.1). These spectra were placed on an absolute scale using the valence shell TRK (VTRK) sum-rule or a related normalization procedure (section 3.2). The low resolution dipole (e,e+ion) spectrometer (section 3.1) was also used to obtain partial photoionization oscillator strengths for molecular and dissociative photoionization. The discrete regions of the photoabsorption spectrum were studied in more detail using a high resolution (0.05–0.15 eV fwhm) dipole (e,e) spectrometer (section 3.3). The photoelectron spectra of CH<sub>3</sub>F, CH<sub>3</sub>Cl and CH<sub>3</sub>Br analysed and reported in chapter 6 of this thesis were recorded at the Canadian Synchrotron Radiation Facility (CSRF) at the Aladdin Storage Ring, University of Wisconsin, Madison, Wisconsin by Dr. G. Cooper, Dr. W. F. Chan and Dr. K. H. Tan (section 3.4). The PIPICO data of BrCN discussed in chapter 7 were measured on the UVSOR synchrotron radiation storage ring at The Institute for Molecular Science (IMS) in Okazaki, Japan by Dr. T. Ibuki and Dr. A. Hiraya (section 3.5).

#### 3.1 Low Resolution Dipole (e,e+ion) Spectrometer

The presently reported low resolution (LR) absolute photoabsorption differential oscillator strengths and the partial differential oscillator strengths for molecular and dissociative

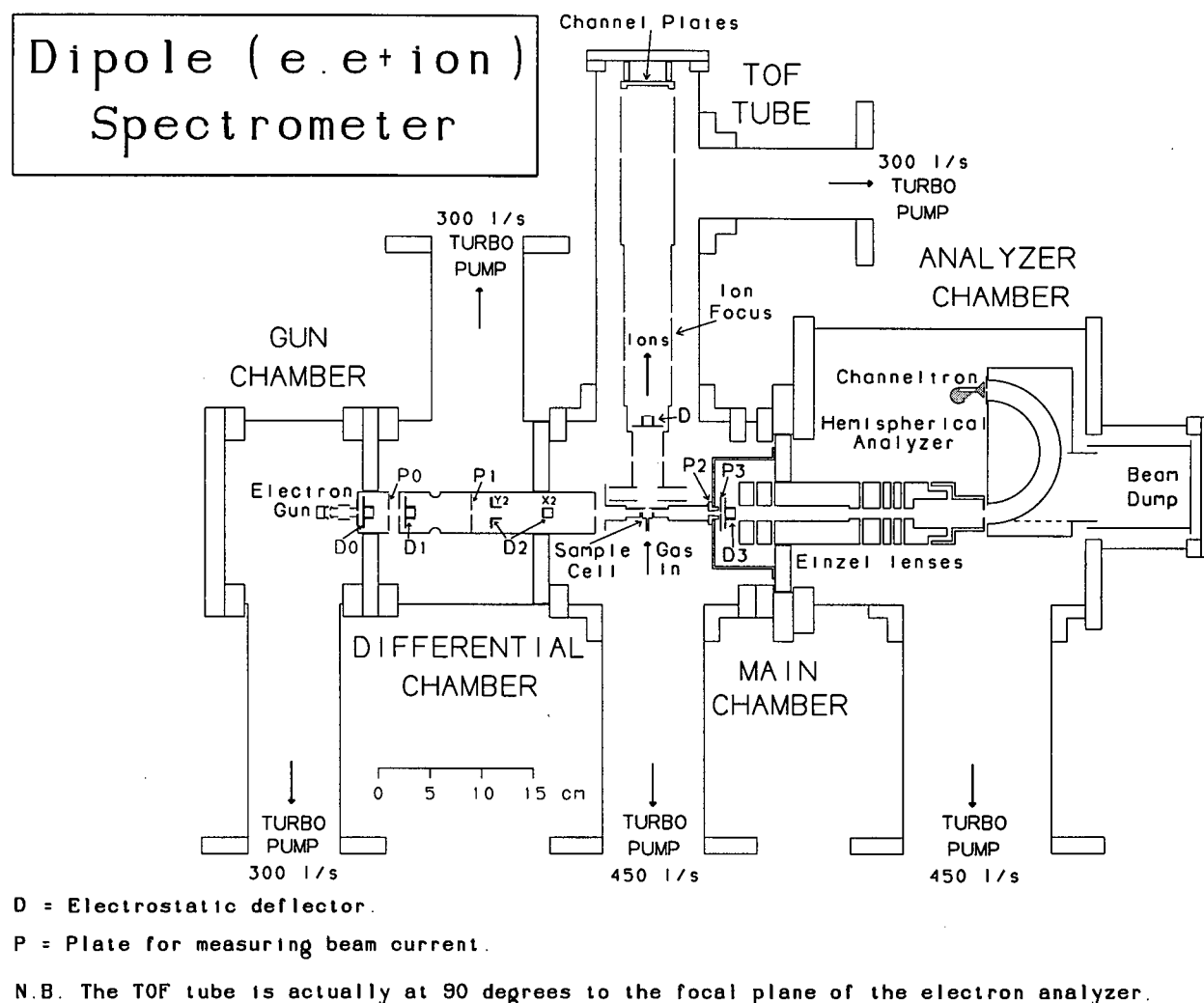


Figure 3.1: Low resolution dipole (e,e<sup>+</sup>ion) spectrometer.

photoionization were measured using electron energy-loss spectroscopy (EELS) and time-of-flight mass spectrometry (TOFMS) on a dipole (e,e<sup>+</sup>ion) spectrometer (figure 3.1) that has been fully described elsewhere [9, 43, 44, 48]. This spectrometer, which was originally constructed at the FOM institute in Amsterdam [41–44] and relocated to UBC in 1981, has undergone several major modifications in the recent years. These changes have improved instrument performance and reliability and have expanded the range of gaseous targets that can be studied by this spectrometer to include highly reactive species [77].

Briefly, the dipole (e,e+ion) spectrometer (figure 3.1) used a narrow (1 mm diameter) beam of electrons produced from an indirectly heated oxide cathode (black and white TV gun, Philips 6AW59) floated at a potential of  $-4$  kV. The electron beam was accelerated to 8 keV and directed using three sets of quadrupole deflectors into the collision chamber which was floated at a potential of  $+4$  kV. In the collision chamber the incident electron beam was scattered by the sample gas and the forward scattered electrons were collected in a small solid angle of acceptance ( $1.4 \times 10^{-4}$  sr) as defined by an angular selection aperture (P3). The forward scattered electrons, which may have imparted a fraction of their energy to the target to excite an electronic transition, were refocused, decelerated and admitted into a hemispherical electron energy analyser. The analyser, which was floated at a potential of  $-3.95$  kV, was operated at a constant pass energy of 50 V to ensure that the transmission, resolution and focusing properties remained constant. The forward scattered electrons were decelerated to the pass energy of the analyser plus the selected energy loss (i.e. decelerated by  $(7.95 \text{ kV} - \text{energy-loss})$ ). Thus electrons of the selected energy-loss were decelerated to 50 eV energy and were deflected by the electrostatic field analyser and detected by a channel electron multiplier (Mullard B419AL) at the analyser exit aperture. The channel electron multiplier was used in the saturated pulse counting mode. The majority of the electron beam, including the primary incident beam, was not of the selected energy loss and maintained an energy, after deceleration, that could not pass through the exit aperture and was thus collected in the beam dump. The resolution of this electron energy-loss spectrometer was  $\sim 1$  eV fwhm.

In the collision chamber a constant  $400 \text{ V}\cdot\text{cm}^{-1}$  electrostatic field was applied at a  $90^\circ$  angle to the incident electron beam to extract all positively charged ions formed by electron scattering (ionization) events into a TOF tube. This electrostatic field and the acceleration and focusing lens system were sufficient to ensure uniform collection of all positive ions formed with up to  $\sim 20$  eV excess kinetic energy of fragmentation, regardless of their initial direction

of dissociation [43–45, 61]. This was important to prevent discrimination against small  $m/e$  ions that could have been formed with significant kinetic energies of fragmentation. Ions were detected by two 40 mm multichannel plates (model VUW-8920ES, Electro-Optical Sensors (Intevac)) in a chevron configuration. The mass spectra were obtained from the TOFMS with a mass resolution ( $m/\Delta m$ ) of better than 50. The ion detection system has been calibrated for differences in detector response to ions of different mass [49].

The collision region was shielded from external magnetic fields by Helmholtz coils and high permeativity mumetal shielding. The spectrometer was controlled by an IBM compatible 80286 PC and the data acquisition and analysis programs were written by Dr G. Cooper. The dipole ( $e, e+ion$ ) spectrometer could be operated in two modes, either the dipole ( $e, e$ ) mode to collect wide energy range photoabsorption data or the dipole ( $e, e+ion$ ) mode to record photoionization mass spectra as a function of energy-loss.

In the dipole ( $e, e$ ) mode an electron energy-loss spectrum was obtained by counting the number of forward scattered electrons detected per unit time as a function of energy-loss. The electron energy-loss spectrum (i.e. relative differential electron scattering cross-section) was converted into a relative optical photoabsorption differential oscillator strength spectrum by multiplication by the known Bethe-Born conversion factor [1, 8, 35, 96] of the spectrometer. The relative photoabsorption spectrum was recorded over a wide energy range in several overlapping regions because the electron scattering cross-section decreases very rapidly with increasing energy-loss (see equation (2.29)). To maintain an acceptable signal-to-noise ratio in each region, a higher incident electron current was required as the average energy-loss of each region increased. The regions were normalized to each other in the overlapping portions and combined to form a wide range relative photoabsorption differential oscillator strength spectrum. The absolute scale for the spectrum was obtained using either the VTRK sum-rule or the dipole polarizability (e.g S(-2)) normalization procedure. These procedures are described below in section 3.2.

The spectrometer was maintained at a background pressure of  $\sim 2 \times 10^{-7}$  torr by five turbomolecular pumps. The ambient sample gas pressure used for data accumulation was  $6-8 \times 10^{-6}$  torr. To eliminate the effects from non-spectral electrons and residual background gases, each spectrum was background subtracted by performing a point for point subtraction of a spectrum recorded immediately after data accumulation at 1/4 of the ambient sample gas pressure.

Photoionization mass spectra were obtained in the dipole (e,e+ion) mode by coincident detection of forward scattered electrons of a particular energy-loss (photon energy) with TOF mass analysed ions. The time-of-flight was proportional to  $\sqrt{m/e}$  for each ion and was determined using a single stop time-to-amplitude converter (TAC) using the ion signal to start the TAC and the delayed electron signal to stop the TAC. The TOF mass spectrum was obtained from the pulse height distribution of the time correlated signals. Branching ratios for all ions were determined by integrating the peaks of the baseline subtracted TOF mass spectra, correcting for the ion multiplier m/e response and then normalizing the total integrated area to 100%. The relative photoionization efficiency was determined by taking the ratio of the total number of electron-ion coincidences to the total number of forward scattered electrons (simultaneously recorded) as a function of energy loss. The value of  $\eta_i$  was constant at higher energies and could not exceed unity with the single stop TAC used in the present instrumentation for single ionization processes or for production of multiply charged ions that do not Coulomb explode, i.e. where there was only one ion which could be detected for each "START" pulse arising from an electron of given energy loss. This situation applies regardless of the ion detection efficiency. Furthermore, in the hypothetical situation that the ion detection efficiency was 100% then only the fastest ion would be detected in dissociative double (or higher) photoionization processes (i.e. Coulomb explosions of multiply charged ions where two or more ions are produced). In reality ion detectors are not 100% efficient. The situation for the present instrumentation used was that the efficiency

of the TOF/MCP detection system has been measured [49] to be 10%. This means that both ions from a Coulomb explosion of a doubly charged ion can be detected with almost equal probability, with the fastest ion being detected 10% of the time and the slower ion being detected 9% of the time (i.e. 10% of 90%). Where such double (or higher) dissociative (multiple) photoionization processes contribute, the  $\eta_i$  value measured with this spectrometer would exceed unity. For example, if 15% of all ionization events were doubly dissociative (i.e. gave two ions) then, although the true overall  $\eta_i$  would be 1.15 (assuming 100% detector efficiency), a value of 1.135 would have resulted with the present experimental arrangement because of the 10% detection efficiency. The absolute partial differential oscillator strengths for molecular and dissociative photoionization were obtained from the triple product of the photoion branching ratio, the absolute differential oscillator strength (obtained in the non-coincident dipole (e,e) mode) and the ionization efficiency using equation (2.9).

### 3.2 Absolute Oscillator Strengths *via* Dipole Sum-rules

The absolute photoabsorption differential oscillator strength scale for the dipole (e,e) photoabsorption spectrum of He [27] was obtained using the TRK sum-rule which is given by

$$S(0) = \int_{E_0}^{\infty} \left( \frac{df}{dE} \right) dE = N \quad (3.1)$$

where  $N$  is simply the total number of electrons in the atomic or molecular target. TRK sum-rule normalization avoids the difficulty of the target number density (i.e. pressure) and pathlength determination necessary in Beer-Lambert law absolute oscillator strength measurements. It does, however, require a correctly shaped relative photoabsorption spectrum (i.e. one with the correct relative intensities). This latter requirement is readily achieved in the dipole (e,e) method because of the “flat” virtual photon field induced by the transit of a fast electron [1, 8]. The placement of a relative photoabsorption spectrum on an absolute

differential oscillator strength scale using the TRK sum-rule requires the normalization of the area under the complete relative spectrum, from threshold up to infinite photon energy (or energy-loss in the dipole (e,e) method), to the total number of electrons in the target. In practice there is an upper limit to the equivalent photon energy (energy-loss) at which dipole (e,e) measurements can be made. However, a good approximation to an infinite energy range data set may be achieved in favorable cases by fitting a suitable polynomial curve to the higher energy continuum region of the measured spectrum and extrapolating to infinite energy. Such a procedure has yielded very high accuracy oscillator strengths for helium [27]. However, the general application of the TRK sum-rule procedure according to equation (3.1) to species containing second or higher row atoms is impractical because relative photoabsorption measurements are then needed not only for the valence shell, but also for all inner shell transitions. For example, for targets containing only first and second row atoms, photoabsorption measurements of up to at least 1000 eV would be needed so that the curve fitting could be performed in the monotonically decreasing ionization continuum region at least 100 to 200 eV above any discrete structure, delayed onsets, or shape resonances associated with excitation of the most tightly bound shell. Therefore, in general, a valence shell-modified form of the TRK sum-rule has been used [1, 11] to obtain absolute photoabsorption differential oscillator strength scales from long-range (i.e. from the first valence shell electronic excitation threshold up to 200 eV) relative photoabsorption measurements.

In the VTRK normalization procedure [1, 27, 30], experimental *valence* shell relative photoabsorption data, collected using the dipole (e,e) method, were extrapolated to infinite energy by fitting a polynomial to the higher energy smoothly decreasing valence shell continuum (typically in the 100 to 200 eV photon energy range). In some earlier studies a fitting function of the form  $df/dE = AE^{-B}$  was used, but more recently a polynomial having the form

$$df/dE = AE^{-2} + BE^{-3} + CE^{-4}, \quad (3.2)$$

where  $A, B$  and  $C$  are fit parameters, generally has been found to be more satisfactory in that it provides a better fit over a wider energy region of the monotonically decreasing ionization continuum at higher energies. The total valence shell spectral area (the area under the measured valence shell photoabsorption spectrum plus the fitted polynomial extrapolated to infinite energy) was then normalized to the number of valence shell electrons in the target,  $N_{val}$ , plus a small estimate for Pauli excluded transitions,  $N_{PE}$ . The Pauli excluded correction allows for the redistribution of oscillator strength because of transitions from the inner shells to levels already occupied in the ground state. The intensity from these transitions, which is redistributed to the valence shell or less tightly bound inner shell regions, can be estimated from atomic calculations [97]. For example, the Pauli excluded K-shell contribution for  $\text{CH}_4$  can be estimated from the calculation for the isoelectronic atom neon [98, 99] for transitions from the Ne K-shell to the occupied Ne 2s and 2p orbitals.

The VTRK sum-rule, given by

$$S_{val}(0) = \int_{E_0}^{\infty} \left( \frac{df}{dE} \right)_{val} dE = N_{val} + N_{PE} , \quad (3.3)$$

has been found to be suitable for targets containing first, second, and in some cases third row atoms. However, in many other cases various spectral features at intermediate energies “distort” the long-range monotonically decreasing direct valence shell ionization continuum needed for an effective polynomial fit and extrapolation. These features include low lying inner shell spectra, Cooper minima, and continuum shape resonances. The use of the VTRK sum-rule may also be precluded because spectral data are available only over a limited photon energy range or because no estimates for the contributions from Pauli excluded transitions are available. For molecules where the TRK or VTRK sum-rules cannot be applied, other sum-rules may be useful for normalization. These other sum-rules can also be used as a check of the accuracy of the absolute scales established with the  $S(0)$  or the  $S_{val}(0)$  sum-rule or those resulting from Beer-Lambert law absolute photoabsorption measurements. The use of

published experimental and theoretical dipole polarizabilities to normalize relative differential oscillator strength spectra and to check absolute scales established by other methods is investigated in chapter 4 of this thesis. The experimental values of the dipole polarizability are generally derived [100] from dielectric constant or refractive index measurements. The static dipole polarizability ( $\alpha_{(\lambda \rightarrow \infty)} = \alpha_\infty$ ) of a molecule is given by the S(-2) sum-rule

$$S(-2) = \int_{E_o}^{\infty} \left( \frac{E}{E_H} \right)^{-2} \left( \frac{df}{dE} \right) dE = \alpha_\infty. \quad (3.4)$$

The wavelength ( $\lambda$ ) dependent molar refractivity ( $R_\lambda$ ) and refractive index ( $n_\lambda$ ) are related to the dynamic polarizability ( $\alpha_\lambda$ ) by the Lorentz-Lorenz equation [101]

$$R_\lambda = \frac{1}{\rho} \left[ \frac{n_\lambda^2 - 1}{n_\lambda^2 + 2} \right] = A_R(\lambda) + B_R(\lambda)\rho + C_R(\lambda)\rho^2 + \dots \simeq \frac{4\pi N_A}{3} \alpha_\lambda \quad (3.5)$$

where  $\rho$  is the molar density and  $N_A$  is Avogadro's number. The virial coefficients ( $B_R(\lambda)$ ,  $C_R(\lambda)$ , etc.) describe the deviations of equation (3.5) from the ideal gas state. These coefficients are very small [102–105] and have not been considered in the present work. The dynamic dipole polarizability,  $\alpha_\lambda$ , and thus the molar refractivity ( $R_\lambda$ ) and refractive index ( $n_\lambda$ ), are related to the differential oscillator strength distribution by

$$\alpha_\lambda = E_H^2 \alpha_o^3 \int_{E_o}^{\infty} \frac{(df/dE)}{(E^2 - \epsilon^2)} dE \quad (3.6)$$

where  $\epsilon = (hc/\lambda)$  is the energy,  $h$  is Planck's constant and  $c$  is the speed of light. The most attractive feature of normalization methods based on experimental values of  $\alpha_\infty$  and  $\alpha_\lambda$  is that they are dominated by the low energy valence shell region of the spectrum (typically the region below 50 eV). Thus the normalization is achieved using the energy region of the measured spectrum which has the advantage of having the highest oscillator strength and typically the best signal-to-noise ratio. This can be an important consideration for the dipole (e,e) electron energy-loss method where the measured electron scattering cross-section decreases with energy faster (by  $\sim E^{-3}$ ) than the photoabsorption cross-section [35].

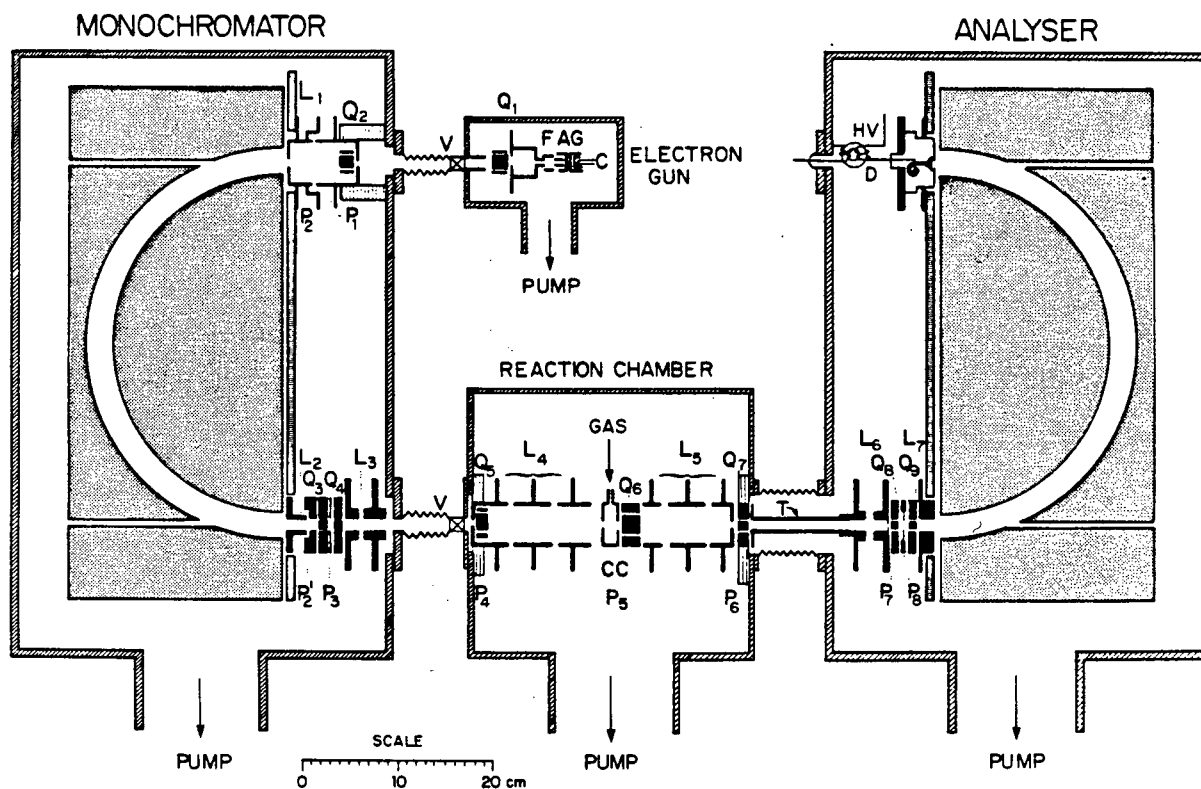


Figure 3.2: High resolution dipole (e,e) spectrometer.

### 3.3 High Resolution Dipole (e,e) Spectrometer

The high resolution (HR) dipole (e,e) spectrometer used to obtain both valence shell and inner shell electron energy-loss spectra in the discrete and near edge continuum regions was built in the early 1980's at UBC [106]. This instrument and the data acquisition procedures [106] were adapted in the early 1990's to provide absolute photoabsorption differential oscillator strength measurements [27, 46] at high resolution (0.05 eV fwhm) in the discrete and low energy continuum valence regions ( $\leq 50$  eV), and moderately high resolution (0.1 eV fwhm) in the discrete and near edge continuum regions of low energy inner shells (below 180 eV). The details of the design and construction of the high resolution dipole (e,e) spectrometer, shown schematically in figure 3.2, have been reported previously [106]. Therefore only a brief description will be given here.

The spectrometer consisted of four adjoining vacuum chambers housing the electron gun, electron beam monochromator, scattering (collision) chamber, and electron beam analyser. Each chamber was evacuated by a separate turbomolecular pump which maintained the base pressure at  $1-4 \times 10^{-7}$  torr. Various regions of the spectrometer were surrounded by hydrogen annealed mumetal to provide shielding from external magnetic fields. The electron beam was produced by a heated thoriated tungsten filament mounted in an oscilloscope electron gun body (Clifftronics CE5AH). The electron gun, which was comprised of the filament (cathode) (C), grid (G), anode (A) and focus (F) elements, was floated at a potential of -3 kV with respect to the collision chamber, which was at ground potential. The narrow ( $\sim 1$  mm) 3 keV energy electron beam, which had an approximate energy spread of 0.8 eV fwhm, was directed into the monochromator chamber where it was retarded by a two element deceleration lens ( $L_1$ ) and was admitted into the electron beam monochromator. The electron beam monochromator and analyser were partial hemispherical analysers with a mean radius of 19 cm that have been truncated in the direction perpendicular to the electron beam path. Side plates hold the truncated hemispheres in place and were biased with appropriate voltages to compensate for any field non-uniformity. Upon exiting the monochromator, the electron beam, which then had a much narrower energy spread, was re-accelerated by  $L_2$  and  $L_3$  to 3 keV and focused by  $L_4$  into the collision chamber (CC) where the beam was scattered off of the sample gas. The forward scattered electrons were refocused by  $L_5$ , decelerated by  $L_6$  and  $L_7$  and admitted in to the electron beam analyser which transmitted only the scattered electrons having a selected energy-loss to the detector. The transmitted electrons were detected by a channel electron multiplier (Mullard B419AL) and the signal was processed by an IBM compatible 80386 PC. The data acquisition and analysis programs were written by Dr G. Cooper.

The electron beam was defined by eight apertures ( $P_1$  to  $P_8$ ) and was guided by nine sets of quadrupole deflectors ( $Q_1$  to  $Q_9$ ). The lens system ( $L_1$  to  $L_7$ ) was designed to ac-

curately focus, to decelerate/accelerate and to transport the electron beam. In the valence shell region, below 60 eV, the electron monochromator and analyser were operated at a pass energy of 10 eV to obtain high resolution. Under these conditions the resolution of the unscattered electron beam, after passing through both the monochromator and analyser regions, was maintained at a resolution of 36 meV fwhm or better. This corresponded to a resolution of 48 meV, or better, for the inelastically scattered electron beam as measured on the  $1^1S \rightarrow 2^1P$  transition of helium. At higher energies, up to 500 eV, where the electron scattering cross-section has decreased significantly, the electron transmission of the monochromator and analyser was increased by using pass energies of 30 or 50 eV. The increase in electron transmission was obtained by sacrificing the spectrometer resolution. Operating at 30 eV pass energy the resolution of the scattered electron beam was 98 meV fwhm, or better, and at 50 eV pass energy the resolution was 150 meV fwhm, or better.

The high resolution spectra were recorded at pressures of  $1-1.5 \times 10^{-5}$  Torr with the background spectra recorded at one quarter of the full pressure. The absolute energy-loss scale was determined at high resolution by simultaneous admission of the sample gas and helium and referencing the spectral features of the sample to the  $1^1S \rightarrow 2^1P$  transition of helium at 21.218 eV [107]. The absolute energy scale for higher energy regions (the C and N K-shell spectra) was determined at high resolution by simultaneous admission of the sample gas and molecular nitrogen and referencing the spectral features of the sample to the  $N 1s \rightarrow \pi^* (v = 1)$  transition of  $N_2$  at 400.88 eV [70]. The calibration corrections were found to be very small, ranging from less than 25 meV in the valence shell to about 50 meV in the nitrogen K-shell region ( $\sim 400$  eV).

The Bethe-Born factor determined for the high resolution spectrometer [27, 46] was used to obtain the relative photoabsorption differential oscillator strength spectrum from the high resolution EELS spectrum. This relative spectrum was placed on an absolute scale by either single point normalization in the smooth continuum region to the absolute photoabsorption

spectrum recorded using the low resolution dipole (e,e) spectrometer or by normalization to an accurate value of the dipole polarizability of the molecule under study using the  $S(-2)$  sum-rule (see section 3.2 and chapter 4 below). The Bethe-Born factor of the high resolution spectrometer has not been determined for energies above 180 eV, and thus inner shell energy-loss spectra recorded above 180 eV (e.g. in the C 1s (300 eV) and N 1s (400 eV) regions) were converted into absolute photoabsorption differential oscillator strength spectra using the following procedure: The electron energy-loss spectra were converted into relative differential oscillator strength spectra by subtraction of a quadratic background function (to remove the contributions from the valence shell, preceding inner shells and any non-spectral background) followed by multiplication by an approximate Bethe-Born factor of the form  $E^{2.5}$ . The relative differential oscillator strength spectra were made absolute by normalization to the low resolution absolute differential oscillator strength spectrum in the pre-edge region, below any discrete structure arising from inner shell transitions. For example C 1s and N 1s inner shell spectra could be normalized near 285 and 395 eV, respectively, in their pre-edge regions where no sharp structures existed.

The accuracy of both the high (below 180 eV) and low resolution absolute photoabsorption differential oscillator strength data is estimated to be better than  $\pm 5\%$ . Above 180 eV the accuracy of the high resolution absolute photoabsorption differential oscillator strength data is estimated to be about  $\pm 10\%$ . An indication of the random errors in both the photoabsorption and photoionization results can be gained by examining the smoothness of the data in the continuum regions.

### 3.4 Photoelectron Spectrometer

The photoelectron spectrometer [108, 109] and the grasshopper grazing incidence monochromator [110] used to record the photoelectron spectral data of  $\text{CH}_3\text{F}$ ,  $\text{CH}_3\text{Cl}$  and  $\text{CH}_3\text{Br}$

(chapter 6) at the Canadian Synchrotron Radiation Facility (CSRF) at the Aladdin Storage Ring, University of Wisconsin, Madison, Wisconsin by Dr. G. Cooper, Dr. W. F. Chan and Dr. K. H. Tan, have been described in detail in previous publications [108–110].

Briefly, a grating with 1800 grooves/mm was used in the grasshopper monochromator, which, in combination with an Al window which was used to isolate the optical elements of the beam line from the high pressure interaction region, provided a usable photon energy range of 21–72 eV. The accuracy of the photon energy was considered to be  $\pm 0.2$  eV at 72 eV. The photoelectron spectrometer consisted of a gas cell plus a 36 cm mean radius McPherson electron energy analyser. This large analyser had both high transmission and high resolution ( $\Delta E/E=0.13\%$  fwhm) capabilities. The analyser was oriented on a frame such that the photon beam was directed across the length of the analyser entrance slit, and photoelectrons were taken from the gas cell and admitted into the analyser at a pseudo magic angle ( $\Theta=55.8^\circ$ ), calculated assuming a 90% polarization of the synchrotron light. This was done to eliminate the effects of the photoelectron asymmetry parameters,  $\beta$ , on the measured PE band intensities.

Binding energy spectra (obtained from electron kinetic energy analysis), measured as a function of photon energy, were obtained by scanning the voltages on the inner and outer analyser plates (i.e. no accelerating/decelerating lens system was used between the gas cell and the analyser). Since the electrons pass through the analyser with varying ejected kinetic energies from the sample gas, it was necessary to characterize the variation of the electron transmission through the analyser with electron kinetic energy. This was achieved by measuring PE spectra of the  $(2p)^{-1}$  band of neon at fixed ionizing photon energies of 26 and 40 eV. At each photon energy the electron kinetic energy through the analyser was varied over a series of spectra by changing the potential of the sample gas cell relative to the potential of the mean path of the analyser (which was kept fixed at ground potential for all spectra). In this way spectra of the  $(2p)^{-1}$  band of neon were obtained over the

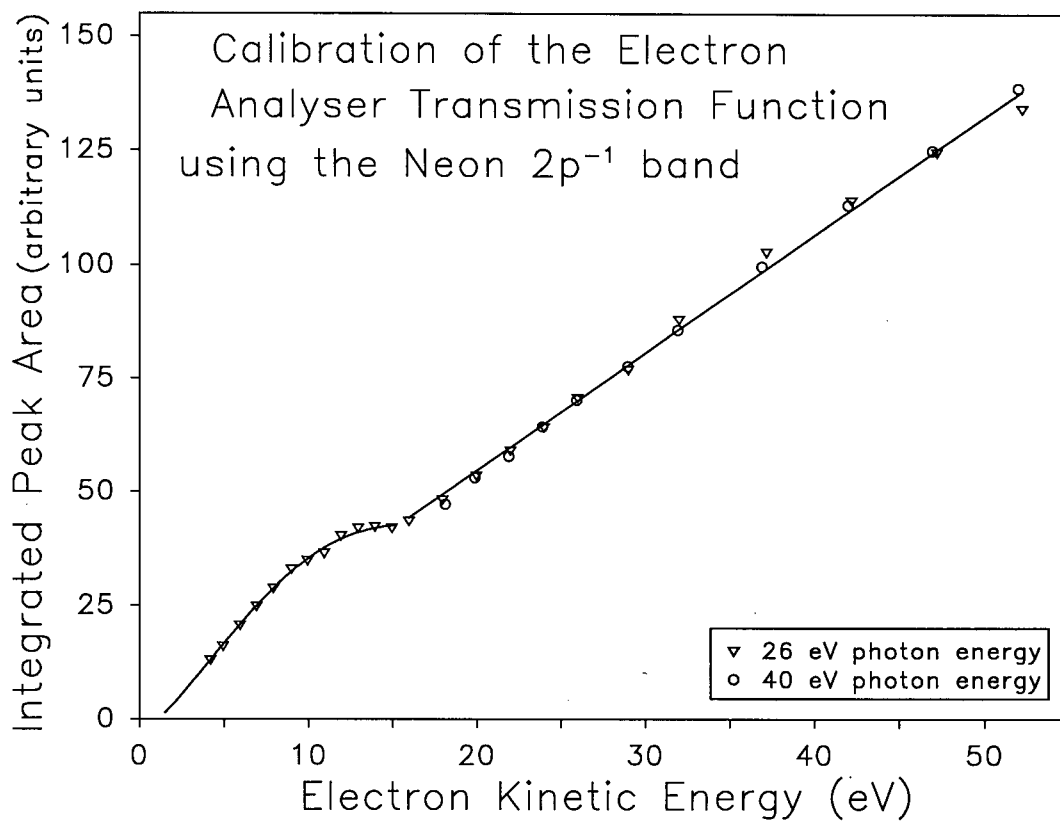


Figure 3.3: Electron analyser transmission calibration curve obtained using neon  $(2p)^{-1}$  ionization with 26 eV (inverted triangles) and 48 eV (circles) radiation.

electron kinetic energy ranges 3.5 to 52.5 eV at 26 eV photon energy, and 18.5 to 52 eV at 40 eV photon energy. The integrated intensity of the  $(2p)^{-1}$  band in each spectrum (after correcting for the variation in synchrotron light beam intensity during the measurements) was then taken as a direct relative measure of the variation in transmission of the analyser with electron kinetic energy (the energy of measurement being taken as that at the PE band maximum). The calibration curve (figure 3.3) shows that, except for some slight curvature at kinetic energies from 10 to 15 eV, the relationship between electron kinetic energy and analyser transmission was linear. In the region from 20 to 52 eV the calibration curves for the two sets of data ( $h\nu = 26$  and 40 eV) were linear and they had virtually the same slope (2.59 and 2.69). This analyser calibration curve was used to correct the intensities of the PE spectra for the methyl halides presented in chapter 6.

A position sensitive detector (Quantar Technology model #3395A) located at the exit focal plane of the electron analyser was used to collect the PE spectra. For each spectrum, the whole of the detector window was scanned across the entire measured PE spectrum. In this way, any effects arising from variations in the sensitivity of the detector across its width were eliminated from the spectra. The precise energy window of the detector was calibrated at several kinetic energies using the Auger electron spectrum of Xe [52]. This calibration spectrum was recorded at 2 to 3 day intervals over the 2 week data collection period at the CSRF during which the present data on the methyl halides were collected. The binding energy scales of the spectra were calibrated using previously reported ionization energies for the outermost  $(2e)^{-1}$  PE bands [111].

The total experimental energy resolution (electron energy analyser resolution plus photon monochromator bandwidth) for the PE spectra reported in the present work was limited essentially by the incident photon bandwidth, and was  $\sim 0.2$  eV at 21 eV photon energy, rising to  $\sim 0.5$  eV at 72 eV photon energy. Note that since many of the PE bands of the methyl halides are substantially broadened by vibrational structure and Jahn-Teller effects, better resolution (obtainable by closing the monochromator entry and exit slits, at the expense of light flux) would not have resulted in a significant improvement in separation of the bands. The spectra were therefore recorded under conditions that enabled a good signal/noise ratio, rather than very high resolution.

### 3.5 PIPICO Spectrometer

The PIPICO spectrometer [112] and grazing incidence monochromator [113] used by Dr. T. Ibuki and Dr. A. Hiraya to record the PIPICO spectra of BrCN at The Institute for Molecular Science (IMS) at the UVSOR synchrotron radiation storage ring have been described in detail elsewhere [112, 113].

Briefly, the PIPICO spectra of BrCN were measured using synchrotron radiation selected with a grazing incidence monochromator [113] and appropriate filters for reducing contributions from higher order radiation. The photon energy range was 40 to 130 eV. The PIPICO spectrometer [112] employs a TOFMS which is rotatable about the primary synchrotron radiation photon beam. In the present work the TOF tube was fixed at the magic angle with respect to the plane of the polarization vector of the incident light. BrCN vapour was admitted into the collision region (ambient pressure  $3 \times 10^{-7}$  torr). The autocorrelation (PIPICO) spectrum was obtained by feeding the TOFMS ion output pulses to both the start and the stop inputs of a time-to-amplitude converter. Ion pairs originating from dissociative multiple photoionization were identified according to their time-of-flight differences. The individual ion flight times were known from normal TOFMS measurements.

### 3.6 Sample Handling

The samples studied in the present work are listed in table 3.1 along with their commercial supplier and the stated sample purity. All gaseous samples were used without further purification. Liquid samples were degassed by several freeze-pump-thaw cycles before being admitted into the spectrometer. The solid sample of  $I_2$  was first purified by vacuum sublimation and then degassed by several freeze-pump-thaw cycles using a dry ice/methanol bath before being introduced into the spectrometer. Also, the solid sample of BrCN was degassed using several freeze-pump-thaw cycles using liquid nitrogen and then purified by bulb-to-bulb distillation under vacuum before being used. No residual air or sample impurities were observed in any of the TOF mass spectra or in the high resolution electron energy-loss spectra. The only detectable impurity in any of the PE spectra was a very small amount of  $N_2$  detected at a binding energy of 15.576 eV in the spectra of methyl fluoride.

Table 3.1: Purity of samples used in the present work.

Compound	Experiment	Sample State	Supplier	Stated Purity
CH <sub>3</sub> F	Dipole <sup>a</sup>	gas	Matheson Gas Products	99.0%
	PES	gas	Liquid Carbonic Specialty Gas Corporation	
CH <sub>3</sub> Cl	Dipole	gas	Matheson Gas Products	99.0%
	PES	gas	Liquid Carbonic Specialty Gas Corporation	
CH <sub>3</sub> Br	Dipole	gas	Matheson Gas Products	>99%
	PES	gas	Liquid Carbonic Specialty Gas Corporation	
CH <sub>3</sub> I	Dipole	liquid	BDH	>99%
BrCN	Dipole	solid	Aldrich Chemical Company	97%
	PIPICO	solid	Nacalai Tesque Company Limited (Japan)	97%

<sup>a</sup>Dipole indicates that the same sample was used for all dipole (e,e) and dipole (e,e+ion) experiments.

## Chapter 4

### Dipole Sum-Rules

#### 4.1 Introduction

Accurate sum-rule evaluation and the related determination of molecular properties for atomic and molecular systems requires, in principle, the entire differential dipole oscillator strength distribution [34,35]. However, direct absolute photoabsorption methods are typically restricted to rather narrow energy ranges because several different types of monochromators are needed to cover the visible, UV, VUV and X-ray regions of the spectrum. While in principle the results obtained using a series of monochromators to cover the wide spectral range could be combined, this has not been done in practice. As such there are no single atomic or molecular data sets covering the photoabsorption spectrum from the electronic excitation threshold out to continuum energies of at least several hundred eV, as is necessary for most sum-rules and for the accurate determination of molecular properties. Alternatively, absolute photoabsorption measurements above and below the first ionization potential, obtained using the conventional Beer Lambert law method and the double ion chamber method, respectively, could be combined. This, however, would suffer from difficulties in absolute number density and pathlength determinations, as well as from errors due to line saturation effects in the discrete region, as discussed above in chapter 1.

Dipole (e,e) spectroscopy [1, 9, 27, 28, 30] offers a versatile and accurate alternative to the use of optical photoabsorption techniques for determining absolute photoabsorption oscillator strength (cross-section) spectra. Many such dipole (e,e) measurements of high accuracy have

been made in recent years covering the valence shell discrete (for example see ref. [12, 27–30, 46, 48, 50, 51, 77, 84, 114–133]), and continuum regions (for example see ref. [1, 27, 28, 46, 84, 114, 115]) as well as inner shell (i.e. core) absolute spectra (for example see ref. [51, 77, 129–131]).

As has been noted above, the relative photoabsorption spectrum recorded using dipole (e,e) spectroscopy is readily made absolute using the VTRK sum-rule, removing the difficult requirements of number density (i.e. pressure) and pathlength determinations which are required in optical measurements. Furthermore, the dipole (e,e) method does not suffer from the difficulties of higher order radiation or stray light, which are problematic when using optical monochromators, or line saturation (i.e. linewidth/bandwidth) errors. Although the energy resolution available in dipole (e,e) spectroscopy (0.05 eV fwhm) is more modest than that available optically, particularly at lower photon energies [9], this is of little consequence for evaluation of sum-rules and determination of molecular properties. Note that, particularly in the discrete valence shell region, the relatively high resolution available using optical methods is optimal for separating closely spaced excited states and thus is the method of choice for such spectral (energy level) studies. However, as was discussed above, the determination of absolute photoabsorption differential oscillator strengths by such optical methods is problematic.

Absolute differential oscillator strength data can be critically evaluated by comparison with other experimental measurements or with theory where sufficiently accurate theoretical calculations are available. However, relatively few accurate calculations have been reported, mainly because of the difficulty of obtaining sufficiently accurate excited state wavefunctions. As a result the theoretical comparisons that can be made are restricted to considerations of a few more prominent discrete transitions in simple targets; for an example see ref. [28] for the case of  $N_2$ . Comparisons between different experiments are complicated in the discrete region by differences in resolution and also in some cases by bandwidth/linewidth interactions

which can result in significant errors where the data have been obtained by Beer-Lambert law photoabsorption methods. In the smooth continuum regions comparison of different experimental data sets is more straight-forward. If the oscillator strength spectrum extends from the first excitation threshold to a sufficiently high energy, application of the sum-rules to the experimental results allows a more global data assessment. For instance, the  $S(0)$  and  $S(-2)$  sum-rules have been used by Berkowitz [74] as a guide in the evaluation of existing photoabsorption data sets and by Meath *et al.* [11, 12, 134–141] to construct dipole oscillator strength distributions (DOSDs) from combinations of previously reported experimental and theoretical atomic and molecular data.

The correspondence between spectral sum-rules and molecular properties has stimulated considerable effort in theoretical [97, 142–146] and empirical (Emp) [147–151] sum-rule determination. The approach implemented by Meath [11, 12, 134–141, 152–156] involves sum-rule evaluation by constructing DOSDs from available, but limited energy range, molecular oscillator strength spectra and, where necessary, filling in the missing experimental gaps with summed experimental and/or theoretical atomic photoabsorption differential oscillator strengths or summed group oscillator strengths determined from mixture rules. This spectral reconstruction, for each system examined, involves discrete energy-regions which have been individually height-renormalized where necessary such that the spectrum, as a whole, satisfies sum-rule based constraints. For many atomic and molecular systems, these semi-empirical DOSDs were, for some time, the only source of “experimentally derived” sums. In contrast, the more recent availability of accurate absolute photoabsorption oscillator strength spectra measured with the dipole (e,e) method [1, 8, 27, 46] over a continuous wide energy range allows direct evaluation of the  $u \leq -1$  sum-rules without appeal to the empirical procedures involved in the DOSD approach. Prediction of the  $u \geq 0$  sums from the presently considered dipole (e,e) measurements, which were made below 500 eV (often only up to 200 eV) energy-loss, is unreliable because of the heavy weighting of the higher energy regions of the

oscillator strength distribution. However, for many of the systems considered here, the sums evaluated in the present work involving  $u \leq -1$  are the best available. Comparison with these presently determined sums provides a direct experimental assessment of the accuracy of the corresponding DOSD-based predictions.

Since dipole (e,e) spectroscopy avoids so many of the difficulties associated with direct wide range absolute photoabsorption measurements, it has been used extensively for the accurate determination of absolute photoabsorption spectra over wide energy ranges. As a result a substantial data base of atomic and molecular absolute photoabsorption spectra, determined by dipole (e,e) spectroscopy and estimated to have an overall accuracy of better than  $\pm 5\%$ , has now been published [12, 27–30, 46, 48, 50, 51, 77, 84, 114–133]. In this chapter the accuracy of this dipole (e,e) data is further evaluated using the S(-2) sum-rule. In addition the absolute photoabsorption oscillator strength spectra are used to evaluate molecular sum-rules and derive molecular and inter-molecular properties. Such an extensive collection of atomic and molecular oscillator strength spectra allows a detailed and systematic analysis of the normalization procedures and subsequent sum-rule determination. Also, the systems investigated in this chapter and chapter 5 span many important atomic and molecular series, for example: the noble gases (He, Ne, Ar, Kr, Xe), the n-alkane series (from CH<sub>4</sub> to C<sub>8</sub>H<sub>18</sub>), halogen substitutions (HCl, HBr, HI), (Cl<sub>2</sub>, Br<sub>2</sub>, I<sub>2</sub>), and (CH<sub>3</sub>F, CH<sub>3</sub>Cl, CH<sub>3</sub>Br, CH<sub>3</sub>I), freons (CF<sub>4</sub>, CF<sub>3</sub>Cl, CF<sub>2</sub>Cl<sub>2</sub>, CFCl<sub>3</sub>, CCl<sub>4</sub>), and common chemical solvents (H<sub>2</sub>CO, CH<sub>3</sub>CHO, (CH<sub>3</sub>)<sub>2</sub>CO, H<sub>2</sub>O).

An assessment of the accuracy of valence shell TRK sum-rule normalization, based on predicted static dipole polarizabilities via the S(-2) sum-rule, is presented in section 4.3.1 for previously published data [12, 27–30, 46, 48, 50, 51, 77, 84, 114–133] obtained for a large number of atoms and molecules using the dipole (e,e) method. Alternative normalizations using the S(-2) sum-rule and related procedures are discussed in section 4.3.2. The evaluation of the S(u) (u=-10 to -1) and L(u) (u=-6 to -1) sum-rules is discussed in section 4.3.3.

Finally, the importance of the sum-rules is illustrated by the calculation of normal Verdet constants and dipole-dipole dispersion energy coefficients in sections 4.3.4 and 4.3.5.

## 4.2 Experimental Background

The previously published absolute oscillator strength spectra [12, 27–30, 46, 48, 50, 51, 77, 84, 114–133] evaluated in the present work were obtained using dipole (e,e) spectroscopy at both high resolution and low resolution as described in chapter 3.

The absolute scale determinations for the low resolution relative photoabsorption oscillator strength spectra were, in most cases, made using the VTRK sum-rule (section 3.2). For H<sub>2</sub> [29] and the noble gases Ar, Kr and Xe [84], the absolute scales for both the low and high resolution oscillator strength spectra were obtained by single point normalization to previously reported absolute optical photoabsorption data. The accuracy of the absolute photoabsorption differential oscillator strength scale was estimated to be within  $\pm 5\%$  in the original publications. Note that errors of 10 to 20%, which occurred in a few earlier low resolution dipole (e,e) measurements, have been found to have been caused by interaction of certain sample gases with the oxide cathode of the electron gun. This affected the background subtraction procedure when using gases such as SiH<sub>4</sub>, C<sub>2</sub>H<sub>2</sub>, C<sub>2</sub>H<sub>4</sub>, and the freons. All of these earlier oscillator strength spectra [157–161] have now been re-measured [125, 126, 130, 132, 133] using a differentially pumped gun chamber [77] which has eliminated these problems. The re-measured data [125, 126, 130, 132, 133] for these targets are used in the present evaluations and sum-rule determinations.

For the present evaluations almost all sum-rule analyses performed on an oscillator strength spectrum which is a combination of the high resolution data in the valence discrete and near edge continuum regions with the low resolution data in the smooth continuum at higher energies when both sets of data are available. The two spectra are matched in the

smooth valence shell continuum region where the data sets overlap (typically between 15 and 25 eV). The resulting long-range spectrum usually extends to  $\sim 200$  eV. In the lower energy discrete valence shell region of the spectrum the more detailed spectra produced at high resolution provide the most accurate integrals particularly for the  $u \leq -1$  sum-rules. For  $\text{H}_2\text{S}$  [119] and  $\text{PH}_3$  [131] the sum-rule calculations are performed on low resolution spectra because high resolution dipole (e,e) measurements are not available. For  $\text{H}_2$ , HD, and  $\text{D}_2$  the recent high resolution measurements [29, 116] from the electronic absorption threshold to 60 eV were sufficient for the sum-rule calculations. Chan *et al.* [29] have earlier reported high resolution dipole (e,e) measurements for  $\text{H}_2$  over the limited energy range 10.5 to 20.8 eV and these results are in good agreement with the more recent wider range measurements [116].

### 4.3 Results and Discussion

#### 4.3.1 Static dipole polarizabilities, the S(-2) sum-rule and the evaluation of VTRK sum-rule normalization

The accuracy of absolute differential oscillator strength scales determined using the VTRK sum-rule can be assessed by comparison of the static dipole polarizability obtained from equation (3.4) with published experimental or theoretical values of  $\alpha_\infty$ . Theoretical and experimental values of the static dipole polarizability are available for a wide range of atoms and molecules. Several sources [162–166] of experimental refractivities and polarizabilities are available. The compilation by Washburn [162] lists reliable dynamic refractive indices ( $n_\lambda$ ) at several wavelengths for some common atomic and molecular gases. The compilations by Stuart [163] and by Maryott and Buckley [164] contain static dipole polarizabilities ( $\alpha_\infty$ ) which have been obtained from both refractive index and dielectric constant measurements. In some cases the static dipole polarizabilities derived from extrap-

olation of refractive index (i.e. optical) measurements as a function of wavelength ( $n_\lambda$ ) are slightly higher than values reported elsewhere because of incomplete extrapolation to the static limit ( $\lambda \rightarrow \infty$ ). A compilation by Miller [166] considers polarizabilities from several sources including the above compilations [163, 164] and lists those values considered to be the most accurate for about 400 compounds. The experimental refractive index measurements reported by Watson [167] and Ramaswamy [168] and the polarizability measurements of Hohm *et al.* [102–105, 151, 169, 170] provide very reliable values of static [167, 168] and dynamic [103–105, 151, 169, 170] polarizabilities. Considerable attention has been focused on the calculation of static polarizabilities [171–188]. In particular, finite-field calculations [171–181], have provided such values for many small systems. The calculated polarizabilities are generally accurate to within 10% of the more reliable experimental values. Dipole polarizabilities derived from DOSD semi-empirical procedures [11, 12, 134–141, 152–156] are also available for many atomic and molecular systems. Finally, additivity methods provide an alternative and reasonably reliable [166] source of static dipole polarizabilities. Such methods can be used to estimate dipole polarizabilities for almost any molecule. Recently Kang and Jhon [189] and Miller [166] have furthered the use of atomic and bond additivity methods by employing an atomic hybrid additivity method which considers the static polarizability of both the individual atom and the atomic environment with respect to hybridization.

The  $S(-2)$  sum-rule, equation (3.4), has been used to obtain values of the static dipole polarizability ( $\alpha_\infty$ ) from the dipole (e,e) oscillator strength spectra [12, 27–30, 46, 48, 50, 51, 77, 84, 114–133] reported earlier from this laboratory. These values are listed in column 2 of table 4.1 for each atom and molecule studied. It can be seen that these “experimentally” derived static dipole polarizabilities are in almost all cases in excellent agreement with the more reliable and highly consistent experimental [103–105, 151, 162–165, 167–170, 183, 190–197] and theoretical [171–185, 187, 188] values and also compare well with DOSD [11, 12, 134–141, 152–156] and additivity [166] data.

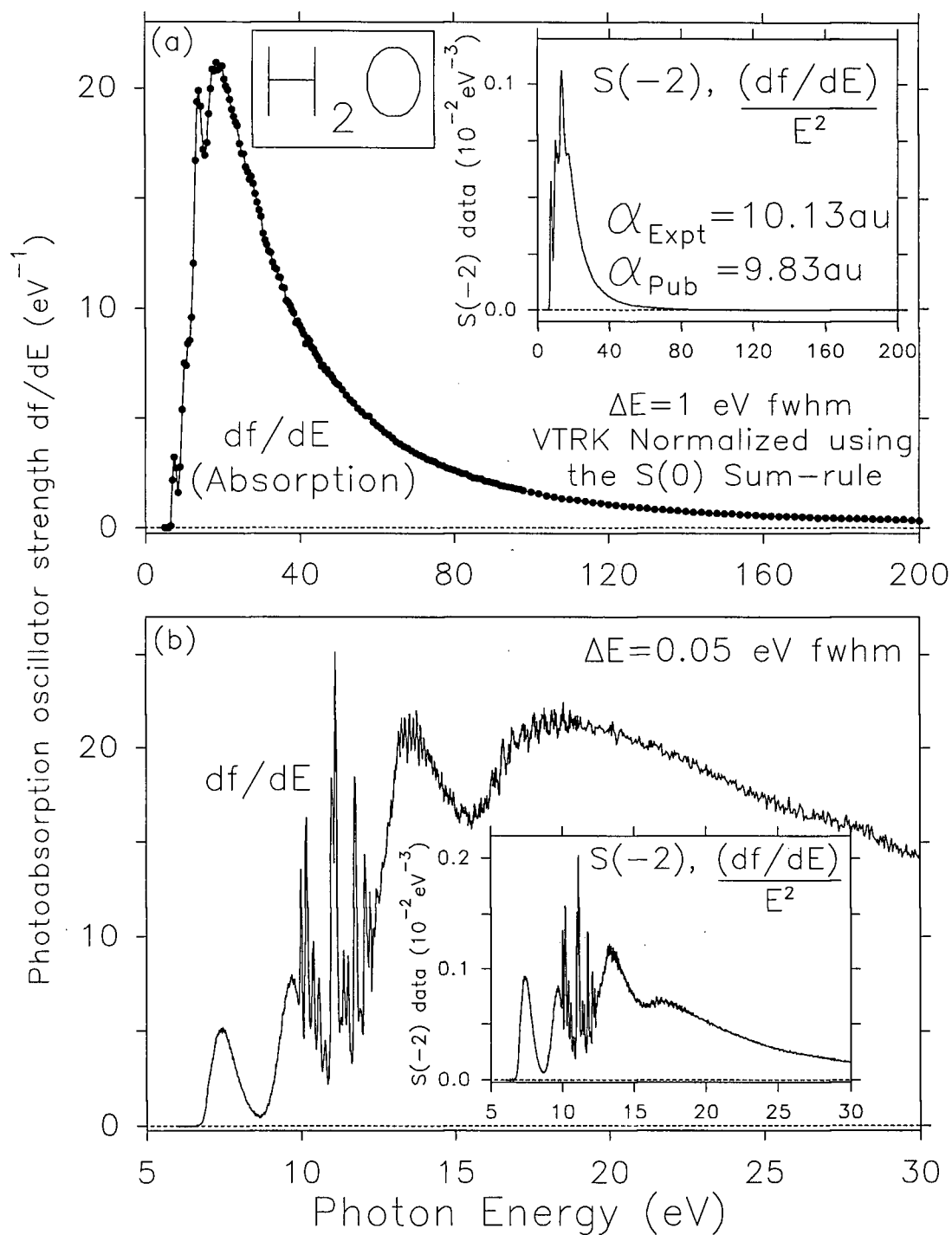


Figure 4.1: Absolute photoabsorption oscillator strength spectrum of water [117]. The upper panel (a) shows the low resolution (1 eV fwhm) oscillator strength spectrum (0 to 200 eV) which was VTRK normalized using the  $S(0)$  sum-rule. The inset shows the  $S(-2)$  spectrum,  $(df/dE)/E^2$ , of water, which gives a static dipole polarizability of 10.13 au. The lower panel (b) shows the high resolution (0.05 eV fwhm) spectrum from 5 to 30 eV and the corresponding  $S(-2)$  spectrum (inset).

Figure 4.1 shows typical long-range low resolution (upper panel) and high resolution (lower panel) dipole (e,e) VTRK (i.e.  $S(0)$ ) normalized spectra in the case of  $\text{H}_2\text{O}$  [117]. The inset in the upper panel shows the  $S(-2)$  analysis giving an experimental value of  $\alpha_\infty$  within 3% of the published value [163,164]. Similar results for  $\text{SiH}_4$  [130] are shown in figure 4.2, where agreement between the  $S(-2)$  experimental value and the published static dipole polarizability [163,167] is better than 1%.

The static dipole polarizabilities obtained from the oscillator strength spectra of the noble gases [27, 46, 84] and  $\text{H}_2$  [29] are within 3.4% of the other experimental values (note that the spectra of Ar, Kr, and Xe [84] and  $\text{H}_2$  [29] were single point normalized to reliable absolute photoabsorption spectra rather than using the VTRK sum-rule). The static dipole polarizabilities obtained from VTRK normalized dipole (e,e) spectra are within  $\pm 5\%$  of the published values for all cases in table 4.1 except for  $\text{CCl}_4$  [51] and  $\text{SiF}_4$  [77] which differ by 10 and 20%, respectively. These larger errors can be traced to errors caused by the fitting and extrapolation procedures used in the original VTRK normalization due to the presence of the Cooper minimum for  $\text{CCl}_4$  and the presence of the valence shell continuum shape resonance and the Si 2p inner shell for  $\text{SiF}_4$  (for further discussion see section 4.3.2 below). With the above exceptions the static dipole polarizabilities derived from the measured oscillator strength spectra are generally slightly lower (but within 3%) than the literature values in all but five cases (He, Ar,  $\text{H}_2\text{O}$ ,  $\text{N}_2\text{O}$ ,  $\text{C}_2\text{H}_2$ ) where they are up to 3% higher. Systematic underestimation of the correction for Pauli excluded transitions could account for the consistently low  $S(-2)$  values. However, this is unlikely to be the main contributing factor and it is more likely that the high energy portion of the extrapolated oscillator strength spectrum is being slightly overestimated by the extrapolation of the fitted polynomial, leading to a systematically low differential oscillator strength scale and thus a somewhat lower derived

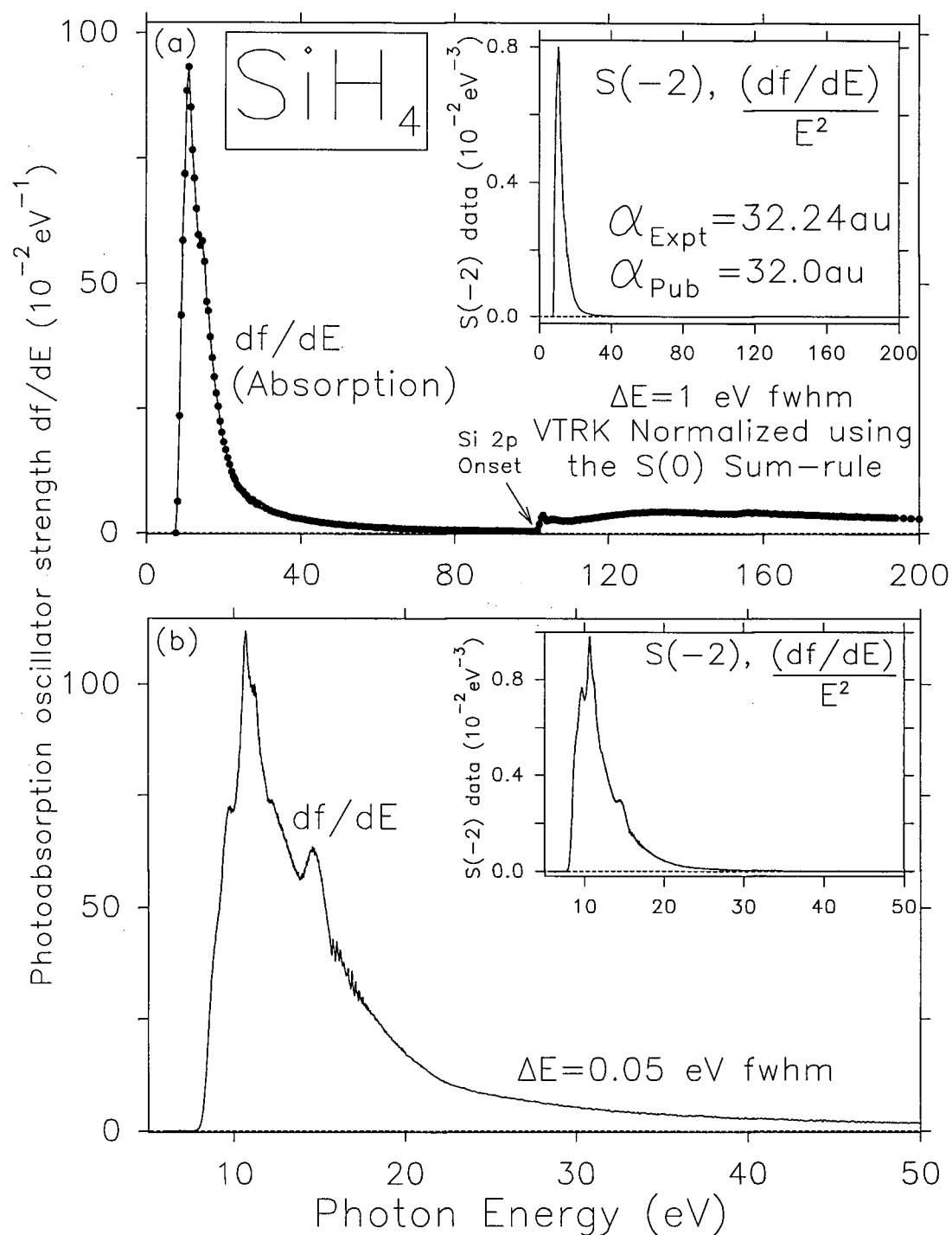


Figure 4.2: Absolute photoabsorption oscillator strength spectrum of silane [130]. The upper panel (a) shows the low resolution (1 eV fwhm) oscillator strength spectrum (0 to 200 eV) which was VTRK normalized using the  $S(0)$  sum-rule. The inset shows the  $S(-2)$  spectrum,  $(df/dE)/E^2$ , of silane, which gives a static dipole polarizability of 32.24 au. The lower panel (b) shows the high resolution (0.05 eV fwhm) spectrum from 5 to 50 eV and the corresponding  $S(-2)$  spectrum (inset).

static dipole polarizability. Although in some earlier studies fitting functions of the form

$$df/dE = AE^{-B} \quad (4.1)$$

and

$$df/dE = AE^{-1.5} + BE^{-2.5} + CE^{-3.5} \quad (4.2)$$

have been used, the polynomial shown in equation (3.2) has generally been found to be even more satisfactory in that it provides a better fit over a wider energy region of the monotonically decreasing ionization continuum at higher energies. However, based on the above sum-rule analysis it seems likely that the polynomial given in equation (3.2) decays slightly too slowly with energy.

The accuracy estimates of the differential oscillator strength scales in the original publications are supported by the fact that the static dipole polarizabilities determined from VTRK sum-rule normalized photoabsorption oscillator strength spectra obtained with the dipole (e,e) method generally agree with the experimentally determined values to better than  $\pm 5\%$  on average. Conversely, this shows that accurate predictions of the dipole polarizability can be obtained from the long-range absolute dipole oscillator strength spectra recorded using dipole (e,e) spectroscopy and normalized using the VTRK sum-rule.

The utility of a comparison of static dipole polarizabilities derived using the S(-2) sum-rule on a photoabsorption spectrum with published experimental polarizability values is demonstrated by the case of CO. The S(-2) evaluation of the absolute photoabsorption spectrum of CO [30] suggests that there are small errors in the published absolute differential oscillator strength data: Static dipole polarizabilities obtained using the S(-2) sum-rule on the combination of the high and low resolution spectra and on only the low resolution spectrum of CO [30] differ by 10%. By a comparison of the contributions to the total S(-2) sum from various regions of the high and low resolution spectra it has been determined that the two spectra differ only below 18 eV, the low resolution spectrum having a small shape

error in this region. This small difference, while being difficult to detect by a comparison of the un-weighted photoabsorption spectra, is readily apparent when the  $E^{-2}$  weighting is applied to the spectra. The incorrect shape and the associated underestimation of the relative differential oscillator strengths at energies below 18 eV in the low resolution spectrum caused a small error in the VTRK sum-rule normalization in the originally published data, resulting in a small over-estimation of the differential oscillator strengths as quoted in tables 1 to 5 of reference [30]. In the present work this error has been eliminated by combining the high resolution data below 18 eV with the low resolution data from 18 to 200 eV. The resulting spectrum, which now has the correct relative shape in all energy regions, has been VTRK normalized using the same fitting procedure and Pauli excluded correction as in the original publication [30]. The renormalized spectrum gives a static dipole polarizability of 13.70 au which is, on average, only 4% higher than the published experimental values [163, 164, 167, 194]. As a result of the new normalization, the low resolution differential oscillator strength data given in table 1 of reference [30] and the high resolution oscillator strength data given in tables 2 to 5 of reference [30] should be decreased by 2.5%. Also, the low resolution data given in table 1 of reference [30] below 18 eV should be disregarded. The 2.5% decrease in the oscillator strengths measured by Chan *et al.* [30] means that the renormalized data are in even better agreement with the most accurate theoretical oscillator strengths [198].

Table 4.1: Static dipole polarizability values derived from absolute photoabsorption oscillator strengths measured by dipole (e,e) spectroscopy, compared with values obtained from experiment and theory.

	Static dipole polarizability (a.u.), $\alpha_\infty$						
	Experiment				Theory	Additivity <sup>b</sup>	
	From Dipole (e,e) This Work <sup>a</sup>	From Refractive Index		From Dielectric Constant			From DOSD
He	1.407 [27]	1.384 <sup>c</sup> 1.383 <sup>e</sup>	1.39 <sup>d</sup>	1.395 <sup>c</sup> 1.383 <sup>f</sup>		1.383 <sup>c</sup> 1.385 <sup>g</sup>	
Ne	2.571 [46]	2.663 <sup>c</sup>	2.75 <sup>d</sup>	2.670 <sup>f</sup>	2.669 <sup>h</sup> 2.670 <sup>i</sup>	2.719 <sup>g</sup> 2.698 <sup>j</sup>	
Ar	11.23 [84]	11.08 <sup>c</sup> 11.1 <sup>d</sup>	11.075 <sup>e</sup>	11.07 <sup>c</sup> 11.075 <sup>f</sup> 11.07 <sup>k</sup>	11.08 <sup>h</sup> 11.08 <sup>i</sup>	11.12 <sup>g</sup>	
Kr	16.86 [84]	16.73 <sup>c</sup>	16.8 <sup>d</sup>	16.765 <sup>f</sup>	16.79 <sup>h</sup> 16.78 <sup>i</sup>	17.08 <sup>l</sup>	
Xe	27.03 [84]	27.29 <sup>c</sup> 27.124 <sup>n</sup>	27.13 <sup>d</sup>	27.1 <sup>m</sup>	27.16 <sup>h</sup> 27.11 <sup>i</sup>	27.76 <sup>l</sup>	
H <sub>2</sub>	5.314 [29, 116]	5.444 <sup>d</sup> 5.33 <sup>k</sup>	5.427 <sup>e</sup> 5.420 <sup>q</sup>		5.428 <sup>o</sup> 5.450 <sup>r</sup> 5.428 <sup>s</sup>	5.414 <sup>p</sup> 5.429 <sup>p</sup> 5.327 <sup>t</sup>	5.20 5.26
D <sub>2</sub>	5.285 [116]	5.368 <sup>e</sup>				5.278 <sup>p</sup> 5.229 <sup>t</sup>	
HD	5.336 [116]					5.382 <sup>p</sup> 5.283 <sup>t</sup>	
N <sub>2</sub>	11.54 [28]	11.74 <sup>d</sup> 11.76 <sup>v</sup>	11.744 <sup>e</sup> 11.76 <sup>w</sup>	11.69 <sup>f</sup> 11.69 <sup>k</sup>	11.74 <sup>o</sup>	11.675 <sup>u</sup> 11.367 <sup>x</sup> 11.87 <sup>y</sup>	12.89 13.09
O <sub>2</sub>	10.54 [115, 118]	10.6 <sup>d</sup> 10.8 <sup>k</sup>	10.670 <sup>e</sup> 10.566 <sup>q</sup>		10.59 <sup>o</sup>		7.69 9.99
CO	13.70 [30]	13.1 <sup>d</sup> 13.08 <sup>w</sup>	13.1 <sup>k</sup> 13.2 <sup>k</sup>	13.1 <sup>m</sup>	13.089 <sup>z</sup> 13.08 <sup>aa</sup>	13.080 <sup>x</sup>	12.48 13.09
NO	11.46 [48, 121]	11.5 <sup>d</sup>	11.5 <sup>k</sup>	11.5 <sup>m</sup>	11.52 <sup>o</sup> 11.518 <sup>bb</sup>		10.80 11.07
CO <sub>2</sub>	16.92 [123]	17.5 <sup>d</sup> 17.79 <sup>f</sup>	17.6 <sup>k</sup> 17.5 <sup>v</sup>	17.5 <sup>m</sup>	17.51 <sup>cc</sup> 17.556 <sup>ee</sup>	17.63 <sup>dd</sup>	16.33 17.95

Table 4.1: (continued) Static dipole polarizability values derived from absolute photoabsorption oscillator strengths measured by dipole (e,e) spectroscopy, compared with values obtained from experiment and theory.

	Static dipole polarizability (a.u.), $\alpha_\infty$						
	Experiment				Theory	Additivity <sup>b</sup>	
	From Dipole (e,e) This Work <sup>a</sup>	From Refractive Index		From Dielectric Constant			From DOSD
N <sub>2</sub> O	20.23 [114]	19.7 <sup>d</sup> 20.2 <sup>k</sup>	19.7 <sup>k</sup> 19.7 <sup>m</sup>	20.9 <sup>m</sup>	19.70 <sup>o</sup>	17.61 17.14	
H <sub>2</sub> O	10.13 [117]	9.82 <sup>ff</sup>	9.82 <sup>k</sup>	9.81 <sup>m</sup> 9.85 <sup>m</sup>	9.642 <sup>o</sup>	9.64 <sup>gg</sup> 9.45 <sup>hh</sup> 9.0658 <sup>x</sup>	9.52 9.52
H <sub>2</sub> S	24.50 [119]	25.51 <sup>k</sup> 24.7 <sup>ii</sup>	24.3 <sup>k</sup>	24.7 <sup>m</sup> 26.6 <sup>m</sup>		24.26 <sup>hh</sup>	25.44 25.51
CH <sub>4</sub>	16.52 [124]	17.3 <sup>d</sup> 17.3 <sup>m</sup>	17.1 <sup>k</sup> 17.257 <sup>kk</sup>	17.5 <sup>m</sup>	17.27 <sup>jj</sup>	16.361 <sup>x</sup> 16.50 <sup>hh</sup>	17.61 17.48
C <sub>2</sub> H <sub>2</sub>	23.53 [125]	22.9 <sup>d</sup> 22.5 <sup>k</sup>	22.3 <sup>k</sup> 22.7 <sup>v</sup>	26.5 <sup>m</sup>	22.96 <sup>ll</sup>	22.449 <sup>x</sup> 22.52 <sup>mm</sup>	22.54 22.47
C <sub>2</sub> H <sub>4</sub>	28.26 [126]	27.66 <sup>d</sup> 28.788 <sup>kk</sup>	28.7 <sup>k</sup>	28.8 <sup>m</sup>	27.70 <sup>nn</sup>	27.29 <sup>oo</sup>	28.68 28.68
C <sub>2</sub> H <sub>6</sub>	28.52 [124]	29.61 <sup>d</sup> 30.2 <sup>k</sup>	29.7 <sup>k</sup> 29.558 <sup>kk</sup>	29.9 <sup>m</sup> 29.6 <sup>m</sup>	29.61 <sup>pp</sup>		29.96 29.89
C <sub>3</sub> H <sub>8</sub>	39.96 [124]	42.08 <sup>d</sup> 42.0 <sup>k</sup>	42.0 <sup>k</sup> 42.927 <sup>kk</sup>		42.09 <sup>pp</sup>		42.38 42.31
C <sub>4</sub> H <sub>10</sub>	51.88 [124]	54.04 <sup>d</sup> 54.044 <sup>kk</sup>	54.8 <sup>k</sup>	55.3 <sup>m</sup>	54.07 <sup>pp</sup>		54.73 54.80
C <sub>5</sub> H <sub>12</sub>	64.64 [124]	67.1 <sup>k</sup>	65.0 <sup>k</sup>	67.4 <sup>m</sup>	66.07 <sup>pp</sup>		67.15 67.21
C <sub>6</sub> H <sub>14</sub>	77.25 [124]	79.49 <sup>k</sup>	78.4 <sup>k</sup>	80.1 <sup>m</sup>	78.04 <sup>pp</sup>		79.50 79.63
C <sub>7</sub> H <sub>16</sub>	89.67 [124]	91.84 <sup>k</sup>	90.1 <sup>k</sup>	92.4 <sup>m</sup>	90.02 <sup>pp</sup>		91.91 92.05
C <sub>8</sub> H <sub>18</sub>	100.7 [124]	104.2 <sup>k</sup>	103 <sup>k</sup>	107 <sup>m</sup>	102.0 <sup>pp</sup>		104.3 104.5
CH <sub>3</sub> OH	20.79 [50]	21.8 <sup>k</sup>		21.8 <sup>k</sup> 22.2 <sup>m</sup>			21.59 21.93

Table 4.1: (continued) Static dipole polarizability values derived from absolute photoabsorption oscillator strengths measured by dipole (e,e) spectroscopy, compared with values obtained from experiment and theory.

	Static dipole polarizability (a.u.), $\alpha_\infty$						
	Experiment				Theory	Additivity <sup>b</sup>	
	From Dipole (e,e) This Work <sup>a</sup>	From Refractive Index		From Dielectric Constant			From DOSD
HCHO	18.69 [127]	16.5 <sup>k</sup>	16.5 <sup>k</sup>	< 18.7 <sup>m</sup>		17.630 <sup>x</sup> 16.0 <sup>qq</sup>	18.15 18.08
CH <sub>3</sub> CHO	28.87 [128]	31.0 <sup>k</sup>		< 31.0 <sup>m</sup>			32.53 31.99
(CH <sub>3</sub> ) <sub>2</sub> CO	41.14 [128]			42.7 <sup>k</sup> < 43.3 <sup>m</sup>			42.92 42.72
HCl	16.97 [122]	17.75 <sup>k</sup> 17.4 <sup>ff</sup>	17.4 <sup>k</sup>	17.4 <sup>m</sup>	17.39 <sup>h</sup>	16.86 <sup>hh</sup> 17.24 <sup>uu</sup>	18.22 18.15
CF <sub>4</sub>	19.06 [132]	19.5 <sup>d</sup>	19.5 <sup>k</sup>	19.1 <sup>m</sup>			15.80 20.54
CF <sub>3</sub> Cl	31.99 [132]						28.82 34.11
CF <sub>2</sub> Cl <sub>2</sub>	42.99 [132]	42.8 <sup>k</sup>					42.40 46.44
CFCl <sub>3</sub>	53.52 [132]	55.6 <sup>k</sup>					56.03 58.79
CCl <sub>4</sub>	67.5 [51]	70.9 <sup>ss</sup>	69.0 <sup>k</sup>	69.0 <sup>k</sup>			69.64 71.05
NH <sub>3</sub>	14.19 [120]	15.2 <sup>k</sup> 14.6 <sup>d</sup>	14.8 <sup>k</sup> 14.6 <sup>ff</sup>	14.2 <sup>m</sup>	14.56 <sup>tt</sup> 14.56 <sup>o</sup>	14.43 <sup>hh</sup> 13.563 <sup>x</sup>	14.37 14.44
NH <sub>2</sub> CH <sub>3</sub>	25.33 [12]	26.46 <sup>ss</sup>	26.75 <sup>k</sup>	27.5 <sup>m</sup>	26.50 <sup>uu</sup>		26.72 28.02
NH(CH <sub>3</sub> ) <sub>2</sub>	36.76 [12]	30.39 <sup>k</sup>	39.06 <sup>k</sup>	40.4 <sup>m</sup>	38.70 <sup>uu</sup>		39.07 40.79
N(CH <sub>3</sub> ) <sub>3</sub>	47.75 [12]	51.9 <sup>k</sup>			49.90 <sup>uu</sup>		51.49 53.67
SiH <sub>4</sub>	32.24 [130]	31.97 <sup>d</sup>		36.7 <sup>m</sup> 36.7 <sup>m</sup>		31.66 <sup>hh</sup>	
PH <sub>3</sub>	28.59 [131]			28.9 <sup>m</sup> 30.93 <sup>hh</sup>		30.57 <sup>hh</sup>	18.21 19.05

Table 4.1: (continued) Static dipole polarizability values derived from absolute photoabsorption oscillator strengths measured by dipole (e,e) spectroscopy, compared with values obtained from experiment and theory.

	Static dipole polarizability (a.u.), $\alpha_\infty$					
	Experiment				Theory	Additivity <sup>b</sup>
	From Dipole (e,e) This Work <sup>a</sup>	From Refractive Index	From Dielectric Constant	From DOSD		
PF <sub>3</sub>	29.79 [133]					16.37 21.81
PF <sub>5</sub>	26.64 [133]	24.6 <sup>k</sup>	25.7 <sup>m</sup>			
PCl <sub>3</sub>	71.76 [133]	69.6 <sup>k</sup>				57.2 58.8

<sup>a</sup>Derived in the present work from previously published absolute dipole (e,e) photoabsorption oscillator strength spectra using the S(-2) sum-rule; see text for details.

<sup>b</sup>Miller [166] additivity methods, first entry is ahp method and second entry is the ahc method, see reference for details.

<sup>c</sup>Teachout and Pack [165] compilation. <sup>d</sup>Watson and Ramaswamy [167]. <sup>e</sup>Newell and Baird [190]. <sup>f</sup>Orcutt and Cole [191]. <sup>g</sup>Woon and Dunning [182]. <sup>h</sup>Kumar and Meath [139]. <sup>i</sup>Leonard and Barker [153]. <sup>j</sup>Maroulis and Thakkar [173]. <sup>k</sup>Stuart's compilation [163] in Landolt-Bornstein. <sup>l</sup>Maroulis and Thakkar [172]. <sup>m</sup>Maryott and Buckley [164] compilation. <sup>n</sup>Hohm and Trümper [169]. <sup>o</sup>Zeiss *et al.* [134]. <sup>p</sup>Kolos and Wolniewicz [183]. <sup>q</sup>Hohm and Kerl [104]. <sup>r</sup>Victor and Dalgarno [152]. <sup>s</sup>Gerhart [154]. <sup>t</sup>Ishiguro *et al.* [188]. <sup>u</sup>Maroulis and Thakkar [171]. <sup>v</sup>Alms *et al.* [192] extrapolated from RI measurements [193]. <sup>w</sup>Oddershede and Svendsen [194] extrapolated from RI measurements of [162]. <sup>x</sup>Sauer and Oddershede [185]. <sup>y</sup>Archibong and Thakkar [181]. <sup>z</sup>Parker and Pack [149]. <sup>aa</sup>Kumar and Meath [141]. <sup>bb</sup>Nielson *et al.* [156]. <sup>cc</sup>Jhanwar and Meath [137]. <sup>dd</sup>Maroulis and Thakkar [174]. <sup>ee</sup>Pack [150]. <sup>ff</sup>Cuthbertson and Cuthbertson [199]. <sup>gg</sup>Maroulis [177]. <sup>hh</sup>Dougherty and Spackman [184]. <sup>ii</sup>Frivold *et al.* [200]. <sup>jj</sup>Thomas and Meath [135]. <sup>kk</sup>Hohm [151]. <sup>ll</sup>Kumar and Meath [140]. <sup>mm</sup>Maroulis and Thakkar [175]. <sup>nn</sup>Jhanwar *et al.* [138]. <sup>oo</sup>Maroulis [178] calculation. <sup>pp</sup>Jhanwar *et al.* [136]. <sup>qq</sup>Alkorta *et al.* [187]. <sup>rr</sup>Sadlej [186]. <sup>ss</sup>Ramaswamy [168]. <sup>tt</sup>Burton *et al.* [11]. <sup>uu</sup>Burton *et al.* [12].

### 4.3.2 Normalization of photoabsorption spectra using the $S(-2)$ sum-rule and dipole polarizabilities

Relative photoabsorption spectra may be normalized using dipole polarizabilities instead of using the TRK sum-rule or single point normalization on an absolute photoabsorption value. Static dipole polarizabilities may be used for normalization by the use of equation (3.4) or, alternatively, a value of the dynamic polarizability at any wavelength may be used with equation (3.6) to yield the absolute scale. The latter approach avoids any uncertainty in the extrapolation procedure needed to determine  $\alpha_\infty$  from  $\alpha_\lambda$ . In addition it means that an absolute scale can be determined even if an accurate value of  $\alpha_\lambda$  (i.e.  $n_\lambda$ ) is available only at a single wavelength. Furthermore, the normalization of a relative oscillator strength spectrum using an accurate value of either the static or dynamic dipole polarizability avoids errors in the absolute scale that can be caused by Pauli excluded correction estimates or the fitting and the extrapolation of the valence shell continuum to infinite energy needed when using VTRK sum-rule normalization. This is because the  $E^{-2}$  energy-weighting of the spectrum means that the contribution to  $S(-2)$  from spectral oscillator strength above  $\sim 50$  eV is negligible and thus the corrections for the Pauli excluded transitions and the valence shell tail are no longer required. The effectiveness of such  $S(-2)$  normalization procedures will, of course, depend on the accuracy of the value of  $\alpha_\infty$  or  $\alpha_\lambda$  used. Table 4.1 shows that variations of  $\pm 5\%$  or more in some less favorable cases occur in the published experimental, theoretical and semi-empirical values of the static dipole polarizability, and this would affect the differential oscillator strength scales accordingly.

As was noted in section 3.2, spectral features can interfere with the VTRK normalization procedure. Dipole polarizability normalization is quite useful for these situations where the TRK sum-rule cannot be applied. Such situations include:

- (a) The presence of Cooper minima, as in Ar [84] and  $\text{Cl}_2$  [129], or shape resonances, as in

SF<sub>6</sub> [80] SiF<sub>4</sub> [77] and CH<sub>3</sub>I (see section 5.6.1), in the ionization continuum [34].

- (b) The existence of one or more low-energy inner shell spectra which limit the energy range available for curve fitting of the valence shell continuum. For example, in the case of CH<sub>3</sub>I (see section 5.6.1) the I 4d discrete transitions and large continuum resonance restrict any valence shell curve fit to the region below ~50 eV, which is insufficient for accurate curve fitting and extrapolation.
- (c) Where relative photoabsorption data are available only over a limited range at lower photon energies. This is not uncommon, for example, in direct photoabsorption experiments which use monochromated synchrotron radiation as the light source. In such situations the usable range and upper energy limit of various types of VUV and soft X-ray monochromators are typically restricted. Such limitations are also often imposed by filters used to suppress the higher order radiation present in grating monochromators.
- (d) Where no estimates for the contributions from Pauli excluded transitions are available - for example for molecules containing 5<sup>th</sup> row atoms.

In these situations published values of the static dipole polarizability, shown in table 4.2, or dynamic dipole polarizabilities [162, 167, 168, 199] are required. The application of an S(-2) normalization procedure to optical data would eliminate the need for the absolute pressure and pathlength determinations required in the Beer-Lambert law experimental method. To the best of our knowledge, although dipole (e,e) data are available over a very wide energy range, to date, no single optical photoabsorption data set exists over a sufficient range for dipole polarizability normalization. However, data from different optical photoabsorption measurements (i.e. Beer-Lambert law measurements in the discrete region plus double ion chamber measurements in the continuum region, etc.) could, in principle, be combined and normalized or re-normalized using a static or dynamic polarizability.

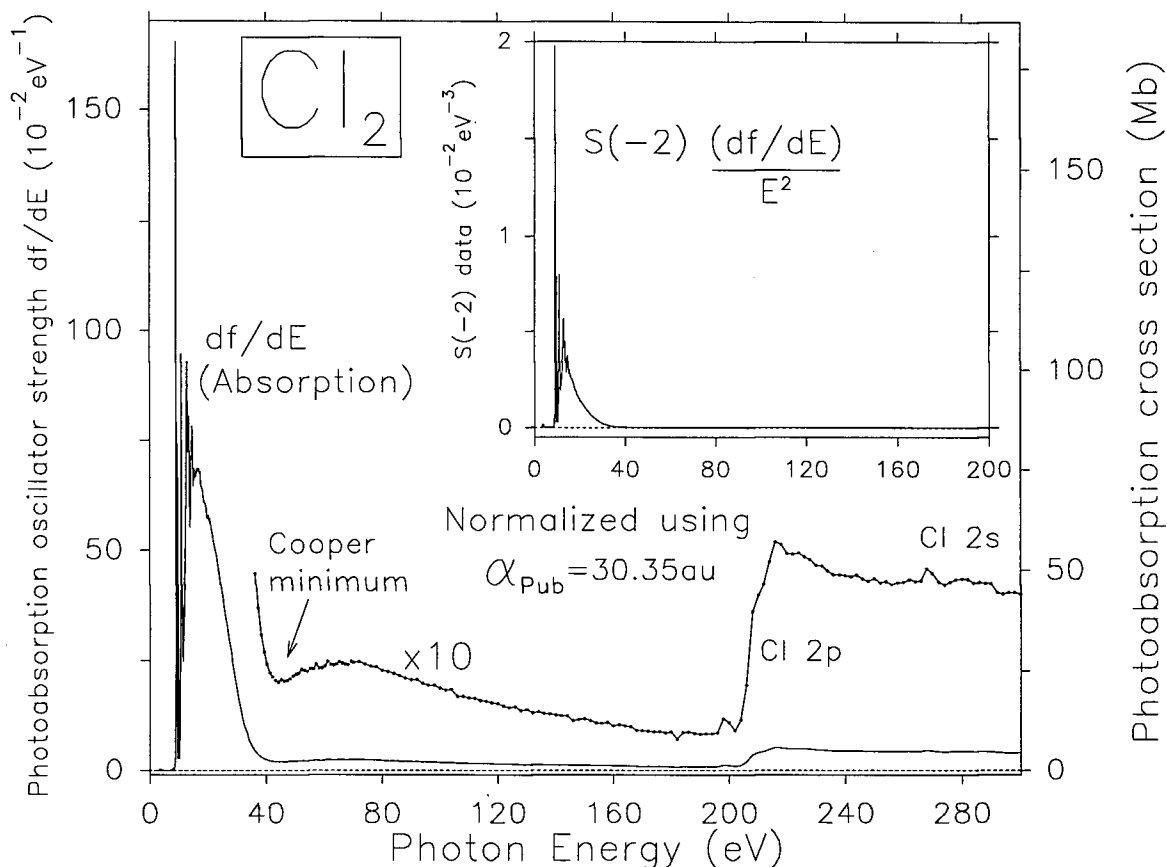


Figure 4.3: Absolute photoabsorption oscillator strength spectrum of chlorine [129]. The inset shows the  $S(-2)$  spectrum,  $(df/dE)/E^2$ , of chlorine, which gives the static dipole polarizability value of 30.40 au. The absolute differential oscillator strength scale was obtained by normalization using the published dynamic dipole polarizability values of Cuthbertson and Cuthbertson [199].

The photoabsorption spectrum of  $\text{Cl}_2$  [129] shown in figure 4.3 contains a Cooper minimum near 40 eV. This minimum, together with the onset of the Cl 2p inner shell spectrum at  $\sim 190$  eV, interferes with the valence continuum fitting procedure required by the VTRK normalization method. Thus, an accurate extrapolation is not possible. It can be seen that the  $\text{Cl}_2$  spectrum weighted by the  $E^{-2}$  factor according to the  $S(-2)$  sum-rule, as shown in the inset of figure 4.3, contains no appreciable intensity above 40 eV. Normalization of this spectrum to published experimental dynamic dipole polarizabilities [199] using equation (3.6) results in the absolute oscillator strength spectrum shown and gives a static dipole

polarizability of 30.40 au using the  $S(-2)$  sum-rule. The  $S(-2)$  sum-rule evaluation of the  $\text{CCl}_4$  spectrum [51] indicates that the differential oscillator strength scale of the previously published [51] data is  $\sim 8\%$  too low. Although the photoabsorption spectrum of  $\text{CCl}_4$  contains a Cooper minimum near 40 eV, there is a sufficiently large region from 90 to 200 eV in which a polynomial may be fitted for VTRK sum-rule normalization. Unfortunately the polynomial used for the VTRK extrapolation in the original publication (equation (4.2)) decayed too slowly with photon energy. Therefore the low resolution spectrum of  $\text{CCl}_4$  has now been renormalized using the same VTRK sum-rule procedure as in reference [51], except that an improved polynomial having the form shown in equation (3.2) has been used. This results in a 2.9% increase in the low resolution oscillator strength values listed in tables 1, 2, 5 and 6 of reference [51]. The polarizabilities obtained using the renormalized spectra with the  $S(-2)$  sum-rule were 68.7 au for the low resolution spectrum and 67.5 au from a combination of the low and high resolution spectra. These compare favorably with the average published experimental dipole polarizability value of 69.6 au obtained from refractive index and dielectric constant measurements [163].

The photoabsorption spectrum of  $\text{SiF}_4$  provides another good example where spectral features preclude the use of the VTRK sum-rule normalization method. As noted above the VTRK sum-rule normalization procedure requires a sufficiently wide energy region of the monotonically decreasing valence shell continuum such that the curve fitting and extrapolation procedures can be reliably performed. In  $\text{SiF}_4$  the onset of the Si 2p discrete spectrum limits the energy region available for the VTRK normalization to between 40 to 100 eV and furthermore, this valence region is not monotonically decreasing because of two continuum features in this region. These are a Cooper minimum, which arises from the radial node in the atomic Si 3p wavefunction, and a shape resonance, which arises from a potential barrier effect caused by the electronegative "cage" of the four F ligands (see Guo *et al.* [77]). These features combine to perturb the shape of the valence shell ionization continuum be-

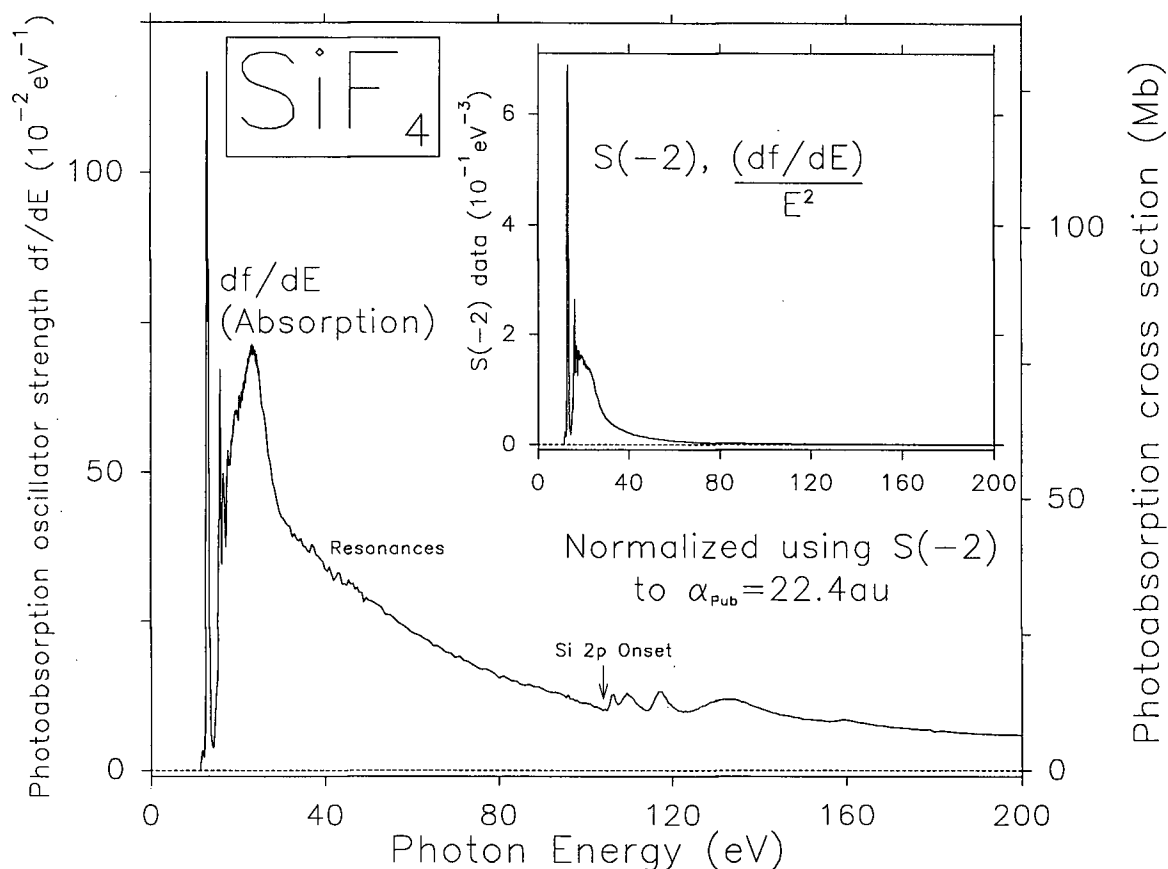


Figure 4.4: Absolute photoabsorption oscillator strength spectrum of  $\text{SiF}_4$  [77]. The inset shows the  $S(-2)$  spectrum,  $(df/dE)/E^2$ , of  $\text{SiF}_4$ , which gives a static dipole polarizability value of 22.42 au. The absolute differential oscillator strength scale was obtained by normalization using the published dynamic dipole polarizability values of Watson and Ramaswamy [167]. (Note that this revises the originally published absolute scale [77] - see text, section 4.3.2, for details).

tween 40 and 100 eV. Consequently the VTRK sum-rule normalized spectrum of  $\text{SiF}_4$  [77] yields a static polarizability of 18.2 au, 19% lower than the published experimental static dipole polarizabilities of 22.4 au [163, 164]. Static and dynamic dipole polarizabilities provide a reliable alternative method for normalization of this spectrum and the absolute scale of the photoabsorption spectrum of  $\text{SiF}_4$  shown in figure 4.4 has been obtained by normalization to published experimental dynamic dipole polarizability values reported by Watson and Ramaswamy [167]. This renormalized spectrum yields a static dipole polarizability of

22.42 au, which compares well with the published experimental values [163,164]. The resulting spectrum, which has differential oscillator strength values 23% higher than those published previously [77], agrees very well with the absolute differential oscillator strengths of the limited range optical photoabsorption spectrum of Suto *et al.* [201].

A further example of interference of the VTRK normalization procedure by a Cooper minimum is the spectrum of argon [84] which could not have been reliably normalized using the VTRK sum-rule. Although originally [84] single point normalized to a photoabsorption cross-section at 21.218 eV [202], the spectrum of Ar could have been made absolute using the S(-2) sum-rule or by using a dynamic dipole polarizability. The static polarizability derived from the published photoabsorption spectrum [84] is within 2% of the published experimental polarizability values.

Due to similar interfering valence shell continuum features and low energy inner shells, normalization of the oscillator strength spectra of Br<sub>2</sub>, I<sub>2</sub>, HBr and HI [122,129] have been achieved using published dynamic [168,199] and static dipole polarizabilities. Shown in table 4.2 are published experimental static dipole polarizabilities for the molecular systems for which the absolute scale must be determined using S(-2)-based normalization.

### 4.3.3 Dipole sum-rules and molecular properties

As shown in section 4.3.1 and in table 4.1, S(-2) analysis of VTRK sum-rule normalized dipole (e,e) absolute photoabsorption oscillator strength spectra [12, 27-30, 46, 48, 50, 51, 77, 84, 114-133] is highly consistent with published values [103-105, 151, 162-165, 167-175, 177-180, 182-185, 187, 190-197] of the dipole polarizabilities. In this regard it should be noted that experimental dipole polarizability and refractive index data can typically be obtained with even higher (typically  $\pm 1-2\%$ ) accuracy than the quoted  $\pm 5\%$  precision for the dipole (e,e) photoabsorption spectra. Thus, to further improve the dipole sums, the absolute scales

Table 4.2: Published static dipole polarizability values from experiment and theory for the molecular systems for which the absolute scale must be determined using  $S(-2)$ -based normalization.

	Static dipole polarizability (a.u.), $\alpha_N$					
	Experiment				Theory	Additivity <sup>a</sup>
	Refractive Index		Dielectric Constant	DOSD		
HBr	24.4 <sup>b</sup>	23.5 <sup>b</sup>	23.7 <sup>c</sup>	23.74 <sup>d</sup>	24.1 <sup>e</sup>	22.94
	23.7 <sup>f</sup>				23.8 <sup>g</sup>	25.91
HI	36.8 <sup>b</sup>	35.3 <sup>b</sup>			36.2 <sup>e</sup>	39.14
	35.3 <sup>f</sup>				36.0 <sup>g</sup>	39.68
Cl <sub>2</sub>	31.11 <sup>b</sup>	30.4 <sup>f</sup>			29.54 <sup>e</sup>	31.24
	30.35 <sup>h</sup>				30.82 <sup>i</sup>	31.78
Br <sub>2</sub>	43.4 <sup>k</sup>	43.6 <sup>b</sup>	47.4 <sup>c</sup>		44.76 <sup>e</sup>	40.66
			47.2 <sup>l</sup>		44.85 <sup>i</sup>	47.79
I <sub>2</sub>	<78.85 <sup>f</sup>				71.32 <sup>e</sup>	73.08
					69.33 <sup>m</sup>	75.22
CH <sub>3</sub> Br	36.81 <sup>n</sup>	38.0 <sup>b</sup>	40.7 <sup>c</sup>		36.15 <sup>e</sup>	35.29
		37.4 <sup>b</sup>				37.32
CH <sub>3</sub> I	49.43 <sup>n</sup>	49.5 <sup>b</sup>	51.6 <sup>c</sup>		49.00 <sup>e</sup>	51.56
						51.02
SiF <sub>4</sub>	22.4 <sup>o</sup>	22.4 <sup>b</sup>	22.4 <sup>c</sup>			

<sup>a</sup>Miller [166] additivity methods, first entry is ahp method and second entry is the ahc method, see ref. [166] for details.

<sup>b</sup>Stuart [163] compilation. <sup>c</sup>Maryott and Buckley [164] compilation. <sup>d</sup>Kumar and Meath [139].

<sup>e</sup>Dougherty and Spackman [184]. <sup>f</sup>Cuthburtson and Cuthburtson [199]. <sup>g</sup>Sadlej [186].

<sup>h</sup>Oddershede and Svendsen [194] extrapolated [162]. <sup>i</sup>Archibong and Thakkar [180].

<sup>j</sup>Maroulis [179]. <sup>k</sup>RI [195] <sup>l</sup>Luft [197]. <sup>m</sup>Maroulis and Thakkar [176]. <sup>n</sup>Ramaswamy [168]. <sup>o</sup>Watson

and Ramaswamy [167].

of the VTRK sum-rule normalized dipole (e,e) spectra for all species in table 4.1 have been further refined by renormalization to the respective more accurate static or dynamic polarizability data [102, 103, 105, 151, 162–164, 167–170, 190, 199] prior to dipole sum-rule evaluation. This should enable even more accurate properties to be obtained by evaluation of the various dipole sum-rules. Where  $\alpha_\lambda$  has been used, the corresponding  $\alpha_\infty$  value has been obtained by applying the S(-2) sum-rule, equation (3.4), to the absolute  $df/dE$  spectrum obtained using  $\alpha_\lambda$ . The static dipole polarizabilities, either the values used directly or those obtained from the  $\alpha_\lambda$  normalized spectra, are given by the first entry for each atom or molecule in column 4 (i.e. S(-2)) of table 4.3. The values of the dipole sum-rules S(u) (u=-1,...,-6,-8,-10) are shown in table 4.3 and those calculated using the logarithmic dipole sum-rules L(u) (u=-1,-2,...,-6) are shown in table 4.4. It can be seen that for many molecules the data in tables 4.3 and 4.4 represent the first reported dipole sums. In the event that the sum-rule values corresponding to the absolute scales of the originally published spectra are required they may be obtained by scaling the sum-rule values from tables 4.3 and 4.4 by the ratio corresponding to the static dipole polarizability of the originally published spectrum, found in column 2 of table 4.1, to the values corresponding to the renormalized spectrum, found as the first entry of column 4 of table 4.3.

As noted previously, the absolute photoabsorption spectra measured using dipole (e,e) spectroscopy are of a sufficient experimental energy range to permit accurate prediction of the sum-rule moments S(u) and L(u) for  $u \leq -1$ . The S(u) sum-rule moments for  $u \leq -2$  can almost all be effectively obtained from spectra that are recorded from the excitation threshold up to 50 eV. In the cases of He and Ne, which have exceptionally high electronic excitation thresholds, higher energy data up to 200 eV are required [27, 46]. It also appears that for most molecules, the S(-1) and L(-1) moments can be accurately determined from an absolute photoabsorption oscillator strength spectrum that has been recorded up to 200 eV. However, for some of the atomic and molecular systems considered here, the accuracy of the

$S(-1)$  and  $L(-1)$  dipole sums is expected to be lower than for  $u \leq -2$  because of appreciable contributions from higher energy regions of the spectrum.

The  $S(-1)$  and  $L(-1)$  sums given in tables 4.3 and 4.4, respectively, are generally slightly lower than previously reported values from DOSD or theoretical studies, reflecting the sensitivity of these sums to regions of the spectrum higher in energy than the upper limit of the dipole (e,e) data. Note that in general the DOSD values involve estimates of the contributions from higher energy inner shell (core) regions to the photoabsorption oscillator strength (usually obtained using experimental and theoretical atomic sums and mixture rules) which are not included in the dipole (e,e) measurements. Figure 4.5 provides an illustration of the energy weighting of the different dipole sums for the measured dipole (e,e) absolute photoabsorption spectrum for  $I_2$  [129]. Shown in panel (a) is the photoabsorption spectrum of  $I_2$  [129], while panels (b), (c), (d) and (e) show the spectra corresponding to the moments  $S(-1)$ ,  $S(-2)$ ,  $S(-4)$  and  $S(-6)$ , respectively (note the different energy scales in the various panels of figure 4.5). The  $S(-1)$  sum still shows some appreciable intensity from the 4d inner shell continuum even at 100 to 150 eV, whereas the  $S(-2)$ ,  $S(-4)$  and  $S(-6)$  sums have all approached zero intensity by much lower energies in the valence shell. Clearly the higher energy contributions will only be important in the  $S(-1)$  and  $L(-1)$  dipole sums.

The most accurate theoretical sums available for He, evaluated from explicitly correlated wavefunctions [203], for  $u = -1$  to  $-10$ , are within 2% of the presently reported values. Sums determined from the polarization-propagator approach are also within 2% for  $u = -1$  to  $-6$ . This high level of agreement between the experimental sum values and the theoretical values confirms the accuracy of the presently employed normalization procedure and the oscillator strength spectrum over the entire range of measurement. The presently determined experimental dipole sum-rule values for  $S(u)$  (table 4.3) for the noble gases Ne to Xe are in excellent agreement with moments determined from DOSD analyses reported by Kumar and Meath [139] for  $u = -2$  to  $-10$  and by Leonard and Barker [153] ( $u = -2$  to

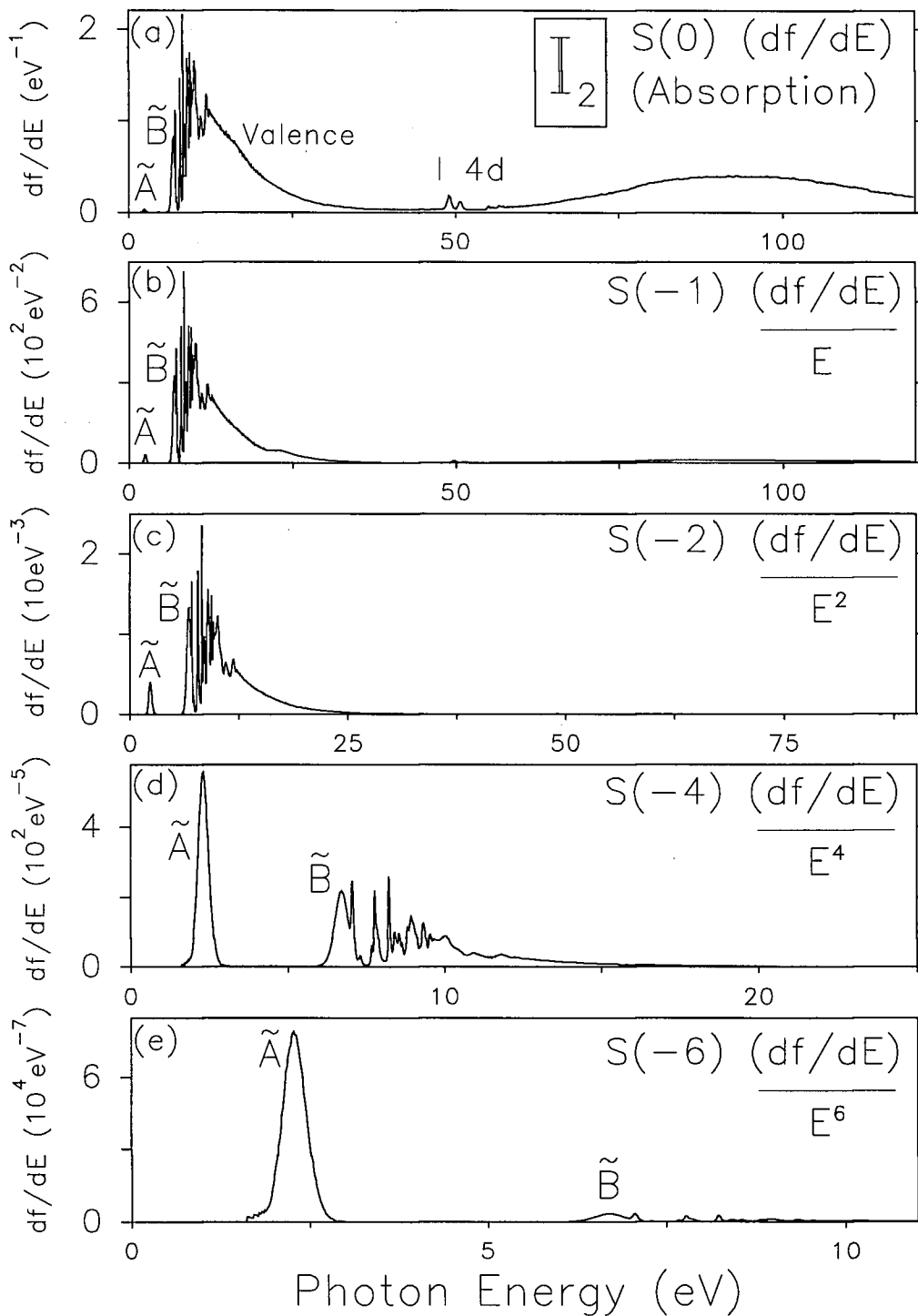


Figure 4.5: (a) The absolute photoabsorption oscillator strength spectrum of molecular iodine. Panels (b), (c), (d) and (e) show the  $S(-1)$  ( $(df/dE)/E$ ), the  $S(-2)$  ( $(df/dE)/E^2$ ), the  $S(-4)$  ( $(df/dE)/E^4$ ), and the  $S(-6)$  ( $(df/dE)/E^6$ ), spectra of molecular iodine, respectively. Note the different photon energy scales in each panel.

-8). The values obtained from the Hartree-Slater oscillator strength distributions calculated by Dehmer and Inokuti [97,143] and the calculations by Cummings [142] for He, Ne, Ar and Kr are generally much higher and moderately higher, respectively, than the present results. The semi-empirically determined moments for Ar by Eggarter [155] are in quite good agreement with the presently reported values. Although the  $L(-1)$  values determined in the present work (table 4.4) decrease from Ne to Xe as expected, they differ considerably from the DOSD-derived values [139]. In particular, the DOSD-derived  $L(-1)$  for Kr [139] is positive, in contrast with expectation based on the decreasing threshold energies for electronic excitation from Ne to Xe.

Molecular hydrogen has been extensively studied and several sets of results are available for  $S(u)$  from DOSD [134,152,154], empirical methods [147,148] and theory [144]. The empirical and DOSD derived  $S(u)$  moments are all in generally very good agreement with the present results with the largest differences (less than 4%) occurring in the lower ( $u=-6$  and  $-10$ ) moments. Polarization propagator calculations [144] are in good agreement for the moments down to  $S(-3)$  but significantly underestimate the experimental values for the lower moments,  $u=-4$  to  $-6$ . Reasonable agreement is obtained with DOSD [134] and theoretical values [144] for the  $L(-1)$  and  $L(-2)$  sums. The present values of  $S(u)$  and  $L(u)$  for  $D_2$  and HD in tables 4.3 and 4.4 are the first to be reported.

For the range of small molecules studied in the present work, the  $S(u)$  and  $L(u)$  moments (tables 4.3 and 4.4 respectively) derived from the absolute oscillator strength spectra agree, in almost all cases, with the DOSD derived moments (where available) reported by Meath and co-workers to better than  $\pm 5\%$  for the moments  $u=-1$  to  $-10$ , with the exception of HCl and some of the alkanes. For the alkanes, the differences from the DOSD-derived  $S(u)$  values [135,138] are limited to less than  $\pm 5\%$  for the moments from  $u=-1$  to  $-4$ , but increase up to 30% by the  $S(-10)$  moment. This indicates a slight overestimation of the oscillator strengths in the low energy region in the DOSD work [135,138]. For  $CH_4$ ,  $C_2H_6$ ,  $C_3H_8$  and

$C_4H_{10}$ , the values determined empirically by Hohm [151] using refractive index data for  $S(-2)$ ,  $S(-4)$ ,  $S(-6)$  and  $S(-8)$  are consistently lower, but within 12%, of the presently reported absolute differential oscillator strength sums. In the case of HCl the presently determined and the DOSD-derived [139]  $S(u)$  for  $u=-1$  to  $-6$  are in excellent agreement, however the  $S(-8)$  and  $S(-10)$  values differ by 14% and 26% respectively. The probable source of this discrepancy is an overestimation of the oscillator strength distribution at very low excitation energy in the DOSD analysis [139].

The limited accuracy of the present  $L(-1)$  values has been discussed above. DOSD and theoretical values for the  $L(-1)$  and  $L(-2)$  sums have been published for a few atoms and molecules. In these cases comparison with the present values is generally quite reasonable, particularly for the  $L(-2)$  sums with the exception of the theoretical value [144] for  $H_2O$  which is only  $\sim 60\%$  of both the DOSD [134] and present experimental values. The largest differences in  $L(-1)$  between the present experimental and DOSD values occur for the noble gases.

The  $S(u)$  and  $L(u)$  sums reported in this work have been obtained from numerical integration of the appropriately energy weighted absolute oscillator strength spectrum obtained using dipole (e,e) spectroscopy. The integrations were performed using standard numerical integration techniques for regularly spaced abscissa [204]. The spectra are sufficiently well characterized such that the sums are largely invariant to the chosen integration method. Instrumental energy resolution was also found to have only a slight effect on the sums. For most targets the sums determined from low resolution spectra alone were found to differ by less than  $\sim 3\%$  for  $S(-10)$  from the sums in tables 4.3 and 4.4 which were obtained from the combination high plus low resolution spectra. Given the significant difference in energy resolution between the high and low resolution dipole (e,e) spectrometers the instrumental resolution contribution to the sums determined here is considered to be negligible. The estimated accuracies of the presently reported sums are 5% for  $S(u)$   $u = -2$  to  $-6$  and for  $L(u)$

$u = -2$  to  $-6$ , 10% for S(-1), 15% for L(-1), 10% for S(-8), and 20% for S(-10).

Table 4.3: Dipole Sums  $S(u)$  obtained from refined<sup>a</sup> dipole (e,e) absolute photo-absorption oscillator strength spectra (first entry of column 2 labeled "Expt") compared with dipole sums from other sources. All values are given in atomic units.

	Source		S(-1)	S(-2) <sup>a</sup>	S(-3)	S(-4)	S(-5)	S(-6)	S(-8)	S(-10)
He	Expt [27]		1.489	1.383 [103]	1.423	1.556	1.771	2.069	2.977	4.475
	Theo [203]		1.505	1.383	1.415	1.542	1.750	2.040	2.923	4.369
	Theo [205]		1.526	1.392	1.411	1.525	1.715	1.984		
	Theo [97]		1.644	1.645	1.818	2.131	2.591	3.231		
	Theo [142]		1.579	1.487	1.43					
Ne	Expt [46]		3.601	2.663 [103]	2.569	2.938	3.749	5.137	10.95	25.65
	DOSD [139]		3.801	2.669	2.533	2.886	3.686	5.063	10.86	25.53
	DOSD [153]		3.830	2.670	2.527	2.884	3.692	5.081	10.90	
	Theo [97]		3.880	2.796	2.726	3.213	4.298	6.241		
	Theo [142]		4.055	2.661	2.31					
Ar	Expt [84]		8.700	11.08 [105]	16.77	27.92	50.06	95.26	392.0	1800
	DOSD [139]		8.768	11.08	16.78	27.91	49.99	95.06	391.5	1802
	DOSD [153]		8.766	11.08	16.81	27.98	50.01	94.56	382.1	
	Theo [97]		10.17	15.07	25.57	45.95	86.59	170.5		
	Theo [142]		10.949	13.377	19.78					
	Emp [155]		8.818	11.09		27.52		92.435	375.73	1712.8
Kr	Expt [84]		11.86	16.80 [105]	29.29	56.51	117.5	258.7	1419	8669
	DOSD [139]		12.33	16.79	29.23	56.32	116.8	256.7	1404	8558
	DOSD [153]		12.13	16.78	29.44	56.65	116.4	251.5	1317	
	Theo [143]		14.67	23.48	45.60	94.69	206.9	472.4		
	Theo [142]		15.753	21.020	35.54					
Xe	Expt [84]		16.55	27.12 [169]	56.43	129.8	319.1	827.0	6250	5.275(4)
	DOSD [139]		17.31	27.16	56.39	129.6	318.4	824.7	6227	5.251(4)
	DOSD [153]		18.05	27.11	55.80	128.3	316.0	816.6	6219	
H <sub>2</sub>	Expt [116]		3.076	5.433 [170]	10.22	20.04	40.43	83.18	367.0	1681
	DOSD [134]		3.100	5.428	10.18	19.96		82.94	367.0	1686
	DOSD [152]		3.135	5.450	10.12	19.63				
	DOSD [154]		3.102	5.428		19.915		82.43	363.0	1660
	Emp [147]			5.4390		20.02		81.61	350	
	Emp [148]			5.447		19.91		80.4		
	Theo [144]		3.054	5.228	9.551	18.174	35.529	70.774		
D <sub>2</sub>	Expt [116]		3.071	5.368 [190]	10.01	19.44	38.85	79.16	342.0	1531
HD	Expt [116]		3.042	5.336 <sup>b</sup>	9.980	19.46	39.04	79.91	348.7	1579
N <sub>2</sub>	Expt [28]		9.258	11.75 [103]	17.82	30.02	53.92	100.8	378.7	1504
	DOSD [134]		9.484	11.74	17.81	30.11		101.8	384.6	1534
	Emp [147]			11.743		30.17		99.21	374	
	Theo [145]			11.42		29.24		98.6		

Table 4.3: (continued) Dipole Sums  $S(u)$  obtained from refined<sup>a</sup> dipole (e,e) absolute photoabsorption oscillator strength spectra (first entry of column 2 labeled "Expt") compared with dipole sums from other sources. All values are given in atomic units.

	Source	S(-1)	S(-2) <sup>a</sup>	S(-3)	S(-4)	S(-5)	S(-6)	S(-8)	S(-10)
O <sub>2</sub>	Theo [146]	13.17	25.64	61.49	162.0	448.7	1281		
	Expt [115]	9.181	10.59 [105]	17.02	35.25	87.63	245.1	2302	2.404(4)
	DOSD [134]	9.304	10.59	16.91	34.75		237.1	2196	2.276(4)
	Emp [147]		10.600		36.97		132.0	480	
CO	Expt [30]	9.086	13.06 [167]	23.81	50.86	121.8	318.1	2587	2.414(4)
	DOSD [141]	9.727	13.08	23.07	48.26	113.8	292.9	2308	
	Emp [149]		13.089		47.842		318.6	2800	2.650(4)
	Theo [145]		13.34		50.2		295		
NO	Expt [121]	9.163	11.53 [167]	19.02	39.02	96.42	278.3	3205	4.696(4)
	DOSD [134]	9.504	11.52	18.80	38.46		276.2	3194	4.657(4)
	DOSD [156]		11.518		39.05		246	4190	1.000(5)
CO <sub>2</sub>	Expt [123]	13.74	17.51 [105]	27.89	50.63	99.68	207.4	1013	5660
	DOSD [137]	14.14	17.51	27.89	50.99		211.4	1030	5642
	Emp [150]		17.556		49.23		235	1200	
N <sub>2</sub> O	Expt [114]	14.20	19.70 [105]	35.23	73.81	171.0	423.5	2942	2.279(4)
	DOSD [134]	14.81	19.70	34.69	72.11		410.7	2847	2.211(4)
H <sub>2</sub> O	Expt [117]	7.244	9.839 [199]	17.09	35.70	86.17	233.1	2165	2.434(4)
	DOSD [134]	7.316	9.642	16.75	35.42		240.1	2299	2.633(4)
	Theo [144]	7.098	8.499	12.83	22.90	46.62	105.8		
H <sub>2</sub> S	Expt [119]	12.79	24.80 [162]	53.71	127.5	327.1	894.5	7742	7.703(4)
CH <sub>4</sub>	Expt [124]	10.76	17.26 [151]	31.36	62.22	132.0	295.0	1660	1.048(4)
	DOSD [135]	10.86	17.27		62.41		289.3	1714	
	Emp [151]		17.257		63.22		293.8	1505	
C <sub>2</sub> H <sub>2</sub>	Expt [125]	13.04	22.95 [167]	48.08	113.3	289.7	786.3	6543	6.100(4)
	DOSD [140]	13.40	22.96	48.06	113.5	290.6	787.3	6467	5.888(4)
	Theo [145]		22.56		112.1		785		
C <sub>2</sub> H <sub>4</sub>	Expt [126]	15.90	27.79 [151]	59.18	147.0	409.8	1240	1.318(4)	1.562(5)
	DOSD [138]	16.31	27.70	58.28	143.5		1202	1.286(4)	1.541(5)
	Emp [151]		27.788		146.7		1227	1.1305(4)	
C <sub>2</sub> H <sub>6</sub>	Expt [124]	18.45	29.54 [151]	54.23	110.1	242.1	567.3	3611	2.651(4)
	DOSD [136]	18.75	29.61	53.96	108.1		531.4	3149	2.116(4)
	Emp [151]		29.558		107.4		573.2	3373	
C <sub>3</sub> H <sub>8</sub>	Expt [124]	26.57	41.97 [151]	75.83	151.6	328.4	759.5	4715	3.369(4)
	DOSD [136]	26.63	42.09	77.34	157.1		804.2	5046	3.627(4)

Table 4.3: (continued) Dipole Sums  $S(u)$  obtained from refined<sup>a</sup> dipole (e,e) absolute photoabsorption oscillator strength spectra (first entry of column 2 labeled "Expt") compared with dipole sums from other sources. All values are given in atomic units.

	Source	S(-1)	S(-2) <sup>a</sup>	S(-3)	S(-4)	S(-5)	S(-6)	S(-8)	S(-10)
	Emp [151]		41.927		158.0		808.3	4558	
C <sub>4</sub> H <sub>10</sub>	Expt [124]	34.35	54.10 [151]	97.81	196.3	428.3	1000	6394	4.751(4)
	DOSD [136]	34.33	54.07	99.66	204.5		1086	7143	5.380(4)
	Emp [151]		54.044		204.9		1025	5655	
C <sub>5</sub> H <sub>12</sub>	Expt [124]	42.20	66.86 [162]	121.6	245.5	538.7	1266	8177	6.133(4)
	DOSD [136]	42.23	66.07	121.4	249.9		1373	9606	7.795(4)
C <sub>6</sub> H <sub>14</sub>	Expt [124]	49.66	78.94 <sup>c</sup>	144.2	292.6	646.8	1534	1.018(4)	7.918(4)
	DOSD [136]	49.85	78.04	144.0	298.1		1650	1.154(4)	9.306(4)
C <sub>7</sub> H <sub>16</sub>	Expt [124]	56.96	90.77 <sup>c</sup>	166.4	339.4	754.4	1799	1.205(4)	9.460(4)
	DOSD [136]	57.59	90.02	166.3	345.6		1928	1.360(4)	1.108(5)
C <sub>8</sub> H <sub>18</sub>	Expt [124]	65.15	103.6 <sup>c</sup>	189.4	384.7	850.0	2012	1.325(4)	1.019(5)
	DOSD [136]	65.26	102.0	188.8	393.4		2206	1.556(4)	1.264(5)
CH <sub>3</sub> OH	Expt [50]	14.91	21.62 [162]	37.83	75.54	167.7	407.1	2996	2.758(4)
HCHO	Expt [127]	12.55	18.69 <sup>b</sup>	34.87	76.97	193.7	541.1	5309	5.629(4)
CH <sub>3</sub> CHO	Expt [128]	20.45	31.00 <sup>d</sup>	58.15	128.2	321.8	896.9	8953	1.198(5)
(CH <sub>3</sub> ) <sub>2</sub> CO	Expt [128]	27.76	42.21 [162]	77.86	166.9	405.9	1099	1.057(4)	1.389(5)
HCl	Expt [122]	10.66	17.42 [199]	32.68	67.67	152.5	370.4	2645	2.323(4)
	DOSD [139]	11.27	17.39	32.27	67.12	154.5	389.3	3102	3.119(4)
HBr	Expt [122]	13.94	23.73 [199]	49.52	115.1	292.2	801.9	7433	8.759(4)
	DOSD [139]	14.68	23.74	49.78	116.9	299.6	827.9	7674	8.831(4)
HI	Expt [122]	17.91	35.33 [199]	84.89	225.2	643.4	1959	2.144(4)	2.846(5)
Cl <sub>2</sub>	Expt [129]	18.78	30.40 [199]	58.30	125.8	312.0	955.7	2.176(4)	1.051(6)
Br <sub>2</sub>	Expt [129]	25.96	44.50 [199]	99.29	271.5	1032	6153	5.129(5)	5.812(7)
I <sub>2</sub>	Expt [129]	36.17	75.00 [199] <sup>e</sup>	210.8	819.2	5139	4.912(4)	7.386(6)	1.356(9)
CF <sub>4</sub>	Expt [132]	20.52	19.54 [167]	23.13	31.42	46.83	74.54	216.4	707.7
CF <sub>3</sub> Cl	Expt [132]	26.07	31.99 <sup>b</sup>	49.19	87.16	170.2	357.1	1826	1.070(4)
CF <sub>2</sub> Cl <sub>2</sub>	Expt [132]	30.00	42.80 <sup>c</sup>	74.18	146.0	316.1	737.9	4831	3.908(4)

Table 4.3: (continued) Dipole Sums  $S(u)$  obtained from refined<sup>a</sup> dipole (e,e) absolute photoabsorption oscillator strength spectra (first entry of column 2 labeled "Expt") compared with dipole sums from other sources. All values are given in atomic units.

	Source	S(-1)	S(-2) <sup>a</sup>	S(-3)	S(-4)	S(-5)	S(-6)	S(-8)	S(-10)
CFCl <sub>3</sub>	Expt [132]	35.27	55.60 <sup>c</sup>	103.3	215.4	493.4	1223	9166	8.644(4)
CCl <sub>4</sub>	Expt [51]	42.97	69.33 [162]	132.8	284.8	672.9	1731	1.417(4)	1.454(5)
NH <sub>3</sub>	Expt [120]	9.253	14.57 [105]	29.00	70.48	202.7	664.0	9133	1.488(5)
	DOSD [11]	9.310	14.56	29.13	71.40	207.3	685.5	9547	1.564(5)
	DOSD [134]	9.319	14.56	29.16	71.44		684.0	9527	1.565(5)
NH <sub>2</sub> CH <sub>3</sub>	Expt [12]	16.97	26.50 [168]	49.95	110.6	284.9	844.1	1.040(4)	1.716(5)
	DOSD [12]	17.06	26.50	50.14	111.3	286.5	846.8	1.036(4)	1.697(5)
NH(CH <sub>3</sub> ) <sub>2</sub>	Expt [12]	25.42	39.95 <sup>d</sup>	75.59	168.0	433.5	1280	1.520(4)	2.333(5)
	DOSD [12]	24.87	38.70	73.27	162.9	420.4	1241	1.472(4)	2.251(5)
N(CH <sub>3</sub> ) <sub>3</sub>	Expt [12]	32.90	51.90 <sup>c</sup>	100.6	235.5	658.6	2147	3.142(4)	5.837(5)
	DOSD [12]	31.92	49.90	96.98	227.7	637.7	2080	3.038(4)	5.619(5)
SiH <sub>4</sub>	Expt [130]	15.83	32.00 [167]	73.51	178.4	449.5	1167	8426	6.527(4)
SiF <sub>4</sub>	Expt [77]	23.00	22.42 [167]	28.58	42.31	68.97	120.3	418.6	1625
PH <sub>3</sub>	Expt [131]	13.59	28.59 <sup>b</sup>	70.09	189.8	559.6	1776	2.130(4)	3.018(5)
PF <sub>3</sub>	Expt [133]	22.92	29.97 <sup>b</sup>	55.81	130.1	350.5	1031	1.025(4)	1.113(5)
PF <sub>5</sub>	Expt [133]	25.86	25.15 <sup>d</sup>	31.25	45.08	72.12	124.5	435.6	1755
PCl <sub>3</sub>	Expt [133]	36.72	67.09 [162]	149.1	384.8	1141	3824	5.671(4)	1.053(6)

<sup>a</sup>The original dipole (e,e) oscillator strength scales as given in Expt[X], column 2, have been refined by renormalizing (see section 4.3.3 for details) to dynamic ( $\alpha_\lambda$ ) or static ( $\alpha_\infty$ ) dipole polarizabilities [102, 103, 105, 151, 162–164, 167–170, 190, 199]. The  $\alpha_\lambda$  or  $\alpha_\infty$  values used for this renormalization correspond to the static polarizability given by the first entry for each atom or molecule in this column.

<sup>b</sup> Due to lack of experimental polarizabilities the VTRK sum-rule normalized spectrum is used.

<sup>c</sup> Normalized to static dipole polarizability value(s) in ref. [163].

<sup>d</sup> Normalized to the average of static dipole polarizability values in refs. [163] and [164].

<sup>e</sup> Normalized only to the dynamic polarizability values in ref. [199] that were measured below the first electronic absorption threshold of  $\sim 2$  eV (i.e only above 6200Å).

Table 4.4: Logarithmic Dipole Sums  $L(u)$  obtained from refined absolute dipole (e,e) oscillator strength spectra (first entry, labeled "Expt") compared with logarithmic dipole sums from other sources. All values given in atomic units.

	Source <sup>a</sup>	L(-1)	L(-2)	L(-3)	L(-4)	L(-5)	L(-6)
He	Expt [27]	0.2175	0.0191	-0.0908	-0.1744	-0.2550	-0.3442
	Theo [205]	0.2582	0.0410	-0.0712	-0.1529	-0.2288	-0.3106
	Theo [97]	0.121	-0.099	-0.244	-0.383	-0.543	-0.745
Ne	Expt [46]	1.707	0.3993	-0.1595	-0.5787	-1.065	-1.755
	DOSD [139]	2.160	0.4735				
Ar	Expt [84]	-0.5531	-3.919	-7.826	-15.34	-30.84	-63.67
	DOSD [139]	-0.2285	-3.932				
	Emp [155]	-0.4262					
Kr	Expt [84]	-1.478	-8.178	-17.96	-39.42	-89.58	-210.4
	DOSD [139]	0.1169	-8.099				
Xe	Expt [84]	-4.125	-17.78	-44.68	-112.9	-296.1	-806.1
	DOSD [139]	-15.88	-17.66				
H <sub>2</sub>	Expt [116]	-1.621	-3.288	-6.701	-13.81	-28.81	-60.70
	DOSD [134]	-1.586	-3.260				
	Theo [144]	-1.504	-3.010				
D <sub>2</sub>	Expt [116]	-1.582	-3.196	-6.468	-13.22	-27.31	-56.97
HD	Expt [116]	-1.579	-3.195	-6.485	-13.31	-27.61	-57.88
N <sub>2</sub>	Expt [28]	-1.042	-4.035	-8.523	-16.77	-32.80	-64.60
	DOSD [134]	-0.3915	-3.980				
O <sub>2</sub>	Expt [115]	0.5173	-3.420	-10.44	-29.30	-85.80	-262.4
	DOSD [134]	0.8785	-3.362				
CO	Expt [30]	-1.853	-6.523	-16.40	-41.78	-112.1	-316.6
	DOSD [141]	-0.8918	-5.966				
NO	Expt [121]	-0.6147	-4.344	-11.71	-31.86	-95.26	-313.2

Table 4.4: (continued) Logarithmic Dipole Sums  $L(u)$  obtained from refined absolute dipole (e,e) oscillator strength spectra (first entry, labeled "Expt") compared with logarithmic dipole sums from other sources. All values given in atomic units.

	Source <sup>a</sup>		L(-1)	L(-2)	L(-3)	L(-4)	L(-5)	L(-6)
	DOSD [134]		0.1192	-4.143				
CO <sub>2</sub>	Expt [123]		-1.199	-6.549	-15.11	-32.53	-70.59	-156.7
N <sub>2</sub> O	Expt [114]		-2.229	-9.338	-23.70	-58.85	-150.2	-394.8
	DOSD [134]		-1.053	-8.909				
H <sub>2</sub> O	Expt [117]		-1.099	-4.356	-11.15	-29.07	-81.26	-243.1
	DOSD [134]		-0.6216	-4.174				
	Theo [144]		-0.1162	-2.655				
H <sub>2</sub> S	Expt [119]		-7.652	-17.88	-44.11	-115.5	-319.3	-924.8
CH <sub>4</sub>	Expt [124]		-4.210	-9.374	-20.24	-44.87	-102.9	-243.9
C <sub>2</sub> H <sub>2</sub>	Expt [125]		-5.878	-15.25	-38.72	-102.2	-281.6	-803.9
	DOSD [140]		-5.046	-15.12				
C <sub>2</sub> H <sub>4</sub>	Expt [126]		-7.011	-18.48	-49.69	-143.1	-438.8	-1412
	DOSD [138]		-6.19	-18.02				
C <sub>2</sub> H <sub>6</sub>	Expt [124]		-7.058	-16.16	-35.92	-82.70	-199.0	-499.0
	DOSD [136]		-6.47	-16.03				
C <sub>3</sub> H <sub>8</sub>	Expt [124]		-9.877	-22.31	-49.01	-111.5	-265.4	-658.3
	DOSD [136]		-9.06	-22.99				
C <sub>4</sub> H <sub>10</sub>	Expt [124]		-12.59	-28.71	-63.44	-145.5	-349.7	-878.8
	DOSD [136]		-11.44	-29.52				
C <sub>5</sub> H <sub>12</sub>	Expt [124]		-15.74	-35.89	-79.58	-183.4	-443.0	-1119
	DOSD [136]		-13.78	-35.68				
C <sub>6</sub> H <sub>14</sub>	Expt [124]		-18.68	-42.65	-95.02	-220.4	-537.3	-1373

Table 4.4: (continued) Logarithmic Dipole Sums  $L(u)$  obtained from refined absolute dipole (e,e) oscillator strength spectra (first entry, labeled "Expt") compared with logarithmic dipole sums from other sources. All values given in atomic units.

	Source <sup>a</sup>	L(-1)	L(-2)	L(-3)	L(-4)	L(-5)	L(-6)
C <sub>7</sub> H <sub>16</sub>	DOSD [136]	-16.16	-42.39				
	Expt [124]	-21.52	-49.34	-110.4	-257.5	-630.8	-1619
	DOSD [136]	-18.48	-48.92				
C <sub>8</sub> H <sub>18</sub>	Expt [124]	-24.46	-56.07	-125.0	-289.8	-705.1	-1796
	DOSD [136]	-20.83	-55.54				
CH <sub>3</sub> OH	Expt [50]	-3.555	-10.37	-23.89	-56.46	-141.6	-377.8
HCHO	Expt [127]	-3.195	-9.785	-24.94	-66.37	-189.6	-580.0
CH <sub>3</sub> CHO	Expt [128]	-5.752	-16.56	-41.65	-110.3	-314.1	-960.6
(CH <sub>3</sub> ) <sub>2</sub> CO	Expt [128]	-8.271	-22.18	-53.93	-138.4	-383.5	-1148
HCl	Expt [122]	-4.079	-9.963	-22.27	-52.24	-129.9	-341.5
	DOSD [139]	-2.719	-9.581				
HBr	Expt [122]	-4.509	-15.79	-39.37	-102.4	-284.0	-838.8
	DOSD [139]	-2.328	-15.70				
HI	Expt [122]	-8.861	-28.53	-79.18	-228.5	-696.8	-2239
Cl <sub>2</sub>	Expt [129]	-6.058	-17.82	-41.42	-104.6	-311.4	-1202
Br <sub>2</sub>	Expt [129]	-6.908	-31.49	-88.71	-309.7	-1606	-1.226(4)
I <sub>2</sub>	Expt [129]	-17.79	-67.84	-246.6	-1294	-1.070(4)	-1.175(5)
CF <sub>4</sub>	Expt [132]	4.008	-1.502	-5.720	-11.26	-20.39	-36.65
CF <sub>3</sub> Cl	Expt [132]	-1.221	-10.76	-25.13	-54.57	-120.6	-275.0

Table 4.4: (continued) Logarithmic Dipole Sums  $L(u)$  obtained from refined absolute dipole (e,e) oscillator strength spectra (first entry, labeled "Expt") compared with logarithmic dipole sums from other sources. All values given in atomic units.

	Source <sup>a</sup>	L(-1)	L(-2)	L(-3)	L(-4)	L(-5)	L(-6)
CF <sub>2</sub> Cl <sub>2</sub>	Expt [132]	-6.517	-20.07	-46.05	-106.4	-256.8	-650.1
CFCl <sub>3</sub>	Expt [132]	-12.06	-30.52	-70.43	-169.1	-429.4	-1153
CCl <sub>4</sub>	Expt [51]	-13.84	-40.46	-94.28	-231.7	-608.6	-1703
NH <sub>3</sub>	Expt [120]	-2.948	-8.428	-23.00	-68.93	-228.6	-822.7
	DOSD [11]	-2.681	-8.496				
	DOSD [134]	-2.641	-8.479				
NH <sub>2</sub> CH <sub>3</sub>	Expt [12]	-5.632	-14.49	-35.81	-96.47	-290.2	-971.1
	DOSD [12]	-5.127	-14.59				
NH(CH <sub>3</sub> ) <sub>2</sub>	Expt [12]	-8.687	-22.03	-54.45	-147.0	-441.4	-1462
	DOSD [12]	-7.590	-21.34				
N(CH <sub>3</sub> ) <sub>3</sub>	Expt [12]	-11.15	-29.25	-76.19	-221.9	-731.2	-2676
	DOSD [12]	-9.574	-28.22				
SiH <sub>4</sub>	Expt [130]	-8.795	-25.34	-63.47	-161.8	-422.7	-1128
SiF <sub>4</sub>	Expt [77]	5.344	-3.088	-9.427	-18.89	-36.29	-70.18
PH <sub>3</sub>	Expt [131]	-8.286	-23.94	-66.57	-197.5	-626.6	-2109
PF <sub>3</sub>	Expt [133]	-0.4870	-14.18	-41.87	-121.0	-365.4	-1145
PF <sub>5</sub>	Expt [133]	5.340	-2.954	-9.438	-19.10	-36.90	-71.91
PCl <sub>3</sub>	Expt [133]	-16.19	-48.12	-130.5	-392.3	-1314	-4835

<sup>a</sup>see footnote a of table 4.3.

### 4.3.4 Verdet constants

The rotation  $\phi$  of the plane of polarization of light as it passes through a sample of pathlength  $l$  in the presence of a static magnetic field  $B$  is known as the Faraday effect [206], and is governed by the Verdet constant,  $V$ , where  $V = \phi/Bl$ . The Verdet constant can also be expressed in terms of the dynamic dipole polarizability according to the Becquerel formula [207]

$$V = r(N_A a_o^3) \epsilon \left( \frac{d\alpha_\lambda}{d\epsilon} \right) \quad (4.3)$$

where  $\epsilon$  is the energy of the incident light,  $N_A$  is Avogadro's number and all quantities are in atomic units. For atoms, Becquerel [207] showed that  $r = 1$ , but for molecules,  $r$  generally varies between 0.5 and 1 [206]. The normal Verdet constant,  $V_N$ , is simply obtained by setting  $r = 1$  for molecules, although it should be noted that  $r$  does have a slight frequency dependence [208].

Differentiation of equation (3.6), the expression for  $\alpha_\lambda$ , with respect to  $\epsilon$  and substitution into equation (4.3), provides an expression for the normal Verdet constant in terms of the dipole oscillator strength distribution

$$V_N = (N_A a_o^3) \int_{E_o}^{\infty} \left( \frac{df}{dE} \right) \left( \frac{2\epsilon^2}{(E^2 - \epsilon^2)^2} \right) dE. \quad (4.4)$$

Using equation (4.4) with the photoabsorption data of Chan *et al.* for H<sub>2</sub> [29], N<sub>2</sub> [28] and O<sub>2</sub> [115, 118] (further refined as explained in section 4.3.3), the experimentally derived  $V_N$  values reproduce those reported by Parkinson *et al.* [208] from *ab initio* calculations to within 9% and from semi-empirical calculations using a sum-rule expansion [208] to within 2%. In addition the values obtained for N<sub>2</sub> [28] agree to within 2% with the values reported by Parkinson *et al.* [208] from determinations using experimental refractive index data [209] and using equation (4.5) below with DOSD derived sum-rule moments [210]. In terms of

$S(u)$ ,  $V_N$  can be approximated as [208]

$$V_N \cong (N_A a_o^3) \sum_{k=1}^{\infty} S(-2k-2) k \epsilon^{2k} = (N_A a_o^3) 2\epsilon^2 \left( S(-4) + 2\epsilon^2 S(-6) + 3\epsilon^4 S(-8) + \dots \right). \quad (4.5)$$

Thus the sum-rules provided in table 4.3 allow an alternative evaluation of normal Verdet constants over a wide range of frequency for any atomic or molecular target using equation (4.5). Normal Verdet constants, as evaluated from equation (4.4) and from the  $S(u)$  expansion, equation (4.5), are in good agreement provided that the selected value of  $\epsilon$  is near to, or less than, the first excitation threshold,  $E_o$ .

The sums provided in table 4.3 and equation (4.5) allow detailed analyses of the Verdet constants at a given photon energy along a molecular series. In general, for a series of molecules, the Verdet constants increase with increasing dipole polarizability. For instance,  $V_N$  increases with chain length for the n-alkanes and with increasing chlorination for the  $CF_n Cl_{4-n}$  freon series. Examples where this behaviour is not observed include the first row hydrides, where  $V_N$  is a maximum for ammonia, and the series  $C_2 H_{2n-m}$  where  $V_N$  would be expected to increase with decreasing  $m$  but the Verdet constant actually increases along the series  $C_2 H_6 < C_2 H_2 < C_2 H_4$ .

### 4.3.5 $C_6$ interaction coefficients

In addition to determining individual molecular properties such as dipole polarizabilities and Verdet constants, as illustrated in sections 4.3.3 and 4.3.4, dipole oscillator strength spectra can also provide some information concerning the interactions between pairs of atoms and/or molecules. For instance, in terms of the dipole oscillator strength distribution, the rotationally averaged dispersion constant [211] for the interaction between molecules A and B,  $C_6(A, B)$ , is given by

$$C_6(A, B) = \frac{3}{2} (E_H a_o^6) \int_{E_o(A)}^{\infty} \int_{E_o(B)}^{\infty} \left( \frac{df}{dE} \right)_A \left( \frac{df}{dE} \right)_B \frac{dE(A) dE(B)}{E(A) E(B) (E(A) + E(B))} \quad (4.6)$$

where  $(df/dE)_A$  is the differential oscillator strength as a function of energy-loss or photon energy,  $E(A)$ , for molecule A, and similarly for molecule B. The  $C_6$  constant plays a very important role in the understanding of van der Waals interactions. Indeed, the quality of model potentials for van der Waals interactions is very sensitive to experimental input data [212], and  $C_6$  plays an important role in this respect. Potential energy surfaces are only available for interactions of small atoms and linear molecules [213]. Direct evaluation of  $C_6(A, B)$  has been performed using equation (4.6) for all possible atomic and/or molecular combinations using the refined dipole (e,e) differential oscillator strength distributions derived in the present work (see section 4.3.3). In those cases where literature values are available for comparison the results are shown in table 4.5. Dispersion coefficients may also be reproduced from sum-rule based approximations such as Kramer's formula [214] for like particle (A,A) interactions,

$$C_6(A, A) \cong \frac{3}{4}(E_H a_0^6)[S(-2)_A]^2 \exp \frac{L(-2)_A}{S(-2)_A}. \quad (4.7)$$

We find that the  $C_6(A, A)$  coefficients obtained using equation (4.7) and the  $S(-2)$  and  $L(-2)$  information from tables 4.3 and 4.4, reproduce those calculated directly from equation (4.6) within 1% for all of the systems studied. Similarly the Moelwyn-Hughes [195] approximation  $C_6(A, B)$  for dissimilar particles,

$$C_6(A, B) \cong \frac{2 C_6(A, A) C_6(B, B)}{C_6(A, A) \frac{S(-2)_B}{S(-2)_A} + C_6(B, B) \frac{S(-2)_A}{S(-2)_B}} \quad (4.8)$$

where  $C_6(A, A)$  and  $C_6(B, B)$  are calculated using equation (4.6), reproduces the values of  $C_6(A, B)$  directly calculated from equation (4.6) to within 3%. In fact, the  $C_6(A, B)$  values estimated using equation (4.8) are within 1% of the directly calculated values (equation (4.6)) for 98% of the A,B systems considered.

The combination of Kramer's formula, equation (4.7), for  $C_6(A, A)$ , and the Moelwyn-

Hughes approximation, equation (4.8) for  $C_6(A, B)$ , gives

$$C_6(A, B) \cong \frac{3}{2}(E_H a_o^6) S(-2)_A S(-2)_B \frac{\exp \left[ \frac{L(-2)_A}{S(-2)_A} + \frac{L(-2)_B}{S(-2)_B} \right]}{\exp \frac{L(-2)_A}{S(-2)_A} + \exp \frac{L(-2)_B}{S(-2)_B}}. \quad (4.9)$$

This provides an expression for  $C_6(A, B)$  which requires only the  $S(-2)$  and  $L(-2)$  sums from tables 4.3 and 4.4, respectively. Equation (4.9) reproduces the  $C_6(A, B)$  values directly calculated from equation (4.6) even better than equation (4.8) does: A mere 1.2% of the  $C_6(A, B)$  values are not reproduced to within 1%. Table 4.6 lists those atomic and molecular combinations for which the result from equation (4.9) differs by more than 0.75% from that obtained using equation (4.6). For all other combinations equation (4.9) and the  $S(-2)$  and  $L(-2)$  sums from tables 4.3 and 4.4 can be used to calculate very accurate values for  $C_6(A, B)$ . Table 4.6 shows that equation (4.9) is generally least accurate for atom-molecule interactions. In general, the dispersion coefficients are proportional to the dipole polarizabilities of A and B, as expected from equation (4.9). The latter is generally least accurate for systems in which  $C_6(A, B)$  is smaller than would be expected based on the polarizabilities, and  $C_6(A, B)$  is underestimated by equation (4.9).

For many of the atomic and molecular systems considered in the present work, the dipole sums given in tables 4.3 and 4.4 allow estimates of the dispersion coefficients to be obtained for the first time by using equation (4.9). DOSD-derived values are also available for several systems (table 4.5). As expected from the sum-rule comparisons discussed in section 4.3.3 above, the present and DOSD-derived values are in good agreement. The  $C_6$  coefficients for which refractivity or theoretical estimates are available are shown in table 4.5. Refractivity experiments produce  $C_6$  coefficients which are lower, but generally within 10% of the present values. The  $C_6(\text{Ar}, \text{Ar})$  and  $C_6(\text{O}_2, \text{B})$  dispersion coefficients from refractivity measurements and the presently determined values differ by as much as 20%. However, as discussed by Hohm [170], the refractivity measurements for these systems are considered to be too low. While theoretical *ab initio* estimates [215–220] of the dispersion coefficients are generally very

difficult to obtain, those that exist (see table 4.5) are within 10% of the present estimates and are, with few exceptions, higher.

The accuracy of the dipole-dipole dispersion coefficients, obtained from dipole (e,e) spectroscopy using equation (4.9) with the  $S(-2)$  and  $L(-2)$  sums given in tables 4.3 and 4.4, or found in table 4.6, is estimated to be better than  $\pm 10\%$  for all the pairs of atoms and molecules considered.

Table 4.5:  $C_6(A, B)$  coefficients derived from refined absolute dipole (e,e) oscillator strength spectra using equation (4.6) compared with values from theory and experiment. All values given in atomic units.

A	B	$C_6(A, B)$ Coefficients					
		Dipole(e,e) This work	Refractivity Hohm <i>et al.</i>	DOSD Meath <i>et al.</i>	Pade Apprx. Tang <i>et al.</i> <sup>b</sup>	Theoretical Wormer <i>et al.</i>	Other Values
He	He	1.450		1.458 <sup>a</sup>	1.47	1.463 <sup>c</sup>	1.461 <sup>d</sup> 1.461 <sup>e</sup> 1.461 <sup>f</sup>
He	Ne	2.977		3.029 <sup>a</sup>	3.13	3.0712 <sup>g</sup>	2.032 <sup>f</sup>
He	Ar	9.530		9.538 <sup>a</sup>	9.82	9.551 <sup>f</sup> 9.567 <sup>g</sup>	
He	Kr	13.35		13.40 <sup>a</sup>	13.6	13.652 <sup>g</sup>	13.42 <sup>f</sup>
He	Xe	19.44		19.54 <sup>a</sup>	18.3	19.916 <sup>g</sup>	19.57 <sup>f</sup>
Ne	Ne	6.180		6.383 <sup>a</sup>	6.87	6.5527 <sup>g</sup> 5.587 <sup>c</sup>	
Ne	Ar	19.29		19.50 <sup>a</sup>	20.7	19.753 <sup>g</sup>	
Ne	Kr	26.93		27.30 <sup>a</sup>	28.7	28.009 <sup>g</sup>	
Ne	Xe	39.05		39.66 <sup>a</sup>	37.8	40.518 <sup>g</sup>	
Ar	Ar	64.37	55.98 <sup>h</sup>	64.57 <sup>a</sup> 64.30 <sup>a</sup>	67.2	64.543 <sup>g</sup>	68.456 <sup>i</sup>
Ar	Kr	91.05		91.13 <sup>a</sup>	94.3	93.161 <sup>g</sup>	
Ar	Xe	134.0		134.5 <sup>a</sup>	129	137.97 <sup>g</sup>	
Xe	Xe	283.9		285.9 <sup>a</sup>	261	302.29 <sup>g</sup>	
Xe	Kr	191.0		191.9 <sup>a</sup>	184	201.27 <sup>g</sup>	
Kr	Kr	129.2		129.6 <sup>a</sup>	133	135.08 <sup>g</sup>	
He	H <sub>2</sub>	3.997				4.0268 <sup>n</sup> 4.030 <sup>c</sup>	4.013 <sup>e</sup> 4.018 <sup>o</sup>
He	N <sub>2</sub>	10.19		10.23 <sup>p</sup>		9.7617 <sup>m</sup>	
He	O <sub>2</sub>	9.367				9.2078 <sup>q</sup>	
He	CO	10.38		10.69 <sup>j</sup>		11.06 <sup>k</sup>	

Table 4.5: (continued)  $C_6(A, B)$  coefficients derived from refined dipole (e,e) oscillator strength spectra using equation (4.6) compared with values from theory and experiment. All values given in atomic units.

A	B	$C_6(A, B)$ Coefficients					
		Dipole(e,e) This work	Refractivity Hohm <i>et al.</i>	DOSD Meath <i>et al.</i>	Pade Apprx. Tang <i>et al.</i> <sup>b</sup>	Theoretical Wormer <i>et al.</i>	Other Values
				10.70 <sup>l</sup>		10.886 <sup>m</sup>	
He	H <sub>2</sub> O	8.096				8.232 <sup>k</sup>	
He	NH <sub>3</sub>	11.06				11.12 <sup>k</sup>	
He	HCl	13.15		13.33 <sup>a</sup>		13.328 <sup>m</sup>	
He	HBr			17.00 <sup>a</sup>		17.294 <sup>m</sup>	
Ne	H <sub>2</sub>	7.998		8.168 <sup>r</sup>		8.2024 <sup>n</sup> 8.1914 <sup>g</sup>	
Ne	N <sub>2</sub>	20.66		20.95 <sup>p</sup>		20.232 <sup>m</sup> 21.525 <sup>g</sup>	
Ne	O <sub>2</sub>	19.10		19.18 <sup>r</sup>		19.196 <sup>q</sup>	
Ne	CO	20.97		21.87 <sup>j</sup> 21.88 <sup>l</sup>		22.407 <sup>m</sup> 23.075 <sup>g</sup> 23.32 <sup>k</sup>	
Ne	H <sub>2</sub> O	16.39		16.23 <sup>r</sup>		17.41 <sup>k</sup>	
Ne	NH <sub>3</sub>	22.28		22.17 <sup>r</sup>		23.33 <sup>k</sup>	
Ne	HCl	26.40		27.05 <sup>a</sup>		27.248 <sup>m</sup>	
Ne	HBr			34.39 <sup>a</sup>		35.182 <sup>m</sup>	
Ar	H <sub>2</sub>	27.62		27.76 <sup>r</sup>		27.773 <sup>n</sup> 27.757 <sup>g</sup>	
Ar	N <sub>2</sub>	68.64		68.64 <sup>l</sup>		65.515 <sup>m</sup> 69.843 <sup>g</sup>	
Ar	O <sub>2</sub>	62.64		62.87 <sup>r</sup>		61.326 <sup>q</sup>	
Ar	CO	70.60		72.26 <sup>j</sup> 72.80 <sup>l</sup>		73.597 <sup>m</sup> 75.806 <sup>g</sup>	
Ar	NH <sub>3</sub>	75.67		75.19 <sup>r</sup>			78.143 <sup>i</sup>
Ar	HCl	90.38		91.21 <sup>a</sup>		91.477 <sup>m</sup>	

Table 4.5: (continued)  $C_6(A, B)$  coefficients derived from refined dipole (e,e) oscillator strength spectra using equation (4.6) compared with values from theory and experiment. All values given in atomic units.

A	B	$C_6(A, B)$ Coefficients					
		Dipole(e,e) This work	Refractivity Hohm <i>et al.</i>	DOSD Meath <i>et al.</i>	Pade Apprx. Tang <i>et al.</i> <sup>b</sup>	Theoretical Wormer <i>et al.</i>	Other Values
Ar	HBr			116.9 <sup>a</sup>		119.73 <sup>m</sup>	
Kr	H <sub>2</sub>	39.36		39.70 <sup>r</sup>		40.433 <sup>n</sup> 40.413 <sup>g</sup>	
Kr	N <sub>2</sub>	97.02		97.20 <sup>p</sup>		94.4 <sup>m</sup> 100.67 <sup>g</sup>	
Kr	O <sub>2</sub>	88.35		89.09 <sup>r</sup>		88.139 <sup>q</sup>	
Kr	CO	100.1		102.5 <sup>j</sup> 102.6 <sup>l</sup>		106.43 <sup>m</sup> 109.63 <sup>g</sup>	
Kr	HCl	128.6		129.9 <sup>a</sup>		132.93 <sup>m</sup>	
Kr	HBr			167.0 <sup>a</sup>		174.59 <sup>m</sup>	
Xe	H <sub>2</sub>	58.48		59.14 <sup>r</sup>		60.563 <sup>n</sup> 60.539 <sup>g</sup>	
Xe	N <sub>2</sub>	142.7		143.3 <sup>p</sup>		139.5 <sup>m</sup> 148.84 <sup>g</sup>	
Xe	O <sub>2</sub>	129.7		131.2 <sup>r</sup>		129.83 <sup>q</sup>	
Xe	CO	147.9		151.6 <sup>j</sup> 151.7 <sup>l</sup>		158.06 <sup>m</sup> 162.8 <sup>g</sup>	
Xe	HCl	190.6		192.8 <sup>a</sup>		198.66 <sup>m</sup>	
Xe	HBr			248.8 <sup>a</sup>		262.11 <sup>m</sup>	
H <sub>2</sub>	H <sub>2</sub>	12.07	11.44 <sup>h</sup> 11.51 <sup>s</sup>	12.11 <sup>u</sup>		12.146 <sup>c</sup>	12.058 <sup>e</sup>
H <sub>2</sub>	O <sub>2</sub>	26.67	23.61 <sup>s</sup>	26.89 <sup>u</sup>			
H <sub>2</sub>	CO	30.47		31.14 <sup>j</sup> 31.17 <sup>l</sup>		33.36 <sup>k</sup>	
H <sub>2</sub>	CO <sub>2</sub>	43.18	40.24 <sup>s</sup>	43.33 <sup>l</sup>			

Table 4.5: (continued)  $C_6(A, B)$  coefficients derived from refined dipole (e,e) oscillator strength spectra using equation (4.6) compared with values from theory and experiment. All values given in atomic units.

A	B	$C_6(A, B)$ Coefficients					
		Dipole(e,e) This work	Refractivity Hohm <i>et al.</i>	DOSD Meath <i>et al.</i>	Pade Apprx. Tang <i>et al.</i> <sup>b</sup>	Theoretical Wormer <i>et al.</i>	Other Values
H <sub>2</sub>	N <sub>2</sub> O	46.45	43.81 <sup>s</sup>	46.97 <sup>u</sup>			
H <sub>2</sub>	H <sub>2</sub> O	23.56		23.25 <sup>u</sup>		24.58 <sup>k</sup>	
H <sub>2</sub>	NH <sub>3</sub>	32.81	32.90 <sup>s</sup>	32.78 <sup>u</sup>		33.98 <sup>k</sup>	
H <sub>2</sub>	C <sub>2</sub> H <sub>6</sub>	67.49	63.46 <sup>s</sup>	68.07 <sup>r</sup>			
N <sub>2</sub>	N <sub>2</sub>	73.22		73.39 <sup>u</sup>		71.46 <sup>c</sup>	
N <sub>2</sub>	CO	75.26		77.21 <sup>j</sup> 77.20 <sup>l</sup>		82.01 <sup>k</sup>	
N <sub>2</sub>	H <sub>2</sub> O	58.44		57.68 <sup>u</sup>		60.74 <sup>k</sup>	
N <sub>2</sub>	NH <sub>3</sub>	80.63		80.48 <sup>u</sup>		83.00 <sup>k</sup>	
O <sub>2</sub>	O <sub>2</sub>	61.24	48.74 <sup>s</sup> 44.20 <sup>h</sup>	62.01 <sup>u</sup>		58.659 <sup>q</sup> 58.49 <sup>v</sup>	
O <sub>2</sub>	CO <sub>2</sub>	98.19	83.22 <sup>s</sup>	98.75 <sup>l</sup>			
O <sub>2</sub>	N <sub>2</sub> O	104.9	90.49 <sup>s</sup>	106.8 <sup>u</sup>			
O <sub>2</sub>	NH <sub>3</sub>	73.38	68.24 <sup>s</sup>	73.62 <sup>u</sup>			
O <sub>2</sub>	C <sub>2</sub> H <sub>6</sub>	150.5	130.37 <sup>s</sup>	152.1 <sup>r</sup>			
CO	CO	77.63		81.31 <sup>j</sup> 81.40 <sup>l</sup>		89.14 <sup>k</sup>	
CO	H <sub>2</sub> O	60.17		60.64 <sup>r</sup>		65.91 <sup>k</sup>	
CO	NH <sub>3</sub>	83.32		84.76 <sup>r</sup>		90.40 <sup>k</sup>	
CO <sub>2</sub>	CO <sub>2</sub>	157.8	142.23 <sup>s</sup>	158.7 <sup>l</sup>			
CO <sub>2</sub>	N <sub>2</sub> O	168.9	154.54 <sup>s</sup>				
CO <sub>2</sub>	NH <sub>3</sub>	118.4	116.71 <sup>s</sup>				
CO <sub>2</sub>	C <sub>2</sub> H <sub>6</sub>	243.1	222.45 <sup>s</sup>				

Table 4.5: (continued)  $C_6(A, B)$  coefficients derived from refined dipole (e,e) oscillator strength spectra using equation (4.6) compared with values from theory and experiment. All values given in atomic units.

A	B	$C_6(A, B)$ Coefficients					
		Dipole(e,e) This work	Refractivity Hohm <i>et al.</i>	DOSD Meath <i>et al.</i>	Pade Apprx. Tang <i>et al.</i> <sup>b</sup>	Theoretical Wormer <i>et al.</i>	Other Values
H <sub>2</sub> O	H <sub>2</sub> O	46.68		45.37 <sup>u</sup>		48.79 <sup>k</sup> 47.623 <sup>i</sup>	
H <sub>2</sub> O	NH <sub>3</sub>	64.53		63.41 <sup>u</sup>		66.76 <sup>k</sup>	
N <sub>2</sub> O	N <sub>2</sub> O	181.0	168.02 <sup>s</sup>	184.9 <sup>u</sup>			
N <sub>2</sub> O	NH <sub>3</sub>	127.2	126.79 <sup>s</sup>	127.9 <sup>r</sup>			
N <sub>2</sub> O	C <sub>2</sub> H <sub>6</sub>	261.1	242.08 <sup>s</sup>	265.9 <sup>r</sup>			
NH <sub>3</sub>	NH <sub>3</sub>	89.55	96.00 <sup>s</sup>	89.09 <sup>u</sup>		91.85 <sup>k</sup>	
NH <sub>3</sub>	C <sub>2</sub> H <sub>6</sub>	184.0	182.02 <sup>s</sup>	184.2 <sup>r</sup>			
C <sub>2</sub> H <sub>6</sub>	C <sub>2</sub> H <sub>6</sub>	378.3	350.22 <sup>s</sup>	381.8 <sup>t</sup>			

<sup>a</sup>Kumar and Meath [221]. <sup>b</sup>Tang *et al.* [222]. <sup>c</sup>Visser *et al.* [218]. <sup>d</sup>Thakkar [203]. <sup>e</sup>Bishop and Pipin [223]. <sup>f</sup>Thakkar *et al.* [212]. <sup>g</sup>Thakkar *et al.* [216]. <sup>h</sup>Hohm and Kerl [104]. <sup>i</sup>Wormer and Hettema [215]. <sup>j</sup>Kumar and Meath [141]. <sup>k</sup>Rijks and Wormer [217]. <sup>l</sup>Jhanwar and Meath [137]. <sup>m</sup>Hettema *et al.* [213]. <sup>n</sup>Wormer *et al.* [219]. <sup>o</sup>Meyer *et al.* [224]. <sup>p</sup>Computed in ref. [213] using DOSD data [221]. <sup>q</sup>Hettema *et al.* [220]. <sup>r</sup>Obtained using equation (4.9) and the DOSD S(-2) and L(-2) sums listed in tables 4.3 and 4.4, respectively. <sup>s</sup>Hohm [170]. <sup>t</sup>Jhanwar and Meath [225]. <sup>u</sup>Zeiss and Meath [226]. <sup>v</sup>Rijks *et al.* [227].

Table 4.6:  $C_6(A, B)$  coefficients derived from refined dipole (e,e) oscillator strength spectra using equation (4.6).  $C_6(A, B)$  coefficients for all other pairs are reproduced to within 0.75% of equation (4.6) values using the sum-rule based approximation and can be generated using equation (4.9) and the S(-2) and L(-2) sums from tables 4.3 and 4.4, respectively. All values given in atomic units.

A	B	$C_6(A, B)$	A	B	$C_6(A, B)$
Xe	Xe	283.9	Ne	H <sub>2</sub> O	16.39
He	Br <sub>2</sub>	30.95	Ne	PF <sub>3</sub>	49.36
He	C <sub>2</sub> H <sub>2</sub>	16.41	Ne	I <sub>2</sub>	92.11
He	C <sub>2</sub> H <sub>4</sub>	19.92	Ne	N <sub>2</sub> O	32.18
He	HCHO	14.64	Ne	N(CH <sub>3</sub> ) <sub>3</sub>	79.87
He	CH <sub>3</sub> CHO	24.12	Ne	NH <sub>3</sub>	22.28
He	(CH <sub>3</sub> ) <sub>2</sub> CO	32.97	Ne	NO	20.05
He	I <sub>2</sub>	46.13	Ne	O <sub>2</sub>	19.10
He	N <sub>2</sub> O	15.91	Ne	HD	7.890
He	N(CH <sub>3</sub> ) <sub>3</sub>	39.69	Ne	D <sub>2</sub>	7.955
He	NH(CH <sub>3</sub> ) <sub>2</sub>	30.72	Ne	H <sub>2</sub>	7.998
He	NH <sub>2</sub> CH <sub>3</sub>	20.43	Ar	I <sub>2</sub>	322.9
He	NH <sub>3</sub>	11.06	Xe	SiH <sub>4</sub>	312.4

Table 4.6: (continued)  $C_6(A, B)$  coefficients derived from refined dipole (e,e) oscillator strength spectra using equation (4.6).  $C_6(A, B)$  coefficients for all other pairs are reproduced to within 0.75% of equation (4.6) values using the sum-rule based approximation and can be generated using equation (4.9) and the  $S(-2)$  and  $L(-2)$  sums from tables 4.3 and 4.4, respectively. All values given in atomic units.

A	B	$C_6(A, B)$	A	B	$C_6(A, B)$
He	NO	9.871	H <sub>2</sub>	PF <sub>5</sub>	68.81
He	CO	10.38	H <sub>2</sub>	SiF <sub>4</sub>	60.73
He	H <sub>2</sub> O	8.096	HD	SiF <sub>4</sub>	59.89
He	O <sub>2</sub>	9.367	D <sub>2</sub>	SiF <sub>4</sub>	60.37
He	PH <sub>3</sub>	18.16	I <sub>2</sub>	CF <sub>4</sub>	629.4
He	PF <sub>3</sub>	24.33	I <sub>2</sub>	CF <sub>3</sub> Cl	936.7
He	PCl <sub>3</sub>	46.37	I <sub>2</sub>	N <sub>2</sub>	343.5
Ne	Br <sub>2</sub>	62.04	I <sub>2</sub>	PF <sub>5</sub>	798.1
Ne	C <sub>2</sub> H <sub>4</sub> O	48.61	I <sub>2</sub>	SiF <sub>4</sub>	705.0
Ne	C <sub>2</sub> H <sub>4</sub>	39.96	O <sub>2</sub>	SiH <sub>4</sub>	140.4
Ne	HCHO	29.54	PF <sub>3</sub>	SiH <sub>4</sub>	373.8
Ne	CO	20.97	PF <sub>3</sub>	CF <sub>4</sub>	330.0

## Chapter 5

# Absolute Photoabsorption Studies of the Methyl Halides

### 5.1 Introduction

With recent interest in atmospheric pollutants, halogenated compounds have received much attention. The main focus has been on refrigerants and propellants such as the chlorofluorocarbons (or freons) because of their profound effect on the stratospheric ozone layer. However, in view of the success of reducing the levels of freons emitted into the atmosphere, the emission of other halocarbon compounds is becoming a significant environmental concern. Some of the simplest halocarbon compounds are the methyl halides, which are released into the atmosphere in large quantities both by natural and man-made sources [13, 14, 16–26]. The most abundant halohydrocarbon species in the upper atmosphere is methyl chloride. The large volume emitted into the atmosphere, estimated to be  $1 \times 10^6$  tonnes of  $\text{CH}_3\text{Cl}$  per year, is believed to arise largely from biological synthesis [19]. The other methyl halides are also released into the atmosphere in large quantities both by natural and man-made sources [16, 20–25]. As part of an ongoing quantitative study of the interaction of energetic UV and soft X-ray radiation with halogen containing species and freons [161, 228] this chapter presents long range absolute photoabsorption measurements, from the electronic excitation threshold up to 350 eV (to 250 eV from  $\text{CH}_3\text{F}$ ), for the methyl halides using dipole (e,e) spectroscopy. This study continues in chapter 6 with the presentation of ionic

photofragmentation and photoelectron measurements for the methyl halides obtained using a combination of dipole electron scattering spectroscopies [1, 9] ( $\text{CH}_3\text{X}$ ; X= F, Cl, Br, I) and synchrotron radiation based techniques ( $\text{CH}_3\text{X}$ ; X= F, Cl, Br) over a wide energy transfer range. These techniques together provide detailed quantitative information on the dipole induced breakdown of the methyl halides under energetic radiation.

To date several studies of the valence shell photoabsorption of the methyl halides have been carried out over limited energy regions (below 70 eV) using helium and hydrogen discharge lamps and synchrotron radiation. To the best of our knowledge no ab-initio calculations of the absolute total photoabsorption of any of the methyl halides have been reported. In 1935 Mulliken [229] proposed a theory of electronic structure for the alkyl halides which was in close agreement with the experimental work carried out the following year by Price [230], who measured the absorption spectra of  $\text{CH}_3\text{Cl}$ ,  $\text{CH}_3\text{Br}$  and  $\text{CH}_3\text{I}$  in the energy range from 6.2 to 12.4 eV. In 1942 Mulliken [231, 232] reviewed all of the experimental data available at that time.

The first detailed experimental photoabsorption study of  $\text{CH}_3\text{F}$  was published in 1958 by Stokes and Duncan [233], who used a helium discharge source to measure the relative photoabsorption spectrum of  $\text{CH}_3\text{F}$  over the energy range 8.5 to 16.1 eV. Edwards and Raymonda [234] recorded the first absolute photoabsorption spectrum from 8.7 to 11.6 eV using a hydrogen discharge source and later Sauvageau *et al.* [235] recorded the absolute photoabsorption spectrum from 8.6 to 20 eV using both hydrogen and helium discharge sources. The electron energy loss spectrum of  $\text{CH}_3\text{F}$  was recorded by Harshbarger *et al.* [236] from 8 to 22 eV under conditions of small momentum transfer, but no absolute cross-sections were reported. The most recent absolute photoabsorption measurements of  $\text{CH}_3\text{F}$  were reported by Wu *et al.* [237], from 16.3 to 70.8 eV using synchrotron radiation as the light source. There are substantial differences in both the shapes and magnitudes of the absolute oscillator strength spectra reported in these previous studies [234, 235, 237].

The first absolute photoabsorption measurement of  $\text{CH}_3\text{Cl}$  was reported by Tsubomura *et al.* [238] in 1964 for the first electronic excitation from 6.6 to 7.75 eV. Russell *et al.* [239] recorded the absolute photoabsorption spectrum over the slightly wider energy region from 6.2 to 11.2 eV using a hydrogen discharge source; later several other absolute spectra [240–244] were published in the same energy region. More recent work, published by Lee and Suto [245] in 1987, reports the absolute photoabsorption spectrum of methyl chloride recorded using synchrotron radiation from 5.6 to 11.8 eV (220 to 105 nm). The only higher energy valence shell absolute photoabsorption data for  $\text{CH}_3\text{Cl}$  is the spectrum obtained by Wu *et al.* [237] from 16.3 to 70.8 eV using synchrotron radiation.

Absolute photoabsorption cross-sections of  $\text{CH}_3\text{Br}$  were first reported by Person and Nicole in 1969 [246, 247] from 10 to 11.8 eV using a hydrogen discharge source. This work was followed by four absolute valence shell spectra being reported in the mid 1970's [241–243, 248], all using hydrogen discharge sources. The first two studies were high resolution spectra published in 1975 from 5 to 11.25 eV [248] and from 6.2 to 11.3 eV [241]. From these spectra [241, 248] several Rydberg series and their associated vibrational structure were identified. The latter two studies [242, 243], which were reported in 1976, focused on the region of the A band from 4.75 to 6.7 eV [243] and on the vibrational structure of the B and C Rydberg bands from 6.7 to 8.55 [242]. Most recently Felps *et al.* [244] re-measured the spectrum from 4.7 to 11.27 eV using a hydrogen discharge source.

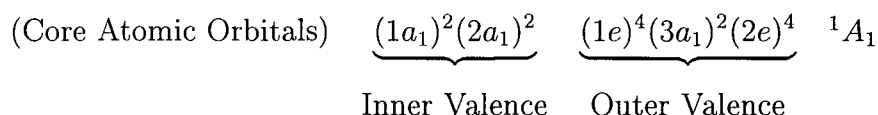
Many valence shell photoabsorption studies of  $\text{CH}_3\text{I}$  have been reported because of the extensive Rydberg structure contained in the valence shell discrete region. The first absolute valence shell spectrum of  $\text{CH}_3\text{I}$  was reported by Boschi and Salahub [249] who, in 1972, recorded the spectra of several 1-iodoalkanes from 4 to 10.6 eV using a hydrogen discharge source. This work was followed by several related publications by McGlynn *et al.* (Hochmann *et al.* [241], Wang *et al.* [250] and Felps *et al.* [242, 244]) between 1975 and 1991. Three of these works [241, 242, 244] involved investigation of the series of methyl halides from

CH<sub>3</sub>Cl to CH<sub>3</sub>I in order to facilitate the assignment of the Rydberg structures observed in the valence shell discrete region. Further assignments of the higher n-Rydberg transitions in CH<sub>3</sub>I were made by Wang *et al.* [250], who identified the 6s to 11s, 9p and 10p and the 5d to 19d Rydberg members. In 1981 Baig *et al.* [251] reported the first photoabsorption spectrum of CH<sub>3</sub>I measured using synchrotron radiation from 6.8 to 11 eV. From this extremely high resolution (0.003 Å) absolute spectrum [251], which was only shown from 9.25 to 10.25 eV in the publication, Baig *et al.* confirmed the assignments of Wang *et al.* [250] and showed vibrational structure which had not previously been observed in this region at lower resolution. Multichannel quantum defect theory (MQDT) has been used [252, 253] to further understand the complex splittings of the Rydberg bands observed in the higher resolution CH<sub>3</sub>I spectra [250, 251]. The most recent photoabsorption study of CH<sub>3</sub>I was published in 1995 by Fahr *et al.* [254] who measured the absolute cross-sections from 3.75 to 7.75 eV in both the gas and liquid phases at temperatures varying from 223 to 333K.

To the best of our knowledge the only inner shell photoabsorption spectrum (absolute or relative) of any of the methyl halides within the energy regions covered in the present work is the I 4d spectrum of CH<sub>3</sub>I reported by O'Sullivan [255]. O'Sullivan [255] photographed the I 4d spectrum of methyl iodide using a laser induced plasma source from 45 to 155 eV. Hitchcock and Brion [256] have studied the inner shell excitation of the methyl halides using EELS and have published long-range energy-loss spectra of CH<sub>3</sub>Cl, CH<sub>3</sub>Br and CH<sub>3</sub>I up to 350 eV energy-loss at moderate resolution (0.35 eV fwhm). They have also reported short range energy-loss spectra at a slightly higher resolution (0.25 eV fwhm) in the discrete regions of the CH<sub>3</sub>Cl Cl 2p, CH<sub>3</sub>Br Br 3d and CH<sub>3</sub>I I 4d spectra and in the carbon 1s inner shell region of each of the methyl halides [256, 257].

## 5.2 Electronic Structure of the Methyl Halides

The photoabsorption, photoionization and binding energy spectra of the methyl halides will be discussed with reference to their valence shell isoelectronic configurations. The molecules  $\text{CH}_3\text{X}$  ( $\text{X} = \text{F}, \text{Cl}, \text{Br}$  or  $\text{I}$ ) are of  $\text{C}_{3v}$  symmetry, and their ground state molecular orbital configurations in the independent particle model may be written in the general form:



In the case of  $\text{CH}_3\text{F}$  most molecular orbital calculations predict the above orbital ordering, but the experimental ionization energies of the  $1e$  (Jahn-Teller split [111]) and  $3a_1$  electrons are very close. In fact, XPS measurements and calculated photoelectron band intensities reported by Banna *et al.* [258, 259] strongly suggest that the order of the  $1e$  and  $3a_1$  ionization energies is reversed in  $\text{CH}_3\text{F}$  from the orbital ordering given above. This reversal in  $\text{CH}_3\text{F}$ , and the ordering shown above for the other three methyl halides, has been convincingly confirmed by Minchinton *et al.* [94, 95] using EMS measurements of the shapes of the respective valence shell momentum distributions for the methyl halides.

He I photoelectron spectra of the outer valence orbitals of the methyl halides were reported by Turner *et al.* in 1970 [53] and several other similar measurements were published at about the same time [260–263]. Further He I studies have also been reported more recently [111, 264–267]. The most detailed high resolution He I spectra have been measured for all four methyl halides by Karlsson *et al.* [111]. He II studies have also been carried out [262, 263, 268, 269], but, with the exception of  $\text{CH}_3\text{I}$ , these have only very limited information on the inner valence region (see section 2.5.4). The XPS measurements by Banna *et al.*, at modest resolution, using  $\text{Y M}\xi$  [259] and also  $\text{Mg}$  and  $\text{Al K}\alpha$  lines [258], were the first to investigate the complete inner valence region of the spectrum in detail for  $\text{CH}_3\text{F}$  only. Earlier, Potts *et al.* [262] had reported rather limited information on the inner valence

Table 5.1: Valence shell ionization potentials<sup>a</sup> of the methyl halides.

Process	CH <sub>3</sub> F	CH <sub>3</sub> Cl	CH <sub>3</sub> Br	CH <sub>3</sub> I
$(2e_{\frac{3}{2}})^{-1}$	13.1 <sup>b</sup>	11.289	10.543	9.540
$(2e_{\frac{1}{2}})^{-1}$		11.316	10.862	10.168
$(3a_1)^{-1}$	17.2 <sup>c</sup>	14.4	13.5	12.5
$(1e_{\frac{3}{2}})^{-1}$	17.2 <sup>b,c</sup>	15.4	15.0	14.7
$(1e_{\frac{1}{2}})^{-1}$		16.0	15.7	15.4
$(2a_1)^{-1}$	23.4	21.7	21.2 <sup>d</sup> 22.0 <sup>d</sup>	19.5 <sup>d</sup> 21.5 <sup>d</sup>
$(1a_1)^{-1}$	38.4	24.1	24.9	23.2

<sup>a</sup>Previously published vertical IPs [111, 268, 269].

<sup>b</sup>Spin orbit components are not resolvable in this band.

<sup>c</sup>Average VIP for the 1e and 3a<sub>1</sub> bands. See text for details on the energy ordering of these bands.

<sup>d</sup>Two bands have been attributed to each of these processes [269].

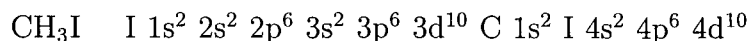
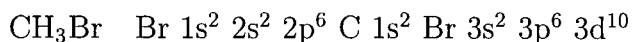
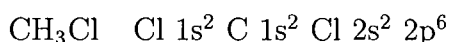
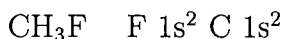
binding energy spectra of each of the methyl halides.

Various PES studies of the methyl halides have also been carried out using synchrotron radiation [270–274]. The studies of Keller *et al.* [270] and Carlson *et al.* [271–273] are mainly concerned with angular distributions and Cooper minimum effects. In other work, Novak *et al.* [274] have reported binding energy spectra of CH<sub>3</sub>F and CH<sub>3</sub>Cl over the outer and inner valence regions at a photon energy of 115 eV. However, the spectra are of modest quality and Novak *et al.* [274] state that better signal/noise ratios than those they obtained would be required for a reliable comparison between theory and experiment. For CH<sub>3</sub>Br and CH<sub>3</sub>I there have been no detailed synchrotron PES studies of the complete inner valence region.

Binding energy spectra covering the complete valence shell region of all four methyl halides have been obtained by Minchinton *et al.* [94, 95] using EMS. Although the energy resolution is limited to  $\sim 1.7$  eV fwhm the spectra at different azimuthal angles provide direct information on the orbital symmetries, the ionization energy ordering and the origins

of the many-body (satellite) structures in the inner valence regions (see sections 2.4 and 2.5.4).

The inner shell electron configurations of the methyl halides can be written as follows:



Many of the inner shell IPs of the methyl halides have been measured using XPS [275–277]. The inner shell IPs within the energy ranges covered in the present work have been reported [275–277] to be  $\text{CH}_3\text{F}$ : C 1s 293.7 eV;  $\text{CH}_3\text{Cl}$ : C 1s 292.48 eV, Cl 2s 277.2 eV, Cl 2p 206.24 eV;  $\text{CH}_3\text{Br}$ : C 1s 292.12 eV, Br  $3d_{5/2}$  76.42 eV;  $\text{CH}_3\text{I}$ : C 1s 291.43 eV. The I  $4d_{5/2,3/2}$  IPs of  $\text{CH}_3\text{I}$  have been determined to be 56.619 and 58.357 eV, respectively, from PES measurements [278] using synchrotron radiation.

The IPs for the Br 3p and 3s subshells of  $\text{CH}_3\text{Br}$  and for the I 4p and 4s subshells of  $\text{CH}_3\text{I}$  have not been measured by XPS. In an attempt to estimate these IPs the following procedure was used: Trends were observed in the behavior of the previously reported Br 3d IPs of  $\text{C}_6\text{H}_5\text{Br}$ ,  $\text{C}_6\text{F}_5\text{Br}$  and  $\text{C}_2\text{H}_3\text{Br}$  [277, 279]. These were compared to the Br 3d IP of  $\text{CH}_3\text{Br}$  reported by Jolly *et al.* [276, 277]. The trends observed between the Br 3d IPs of the aforementioned molecules and  $\text{CH}_3\text{Br}$  were then applied to the 3p and 3s IPs of those molecules in order to estimate the energies of the  $\text{CH}_3\text{Br}$  Br 3p ionization (190 eV) and 3s ionization (263 eV). In the case of  $\text{CH}_3\text{I}$  trends were observed between the previously reported I 4d IPs of  $\text{I}_2$ ,  $\text{BI}_3$  and  $\text{TiI}_4$  [277], and were compared to the I 4d IP of  $\text{CH}_3\text{I}$  [278]. These trends were then applied to the 4p and 4s IPs in order to estimate the energies of the  $\text{CH}_3\text{I}$  I 4p ionization (129 eV) and 4s ionization (194 eV).

## 5.3 Methyl Fluoride Results and Discussion

### 5.3.1 Low resolution photoabsorption (7 to 250 eV)

The absolute photoabsorption oscillator strength spectrum of methyl fluoride from 7 to 250 eV obtained at a resolution of 1 eV fwhm is shown in figure 5.1. The corresponding differential oscillator strengths are given numerically in table 5.2. The results are compared graphically to the previously reported photoabsorption data of Wu *et al.* [237] and to theoretical [280] and experimental [281] summed (3H + C + F) atomic oscillator strengths in figure 5.1.

The absolute scale was obtained using the VTRK sum-rule by normalizing the total area under the valence shell Bethe-Born converted electron energy loss spectrum to a total integrated oscillator strength of 14.54 electrons. This value corresponds to the 14 valence electrons in CH<sub>3</sub>F plus a small estimated contribution due to Pauli excluded transitions [98, 99]. The area under the valence shell spectrum above 250 eV was estimated by fitting the polynomial given in equation (3.1) to the relative oscillator strength data from 100 to 250 eV (where the fit parameters were determined by a least squares fit to be  $A = 7.7464 \times 10^4$  eV,  $B = -3.05054 \times 10^6$  eV<sup>2</sup>,  $C = 2.05793 \times 10^8$  eV<sup>3</sup>) and integrating to infinite energy. The area under the fitted polynomial from 250 eV to infinite energy was 8.4% of the total valence shell area.

The low resolution dipole (e,e) spectrum in figure 5.1(a) shows several prominent features which have been assigned by Harshbarger *et al.* [236] to Rydberg transitions. These are discussed in more detail for the high resolution dipole (e,e) spectrum (0.05 eV fwhm) of methyl fluoride in section 5.3.2. From figure 5.1(a) it can be seen that the photoabsorption oscillator strength data obtained by Wu *et al.* [237] using a double ion chamber with synchrotron radiation as the light source are considerably lower below 20 eV, but agree quite well between 20 and 70 eV with the present low-resolution data, with only a slight discrepancy between the

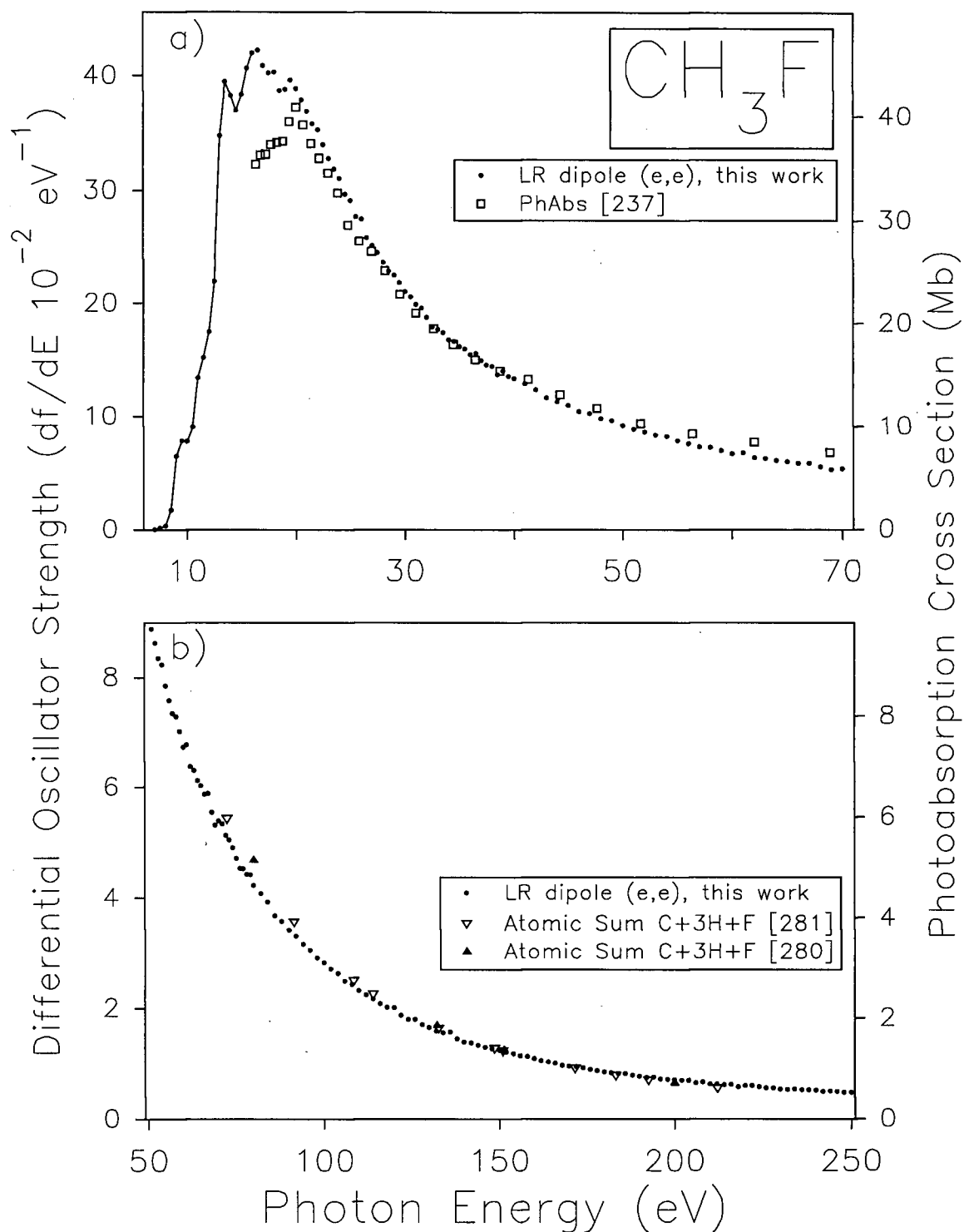


Figure 5.1: Absolute low resolution (1 eV fwhm) photoabsorption oscillator strength spectrum of methyl fluoride. (a) The valence shell region from 6 to 71 eV. (b) The higher energy valence region shown from 49 to 251 eV. Also shown are previously published photoabsorption measurements [237] and summed atomic oscillator strengths [280, 281].

shapes of the continua. The reason for the lower intensity of the data in reference [237] below 20 eV is unclear. There is excellent agreement between the present data and the summed atomic oscillator strengths [280, 281] above 100 eV.

Table 5.2: Absolute differential oscillator strengths for the total photoabsorption of CH<sub>3</sub>F from 7 to 250 eV.

Photon Energy eV	Oscillator Strength (10 <sup>-2</sup> eV <sup>-1</sup> ) <sup>a</sup>	Photon Energy eV	Oscillator Strength (10 <sup>-2</sup> eV <sup>-1</sup> )	Photon Energy eV	Oscillator Strength (10 <sup>-2</sup> eV <sup>-1</sup> )	Photon Energy eV	Oscillator Strength (10 <sup>-2</sup> eV <sup>-1</sup> )
7	0.10	25.5	27.72	57	7.34	108	2.44
7.5	0.16	26	27.51	58	7.28	110	2.33
8	0.36	26.5	25.86	59	7.01	112	2.24
8.5	1.77	27	25.14	60	6.73	114	2.17
9	6.47	27.5	24.52	61	6.78	116	2.08
9.5	7.83	28	23.61	62	6.38	118	2.02
10	7.80	28.5	22.87	63	6.31	120	2.01
10.5	9.08	29	22.49	64	6.12	122	1.87
11	13.46	29.5	21.84	65	6.03	124	1.80
11.5	15.21	30	21.04	66	5.88	126	1.80
12	17.49	31	19.90	67	5.89	128	1.71
12.5	21.97	32	18.77	68	5.55	130	1.66
13	34.78	33	17.71	69	5.32	132	1.59
13.5	39.50	34	16.81	70	5.39	134	1.56
14	38.30	35	16.22	71	5.35	136	1.57
14.5	37.02	36	15.48	72	5.14	138	1.45
15	38.36	37	14.98	73	5.06	140	1.39
15.5	40.67	38	14.49	74	4.92	142	1.38
16	41.99	39	14.05	75	4.73	144	1.34
16.5	42.22	40	13.39	76	4.55	146	1.30
17	40.90	41	12.94	77	4.54	148	1.27
17.5	40.27	42	12.39	78	4.44	150	1.24
18	40.32	43	11.70	79	4.44	152	1.21
18.5	38.71	44	11.34	80	4.24	154	1.18
19	38.80	45	11.03	82	4.08	156	1.15
19.5	39.60	46	10.48	84	3.93	158	1.13
20	38.86	47	10.28	86	3.69	160	1.09
20.5	37.87	48	9.84	88	3.58	162	1.06
21	36.92	49	9.66	90	3.42	164	1.04
21.5	35.83	50	9.18	92	3.31	166	1.01
22	35.30	50	9.18	94	3.16	168	0.97
22.5	33.99	51	8.89	96	3.06	170	0.96
23	32.80	52	8.63	98	2.92	172	0.95
23.5	31.89	53	8.35	100	2.83	174	0.82
24	31.06	54	8.24	102	2.72	176	0.90
24.5	29.70	55	7.85	104	2.64	178	0.88
25	29.11	56	7.58	106	2.49	180	0.86

Table 5.2: (continued) Absolute differential oscillator strengths for the total photoabsorption of CH<sub>3</sub>F from 7 to 250 eV.

Photon Energy eV	Oscillator Strength (10 <sup>-2</sup> eV <sup>-1</sup> ) <sup>a</sup>	Photon Energy eV	Oscillator Strength (10 <sup>-2</sup> eV <sup>-1</sup> )	Photon Energy eV	Oscillator Strength (10 <sup>-2</sup> eV <sup>-1</sup> )	Photon Energy eV	Oscillator Strength (10 <sup>-2</sup> eV <sup>-1</sup> )
182	0.84	200	0.71	218	0.58	236	0.52
184	0.82	202	0.70	220	0.61	238	0.52
186	0.82	204	0.70	222	0.61	240	0.52
188	0.79	206	0.66	224	0.51	242	0.50
190	0.78	208	0.67	226	0.56	244	0.50
192	0.75	210	0.64	228	0.56	246	0.50
194	0.76	212	0.64	230	0.54	248	0.48
196	0.72	214	0.62	232	0.53	250	0.50
198	0.71	216	0.62	234	0.54		

$\sigma(\text{Mb})=109.75 \, df/dE \, (\text{eV}^{-1})$ .

### 5.3.2 High resolution photoabsorption (7.5 to 50 eV)

The high-resolution (0.05 eV fwhm) valence shell photoabsorption spectrum of  $\text{CH}_3\text{F}$  recorded in the present work is shown in figure 5.2(a) from 7.5 to 50 eV. Figure 5.2(b) shows an expanded view of the energy region from 8.4 to 13 eV. The presently measured high-resolution oscillator strength spectrum was normalized to the low resolution absolute spectrum (figure 5.1) in the smooth continuum region at 28 eV where no sharp structures exist.

For comparison to the presently reported high-resolution oscillator strengths, figure 5.2(a) shows the photoabsorption spectrum recorded by Sauvageau *et al.* [235] using a helium Hopfield discharge source from 11.7 to 20 eV. Below 17 eV these data are consistently higher than the presently reported data, up to and above the 25 % accuracy reported [235]. Above 17 eV the data of Sauvageau *et al.* [235] decrease to well below the present data probably because of the drop off in photon intensity at the upper energy limit of the Helium Hopfield continuum discharge lamp used in their work.

Figure 5.2(b) compares the presently reported high resolution data with the photoabsorption data of Edwards and Raymonda [234] from 8.7 to 11.6 eV and the data of Sauvageau *et al.* [235] from 8.6 to 11.7 eV, which were both obtained using hydrogen discharge sources. The data of Sauvageau *et al.* [235] are consistently higher than the presently reported data, but, in contrast to the higher energy data shown in figure 5.2(a), are for the most part less than 10 % higher. The data of Edwards and Raymonda [234] are consistently up to 10 % lower than the present work. No direct comparison is made on figure 5.2(b) in the region from 10.0 to 10.7 eV where sharp discrete structures occur, because the different energy resolutions of different data sets make direct comparison misleading.

The accuracy of the presently reported absolute differential oscillator strengths for  $\text{CH}_3\text{F}$  is supported by application of the S(-2) sum-rule to the photoabsorption spectrum. The

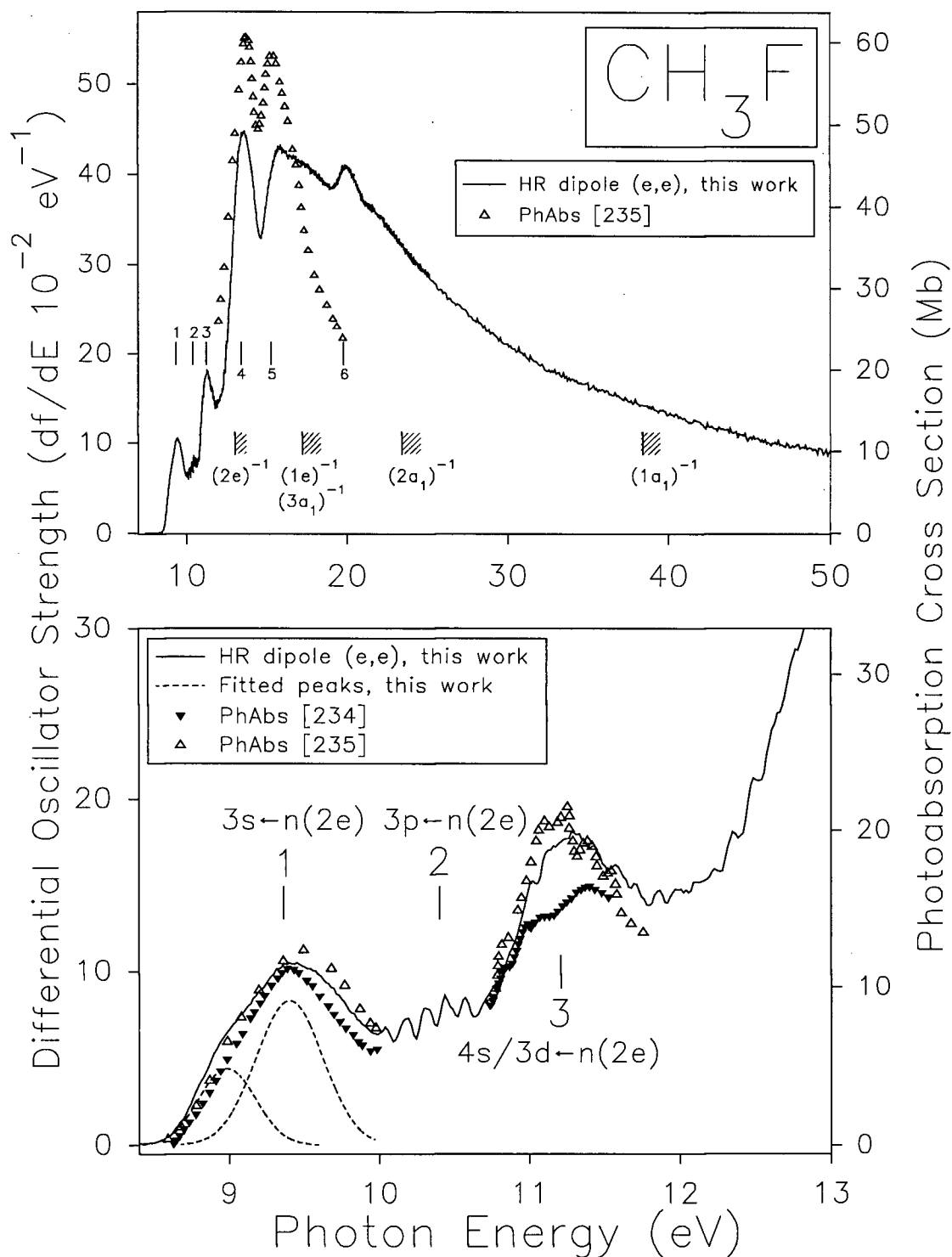


Figure 5.2: Absolute photoabsorption oscillator strengths for methyl fluoride. (a) The high resolution (0.05 eV fwhm) dipole ( $e,e$ ) measurements from 7 to 51 eV. (b) Expanded view from 8.4 to 13 eV. Gaussian peaks fitted to the present high resolution spectrum (solid line) are shown as dashed lines. Also shown are previously published ionization potentials (see table 5.1), photoabsorption measurements [234, 235] and assignments [233, 236].

presently reported absolute spectrum (combined high plus low resolution) from 7 to 350 eV gives an  $S(-2)$  sum of 17.14 au, which is within 5% of the experimentally measured static dipole polarizabilities of 17.9 and 17.6 au [163]. It is also in good agreement with the value of 16.13 au obtained from theoretical calculations [184] using the finite field method at the MP2 level and the values of 17.00 and 16.53 au obtained from additivity methods [166].

Stokes and Duncan [233] recorded a relative photoabsorption spectrum of  $\text{CH}_3\text{F}$  in the region from 8.5 to 16 eV using a hydrogen discharge source. The features in this high-resolution spectrum were extensively analysed and the relative energy positions of the features are considered highly accurate. The Rydberg assignment proposed by Stokes and Duncan [233] has since been revised [236] as more accurate measurements of IPs have been published. The assignment of vibronic structure in the Rydberg transition in the energy region from 10.0 to 10.9 eV proposed by Stokes and Duncan [233] has been upheld and is consistent with the structure observable in the present work from 10 to 10.9 eV shown in figure 5.2(b). The Rydberg transitions of methyl fluoride in the discrete valence shell were re-assigned by Harshbarger *et al.* [236] using their electron energy loss spectrum which was recorded using 400 eV electron impact energy and a mean scattering angle of  $0^\circ$ . There is good agreement between the energy positions of the transitions observed in the present high-resolution spectrum and the energies quoted for the corresponding transitions detailed by Harshbarger *et al.* [236].

The  $3s \leftarrow 2e$  Rydberg transition, feature 1 on figures 5.2(a) and (b), centered at 9.3 eV, is made up of two peaks at 8.98 and 9.40 eV (fitted peaks are shown as dashed lines on figure 5.2(b)) due to Jahn-Teller splitting in the  $2e$  orbital. The splitting of about 0.4 eV is similar to the 0.6 eV splitting reported by Karlsson *et al.* [111] for the Jahn-Teller splitting of the  $(2e)^{-1}$  photoelectron band in the PE spectrum of methyl fluoride. Feature 2 on figures 5.2(a) and (b) is the  $3p \leftarrow 2e$  Rydberg transition centered at about 10.4 eV, which involves an extensive vibronic envelope from 10.04 to 10.84 eV. This envelope was interpreted

by Stokes and Duncan [233] to contain 15 peaks from excitations of various vibrational modes of  $\text{CH}_3\text{F}$ . Seven vibronic peaks are observed at the 0.05 eV fwhm resolution of the present work and correspond to the more intense peaks described by Stokes and Duncan [233]. Feature 3 at 11.2 eV on figures 5.2(a) and (b) is assigned to the transition from the 2e orbital to either the 3d or 4s Rydberg orbitals. This gives quantum defects of  $\delta=0.07$  and 1.07, respectively, which are both consistent with those expected for 3d and 4s Rydberg orbitals. The remaining transitions, shown as features 4, 5, and 6 on figure 5.2(a), have been assigned by Harshbarger *et al.* [236] to the Rydberg transitions  $3s/3p \leftarrow 3a_1/1e$  (feature 4),  $3d/4s \leftarrow 3a_1/1e$  (feature 5), and  $3s \leftarrow 2a_1$  (feature 6).

Many partially resolved vibronic peaks are observed in the present high resolution spectrum of  $\text{CH}_3\text{F}$  in the energy region from 11 to 13 eV (figure 5.2(b)). These peaks were not discussed by Stokes and Duncan [233] nor by Edwards and Raymond [234], even though several can be observed from 10.8 to 11.0 eV in their spectra. These peaks were also observed in the spectrum reported by Sauvageau *et al.* [235] from 10.8 to 11.55 eV. They concluded [235] that for both this band and the previous band displaying vibronic structure (feature 2) there is likely to be a coincidence between two electronic transitions. It would appear that the first nine peaks of feature 3, from 11.02 to 11.86 eV, are associated with the  $3d$  or  $4s \leftarrow 2e$  transition. The remaining vibronic peaks suggest the presence of extended Rydberg structure from  $4p$ ,  $4d$ , or  $5s \leftarrow 2e$  Rydberg transitions or possibly a  $3s \leftarrow 3a_1/1e$  Rydberg transition.

## 5.4 Methyl Chloride Results and Discussion

### 5.4.1 Low resolution photoabsorption (6 to 350 eV)

The absolute low resolution (1 eV fwhm) photoabsorption oscillator strength spectrum of methyl chloride obtained in the present work from 6 to 350 eV is shown in figure 5.3. The corresponding differential oscillator strengths are given numerically in table 5.3. The

results are compared graphically in figure 5.3 to the previously reported photoabsorption data of Wu *et al.* [237] and to theoretical [280] and experimental [281] summed (3H + C + Cl) atomic oscillator strengths.

The absolute scale of the presently reported spectrum was obtained using the VTRK sum-rule by normalizing the total area under the valence shell Bethe-Born converted electron energy loss spectrum to a total integrated oscillator strength of 14.53 electrons. This value corresponds to the 14 valence electrons in CH<sub>3</sub>Cl plus a small estimated contribution due to Pauli excluded transitions [98, 99]. The area under the valence shell spectrum above 194 eV was estimated by fitting the polynomial given in equation (3.1) to the relative oscillator strength data from 80 to 194 eV and integrating to infinite energy. The best fit parameters from equation (3.1) were determined to be  $A = 227.2$  eV,  $B = -1.462 \times 10^4$  eV<sup>2</sup>,  $C = 3.774 \times 10^5$  eV<sup>3</sup>. The area under the fitted polynomial from 194 eV to infinite energy was 6.8% of the total valence shell area.

Figure 5.3(a) shows that the photoabsorption data of Wu *et al.* [237], obtained using a double ion chamber with synchrotron radiation as the light source, are considerably lower than the presently reported oscillator strengths measurements below 20 eV, but agree reasonably well between 20 and 70 eV. Similar discrepancies occur in the case of CH<sub>3</sub>F [237] (see section 5.3.1).

Prominent structures in the Cl 2p, 2s, and C 1s inner shell excitation regions of CH<sub>3</sub>Cl can be seen in the extended range absolute photoabsorption spectrum in figure 5.3(b). These structures are shown at higher resolution (0.25-0.35 eV fwhm) in the energy loss spectra reported earlier by Hitchcock and Brion [256, 257, 282]. There is good agreement between the present data and the summed atomic oscillator strengths [280, 281] with the exceptions of the region below 100 eV and at the Cl 2p edge where molecular effects are expected to be significant.

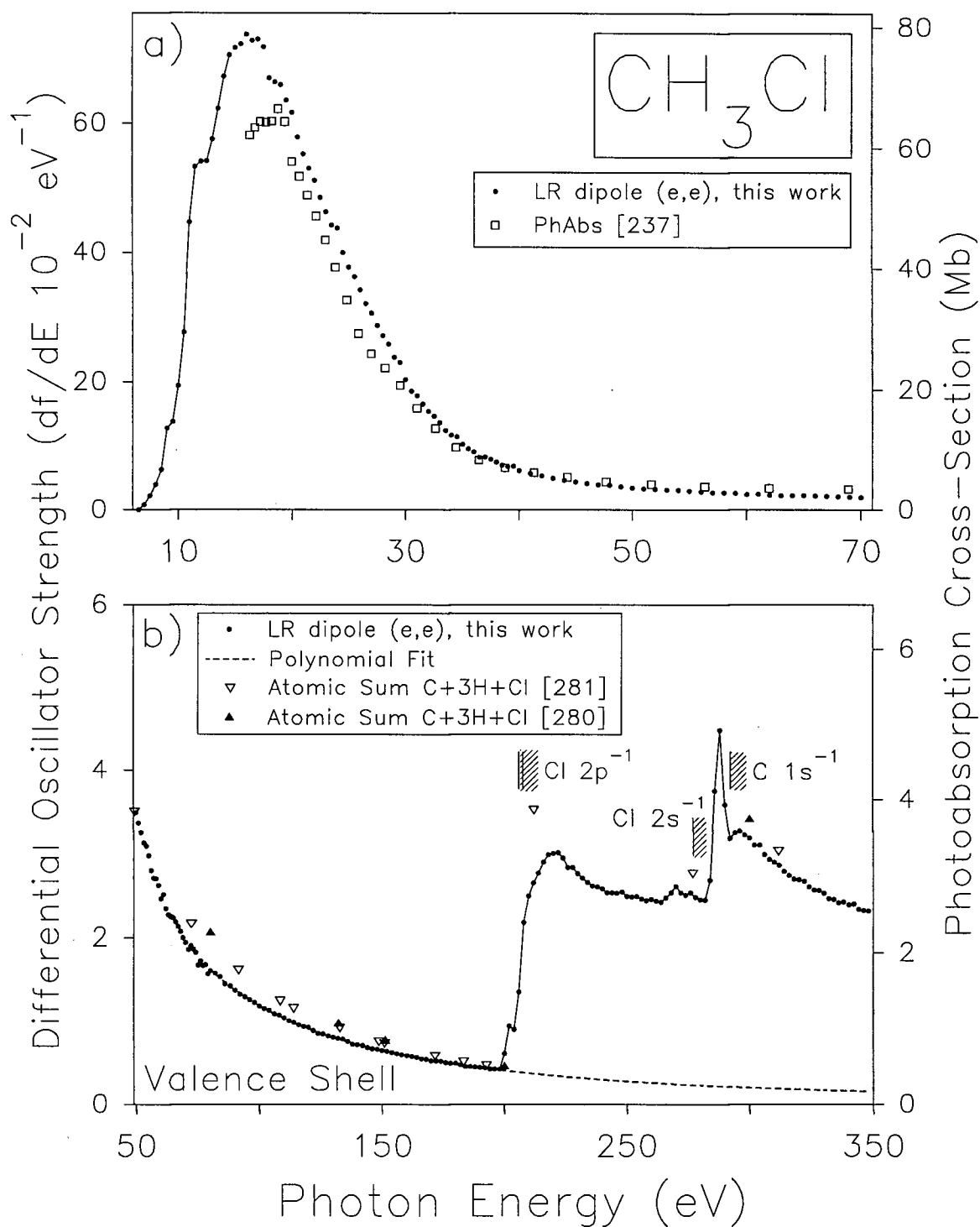


Figure 5.3: Absolute low resolution (1 eV fwhm) photoabsorption oscillator strength spectrum of methyl chloride. (a) The valence shell region from 6 to 70 eV. (b) The higher energy region shown from 50 to 350 eV. Also shown are previously published inner shell ionization potentials [275–277], photoabsorption measurements [237] and summed atomic oscillator strengths [280, 281].

Table 5.3: Absolute differential oscillator strengths for the total photoabsorption of  $\text{CH}_3\text{Cl}$  from 6 to 348 eV.

Photon Energy eV	Oscillator Strength ( $10^{-2} \text{ eV}^{-1}$ ) <sup>a</sup>	Photon Energy eV	Oscillator Strength ( $10^{-2} \text{ eV}^{-1}$ )	Photon Energy eV	Oscillator Strength ( $10^{-2} \text{ eV}^{-1}$ )	Photon Energy eV	Oscillator Strength ( $10^{-2} \text{ eV}^{-1}$ )
6.0	0.00	24.5	39.98	56	2.80	106	1.09
6.5	0.03	25.0	37.68	57	2.70	108	1.07
7.0	0.85	25.5	36.20	58	2.70	110	1.04
7.5	2.19	26.0	34.21	59	2.62	112	1.01
8.0	3.96	26.5	32.05	60	2.46	114	0.98
8.5	6.28	27.0	30.65	61	2.50	116	0.96
9.0	12.78	27.5	28.78	62	2.34	118	0.94
9.5	13.79	28.0	27.23	63	2.26	120	0.93
10.0	19.42	28.5	25.92	64	2.25	122	0.89
10.5	27.74	29.0	23.84	65	2.23	124	0.86
11.0	44.74	29.5	23.04	66	2.18	126	0.85
11.5	53.28	30.0	20.37	67	2.13	128	0.82
12.0	54.08	31.0	17.83	68	2.07	130	0.81
12.5	54.13	32.0	15.41	69	2.00	132	0.80
13.0	57.52	33.0	13.69	70	1.94	134	0.79
13.5	62.33	34.0	11.68	71	1.86	136	0.76
14.0	67.21	35.0	10.27	72	1.90	138	0.73
14.5	70.55	36.0	9.07	73	1.86	140	0.72
15.0	71.70	37.0	8.23	74	1.83	142	0.71
15.5	72.22	38.0	7.42	75	1.67	144	0.68
16.0	73.73	39.0	6.76	76	1.72	146	0.67
16.5	72.81	40.0	6.14	77	1.67	148	0.66
17.0	72.97	41.0	5.72	78	1.68	150	0.65
17.5	71.81	42.0	5.32	79	1.56	152	0.64
18.0	67.02	43.0	4.93	80	1.60	154	0.63
18.5	66.34	44.0	4.61	82	1.58	156	0.61
19.0	65.95	45.0	4.41	84	1.53	158	0.60
19.5	63.55	46.0	4.14	86	1.45	160	0.58
20.0	61.72	47.0	3.94	88	1.43	162	0.58
20.5	57.83	48.0	3.88	90	1.37	164	0.57
21.0	55.23	49.0	3.65	92	1.32	166	0.55
21.5	53.06	50	3.48	94	1.29	168	0.55
22.0	51.16	51	3.35	96	1.26	170	0.53
22.5	48.54	52	3.24	98	1.22	172	0.52
23.0	46.27	53	3.12	100	1.18	174	0.52
23.5	44.23	54	3.08	102	1.15	176	0.51
24.0	43.80	55	2.97	104	1.13	178	0.49

Table 5.3: (continued) absolute differential oscillator strengths for the total photoabsorption of CH<sub>3</sub>Cl from 6 to 348 eV.

Photon Energy eV	Oscillator Strength (10 <sup>-2</sup> eV <sup>-1</sup> ) <sup>a</sup>	Photon Energy eV	Oscillator Strength (10 <sup>-2</sup> eV <sup>-1</sup> )	Photon Energy eV	Oscillator Strength (10 <sup>-2</sup> eV <sup>-1</sup> )	Photon Energy eV	Oscillator Strength (10 <sup>-2</sup> eV <sup>-1</sup> )
180	0.49	224	2.95	268	2.53	312	2.86
182	0.47	226	2.83	270	2.61	314	2.79
184	0.46	228	2.83	272	2.53	316	2.74
186	0.46	230	2.76	274	2.50	318	2.70
188	0.45	232	2.71	276	2.53	320	2.69
190	0.45	234	2.65	278	2.48	322	2.67
192	0.44	236	2.61	280	2.45	324	2.60
194	0.43	238	2.60	282	2.44	326	2.56
196	0.43	240	2.58	284	2.68	328	2.56
198	0.43	242	2.53	286	3.75	330	2.52
200	0.62	244	2.53	288	4.48	332	2.46
202	0.94	246	2.52	290	3.58	334	2.45
204	0.91	248	2.54	292	3.18	336	2.41
206	1.35	250	2.48	294	3.25	338	2.42
208	2.18	252	2.48	296	3.26	340	2.39
210	2.49	254	2.49	298	3.22	342	2.40
212	2.65	256	2.46	300	3.18	344	2.33
214	2.77	258	2.44	302	3.10	346	2.32
216	2.90	260	2.45	304	3.10	348	2.32
218	2.98	262	2.43	306	2.99		
220	3.00	264	2.41	308	2.93		
222	3.01	266	2.47	310	2.90		

$\sigma(\text{Mb})=109.75 df/dE$  (eV<sup>-1</sup>).

### 5.4.2 High resolution photoabsorption (5 to 50 eV)

The high-resolution (0.05 eV fwhm) valence shell photoabsorption spectrum of CH<sub>3</sub>Cl recorded in the present work is shown in figure 5.4(a) from 6 to 25 eV, while figure 5.4(b) shows an expanded view of the discrete absorption bands in the 6 to 12 eV region. The presently reported high resolution data was placed on an absolute scale by normalization to the absolute low resolution spectrum (figure 5.3) in the smooth continuum region at 28 eV where no sharp structures exist.

In 1936 Price [230] reported the energies of the A ( $\sigma^* \leftarrow n$ ), B ( $4s \leftarrow n$ ), and the D ( $4p \leftarrow n$ ) photoabsorption bands of CH<sub>3</sub>Cl (where n represents the 2e orbital which is mainly Cl 3p non-bonding in character). Price also assigned several bands to the np-Rydberg series leading up to the  $(2e_{\frac{3}{2}})^{-1}$  and the  $(2e_{\frac{1}{2}})^{-1}$  ionization limits. The assignments of bands A to D given by Price [230] were confirmed by Russell [239] and Raymond [240], who expanded the work by identifying the first component of the nd-Rydberg series and the second component of the ns-series as well as the first band of the ns-series terminating at the  $(3a_1)^{-1}$  ionization limit. Hochmann *et al.* [241] identified many more of the components of the ns, np, and nd Rydberg series that terminate at the  $(2e_{\frac{3}{2}})^{-1}$  and the  $(2e_{\frac{1}{2}})^{-1}$  limits. A combination of these assignments [230, 241] is shown on figure 5.4(b).

As a result of the large difference in energy resolution, the presently reported high resolution (0.05 eV fwhm) oscillator strength spectrum of CH<sub>3</sub>Cl cannot be compared directly, in the discrete valence shell region, with the absolute photoabsorption spectrum recorded by Lee and Suto [245] using synchrotron radiation from 6–11.5 eV (107.5–205 nm) at a resolution of 0.04 nm (3 meV fwhm at 9.65 eV). A meaningful quantitative comparison can, however, be achieved by convolution of the (digitized) spectrum of Lee and Suto [245] with a gaussian function of 0.05 eV fwhm, in order to mathematically degrade the resolution of the optical experiment to match the resolution of the presently reported dipole (e,e) spectrum.

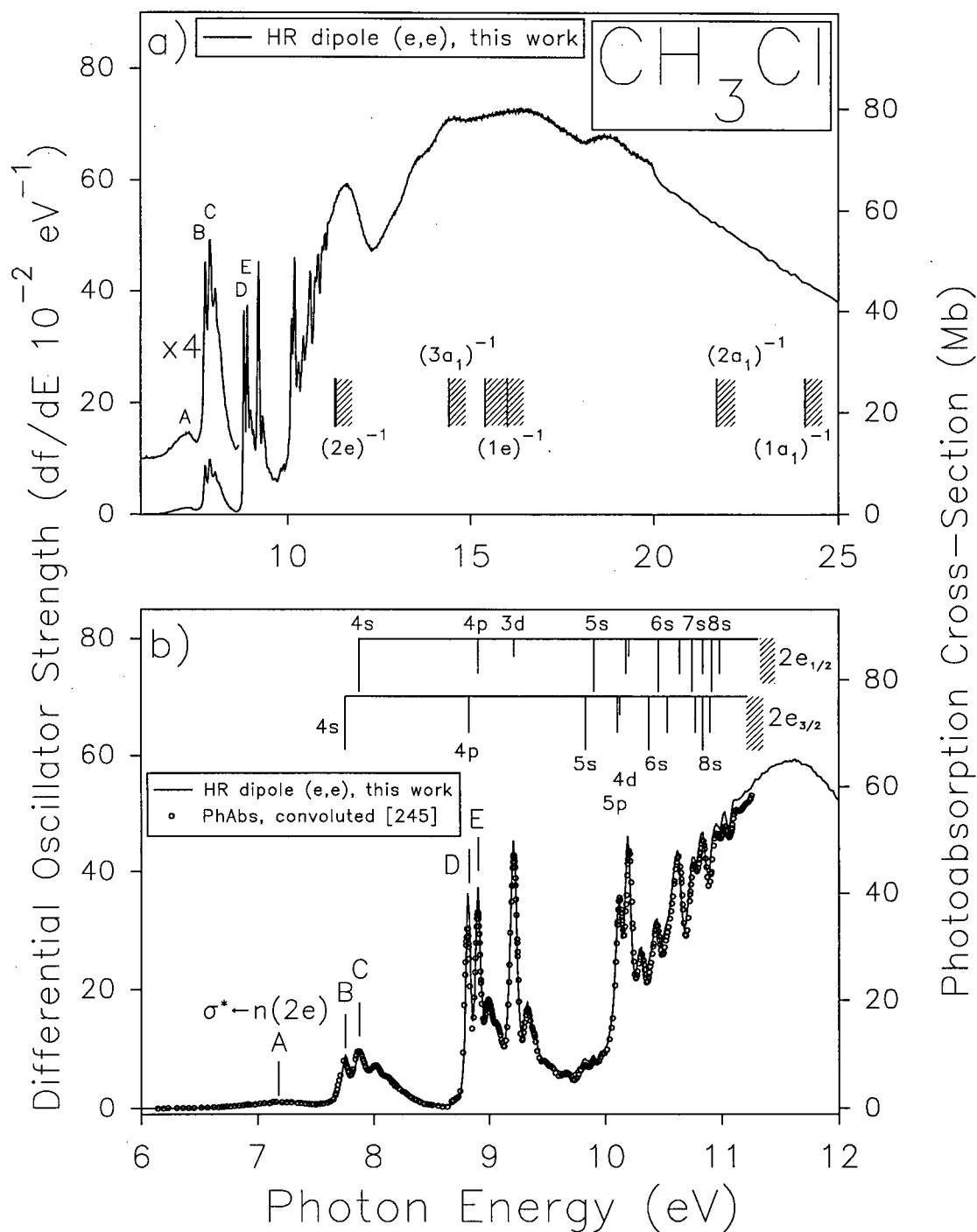


Figure 5.4: Absolute photoabsorption oscillator strength spectrum for methyl chloride. (a) High resolution (0.05 eV fwhm) dipole (e,e) measurements from 6 to 25 eV. (b) Expanded view of (a) from 6 to 12 eV. Shown for comparison are the high resolution data of Lee and Suto [245] convoluted with a 0.05 eV fwhm gaussian function (see text for details). Also shown are previously published assignments [230, 241] (transitions to ns, np and nd Rydberg orbitals represented as long, medium, and short vertical lines, respectively) and ionization potentials (see table 5.1).

Figure 5.4(b) shows that the quantitative agreement between the presently reported dipole (e,e) data and the (convoluted) experimental photoabsorption data of Lee and Suto [245] is generally excellent, for the most part being well within the 10% uncertainty quoted for the optical measurements. The largest discrepancies occur for the D and E bands ( $4p \leftarrow 2e$ ) at 8.81 and 8.90 eV, respectively, which are between 5 and 15% lower in intensity in the spectrum of Lee and Suto [245] than in the present work. This may be caused by line-saturation errors (see chapter 1) in the optical spectrum. The spectrum reported by Lee and Suto [245] is also slightly lower ( $< 5\%$ ) in the continuum region above 11 eV. The region from 6.0 to 11.5 eV in the presently reported high resolution spectrum has a total oscillator strength of 0.832. The oscillator strength of the spectrum reported by Lee and Suto [245] over the same energy range is 0.797, which is 4% lower than the present work.

The  $S(-2)$  sum for methyl chloride using the presently reported (high plus low resolution) data from 6 to 350 eV gives a value of 29.80 a.u., which is in excellent agreement with experimental dipole polarizability values which range from 30.0 to 30.7 au from refractive index measurements [163, 192] and the theoretical value of 28.57 a.u. [184] calculated using the finite field method at the MP2 level. This good agreement lends strong support to the accuracy of the absolute oscillator strength scale determined in the present work by the  $S(0)$  sum-rule.

Several other studies [239–242, 244] have reported absolute spectra which are qualitatively the same as the presently reported spectrum. However, the intensities of many of the bands in the previously reported spectra differ from those in the presently reported spectrum. While the intensity differences may in partially be a result of different spectral resolutions in the various studies, line-saturation effects [6, 27, 28] (see chapter 1) will also cause differences in band intensities where the natural line-width of a transition is smaller than, or comparable to, the resolution of the optical photoabsorption experiment. Table 5.4 compares oscillator strengths for several bands determined in the present work with those from various other

Table 5.4: Absolute oscillator strengths for selected regions of the valence shell photoabsorption spectrum of CH<sub>3</sub>Cl.

Assignment	Energy Region (eV)	Oscillator Strength <sup>a</sup>				
		This Work	[239]	[240]	[244]	[245]
A: $\sigma^* \leftarrow 2e$	6.00 – 7.60	0.0077	0.0066	0.0066	0.0067	0.0071
B,C: $4s \leftarrow 2e$	7.50 – 8.65	0.0431	0.0531	0.0531		0.0410
D,E: $4p \leftarrow 2e$	8.65 – 9.70	0.1563	0.1328	0.0996		0.1444
	6.00 – 11.50	0.832				0.797

<sup>a</sup>Oscillator strength values that were not tabulated in the original publications [239, 240, 244, 245] were obtained from integration of the digitized (unconvoluted) spectra.

studies of the CH<sub>3</sub>Cl spectrum [239, 240, 244, 245].

## 5.5 Methyl Bromide Results and Discussion

### 5.5.1 Low resolution photoabsorption (6 to 350 eV)

The absolute photoabsorption oscillator strength spectrum of methyl bromide obtained in the present work from 6 to 350 eV at a resolution of 1 eV fwhm is shown in figure 5.5. The corresponding differential oscillator strengths are given numerically in table 5.5. Figure 5.5(a) shows the absolute photoabsorption spectrum of CH<sub>3</sub>Br from 6 to 71 eV in the valence shell region. Figure 5.5(b) shows the absolute photoabsorption spectrum of CH<sub>3</sub>Br from 60 to 285 eV in the region of the Br 3d, 3p, 3s and C 1s subshells. The results are compared graphically to the previously reported theoretical [280] and experimental [281] summed (3H + C + Br) atomic oscillator strengths in figure 5.5(b).

The low energy Br 3d inner shell discrete region and delayed onset complicate the application of the VTRK sum-rule to establish the absolute scale of the CH<sub>3</sub>Br photoabsorption

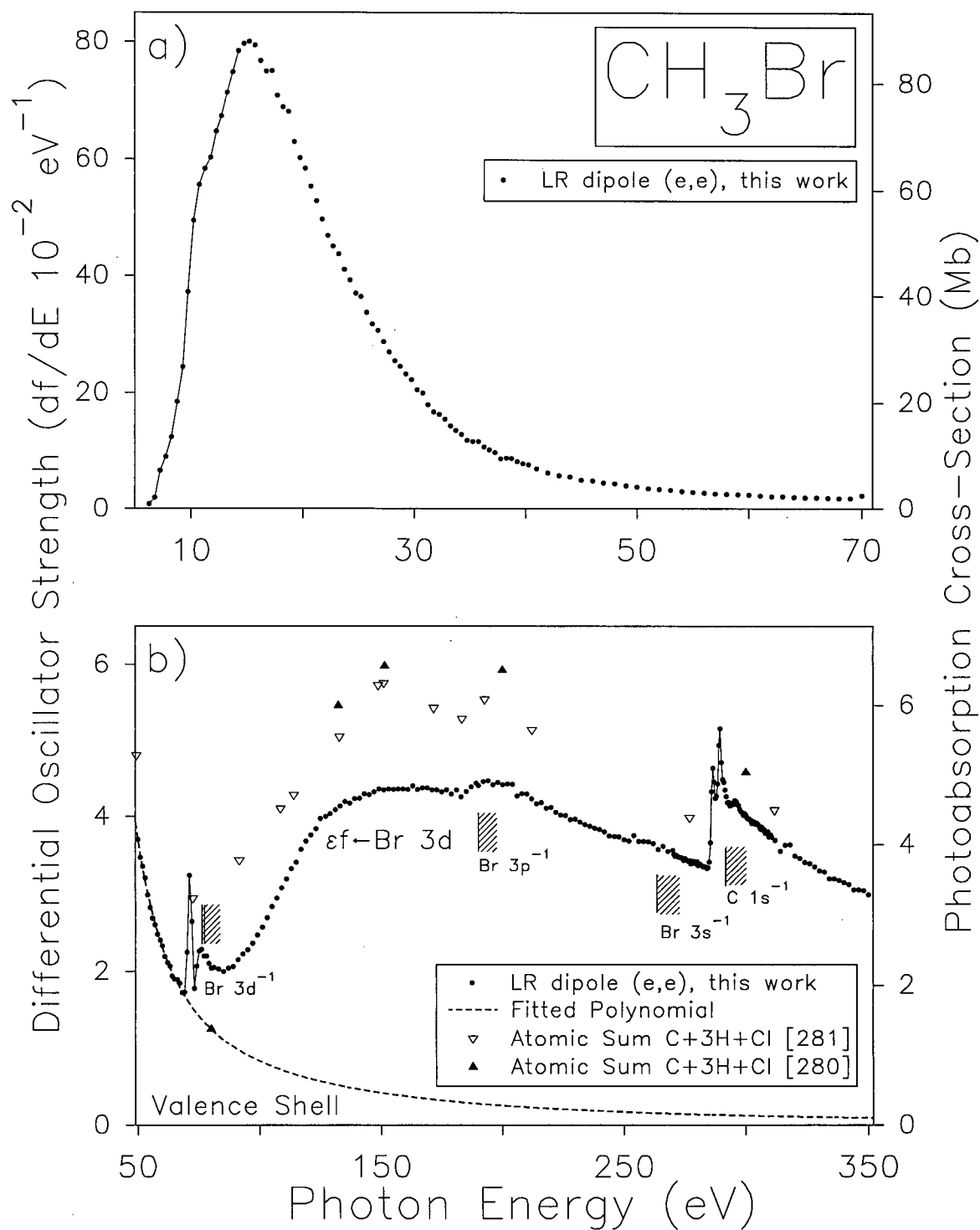


Figure 5.5: Absolute low resolution (1 eV fwhm) photoabsorption oscillator strength spectrum of methyl bromide. (a) The valence shell region from 5 to 71 eV. (b) The higher energy region shown from 49 to 352 eV. Also shown are previously published inner shell ionization potentials [275–277, 279] and summed atomic oscillator strengths [280, 281].

spectrum. For this reason the absolute scale was obtained by normalization of a combination high (5 to 18 eV) (see section 5.5.2 below) and low (18 to 350 eV) resolution relative photoabsorption spectrum to the dynamic dipole polarizability values reported by Ramaswamy [168]. Application of the  $S(-2)$  sum-rule to the resulting absolute spectrum yields a sum of 36.81 au which, when compared to published static dipole polarizabilities for  $\text{CH}_3\text{Br}$  listed in table 4.2, is only slightly lower than the experimental values [163, 164] and compares well with the theoretical [184] and additivity [166] values.

An estimation of the valence shell oscillator strength underlying the Br 3d, 3p, 3s and C 1s inner shells, obtained by fitting a polynomial of the form given in equation (3.1) to the absolute spectrum in the valence region from 36 to 68 eV, is shown by the dashed line in figure 5.5(b). The area under the photoabsorption spectrum from 4 to 68 eV plus the area under the fitted polynomial from 68 eV to infinite energy is 14.7. This can be compared to a total oscillator strength of 14.87 corresponding to the 14 valence electrons in  $\text{CH}_3\text{Br}$  plus a small estimated contribution due to Pauli excluded transitions [98, 99]. This excellent agreement supports the accuracy of the absolute oscillator strength scale established using the experimental dynamic dipole polarizabilities of Ramaswamy [168].

The valence shell discrete spectrum, which appears relatively featureless at low resolution (figure 5.5(a)), contains an abundance of discrete structure that can be observed in the high resolution (0.05 eV fwhm) dipole (e,e) spectrum discussed in the following section. However, several prominent features are observed in the extended range low resolution photoabsorption spectrum shown in figure 5.5(b). A prominent sharp structure from excitation from the Br 3d to the  $\sigma^*$  virtual valence orbital is visible below the Br 3d ionization edge. Also present is a large, broad continuum resonance ( $\epsilon f \leftarrow 3d$ ) from 95 to above 300 eV with a maximum at  $\sim 160$  eV. This is a delayed onset of the  $\epsilon f \leftarrow 3d$  transitions caused by a potential barrier to continuum  $f$ -waves (see section 2.5.2). To the best of our knowledge the only published photoabsorption or energy-loss spectrum in the inner shell region of  $\text{CH}_3\text{Br}$  is the long

range electron energy-loss spectrum (0.35 eV fwhm) from 60 to 350 eV by Hitchcock and Brion [256]. Their energy-loss spectrum [256] shows a maximum at  $\sim 120$  eV energy-loss from the Br 3d delayed onset. They [256] noted that there was an absence of any structure associated with the excitation of Br 3p and 3s electrons in the long range spectrum which would be expected to appear in the region about 10 eV below the respective IPs. In the presently reported photoabsorption spectra there are definite pre-edge excitation features visible in the regions just below the Br 3p and 3s ionization thresholds. The broad nature of these transitions is likely a result of the very short lifetimes of the excited states which would likely decay via fast (super) Coster-Kronig type processes to lower continua within the same (sub-) shell. Two intense features occurring at 286.5 and 289.5 eV are from the  $\sigma \leftarrow \text{C } 1s$  and  $5p \leftarrow \text{C } 1s$  inner shell transitions. There is reasonable agreement between the present data and the summed atomic oscillator strengths [280, 281] in the high energy region above 250 eV, but in the lower energy region, particularly near the delayed maximum where molecular effects are expected to be significant, the atomic oscillator strengths are about 30% higher than the present data.

Table 5.5: Absolute differential oscillator strengths for the total photoabsorption of CH<sub>3</sub>Br from 6.25 to 350 eV.

Photon Energy eV	Oscillator Strength (10 <sup>-2</sup> eV <sup>-1</sup> ) <sup>a</sup>	Photon Energy eV	Oscillator Strength (10 <sup>-2</sup> eV <sup>-1</sup> )	Photon Energy eV	Oscillator Strength (10 <sup>-2</sup> eV <sup>-1</sup> )	Photon Energy eV	Oscillator Strength (10 <sup>-2</sup> eV <sup>-1</sup> )
6.25	0.84	24.75	36.96	46	4.78	85	2.00
6.75	1.93	25.25	36.43	47	4.41	87	2.04
7.25	6.55	25.75	33.73	48	4.30	89	2.06
7.75	9.00	26.25	31.74	49	3.92	91	2.15
8.25	12.39	26.75	30.67	50	3.71	93	2.21
8.75	18.50	27.25	28.74	51	3.47	95	2.28
9.25	24.38	27.75	26.92	52	3.36	97	2.37
9.75	37.23	28.25	25.45	53	3.20	99	2.47
10.25	49.56	28.75	24.45	54	2.98	101	2.57
10.75	55.68	29.25	23.13	55	2.82	103	2.69
11.25	58.30	29.75	22.16	56	2.68	105	2.83
11.75	60.24	30.25	20.48	57	2.60	107	2.94
12.25	64.76	30.75	19.93	58	2.48	109	3.08
12.75	67.33	31.25	17.91	59	2.41	111	3.19
13.25	71.32	31.75	16.71	60	2.33	113	3.33
13.75	74.87	32.25	16.28	61	2.20	115	3.41
14.25	78.44	32.75	15.46	62	2.11	117	3.58
14.75	79.65	33.25	14.27	63	2.07	119	3.69
15.25	79.99	33.75	13.53	64	1.94	121	3.76
15.75	79.38	34.25	12.85	65	1.90	123	3.84
16.25	76.78	34.75	11.80	66	1.89	125	3.98
16.75	74.95	35.25	11.59	67	1.85	127	4.00
17.25	75.09	35.75	11.59	68	1.73	129	4.04
17.75	70.83	36.25	10.58	69	1.73	131	4.09
18.25	68.88	36.75	10.12	70	2.25	133	4.14
18.75	68.12	37.25	9.68	71	3.24	135	4.19
19.25	62.96	37.75	8.53	72	2.64	137	4.18
19.75	60.22	38.25	8.69	73	1.78	139	4.23
20.25	58.39	38.75	8.63	74	2.07	141	4.24
20.75	55.34	39.25	8.04	75	2.26	143	4.30
21.25	52.91	39.75	7.71	76	2.28	145	4.28
21.75	49.78	40.25	7.52	77	2.20	147	4.32
22.25	47.01	41	6.81	78	2.20	149	4.36
22.75	45.13	42	6.15	79	2.11	151	4.35
23.25	43.74	43	5.70	80	2.04	153	4.36
23.75	41.05	44	5.44	81	2.05	155	4.35
24.25	39.24	45	4.93	83	2.03	157	4.36

Table 5.5: (continued) absolute differential oscillator strengths for the total photoabsorption of CH<sub>3</sub>Br from 6.25 to 350 eV.

Photon Energy eV	Oscillator Strength (10 <sup>-2</sup> eV <sup>-1</sup> ) <sup>a</sup>	Photon Energy eV	Oscillator Strength (10 <sup>-2</sup> eV <sup>-1</sup> )	Photon Energy eV	Oscillator Strength (10 <sup>-2</sup> eV <sup>-1</sup> )	Photon Energy eV	Oscillator Strength (10 <sup>-2</sup> eV <sup>-1</sup> )
159	4.36	228	3.96	280	3.42	297.5	4.10
161	4.35	230	3.97	280.5	3.37	298	4.07
163	4.40	232	3.93	281	3.40	298.5	4.06
165	4.35	234	3.90	281.5	3.38	299	4.02
167	4.37	236	3.88	282	3.37	299.5	4.04
169	4.37	238	3.85	282.5	3.35	300	4.02
171	4.35	240	3.84	283	3.36	300.5	3.99
173	4.35	242	3.81	283.5	3.35	301	3.98
175	4.32	244	3.75	284	3.33	301.5	3.98
177	4.35	246	3.75	284.5	3.35	302	3.95
179	4.29	248	3.74	285	3.42	302.5	3.92
181	4.35	250	3.71	285.5	3.67	303	3.94
183	4.26	252	3.69	286	4.33	303.5	3.93
185	4.33	254	3.76	286.5	4.64	304	3.91
187	4.39	256	3.69	287	4.45	304.5	3.92
189	4.44	258	3.68	287.5	4.24	305	3.91
190	4.40	260	3.68	288	4.27	305.5	3.88
192	4.46	262	3.66	288.5	4.43	306	3.84
194	4.47	264	3.58	289	4.94	306.5	3.87
196	4.42	266	3.62	289.5	5.16	307	3.83
198	4.45	268	3.55	290	4.71	307.5	3.84
200	4.41	270	3.57	290.5	4.49	308	3.79
202	4.43	271	3.49	291	4.45	309	3.81
204	4.42	272	3.49	291.5	4.35	310	3.74
206	4.27	273	3.48	292	4.26	312	3.70
208	4.30	274	3.46	292.5	4.19	314	3.56
210	4.30	275	3.46	293	4.19	316	3.64
212	4.23	276	3.43	293.5	4.14	318	3.64
214	4.17	276.5	3.42	294	4.15	320	3.50
216	4.18	277	3.44	294.5	4.18	325	3.40
218	4.11	277.5	3.39	295	4.17	330	3.30
220	4.12	278	3.40	295.5	4.21	335	3.20
222	4.06	278.5	3.43	296	4.20	340	3.15
224	4.02	279	3.40	296.5	4.16	345	3.06
226	4.01	279.5	3.40	297	4.15	350	2.99

 $\sigma(\text{Mb})=109.75 \, df/dE \, (\text{eV}^{-1}).$

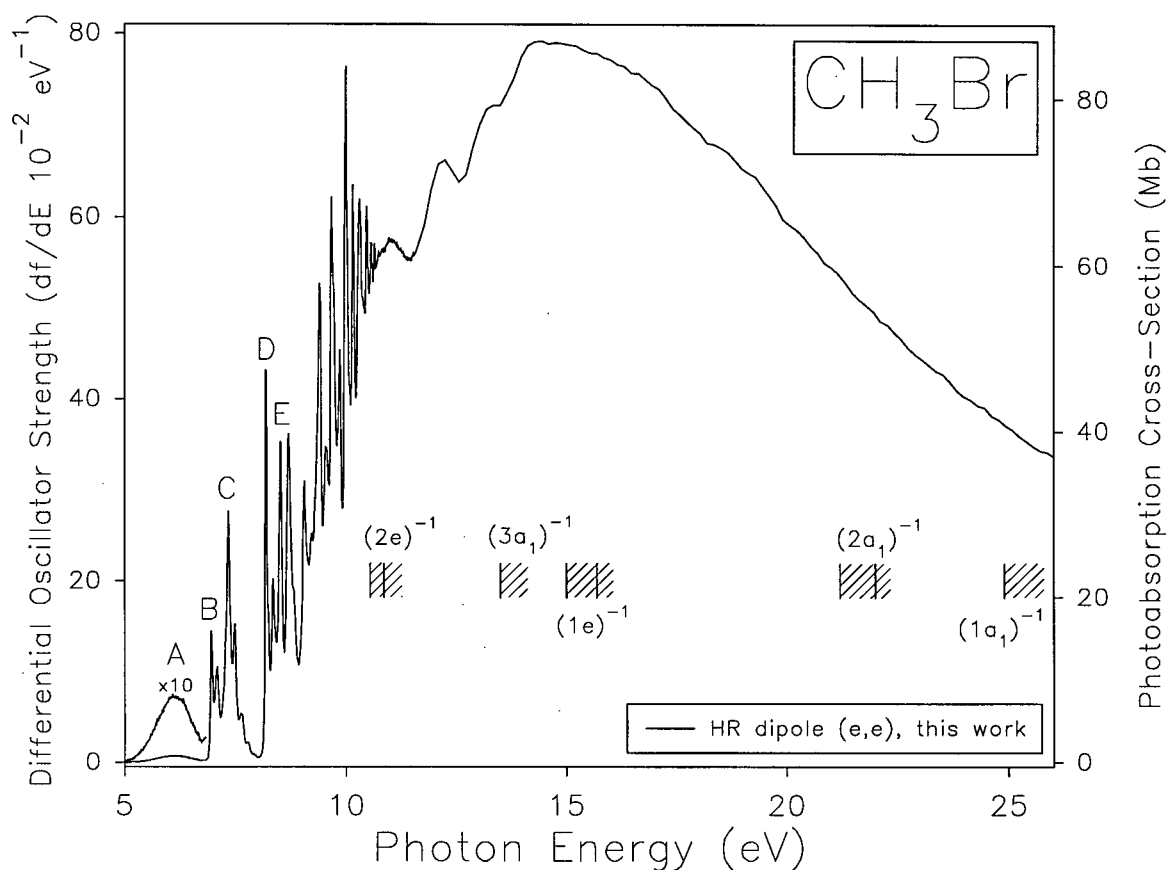


Figure 5.6: Absolute high resolution (0.05 eV fwhm) dipole (e,e) photoabsorption oscillator strength spectrum of methyl bromide from 5 to 26 eV. Also shown are previously published ionization potentials (see table 5.1).

### 5.5.2 High resolution valence shell photoabsorption (5 to 26 eV)

The valence shell photoabsorption spectrum of  $\text{CH}_3\text{Br}$  recorded in the present work at high resolution (0.05 eV fwhm) is shown in figure 5.6 from 5 to 26 eV. Expanded views of the discrete absorption bands from 5 to 9 eV are shown in figure 5.7(a) and from 8.5 to 12.5 eV in figure 5.7(b).

In 1936 Price [230] reported the excitation energies for the A ( $\sigma^* \leftarrow n$ ), B ( $5s \leftarrow n$ ), and D ( $5p \leftarrow n$ ) photoabsorption bands of  $\text{CH}_3\text{Br}$  (where  $n$  is the  $2e$  orbital which is non-bonding and has a large Br  $4p$  character) and several other bands were assigned to the  $ns$ -Rydberg series leading up to the  $(2e_{\frac{3}{2}})^{-1}$  and the  $(2e_{\frac{1}{2}})^{-1}$  limits. In 1975 both Causley and Russell [248]

and Hochmann *et al.* [241] identified several members of the ns, np and nd Rydberg series terminating at the  $(2e_{\frac{3}{2}})^{-1}$  and the  $(2e_{\frac{1}{2}})^{-1}$  limits. Causley and Russell [248] have also attributed the intensity near 8.8 eV underlying the np and nd Rydbergs to the  $\sigma^* \leftarrow 3a_1$  transition. A combination of these assignments [230, 241, 248] is shown on figures 5.7(a) and (b).

As a result of the large difference in energy resolution, the presently reported high resolution (0.05 eV fwhm) oscillator strength spectrum cannot be compared directly to the much higher resolution optical measurements [248] in the discrete valence shell except in the region of the broad A band. In order to obtain a meaningful comparison with the presently reported data the absolute photoabsorption spectrum reported by Causley and Russell [248] has been convoluted with a 0.05 eV fwhm gaussian function in order to degrade the resolution of the optical experiment to  $\sim 0.05$  eV fwhm. The resulting spectrum is shown in figure 5.7(a). Figure 5.7(a) shows that in the region of the A band there is good agreement between the presently reported differential oscillator strengths and the data published by Felps *et al* [244], but that the measurements of Causley and Russell [248] are almost two times higher than the presently reported data. Above the A band the presently reported dipole (e,e) data and the (convoluted) photoabsorption experimental data of Causley and Russell [248] are in excellent quantitative agreement and the two spectra are well within the 10% uncertainty quoted for the optical measurements over the entire energy range from 6.8 to 8.8 eV. The largest discrepancies occur for the D and E bands ( $5p \leftarrow 2e_{3/2,1/2}$ ) at 8.19 and 8.52 eV, respectively, which are at most 8% lower in intensity in the spectrum of Causley and Russell [248] than in the present work. These differences are likely caused by line-saturation errors in the optical spectrum (see chapter 1). In the higher energy region from 10.09 to 11.78 eV there is good agreement between the presently reported spectrum and the data reported by Person and Nicole [246, 247] shown (unconvoluted) in figure 5.7(b). The disagreement in the discrete region from 10.09 to 10.5 is most likely because of the difference in resolution between the

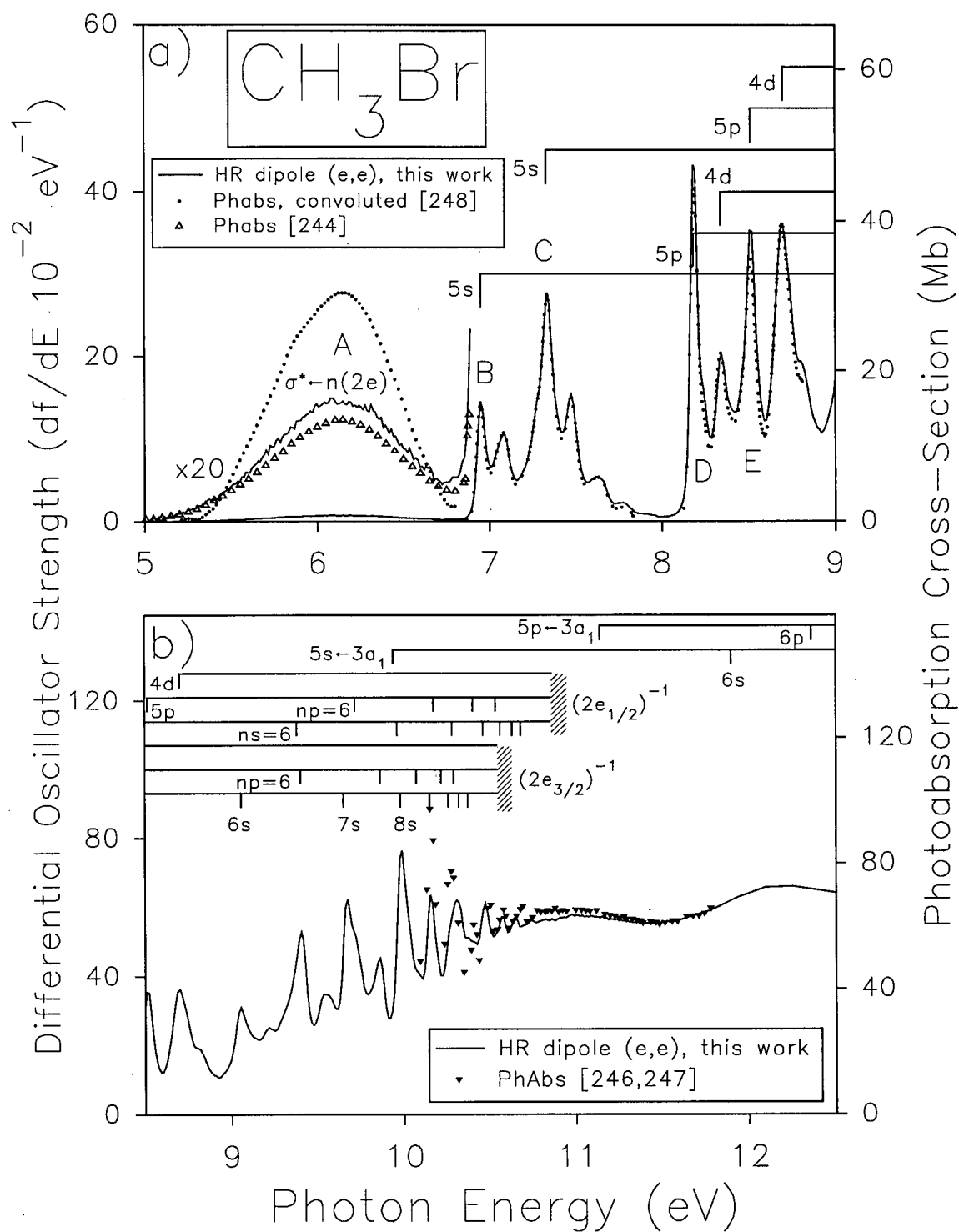


Figure 5.7: Absolute high resolution (0.05 eV fwhm) photoabsorption oscillator strength spectrum of methyl bromide. Expanded view of the valence shell photoabsorption spectrum (a) from 5 to 9 eV and (b) from 8.5 to 12.5 eV. Shown for comparison are previously published high resolution data [248] convoluted with a 0.05 eV fwhm gaussian function (see text for details). Also shown are previously published data [244, 246, 247], assignments [241, 248] and ionization potentials (see table 5.1).

Table 5.6: Absolute oscillator strengths for selected regions of the valence shell photoabsorption spectrum of CH<sub>3</sub>Br.

Assignment	Energy Region (eV)	Oscillator Strength <sup>a</sup>			
		This Work	[242]	[244]	[246] [248]
A: $\sigma^* \leftarrow 2e$	5.00 – 6.80	0.0069		0.0066	0.011
B,C: $5s \leftarrow 2e$	6.80 – 8.10	0.085	0.087		0.080
D,E: $5p \leftarrow 2e$	8.10 – 8.80	0.141			0.146
	10.09 – 11.78	0.936			0.960
	5.00 – 11.78	1.600			

<sup>a</sup>Oscillator strength values that were not tabulated in the original publications [242, 246, 248] were obtained from integration of the digitized (unconvoluted) spectra.

two experiments.

Other studies [241, 242, 244] have reported absolute spectra throughout the discrete photoabsorption region which are qualitatively the same as the presently reported spectrum. However, the intensities of many of the bands in the previously reported spectra differ from those in the present spectrum because of the different spectral resolutions of the various experiments. Table 5.6 compares oscillator strengths for several bands determined in the present work with those from various other studies of the CH<sub>3</sub>Br spectrum [242, 244, 246, 248].

### 5.5.3 High resolution Br 3d photoabsorption

The absolute photoabsorption spectrum of CH<sub>3</sub>Br recorded in the Br 3d discrete region at high resolution (0.1 eV fwhm) is shown in figure 5.8(b) from 68 to 81 eV. This high resolution spectrum was placed onto an absolute scale by normalization to the absolute low resolution differential oscillator strength spectrum in the smooth valence shell continuum region at 66 eV where no sharp structure exists. The Br 3d<sub>3/2</sub> IP was obtained

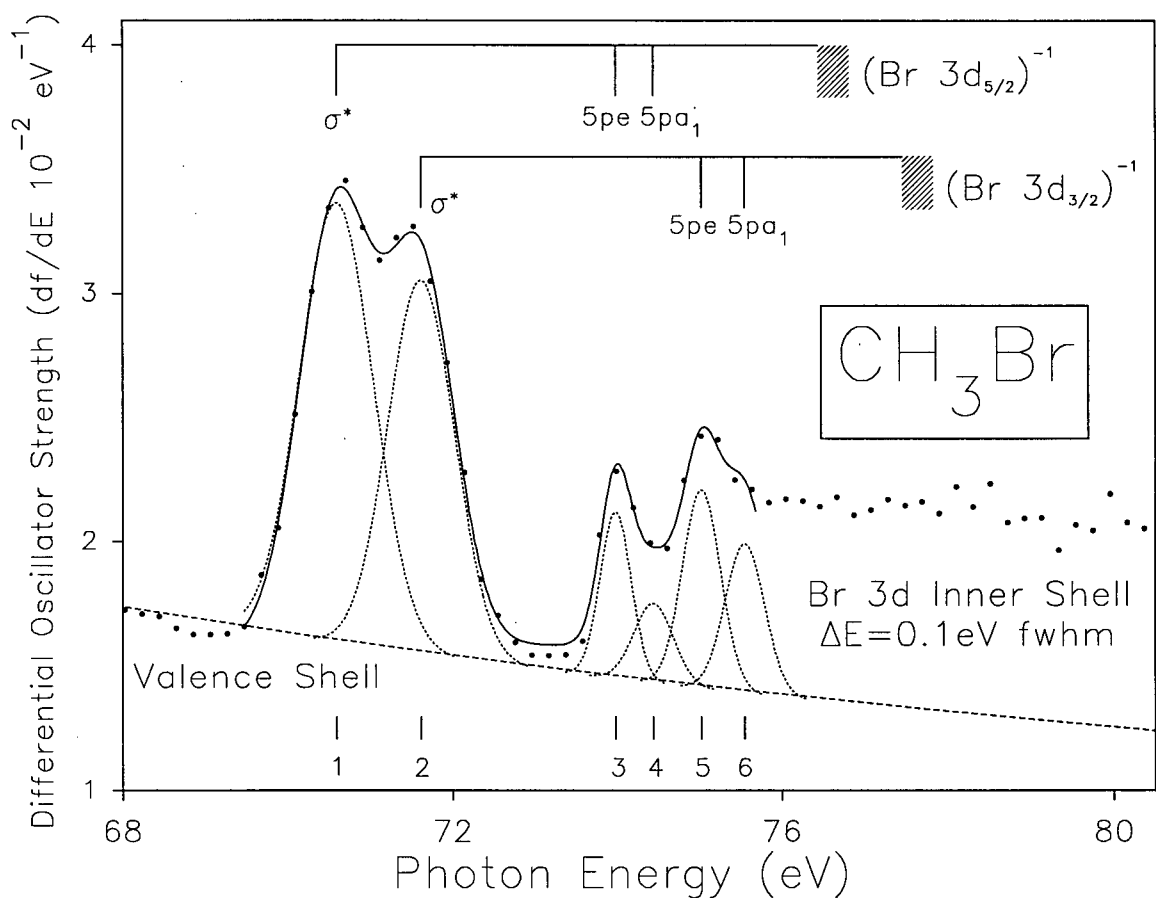


Figure 5.8: Absolute high resolution (0.1 eV fwhm) dipole (e,e) photoabsorption oscillator strength spectrum of methyl bromide in the Br 3d region from 68 to 81 eV. Also shown are previously published IPs [276, 277] and assignments [256]. An estimation of the valence shell oscillator strength contribution is shown by the dashed line (see section 5.5.1 for details).

EELS spectrum reported by Shaw *et al.* [284].

In addition to their long range EELS spectrum [256], Hitchcock and Brion [256] have reported the energy-loss spectrum of CH<sub>3</sub>Br in the Br 3d discrete region at a resolution of 0.25 eV fwhm. From this they identified the Br 3d<sub>5/2,3/2</sub> transitions to the  $\sigma^*$  and 5pe final orbitals as well as the 5pa<sub>1</sub>  $\leftarrow$ Br 3d<sub>3/2</sub> transition. The presently reported high resolution photoabsorption spectrum was fitted using a least squares fitting procedure with five gaussian profiles based on the assignment proposed by Hitchcock and Brion [256]. An adequate fit could not be obtained in the region from 74 to 75 eV using this scheme, but a satisfactory fit was achieved by adding a sixth gaussian peak to this region. The resulting least squares fit is shown in figure 5.8(b) where the individual peaks and the total fit to the experimental data are shown as the dotted and solid lines, respectively. The additional peak required for a satisfactory fit (feature 4 on figure 5.8(b)) has an energy of 74.44 eV which gives a term value of 1.98 eV with respect to the Br 3d<sub>5/2</sub> IP. This is in excellent agreement with the term value of 1.90 eV for the 5pa<sub>1</sub>  $\leftarrow$ Br 3d<sub>3/2</sub> transition and thus feature 4 is assigned as 5pa<sub>1</sub>  $\leftarrow$ Br 3d<sub>5/2</sub>. The energies, term values and oscillator strengths resulting from the fit are shown in table 5.7 along with previously published assignments [256].

The ratio of the oscillator strengths of the  $\sigma^* \leftarrow$ Br 3d<sub>5/2,3/2</sub> transitions (features 1 and 2) was found to be 1.3, which is closer to the statistical ratio of 1.5 than the value of 1.2 which was obtained from peak areas for these features in the energy-loss spectrum of Hitchcock and Brion [256]. The transition energies given in table 5.7 are within 0.1 eV of those given by Hitchcock and Brion [256], but, as a result of recent corrections [277] to the XPS IP measurements [276], the presently reported term values and Br 3d<sub>3/2</sub> IP are  $\sim$ 0.2 eV larger. Hitchcock and Brion [256] have pointed out that features 3 to 6, which were assigned to the various 5p $\leftarrow$ Br 3d transitions, may alternatively have been assigned to the 4f $\leftarrow$ Br 3d<sub>5/2,3/2</sub> transitions, but this was discounted [256] on the grounds that the 4f $\leftarrow$ Br 3d<sub>5/2,3/2</sub> transitions were expected to be small because of the centrifugal potential barrier to *f* waves. Further-

Table 5.7: Energy, term value, oscillator strength, and assignment of features in the Br 3d spectrum of CH<sub>3</sub>Br.

Feature	Photon	Term Value (eV) <sup>a</sup>	Oscillator Strength <sup>b</sup> (10 <sup>-2</sup> )	Assignment	
	Energy (eV)			Br 3d <sub>5/2</sub>	Br 3d <sub>3/2</sub>
1	70.59	5.83	1.98	σ* (4a <sub>1</sub> )	
2	71.62	5.83	1.52		σ* (4a <sub>1</sub> )
3	73.98	2.44 (2.64)	0.32	5pe	
4	74.44	1.98 (2.38)	0.19	5pa <sub>1</sub>	
5	75.02	2.43 (2.63)	0.46		5pe
6	75.55	1.90 (2.32)	0.36		5pa <sub>1</sub>
IP	76.42 <sup>c</sup>				
IP	77.45 <sup>c</sup>				
	160 <sup>d</sup>			εf ← Br 3d	

<sup>a</sup>quantum defect values given in parentheses.

<sup>b</sup>Oscillator strengths taken from the fitted gaussian peaks shown in figure 5.8.

<sup>d</sup>The 3d<sub>3/2</sub> IP was obtained from the 3d<sub>5/2</sub> IP XPS value [276] and the average spin-orbit splittings (1.03 eV) of the σ\* ← 3d<sub>5,2,3/2</sub> and 5p ← 3d<sub>5,2,3/2</sub> transitions.

<sup>d</sup>From figure 5.5(b).

more, the barrier would likely cause the 4f ← Br 3d<sub>5/2,3/2</sub> transitions to appear at energies outside the potential barrier, above the Br 3d ionization threshold.

## 5.6 Methyl Iodide Results and Discussion

### 5.6.1 Low resolution photoabsorption (4.5 to 350 eV)

The absolute photoabsorption differential oscillator strengths of methyl iodide from 4.5 to 350 eV obtained at low resolution (1 eV fwhm) in the present work are shown graphically in figure 5.9 and are given numerically in table 5.8. The results are compared to previously reported theoretical [280] and experimental [281] summed (3H + C + I) atomic oscillator strengths in figure 5.9.

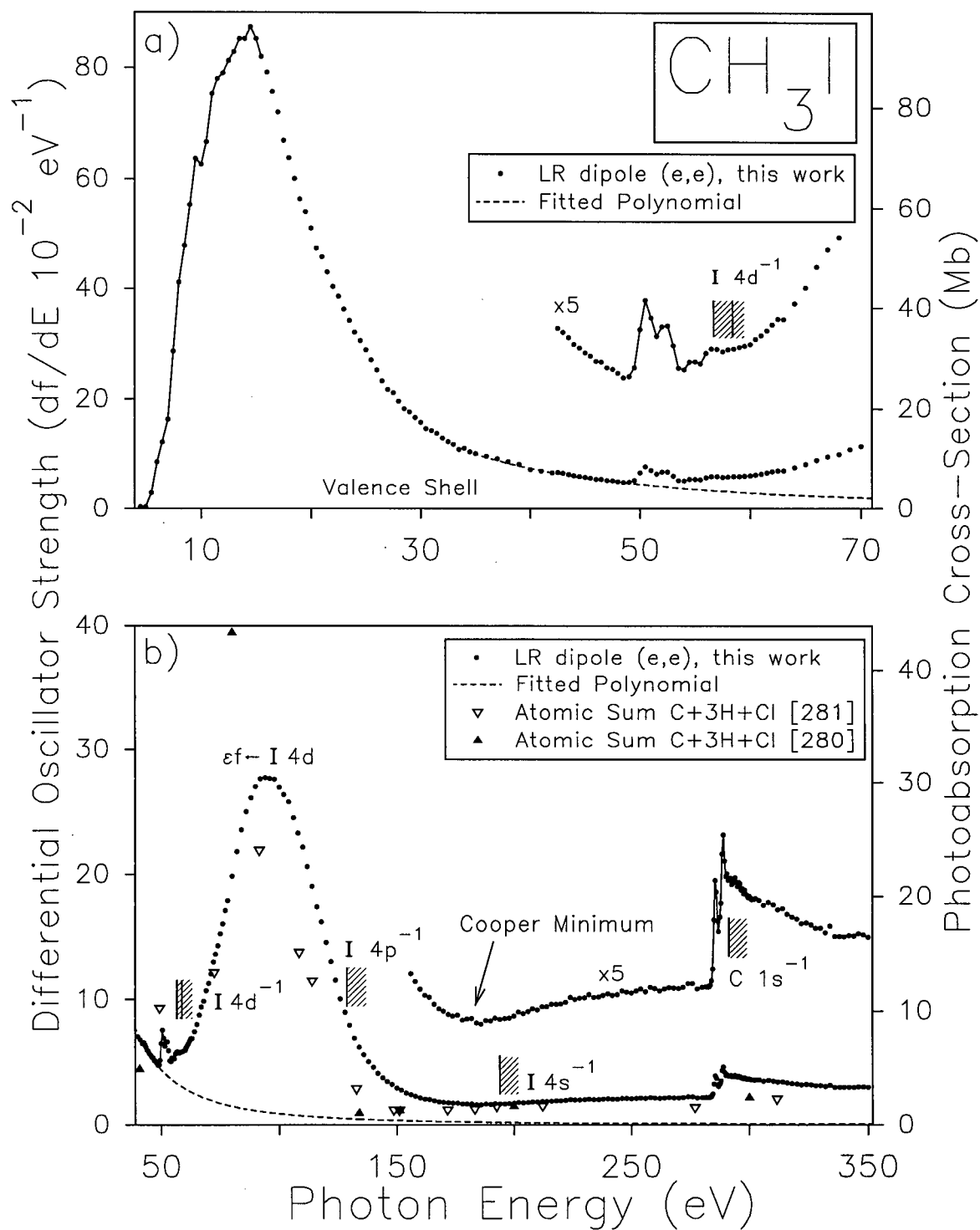


Figure 5.9: Absolute low resolution (1 eV fwhm) photoabsorption oscillator strength spectrum of methyl iodide. (a) The valence shell region from 4 to 71 eV. (b) The higher energy region shown from 39 to 352 eV. Also shown are previously published inner shell ionization potentials [275–277] and summed atomic oscillator strengths [280, 281].

The VTRK sum-rule cannot be used to establish the absolute scale of the  $\text{CH}_3\text{I}$  photoabsorption spectrum because the low energy I 4d inner shell discrete region and the delayed onset of the  $\epsilon f \leftarrow \text{I } 4d$  continuum resonance interferes with the polynomial fitting procedure which would be required to obtain the absolute scale. For these reasons the absolute differential oscillator strength scale was obtained by normalization of the combined high (4 to 18 eV) (see section 5.6.2 below) and low resolution (18 to 350 eV) relative photoabsorption spectrum to the dynamic dipole polarizability values reported by Ramaswamy [168]. Application of the S(-2) sum-rule to the resulting absolute spectrum yields a sum of 49.43 au which compares well with a static dipole polarizability value of 49.5 au obtained from refractive index measurements [163]. It is also within 4% of the other experimental [164], theoretical [184] and additivity [166] values listed in table 4.2.

An estimation of the valence shell oscillator strength contribution underlying the I 4d, 4p, 4s and C 1s inner shells, shown by the dashed line in figure 5.9(b), was obtained by fitting a polynomial of the form given in equation (3.1) to the absolute spectrum in the valence region from 30 to 48 eV. The area under the measured photoabsorption spectrum from 4 to 35 eV plus the area under the fitted polynomial from 35 eV to infinite energy is 15.1. This can be compared with a total oscillator strength of 15 which corresponds to the 14 valence electrons in  $\text{CH}_3\text{I}$  plus an estimated contribution due to Pauli excluded transitions. Although it has not been calculated [98,99], the contribution due to Pauli excluded transitions is estimated to be 1 electron based on the increase in this correction on going from  $\text{CH}_3\text{F}$  (0.54) to  $\text{CH}_3\text{Br}$  (0.87). As was the case with  $\text{CH}_3\text{Br}$ , the agreement of the spectral area based on this polynomial fit with the value of 15 supports the accuracy of the absolute oscillator strength scale of  $\text{CH}_3\text{I}$  established in the present work using the experimental dynamic dipole polarizabilities of Ramaswamy [168].

The extensive Rydberg structure reported in previously published high resolution valence shell discrete spectra of  $\text{CH}_3\text{I}$  [241, 242, 244, 249–251] is observed as a broad, almost

featureless band in the presently reported low resolution photoabsorption spectrum shown in figure 5.9(a). A high resolution (0.05 eV fwhm) spectrum showing the extensive discrete structure in the region below the first IP has been measured in the present work and will be discussed in the following section. The two features at  $\sim 50$  eV in figure 5.9(a) arise from discrete excitation of the I 4d inner shell to the  $\sigma^*$  virtual valence orbital. In the extended range photoabsorption spectrum of  $\text{CH}_3\text{I}$ , shown in figure 5.9(b) from 40 to 350 eV, discrete structures associated with excitation from the C 1s inner shell are observed  $\sim 285$  eV. Also shown on figure 5.9(b) is a delayed onset of the  $\epsilon f \leftarrow 4d$  transitions caused by a potential barrier effect (see section 2.5.2) which gives rise to a giant resonance between 60 and 150 eV that increases to a maximum differential oscillator strength of  $0.277 \text{ eV}^{-1}$  at 94 eV. Using photographic techniques and a laser-produced plasma source O'Sullivan [255] reported that the giant resonance went through a maximum cross-section ( $0.155 \text{ eV}^{-1}$ ) at 88.5 eV which, when compared to the present work, is lower in intensity by a factor of 1.75 and occurs at a photon energy 5 eV lower. Hitchcock and Brion [256, 257] reported that the maximum in the I 4d delayed onset of  $\text{CH}_3\text{I}$  occurred at  $\sim 85$  eV in their long range (40 to 350 eV) energy-loss spectrum (0.35 eV fwhm). In the vicinity of  $\sim 185$  eV the photoabsorption curve shown in figure 5.9(b) goes through a Cooper minimum, which is associated with the radial node in the atomic I 4d wavefunction (see section 2.5.2). A similar minimum is observed in the photoabsorption spectrum of xenon [74, 84], which is associated with the radial node in the Xe 4d wavefunction. Hitchcock and Brion [256] observed that there was an absence of any structure associated with the excitation of Br 3p and 3s electrons in their energy-loss spectrum of  $\text{CH}_3\text{Br}$ , and of the I 4p and 4s electrons in their energy-loss spectrum of  $\text{CH}_3\text{I}$ . These features, however, are observed in the present work in the region just below their respective IPs in the photoabsorption spectrum of  $\text{CH}_3\text{Br}$  (figure 5.5(b)), but they are not observed in the photoabsorption spectrum of  $\text{CH}_3\text{I}$  shown in figure 5.9(b). This is consistent with noble gas photoabsorption spectra [84], which show structure in the spectrum of Kr

below the Kr 3p and 3s ionization thresholds, but do not show any structure associated with Xe 4p or 4s excitation in the spectrum of Xe.

There is reasonable agreement between the presently reported data and the summed atomic cross-sections [280, 281] in the energy region from 170 to 280 eV, but above the C 1s threshold the atomic sums are about 30% lower than the presently reported differential oscillator strengths. At lower energy, particularly near the I 4d delayed maximum where molecular effects are expected to be significant, the summed atomic data [280, 281] is both lower and the maximum is shifted to lower energies with respect to the presently reported data for CH<sub>3</sub>I.

Table 5.8: Absolute differential oscillator strengths for the total photoabsorption of CH<sub>3</sub>I from 4.5 to 350 eV.

Photon Energy eV	Oscillator Strength (10 <sup>-2</sup> eV <sup>-1</sup> ) <sup>a</sup>	Photon Energy eV	Oscillator Strength (10 <sup>-2</sup> eV <sup>-1</sup> )	Photon Energy eV	Oscillator Strength (10 <sup>-2</sup> eV <sup>-1</sup> )	Photon Energy eV	Oscillator Strength (10 <sup>-2</sup> eV <sup>-1</sup> )
4.5	0.41	23	36.27	45	5.68	64	7.45
5	0.38	23.5	34.18	45.5	5.56	65	8.02
5.5	2.91	24	32.13	46	5.37	66	8.78
6	8.50	24.5	30.54	46.5	5.33	67	9.42
6.5	12.15	25	28.86	47	5.13	68	9.87
7	16.36	25.5	27.09	47.5	5.08	69	10.72
7.5	28.65	26	25.24	48	4.93	70	11.30
8	41.13	26.5	23.28	48.5	4.78	71	12.04
8.5	47.80	27	21.78	49	4.81	72	13.02
9	55.33	27.5	21.20	49.5	5.14	73	13.64
9.5	63.62	28	19.66	50	6.52	74	14.31
10	62.67	28.5	18.26	50.5	7.57	75	15.27
10.5	66.75	29	17.67	51	6.94	76	16.05
11	75.29	29.5	16.62	51.5	6.28	77	17.10
11.5	78.01	30	15.75	52	6.63	78	17.87
12	79.04	30.5	14.60	52.5	6.65	80	19.86
12.5	81.29	31	14.23	53	5.93	82	21.82
13	82.89	31.5	13.73	53.5	5.13	84	23.53
13.5	85.24	32	12.85	54	5.06	86	24.98
14	85.21	32.5	12.17	54.5	5.34	88	26.09
14.5	87.34	33	11.72	55	5.35	90	27.00
15	85.20	33.5	10.72	55.5	5.28	92	27.63
15.5	82.06	34	10.95	56	5.66	94	27.73
16	79.19	34.5	10.29	56.5	5.82	96	27.67
16.5	75.71	35	10.01	57	5.81	98	27.61
17	72.01	36	9.48	57.5	5.72	100	26.94
17.5	66.94	37	9.08	58	5.80	102	26.36
18	63.79	38	8.55	58.5	5.81	104	25.78
18.5	60.09	39	8.01	59	5.88	106	24.48
19	56.35	40	7.06	59.5	5.92	108	23.27
19.5	54.05	41	6.80	60	5.97	110	22.17
20	51.04	42	6.47	60.5	6.17	112	20.65
20.5	47.30	42.5	6.56	61	6.31	114	19.04
21	45.69	43	6.42	61.5	6.48	116	17.40
21.5	42.93	43.5	6.23	62	6.70	118	16.21
22	40.32	44	5.98	62.5	6.89	120	14.59
22.5	38.58	44.5	5.86	63	6.89	122	13.04

Table 5.8: (continued) absolute differential oscillator strengths for the total photoabsorption of CH<sub>3</sub>I from 4.5 to 350 eV.

Photon Energy eV	Oscillator Strength (10 <sup>-2</sup> eV <sup>-1</sup> ) <sup>a</sup>	Photon Energy eV	Oscillator Strength (10 <sup>-2</sup> eV <sup>-1</sup> )	Photon Energy eV	Oscillator Strength (10 <sup>-2</sup> eV <sup>-1</sup> )	Photon Energy eV	Oscillator Strength (10 <sup>-2</sup> eV <sup>-1</sup> )
124	11.57	194	1.69	264	2.18	295.5	3.88
126	10.06	196	1.70	266	2.20	296	3.86
128	9.01	198	1.71	268	2.19	296.5	3.75
130	7.98	200	1.75	270	2.18	297	3.78
132	6.95	202	1.81	272	2.20	297.5	3.69
134	6.21	204	1.78	274	2.26	298	3.75
136	5.62	206	1.82	276	2.26	298.5	3.68
138	5.05	208	1.86	278	2.18	299	3.67
140	4.59	210	1.84	280	2.20	300	3.65
142	4.13	212	1.89	282	2.21	301	3.59
144	3.76	214	1.89	283	2.21	302	3.61
146	3.47	216	1.93	283.5	2.24	304	3.58
148	3.24	218	1.93	284	2.30	306	3.51
150	2.96	220	1.94	284.5	2.49	308	3.55
152	2.79	222	1.96	285	3.27	310	3.51
154	2.57	224	2.04	285.5	3.91	312	3.44
156	2.42	226	2.01	286	3.72	314	3.45
158	2.29	228	2.03	286.5	3.25	316	3.36
160	2.17	230	2.04	287	3.09	318	3.31
162	2.08	232	2.09	287.5	3.31	320	3.29
164	2.04	234	2.04	288	3.54	322	3.22
166	1.93	236	2.04	288.5	4.33	324	3.23
168	1.86	238	2.07	289	4.63	326	3.19
170	1.82	240	2.10	289.5	4.21	328	3.14
172	1.77	242	2.08	290	3.97	330	3.14
174	1.74	244	2.09	290.5	4.02	332	3.07
176	1.76	246	2.14	291	3.91	334	3.18
178	1.68	248	2.13	291.5	3.93	336	3.01
180	1.70	250	2.11	292	3.95	338	3.02
182	1.70	252	2.14	292.5	3.84	340	3.01
184	1.63	254	2.18	293	3.91	342	3.03
186	1.61	256	2.13	293.5	3.87	344	3.02
188	1.67	258	2.20	294	3.95	346	3.06
190	1.67	260	2.18	294.5	3.88	348	3.04
192	1.71	262	2.14	295	3.81	350	3.00

$\sigma(\text{Mb})=109.75 df/dE$  (eV<sup>-1</sup>).

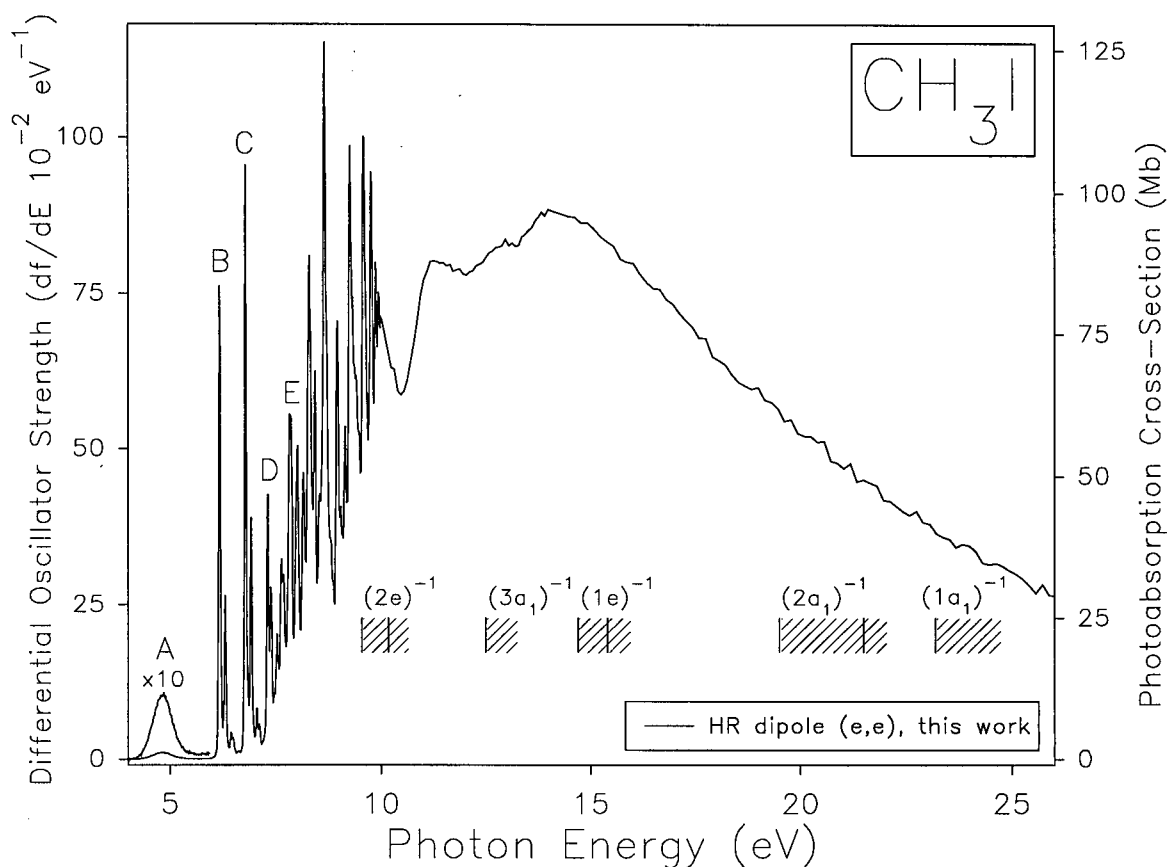


Figure 5.10: Absolute high resolution (0.05 eV fwhm) dipole (e,e) photoabsorption oscillator strength spectrum of methyl iodide from 4 to 26 eV. Also shown are previously published ionization potentials (see table 5.1).

### 5.6.2 High resolution valence shell photoabsorption (4 to 26 eV)

The high resolution (0.05 eV fwhm) valence shell photoabsorption spectrum of  $\text{CH}_3\text{I}$  recorded in the present work is shown in figure 5.10 from 4 to 26 eV. Figure 5.11 shows expanded views of the discrete absorption bands, in panel (a) from 4 to 8 eV, and in panel (b) from 7.5 to 11.5 eV.

Much of the earliest theory regarding the electronic structure and spectrum of methyl iodide was proposed by Mulliken [229, 231, 232] and this was supported by the experimental spectra reported by Price [230], who reported the energies of the A, B and the D photoabsorption bands of  $\text{CH}_3\text{I}$  and also assigned several bands to the ns-Rydberg series leading up

to the  $(2e_{\frac{3}{2}})^{-1}$  and  $(2e_{\frac{1}{2}})^{-1}$  limits. Hochmann *et al.* [241] later identified several of the lower energy members of the ns, np and nd-Rydberg series. Assignment of the higher n Rydberg transitions was made by Wang *et al.* [250], who identified the 6s to 11s, 9p and 10p and the 5d to 19d members of the Rydberg series terminating at the  $(2e_{\frac{3}{2}})^{-1}$  and the  $(2e_{\frac{1}{2}})^{-1}$  limits. These assignments [250] were confirmed by the very high resolution (equivalent to a maximum resolution of 0.025 meV fwhm at 10 eV photon energy) photoabsorption spectrum reported by Baig *et al.* [251]. A combination of the previously published assignments [230, 241, 250] is shown on figure 5.11(a) and (b).

Figure 5.11(a) shows that there is excellent agreement in the region of the A band between the present data and the work of Felps *et al.* [244], but the cross-section measurements by Boschi and Salahub [249] and by Fahr *et al.* [254] are about 25% lower and 15% higher, respectively, than the presently reported data. However, there is good agreement between the presently reported measurements and the five data points reported by Fahr *et al.* [254] from 6 to 7.75 eV. The absolute photoabsorption spectrum reported by Hochmann *et al.* [241] has been convoluted with a gaussian function of 0.05 eV fwhm, in order to obtain a meaningful comparison with the presently reported data above 6 eV. Figures 5.11(a) and (b) show that the quantitative agreement between the presently reported dipole (e,e) data and the (convoluted) photoabsorption experimental data [241] is, in general, quite good. However, the B, C ( $6s \leftarrow 2e$ ) and D ( $6p \leftarrow 2e$ ) bands at 6.16, 6.77, and 7.30 eV, respectively, are on the order of 50% lower in intensity in the spectrum of Hochmann *et al.* [241] than in the present work. These bands are the most intense and the sharpest lines in the spectrum and thus will suffer the largest errors due to line-saturation effects (see chapter 1). The only other major discrepancy occurs in the region from 9.3 to 9.55 eV where the spectrum of Hochmann *et al.* [241] is again lower than the present work. The most recent, very high resolution measurements by Baig *et al.* [251] show several very narrow bands in this energy region which are all likely candidates for line-saturation errors in Beer-Lambert law

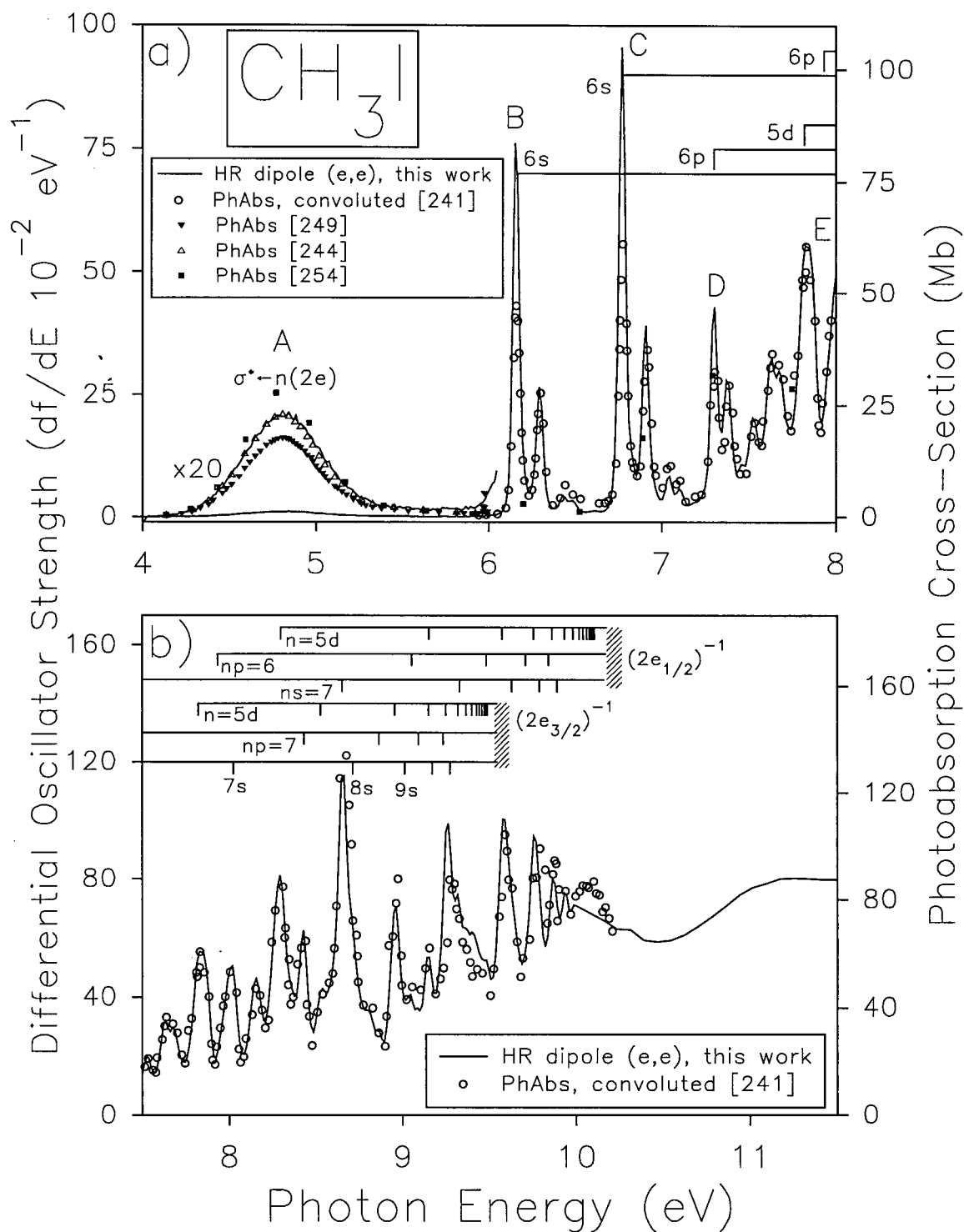


Figure 5.11: High resolution (0.05 eV fwhm) absolute photoabsorption oscillator strength spectrum of methyl iodide. Expanded views of the valence shell spectrum from (a) 4 to 8 eV and (b) 7.5 to 11.5 eV. Shown for comparison are previously published high resolution data [241] convoluted with a 0.05 eV fwhm gaussian function (see text for details). Also shown are previously published data [244, 249, 254], assignments [230, 241, 250] and ionization potentials (see table 5.1).

Table 5.9: Absolute oscillator strengths for selected regions of the valence shell photoabsorption spectrum of CH<sub>3</sub>I.

Assignment	Energy Region (eV)	Oscillator Strength <sup>a</sup>				
		This Work	[241]	[244]	[249]	[254]
A: $\sigma^* \leftarrow 2e$	4.00 – 5.95	0.0065		0.0062	0.0048	0.0075
B: $6s \leftarrow 2e_{3/2}$	5.95 – 6.65	0.061	0.052			
C: $6s \leftarrow 2e_{1/2}$	6.65 – 7.20	0.085	0.078			
D: $6p \leftarrow 2e_{3/2}$	7.20 – 7.45	0.045	0.045			
	7.45 – 8.50	0.378	0.385			
	8.50 – 10.20	1.030	1.097			
	4.00 – 10.20	1.605	1.685			

<sup>a</sup>Oscillator strength values that were not tabulated in the original publications [241, 249, 254] were obtained from integration of the digitized (unconvoluted) spectra.

photoabsorption measurements made at lower resolution. In the spectrum reported by Baig *et al.* [251] these very narrow bands have relative intensities which are higher than the surrounding bands at lower and higher energies. In the lower resolution work of Hochmann *et al.* [241] the relative intensities of the same narrow bands are at about half the intensity of the surrounding bands. Thus, it is likely that these cross-section measurements [241] in the region from 9.3 to 9.55 eV suffer from line-saturation errors.

Other studies [242, 244, 249, 250] that have reported absolute spectra in the discrete valence shell region of CH<sub>3</sub>I are qualitatively the same as the presently reported spectrum. However, there are differences in the relative intensities of the bands within each of the previously reported spectra. These differences in relative intensities are in part a result of the different resolutions, but because of the many intense and narrow discrete lines in the valence shell spectrum of CH<sub>3</sub>I, line-saturation errors will also occur in all of the Beer-Lambert law measurements, except those made at the highest resolutions. Table 5.9 compares oscillator

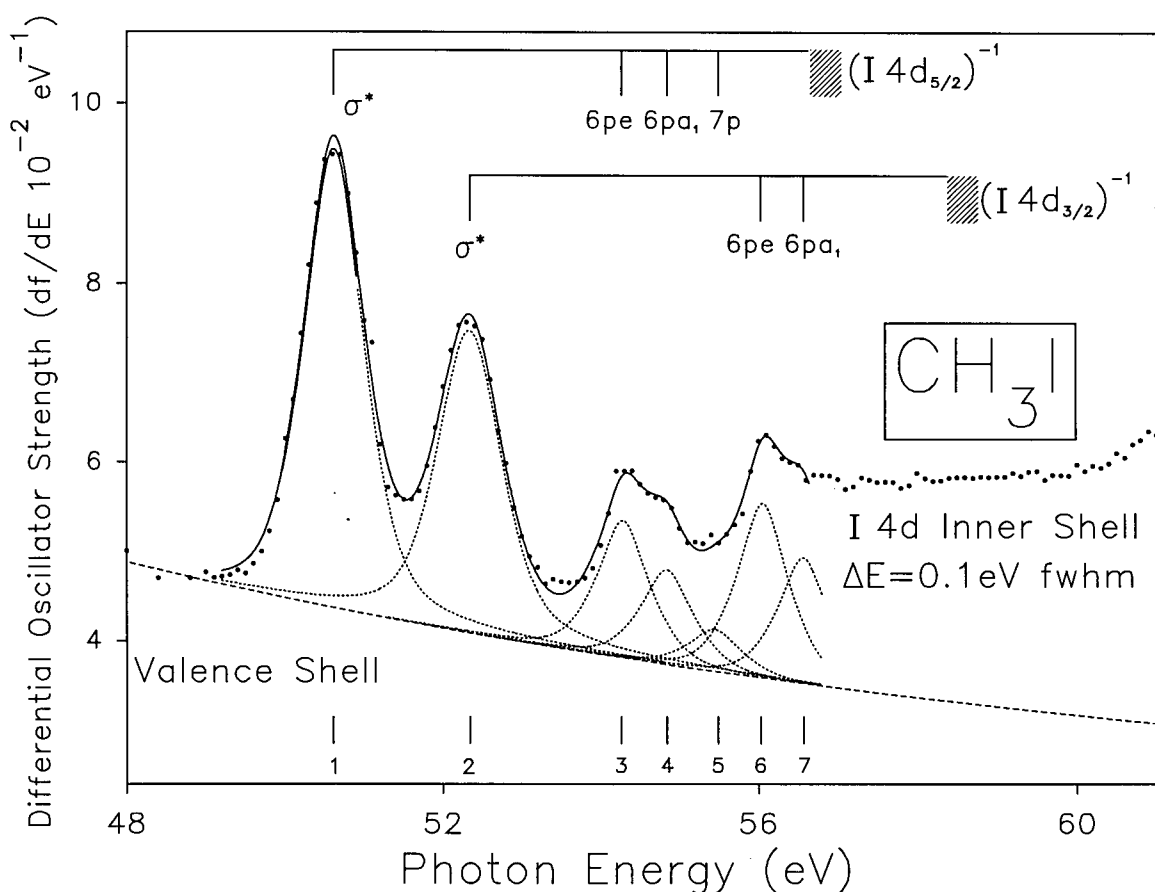


Figure 5.12: Absolute high resolution (0.1 eV fwhm) dipole (e,e) photoabsorption oscillator strength spectrum of methyl iodide in the I 4d region from 48 to 61 eV. Also shown are previously published IPs [278] and assignments [255]. An estimation of the valence shell oscillator strength contribution is shown by the dashed line (see section 5.6.1 for details).

strengths of several bands determined in the present work with those from various other valence shell photoabsorption studies [241, 244, 249] of  $\text{CH}_3\text{I}$ .

### 5.6.3 High resolution I 4d photoabsorption

The I 4d differential oscillator strength data of  $\text{CH}_3\text{I}$  recorded at high resolution (0.1 eV fwhm) in the present work are shown graphically in figure 5.12 from 48 to 61 eV. The I  $4d_{5/2,3/2}$  IPs have been taken from PES measurements [278]. Hitchcock and Brion [256] and O'Sullivan [255] have both proposed the same assignment scheme for the electronic

excitation spectrum of  $\text{CH}_3\text{I}$  in the discrete I 4d region, with one additional assignment being made by O'Sullivan [255], that being the  $7p \leftarrow 4d_{5/2}$  transition at 55.58 eV. It has also been noted [255, 256] that the transition that is assigned to the  $6pa_1$  upper state may alternatively be assigned to a  $4fa_1$  or  $4fe$  upper state, which has been proposed in the assignment of the I 4d photoabsorption spectrum of  $\text{I}_2$  by Comes *et al.* [285]. This, however, is not likely because the centrifugal potential barrier (see section 2.5.2), which is responsible for the enhancement of the inner well  $\sigma^* \leftarrow \text{I } 4d$  transitions and for the delayed maximum of the outer well  $\epsilon f \leftarrow \text{I } 4d$  transitions, will cause the  $4f \leftarrow \text{I } 4d_{5/2,3/2}$  transitions to be small because of the potential barrier to  $f$  waves. These transitions would, in fact, be expected to appear at energies outside the potential barrier, i.e. above the I 4d ionization threshold.

A satisfactory fit of the presently reported high resolution photoabsorption spectrum was obtained using a least squares fitting procedure with seven voigt profiles (constant gaussian width of 0.4 eV) based on the assignment of O'Sullivan [255]. The resulting fit is shown in figure 5.12(b) where the individual peaks and the total fit to the experimental data are shown as the dotted and solid lines, respectively. The energies, term values and oscillator strengths resulting from this fit are shown in table 5.10 along with the previously published assignments [255, 256]. The transition energies determined in the present work are 0 to 0.14 eV higher than those reported by Hitchcock and Brion [256] and are 0.01 to 0.13 eV lower than those reported by O'Sullivan [255].

As a result of the large natural widths of the features in the I 4d spectrum of  $\text{CH}_3\text{I}$ , the higher resolution in the present work does not provide significantly better excitation energies than the work by Hitchcock and Brion [256]. The I  $4d_{5/2,3/2}$  spin-orbit splitting of  $\text{CH}_3\text{I}$  was determined to be 1.74 eV in the present work from the average spin-orbit splitting of the  $\sigma^* \leftarrow \text{I } 4d$  and  $6p \leftarrow \text{I } 4d$  transitions. This is consistent with the value of 1.738 eV from PES [278], 1.70 eV from EELS [256] and 1.72 eV from photoabsorption [255] measurements. The ratio of the oscillator strengths of the two  $\sigma^* \leftarrow \text{I } 4d_{5/2,3/2}$  transitions (features 1 and 2)

Table 5.10: Energy, term value, oscillator strength, and assignment of features in the I 4d spectrum of CH<sub>3</sub>I.

Feature	Photon	Term Value (eV) <sup>a</sup>	Oscillator Strength <sup>b</sup> (10 <sup>-2</sup> )	Assignment	
	Energy (eV)			I 4d <sub>5/2</sub>	I 4d <sub>3/2</sub>
1	50.62	6.01	0.060	σ* (4a <sub>1</sub> )	
2	52.34	6.02	0.043		σ* (4a <sub>1</sub> )
3	54.29	2.33 (3.58)	0.016	6pe	
4	54.84	1.78 (3.24)	0.010	6pa <sub>1</sub>	
5	55.45	1.17 (3.59)	0.004	7p	
6	56.05	2.31 (3.57)	0.019		6pe
7	56.57	1.79 (3.24)	0.014		6pa <sub>1</sub>
IP	56.62 <sup>c</sup>				
IP	58.36 <sup>c</sup>				
	95 <sup>d</sup>			εf ← I 4d	

<sup>a</sup>Quantum defect values given in parentheses.

<sup>b</sup>Oscillator strengths taken from the fitted voigt peaks shown in figure 5.12.

<sup>c</sup>From PES measurements [278].

<sup>d</sup>From figure 5.9(b).

was found to be 1.4, which is closer to the expected statistical ratio of 1.5 than the value of 1.7 obtained from the peak areas in the energy-loss spectrum of Hitchcock and Brion [256]. This difference is partly caused by the fact that the electron scattering cross-section decreases by a factor of  $E^3$  (see equation (2.29)) faster than the photoabsorption oscillator strength. Taking this into consideration, Hitchcock and Brion [256] found that this intensity ratio for CH<sub>3</sub>I became 1.55. The corresponding ratio in the xenon Xe 4d spectrum is 1.5. This may indicate that there is a small error in the fitted polynomial used to estimate the valence shell contribution underlying these peaks in the present work (see section 5.6.1).

## 5.7 Dipole Sum-rules of the Methyl Halides

Using  $S(-2)$  analysis it was shown in section 4.3.1 that VTRK normalized dipole (e,e) absolute photoabsorption oscillator strength spectra are highly consistent with published experimental values of static dipole polarizability. In addition, experimental dipole polarizabilities can typically be obtained with even higher (typically  $\pm 1-2\%$ ) accuracy than the quoted  $\pm 5\%$  precision for the VTRK normalized dipole (e,e) photoabsorption spectra. Thus, to further improve the dipole sums, the absolute scales of the VTRK sum-rule normalized dipole (e,e) spectra of  $\text{CH}_3\text{F}$  and  $\text{CH}_3\text{Cl}$ , presented in sections 5.3.1 and 5.4.1, respectively, have been further refined by renormalization to the respective more accurate dynamic polarizability data of Ramaswamy [168] for the purpose of dipole sum-rule evaluation. This should enable even more accurate properties to be obtained by evaluation of the various dipole sum-rules. The values of the dipole sum-rules  $S(u)$  ( $u=-1, \dots, -6, -8, -10$ ) and logarithmic dipole sum-rules  $L(u)$  ( $u=-1, -2, \dots, -6$ ) for the methyl halides so obtained are shown in table 5.11. These values are the first reported dipole sums for the methyl halides. The estimated accuracies of the presently reported sums are 5% for  $S(u)$   $u=-2$  to  $-6$  and for  $L(u)$   $u=-2$  to  $-6$ , 10% for  $S(-1)$ , 15% for  $L(-1)$ , 10% for  $S(-8)$ , and 20% for  $S(-10)$ .

Values of the Verdet constant for the methyl halides have been reported [286] at a wavelength of 589  $\mu\text{m}$  to be  $1.25 \times 10^{-13}$ ,  $1.86 \times 10^{-13}$  and  $3.06 \times 10^{-13}$  au for  $\text{CH}_3\text{Cl}$ ,  $\text{CH}_3\text{Br}$  and  $\text{CH}_3\text{I}$ , respectively. Using the presently reported absolute photoabsorption oscillator strength spectra with equation (4.4) the values for the normal Verdet constants at 589  $\mu\text{m}$  are  $1.23 \times 10^{-13}$ ,  $1.85 \times 10^{-13}$  and  $3.27 \times 10^{-13}$  au, for  $\text{CH}_3\text{Cl}$ ,  $\text{CH}_3\text{Br}$  and  $\text{CH}_3\text{I}$ , respectively, which are in excellent agreement with literature values [286] given above. These same values can also be obtained by substituting the appropriate dipole sums from table 5.11 into equation (4.5).

The values of the dipole dispersion coefficients involving the methyl halides have been

Table 5.11: Dipole sums  $S(u)$  and logarithmic dipole sums  $L(u)$  obtained from refined<sup>a</sup> absolute photoabsorption oscillator strength spectra of the methyl halides. All values are given in atomic units.

	S(-1)	S(-2) <sup>a</sup>	S(-3)	S(-4)	S(-5)	S(-6)	S(-8)	S(-10)
CH <sub>3</sub> F	13.12	17.62 [168]	28.66	52.77	106.4	230.6	1278	8310
CH <sub>3</sub> Cl	18.94	30.40 [168]	56.42	115.6	257.5	615.6	4215	3.509(4)
CH <sub>3</sub> Br	22.15	36.81	74.51	169.4	423.4	1148	1.037(4)	1.177(5)
CH <sub>3</sub> I	28.57	49.43	113.5	299.8	879.1	2819	3.662(4)	6.271(5)
	L(-1)	L(-2)	L(-3)	L(-4)	L(-5)	L(-6)		
CH <sub>3</sub> F	-2.088	-7.172	-15.93	-34.81	-78.72	-185.5		
CH <sub>3</sub> Cl	-6.725	-17.00	-37.89	-88.03	-215.7	-556.8		
CH <sub>3</sub> Br	-7.086	-23.28	-57.25	-147.6	-405.9	-1188		
CH <sub>3</sub> I	-7.914	-36.24	-103.4	-307.9	-986.7	-3401		

<sup>a</sup>The original dipole (e,e) oscillator strength scales of CH<sub>3</sub>F and CH<sub>3</sub>Cl established in sections 5.3.1 and 5.4.1, respectively, have been refined by renormalizing to experimental dynamic ( $\alpha_\lambda$ ) dipole polarizabilities [168]. The static limit ( $\alpha_\infty$ ) of the  $\alpha_\lambda$  values used for this renormalization correspond to their respective value of S(-2).

evaluated directly from equation (4.6) using the appropriate absolute photoabsorption spectra. They have also been evaluated from equation (4.9) using the S(-2) and L(-2) sums (tables 4.3, 4.4 and 5.11) for all (A,A) and (A,B) combinations involving the methyl halides and all of the atoms and molecules discussed in chapter 4. The only combinations for which equation (4.9) differs by more than 0.75% from those obtained using equation (4.6) occur for the combination of CH<sub>3</sub>I with each of Ne, Ar and SiH<sub>4</sub>. The values for these combinations determined using equation (4.6) are  $C_6(\text{He}, \text{CH}_3\text{I})=33.88$ ,  $C_6(\text{Ne}, \text{CH}_3\text{I})=68.00$  and  $C_6(\text{SiH}_4, \text{CH}_3\text{I})=549.0$ . For the methyl halides, equation (4.9) and the sum-rules of tables 4.3, 4.4 and 5.11 allow estimates of the dispersion coefficients to be obtained for the first time. The accuracy of the dipole-dipole dispersion coefficients, obtained from dipole (e,e) spectroscopy using equation (4.9) with the S(-2) and L(-2) sums (tables 4.3, 4.4 and 5.11), or those given above using equation (4.6), is estimated to be better than  $\pm 10\%$ .

## Chapter 6

# Photoionization Studies of the Methyl Halides

### 6.1 Introduction

Although various aspects of the photoionization of the methyl halides have been the subjects of numerous studies using a variety of techniques, very little information on the partial or complete dipole induced breakdown of any of these molecules has been published. As noted in section 5.2 extensive studies of the binding energy spectrum of the methyl halides have been carried out experimentally by PES [53, 111, 258–270, 274, 287, 288] and EMS [94, 95, 289] and also by several computational methods from simple ionization potential calculations [290–295] to more extensive Green's function calculations [67, 88, 94, 95, 268, 269, 289]. Novak *et al.* [274], using synchrotron radiation, recorded binding energy spectra of both  $\text{CH}_3\text{F}$  and  $\text{CH}_3\text{Cl}$  over the outer and inner valence regions at various incident photon energies from 19 to 115 eV [274]. The photoelectron branching ratios obtained from these measurements were combined with the absolute photoabsorption measurements reported by Wu *et al.* [237] to yield partial photoionization cross-sections (oscillator strengths) for production of the electronic states of  $\text{CH}_3\text{F}^+$  and of  $\text{CH}_3\text{Cl}^+$ . However, the results of this study [274] are complicated by the fact that they did not include any corrections for electron analyser transmission efficiency as a function of electron kinetic energy, nor did they include explicit measurements of the  $(1a_1)^{-1}$  inner valence state. In other work Carlson *et al.* [273] have measured the electronic state partial cross-sections for only the three outer valence

orbitals of  $\text{CH}_3\text{I}$  from 13 to 91.4 eV. No electronic state partial cross-section measurements of  $\text{CH}_3\text{Br}$  have been published.

Previous photoionization studies of the methyl halides have been used to determine ion appearance potentials [296–302], ionization efficiencies [246, 247, 298, 299], fragmentation kinetic energies [303–305], and photoionization branching ratios [288, 306, 307]. In other work photoelectron–photoelectron coincidence (PEPECO) [308], photoelectron–photoion coincidence (PEPICO) [288], photoion–photoion coincidence (PIPICO) [306, 309–313] and photoelectron–photoion–photoion coincidence (PEPIPICO) [314] techniques have been used to study further details of the photoionization process.

This chapter presents the branching ratios and partial oscillator strength data for the molecular and dissociative photoionization of the methyl halides measured using dipole (e,e+ion) spectroscopy. An examination of the appearance potentials [296–306, 315, 316], the ionization potentials (see section 5.2) and Franck-Condon widths [53, 111, 258–270, 274, 287, 288] for the various primary ionization processes of the methyl halides as well as the shapes and possible higher onsets in their respective photoion branching ratio and partial oscillator strength curves provides an estimate of the partial oscillator strengths for the electronic ion states in the methyl halides. From these partial oscillator strength data a dipole-induced breakdown scheme is deduced for each of the methyl halides.

Electronic state partial oscillator strengths of the methyl halides ( $\text{CH}_3\text{X}$ ; X=F, Cl, Br) have also been determined in the present work from photoelectron spectra obtained by Dr. G. Cooper and Dr. W. F. Chan at the Canadian Synchrotron Radiation Facility (CSRF) at the Aladdin Storage Ring, University of Wisconsin, Madison, Wisconsin using variable photon energy PES. In the present work the analyser calibration curve was determined (see section 3.4) and used to correct the intensities of the PE spectra. These spectra were then analysed using curve fitting and background subtraction procedures (see below in section 6.2.4) to obtain quantitative photoelectron branching ratios and absolute electronic

state POSs. These POS data are compared with the estimates made from dipole ( $e, e^+ion$ ) molecular and dissociative photoionization results.

## 6.2 Methyl Fluoride Results and Discussion

### 6.2.1 Binding energy spectrum

The photoelectron spectrum of  $CH_3F$ , recorded in the present work at a photon energy of 72 eV, is shown in figure 6.1(a) together with synthetic spectra in figures 6.1(b), 6.1(c), and 6.1(d) generated from a range of previously published Green's function calculations. The experimental spectrum as shown has been corrected for the electron analyser transmission efficiency and the dotted line represents the estimated position of the base line. The calculations have been taken from previously published work [94, 289] using many-body Green's function methods [88, 89] to incorporate the effects of electron correlation and relaxation. The calculations each employ two levels of approximation. Firstly, the outer valence (OV) approximation provides very accurate values for the outer valence ionization energies, since in this region correlation effects are small and pole strengths are essentially unity, as can be seen from the measured spectrum. In the inner valence region the intensity associated with a given single hole configuration is typically spread out over many lines arising from correlation effects, which can be seen in the experimental spectrum of  $CH_3F$  above  $\sim 25$  eV. In such circumstances the 2ph-Tamm-Dancoff approximation (TDA) has been found [88, 89] to yield a good description of the binding energy spectrum and a reasonable, but usually less accurate, representation of the outer valence ionization energies than the OV approximation. In figure 6.1 (and also figures 6.8, 6.14 and 6.20 below) the calculated pole strengths are shown as vertical bars at the ionization energies given by the OV and ext-TDA approximations in the outer and inner valence regions respectively. For each calculation the synthetic spectrum was generated by convoluting the calculated pole strengths with Gaussian curves, the widths

of which were estimated from those of the main peaks of each symmetry manifold in the experimental PE spectra (figure 6.1(a)). The degeneracies of the 2e and 1e orbitals have not been included in the intensities of the synthetic spectra shown in figures 6.1, 6.8, 6.14 and 6.20.

In the case of CH<sub>3</sub>F the three Green's function calculations are:

(i) The OV/TDA calculation of Cambi *et al.* [268, 289] using Dunning contracted Gaussian basis sets (9s5p)/[4s2p] for C and F and (4s)/[2s] for H. See figure 6.1(b).

(ii) The OV/ext-TDA calculation reported by Minchinton *et al.* [94] using an improved (9s5p/4s)/[4s2p/2s] basis set and the extended 2ph-TDA with the ADC(4) approach [89]. This employs additional higher excitations (3h2p) above those used in the simpler 2ph-TDA treatment. See figure 6.1(c).

(iii) The OV/ext-TDA-pol calculations reported by Minchinton *et al.* [94] which use a (9s5p1d/4s1p)/[4s2p1d/2s1p] basis set similar to that in (ii), but with additional d polarization functions on the C and F atoms. See figure 6.1(d).

For all three calculations only poles with strengths greater than  $\sim 0.01$  are shown on figures 6.1(b), 6.1(c), and 6.1(d). A coarse indication of the pole strengths is given by the vertical pole strength indicators under the synthetic spectra. The specific values of the pole strengths and energies can be found in the original publications [94, 289].

It is important to bear in mind the perspectives of sections 2.4 and 2.5.4 above in making any detailed comparison of the measured and calculated spectra in figure 6.1 and in comparing these to previously published EMS measurements [94]. The essentially single particle picture of ionization predicted by theory for the three outer valence orbitals of CH<sub>3</sub>F is reflected by the three peaks observed below  $\sim 25$  eV in the experimental PE spectrum. There is, however, experimental evidence for the minor poles (less than a few percent) from the  $(2a_1)^{-1}$  and  $(1a_1)^{-1}$  ion states predicted to occur in the 28–37 eV region by the calculations. While the ionization energies of the three outermost orbitals are well reproduced by the OV

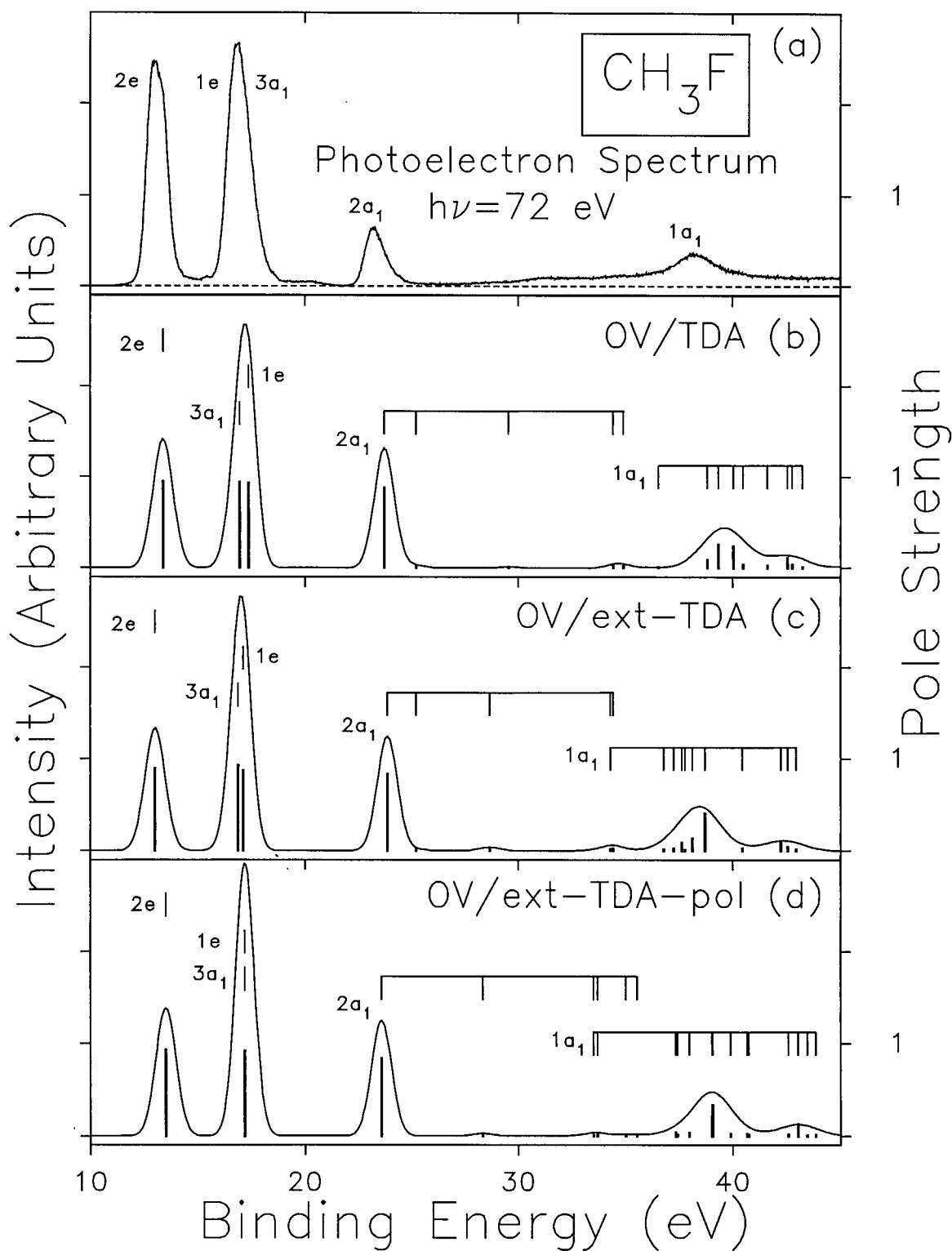


Figure 6.1: The photoelectron spectrum of  $\text{CH}_3\text{F}$  at a photon energy of 72 eV (a) compared with pole-strength calculations and synthetic spectra (b), (c), and (d) generated from Green's function calculations using the OV/TDA [268, 289], OV/ext-TDA [94], and OV/ext-TDA-pol [94] approximations respectively—see text for details.

approximation the predicted ordering of the closely spaced  $1e$  and  $3a_1$  ionization energies is incorrect (see discussion in 5.2 above). The different relative peak areas between experiment and theory in the outer valence regions of figure 6.1 are to be expected since the measured spectrum includes the (final state dependent) full dipole matrix elements for photoionization whereas the synthetic spectrum (based on pole strength) is simply a wavefunction overlap convoluted with appropriate energy widths without allowances for the orbital degeneracies (see sections 2.4 and 2.5.4).

In the inner valence region there are prominent peaks in the measured spectrum at 23.2 to 38.2 eV, but additional broad structures involving appreciable intensity are located in the 27-45 eV region. The peak at 23.2 eV is from  $2a_1$  ionization and it can be seen that all three calculations predict a very large pole strength (0.84–0.88) close to the observed energy and only very low intensity poles arising from ionization of this orbital elsewhere. Thus it can be concluded that this ionization process is quite well described by the independent particle model. This assignment for the  $(2a_1)^{-1}$  band is well supported by the EMS measurements [94]. The EMS binding energy spectra [94] at two angles ( $\phi=0^\circ$  and  $9^\circ$ ) and the momentum distributions show that the structure above 27 eV is predominantly "s-type" in character and that it belongs to the  $(1a_1)^{-1}$  symmetry manifold, as predicted by all three calculations. It can be seen from figure 6.1 that the calculations reproduce the general shape of the inner valence spectral envelope quite well. However, the ext-TDA and ext-TDA-pol calculations both give a much more satisfactory prediction of the energies than the simpler TDA calculation, with little further change arising from the addition of polarization functions. Note that the comparison between the intensities in the pole strength calculation and the photoelectron spectrum in the inner valence region is reasonably straight forward since only one  $(1a_1)$  symmetry manifold appears to be contributing above  $\sim 27$  eV (see discussion in sections 2.4 and 2.5.4 above).

### 6.2.2 Molecular and dissociative photoionization

Information about the molecular and dissociative photoionization processes in  $\text{CH}_3\text{F}$  in the valence region from the first ionization potential up to 100 eV was obtained in the present work from TOF mass spectra using dipole (e,e+ion) spectroscopy. Figure 6.2(a) shows the TOF mass spectrum obtained at an equivalent photon energy of 80 eV. The positive ions observed were:  $\text{H}^+$ ,  $\text{H}_2^+$ ,  $\text{CH}_n^+$ ,  $\text{F}^+$ , and  $\text{CH}_n\text{F}^+$  where  $n = 0$  to 3. The broadness of the  $\text{F}^+$  peak is indicative of considerable excess kinetic energy of fragmentation. No stable doubly charged ions were observed although the products of a small amount of dissociative double photoionization have been studied previously using PIPICO techniques [306]. observed in the TOF mass spectra.

The branching ratio for each molecular and dissociative photoion, determined as the percentage of the total photoionization from integration of the background subtracted TOF peaks, are shown in figure 6.3 (the corresponding numerical values can be calculated from the data given in table 6.1 by dividing the partial photoionization oscillator strength for a particular ion at a particular energy by the sum of all of the ion partial oscillator strengths at that energy).

The photoionization efficiency curve for  $\text{CH}_3\text{F}$  is shown in figure 6.2(b). The data are given numerically in table 6.1. Relative photoionization efficiency values were determined from the TOF mass spectra by taking the ratio of the total number of electron-ion coincidences to the total number of forward scattered electrons as a function of energy loss. Making the reasonable assumption that the absolute photoionization efficiency is unity at higher photon energies we conclude that  $\eta_i$  is 1 above 18.5 eV.

Absolute partial photoionization oscillator strengths for the production of molecular and dissociative ions were obtained from the triple product of the absolute photoabsorption oscillator strength (from dipole (e,e) measurements, see section 5.3.1), the absolute photo-

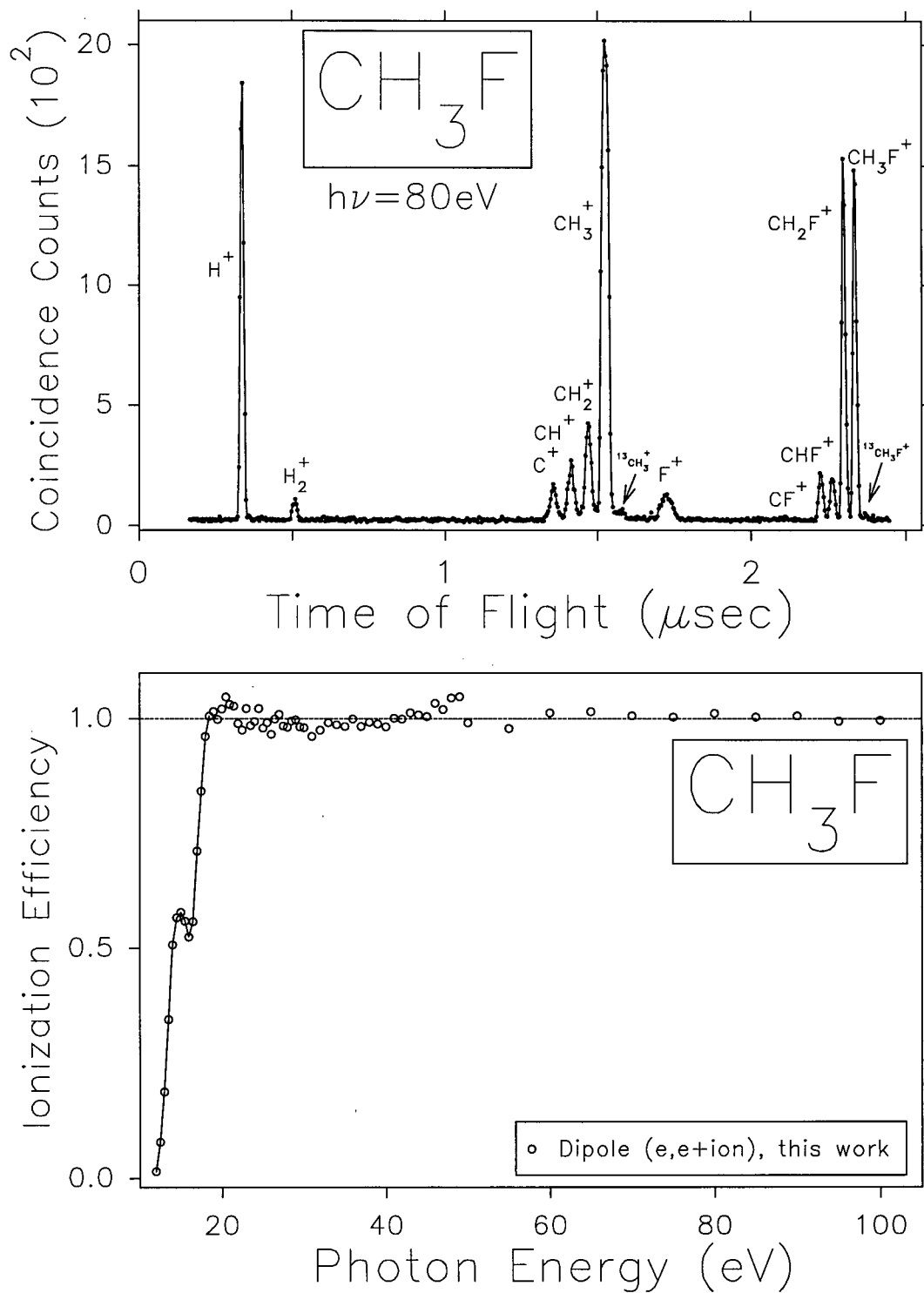


Figure 6.2: (a) TOF mass spectrum of  $\text{CH}_3\text{F}$  recorded at an equivalent photon energy of 80 eV. (b) The photoionization efficiency of methyl fluoride from 12 to 100 eV.

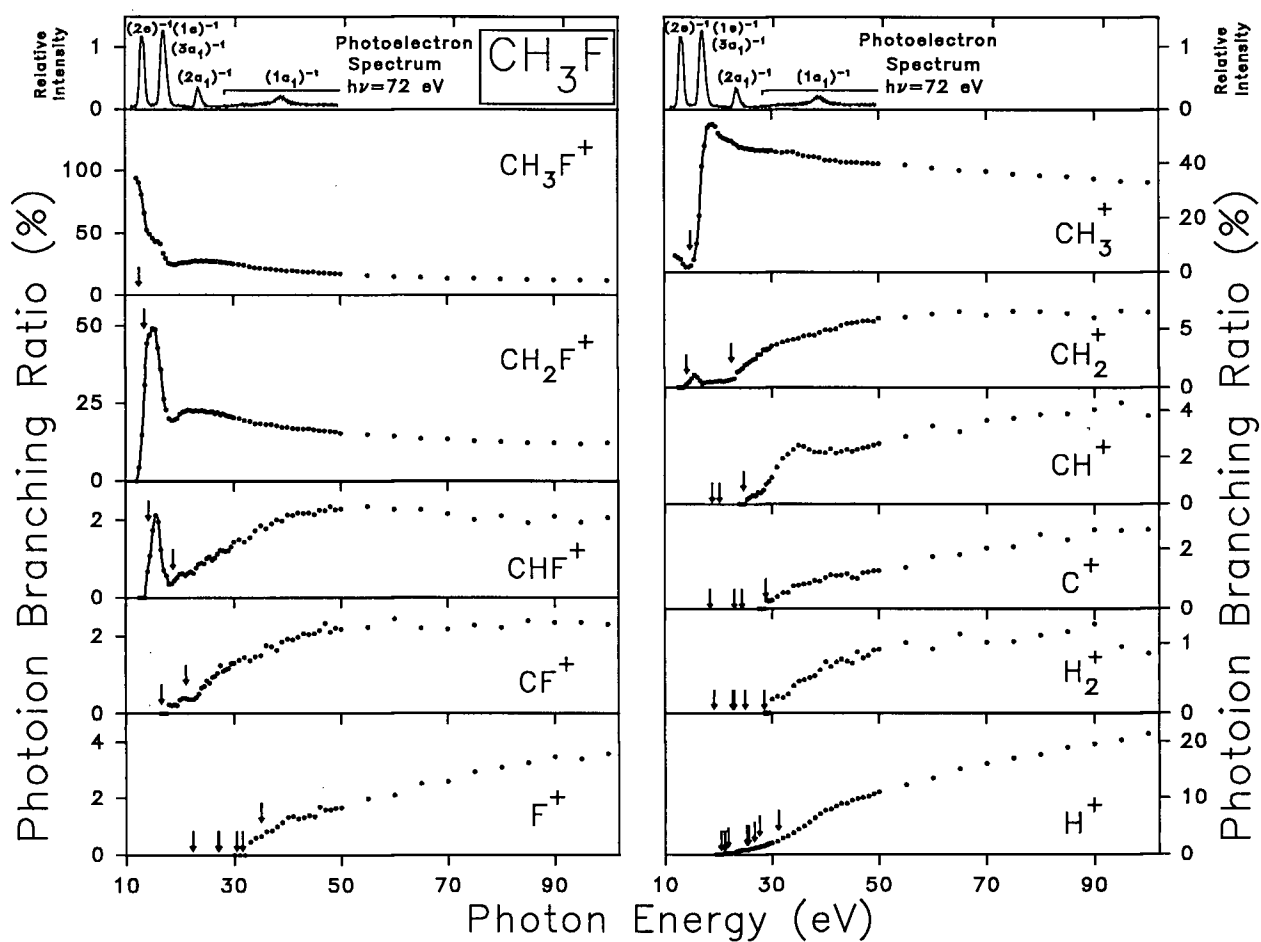


Figure 6.3: Branching ratios for the molecular and dissociative photoionization of  $\text{CH}_3\text{F}$ . Vertical arrows represent the calculated thermodynamic appearance potentials [317] of the ions from  $\text{CH}_3\text{F}$  (see table 6.2). Top panels show the photoelectron spectrum reported in the present work at  $h\nu = 72$  eV (from figure 6.1(a)).

ionization efficiency, and the branching ratio for each ion as a function of photon energy. These absolute partial photoionization oscillator strengths are shown in figure 6.4 and are given numerically in table 6.1. Figures 6.3 and 6.4 show that the major ions formed in the 5 eV energy region above the ionization threshold of the  $(2e)^{-1}$  state are  $\text{CH}_3\text{F}^+$  and  $\text{CH}_2\text{F}^+$ . Small amounts of  $\text{CHF}^+$ ,  $\text{CH}_3^+$ , and  $\text{CH}_2^+$  are also observed in the region just above the first IP. The  $\text{CH}_3^+$  ion appears weakly from 12 to 16 eV, then increases strongly in intensity above 17 eV. This energy corresponds to the ionization potentials for the overlapped  $(1e)^{-1}$  and  $(3a_1)^{-1}$  states. The  $\text{CH}_3^+$  ion is the predominant ion observed at energies above 17 eV. At photon energies below 60 eV the ions  $\text{CH}_3\text{F}^+$ ,  $\text{CH}_2\text{F}^+$ , and  $\text{CH}_3^+$  account for most of the ions produced. In fact at 20 eV these three ions account for 98.5 % of all ions produced, which is consistent with the branching ratios reported by Masuoka and Koyano [306] at 20 eV for this limited m/e range. However, at higher photon energies the present results show appreciable quantitative differences from the branching ratios reported by Masuoka and Koyano [306]. Such differences have been observed in earlier work on  $\text{SiF}_4$  [318, 319]. The presently used dipole (e,e+ion) instrumentation is considered to give more accurate measurements (see references [318, 319] for a discussion of these matters). At 21 eV the branching ratio of  $\text{CH}_2^+$  is 0.5 %, which is consistent with the observations of Momigny *et al.* [304]. The  $\text{H}^+$  ion branching ratio gradually increases over the energy region from 20 to 100 eV, having a larger partial photoionization oscillator strength in the 65 to 100 eV energy region than either  $\text{CH}_3\text{F}^+$  or  $\text{CH}_2\text{F}^+$ . The ions  $\text{CHF}^+$ ,  $\text{CF}^+$ ,  $\text{F}^+$ ,  $\text{CH}^+$ ,  $\text{C}^+$ , and  $\text{H}_2^+$  are all minor products, each contributing less than 6% to the total photoionization oscillator strength even at higher energies.

The presently measured appearance potentials for the ions formed from the molecular and dissociative photoionization of  $\text{CH}_3\text{F}$  are given in table 6.2 where they are compared with both calculated and previously published experimental appearance potentials. Calculated appearance potentials for all possible fragmentation pathways leading to singly charged

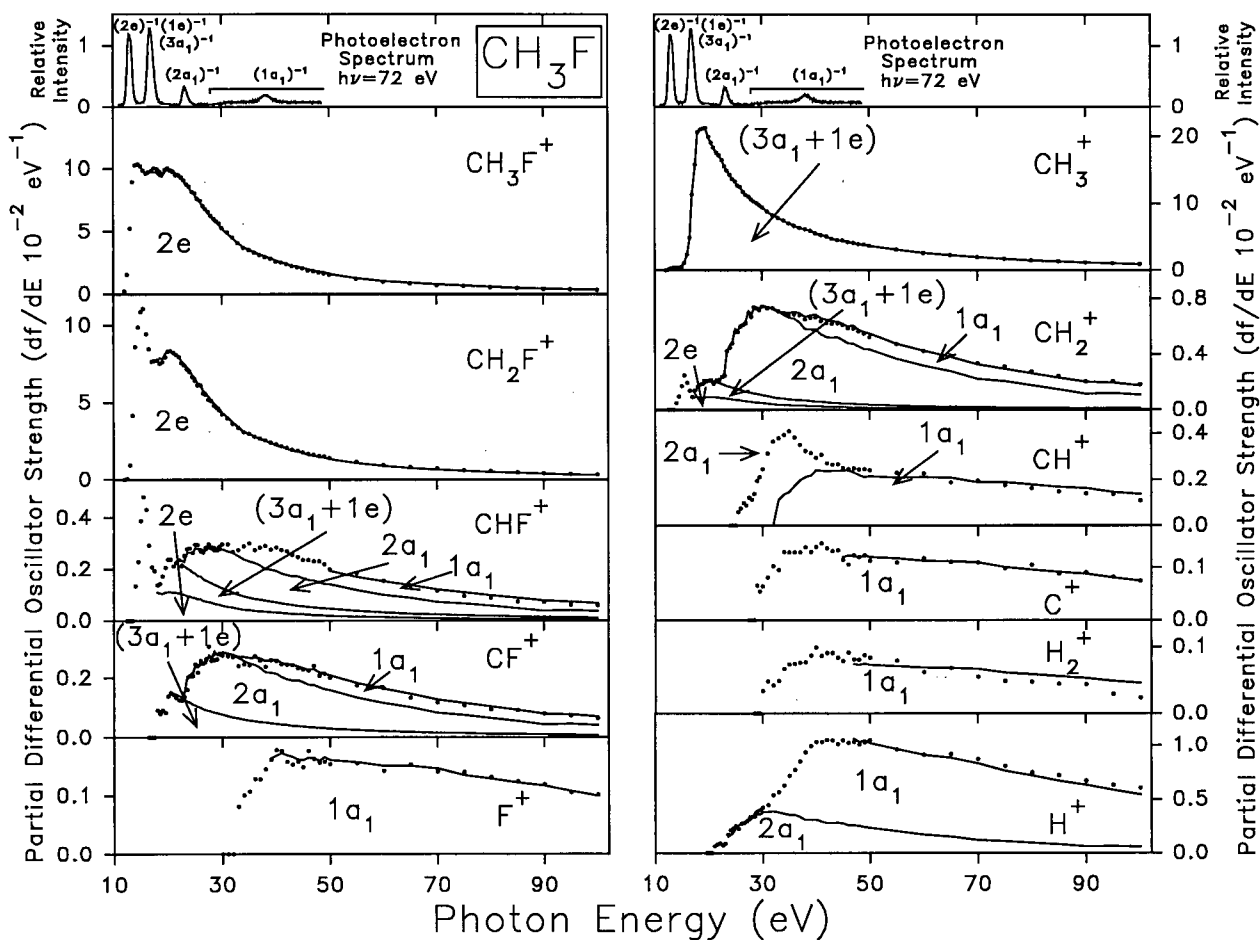


Figure 6.4: Absolute partial photoionization oscillator strengths for the molecular and dissociative photoionization of  $\text{CH}_3\text{F}$ . Points represent the measured partial photoionization oscillator strengths for the molecular and dissociative photoionization. Lines show the sums and partial sums of the electronic state partial photoionization oscillator strength contributions derived from the proposed dipole-induced breakdown scheme (see text, section 6.2.3, for details). Top panels show the photoelectron spectrum recorded in the present work at  $h\nu = 72$  eV (from figure 6.1(a)).

cations from  $\text{CH}_3\text{F}$  are shown as vertical arrows in figure 6.3. These appearance potentials were calculated from thermodynamic heats of formation [317] assuming zero kinetic energy of fragmentation, so the actual thresholds may be higher. Previously published appearance potentials were obtained using either electron impact [297–299] or photoionization [303–306] methods. The presently measured appearance potentials agree well in most cases with the limited number of previously published appearance potentials (within the present experimental uncertainty of  $\pm 1$  eV). It is worth noting that the TOF mass spectral data of Masuoka and Koyano [306], obtained using synchrotron radiation from 20 to 23 eV, showed  $\text{CH}_3\text{F}^+$ ,  $\text{CH}_2\text{F}^+$ ,  $\text{CHF}^+$ ,  $\text{CH}_3^+$ , and  $\text{CH}_2^+$  ions and small amounts of  $\text{CH}^+$  and  $\text{H}^+$ . At these lower energies the  $\text{CH}^+$  and  $\text{H}^+$  ions observed [306] are most likely from ionizing events caused by second or third order radiation.

Table 6.1: Absolute partial differential oscillator strengths for the molecular and dissociative photoionization of CH<sub>3</sub>F from 12 to 100 eV.

Photon Energy eV	Differential Oscillator Strength ( $df/dE$ $10^{-2}eV^{-1}$ ) <sup>a</sup>											Ionization Efficiency <sup>b</sup>
	CH <sub>3</sub> F <sup>+</sup>	CH <sub>2</sub> F <sup>+</sup>	CHF <sup>+</sup>	CF <sup>+</sup>	F <sup>+</sup>	CH <sub>3</sub> <sup>+</sup>	CH <sub>2</sub> <sup>+</sup>	CH <sup>+</sup>	C <sup>+</sup>	H <sub>2</sub> <sup>+</sup>	H <sup>+</sup>	$\eta_i$
12.0	0.24	0.00				0.02						0.01
12.5	1.56	0.07	0.00			0.09	0.00					0.07
13.0	5.23	0.95	0.00			0.31	0.00					0.18
13.5	8.95	4.18	0.00			0.43	0.00					0.34
14.0	10.25	8.62	0.13			0.39	0.05					0.50
14.5	10.35	9.86	0.23			0.42	0.10					0.56
15.0	10.18	10.87	0.39			0.56	0.17					0.57
15.5	9.86	11.07	0.48			1.08	0.25					0.55
16.0	9.61	9.44	0.43			2.34	0.19					0.52
16.5	9.74	8.47	0.29	0.00		4.92	0.14					0.55
17.0	9.83	7.66	0.21	0.00		11.38	0.09					0.71
17.5	10.04	7.71	0.19	0.00		15.78	0.14					0.84
18.0	9.96	7.74	0.14	0.09		20.63	0.17					0.96
18.5	9.75	7.52	0.14	0.08		21.04	0.18					1.00 <sup>b</sup>
19.0	9.54	7.62	0.17	0.09		21.19	0.19					
19.5	9.91	7.95	0.20	0.08		21.26	0.20				0.00	
20.0	10.02	8.32	0.24	0.14		19.94	0.21				0.00	
20.5	9.86	8.34	0.24	0.15		19.06	0.21				0.00	
21.0	9.78	8.25	0.21	0.14		18.28	0.19				0.07	
21.5	9.49	8.11	0.22	0.13		17.57	0.21				0.08	

Table 6.1: (continued) Absolute partial differential oscillator strengths for the molecular and dissociative photoionization of CH<sub>3</sub>F from 12 to 100 eV.

Photon Energy eV	Differential Oscillator Strength ( $df/dE$ $10^{-2}\text{eV}^{-1}$ ) <sup>a</sup>											Ionization Efficiency <sup>b</sup> $\eta_i$
	CH <sub>3</sub> F <sup>+</sup>	CH <sub>2</sub> F <sup>+</sup>	CHF <sup>+</sup>	CF <sup>+</sup>	F <sup>+</sup>	CH <sub>3</sub> <sup>+</sup>	CH <sub>2</sub> <sup>+</sup>	CH <sup>+</sup>	C <sup>+</sup>	H <sub>2</sub> <sup>+</sup>	H <sup>+</sup>	
22.0	9.49	7.97	0.24	0.12		17.17	0.22					0.09
22.5	9.31	7.57	0.21	0.12		16.46	0.24					0.07
23.0	9.09	7.42	0.25	0.14		15.56	0.24					0.09
23.5	8.76	7.16	0.28	0.16		14.94	0.42					0.18
24.0	8.58	7.01	0.28	0.20		14.31	0.45	0.00				0.22
24.5	8.17	6.66	0.26	0.21		13.69	0.48	0.00				0.23
25.0	8.06	6.42	0.30	0.24		13.27	0.56	0.00				0.26
25.5	7.61	6.11	0.29	0.22		12.64	0.56	0.06				0.23
26.0	7.47	6.11	0.27	0.26		12.45	0.60	0.08				0.23
26.5	7.03	5.58	0.26	0.25		11.73	0.61	0.01				0.28
27.0	6.80	5.52	0.28	0.26		11.26	0.62	0.09				0.30
27.5	6.55	5.19	0.30	0.30		11.04	0.70	0.12	0.00			0.32
28.0	6.26	5.10	0.29	0.26		10.58	0.67	0.11	0.00			0.34
28.5	6.02	4.81	0.27	0.26		10.28	0.74	0.14	0.00	0.00		0.35
29.0	5.82	4.68	0.27	0.26		10.07	0.73	0.19	0.06	0.00		0.39
29.5	5.64	4.51	0.29	0.28		9.73	0.72	0.21	0.05	0.00		0.40
30.0	5.27	4.25	0.30	0.28	0.00	9.39	0.74	0.24	0.06	0.03		0.42
31.0	4.92	3.98	0.30	0.27	0.00	8.80	0.73	0.31	0.08	0.05		0.45
32.0	4.55	3.64	0.27	0.27	0.00	8.26	0.73	0.36	0.10	0.04		0.54
33.0	4.08	3.39	0.27	0.24	0.08	7.84	0.71	0.38	0.09	0.05		0.57

Table 6.1: (continued) Absolute partial differential oscillator strengths for the molecular and dissociative photoionization of CH<sub>3</sub>F from 12 to 100 eV.

Photon Energy eV	Differential Oscillator Strength ( $df/dE$ 10 <sup>-2</sup> eV <sup>-1</sup> ) <sup>a</sup>											Ionization Efficiency <sup>b</sup> $\eta_i$
	CH <sub>3</sub> F <sup>+</sup>	CH <sub>2</sub> F <sup>+</sup>	CHF <sup>+</sup>	CF <sup>+</sup>	F <sup>+</sup>	CH <sub>3</sub> <sup>+</sup>	CH <sub>2</sub> <sup>+</sup>	CH <sup>+</sup>	C <sup>+</sup>	H <sub>2</sub> <sup>+</sup>	H <sup>+</sup>	
34.0	3.72	3.09	0.29	0.24	0.10	7.45	0.69	0.39	0.13	0.07	0.63	
35.0	3.54	2.98	0.30	0.24	0.11	7.04	0.68	0.41	0.13	0.07	0.71	
36.0	3.32	2.80	0.28	0.27	0.13	6.64	0.69	0.38	0.13	0.07	0.77	
37.0	3.15	2.70	0.28	0.26	0.13	6.37	0.68	0.35	0.13	0.08	0.85	
38.0	2.96	2.56	0.29	0.24	0.14	6.17	0.65	0.32	0.14	0.08	0.93	
39.0	2.84	2.42	0.28	0.26	0.16	5.91	0.66	0.31	0.13	0.09	1.00	
40.0	2.61	2.31	0.28	0.26	0.18	5.52	0.66	0.29	0.14	0.10	1.03	
41.0	2.54	2.17	0.27	0.25	0.17	5.32	0.64	0.31	0.15	0.09	1.03	
42.0	2.38	2.07	0.27	0.24	0.16	5.09	0.62	0.27	0.14	0.09	1.05	
43.0	2.22	1.94	0.25	0.24	0.15	4.74	0.62	0.26	0.13	0.09	1.05	
44.0	2.11	1.89	0.25	0.23	0.16	4.58	0.62	0.26	0.13	0.08	1.01	
45.0	2.07	1.79	0.24	0.23	0.15	4.45	0.61	0.25	0.11	0.08	1.05	
46.0	1.87	1.68	0.24	0.22	0.18	4.23	0.59	0.24	0.11	0.09	1.02	
47.0	1.83	1.63	0.23	0.24	0.16	4.12	0.58	0.25	0.12	0.08	1.03	
48.0	1.72	1.55	0.23	0.21	0.16	3.95	0.56	0.24	0.12	0.08	1.01	
49.0	1.66	1.51	0.22	0.21	0.16	3.86	0.55	0.24	0.12	0.09	1.03	
50.0	1.56	1.40	0.20	0.20	0.15	3.67	0.52	0.24	0.11	0.08	1.05	
55.0	1.22	1.16	0.18	0.18	0.15	3.10	0.47	0.23	0.11	0.08	0.96	
60.0	0.99	0.96	0.15	0.16	0.14	2.58	0.42	0.23	0.12	0.06	0.91	
65.0	0.86	0.81	0.14	0.13	0.15	2.26	0.39	0.19	0.11	0.07	0.92	

Table 6.1: (continued) Absolute partial differential oscillator strengths for the molecular and dissociative photoionization of CH<sub>3</sub>F from 12 to 100 eV.

Photon Energy eV	Differential Oscillator Strength ( $df/dE$ $10^{-2}eV^{-1}$ ) <sup>a</sup>											Ionization Efficiency <sup>b</sup> $\eta_i$
	CH <sub>3</sub> F <sup>+</sup>	CH <sub>2</sub> F <sup>+</sup>	CHF <sup>+</sup>	CF <sup>+</sup>	F <sup>+</sup>	CH <sub>3</sub> <sup>+</sup>	CH <sub>2</sub> <sup>+</sup>	CH <sup>+</sup>	C <sup>+</sup>	H <sub>2</sub> <sup>+</sup>	H <sup>+</sup>	
70.0	0.73	0.72	0.12	0.12	0.14	2.01	0.33	0.19	0.11	0.05	0.87	
75.0	0.64	0.60	0.10	0.11	0.14	1.71	0.31	0.17	0.10	0.05	0.80	
80.0	0.54	0.53	0.09	0.09	0.13	1.51	0.28	0.16	0.10	0.05	0.75	
85.0	0.47	0.46	0.07	0.09	0.12	1.34	0.24	0.15	0.09	0.04	0.72	
90.0	0.41	0.31	0.07	0.08	0.12	1.18	0.20	0.14	0.09	0.04	0.67	
95.0	0.38	0.36	0.06	0.07	0.10	1.04	0.20	0.14	0.08	0.03	0.63	
100.0	0.34	0.34	0.06	0.06	0.10	0.93	0.18	0.11	0.07	0.02	0.60	

<sup>a</sup> $\sigma(\text{Mb})=109.75 df/dE$  ( $eV^{-1}$ ).

<sup>b</sup>The photoionization efficiency is normalized to unity above 18.5 eV (see text for details).



Table 6.2: (continued) Calculated and measured appearance potentials for the production of positive ions from CH<sub>3</sub>F.

Process	Appearance Potential (eV)								
	Calc- ulated <sup>a</sup>	Experimental							
		This work <sup>b</sup>	[297]	[298]	[299]	[303]	[304]	[305]	[306]
(27) H <sub>2</sub> <sup>+</sup> + CH + F	24.98								
(28) H <sub>2</sub> <sup>+</sup> + F + C + H	28.50	30							
(29) H <sup>+</sup> + CH <sub>2</sub> F	20.48								≤20
(30) H <sup>+</sup> + CF + H <sub>2</sub>	21.06								
(31) H <sup>+</sup> + CH <sub>2</sub> + F	21.30	21.5							
(32) H <sup>+</sup> + HF + CH	21.77								
(33) H <sup>+</sup> + CHF + H	21.81								
(34) H <sup>+</sup> + HF + C + H	25.28								
(35) H <sup>+</sup> + CF + 2H	25.58								
(36) H <sup>+</sup> + F + H <sub>2</sub> + C	26.67								
(37) H <sup>+</sup> + F + CH + H	27.67								
(38) H <sup>+</sup> + F + C + 2H	31.19								

<sup>a</sup>Values calculated using thermodynamic data for the enthalpy of formation of ions and neutrals (taken from [317]) assuming zero kinetic energy of fragmentation.

<sup>b</sup>±1 eV.

### 6.2.3 Dipole-induced breakdown

Above the first ionization threshold it is useful to partition the photoabsorption oscillator strength into either partial photoionization contributions from all ions formed (see section 6.2.2) or into partial photoionization contributions from all electronic ion states (see below and see section 6.2.4). At photon energies above the ionization threshold of a particular electronic state, beyond the upper limit of the Franck-Condon region, the fragmentation branching ratios for molecular and dissociative photoionization from that electronic state will be constant [61]. Therefore, it is possible to partition the partial oscillator strength (POS) for production of any stable molecular or fragment ion into a linear combination of contributions from the various partial photoionization oscillator strengths for the electronic states of at all photon energies above the upper limit of their Franck-Condon regions. For  $\text{CH}_3\text{F}$  this process is assisted by a consideration of ion appearance potentials (table 6.2), vertical ionization potentials (table 5.1 on page 112), PEPICO data [288], and Green's function calculations [94].

The major ions formed by the photoionization of  $\text{CH}_3\text{F}$  were  $\text{CH}_3\text{F}^+$ ,  $\text{CH}_2\text{F}^+$ , and  $\text{CH}_3^+$ . The  $\text{CH}_3\text{F}^+$  and  $\text{CH}_2\text{F}^+$  ions appear (see figure 6.4) near the ionization threshold of the  $(2e)^{-1}$  state and the  $\text{CH}_3^+$  ion appears at energies above the  $(2e)^{-1}$  VIP. The HeI PEPICO data of Eland *et al.* [288] show clearly that the  $\text{CH}_3\text{F}^+$  and  $\text{CH}_2\text{F}^+$  ions are formed only from the  $(2e)^{-1}$  electronic state, while the  $\text{CH}_3^+$  ion is formed only from the  $(1e)^{-1}$  and  $(3a_1)^{-1}$  electronic ion states. It is interesting to note that as shown in the PEPICO spectrum [288], the  $\text{CH}_3\text{F}^+$  ion is formed from the first component of the Jahn-Teller split  $(2e)^{-1}$  band, while the  $\text{CH}_2\text{F}^+$  ion is formed from the second component of the  $(2e)^{-1}$  band. This is observed in the TOF data in the present work, where the onset of the  $\text{CH}_3\text{F}^+$  ion is about 0.5 eV lower than that for the  $\text{CH}_2\text{F}^+$  ion, which corresponds to the estimate by Karlsson *et al.* [111] of 0.6 eV for the magnitude of the Jahn-Teller splitting in the  $\text{CH}_3\text{F}$   $(2e)^{-1}$  band. The shapes

of the POS curves for the  $\text{CH}_3\text{F}^+$  and  $\text{CH}_2\text{F}^+$  ions are essentially the same above 20 eV photon energy, beyond the upper limit of the Franck-Condon region of the  $(2e)^{-1}$  state. From this observation and the PEPICO data [288], it can be concluded that the  $\text{CH}_3\text{F}^+$  and  $\text{CH}_2\text{F}^+$  ions are formed solely by ionization of the  $(2e)^{-1}$  state. The sum of these two partial oscillator strength curves (POS) was therefore used to obtain the shape of the  $(2e)^{-1}$  POS curve.

The onset of the  $\text{CH}_3^+$  ion corresponds to the VIP of the  $(2e)^{-1}$  band, but its intensity is less than 2 % of the total intensity of all ions at this energy. The initial formation of  $\text{CH}_3^+$  is from the ion pair formation,  $\text{CH}_3\text{F} \rightarrow \text{F}^- + \text{CH}_3^+$ , which was reported by Suzuki *et al.* [315] to produce  $\text{F}^-$  from 12.4 to 19 eV. The second  $\text{CH}_3^+$  onset, which is much larger, occurs at about 16.5 eV and corresponds to the ionization energies of the  $(1e+3a_1)^{-1}$  states. Since the POS curve of the  $\text{CH}_3^+$  ion shows no higher thresholds it can be used to represent the shape of the  $(1e+3a_1)^{-1}$  electronic ion state POS curve. This is also consistent with the PEPICO data [288], which indicate that the  $\text{CH}_3^+$  ion is produced solely from dissociative photoionization of the  $(1e)^{-1}$  and  $(3a_1)^{-1}$  states. The electronic state POS shapes so-obtained for the  $(2e)^{-1}$  and  $(1e+3a_1)^{-1}$  states can then be used to assess their contributions to the POSs for  $\text{CH}_3\text{F}^+$ ,  $\text{CH}_2\text{F}^+$ ,  $\text{CHF}^+$ ,  $\text{CF}^+$ ,  $\text{CH}_3^+$ , and  $\text{CH}_2^+$  as shown on figure 6.4. The  $\text{CHF}^+$  and  $\text{CH}_2^+$  ion POS curves show large maxima at 14 eV similar to that in the  $\text{CH}_2\text{F}^+$  POS curve. These are assigned as autoionization to the  $(2e)^{-1}$  state. There are three other onsets in the  $\text{CHF}^+$  ion POS curve which indicate contributions from the  $(1e+3a_1)^{-1}$ ,  $(2a_1)^{-1}$ , and  $(1a_1)^{-1}$  electronic ion states. The  $\text{CF}^+$  ion POS curve has onsets corresponding to the energies of the  $(1e+3a_1)^{-1}$ ,  $(2a_1)^{-1}$ , and  $(1a_1)^{-1}$  states.

The appearance potentials of the  $\text{F}^+$ ,  $\text{C}^+$ , and  $\text{H}_2^+$  ions are 33, 29.5, and 30 eV, respectively, which correspond to the region where several many-body states associated with the  $(1a_1)^{-1}$  electronic ion state exist. The thresholds are well above the Franck-Condon regions of the other electronic ion states, so the  $\text{F}^+$ ,  $\text{C}^+$ , and  $\text{H}_2^+$  ions must be formed from ioniza-

tion processes corresponding to production of the various many-body states of the  $(1a_1)^{-1}$  photoionization process. Therefore the shape of the  $(1a_1)^{-1}$  POS was estimated from the sum of the  $F^+$ ,  $C^+$ , and  $H_2^+$  POSs, since these all show similar shapes and have thresholds consistent with onsets of the  $(1a_1)^{-1}$  many-body ion states observed in the photoelectron spectrum (see figure 6.1 and section 6.2.1). The  $(2e)^{-1}$  and  $(1e+3a_1)^{-1}$  contributions to the  $CH_2^+$  POS were then subtracted from it to leave a contribution which (from the sharp higher threshold at 22.5 eV) is clearly from a  $(2a_1)^{-1}$  contribution plus a small  $(1a_1)^{-1}$  contribution (as indicated by the highest threshold at  $\sim 35$  eV). This small  $(1a_1)^{-1}$  contribution was subtracted (using the shape determined above from the  $F^+$ ,  $C^+$ , and  $H_2^+$  POSs) to give the shape of the  $(2a_1)^{-1}$  POS curve.

The appearance potential of the  $H^+$  ion is 21.5 eV, which is close to the adiabatic ionization potential of the  $(2a_1)^{-1}$  state. Therefore, part of the  $H^+$  ion intensity comes from the  $(2a_1)^{-1}$  electronic ion state. The shape of the  $(2a_1)^{-1}$  POS was fit to the total  $H^+$  POS to determine the  $(2a_1)^{-1}$  contribution to  $H^+$ . The remainder of the  $H^+$  ion is produced from the  $(1a_1)^{-1}$  state, as indicated by the onset in the  $H^+$  POS curve at 32 eV. This higher threshold for  $H^+$  clearly corresponds to a  $(1a_1)^{-1}$  contribution, which is indicated by comparing its threshold and shape with those of the  $F^+$ ,  $C^+$ , and  $H_2^+$  ions.

The contributions from the  $(2e)^{-1}$  and  $(1e+3a_1)^{-1}$  POSs to each of the  $CHF^+$  and  $CF^+$  POS were subtracted from them to yield the contributions from  $(2a_1)^{-1}$  and  $(1a_1)^{-1}$  to each (this was done using the shapes of these two electronic ion state POSs as determined above). The main contribution to the  $CH^+$  POS fits the shape of the  $(1a_1)^{-1}$  POS at high energy. The slightly lower threshold for  $CH^+$  than for  $F^+$ ,  $C^+$ , or  $H_2^+$  suggests that it comes from a very low energy many-body state of the  $(1a_1)^{-1}$  process (see section 6.2.1 and ref. [94]), just above the  $(2a_1)^{-1}$  peak. The broad peak between 30 and 40 eV on the  $CH^+$  POS is thought to arise from neutral excited states approaching the  $(1a_1)^{-1}$  many-body ion state limits which autoionize down to the underlying  $(2a_1)^{-1}$  continuum.

The various portions (areas) for each of the  $(2e)^{-1}$ ,  $(1e+3a_1)^{-1}$ ,  $(2a_1)^{-1}$  (including the peak in the  $\text{CH}^+$  POS), and  $(1a_1)^{-1}$  electronic ion states contributing to the molecular and dissociative ion POSs (as shown in figure 6.4) were then summed to provide estimates of the partial photoionization oscillator strengths for the production of molecular ions in these specific electronic states of  $\text{CH}_3\text{F}^+$ . These electronic state partial photoionization oscillator strength estimates, shown in figure 6.5 and listed in table 6.3, can be compared with direct measurements obtained using tunable photon energy photoelectron spectroscopy (see section 6.2.4 below).

The resulting dipole-induced breakdown pattern for  $\text{CH}_3\text{F}$  above 50 eV suggested by the above analysis is summarized in figure 6.6.

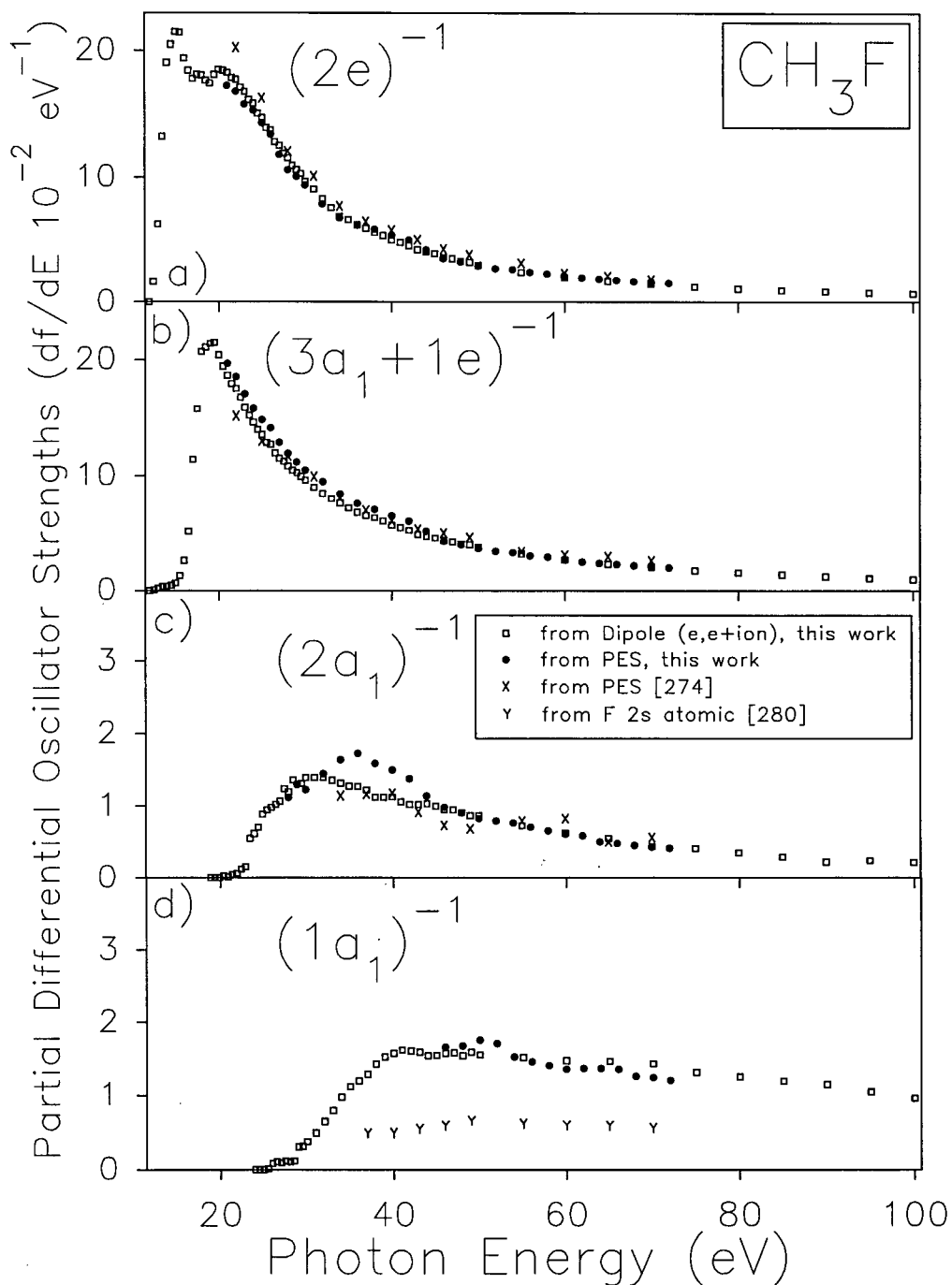


Figure 6.5: Absolute partial photoionization oscillator strengths for production of electronic states of  $\text{CH}_3\text{F}^+$ . Open squares show the estimates from appropriate linear combinations of the present molecular and dissociative photoionization POSs of  $\text{CH}_3\text{F}$  and the dipole-induced breakdown scheme (see section 6.2.3). Filled circles represent estimates from photoelectron binding energy spectra recorded in the present work using tunable synchrotron radiation (see section 6.2.4). The crosses are the previously published electronic state partial photoionization oscillator strengths of Novak *et al.* [274] renormalized using the presently reported photoabsorption data (see text in section 6.2.4 for details).

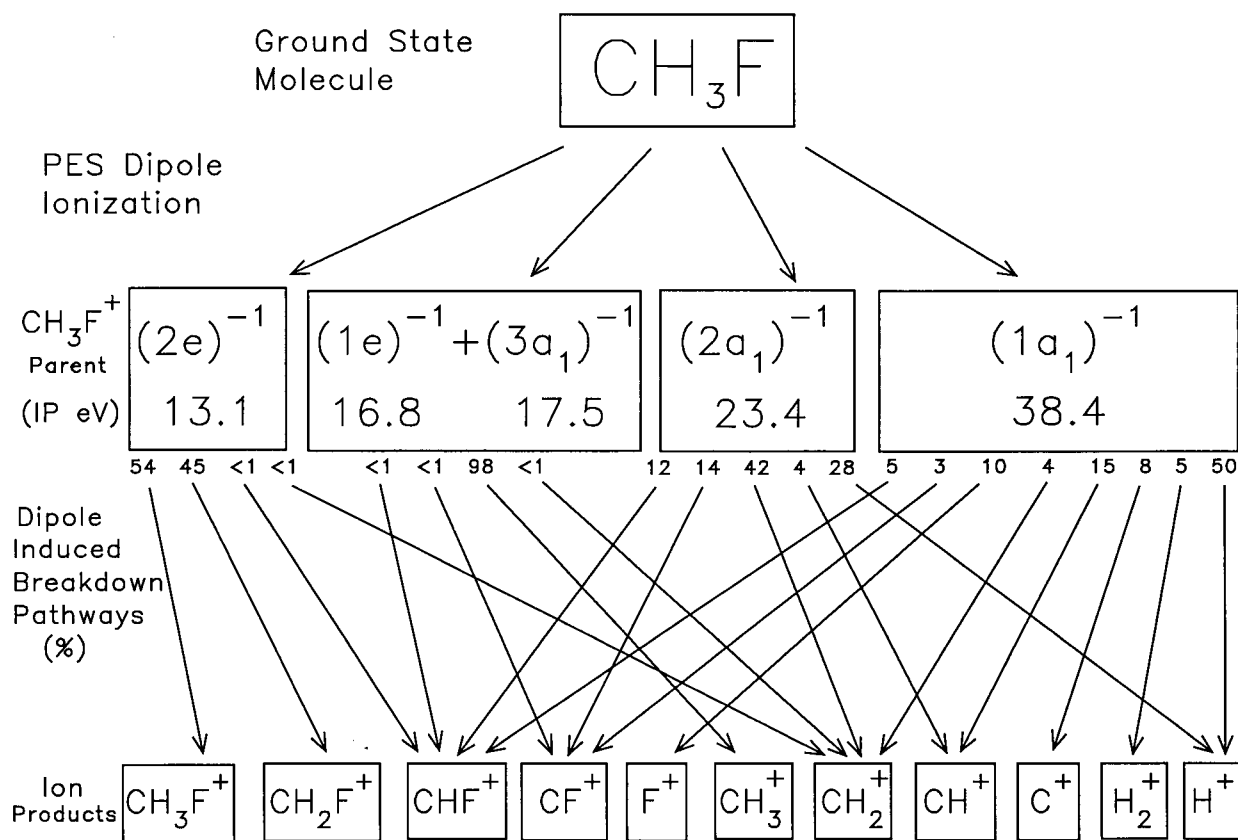


Figure 6.6: Proposed dipole-induced breakdown scheme for the ionic photofragmentation of CH<sub>3</sub>F above  $h\nu = 50$  eV.

Table 6.3: Absolute partial differential oscillator strengths for production of electronic states<sup>a</sup> of CH<sub>3</sub>F<sup>+</sup>.

Photon Energy eV	Partial Differential Oscillator Strength $df/dE$ ( $10^{-2}eV^{-1}$ ) <sup>b</sup>				Photon Energy eV	Partial Differential Oscillator Strength $df/dE$ ( $10^{-2}eV^{-1}$ ) <sup>b</sup>			
	(2e) <sup>-1</sup>	(1e+3a <sub>1</sub> ) <sup>-1</sup>	(2a <sub>1</sub> ) <sup>-1</sup>	(1a <sub>1</sub> ) <sup>-1</sup>		(2e) <sup>-1</sup>	(1e+3a <sub>1</sub> ) <sup>-1</sup>	(2a <sub>1</sub> ) <sup>-1</sup>	(1a <sub>1</sub> ) <sup>-1</sup>
12.5	1.67	0.05			29	10.62	10.25	1.30	0.31
13	6.28	0.21			29.5	10.30	9.92	1.31	0.31
13.5	13.21	0.35			30	9.68	9.59	1.39	0.38
14	19.04	0.40			31	9.03	8.98	1.39	0.50
14.5	20.50	0.47			32	8.29	8.42	1.40	0.65
15	21.51	0.65			33	7.57	7.99	1.35	0.80
15.5	21.44	1.30			34	6.91	7.61	1.31	0.98
16	19.41	2.61			35	6.62	7.20	1.28	1.12
16.5	18.42	5.15			36	6.22	6.79	1.27	1.20
17	17.78	11.39			37	5.95	6.52	1.22	1.29
17.5	18.12	15.75			38	5.62	6.32	1.12	1.43
18	18.06	20.68			39	5.36	6.06	1.12	1.52
18.5	17.65	21.06			40	5.02	5.67	1.12	1.58
19	17.42	21.39			41	4.81	5.46	1.06	1.62
19.5	18.11	21.49			42	4.55	5.22	1.02	1.61
20	18.50	20.37	0		43	4.24	4.86	1.02	1.59
20.5	18.44	19.41	0.02		44	4.08	4.69	1.03	1.54
21	18.27	18.62	0.01		45	3.93	4.55	1.00	1.55
21.5	17.86	17.93	0.04		46	3.63	4.34	0.95	1.58
22	17.72	17.52	0.06		47	3.53	4.23	0.95	1.58
22.5	17.10	16.77	0.12		48	3.34	4.05	0.91	1.54
23	16.76	15.88	0.15		49	3.24	3.96	0.87	1.60
23.5	16.12	15.22	0.55		50	3.01	3.76	0.86	1.55
24	15.83	14.61	0.62		55	2.43	3.18	0.73	1.52
24.5	15.03	13.96	0.71		60	1.99	2.64	0.63	1.48
25	14.69	13.53	0.89	0	65	1.70	2.31	0.55	1.46
25.5	13.89	12.87	0.95	0.01	70	1.47	2.05	0.44	1.43
26	13.75	12.69	0.98	0.08	75	1.26	1.74	0.41	1.32
26.5	12.78	11.95	1.02	0.10	80	1.09	1.54	0.35	1.25
27	12.49	11.49	1.06	0.09	85	0.95	1.37	0.29	1.20
27.5	11.89	11.24	1.24	0.12	90	0.84	1.21	0.22	1.15
28	11.52	10.79	1.20	0.10	95	0.76	1.07	0.24	1.05
28.5	10.94	10.44	1.36	0.12	100	0.70	0.96	0.22	0.96

<sup>a</sup>Estimates obtained from a consideration of the partial oscillator strengths for the molecular and dissociative photoionization of CH<sub>3</sub>F using the dipole-induced breakdown scheme derived in section 6.2.3. See text for details (section 6.2.3) and comparison with synchrotron radiation PES measurements (section 6.2.4).

<sup>b</sup> $\sigma$ (Mb)=109.75  $df/dE$  (eV<sup>-1</sup>).

### 6.2.4 Photoelectron spectroscopy

Photoelectron (binding energy) spectra of  $\text{CH}_3\text{F}$  have been recorded using monochromated synchrotron radiation at photon energies from 21 to 72 eV. The photoelectron spectrum recorded at 72 eV photon energy has already been shown in figure 6.1. The experimental spectra have been corrected for the electron analyser transmission efficiency as detailed in section 3.4. At lower incident photon energies the vibronic peaks of the  $(2e)^{-1}$  ion state were resolved. These have been studied by Karlsson *et al.* [111] at high resolution. The photoelectron spectra were put onto an absolute binding energy scale by normalizing the energies of the vibronic peaks observed in the  $(2e)^{-1}$  band to those reported for the  $(2e)^{-1}$  band in the high resolution HeI photoelectron spectra of Karlsson *et al.* [111]. The inner valence photoelectron bands are split into several many-body states by electron correlation effects. These effects have been discussed in section 6.2.1 and it was determined that the  $(2a_1)^{-1}$  band is not significantly split, but is mostly localized in one main pole at 23.2 eV. The  $(1a_1)^{-1}$  band, however, is split into many small poles which are spread out over the 27 to  $\sim 45$  eV energy region with the main pole being centered at 38.2 eV. Reasonable predictions of these effects are given by many-body Green's function calculations [94, 289].

The branching ratios for the production of the electronic ion states of methyl fluoride were obtained by integrating the peak area for each electronic ion state in the transmission corrected photoelectron spectra. Note that even if only one peak area is in error then all branching ratios and thus all electronic state partial photoionization oscillator strengths will exhibit corresponding errors. Quantitative studies of photoelectron branching ratios require accurate background subtraction of the photoelectron spectra to obtain the true relative peak areas for each electronic ion state. However, this background subtraction process is complicated: First by the rising background caused by stray electrons which is observed increasingly in the low kinetic energy regions of the photoelectron spectra in all

photoelectron spectrometers. In addition, difficulties in assessing the background are also caused by electron correlation effects that can split the ionization of inner valence orbitals into a number of many-body states, many of which are of low intensity.

The rising background at low electron kinetic energies is mainly caused by stray electrons ejected from the metal surfaces in the electron spectrometer. Since most stray electrons have lower kinetic energies, the background decreases significantly at higher electron kinetic energies. This means that the background "ramp" problem is much more serious at lower photon energies (i.e. when the incident photon energy is near the electronic ion state threshold) and it is in these regions that the largest quantitative errors are to be expected. Thus, the background subtraction procedures used for determining peak areas are expected to be less accurate near threshold where the ionization energy is only a few electron volts below the ionizing photon energy. At electron kinetic energies greater than 10 eV the background becomes more constant and less curved, and therefore it is easier to estimate and subtract (see figure 6.7). The assessment of this rising background is particularly difficult in the photoelectron spectra of molecules in which electron correlation effects split each of the inner valence orbitals into several low intensity many-body states. These many-body states, giving a general rise in intensity, can easily be misinterpreted as part of the rising background (or vice-versa). Methyl fluoride shows such extensive many-body effects in the  $(1a_1)^{-1}$  inner valence region (see figure 6.7).

In the present work the shape and intensity of the  $(1a_1)^{-1}$  band including the low intensity many-body states was determined at high photon energy (72 eV, see figure 6.7) where the background is relatively flat and could therefore be estimated for all binding energies of interest. The resulting shape of the  $(1a_1)^{-1}$  binding energy profile at  $h\nu = 72$  eV was used to differentiate the  $(1a_1)^{-1}$  band from the rising background at the lower photon energies where the background became severe, as can be seen in figure 6.7. This procedure was most important for the  $(1a_1)^{-1}$  band for two reasons. First, the intensity of the  $(1a_1)^{-1}$

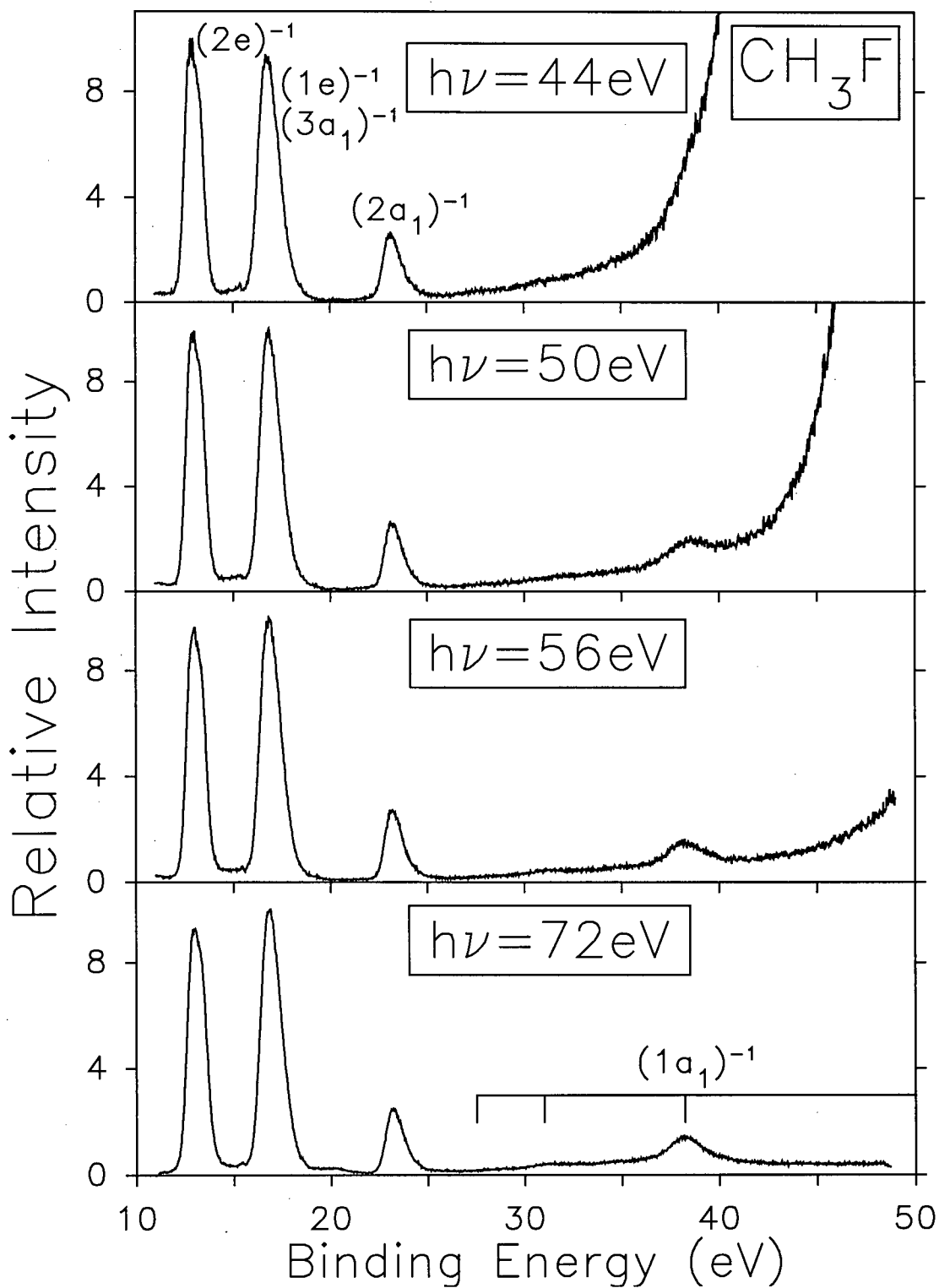


Figure 6.7: Photoelectron spectra of  $\text{CH}_3\text{F}$  recorded at photon energies of 44, 50, 56, and 72 eV. Note the steeply rising non-spectral background obscuring the  $(1a_1)^{-1}$  many-body region at lower incident photon energies.

state is spread out into several many-body states over more than 20 eV binding energy. Some additional many-body states were reported at binding energies above 45 eV in the EMS experiments of Minchinton *et al.* [94]. The small contributions from these states above 45 eV, higher in binding energy than the present measurements, were unaccounted for in the present work. Secondly, the determination of the background in the region of the  $(1a_1)^{-1}$  band could seriously overestimate or underestimate the band area depending on where it was assigned.

The photoelectron branching ratios for the  $(2e)^{-1}$ ,  $(1e+3a_1)^{-1}$ ,  $(2a_1)^{-1}$ , and  $(1a_1)^{-1}$  electronic ion states of  $\text{CH}_3\text{F}$  resulting from the preceding analysis were obtained at each photon energy by integrating the photoelectron peaks for each state in the transmission corrected, background subtracted photoelectron spectra and normalizing the sum of all states to 100%. The kinetic energy resolution was sufficient to resolve all states in the photoelectron spectra with the exception of the  $(1e)^{-1}$  and  $(3a_1)^{-1}$  states, which are significantly overlapped. Thus, this intensity is reported as the sum of the  $(1e+3a_1)^{-1}$  states.

The difficulties caused by the rising background at low kinetic energies make it impossible to determine the contribution from a state in the region immediately above that state's ionization threshold. The branching ratio determined for each state from 10 to 20 eV above its ionization threshold is therefore approximate because of the rising background. It is also important to note that the absence of or uncertainty in any one branching ratio will cause errors in the branching ratios and the partial photoionization oscillator strengths for production of all ionic states in these near threshold regions.

Absolute partial photoionization oscillator strengths for production of the electronic states of  $\text{CH}_3\text{F}^+$  were obtained from the triple product of the absolute photoabsorption oscillator strength (from dipole (e,e) measurements, see section 5.3.1), the absolute photoionization efficiency, and the photoelectron branching ratio for each electronic ion state as a function photon energy. The absolute electronic state partial photoionization oscillator

strengths so derived are shown as solid circles on figure 6.5 in comparison with the estimates (open squares) obtained from a consideration of the molecular and dissociative photoionization breakdown scheme derived above (section 6.2.3). The electronic state partial photoionization cross-sections (oscillator strengths) reported by Novak *et al.* [274] (which were not corrected for electron analyser kinetic energy effects) were originally placed on an absolute scale using the photoabsorption data reported by Wu *et al.* [237]. For the purpose of consistency in the present comparison, branching ratios were computed from the electronic state partial photoionization cross-sections given by Novak *et al.* [274], then renormalized electronic state partial photoionization oscillator strengths were calculated using the photoabsorption data from the present work. These renormalized POSs (crosses on figure 6.5) derived from the data of Novak *et al.* [274] are compared to the presently reported electronic ion state POSs in figure 6.5. The contribution from the  $(1a_1)^{-1}$  state was not measured by Novak *et al.* [274], but was estimated from the F 2s atomic cross sections calculated by Yeh and Lindau [280]. Figure 6.5 also shows the F 2s theoretical data [280]. It can be seen from figure 6.5 that there is quite good agreement between the present work and the “reworked” results of Novak *et al.* [274] for the  $(2e)^{-1}$ ,  $(1e+3a_1)^{-1}$ , and the  $(2a_1)^{-1}$  partial oscillator strengths. There are significant differences between intensities of the presently reported  $(1a_1)^{-1}$  state POSs and the atomic F 2s partial cross sections of Yeh and Lindau [280] used as an approximation for the  $(1a_1)^{-1}$  partial cross-sections by Novak *et al.* [274]. Note that the underestimation of the  $(1a_1)^{-1}$  POSs obtained by using the F 2s atomic data will result in a corresponding slight overestimate in the other POSs in the work of Novak *et al.* [274].

Figure 6.5 shows that there is generally quite good agreement between the electronic ion state POSs measured directly in the present work using synchrotron radiation and the estimates derived from the molecular and dissociative photoionization POSs and breakdown scheme (see section 6.2.3) for all states above 45 eV. However, there are serious discrepancies below 45 eV for the  $(2a_1)^{-1}$  and the  $(1a_1)^{-1}$  POSs and corresponding minor discrepancies for

the  $(2e)^{-1}$  and the  $(1e+3a_1)^{-1}$  POSs. These discrepancies are a result of errors in assessing the rising PES background at lower photon energies for the inner valence states (see above) particularly in the case of the  $(1a_1)^{-1}$  ionization which has many low intensity many-body states spread out over a wide range of binding energies. Indeed the  $(1a_1)^{-1}$  integrated area could not be assessed at all below a photon energy of  $\sim 45$  eV, which results in corresponding errors in the other photoelectron branching ratios and partial photoionization oscillator strengths. Errors near the  $(2a_1)^{-1}$  threshold result in (small percentage) errors in the 21 to 30 eV region of the  $(2e)^{-1}$  and  $(1e+3a_1)^{-1}$  POSs. Similar errors near the  $(1e+3a_1)^{-1}$  threshold also result in small errors in the 21 to 25 eV region of the  $(2e)^{-1}$  POSs. As such the present direct synchrotron radiation electronic state photoionization POS measurements are only considered to be reasonably accurate for the lower intensity  $(2a_1)^{-1}$  and  $(1a_1)^{-1}$  states above 45 eV. For the  $(2e)^{-1}$  and  $(1e+3a_1)^{-1}$  states the PES results agree with the molecular and dissociative photoionization estimates to better than 10% over the whole energy range studied. In summary, the present estimates of the electronic state photoionization POSs from the molecular and dissociative photoionization POSs and breakdown scheme (section 6.2.3) are considered to be of higher accuracy than the direct measurements using PES and synchrotron radiation.

The present work illustrates the accuracy and utility of the dipole (e,e+ion) method for estimating electronic state partial photoionization oscillator strengths from molecular and dissociative photoionization data. This has also been seen in earlier work [161, 320, 321]. It also illustrates the difficulties and inaccuracies involved in quantitative PES studies at lower electron kinetic energies, especially where low intensity inner valence many-body ion states occur. This latter phenomenon is wide spread [88, 89] and is expected to complicate most PES measurements of inner valence regions. Recent advances in PES instrumentation by Baltzer *et al.* [322], including a new gas cell for PES use which incorporates an "electron dump", are expected to greatly improve the quantitative aspect of PES and techniques

could possibly be significantly improved by employing background subtraction techniques at quarter sample pressure, as used (see section 3.1) in the present dipole (e,e) methods [27, 46]. This latter procedure will of course double the amount of beamtime required at the synchrotron light source, but should result in improved accuracy. Furthermore, a careful instrumental design which minimizes the amount of light striking the metal surfaces in the source region would also diminish the non-spectral background of low kinetic energy electrons.

## 6.3 Methyl Chloride Results and Discussion

### 6.3.1 Binding energy spectrum

The photoelectron spectrum of  $\text{CH}_3\text{Cl}$  reported in the present work at a photon energy of 72 eV is shown in figure 6.8(a) where it is compared with several calculations (see section 6.2.1 above for general information concerning the calculations and the details of the various presentations in the figure).

The three Green's function calculations for  $\text{CH}_3\text{Cl}$  are:

(i) The OV/TDA calculation by von Niessen *et al.* [269] using the ADC(3) method and a  $[12s9p/9s5p/4s]/(6s4p/4s2p/2s)$  basis set. See figure 6.8(b).

(ii) The OV/ext-TDA calculation by Minchinton *et al.* [94] using the ADC(4) method and the same basis set as in (i). See figure 6.8(c).

(iii) The OV/ext-TDA-pol calculation of Minchinton *et al.* [94] using the ADC(4) method and a  $[12s9p1d/9s5p1d/4s1p]$  basis set containing extra polarization functions on the C and Cl atoms. See figure 6.8(d).

The binding energies of the outer valence PE spectrum are reproduced well by the OVGF calculations [94, 269]. The calculations indicate that these ionization processes are all well described by the independent particle model, with essentially unit pole strength in the main

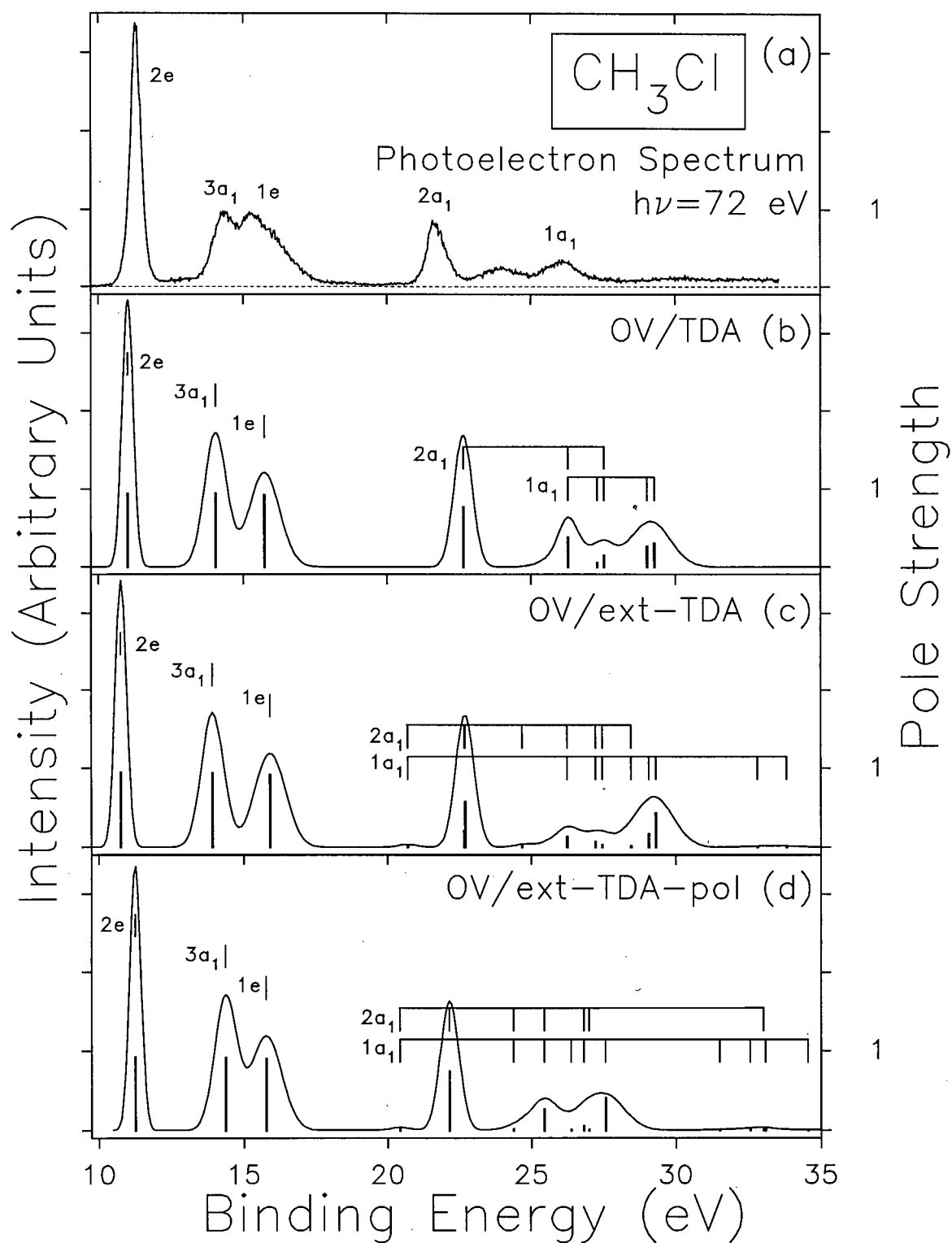


Figure 6.8: The photoelectron spectrum of  $\text{CH}_3\text{Cl}$  at a photon energy of 72 eV (a) compared with pole-strength calculations and synthetic spectra (b), (c), and (d) generated from Green's function calculations using the OV/TDA [269], OV/ext-TDA [94], and OV/ext-TDA-pol [94] approximations respectively—see text for details.

peaks. In contrast, the structured inner valence region of the spectrum shows clear evidence of the breakdown of the independent particle model and the observed spectral envelope is qualitatively consistent with the various theoretical predictions of the pole strength distributions.

In  $\text{CH}_3\text{Cl}$ , the inner valence manifolds corresponding to ionization of the  $2a_1$  and  $1a_1$  electrons in the neutral molecules, are more complex than for  $\text{CH}_3\text{F}$ . Three major inner valence peaks are observed at 21.6, 23.8 and 26.1 eV, together with higher energy broader structures. The calculations all predict a major pole between 22 and 23 eV  $(2a_1)^{-1}$  with a pole strength ranging between 0.56 and 0.77, and another between 27 and 29 eV  $(1a_1)^{-1}$  with a pole strength ranging between 0.26 and 0.42. The superior ext-TDA and ext-TDA-pol calculations predict slightly larger pole strengths for both these peaks than the simpler TDA calculation. A third structure between the two peaks is also predicted in all calculations. Clearly the ext-TDA-pol calculation gives the best overall description of the energies and shape of the inner valence region. Both ext-TDA calculations predict higher energy poles between 30 and 35 eV in accord with the experimental spectrum whereas no poles were reported [269] above 30 eV in the TDA calculation. It is of interest to consider the predictions for the origin of the structure at 23.8 eV between the two main inner valence peaks. All calculations predict contributions from both the  $(2a_1)^{-1}$  and  $(1a_1)^{-1}$  processes with the ext-TDA and the ext-TDA-pol predicting ratios of  $\sim 3:1$  and  $\sim 5:1$  respectively in favour of the  $(1a_1)^{-1}$  process, whereas the less accurate TDA calculation predicts approximately equal contributions. The EMS measurements of binding energy spectra and momentum distributions [94] strongly support the conclusions of the better calculations, confirming that the vast majority of the  $(2a_1)^{-1}$  pole strength is located at  $\sim 21.9$  eV and that 50 % of the  $(1a_1)^{-1}$  pole strength is located in a peak at 25.5 eV, with the bulk of the remaining  $(1a_1)^{-1}$  strength making up the low intensity continuum to higher binding energy.

### 6.3.2 Molecular and dissociative photoionization

The formation of the molecular and fragment ions by molecular and dissociative photoionization processes in  $\text{CH}_3\text{Cl}$  in the valence region from the first ionization potential up to 80 eV has been studied in the present work using TOF mass spectra measured in coincidence with energy loss electrons by dipole (e,e+ion) spectroscopy. Figure 6.9(a) shows a typical TOF mass spectrum obtained at an equivalent photon energy of 80 eV. The positive ions observed are:  $\text{H}^+$ ,  $\text{H}_2^+$ ,  $\text{CH}_n^+$ ,  $\text{Cl}^+$ , and  $\text{CH}_n\text{Cl}^+$  where  $n = 0$  to 3. The broadness of the  $\text{Cl}^+$  peaks is indicative of considerable excess kinetic energy of fragmentation. No stable doubly charged ions were observed, thus it can be concluded that any double ionization events produce two positively charged fragments within the time scale of this experiment.

The branching ratios for each molecular and dissociative photoionization channel of  $\text{CH}_3\text{Cl}$ , determined as the percentage of the total photoionization from integration of the background subtracted TOF peaks, are shown in figure 6.10 (the corresponding numerical values can be calculated from the data given in table 6.4 by dividing the partial photoionization oscillator strength for a particular ion at a particular energy by the sum of the ion partial oscillator strengths at that energy).

The photoionization efficiency curve for  $\text{CH}_3\text{Cl}$  is shown in figure 6.9(b) and given numerically in table 6.4. Relative photoionization efficiency values were determined from the TOF mass spectra by taking the ratio of the total number of electron-ion coincidences to the total number of forward scattered electrons as a function of energy loss. Making the reasonable assumption that the absolute photoionization efficiency is unity at higher photon energies we conclude that  $\eta_i$  is 1 above 18 eV.

Absolute partial photoionization oscillator strengths for the production of molecular and dissociative ions were obtained from the triple product of the absolute photoabsorption oscillator strength (from dipole (e,e) measurements, see section 5.4.1), the absolute photo-

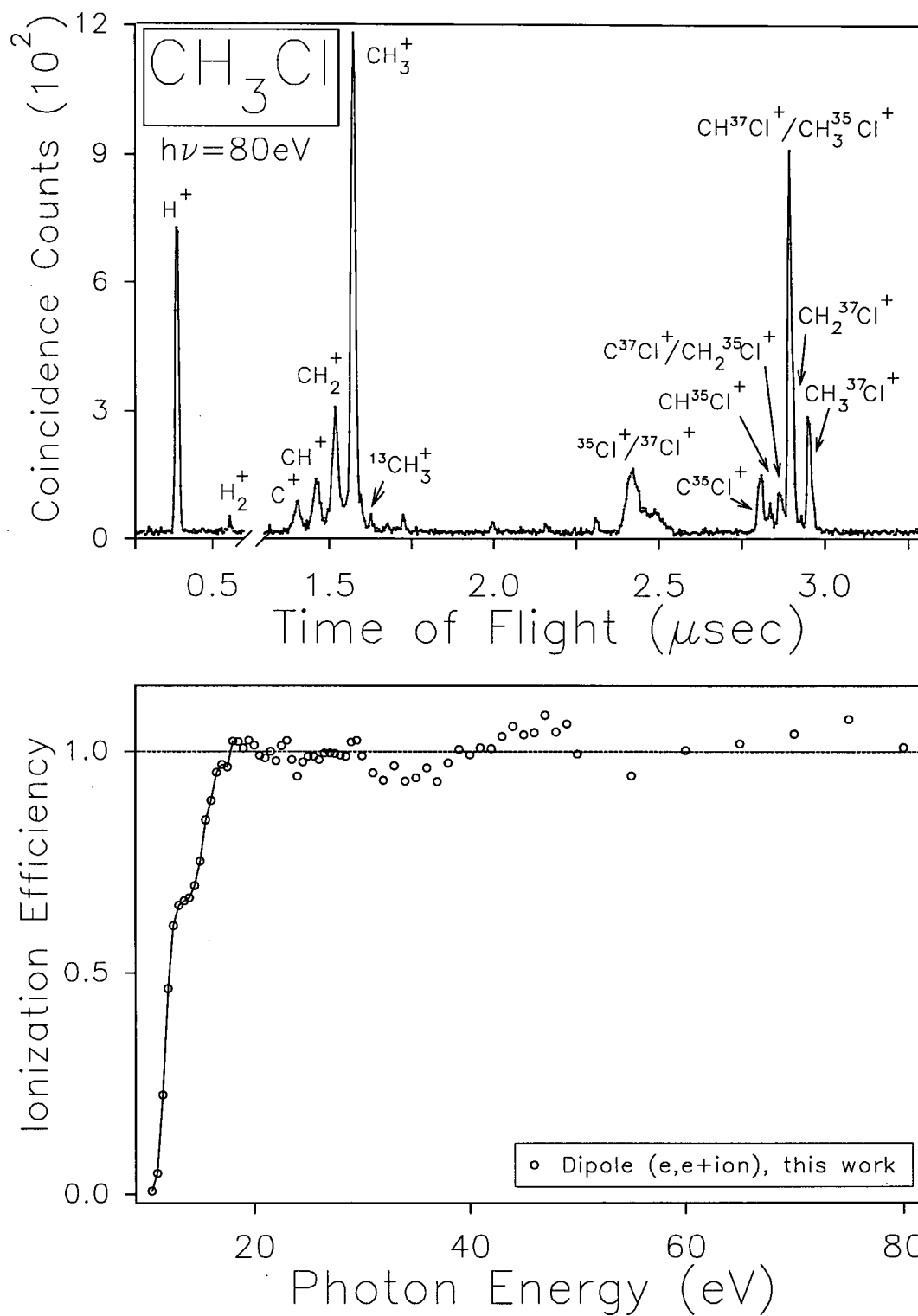


Figure 6.9: (a) TOF mass spectrum of  $\text{CH}_3\text{Cl}$  recorded at an equivalent photon energy of 80 eV. (b) The photoionization efficiency of methyl chloride from 11 to 80 eV.

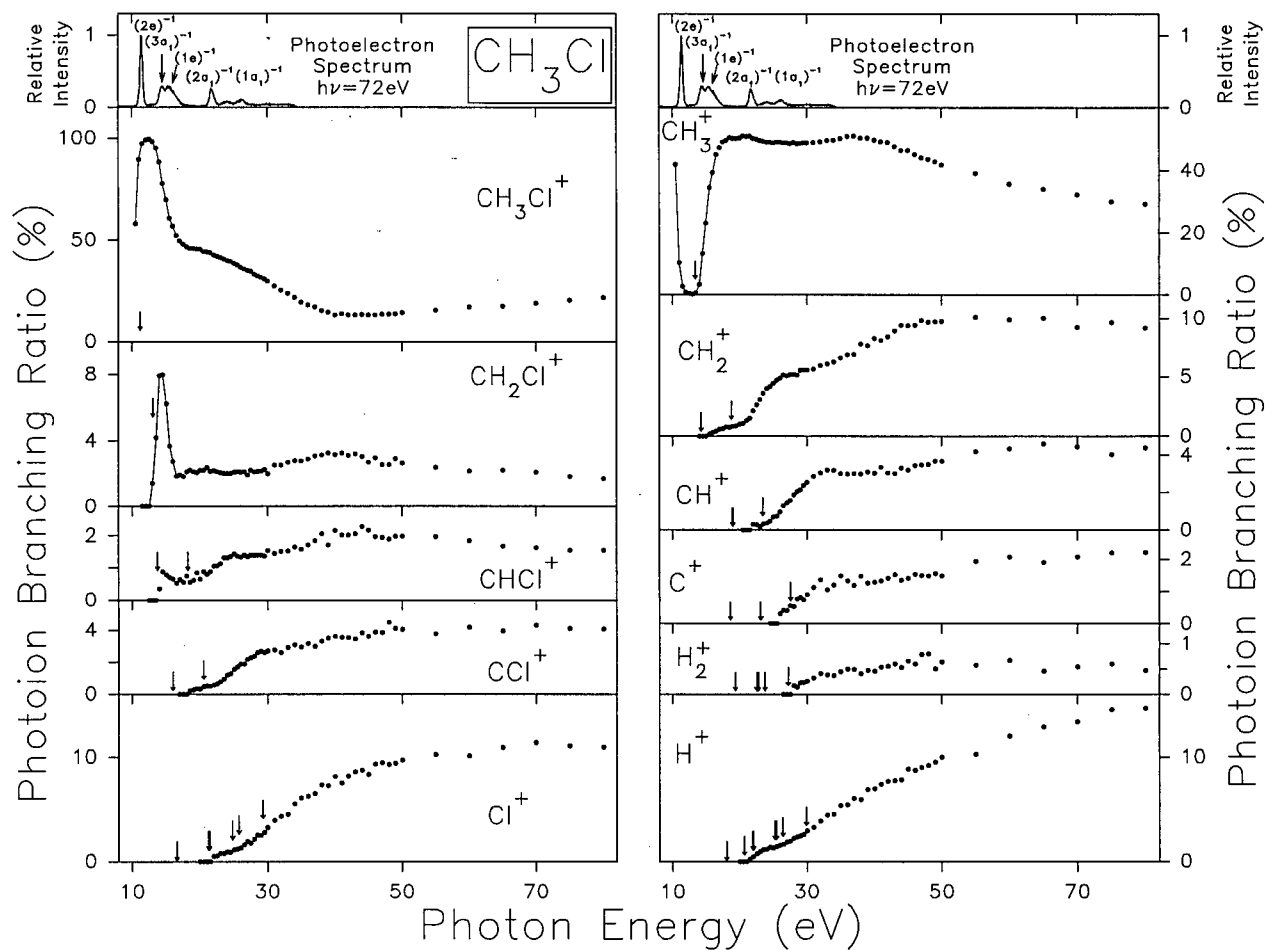


Figure 6.10: Branching ratios for the molecular and dissociative photoionization of  $\text{CH}_3\text{Cl}$ . Vertical arrows represent the calculated thermodynamic appearance potentials [317] of the ions from  $\text{CH}_3\text{Cl}$  (see table 6.5). Top panels show the photoelectron spectrum recorded in the present work at  $h\nu = 72 \text{ eV}$  (from figure 6.8(a)).

ionization efficiency, and the branching ratio for each ion as a function of photon energy. These absolute partial photoionization oscillator strengths are shown in figure 6.11 and are given numerically in table 6.4. Figures 6.10 and 6.11 show that the major ions formed in the 3 eV energy region above the ionization threshold of the  $(2e)^{-1}$  state are  $\text{CH}_3\text{Cl}^+$  and  $\text{CH}_2\text{Cl}^+$ . A small amount of  $\text{CH}_3^+$  was also observed in the region just above the first IP. The  $\text{CH}_3^+$  ion appears weakly from below 10.5 to 14 eV, then increases strongly in intensity above 14 eV which corresponds to the ionization potential of the  $(3a_1)^{-1}$  state. The  $\text{CH}_3\text{Cl}^+$  and  $\text{CH}_3^+$  ions are the predominant ions observed at energies between 17 and 50 eV. At photon energies below 50 eV the ions  $\text{CH}_3\text{Cl}^+$ ,  $\text{CH}_2\text{Cl}^+$ , and  $\text{CH}_3^+$  account for most of the ions produced; in fact at 21 eV these three ions account for 98 % of all ionization processes. This is supported by the mass spectra reported by Eland *et al.* [288]: these were the only ions observed by photoionization using He I radiation (21.21 eV). However, the reported intensity ratios [288] of 1.00 : 0.06 : 0.38 for  $\text{CH}_3\text{Cl}^+:\text{CH}_2\text{Cl}^+:\text{CH}_3^+$  are significantly different from those (1.00 : 0.06 : 1.15) found in the present work at 21 eV. This suggests that the mass spectrometer used by Eland *et al.* [288] suffers from serious mass discrimination problems for ions of lower  $m/e$ . The  $\text{Cl}^+$ ,  $\text{CH}_2^+$ , and  $\text{H}^+$  ion branching ratios gradually increase over the energy region from 20 to 80 eV, each contributing at least 10% to the total photoionization oscillator strength in the 50 to 80 eV energy region. The ions  $\text{CHCl}^+$ ,  $\text{CCl}^+$ ,  $\text{CH}^+$ ,  $\text{C}^+$ , and  $\text{H}_2^+$  are all minor products, each contributing less than 5% to the total photoionization oscillator strength, even at the highest energies studied.

The presently measured appearance potentials for the ions formed from the molecular and dissociative photoionization of  $\text{CH}_3\text{Cl}$  are shown in table 6.5 compared with calculated and previously published experimental appearance potentials. Calculated appearance potentials for all possible fragmentation pathways leading to singly charged cations from  $\text{CH}_3\text{Cl}$  are shown as vertical arrows in figure 6.10. These appearance potentials were calculated from thermodynamic heats of formation [317] assuming zero kinetic energy of fragmentation, so the



actual thresholds may be higher. Previously published appearance potentials were obtained by electron impact [296–299, 301] and photoionization [302, 315] techniques. The presently measured values agree well in all cases with the limited number of previously published appearance potentials (within the present experimental uncertainty of  $\pm 1$  eV) with the exception of  $\text{Cl}^+$ . Although  $\text{Cl}^+$  was reported to appear at 16.6 eV by Branson [296] and by Tsuda [298] no  $\text{Cl}^+$  can be observed in the present mass spectra until 22 eV.

Table 6.4: Absolute partial differential oscillator strengths for the molecular and dissociative photoionization of CH<sub>3</sub>Cl from 11 to 80 eV.

Photon Energy eV	Differential Oscillator Strength ( $df/dE$ 10 <sup>-2</sup> eV <sup>-1</sup> ) <sup>a</sup>											Ionization Efficiency <sup>b</sup> $\eta_i$
	CH <sub>3</sub> Cl <sup>+</sup>	CH <sub>2</sub> Cl <sup>+</sup>	CHCl <sup>+</sup>	CCl <sup>+</sup>	Cl <sup>+</sup>	CH <sub>3</sub> <sup>+</sup>	CH <sub>2</sub> <sup>+</sup>	CH <sup>+</sup>	C <sup>+</sup>	H <sub>2</sub> <sup>+</sup>	H <sup>+</sup>	
11.0	1.87					0.22						0.05
11.5	11.43					0.31						0.22
12.0	24.31					0.22						0.46
12.5	31.85	0.00				0.18						0.59
13.0	35.98	0.52				0.09						0.64
13.5	38.32	1.68	0.00			0.25						0.64
14.0	38.81	3.48	0.16			1.47						0.65
14.5	37.41	3.84	0.43			6.48						0.68
15.0	37.07	3.31	0.42			12.35	0.00					0.74
15.5	36.80	2.22	0.42			20.90	0.12					0.84
16.0	37.03	1.79	0.42			25.57	0.22					0.88
16.5	35.95	1.27	0.36			31.06	0.32					0.95
17.0	35.00	1.35	0.45			33.29	0.43					0.97
17.5	33.09	1.27	0.38			33.85	0.44					0.96
18.0	31.33	1.42	0.50	0.00		33.25	0.51					1.00 <sup>b</sup>
18.5	30.40	1.47	0.37	0.14		33.48	0.49					
19.0	30.28	1.40	0.41	0.17		33.12	0.57					
19.5	28.99	1.31	0.54	0.22		31.93	0.56					
20.0	28.08	1.36	0.40	0.19		31.05	0.63					
20.5	25.66	1.28	0.51	0.28		29.47	0.63					

Table 6.4: (continued) Absolute partial differential oscillator strengths for the molecular and dissociative photoionization of CH<sub>3</sub>Cl from 11 to 80 eV.

Photon Energy eV	Differential Oscillator Strength ( $df/dE$ $10^{-2}eV^{-1}$ ) <sup>a</sup>											Ionization Efficiency <sup>b</sup> $\eta_i$
	CH <sub>3</sub> Cl <sup>+</sup>	CH <sub>2</sub> Cl <sup>+</sup>	CHCl <sup>+</sup>	CCl <sup>+</sup>	Cl <sup>+</sup>	CH <sub>3</sub> <sup>+</sup>	CH <sub>2</sub> <sup>+</sup>	CH <sup>+</sup>	C <sup>+</sup>	H <sub>2</sub> <sup>+</sup>	H <sup>+</sup>	
21.0	24.40	1.31	0.44	0.29		28.07	0.73					0.00
21.5	23.25	1.14	0.47	0.26	0.00	27.01	0.81	0.00				0.12
22.0	21.76	1.12	0.54	0.29	0.27	25.68	1.10	0.15				0.25
22.5	20.40	1.02	0.52	0.32	0.26	24.22	1.29	0.13				0.38
23.0	19.18	0.96	0.52	0.36	0.38	22.94	1.43	0.08				0.44
23.5	17.96	0.89	0.58	0.42	0.35	21.78	1.59	0.14				0.51
24.0	17.50	0.89	0.58	0.52	0.41	21.46	1.75	0.16				0.53
24.5	15.75	0.81	0.54	0.51	0.36	19.61	1.67	0.19				0.54
25.0	14.54	0.79	0.54	0.58	0.44	18.37	1.68	0.26				0.49
25.5	13.63	0.76	0.50	0.61	0.44	17.73	1.71	0.27	0.00			0.53
26.0	12.53	0.72	0.46	0.64	0.44	16.76	1.67	0.34	0.11			0.54
26.5	11.44	0.68	0.45	0.60	0.52	15.64	1.65	0.41	0.14			0.52
27.0	10.70	0.59	0.41	0.67	0.59	14.97	1.57	0.45	0.13			0.57
27.5	9.93	0.64	0.40	0.66	0.51	13.97	1.49	0.46	0.16	0.00		0.56
28.0	8.99	0.58	0.38	0.65	0.59	13.31	1.43	0.51	0.15	0.05		0.61
28.5	8.36	0.56	0.36	0.67	0.66	12.59	1.34	0.53	0.20	0.04		0.61
29.0	7.47	0.52	0.34	0.64	0.59	11.61	1.32	0.51	0.20	0.05		0.59
29.5	7.08	0.52	0.31	0.60	0.64	11.23	1.29	0.55	0.17	0.06		0.59
30.0	5.99	0.41	0.31	0.55	0.66	9.95	1.14	0.52	0.18	0.05		0.60

Table 6.4: (continued) Absolute partial differential oscillator strengths for the molecular and dissociative photoionization of CH<sub>3</sub>Cl from 11 to 80 eV.

Photon Energy eV	Differential Oscillator Strength ( $df/dE$ 10 <sup>-2</sup> eV <sup>-1</sup> ) <sup>a</sup>											Ionization Efficiency <sup>b</sup> $\eta_i$
	CH <sub>3</sub> Cl <sup>+</sup>	CH <sub>2</sub> Cl <sup>+</sup>	CHCl <sup>+</sup>	CCl <sup>+</sup>	Cl <sup>+</sup>	CH <sub>3</sub> <sup>+</sup>	CH <sub>2</sub> <sup>+</sup>	CH <sup>+</sup>	C <sup>+</sup>	H <sub>2</sub> <sup>+</sup>	H <sup>+</sup>	
31.0	4.84	0.45	0.26	0.49	0.71	8.73	1.01	0.51	0.20	0.06	0.58	
32.0	3.89	0.39	0.23	0.40	0.67	7.57	0.92	0.47	0.21	0.06	0.59	
33.0	3.22	0.37	0.21	0.40	0.62	6.79	0.84	0.44	0.14	0.05	0.61	
34.0	2.53	0.33	0.19	0.36	0.65	5.80	0.74	0.37	0.14	0.04	0.53	
35.0	1.99	0.29	0.16	0.30	0.63	5.16	0.68	0.31	0.15	0.05	0.55	
36.0	1.62	0.26	0.16	0.29	0.57	4.61	0.63	0.27	0.12	0.05	0.50	
37.0	1.39	0.26	0.15	0.25	0.54	4.20	0.57	0.25	0.10	0.04	0.50	
38.0	1.13	0.23	0.15	0.25	0.55	3.73	0.58	0.22	0.11	0.03	0.44	
39.0	0.98	0.22	0.12	0.24	0.49	3.40	0.52	0.21	0.09	0.03	0.47	
40.0	0.81	0.19	0.13	0.22	0.50	3.05	0.51	0.19	0.08	0.03	0.43	
41.0	0.78	0.19	0.12	0.20	0.43	2.81	0.47	0.19	0.08	0.03	0.43	
42.0	0.70	0.17	0.11	0.19	0.44	2.60	0.45	0.16	0.08	0.03	0.41	
43.0	0.65	0.16	0.10	0.17	0.42	2.35	0.44	0.15	0.08	0.03	0.38	
44.0	0.61	0.14	0.10	0.18	0.40	2.14	0.43	0.15	0.06	0.02	0.36	
45.0	0.58	0.12	0.10	0.16	0.37	2.05	0.41	0.14	0.06	0.03	0.39	
46.0	0.54	0.12	0.08	0.16	0.39	1.87	0.39	0.14	0.06	0.02	0.36	
47.0	0.53	0.10	0.08	0.15	0.37	1.74	0.39	0.14	0.06	0.03	0.36	
48.0	0.52	0.10	0.07	0.17	0.36	1.69	0.38	0.14	0.06	0.03	0.36	
49.0	0.50	0.11	0.07	0.15	0.34	1.56	0.36	0.13	0.06	0.02	0.35	
50.0	0.50	0.09	0.07	0.14	0.34	1.45	0.34	0.13	0.05	0.02	0.35	

Table 6.4: (continued) Absolute partial differential oscillator strengths for the molecular and dissociative photoionization of CH<sub>3</sub>Cl from 11 to 80 eV.

Photon Energy eV	Differential Oscillator Strength ( $df/dE$ $10^{-2}eV^{-1}$ ) <sup>a</sup>											Ionization Efficiency <sup>b</sup> $\eta_i$
	CH <sub>3</sub> Cl <sup>+</sup>	CH <sub>2</sub> Cl <sup>+</sup>	CHCl <sup>+</sup>	CCl <sup>+</sup>	Cl <sup>+</sup>	CH <sub>3</sub> <sup>+</sup>	CH <sub>2</sub> <sup>+</sup>	CH <sup>+</sup>	C <sup>+</sup>	H <sub>2</sub> <sup>+</sup>	H <sup>+</sup>	
55.0	0.46	0.07	0.06	0.11	0.30	1.16	0.30	0.12	0.06	0.02	0.31	
60.0	0.42	0.05	0.05	0.10	0.25	0.88	0.24	0.11	0.05	0.02	0.29	
65.0	0.39	0.05	0.04	0.09	0.24	0.76	0.22	0.10	0.04	0.01	0.29	
70.0	0.36	0.04	0.03	0.08	0.22	0.63	0.18	0.09	0.04	0.01	0.26	
75.0	0.34	0.03	0.03	0.07	0.19	0.50	0.16	0.07	0.04	0.01	0.24	
80.0	0.35	0.03	0.02	0.07	0.18	0.47	0.15	0.07	0.04	0.01	0.23	

<sup>a</sup> $\sigma(\text{Mb})=109.75 df/dE$  ( $eV^{-1}$ ).

<sup>b</sup>The photoionization efficiency is normalized to unity above 18 eV (see text for details).



Table 6.5: (continued) Calculated and measured appearance potentials for the production of positive ions from CH<sub>3</sub>Cl.

Process	Appearance Potential (eV)							
	Calc- ulated <sup>a</sup>	Experimental						
		This work <sup>b</sup>	[296]	[297]	[298]	[299]	[301]	[302]
(27) H <sub>2</sub> <sup>+</sup> + CH + Cl	23.71							
(28) H <sub>2</sub> <sup>+</sup> + Cl + C + H	27.22	28						
(29) H <sup>+</sup> + CH <sub>2</sub> Cl	18.05							
(30) H <sup>+</sup> + CCl + H <sub>2</sub>	20.69							
(31) H <sup>+</sup> + HCl + CH	21.92	21.5						
(32) H <sup>+</sup> + CH <sub>2</sub> + Cl	22.01							
(33) H <sup>+</sup> + CHCl + H	22.04							
(34) H <sup>+</sup> + CCl + 2H	25.20							
(35) H <sup>+</sup> + Cl + C + H <sub>2</sub>	25.39							
(36) H <sup>+</sup> + HCl + C + H	25.44							
(37) H <sup>+</sup> + Cl + CH + H	26.40							
(38) H <sup>+</sup> + Cl + C + 2H	29.91							

<sup>a</sup>Values calculated using thermodynamic data for the enthalpy of formation of ions and neutrals (taken from [317]) assuming zero kinetic energy of fragmentation.

<sup>b</sup>±1 eV.

### 6.3.3 Dipole-induced breakdown

The major ions formed by the photoionization of  $\text{CH}_3\text{Cl}$  below 20 eV are  $\text{CH}_3\text{Cl}^+$ ,  $\text{CH}_2\text{Cl}^+$ , and  $\text{CH}_3^+$ . The  $\text{CH}_3\text{Cl}^+$  ion appears (see figure 6.11) as expected at the ionization threshold of the  $(2e)^{-1}$  state while the  $\text{CH}_2\text{Cl}^+$  and  $\text{CH}_3^+$  ions appear at slightly higher energies. The He I PEPICO data of Eland *et al.* [288] show clearly that the  $\text{CH}_3\text{Cl}^+$  ion is formed only from the  $(2e)^{-1}$  electronic state, while the  $\text{CH}_3^+$  ion is formed only from the  $(3a_1)^{-1}$  and  $(1e)^{-1}$  electronic ion states. The  $\text{CH}_2\text{Cl}^+$  ion appears at 13 eV, beyond the upper limit of the Franck-Condon region of the  $(2e)^{-1}$  state, and the POS curve for this ion shows a strong local maximum at 14.5 eV, suggesting that the  $\text{CH}_2\text{Cl}^+$  yield in this region comes from an excited state of  $\text{CH}_3\text{Cl}$  (associated with a higher ionization limit) which autoionizes down to the  $(2e)^{-1}$  state. The  $\text{CH}_3^+$  ion is first observed at 10.5 eV, which is the lower energy limit of the present measurements and located below the VIP of the  $(2e)^{-1}$  band (see table 5.1 on page 112). This initial formation of  $\text{CH}_3^+$  is from ion pair formation,  $\text{CH}_3\text{Cl} \rightarrow \text{CH}_3^+ + \text{Cl}^-$ , which has been reported earlier by several authors [298, 301, 315] to begin at about 10 eV. A second  $\text{CH}_3^+$  onset, which is much larger, occurs at about 14.0 eV and corresponds to the ionization energy of the  $(3a_1)^{-1}$  state. The  $(3a_1)^{-1}$  and  $(1e)^{-1}$  states are significantly overlapped in the photoelectron spectrum because of their large natural band-widths. When this is considered, along with the 1 eV fwhm resolution of the present dipole (e,e+ion) technique, it is necessary that the  $(3a_1)^{-1}$  and  $(1e)^{-1}$  states are treated together as the sum  $(3a_1+1e)^{-1}$ . The POS curve of the  $\text{CH}_3^+$  ion can be used to represent the shapes of the combined  $(3a_1+1e)^{-1}$  electronic ion state POS curve because it shows no obvious higher thresholds corresponding to higher ionic states. This is consistent with the PEPICO data [288], which indicate that the  $\text{CH}_3^+$  ion is produced solely from dissociative photoionization of the  $(3a_1)^{-1}$  and  $(1e)^{-1}$  states. The electronic ion state POS shapes for the  $(2e)^{-1}$  and  $(3a_1+1e)^{-1}$  states obtained from the  $\text{CH}_3\text{Cl}^+$  and  $\text{CH}_3^+$  ion POSs, respectively,

as described above, have been used to assess their contributions to the POSs for  $\text{CH}_3\text{Cl}^+$ ,  $\text{CH}_2\text{Cl}^+$ ,  $\text{CHCl}^+$ ,  $\text{CH}_3^+$ , and  $\text{CH}_2^+$  as shown on figure 6.11.

The  $\text{CH}_2^+$  ion has a low energy contribution from the  $(3a_1+1e)^{-1}$  ion states (which from its appearance potential of 15.5 eV indicates this is most likely to be from the  $(1e)^{-1}$  state, i.e. the  $\text{CH}_3$  system [54, 94, 294, 323]), but most of the intensity for this ion comes from a higher threshold corresponding to the IP of the  $(2a_1)^{-1}$  ion state. The  $\text{CH}_2^+$  ion yield has therefore been used to estimate the shape of the  $(2a_1)^{-1}$  POS curve by subtracting the small contribution from the lower lying  $(3a_1+1e)^{-1}$  ion states from it. The appearance potentials of the  $\text{C}^+$  and  $\text{H}_2^+$  ions, at 26.0 and 28.0 eV respectively, correspond to regions where strong poles from the  $(1a_1)^{-1}$  electronic ion state exist (see section 6.3.1 and ref. [323]). These thresholds are well above the Franck-Condon regions of the other electronic ion states, so the  $\text{C}^+$  and  $\text{H}_2^+$  ions must be formed from ionization processes corresponding to production of the various many-body states of the  $(1a_1)^{-1}$  process. Therefore, the shape of the  $(1a_1)^{-1}$  POS was estimated from the sum of the  $\text{C}^+$  and  $\text{H}_2^+$  POSs, since they show similar shapes and have thresholds consistent with onsets of the  $(1a_1)^{-1}$  many-body ion states observed in the photoelectron spectrum (see figure 6.8 and section 6.3.1).

The contributions from the various electronic states to the other ions were estimated as follows: In addition to the strong resonance in the  $\text{CH}_2\text{Cl}^+$  POS from dissociative autoionization to the  $(2e)^{-1}$  state, the  $\text{CH}_2\text{Cl}^+$  ion has two higher onsets, which are most clearly observed in the branching ratio curve (see figure 6.10). The first occurs in the region of the  $(3a_1+1e)^{-1}$  ion states at  $\sim 13$  eV with the process being hydrogen loss to produce  $\text{CH}_2\text{Cl}^+$ . This intensity most likely comes from the  $(1e)^{-1}$  state which involves ionization of the  $\text{CH}_3$  system. The second rather weak onset at  $\sim 30$  eV comes from the  $(1a_1)^{-1}$  ion state manifold (see figure 6.8). The  $\text{CHCl}^+$  ion has a low first appearance potential in the region of the  $(3a_1+1e)^{-1}$  ion states, plus a higher onset in the region of the  $(1a_1)^{-1}$  ion state. The  $\text{CCl}^+$  ion first appears at 18.5 eV, which is well above the  $(3a_1+1e)^{-1}$  ion state Franck-Condon

region, so the lower energy process leading to this ion probably comes from autoionization of excited neutral states down to the  $(3a_1+1e)^{-1}$  ion states. Higher contributions from the  $(2a_1)^{-1}$  and  $(1a_1)^{-1}$  ion states are also observed corresponding to further onsets at about  $\sim 21$  and  $\sim 30$  eV in the  $\text{CCl}^+$  POS curve (see figure 6.11). The appearance potentials of the  $\text{Cl}^+$  and  $\text{CH}^+$  ions are both around 22 eV, which corresponds to a region where several many-body states of the  $(2a_1)^{-1}$  and  $(1a_1)^{-1}$  electronic ion states exist as discussed in section 6.3.1. For the  $(2a_1)^{-1}$  ion state, a strong pole at 21.6 eV and a weaker one at 23.8 eV have been predicted by Green's Function calculations [94, 269]. This weaker pole accounts for about 25% of the intensity in the 23 to 25 eV region, while the pole from the  $(1a_1)^{-1}$  ion state in this region accounts for the remaining 75% of the intensity. The main pole of the  $(1a_1)^{-1}$  ion state occurs at 26.1 eV (see figure 6.8). Many small  $(1a_1)^{-1}$  poles are found above this region. Only small contributions to the  $\text{Cl}^+$  and  $\text{CH}^+$  ions arise from the  $(2a_1)^{-1}$  state. The main contributions to these ions, seen as onsets at about 25 eV in the ion POS curves (see figure 6.11), come from the  $(1a_1)^{-1}$  state. The appearance potential of the  $\text{H}^+$  ion is 21.5 eV, which is close to the adiabatic ionization potential of the  $(2a_1)^{-1}$  state. Therefore, part of the  $\text{H}^+$  ion intensity comes from the  $(2a_1)^{-1}$  electronic ion state. The remainder of the  $\text{H}^+$  ion is produced from the  $(1a_1)^{-1}$  state, as indicated by the higher onset in the  $\text{H}^+$  POS curve in the 28 to 30 eV region (see figure 6.11).

The electronic ion state POSs of the  $(2e)^{-1}$ ,  $(3a_1)^{-1}$ ,  $(1e)^{-1}$ ,  $(2a_1)^{-1}$ , and  $(1a_1)^{-1}$  states of  $\text{CH}_3\text{Cl}^+$  have been estimated by summing their contributions to the molecular and dissociative ion POSs (as shown in figure 6.11). These estimates, shown in figure 6.12 and listed in table 6.6, can be compared with the electronic state POSs obtained from photoelectron branching ratios made using tunable photon energy photoelectron spectroscopy (see section 6.3.4 below). In making this comparison it should be remembered that the estimates of the electronic ion state POSs are based upon the partitioning shown in figure 6.11 and the other information involved in this process. However, these estimates are considered more

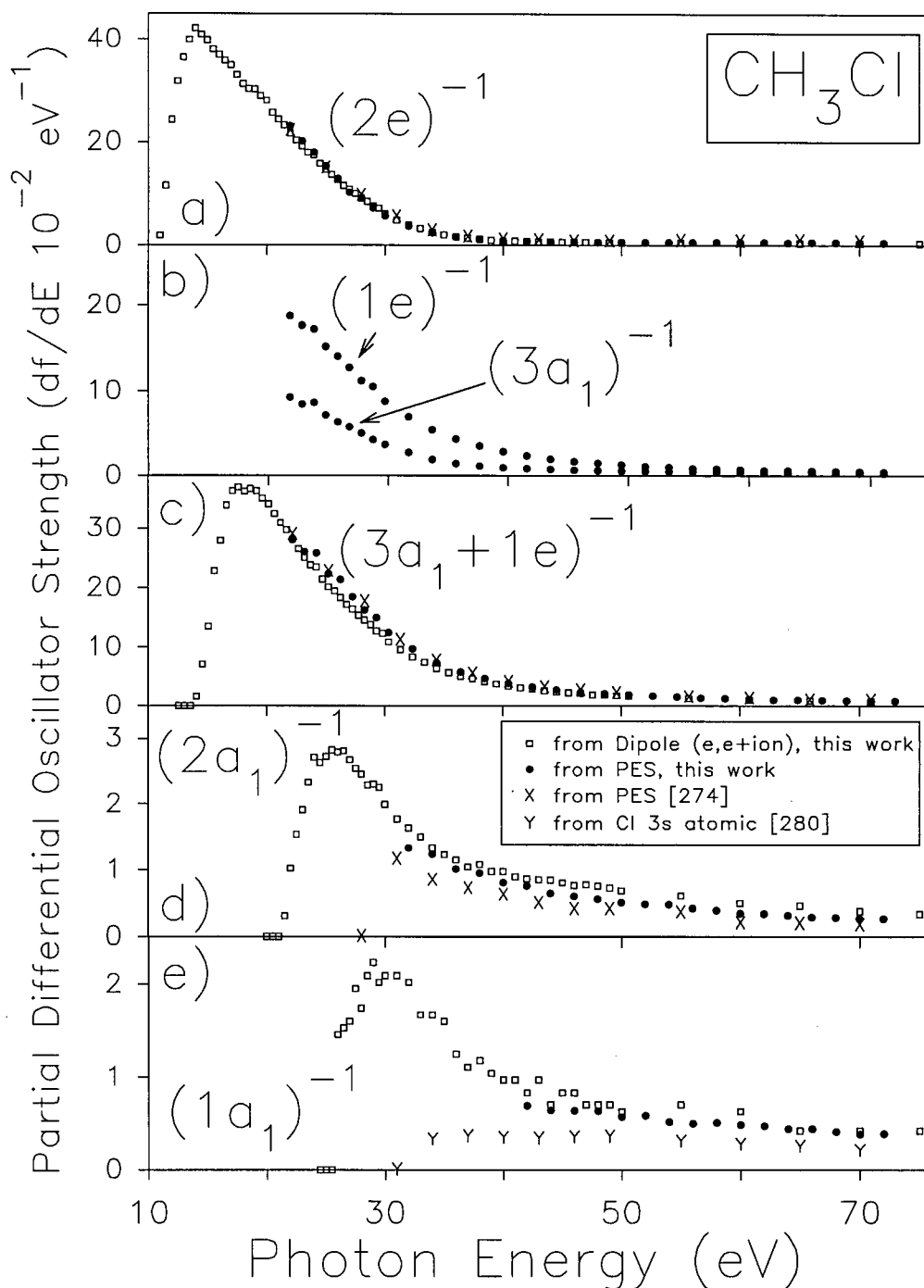


Figure 6.12: Absolute partial photoionization oscillator strengths for production of electronic states of  $\text{CH}_3\text{Cl}^+$ . Open squares show the estimates from appropriate linear combinations of the present molecular and dissociative photoionization POSs of  $\text{CH}_3\text{Cl}$  and the dipole-induced breakdown scheme (see section 6.3.3). Filled circles represent estimates from photoelectron binding energy spectra recorded in the present work using tunable synchrotron radiation (see section 6.3.4). The crosses are the previously published electronic state partial photoionization oscillator strengths of Novak *et al.* [274], renormalized using the presently reported photoabsorption data (see text in section 6.3.4 for details).

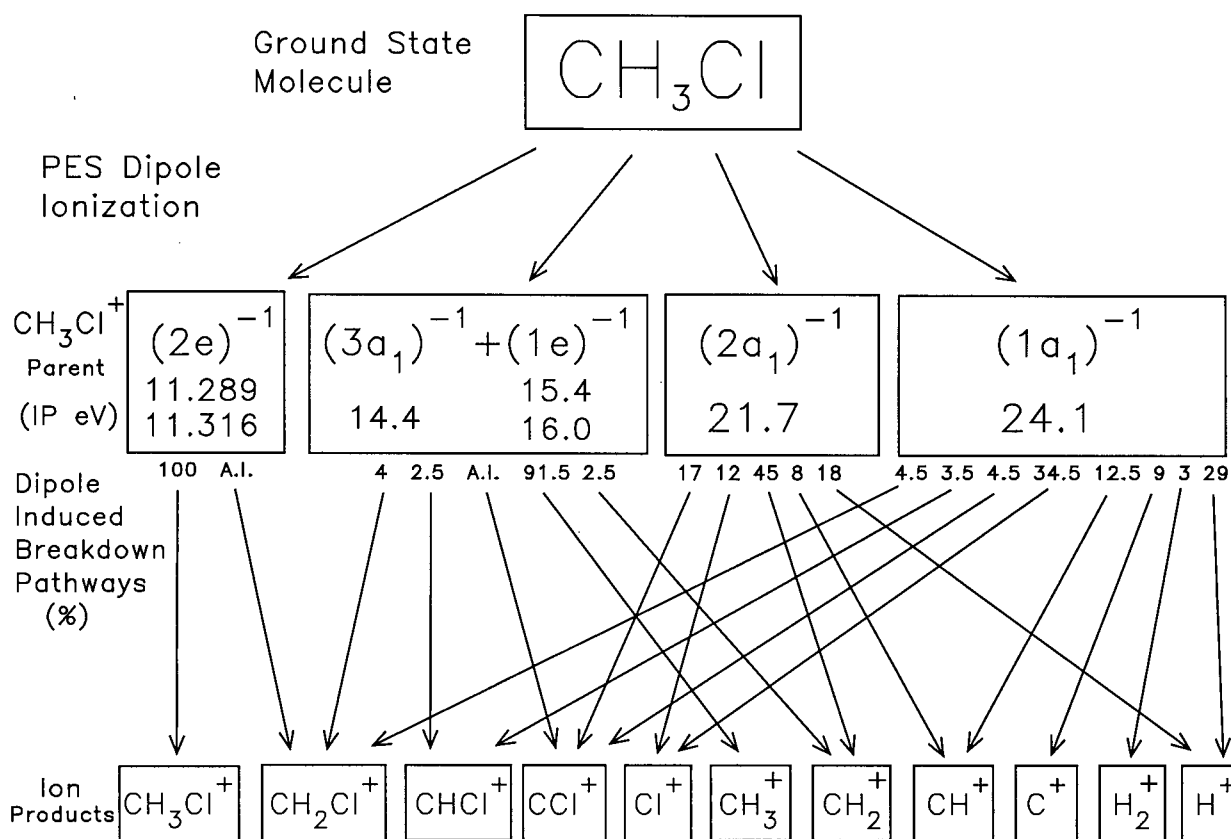


Figure 6.13: Proposed dipole-induced breakdown scheme for the ionic photofragmentation of CH<sub>3</sub>Cl above  $h\nu = 50$  eV. A.I.=autoionization.

accurate than those obtained from the photoelectron spectra, since the processing and interpretation of the latter is complicated by the factors discussed in section 6.2.3 above. In particular the photon energy region in the first 5 to 10 eV above each ionization threshold is particularly subject to errors because of the rising non-spectral PES background (figure 6.7) and uncertainties in the transmission correction factor in this region. Cumulative errors in successive threshold regions can give rise to significant errors in the branching ratios (and thus the individual POSs) over extended energy regions.

The dipole-induced breakdown scheme for CH<sub>3</sub>Cl above 50 eV suggested by the above analysis is summarized in figure 6.13.

Table 6.6: Absolute partial differential oscillator strengths for production of electronic states<sup>a</sup> of CH<sub>3</sub>Cl<sup>+</sup>.

Photon Energy eV	Partial Differential Oscillator Strength $df/dE$ ( $10^{-2}eV^{-1}$ ) <sup>b</sup>				Photon Energy eV	Partial Differential Oscillator Strength $df/dE$ ( $10^{-2}eV^{-1}$ ) <sup>b</sup>			
	$(2e)^{-1}$	$(3a_1+1e)^{-1}$	$(2a_1)^{-1}$	$(1a_1)^{-1}$		$(2e)^{-1}$	$(3a_1+1e)^{-1}$	$(2a_1)^{-1}$	$(1a_1)^{-1}$
11.0	1.87				27.5	9.93	15.27	2.54	1.95
11.5	11.43				28.0	8.99	14.55	2.45	1.74
12.0	24.31				28.5	8.36	13.76	2.29	2.09
12.5	31.85				29.0	7.47	12.69	2.30	2.23
13.0	36.50				29.5	7.08	12.27	2.25	2.02
13.5	40.00	0			30.0	5.99	10.87	1.99	2.09
14.0	42.23	1.61			31.0	4.84	9.54	1.77	2.09
14.5	40.97	7.08			32.0	3.89	8.27	1.63	2.02
15.0	39.85	13.50			33.0	3.22	7.42	1.49	1.67
15.5	38.12	22.84			34.0	2.53	6.34	1.33	1.67
16.0	37.03	27.95			35.0	1.99	5.64	1.23	1.60
16.5	35.95	33.95			36.0	1.62	5.04	1.15	1.25
17.0	35.00	36.39			37.0	1.39	4.59	1.04	1.11
17.5	33.09	37.00			38.0	1.13	4.08	1.08	1.18
18.0	31.33	36.34			39.0	0.98	3.72	0.97	1.04
18.5	30.40	36.73			40.0	0.81	3.33	0.97	0.97
19.0	30.28	36.37			41.0	0.78	3.07	0.89	0.97
19.5	28.99	35.12			42.0	0.70	2.84	0.86	0.83
20.0	28.08	34.13			43.0	0.65	2.57	0.85	0.97
20.5	25.66	32.49			44.0	0.61	2.34	0.84	0.70
21.0	24.40	30.97	0		45.0	0.58	2.24	0.80	0.83
21.5	23.25	29.73	0.30		46.0	0.54	2.04	0.76	0.83
22.0	21.76	28.18	1.02		47.0	0.53	1.90	0.77	0.70
22.5	20.40	26.53	1.53		48.0	0.52	1.85	0.75	0.70
23.0	19.18	25.07	1.91		49.0	0.50	1.70	0.72	0.70
23.5	17.96	23.80	2.33		50.0	0.50	1.59	0.68	0.63
24.0	17.50	23.46	2.71		55.0	0.46	1.27	0.60	0.70
24.5	15.75	21.43	2.63		60.0	0.42	0.96	0.49	0.63
25.0	14.54	20.08	2.72		65.0	0.39	0.83	0.45	0.42
25.5	13.63	19.38	2.82	0	70.0	0.36	0.69	0.37	0.42
26.0	12.53	18.32	2.79	1.46	75.0	0.34	0.55	0.33	0.42
26.5	11.44	17.09	2.81	1.53	80.0	0.35	0.51	0.31	0.42
27.0	10.70	16.36	2.67	1.60					

<sup>a</sup>Estimates obtained from a consideration of the partial oscillator strengths for the molecular and dissociative photoionization of CH<sub>3</sub>Cl using the dipole induced breakdown scheme derived in section 6.3.3. See text for details (section 6.3.3) and comparison with synchrotron radiation PES measurements (section 6.3.4).

<sup>b</sup> $\sigma$ (Mb)=109.75  $df/dE$  ( $eV^{-1}$ ).

### 6.3.4 Photoelectron spectroscopy

Information about the valence shell photoionization processes of  $\text{CH}_3\text{Cl}$  have also been obtained in the present work using photoelectron spectroscopy with monochromated synchrotron radiation over the photon energy range 21 to 72 eV. Typical photoelectron spectrum recorded at 72 eV photon energy has already been shown in figure 6.8(a). The binding energy scales of the photoelectron spectra were calibrated using the same procedure outlined in section 6.2.4 for  $\text{CH}_3\text{F}$ . The inner valence photoelectron bands of  $\text{CH}_3\text{Cl}$  are split by many-body effects into several states. These effects have been discussed in section 6.3.1. It was determined that the  $(2a_1)^{-1}$  band is not significantly split, but is mostly localized in one main band at 21.6 eV, with only a small amount of intensity in the 22 to 24 eV binding energy region. In contrast the  $(1a_1)^{-1}$  band is split into many states of low intensity which are spread out over the 22 to 35 eV energy region, with the main band being centered at 26.1 eV and smaller bands contributing much of the intensity between 22 to 24 eV. Reasonable predictions of these effects are given by many-body Green's function calculations [94, 269]. Note that the intensity ascribed to the many-body states in the photoelectron spectrum can be subject to appreciable errors from uncertainties in the background and transmission functions. This effects both the branching ratios and the POSs.

The branching ratios for the production of the electronic ion states of methyl chloride were obtained by integrating the peak area for each electronic ion state in the transmission corrected, background subtracted, photoelectron spectra. Problems associated with the quantitative determination of electronic ion state branching ratios, namely the non-spectral background at low kinetic energies and complications due to the splitting of states by many-body effects, have been discussed above in sections 2.4, 2.5.4 and 6.2.4.

In the present work the shape and intensity of the  $(1a_1)^{-1}$  photoelectron band was determined at high photon energy (72 eV, see figure 6.8) where the background is relatively flat

and therefore could be estimated for all binding energies of interest. The resulting shape of the  $(1a_1)^{-1}$  binding energy profile at  $h\nu = 72$  eV was used to differentiate the  $(1a_1)^{-1}$  band from the rising non-spectral low kinetic energy background at the lower photon energies. Additional intensity from  $(1a_1)^{-1}$  many-body states has been reported at binding energies above 34 eV in EMS experiments [94, 323] and this appeared to continue weakly even above 45 eV. The small contribution from this intensity above 34 eV, higher in binding energy than the present measurements, was unaccounted for in the present work.

The photoelectron branching ratios for the  $(2e)^{-1}$ ,  $(3a_1)^{-1}$ ,  $(1e)^{-1}$ ,  $(2a_1)^{-1}$ , and  $(1a_1)^{-1}$  electronic ion states of  $\text{CH}_3\text{Cl}$  resulting from the considerations described above were obtained at each photon energy by integrating the photoelectron peaks for each state in the transmission corrected, background subtracted photoelectron spectra and normalizing the sum of all states to 100%. The kinetic energy resolution was sufficient to resolve all states in the photoelectron spectra with the exception of the  $(3a_1)^{-1}$  and the spin-orbit split  $(1e)^{-1}$  states, which are partially overlapped. The photoelectron bands of these ion states were fit with three gaussians, fixed to their estimated vertical ionization potentials, and the fitted gaussian peak areas were used to determine the individual areas for both the  $(3a_1)^{-1}$  and  $(1e)^{-1}$  ion states. Thus, this intensity is reported both as the sum of the  $(3a_1+1e)^{-1}$  states and as an estimate of the separate components of the two states (see figure 6.12(b)).

Absolute partial photoionization oscillator strengths for production of the electronic states of  $\text{CH}_3\text{Cl}^+$  were obtained from the triple product of the absolute photoabsorption oscillator strength (from dipole (e,e) measurements, see section 5.4.1, the absolute photoionization efficiency, and the photoelectron branching ratio for each electronic ion state as a function photon energy. The absolute electronic state partial photoionization oscillator strengths so derived are shown as solid circles in figure 6.12, in comparison with the estimates (open squares) obtained from the molecular and dissociative photoionization breakdown scheme derived above (section 6.3.3). The electronic state partial photoionization

cross-sections reported by Novak *et al.* [274] (which were not corrected for electron analyser kinetic energy effects) were originally placed on an absolute scale using the photoabsorption data reported by Wu *et al.* [237]. To provide a meaningful comparison with the present work, their [237] branching ratios were renormalized to the photoabsorption data measured in the present work (see section 6.2.4 for full details). The contributions from the  $(1a_1)^{-1}$  state were not measured by Novak *et al.* [274], but instead were estimated from the Cl 3s atomic cross-sections calculated by Yeh and Lindau [280], which are shown in figure 6.12(e). It can be seen from figures 6.12(a) and (c) that there is quite good agreement between the present work and the “renormalized” results of Novak *et al.* [274] for the  $(2e)^{-1}$  and the  $(3a_1+1e)^{-1}$  partial oscillator strengths. However, figure 6.12(d) shows that there are substantial differences between the intensities of the  $(2a_1)^{-1}$  state measured in the present work and those reported by Novak *et al.* [274]. These differences are in part because Novak *et al.* [274] neglected any contribution from  $(2a_1)^{-1}$  intensity at higher energies than the main  $(2a_1)^{-1}$  band at 21.6 eV. There are also significant differences between intensities of the presently reported  $(1a_1)^{-1}$  state POSs and the atomic Cl 3s partial cross sections of Yeh and Lindau [280], which were used as an approximation for the  $(1a_1)^{-1}$  partial cross-sections by Novak *et al.* [274]. Note that the underestimation of the  $(1a_1)^{-1}$  POSs obtained by using the Cl 3s atomic data will result in a corresponding slight overestimate in all the other POSs in the work of Novak *et al.* [274].

The agreement between the electronic ion state POSs measured directly in the present work using synchrotron radiation and the estimates derived from the POSs for the molecular and dissociative photoionization of  $\text{CH}_3\text{Cl}$  via the dipole-induced breakdown scheme (see section 6.3.3), as shown in figure 6.12, is generally quite good for all states except the  $(2a_1)^{-1}$  state above 45 eV. This may be a result of an underestimation of the contributions from the higher energy peaks of the  $(2a_1)^{-1}$  state which occur at energies higher than 22 eV, in the region of the  $(1a_1)^{-1}$  many-body states. There are also some discrepancies below 45 eV

for the  $(1a_1)^{-1}$  POSs and corresponding minor discrepancies for the  $(2e)^{-1}$ ,  $(3a_1+1e)^{-1}$ , and  $(2a_1)^{-1}$  POSs. The errors that can cause these discrepancies, which include difficulties in assessing the rising PES background at lower photon energies, have been discussed above in section 6.2.4. Errors near the  $(2a_1)^{-1}$  threshold also result in small errors in the 21 to 30 eV region of the  $(2e)^{-1}$  and  $(3a_1+1e)^{-1}$  POSs. Likewise, errors near the  $(3a_1+1e)^{-1}$  threshold result in small errors will occur in the 21 to 25 eV region of the  $(2e)^{-1}$  POSs. For these reasons the present direct synchrotron radiation electronic state photoionization POS measurements are only considered to be reasonably accurate for the lower intensity  $(2a_1)^{-1}$  and  $(1a_1)^{-1}$  states above 45 eV. For the  $(2e)^{-1}$  and  $(3a_1+1e)^{-1}$  states, the PES results agree with the molecular and dissociative photoionization estimates to better than 10% over the whole energy range studied.

## 6.4 Methyl Bromide Results and Discussion

### 6.4.1 Binding energy spectrum

The PE spectrum of  $\text{CH}_3\text{Br}$  is shown at a photon energy of 70 eV in figure 6.14(a) in comparison with a similar range of calculations as used for  $\text{CH}_3\text{F}$  (section 6.2.1) and  $\text{CH}_3\text{Cl}$  (section 6.3.1). The same general details given in section 6.2.1 for figure 6.1 also apply to the various respective presentations on figure 6.14. The three Green's function calculations for  $\text{CH}_3\text{Br}$  are:

(i) The OV/TDA calculations of von Niessen *et al.* [269] using the ADC(3) method and a  $[14s11p5d/9s5p/4s]/(9s6p2d/4s2p/2s)$  basis set. See figure 6.14(b).

(ii) The OV/ext-TDA calculations of Minchinton *et al.* [95] using the ADC(4) method and the same basis set as in (i). See figure 6.14(c).

(iii) The OV/ext-TDA-pol calculation of Minchinton *et al.* [95] which uses the ADC(4) method and a  $[14s11p7d/9s5p1d/4s]/(9s6p4d/4s2p1d/2s)$  basis set with polarization func-

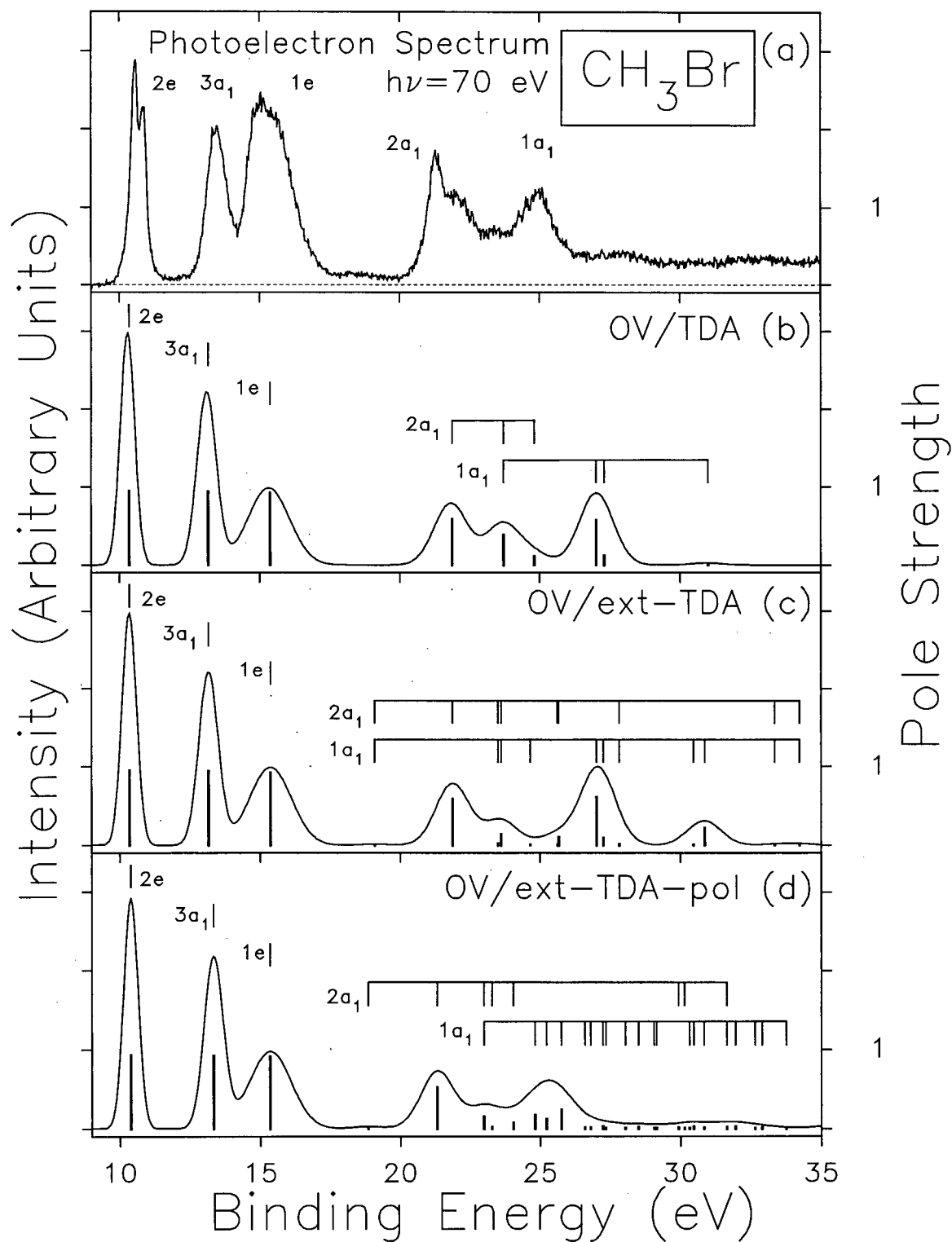


Figure 6.14: The photoelectron spectrum of  $\text{CH}_3\text{Br}$  at a photon energy of 70 eV (a) compared with pole-strength calculations and synthetic spectra (b), (c), and (d) generated from Green's function calculations using the OV/TDA [269], OV/ext-TDA [95], and OV/ext-TDA-pol [95] approximations respectively—see text for details.

tions on the C and Br atoms. See figure 6.14(d).

As in the cases of  $\text{CH}_3\text{F}$  and  $\text{CH}_3\text{Cl}$  the energies of the three outer valence ionization processes are all well predicted by the three OVGf calculations. The pole strengths for the three processes are predicted to be close to unity and are therefore well described by the independent particle model. In the  $(2a_1)^{-1}$  and  $(1a_1)^{-1}$  inner valence region, however, there are a number of major structures indicating breakdown of the independent particle model due to significant electron correlation and relaxation effects in the ionization processes. Peaks are observed in the PE spectrum at  $\sim 21.3, 22.1, 23.6, 24.9,$  and  $27.8$  eV and broad structure exists at higher energies. All three calculations again predict the general shape of the observed structure quite well. The ext-TDA-pol treatment gives the best overall description of both the energies and pole strength distribution. The ext-TDA calculation seriously overestimates the pole at 30.87 eV [95]. The ext-TDA-pol calculation suggests that the measured peak at 21.3 eV is overwhelmingly from the  $(2a_1)^{-1}$  process with a predicted pole strength of 0.52 with only 4 % of this peak intensity being from  $(1a_1)^{-1}$ . The second feature observed as a shoulder at 22.1 eV has contributions from both processes but is predicted to be mainly a result of  $(2a_1)^{-1}$  ionization. The smaller third peak at 23.6 eV can be identified as predominantly  $(2a_1)^{-1}$  in origin while the larger fourth peak at 24.9 eV is predicted to contain 71 % (ext-TDA) or 65 % (ext-TDA-pol) of the  $(1a_1)^{-1}$  pole strength. The calculations indicate that the vast majority of the structure above 26 eV is from the  $(1a_1)^{-1}$  process and this, as well as the other conclusions for the inner valence region, is consistent with the conclusions reached from a consideration of the EMS binding energy spectra and momentum distribution measurements for  $\text{CH}_3\text{Br}$  [95].

### 6.4.2 Molecular and dissociative photoionization

Information about the molecular and dissociative photoionization processes in  $\text{CH}_3\text{Br}$  in the valence region from the first ionization potential up to 79 eV was obtained in the present work using dipole (e,e+ion) spectroscopy. Figure 6.15(a) shows the TOF mass spectrum obtained at an equivalent photon energy of 71 eV. The positive ions observed were:  $\text{H}^+$ ,  $\text{H}_2^+$ ,  $\text{H}_3^+$ ,  $\text{CH}_n^+$ ,  $\text{Br}^+$ ,  $\text{Br}^{2+}$  and  $\text{CH}_n\text{Br}^+$  where  $n = 0$  to 3. The broadness of the  $\text{Br}^+$  peak is indicative of considerable excess kinetic energy of fragmentation. The only double charged ion observed was  $\text{Br}^{2+}$ , no stable doubly charged molecular ions were detected. Thus, it is concluded that any double ionization events taking place result in either two positively charged fragments or in  $\text{Br}^{2+}$ , plus other associated neutral fragments, within the time scale of this experiment.

The branching ratio for each molecular and dissociative photoion of  $\text{CH}_3\text{Br}$ , determined as the percentage of the total photoionization from integration of the background subtracted TOF peaks, are shown in figure 6.16. The corresponding numerical values can be calculated from the data given in table 6.7 by dividing the partial photoionization oscillator strength for a particular ion at a particular energy by the sum of all of the ion partial oscillator strengths at that energy. The mass resolution was not sufficient to completely resolve the individual  $\text{CH}_n\text{Br}^+$  ions in the TOF mass spectra, thus this region was least squares fitted using six gaussian peak profiles, corresponding to individual mass units from 91 ( $\text{C}^{79}\text{Br}^+$ ) to 96 ( $\text{CH}_3^{81}\text{Br}^+$ ) amu. From this procedure the TOF peak areas for the individual  $\text{CH}_n\text{Br}^+$  ions were determined at each energy and their branching ratios were calculated. The peak fit of the  $\text{CH}_n\text{Br}^+$  region of the TOF mass spectrum recorded at 71 eV is shown in the inset to figure 6.15(a).

The ionization efficiency curve for  $\text{CH}_3\text{Br}$  is shown in figure 6.15(b). The data are given numerically in table 6.7. Relative photoionization efficiency values were determined from

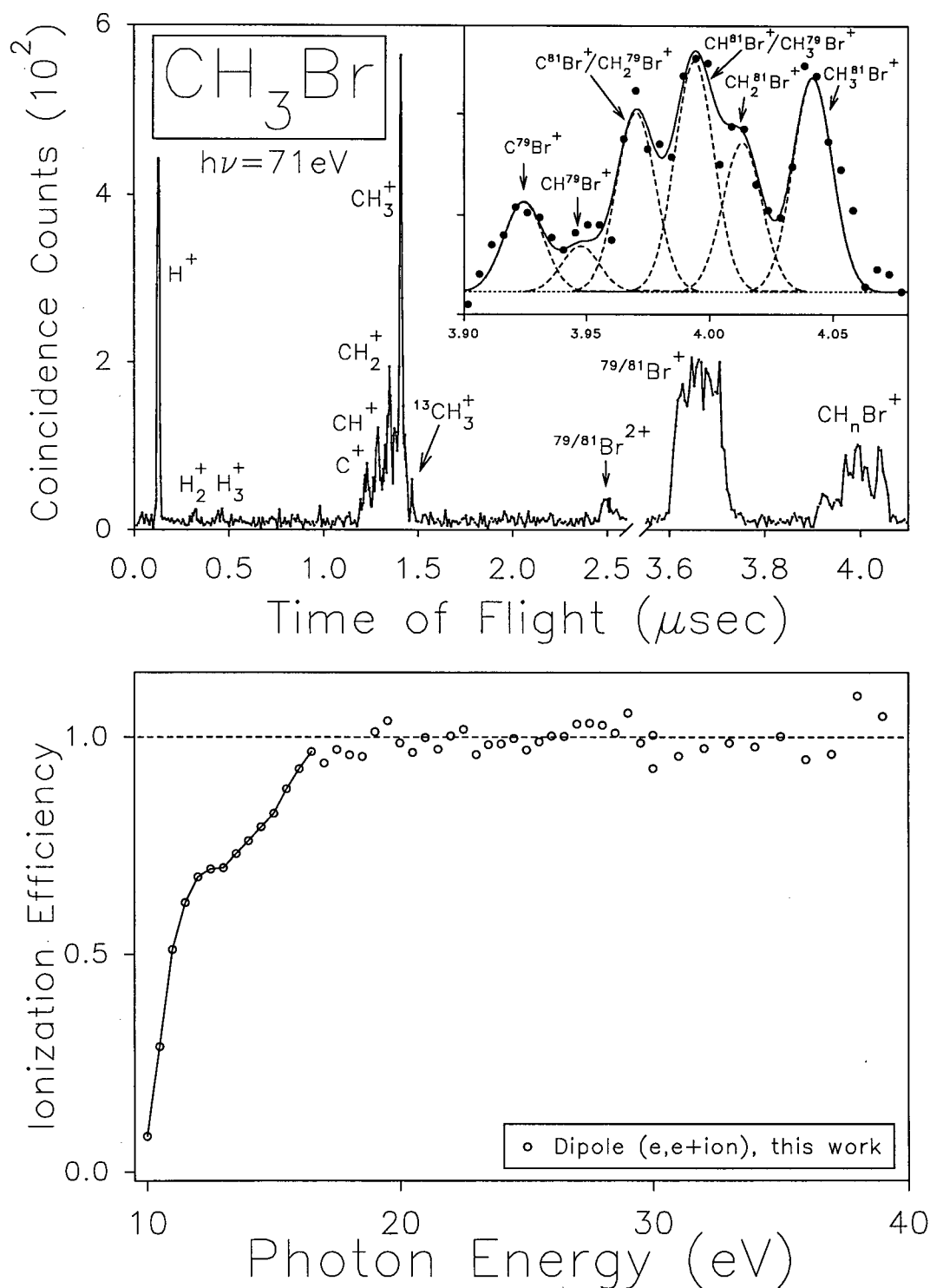


Figure 6.15: (a) TOF mass spectrum of  $\text{CH}_3\text{Br}$  recorded at an equivalent photon energy of 71 eV. The inset to (a) shows an expanded view of the TOF mass spectrum in the region of the  $\text{CH}_n\text{Br}^+$  ions. The individual mass peaks and the total fit to the experimental data are shown as the dashed and solid lines, respectively. (b) The photoionization efficiency of methyl bromide from 10 to 40 eV.

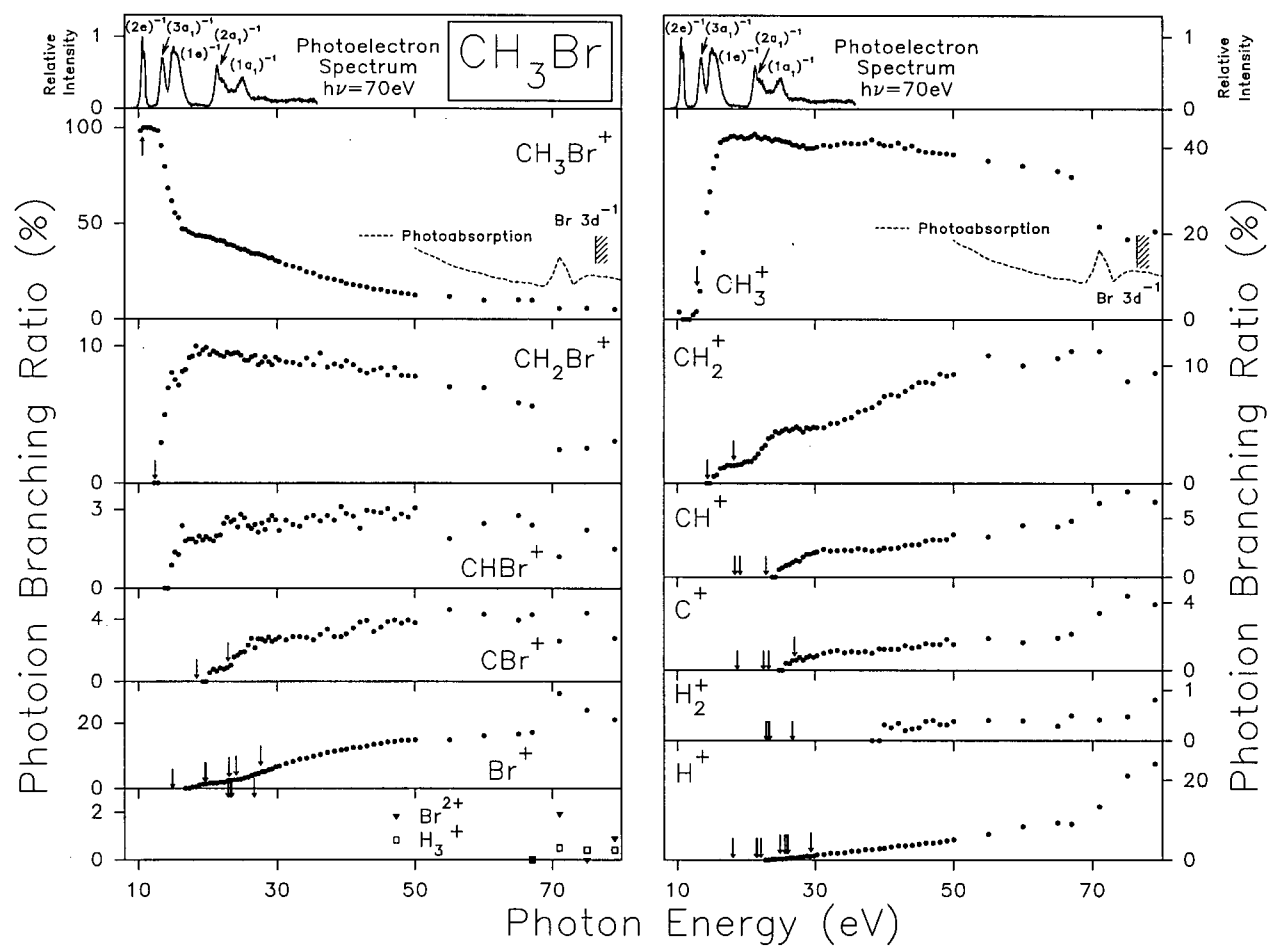


Figure 6.16: Branching ratios for the molecular and dissociative photoionization of  $\text{CH}_3\text{Br}$ . Vertical arrows represent the calculated thermodynamic appearance potentials [317] of the ions from  $\text{CH}_3\text{Br}$  (see table 6.8). Top panels show the photoelectron spectrum recorded in the present work at  $h\nu = 70 \text{ eV}$  (see figure 6.14(a)).

the TOF mass spectra by taking the ratio of the total number of electron-ion coincidences to the total number of forward scattered electrons as a function of energy loss. Making the reasonable assumption that the absolute photoionization efficiency is unity at higher photon energies we conclude that  $\eta_i$  is 1 above 19.25 eV.

Absolute partial photoionization oscillator strengths for the production of molecular and dissociative ions were obtained from the triple product of the absolute photoabsorption oscillator strength (from dipole (e,e) measurements, see section 5.5.1), the absolute photoionization efficiency, and the branching ratio for each ion as a function of photon energy. These absolute partial photoionization oscillator strengths are shown in figure 6.17 and are given numerically in table 6.7. Figures 6.16 and 6.17 show that the only ions formed in the 3 eV energy region above the ionization threshold of the  $(2e)^{-1}$  state are  $\text{CH}_3\text{Br}^+$  and  $\text{CH}_3^+$ . The  $\text{CH}_3^+$  ion appears weakly in intensity at  $\sim 10.25$ , then appears again much more strongly above 12.75 eV, just below the vertical ionization potential for the  $(3a_1)^{-1}$  state. Between 13 and 20 eV the  $\text{CH}_2\text{Br}^+$ ,  $\text{CHBr}^+$ ,  $\text{Br}^+$  and  $\text{CH}_2^+$  ions appear. At energies between 20 and 50 eV the predominant ions are  $\text{CH}_3\text{Br}^+$ ,  $\text{CH}_2\text{Br}^+$  and  $\text{CH}_3^+$ . At 21.25 eV these three ions account for 84% of all ionization processes. This is in agreement with the photoionization mass spectrum recorded using HeI radiation (21.21 eV) by Eland *et al.* [288], where these three ions and  $\text{Br}^+$  were the only ions observed. However, the intensity ratios reported by Eland *et al.* [288] were 1.00 : 0.35 : 0.02 : 0.38 for  $\text{CH}_3\text{Br}^+:\text{CH}_2\text{Br}^+:\text{Br}^+:\text{CH}_3^+$  which are significantly different from those (1.00 : 0.23 : 0.04 : 1.05) found in the present work at 21 eV. This same discrepancy was also observed in the measurements of  $\text{CH}_3\text{F}$  and  $\text{CH}_3\text{Cl}$  which supports the conclusion that the mass spectrometer used by Eland *et al.* [288] suffers from serious mass discrimination for ions of lower  $m/e$ . The  $\text{CH}^+$ ,  $\text{C}^+$  and  $\text{H}^+$  ions appear between 24 to 26.5 eV and their branching ratios increase steadily over the energy region from 27 to 70 eV. A small amount of  $\text{H}_2^+$  appears above 40 eV. At 50 eV the major ion formed is  $\text{CH}_3^+$ , with a branching ratio of 38.6%, and the  $\text{CH}_3\text{Br}^+$ ,  $\text{CH}_2\text{Br}^+$ ,  $\text{Br}^+$  and  $\text{CH}_2^+$

ions are also formed in significant quantities, having branching ratios greater than 7% each. These trends continue up to 67 eV, just below the onset of the Br 3d discrete excitation region at 71 eV. This indicates that below the Br 3d excitation and ionization region the major breakdown pathways are direct ionization, C-Br bond breakage and H loss. The ions  $\text{CHBr}^+$ ,  $\text{CBr}^+$ ,  $\text{CH}^+$ ,  $\text{C}^+$ , and  $\text{H}_2^+$  are all minor products, each contributing less than 5% to the total photoionization oscillator strength below 71 eV.

Above 67 eV, in the Br 3d discrete excitation and ionization region of  $\text{CH}_3\text{Br}$ , a dramatic increase in the amount of fragmentation is observed, with larger amounts of the smallest fragments ions  $\text{Br}^+$ ,  $\text{CH}^+$ ,  $\text{C}^+$  and  $\text{H}^+$  being formed. This may be a result of autoionization, dissociative photoionization or Coulomb explosion of doubly charged ions (formed from Auger decay) in the Br 3d excitation and ionization region. Further discussion of these effects will be given in the following section on the dipole-induced breakdown of  $\text{CH}_3\text{Br}$ .

The presently measured appearance potentials for the ions formed from the molecular and dissociative photoionization of  $\text{CH}_3\text{Br}$  are given in table 6.8 where they are compared with both calculated and previously published experimental appearance potentials. Calculated appearance potentials for most fragmentation pathways leading to singly charged cations from  $\text{CH}_3\text{Br}$  are shown as vertical arrows in figure 6.16. Only the appearance potentials for pathways involving  $\text{CHBr}$  were not calculated because a heat of formation for this fragment was not available from the literature. The appearance potentials were calculated from thermodynamic heats of formation [317] assuming zero kinetic energy of fragmentation, so the actual thresholds may be higher. Previously published appearance potentials were obtained using electron impact [296-301] and photoionization [316] methods. The presently measured appearance potentials agree well in most cases with the limited number of previously published appearance potentials (within the present experimental uncertainty of  $\pm 1$  eV). The exceptions are the  $\text{Br}^+$  and  $\text{CH}^+$  ions which are found to appear at energies  $\sim 3.5$  eV higher in the present work than in previously reported electron impact measurements [296, 298].

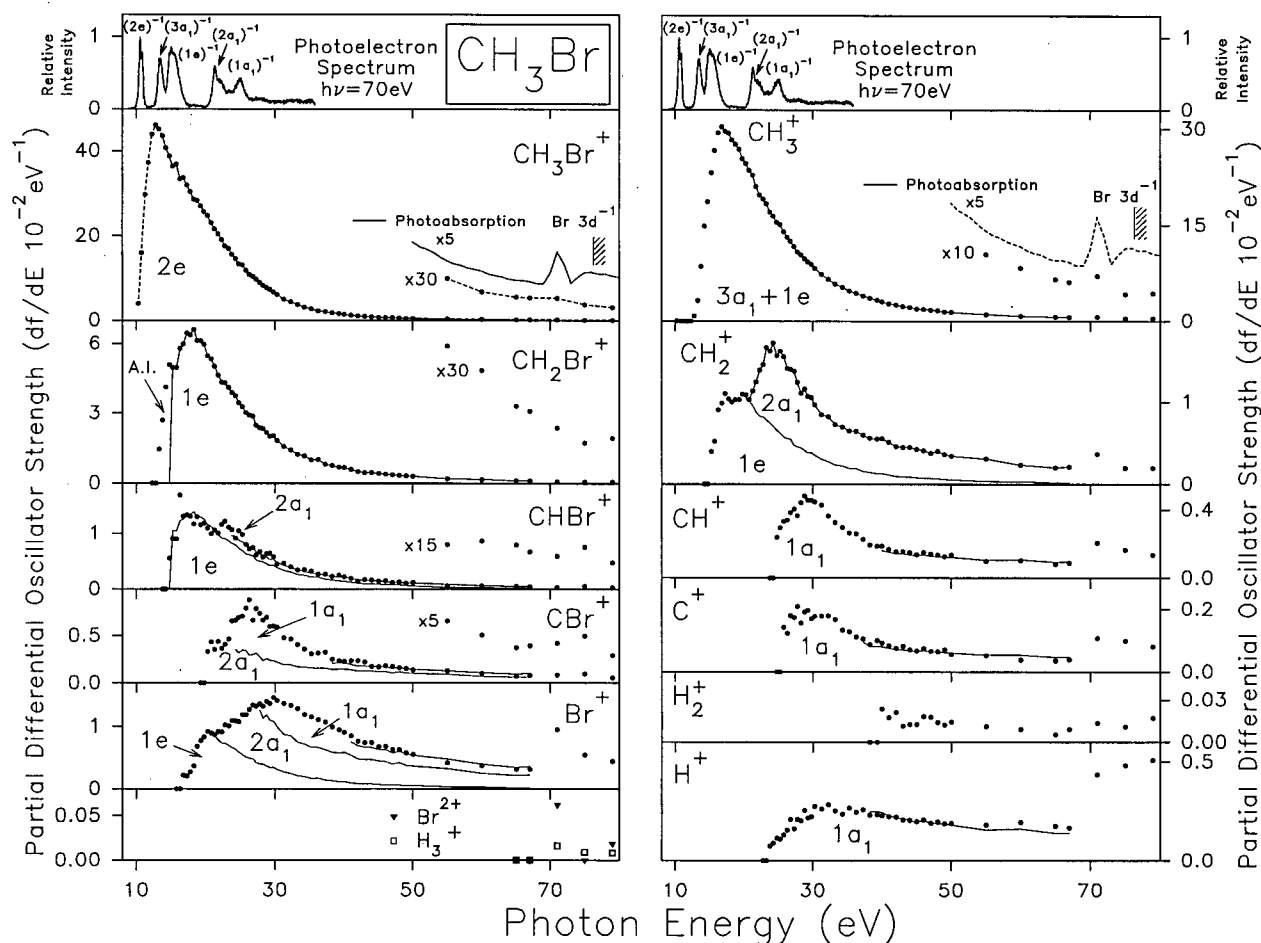


Figure 6.17: Absolute partial photoionization oscillator strengths for the molecular and dissociative photoionization of  $\text{CH}_3\text{Br}$ . Points represent the measured partial photoionization oscillator strengths for the molecular and dissociative photoionization. Lines show the sums and partial sums of the electronic state partial photoionization oscillator strength contributions derived from the proposed dipole-induced breakdown scheme (see text, section 6.4.3, for details). Vertical arrows represent calculated thermodynamic appearance potentials [317] of the ions from  $\text{CH}_3\text{Br}$  (see table 6.8). Top panels show the photoelectron spectrum recorded in the present work at  $h\nu = 70$  eV (see figure 6.14(a)).

A similar discrepancy was found in the photoionization of  $\text{CH}_3\text{Cl}$  (section 6.3.2) where the appearance potential of  $\text{Cl}^+$  was found to be 22 eV in the present work and 16.6 eV in electron impact measurements [296, 298]. This is possibly a result of an ionization channel available to the electron impact method which is dipole forbidden and thus is not observed in the dipole electron impact experiment.

Table 6.7: Absolute partial differential oscillator strengths for the molecular and dissociative photoionization of CH<sub>3</sub>Br from 10.25 to 79 eV.

Photon Energy eV	Differential Oscillator Strength ( $df/dE$ $10^{-2}\text{eV}^{-1}$ ) <sup>a</sup>													Ionization Efficiency <sup>b</sup>
	CH <sub>3</sub> Br <sup>+</sup>	CH <sub>2</sub> Br <sup>+</sup>	CHBr <sup>+</sup>	CBr <sup>+</sup>	Br <sup>+</sup>	Br <sup>2+</sup>	CH <sub>3</sub> <sup>+</sup>	CH <sub>2</sub> <sup>+</sup>	CH <sup>+</sup>	C <sup>+</sup>	H <sub>3</sub> <sup>+</sup>	H <sub>2</sub> <sup>+</sup>	H <sup>+</sup>	$\eta_i$
10.25	4.00						0.07							0.08
10.75	16.01						0.01							0.29
11.25	29.83						0							0.51
11.75	37.35						0							0.62
12.25	43.52						0.43							0.68
12.75	46.08	0					0.80							0.70
13.25	45.19	1.46					3.24							0.70
13.75	43.52	2.70					8.53							0.73
14.25	40.71	4.12	0				14.83							0.76
14.75	38.84	5.08	0.56				18.69	0						0.79
15.25	36.48	4.95	0.91				23.21	0.39						0.82
15.75	36.91	4.97	0.90				26.62	0.52						0.88
16.25	33.49	5.74	1.69				29.36	0.90						0.93
16.75	33.85	5.99	1.31				30.36	0.99						0.97
17.25	32.07	6.46	1.33		0		29.67	1.10						0.94
17.75	30.55	6.37	1.30		0.27		29.30	1.04						0.97
18.25	28.76	6.60	1.16		0.37		28.23	1.00						0.96
18.75	28.45	6.12	1.30		0.68		27.57	1.03						0.96
19.25	27.08	6.11	1.15		0.77		26.81	1.03						1.00 <sup>b</sup>
19.75	25.77	5.96	1.18	0	0.83		25.37	1.09						

Table 6.7: (continued) Absolute partial differential oscillator strengths for the molecular and dissociative photoionization of CH<sub>3</sub>Br from 10.25 to 79 eV.

Photon Energy eV	Differential Oscillator Strength ( $df/dE$ 10 <sup>-2</sup> eV <sup>-1</sup> ) <sup>a</sup>													Ionization Efficiency <sup>b</sup> $\eta_i$
	CH <sub>3</sub> Br <sup>+</sup>	CH <sub>2</sub> Br <sup>+</sup>	CHBr <sup>+</sup>	CBr <sup>+</sup>	Br <sup>+</sup>	Br <sup>2+</sup>	CH <sub>3</sub> <sup>+</sup>	CH <sub>2</sub> <sup>+</sup>	CH <sup>+</sup>	C <sup>+</sup>	H <sub>3</sub> <sup>+</sup>	H <sub>2</sub> <sup>+</sup>	H <sup>+</sup>	
20.25	24.86	5.47	1.09	0.33	0.91		24.62	1.08						
20.75	23.10	5.33	0.99	0.43	0.89		23.54	1.03						
21.25	21.64	5.01	1.06	0.35	0.87		22.83	1.13						
21.75	20.44	4.64	1.01	0.44	0.92		21.09	1.25						
22.25	19.07	4.34	1.16	0.37	0.91		19.77	1.39						
22.75	17.56	4.30	1.21	0.41	1.02		19.16	1.46						
23.25	16.96	4.11	1.11	0.46	1.01		18.42	1.66					0	
23.75	15.58	3.89	1.07	0.66	1.09		17.00	1.62					0.08	
24.25	14.55	3.74	0.91	0.66	1.09		16.47	1.72	0				0.09	
24.75	13.35	3.44	1.04	0.69	1.07		15.45	1.56	0.24				0.11	
25.25	13.17	3.27	0.97	0.70	1.19		15.09	1.62	0.29	0			0.11	
25.75	11.83	3.01	0.80	0.79	1.19		13.94	1.56	0.33	0.14			0.13	
26.25	10.85	2.92	0.72	0.88	1.27		13.07	1.41	0.34	0.12			0.16	
26.75	10.42	2.86	0.74	0.66	1.34		12.46	1.40	0.38	0.18			0.21	
27.25	9.75	2.48	0.61	0.79	1.32		11.67	1.37	0.40	0.17			0.16	
27.75	8.95	2.37	0.67	0.73	1.36		10.81	1.24	0.36	0.21			0.21	
28.25	8.32	2.34	0.57	0.66	1.32		10.30	1.10	0.44	0.15			0.20	
28.75	7.75	2.16	0.63	0.69	1.40		9.73	1.15	0.48	0.19			0.25	
29.25	7.37	1.99	0.64	0.59	1.37		9.23	1.06	0.45	0.20			0.22	
29.75	6.73	2.03	0.57	0.60	1.46		8.85	1.05	0.46	0.17			0.22	

Table 6.7: (continued) Absolute partial differential oscillator strengths for the molecular and dissociative photoionization of CH<sub>3</sub>Br from 10.25 to 79 eV.

Photon Energy eV	Differential Oscillator Strength ( $df/dE$ 10 <sup>-2</sup> eV <sup>-1</sup> ) <sup>a</sup>													Ionization Efficiency <sup>b</sup> $\eta_i$
	CH <sub>3</sub> Br <sup>+</sup>	CH <sub>2</sub> Br <sup>+</sup>	CHBr <sup>+</sup>	CBr <sup>+</sup>	Br <sup>+</sup>	Br <sup>2+</sup>	CH <sub>3</sub> <sup>+</sup>	CH <sub>2</sub> <sup>+</sup>	CH <sup>+</sup>	C <sup>+</sup>	H <sub>3</sub> <sup>+</sup>	H <sub>2</sub> <sup>+</sup>	H <sup>+</sup>	
30.25	6.10	1.83	0.45	0.58	1.41		8.23	0.96	0.44	0.18				0.27
31.25	5.03	1.58	0.46	0.48	1.37		7.28	0.84	0.43	0.18				0.26
32.25	4.44	1.43	0.39	0.47	1.34		6.57	0.82	0.36	0.18				0.28
33.25	3.74	1.23	0.34	0.41	1.28		5.81	0.72	0.32	0.17				0.25
34.25	3.14	1.17	0.34	0.36	1.19		5.28	0.69	0.30	0.13				0.23
35.25	2.75	1.00	0.32	0.31	1.15		4.76	0.65	0.26	0.13				0.27
36.25	2.30	1.00	0.27	0.32	1.10		4.33	0.64	0.26	0.11				0.24
37.25	2.03	0.81	0.27	0.32	1.07		3.98	0.60	0.23	0.11				0.26
38.25	1.77	0.75	0.22	0.25	0.99		3.63	0.56	0.19	0.09				0.23
39.25	1.56	0.68	0.25	0.23	0.95		3.30	0.55	0.18	0.10		0		0.23
40	1.37	0.67	0.21	0.23	0.90		3.05	0.55	0.19	0.09		0.02		0.23
41	1.20	0.59	0.19	0.23	0.85		2.75	0.51	0.17	0.08		0.02		0.22
42	1.04	0.50	0.14	0.23	0.77		2.53	0.46	0.15	0.08		0.02		0.22
43	0.93	0.46	0.17	0.22	0.74		2.27	0.44	0.15	0.08		0.01		0.21
44	0.84	0.45	0.16	0.17	0.74		2.20	0.44	0.15	0.07		0.01		0.20
45	0.75	0.41	0.14	0.17	0.67		1.94	0.42	0.14	0.07		0.01		0.20
46	0.67	0.38	0.14	0.18	0.68		1.87	0.41	0.15	0.07		0.02		0.21
47	0.61	0.37	0.12	0.17	0.63		1.72	0.37	0.14	0.07		0.02		0.19
48	0.59	0.34	0.12	0.16	0.63		1.66	0.40	0.14	0.06		0.01		0.19
49	0.52	0.31	0.10	0.15	0.58		1.51	0.36	0.13	0.07		0.01		0.19

Table 6.7: (continued) Absolute partial differential oscillator strengths for the molecular and dissociative photoionization of CH<sub>3</sub>Br from 10.25 to 79 eV.

Photon Energy eV	Differential Oscillator Strength ( $df/dE$ $10^{-2}eV^{-1}$ ) <sup>a</sup>													Ionization Efficiency <sup>b</sup> $\eta_i$
	CH <sub>3</sub> Br <sup>+</sup>	CH <sub>2</sub> Br <sup>+</sup>	CHBr <sup>+</sup>	CBr <sup>+</sup>	Br <sup>+</sup>	Br <sup>2+</sup>	CH <sub>3</sub> <sup>+</sup>	CH <sub>2</sub> <sup>+</sup>	CH <sup>+</sup>	C <sup>+</sup>	H <sub>3</sub> <sup>+</sup>	H <sub>2</sub> <sup>+</sup>	H <sup>+</sup>	
50	0.45	0.29	0.11	0.14	0.55		1.42	0.34	0.13	0.05		0.01	0.19	
55	0.33	0.20	0.05	0.13	0.42		1.04	0.31	0.10	0.05		0.01	0.18	
60	0.23	0.16	0.06	0.10	0.37		0.83	0.23	0.10	0.04		0.01	0.19	
65	0.19	0.11	0.05	0.07	0.31		0.65	0.20	0.08	0.04		0.01	0.18	
67	0.18	0.10	0.04	0.08	0.31	0	0.61	0.21	0.09	0.04	0	0.01	0.17	
71	0.18	0.08	0.04	0.08	0.95	0.06	0.70	0.37	0.20	0.11	0.02	0.01	0.44	
75	0.12	0.06	0.05	0.10	0.54	0.00	0.42	0.20	0.16	0.10	0.01	0.01	0.48	
79	0.10	0.06	0.03	0.06	0.44	0.02	0.43	0.20	0.13	0.08	0.01	0.02	0.51	

<sup>a</sup> $\sigma(\text{Mb})=109.75 df/dE$  ( $eV^{-1}$ ).

<sup>b</sup>The photoionization efficiency is normalized to unity above 19.25 eV (see text for details).

Table 6.8: Calculated and measured appearance potentials for the production of positive ions from CH<sub>3</sub>Br.

	Process	Appearance Potential (eV)								
		Calculated <sup>a</sup>	This work <sup>b</sup>	[297]	[298]	[299]	[296]	[300]	[301]	[316]
(1)	CH <sub>3</sub> Br <sup>+</sup>	10.54	10.75		10.5		10.5	10.528	10.56	10.54
(2)	CH <sub>2</sub> Br <sup>+</sup> + H	12.36	13.75			13.6				
(3)	CHBr <sup>+</sup> + H <sub>2</sub>		15.25							
(4)	CHBr <sup>+</sup> + 2H									
(5)	CBr <sup>++</sup> + H <sub>2</sub> + H	18.37	20.75							
(6)	CBr <sup>++</sup> + 3H	22.89								
(7)	Br <sup>+</sup> + CH <sub>3</sub>	14.88	18.25		14.7		15.0			
(8)	Br <sup>+</sup> + CH + H <sub>2</sub>	19.54								
(9)	Br <sup>+</sup> + CH <sub>2</sub> + H	19.67								
(10)	Br <sup>+</sup> + C + H <sub>2</sub> + H	23.05								
(11)	Br <sup>+</sup> + CH + 2H	24.06								
(12)	Br <sup>+</sup> + C + 3H	27.57								
(13)	Br <sup>2+</sup> + CH <sub>3</sub>		71							
(14)	CH <sub>3</sub> <sup>+</sup> + Br <sup>-</sup>	9.299	<10.25		10.7				9.60	
(15)	CH <sub>3</sub> <sup>+</sup> + Br	12.88	12.75	12.83	13.0		13.2			12.80
(16)	CH <sub>2</sub> <sup>+</sup> + HBr	14.39	15.75			14.9	15.0			
(17)	CH <sub>2</sub> <sup>+</sup> + Br + H	18.18				18.7				
(18)	CH <sup>+</sup> + Br + H <sub>2</sub>	18.37								
(19)	CH <sup>+</sup> + HBr + H	19.10								
(20)	CH <sup>+</sup> + Br + 2H	22.89	25.25				21.8			
(21)	C <sup>+</sup> + HBr + H <sub>2</sub>	18.71								
(22)	C <sup>+</sup> + Br + H <sub>2</sub> + H	22.50								
(23)	C <sup>+</sup> + HBr + 2H	23.23								
(24)	C <sup>+</sup> + Br + 3H	27.02	26.25				25.4			
(25)	H <sub>3</sub> <sup>+</sup> + CBr		71							

Table 6.8: (continued) Calculated and measured appearance potentials for the production of positive ions from CH<sub>3</sub>Br.

Process	Calc- ulated <sup>a</sup>	Appearance Potential (eV)							
		Experimental							
		This work <sup>b</sup>	[297]	[298]	[299]	[296]	[300]	[301]	[316]
(26) H <sub>2</sub> <sup>+</sup> + CHBr									
(27) H <sub>2</sub> <sup>+</sup> + HBr + C	22.87								
(28) H <sub>2</sub> <sup>+</sup> + CH + Br	23.15								
(29) H <sub>2</sub> <sup>+</sup> + CBr + H	23.37								
(30) H <sub>2</sub> <sup>+</sup> + Br + C + H	26.67	40							
(31) H <sup>+</sup> + CH <sub>2</sub> Br	18.06								
(32) H <sup>+</sup> + CH <sub>2</sub> + Br	21.45								
(33) H <sup>+</sup> + CBr + H <sub>2</sub>	21.54								
(34) H <sup>+</sup> + HBr + CH	22.05	24.25							
(35) H <sup>+</sup> + CHBr + H									
(36) H <sup>+</sup> + Br + C + H <sub>2</sub>	24.84								
(37) H <sup>+</sup> + HBr + C + H	25.57								
(38) H <sup>+</sup> + Br + CH + H	25.85								
(39) H <sup>+</sup> + CBr + 2H	26.06								
(40) H <sup>+</sup> + Br + C + 2H	29.36								

<sup>a</sup>Values calculated using thermodynamic data for the enthalpy of formation of ions and neutrals (taken from [317]) assuming zero kinetic energy of fragmentation.

<sup>b</sup>±1 eV.

### 6.4.3 Dipole-induced breakdown

The major ions formed by the photoionization of  $\text{CH}_3\text{Br}$  were  $\text{CH}_3\text{Br}^+$ ,  $\text{CH}_2\text{Br}^+$ , and  $\text{CH}_3^+$ . The  $\text{CH}_3\text{Br}^+$  ion appears (see figure 6.17) near the ionization threshold of the  $(2e)^{-1}$  state and the  $\text{CH}_3^+$  ion also appears weakly at energies near the  $(2e)^{-1}$  VIP (see table 5.1 on page 112). However, the HeI PEPICO data of Eland *et al.* [288] clearly show that  $\text{CH}_3\text{Br}^+$  is the only ion formed from the  $(2e)^{-1}$  electronic state. The  $\text{CH}_3\text{Br}^+$  POS (figure 6.17) curve does not show any higher energy onsets which indicates that it is formed only from the  $(2e)^{-1}$  state. Thus, the  $\text{CH}_3\text{Br}^+$  POS curve is equal to the entire  $(2e)^{-1}$  POS curve.

The  $\text{CH}_3^+$  ion, which has an onset near the VIP of the  $(2e)^{-1}$  band, is less than 2 % of the total intensity of all ions at this energy. No  $\text{CH}_3^+$  is observed from 11.25 to 12.25 eV. The initial appearance of  $\text{CH}_3^+$  is from ion pair formation,  $\text{CH}_3\text{Br} \rightarrow \text{CH}_3^+ + \text{Br}^-$ , which has been reported by Suzuki *et al.* [315] to produce  $\text{Br}^-$  from below the limit of their data at 9.4 eV. The second  $\text{CH}_3^+$  onset at 12.75 eV, which is much stronger, occurs near the adiabatic IP (13.0 eV [111]) of the  $(3a_1)^{-1}$  state. PEPICO data [288] indicates that the  $\text{CH}_3^+$  ion is the sole product from dissociative photoionization of the  $(3a_1)^{-1}$  state and that  $\text{CH}_3^+$  is also formed from the  $(1e)^{-1}$  state. Since the POS curve of the  $\text{CH}_3^+$  ion shows no higher energy thresholds it can be concluded that curve is equal to the entire  $(3a_1)^{-1}$  POS curve plus some additional contribution from the  $(1e)^{-1}$  POS curve.

The ions with the next lowest appearance potentials are the  $\text{CH}_2\text{Br}^+$ ,  $\text{CHBr}^+$ ,  $\text{CH}_2^+$  and  $\text{Br}^+$  ions at 13.75, 15.25, 15.75 and 18.25 eV, respectively. Since the only ion formed from the  $(3a_1)^{-1}$  state is  $\text{CH}_3^+$ , the  $\text{CH}_2\text{Br}^+$ ,  $\text{CHBr}^+$ ,  $\text{Br}^+$  and  $\text{CH}_2^+$  ions must all be formed from the photoionization of the  $(1e)^{-1}$  state. Formation of the  $\text{CH}_2\text{Br}^+$  ion below the  $(1e)^{-1}$  adiabatic IP of 14.5 eV [111] is likely the result of neutral excited states converging to the  $(1e)^{-1}$  limit which autoionize to the  $(2e)^{-1}$  or  $(3a_1)^{-1}$  state. It is clear from the broad nature of the  $\text{Br}^+$  peak in the TOF spectrum (see figure 6.15) that the  $\text{Br}^+$  ion is formed with considerable

kinetic energy of fragmentation, which is reflected in the high appearance potential of  $\text{Br}^+$ . The  $\text{CHBr}^+$ ,  $\text{Br}^+$  and  $\text{CH}_2^+$  POS curves each show a higher energy onset near 21.5 eV which corresponds to the main photoelectron band of the  $(2a_1)^{-1}$  state. Since the  $\text{CH}_2\text{Br}^+$  ion shows no higher energy thresholds its shape can be used as the shape of the  $(1e)^{-1}$  POS curve to assess the  $(1e)^{-1}$  contributions to  $\text{CH}_2\text{Br}^+$ ,  $\text{CHBr}^+$ ,  $\text{Br}^+$  and  $\text{CH}_2^+$ . Both the  $\text{Br}^+$  and  $\text{CH}_2^+$  POSs have large contributions from the  $(2a_1)^{-1}$  state, but the  $\text{Br}^+$  POS curve has one further onset at  $\sim 26$  eV indicating a further contribution from the  $(1a_1)^{-1}$  state. The  $\text{CH}_2^+$  POS curve can be used to obtain the shape of the  $(2a_1)^{-1}$  POS curve by subtracting the contribution of the  $(1e)^{-1}$  state (represented by the shape of the  $\text{CH}_2\text{Br}^+$  POS curve) from the  $\text{CH}_2^+$  POSs.

The appearance potentials of the  $\text{CH}^+$ ,  $\text{C}^+$ , and  $\text{H}^+$  ions are 25.25, 26.25, and 24.25 eV respectively, and these all occur in a region where several many-body states of the  $(1a_1)^{-1}$  process exist (see section 6.4.1 above). These ions appear well above the Franck-Condon regions of the other electronic ion states, so the  $\text{CH}^+$ ,  $\text{C}^+$ , and  $\text{H}^+$  ions must be formed only from ionization processes corresponding to production of the various  $(1a_1)^{-1}$  many-body states. The shape of the  $(1a_1)^{-1}$  POS can be obtained from the sum of the  $\text{CH}^+$ ,  $\text{C}^+$ , and  $\text{H}^+$  POSs.

In summary, the shapes of the electronic state POS curves have been obtained from the molecular and dissociative photoion POS curves as follows: The shape and magnitude of the  $(2e)^{-1}$  state is given by the  $\text{CH}_3\text{Br}^+$  POS curve. The shape of the  $(1e)^{-1}$  state is given by the  $\text{CH}_2\text{Br}^+$  POS curve. The shape of the  $(1a_1)^{-1}$  state is given by the sum of the  $\text{CH}^+$ ,  $\text{C}^+$  and  $\text{H}^+$  POS curves. The  $\text{CH}_2^+$  POS curve has contributions from both the  $(1e)^{-1}$  and  $(2a_1)^{-1}$  states, thus, the shape of the  $(2a_1)^{-1}$  POS curve has been obtained by subtracting from the  $\text{CH}_2^+$  POS the appropriate contribution from the  $(1e)^{-1}$  state. The entire  $(3a_1)^{-1}$  POS curve is contained within the  $\text{CH}_3^+$  POS curve, which also has a contribution from the  $(1e)^{-1}$  state of unknown magnitude.

The  $\text{CBr}^+$  ion has an appearance potential of 20.75 eV which must come from photoionization of the  $(2a_1)^{-1}$  state. One further onset is observed in the  $\text{CBr}^+$  POS curve at  $\sim 24$  eV. This onset, along with the higher energy onset at 25 eV in the  $\text{Br}^+$  POS curve, is from production of these ions from the  $(1a_1)^{-1}$  ion state, which also forms the other small fragment ions  $\text{CH}^+$ ,  $\text{C}^+$  and  $\text{H}^+$ .

The appearance potential of the  $\text{H}_2^+$  ion is 40 eV. No measurements of multiple photoionization of  $\text{CH}_3\text{Br}$  have been published below 68 eV, but the high energy onset of this ion, so far above any of the significant many-body states of the  $(1a_1)^{-1}$  state, is probably a result of dissociative double photoionization. The absence of any doubly charged species in the TOF mass spectra measured below the Br 3d excitation threshold of  $\text{CH}_3\text{Br}$  means that any multiple photoionization events must decay into singly charged fragment ions within the time scale of the dipole (e,e+ion) experiment. The PIPICO spectrum of Nenner *et al.* [309–311] recorded at 68 eV photon energy has shown that the majority of double photoionization (DPI) events result in formation of  $\text{Br}^+/\text{CH}_n^+$  pairs of ions. Small amounts of the  $\text{H}^+/\text{CH}_n^+$  and  $\text{H}^+/\text{Br}^+$  pairs were also reported [309–311]. The formation of  $\text{H}_2^+$  was not reported by Nenner *et al.* [309–311], but this is not surprising because its branching ratio has been found to be very small in the present work ( $\leq 2\%$ ) thus the detection of this ion in the PIPICO spectrum would be obscured by coincidence peaks involving  $\text{H}^+$  which are formed in much higher abundance ( $\sim 20\%$ ). In the presently reported ion POS curves there are no features above 30 eV to indicate the onset of any DPI channels.

The various portions (areas) for each of the  $(2e)^{-1}$ ,  $(3a_1)^{-1}$ ,  $(1e)^{-1}$ ,  $(2a_1)^{-1}$  and  $(1a_1)^{-1}$  electronic ion states contributing to the molecular and dissociative ion POSs (as shown in figure 6.17) were summed to provide estimates of the valence shell partial photoionization oscillator strengths for the production of molecular ions in these specific electronic states of  $\text{CH}_3\text{Br}^+$ . The unknown magnitude of the  $(1e)^{-1}$  contribution to the  $\text{CH}_3^+$  ion POS necessitates that the  $(3a_1)^{-1}$  and  $(1e)^{-1}$  POSs are reported as the sum  $(1e+3a_1)^{-1}$ . These

electronic state partial photoionization oscillator strength estimates, which are shown in figure 6.18 and listed in table 6.9, can be compared with direct measurements obtained using tunable photon energy photoelectron spectroscopy (see section 6.4.4 below).

Throughout the Br 3d excitation and ionization region (above  $\sim 70$  eV) increases in the yields of the small fragment ions are observed while the amount of the larger  $\text{CH}_n\text{Br}^+$  ions formed remains unchanged. Above 71 eV both the larger  $\text{CH}_n\text{Br}^+$  ions and the small fragment ions continue to be formed *via* the ionization channels from the underlying valence shell continuum, but Br 3d excitation and ionization open new channels which form only the smaller fragment ions. To investigate these processes on detail, TOF mass spectra were recorded in the present work at 67, 71, 75 and 79 eV which correspond to regions in the  $\text{CH}_3\text{Br}$  spectrum (see section 5.5.3) below the Br 3d excitation threshold, on the  $\sigma^* \leftarrow \text{Br}$  3d transition, on the Rydberg  $\leftarrow \text{Br}$  3d transitions and above the Br 3d ionization edge, respectively. The ions  $\text{Br}^{2+}$  and  $\text{H}_3^+$  appear for the first time in this region. At 71 eV ( $\sigma^* \leftarrow \text{Br}$  3d) large increases in the yields of the  $\text{Br}^+$  and  $\text{H}^+$  are observed along with smaller increases in the  $\text{CH}_2^+$ ,  $\text{CH}^+$ ,  $\text{C}^+$  and  $\text{H}^+$  ion yields. This excited state is expected to decay *via* a resonance MVV Auger pathway (see section 2.5.3) to form either a singly or doubly ionized state. The ionized state may decompose further into several fragments [309]. The influence of the  $\sigma^*$  virtual valence orbital, which is largely C-Br anti-bonding in character, is expected to be towards breakage of the C-Br bond. This would result in a  $\text{Br}^{2+}$  ion fragment or in  $\text{Br}^+$  and/or  $\text{CH}_3^+$  fragment ion(s) (in which  $\text{CH}_3^+$  may decompose further). Beyond the  $\sigma^*$  resonance, both below and above the Br 3d ionization edge, there remain only small increases in the yields of the  $\text{Br}^+$ ,  $\text{CH}^+$ ,  $\text{C}^+$  and  $\text{H}_2^+$  ions, but the yield of the  $\text{H}^+$  ion continues to increase rapidly. In this region Coulomb explosion of multiply charged  $\text{CH}_3\text{Br}^{n+}$ , which is formed from MVV Auger decay of the Br 3d excited or ionized molecule, appears to result in small fragment ions. Furthermore, in the Br 3d continuum there is no involvement of the  $\sigma^*$  orbital (and therefore no bias toward C-Br bond breakage), thus larger increases in the

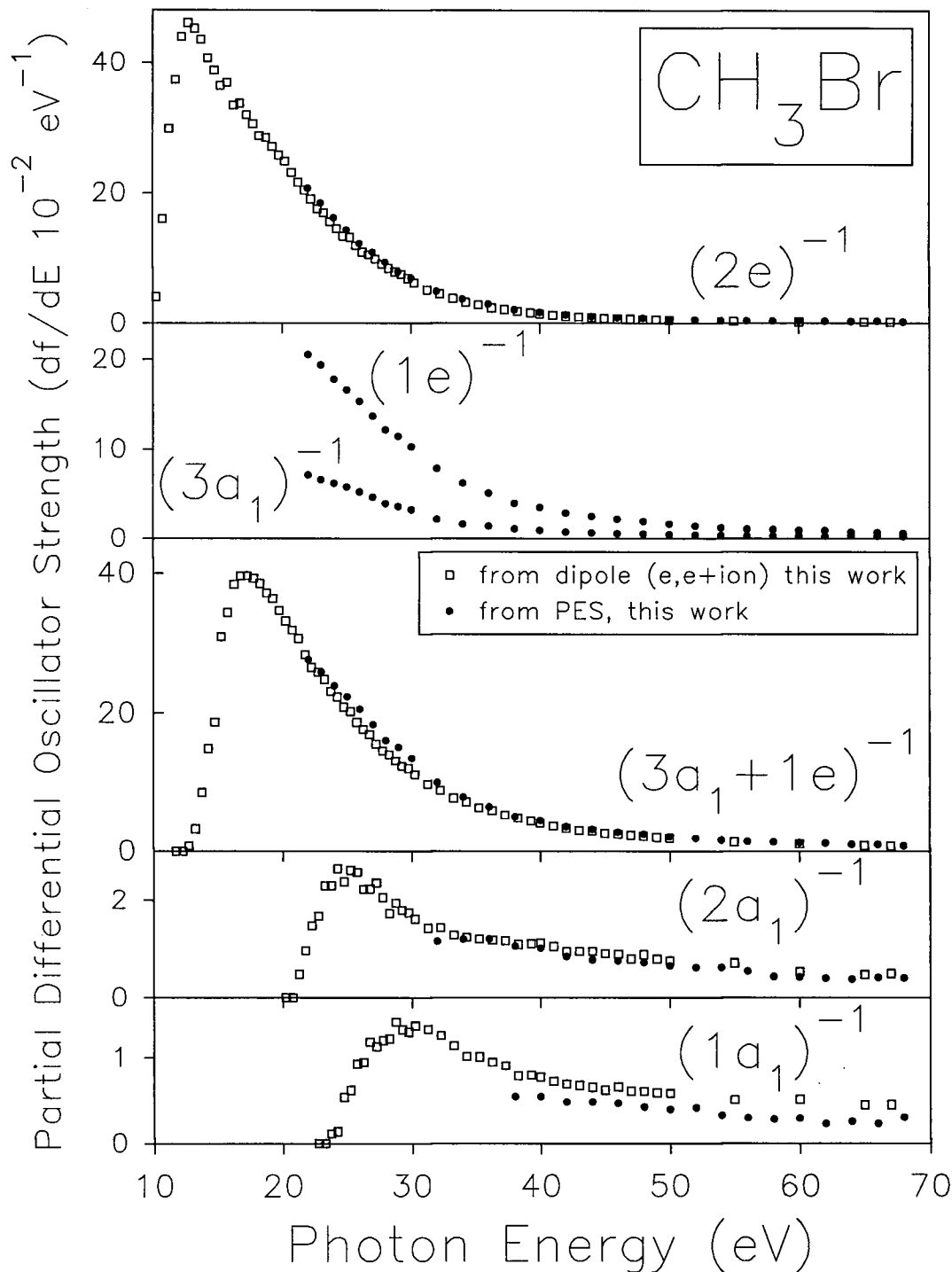


Figure 6.18: Absolute partial photoionization oscillator strengths for production of electronic states of  $\text{CH}_3\text{Br}^+$ . Open squares show the estimates from appropriate linear combinations of the present molecular and dissociative photoionization POSs and breakdown scheme (see section 6.4.3). Filled circles represent estimates from photoelectron binding energy spectra recorded in the present work with tunable synchrotron radiation (see section 6.4.4).

$H^+/CH_n^+$  and  $H^+/Br^+$  channels are observed [309–311] as expected.

The resulting dipole-induced breakdown pattern above 70 eV suggested by the above analysis, including the breakdown pathways from excitation and ionization from the Br 3d inner shell, is summarized in figure 6.19. The  $(3a_1)^{-1}$  and  $(1e)^{-1}$  POSs were reported above as the sum  $(1e+3a_1)^{-1}$  because the magnitude of the  $(1e)^{-1}$  contribution to the  $CH_3^+$  ion POS could not be determined from the  $CH_3^+$  POS curve. As a result only the relative proportions of the other ions formed from the  $(1e)^{-1}$  state could be determined. In an attempt to address this problem the magnitude of the  $(1e)^{-1}$  POS which results in the  $CH_3^+$  ion was estimated using the  $(3a_1)^{-1}$  and  $(1e)^{-1}$  POS curves measured using PES, which are presented below in section 6.4.4. Based on the magnitude of the measured  $(3a_1)^{-1}$  POS curve (see section 6.4.4 below) it was determined that the contribution from ionization of the  $(1e)^{-1}$  state to the  $CH_3^+$  ion was two times the sum of the  $(1e)^{-1}$  contributions to the  $CH_2Br^+$ ,  $CHBr^+$ ,  $Br^+$  and  $CH_2^+$  ions. The resulting partition of the  $(1e)^{-1}$  state into formation of the  $CH_2Br^+$ ,  $CHBr^+$ ,  $Br^+$ ,  $CH_3^+$  and  $CH_2^+$  ions is shown in figure 6.19.

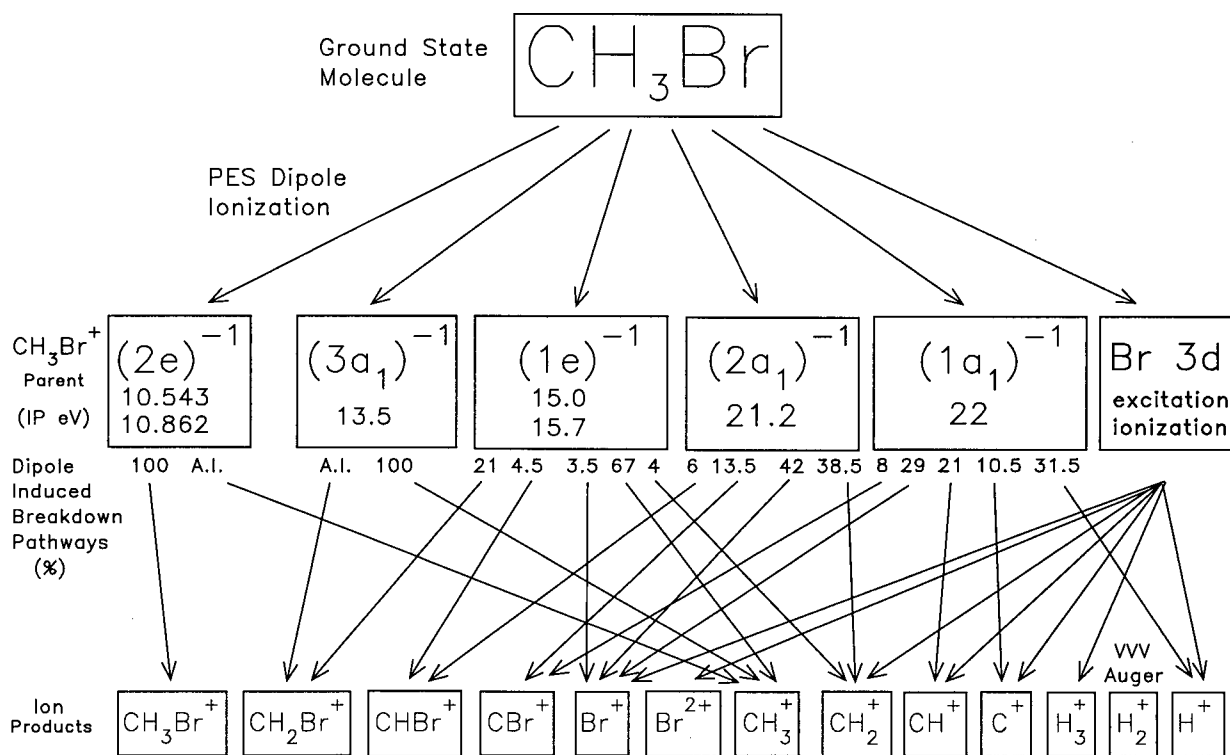


Figure 6.19: Proposed dipole-induced breakdown scheme for the ionic photofragmentation of CH<sub>3</sub>Br above  $h\nu = 70$  eV.

Table 6.9: Absolute partial differential oscillator strengths for production of electronic states<sup>a</sup> of CH<sub>3</sub>Br<sup>+</sup>.

Photon Energy eV	Partial Differential Oscillator Strength $df/dE$ ( $10^{-2}eV^{-1}$ ) <sup>b</sup>				Photon Energy eV	Partial Differential Oscillator Strength $df/dE$ ( $10^{-2}eV^{-1}$ ) <sup>b</sup>			
	(2e) <sup>-1</sup>	(3a <sub>1</sub> +1e) <sup>-1</sup>	(2a <sub>1</sub> ) <sup>-1</sup>	(1a <sub>1</sub> ) <sup>-1</sup>		(2e) <sup>-1</sup>	(3a <sub>1</sub> +1e) <sup>-1</sup>	(2a <sub>1</sub> ) <sup>-1</sup>	(1a <sub>1</sub> ) <sup>-1</sup>
10.25	4.00				26.75	10.42	16.94	2.11	0.75
10.75	16.01				27.25	9.75	15.55	2.22	0.72
11.25	29.83				27.75	8.95	14.53	2.15	0.76
11.75	37.35				28.25	8.32	13.99	1.96	0.78
12.25	43.95	0			28.75	7.75	13.12	2.18	0.90
12.75	46.08	0.80			29.25	7.37	12.34	2.11	0.85
13.25	45.19	3.24			29.75	6.73	12.03	2.19	0.83
13.75	43.52	8.53			30.25	6.10	11.10	2.11	0.87
14.25	40.71	14.84			31.25	5.03	9.76	2.01	0.85
14.75	38.84	18.69			32.25	4.44	8.81	2.01	0.80
15.25	36.48	30.96			33.25	3.74	7.73	1.91	0.72
15.75	36.91	34.39			34.25	3.14	7.12	1.79	0.65
16.25	33.49	38.43			35.25	2.75	6.32	1.75	0.64
16.75	33.75	39.62			36.25	2.30	5.90	1.69	0.60
17.25	31.97	39.68			37.25	2.03	5.26	1.68	0.58
17.75	30.55	39.28			38.25	1.77	4.81	1.56	0.50
18.25	28.76	38.56			39.25	1.56	4.37	1.53	0.51
18.75	28.45	37.16			40	1.37	4.09	1.48	0.49
19.25	27.08	36.38			41	1.20	3.67	1.40	0.46
19.75	25.77	34.71			42	1.04	3.32	1.27	0.44
20.25	24.86	33.19			43	0.93	2.99	1.24	0.43
20.75	23.10	31.90	0		44	0.84	2.90	1.24	0.42
21.25	21.64	30.69	0.30		45	0.75	2.59	1.16	0.39
21.75	20.44	28.35	0.66		46	0.68	2.45	1.16	0.42
22.25	19.07	26.56	0.95		47	0.61	2.30	1.06	0.39
22.75	17.56	25.90	1.18		48	0.57	2.19	1.11	0.39
23.25	16.96	24.86	1.50	0	49	0.51	1.99	1.01	0.38
23.75	15.58	23.15	1.64	0.07	50	0.45	1.88	0.97	0.37
24.25	14.55	22.33	1.82	0.09	55	0.33	1.35	0.80	0.32
24.75	13.35	20.84	1.74	0.34	60	0.23	1.08	0.67	0.33
25.25	13.17	20.22	2.02	0.39	65	0.19	0.83	0.58	0.29
25.75	11.83	18.66	2.06	0.59	67	0.18	0.77	0.59	0.29
26.25	10.85	17.64	2.02	0.60					

<sup>a</sup>Estimates obtained from a consideration of the partial oscillator strengths for the molecular and dissociative photoionization of CH<sub>3</sub>Br using the dipole induced breakdown scheme derived in section 6.4.3. See text for details (section 6.4.3) and comparison with synchrotron radiation PES measurements (section 6.4.4).

<sup>b</sup> $\sigma$ (Mb)=109.75  $df/dE$  ( $eV^{-1}$ ).

#### 6.4.4 Photoelectron spectroscopy

Valence shell photoionization of  $\text{CH}_3\text{Br}$  has been studied in the present work using photoelectron spectroscopy over the photon energy range 21 to 70 eV. A typical photoelectron spectrum recorded at 70 eV photon energy has already been shown in figure 6.14. The binding energy scales of the  $\text{CH}_3\text{Br}$  photoelectron spectra were calibrated using the same procedure used in section 6.2.4 for the photoelectron spectra of  $\text{CH}_3\text{F}$ . The inner valence photoelectron bands of  $\text{CH}_3\text{Br}$  are split by many-body effects into a number of states involving with inner valence ionization (see section 6.4.1). The origins of the peaks observed in the PE spectrum at  $\sim 21.3$ , 22.1, 23.6, 24.9, and 27.8 eV binding energy and the broad structure at higher energies were identified above, in section 6.4.4, with the aid of Green's function calculations [95] and EMS measurements [95]. The features at 21.3, 22.1 and 23.6 eV are predominantly resulting from the  $(2a_1)^{-1}$  ionization process with only a small contribution from the  $(1a_1)^{-1}$  process. The larger fourth peak at 24.9 eV is predicted [95] to be mainly from the  $(1a_1)^{-1}$  state. The Green's function calculations [95] and the EMS binding energy spectra and momentum distribution measurements for  $\text{CH}_3\text{Br}$  [95] indicate that the vast majority of the structure above 26 eV is from the  $(1a_1)^{-1}$  process.

In the present work the shape and intensity of the  $(1a_1)^{-1}$  photoelectron band, including the small many-body peaks above 26 eV binding energy, was determined from the photoelectron spectrum recorded at high photon energy (70 eV, see figure 6.14) where the background is relatively flat and could therefore be estimated for all binding energies of interest. The resulting shape of the  $(1a_1)^{-1}$  photoelectron band profile at 70 eV was used to differentiate the  $(1a_1)^{-1}$  band from the rising non-spectral low kinetic energy background at the lower photon energies. The importance of this procedure has already been discussed above for the cases of  $\text{CH}_3\text{F}$  and  $\text{CH}_3\text{Cl}$ . The small contribution from low intensity many-body states above 35 eV to the  $(1a_1)^{-1}$  branching ratio, higher in binding energy than the present measurements, was

unaccounted for in the present work.

The photoelectron branching ratios for the  $(2e)^{-1}$ ,  $(3a_1)^{-1}$ ,  $(1e)^{-1}$ ,  $(2a_1)^{-1}$ , and  $(1a_1)^{-1}$  electronic ion states of  $\text{CH}_3\text{Br}$  resulting from the considerations described above were obtained at each photon energy by integrating the photoelectron peaks for each state in the transmission corrected, background subtracted photoelectron spectra and normalizing the sum of all states to 100%. The kinetic energy resolution was sufficient to resolve all states in the photoelectron spectra with the exception of the  $(3a_1)^{-1}$  and the spin-orbit split  $(1e)^{-1}$  states, which are slightly overlapped. The photoelectron bands of these ion states were fitted with three gaussians, fixed to the estimated vertical ionization potentials of the states, and the fitted gaussian peak areas were used to determine the individual areas for both the  $(3a_1)^{-1}$  and  $(1e)^{-1}$  ion states.

Absolute partial photoionization oscillator strengths for production of the electronic states of  $\text{CH}_3\text{Br}^+$  were obtained from the triple product of the absolute photoabsorption oscillator strength (from dipole (e,e) measurements, see section 5.5.1), the absolute photoionization efficiency, and the photoelectron branching ratio for each electronic ion state as a function photon energy. The absolute electronic state partial photoionization oscillator strengths so derived are shown as the solid circles in figure 6.18, in comparison with the estimates (open squares) obtained from the molecular and dissociative photoionization breakdown scheme derived above (section 6.4.3). The POS curves of the  $(3a_1)^{-1}$  and  $(1e)^{-1}$  states are reported both individually (figure 6.18(b)) and as a sum of the  $(3a_1+1e)^{-1}$  states (figure 6.18(c)) in order to compare with the  $(3a_1+1e)^{-1}$  POS curve determined from molecular and dissociative photoionization POSs in section 6.4.3.

Figure 6.18 shows that there is quite good agreement between the electronic ion state POSs determined directly in the present work using synchrotron radiation PES measurements and the estimates derived from the molecular and dissociative photoion POSs for all states except the  $(1a_1)^{-1}$  state. This may result from: 1) underestimation of the  $(1a_1)^{-1}$

many-body states in the 20 to 23.5 eV region, which was predicted in section 6.4.1 to be mainly from  $(2a_1)^{-1}$  ionization; 2) from neglecting the higher energy many-body states of the  $(1a_1)^{-1}$  process which occur at binding energies higher than 35 eV; 3) from an overestimation of the photoelectron spectrum background in the region of the  $(1a_1)^{-1}$  states. There are also some discrepancies below 35 eV for the  $(2a_1)^{-1}$  POSs and corresponding minor discrepancies for the  $(2e)^{-1}$  and  $(3a_1+1e)^{-1}$  POSs. This may be a result of an underestimation of the  $(1e)^{-1}$  contribution to one or more of the  $\text{CHBr}^+$ ,  $\text{Br}^+$  and  $\text{CH}_2^+$  ions, but it is more likely that these discrepancies are from errors in assessing the rising PES background at lower photon energies for the inner valence states (see above). As noted in sections 6.2.4 and 6.3.4, errors near the electronic state thresholds of one state will result in small errors in the POS curves of all states present at those energies. As such the present direct synchrotron radiation electronic state photoionization POS measurements are only considered to be reasonably accurate for the lower intensity  $(2a_1)^{-1}$  and  $(1a_1)^{-1}$  states above 40 eV. For the  $(2e)^{-1}$  and  $(3a_1+1e)^{-1}$  states, the PES results agree with the molecular and dissociative photoionization estimates to better than 10% over the whole energy range studied. The present estimates of the electronic state photoionization POSs from the POSs for the molecular and dissociative photoionization of  $\text{CH}_3\text{Br}$  and the dipole-induced breakdown scheme (section 6.4.3) are considered to be of higher accuracy than the direct measurements using PES and synchrotron radiation.

## 6.5 Methyl Iodide Results and Discussion

### 6.5.1 Binding energy spectrum

To assess the effects of electron correlation on the inner valence photoionization of  $\text{CH}_3\text{I}$  with the aim of providing a better understanding of its molecular and dissociative photoionization, figure 6.20 shows a comparison of a previously published photoelectron spectrum

reported by von Niessen *et al.* [269] with previously published Green's function calculations. The photoelectron spectrum of CH<sub>3</sub>I shown in figure 6.20(a), which has been digitized from ref. [269], was recorded using HeII radiation (40.8140 eV) and this is compared with a limited range of calculations similar to those used for CH<sub>3</sub>F (section 6.2.1), CH<sub>3</sub>Cl (section 6.3.1) and CH<sub>3</sub>Br (section 6.4.1). The same general details given in section 6.2.1 for figure 6.1 also apply to the various respective presentations on figure 6.20. The two Green's function calculations shown for CH<sub>3</sub>I are:

(i) The OV/TDA calculations of von Niessen *et al.* [269] using the ADC(3) method and a [18s14p8d/9s5p/4s]/(13s9p4d/4s2p/2s) basis set. See figure 6.20(b).

(ii) The OV/ext-TDA calculations of Minchinton *et al.* [95] using the ADC(4) method and the same basis set as in (i). See figure 6.20(c).

As in the cases of the other methyl halides the binding energies of the three outer valence ionization processes of CH<sub>3</sub>I are all well predicted by the two OVGf calculations. Both calculations predict that the main poles for each of the outer valence orbitals are close to unity and that no significant splitting occurs. The inner valence region, however, is predicted to be severely split by electron correlation effects. The PE spectrum reported by von Niessen *et al.* [269] (figure 6.20(a)) shows three peaks in the inner valence region at 19.5, 21.5 and 23.2 eV. Both of the calculations provide similar descriptions of this region. The calculations predict a strong pole at ~19.5 eV with a pole strength of 0.45 and two smaller poles at ~21 and 22.5 eV containing pole strengths of 0.15 and 0.25, respectively, from the (2a<sub>1</sub>)<sup>-1</sup> ionization process. Ionization resulting in the (1a<sub>1</sub>)<sup>-1</sup> state is predicted to be concentrated in one band at ~25 eV containing 0.7 of the pole strength. Thus, the bands in the photoelectron spectrum at 19.5 and 21.5 eV are assigned to (2a<sub>1</sub>)<sup>-1</sup> ionization and the peak at 23.2 eV is attributed to the (1a<sub>1</sub>)<sup>-1</sup> state. Both calculations predict very little overlap of the (2a<sub>1</sub>)<sup>-1</sup> and (1a<sub>1</sub>)<sup>-1</sup> many-body states. In fact, both calculation predict that above 23 eV less than 0.02 of the (2a<sub>1</sub>)<sup>-1</sup> pole strength occurs and below 23 eV no poles from

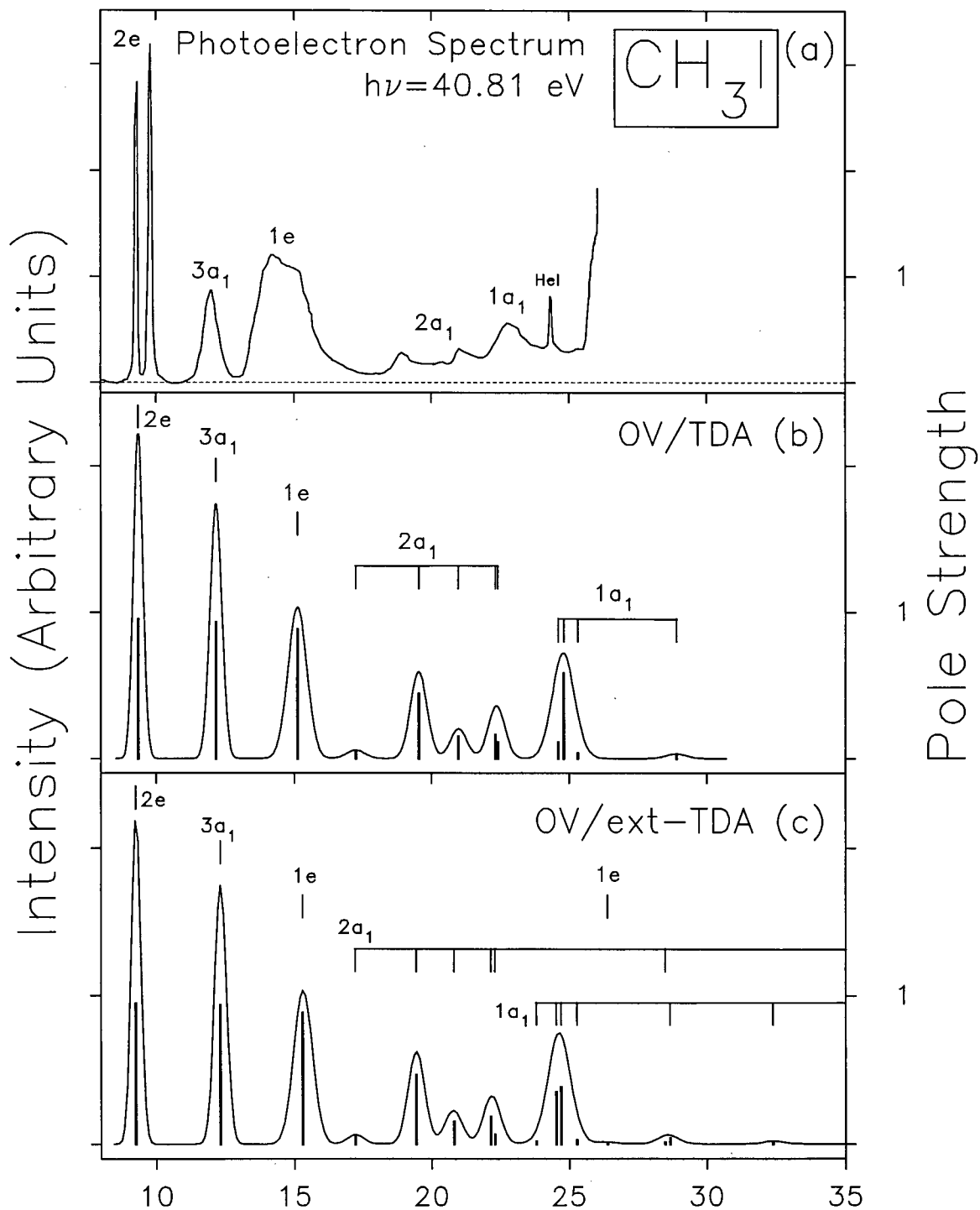


Figure 6.20: The previously published photoelectron spectrum of  $\text{CH}_3\text{I}$  recorded a photon energy of 40.81 eV (HeII) by von Niessen *et al.* [269] (a) compared with pole-strength calculations and synthetic spectra (b) and (c) generated from Green's function calculations using the OV/TDA [269] and OV/ext-TDA [95] approximations respectively—see text for details.

the  $(1a_1)^{-1}$  exist. Figure 6.20(a) shows a possible shoulder on the high energy side of the  $(1e)^{-1}$  photoelectron band at  $\sim 16.5$  eV. Both calculations predict a weak pole (0.05) from the  $(2a_1)^{-1}$  state at  $\sim 17.5$  eV which may be the origin of this shoulder. In contrast to the other methyl halides, few many-body states are predicted to occur at high binding energies. Outside of the main  $(1a_1)^{-1}$  band the OV/TDA calculation predicts only one other significant many-body state at 28.9 eV with a pole strength of 0.03, and the OV/ext-TDA calculation predicts five low intensity many-body states above 28 eV having a combined pole strength of 0.08. This assessment is consistent with the conclusions reached from a consideration of the EMS binding energy spectra and momentum distribution measurements for  $\text{CH}_3\text{I}$  [95].

### 6.5.2 Molecular and dissociative photoionization

Information about the molecular and dissociative photoionization processes of  $\text{CH}_3\text{I}$  in the valence and I 4d regions from the first ionization potential up to 59.5 eV was obtained in the present work using dipole (e,e+ion) spectroscopy. Figure 6.21(a) shows the TOF mass spectrum obtained at an equivalent photon energy of 58.5 eV. The mass resolution was sufficient to fully resolve all but the higher mass ions ( $\text{CH}_n\text{I}^+$ ) in the TOF mass spectra. The positive ions observed were:  $\text{H}^+$ ,  $\text{H}_2^+$ ,  $\text{CH}_n^+$ ,  $\text{I}^+$ ,  $\text{I}^{2+}$  and  $\text{CH}_n\text{I}^+$  where  $n = 0$  to 3. The broadness of the  $\text{I}^+$  peak is indicative of excess kinetic energy of fragmentation.

The branching ratio for each ion is shown in figure 6.22 (the corresponding numerical values can be calculated from the data given in table 6.10 by dividing the partial photoionization oscillator strength for a particular ion at a particular energy by the sum of all of the photoion partial oscillator strengths at that energy). These branching ratios were obtained for the molecular and dissociative photoionization channels of  $\text{CH}_3\text{I}$  by integrating the peaks for each ion in the background subtracted TOF mass spectrum and normalizing the sum of all ions to 100%. Separation of the  $\text{CH}_n\text{I}^+$  peaks in the TOF mass spectrum

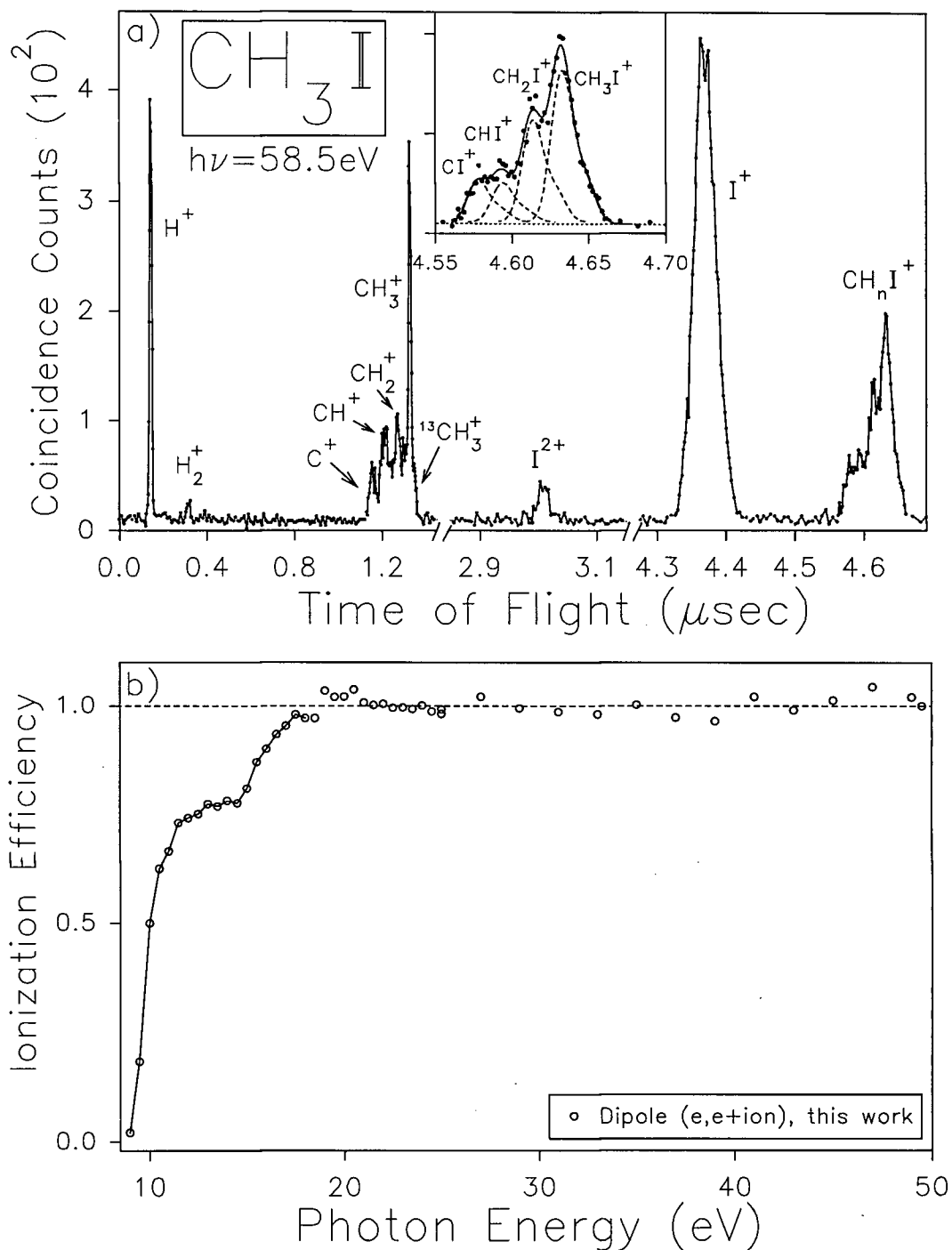


Figure 6.21: (a) TOF mass spectrum of  $\text{CH}_3\text{I}$  recorded at an equivalent photon energy of 58.5 eV. The inset to (a) shows an expanded view of the TOF mass spectrum in the region of the  $\text{CH}_n\text{I}^+$  ions. The individual mass peaks and the total fit to the experimental data are shown as the dashed and solid lines, respectively. (b) The photoionization efficiency of methyl iodide from 9 to 50 eV.

was achieved using a curve fit comprising four peaks, corresponding to individual masses from 139 ( $\text{CI}^+$ ) to 142 amu ( $\text{CH}_3\text{I}^+$ ). The shapes of the peaks in this region of the TOF spectrum were found to be asymmetric which required asymmetric peaks to be used in the fitting procedure. Each peak profile used was comprised of two gaussian peaks separated by  $0.15 \mu\text{s}$ . The relative areas and widths of the two peaks were fixed such that the area of the peak with the longer flight time was one-third of the area of the other peak and the widths of the two peaks were equal. From this procedure the TOF peak areas for the individual  $\text{CH}_n\text{I}^+$  ions were determined at each energy and their branching ratios were calculated. The fit to the  $\text{CH}_n\text{I}^+$  region of the TOF mass spectrum recorded at 58.5 eV is shown in the inset to figure 6.21(a).

The ionization efficiency data for  $\text{CH}_3\text{I}$  are shown graphically in figure 6.21(b) and the corresponding numerical values are given in table 6.10. Relative photoionization efficiency values were determined from the TOF mass spectra by taking the ratio of the total number of electron-ion coincidences to the total number of forward scattered electrons as a function of energy loss. Making the reasonable assumption that the absolute photoionization efficiency is unity at higher photon energies we conclude that  $\eta_i$  is 1 above 19 eV.

Absolute partial photoionization oscillator strengths for the production of molecular and dissociative ions were obtained from the triple product of the absolute photoabsorption oscillator strength (from dipole (e,e) measurements, see section 5.6.1), absolute photoionization efficiency, and branching ratio for each ion as a function of photon energy. These absolute partial photoionization oscillator strengths are shown in figure 6.23 and are given numerically in table 6.10. Figures 6.22 and 6.23 show that the only ion formed within the Franck-Condon region of the of the  $(2e)^{-1}$  state is  $\text{CH}_3\text{I}^+$ . The next ion to appear in the TOF mass spectra is  $\text{CH}_3^+$  at an equivalent photon energy of 12.0 eV, which corresponds to the  $(3a_1)^{-1}$  adiabatic IP [111]. Between 13.5 and 16 eV the  $\text{CH}_2\text{I}^+$ ,  $\text{CHI}^+$ ,  $\text{I}^+$  and  $\text{CH}_2^+$  ions appear. The predominant ions formed between 16 and 45 eV are  $\text{CH}_3\text{I}^+$ ,  $\text{CH}_2\text{I}^+$ ,  $\text{I}^+$  and  $\text{CH}_3^+$ . At 21 eV

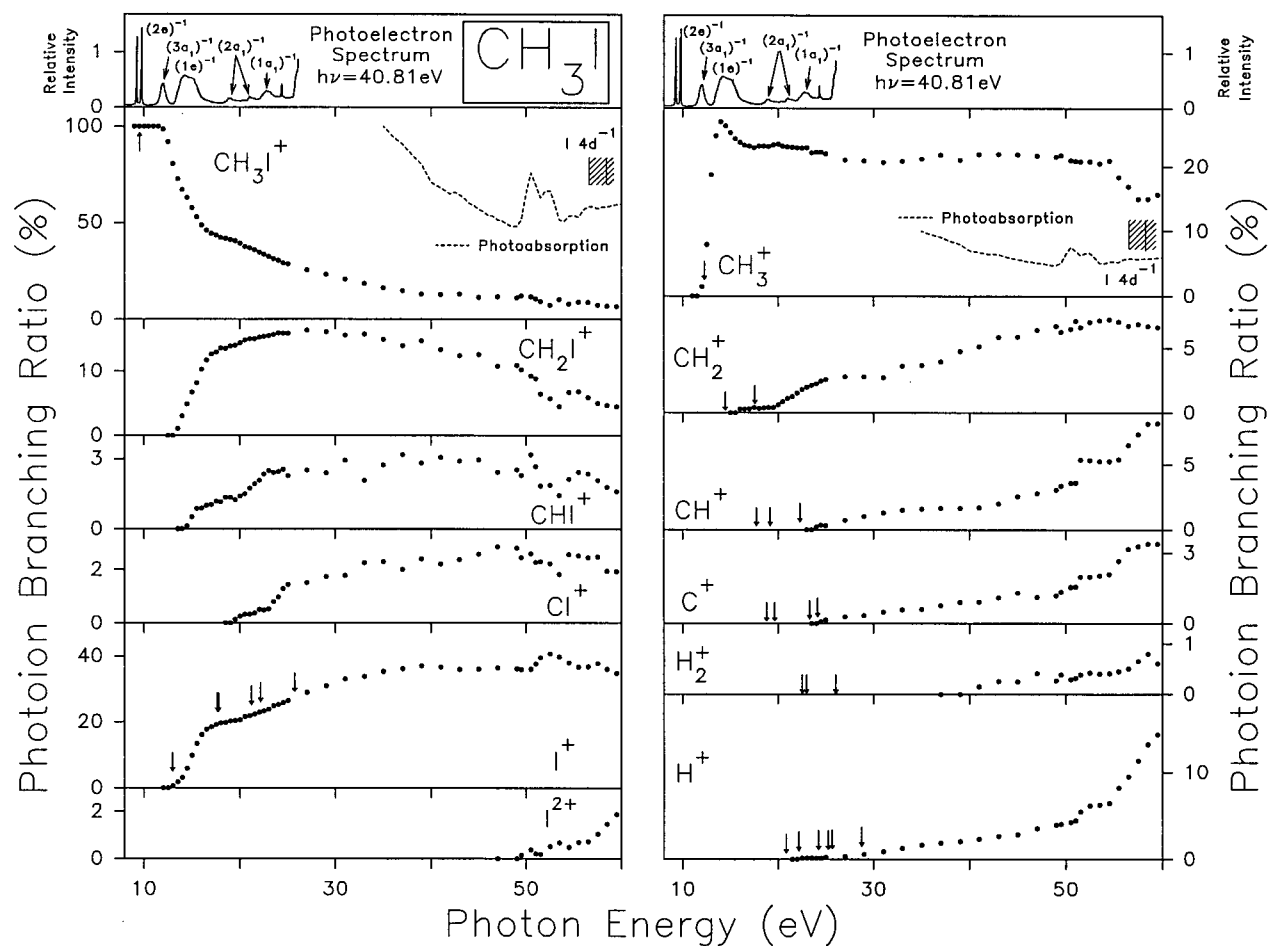


Figure 6.22: Branching ratios for the molecular and dissociative photoionization of  $\text{CH}_3\text{I}$ . Vertical arrows represent the calculated thermodynamic appearance potentials [317] of the ions from  $\text{CH}_3\text{I}$  (see table 6.11). The top panels show a digitized representation of the previously published HeII photoelectron spectrum reported by von Niessen *et al* [269] at  $h\nu = 40.81 \text{ eV}$  (see figure 6.20).

these four ions account for 97% of all ionization processes. This is in agreement with the photoionization mass spectrum recorded using HeI radiation (21.21 eV) by Eland *et al.* [288], in which these four ions were the only ions observed. The intensity ratios reported by Eland *et al.* [288] were 1.00 : 0.30 : 0.30 : 0.45 for  $\text{CH}_3\text{I}^+:\text{CH}_2\text{I}^+:\text{I}^+:\text{CH}_3^+$  which are different from those (1.00 : 0.41 : 0.61 : 0.63) found in the present work at 21 eV. This difference must be the result of discrimination towards low mass ions in the spectra of Eland *et al.* [288], which is consistent with similar differences found in the photoion ratios reported for the other methyl halides (see sections 6.2.2, 6.2.2 and 6.2.2). The  $\text{CI}^+$  ion appears at 20 eV and the  $\text{CH}^+$ ,  $\text{C}^+$  and  $\text{H}^+$  ions appear between 22 to 25 eV. The branching ratios for these ions increase steadily over the energy region from 26 to 45 eV. A small amount of  $\text{H}_2^+$  appears at 41 eV. At 47 eV, just below the onset of the I 4d excitation region, the major ion formed is  $\text{I}^+$ , having a branching ratio of 36.3%. The  $\text{CH}_3\text{I}^+$ ,  $\text{CH}_2\text{I}^+$  and  $\text{CH}_3^+$  ions are also formed in significant quantities at 47 eV, all having branching ratios between 11 and 22%. The  $\text{CHI}^+$ ,  $\text{CI}^+$ ,  $\text{CH}_2^+$ ,  $\text{CH}^+$ ,  $\text{C}^+$ ,  $\text{H}_2^+$  and  $\text{H}^+$  ions are all minor products, each contributing less than 3.5%, except for  $\text{CH}_2^+$  which contributes 6.4%, to the total photoionization oscillator strength below 47 eV.

Above 47 eV the degree of fragmentation increases throughout the I 4d excitation and ionization region of  $\text{CH}_3\text{I}$ . This is demonstrated by the steady rise in the branching ratios of the smaller fragments ions  $\text{CH}^+$ ,  $\text{C}^+$  and  $\text{H}^+$  from 47 to 59.5 eV. This behavior was also observed in the Br 3d excitation and ionization region of  $\text{CH}_3\text{Br}$ , but the dramatic increase in  $\text{Br}^+$  formation from photoionization of  $\text{CH}_3\text{Br}$  is not mirrored in the photoionization of  $\text{CH}_3\text{I}$  by a large increase in the yield of  $\text{I}^+$ . There is an increase in the yield of  $\text{I}^+$  from photoionization of  $\text{CH}_3\text{I}$  in the I 4d region at the energy of the  $\sigma^* \leftarrow \text{I } 4\text{d}$  transition. The only doubly charged ion observed in the present work is  $\text{I}^{2+}$  and this has an appearance potential of 50 eV, which coincides with the I 4d excitation threshold (see section 5.6.3). Further discussion of the photoionization products resulting from I 4d excitation and ionization will

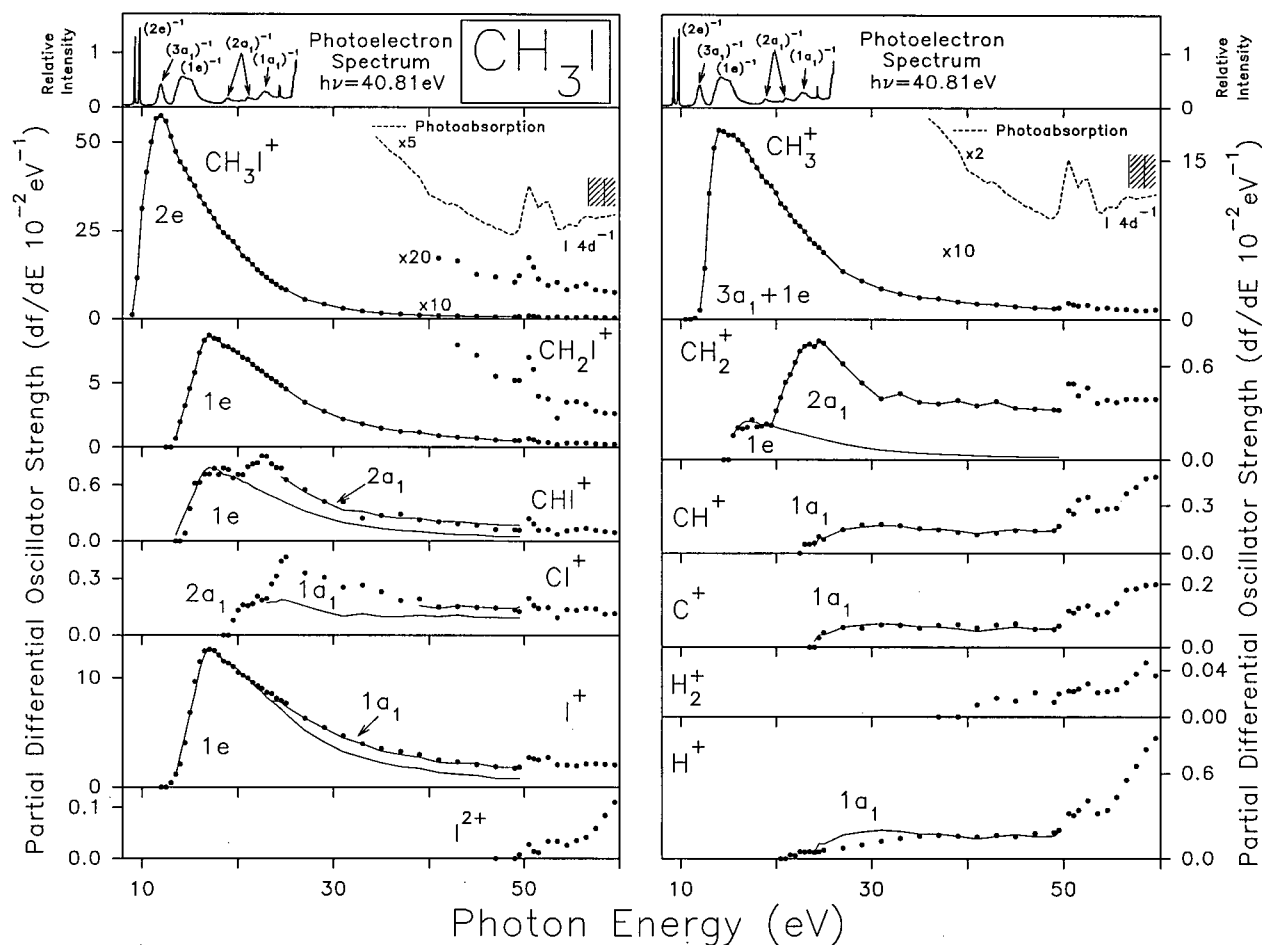


Figure 6.23: Absolute partial photoionization oscillator strengths for the molecular and dissociative photoionization of  $\text{CH}_3\text{I}$ . Points represent the measured partial photoionization oscillator strengths for the molecular and dissociative photoionization. Lines show the sums and partial sums of the electronic state partial photoionization oscillator strength contributions derived from the proposed dipole-induced breakdown scheme (see text, section 6.5.3, for details). The top panels show a digitized representation of the previously published HeII photoelectron spectrum reported by von Niessen *et al* [269] at  $h\nu = 40.81$  eV (see figure 6.20).

be given in the following section on the dipole-induced breakdown of  $\text{CH}_3\text{I}$ .

The presently measured appearance potentials for the ions formed from the molecular and dissociative photoionization of  $\text{CH}_3\text{I}$  are given in table 6.11 where they are compared with both calculated and previously published experimental appearance potentials. Calculated appearance potentials for many of the fragmentation pathways leading to singly charged cations from  $\text{CH}_3\text{I}$  are shown as vertical arrows in figure 6.22. The appearance potentials were calculated from thermodynamic heats of formation [317] assuming zero kinetic energy of fragmentation, so the actual thresholds may be higher. The appearance potentials for pathways involving  $\text{CH}_2\text{I}$ ,  $\text{CHI}$  and  $\text{CI}$  have not been calculated because values of the heats of formation for these fragments were not available from the literature. Previously published experimental appearance potentials were obtained using electron impact [296–299] and photoionization [316] methods. The presently measured appearance potentials agree well, in most cases, with the limited number of previously published values (within the present experimental uncertainty of  $\pm 1$  eV). The exceptions are the  $\text{CH}_2^+$  and  $\text{CH}^+$  ions which are found to appear at ionizing energies  $\sim 1.5$  eV and 2.3 eV higher, respectively, in the present work than in previously reported electron impact measurements [296, 299]. Similar discrepancies have been found for photoionization of  $\text{CH}_3\text{Cl}$  (section 6.3.2) and  $\text{CH}_3\text{Br}$  (section 6.4.2) where the  $\text{Cl}^+$ ,  $\text{Br}^+$  and  $\text{CH}^+$  ions were found have appearance potentials 6.5, 3.5 and 3.5 eV higher, respectively, in the present work than their appearance potentials measured using electron impact methods [296, 298]. As noted in the above sections, these differences may be due to ionization channels available *via* electron impact which are forbidden by dipole selection rules and thus would not be observed in the presently reported dipole (e,e+ion) photoionization studies.

Table 6.10: Absolute differential oscillator strengths for the molecular and dissociative photoionization of CH<sub>3</sub>I from 9 to 59.5 eV.

Photon Energy eV	Differential Oscillator Strength ( $df/dE$ 10 <sup>-2</sup> eV <sup>-1</sup> ) <sup>a</sup>												Ionization Efficiency <sup>b</sup> $\eta_i$
	CH <sub>3</sub> I <sup>+</sup>	CH <sub>2</sub> I <sup>+</sup>	CHI <sup>+</sup>	CI <sup>+</sup>	I <sup>+</sup>	I <sup>2+</sup>	CH <sub>3</sub> <sup>+</sup>	CH <sub>2</sub> <sup>+</sup>	CH <sup>+</sup>	C <sup>+</sup>	H <sub>2</sub> <sup>+</sup>	H <sup>+</sup>	
9.0	1.12												0.02
9.5	11.65												0.18
10.0	31.28												0.50
10.5	41.64												0.62
11.0	49.94						0						0.66
11.5	56.81						0						0.73
12.0	57.54				0		0.88						0.74
12.5	55.93	0			0		4.85						0.75
13.0	51.60	0			0.39		11.94						0.77
13.5	47.26	0.69	0		1.16		16.15						0.76
14.0	44.46	1.98	0		2.07		17.83						0.78
14.5	42.44	3.25	0.08		4.05		17.73						0.77
15.0	39.67	4.59	0.35		6.82		17.37	0					0.81
15.5	37.64	5.81	0.62		9.64		17.36	0					0.87
16.0	34.65	7.34	0.63		11.54		16.93	0.21					0.90
16.5	32.53	8.28	0.72		12.53		16.50	0.20					0.93
17.0	30.48	8.68	0.72		12.69		15.93	0.21					0.95
17.5	28.46	8.45	0.78		12.57		15.02	0.26					0.98
18.0	26.11	8.36	0.71		12.18		14.36	0.21					0.97
18.5	24.40	7.85	0.78	0	11.59		13.52	0.22					0.97

Table 6.10: (continued) Absolute differential oscillator strengths for the molecular and dissociative photoionization of CH<sub>3</sub>I from 9 to 59.5 eV.

Photon Energy eV	Differential Oscillator Strength ( $df/dE$ 10 <sup>-2</sup> eV <sup>-1</sup> ) <sup>a</sup>												Ionization Efficiency <sup>b</sup> $\eta_i$
	CH <sub>3</sub> I <sup>+</sup>	CH <sub>2</sub> I <sup>+</sup>	CHI <sup>+</sup>	CI <sup>+</sup>	I <sup>+</sup>	I <sup>2+</sup>	CH <sub>3</sub> <sup>+</sup>	CH <sub>2</sub> <sup>+</sup>	CH <sup>+</sup>	C <sup>+</sup>	H <sub>2</sub> <sup>+</sup>	H <sup>+</sup>	
19.0	23.17	7.78	0.76	0	11.39		13.02	0.23					1.00 <sup>b</sup>
19.5	21.85	7.55	0.68	0.08	11.05		12.62	0.22					
20.0	20.04	7.32	0.71	0.13	10.53		11.99	0.32					
20.5	17.85	6.96	0.71	0.16	10.25		10.97	0.40					
21.0	16.88	6.82	0.79	0.16	10.00		10.55	0.50					
21.5	15.46	6.42	0.82	0.16	9.59		9.86	0.55				0	
22.0	13.99	6.11	0.84	0.21	9.25		9.26	0.62				0	
22.5	12.98	5.91	0.91	0.18	9.02		8.83	0.70				0.05	
23.0	11.73	5.59	0.90	0.19	8.63		8.32	0.73	0			0.05	
23.5	10.74	5.34	0.82	0.27	8.51		7.59	0.74	0	0		0.05	
24.0	9.79	5.10	0.79	0.31	8.14		7.16	0.73	0.07	0		0.05	
24.5	8.88	4.83	0.78	0.39	7.90		6.81	0.76	0.11	0.03		0.05	
25.0	8.30	4.55	0.66	0.41	7.64		6.35	0.75	0.09	0.05		0.07	
27.0	5.57	3.55	0.55	0.33	6.30		4.58	0.62	0.15	0.06		0.08	
29.0	4.13	2.83	0.42	0.31	5.45		3.69	0.50	0.18	0.06		0.10	
31.0	2.94	2.21	0.42	0.25	4.70		2.94	0.40	0.18	0.07		0.13	
33.0	2.16	1.84	0.24	0.26	3.96		2.44	0.43	0.18	0.07		0.15	
35.0	1.62	1.49	0.27	0.23	3.52		2.13	0.37	0.16	0.06		0.16	
37.0	1.33	1.26	0.29	0.18	3.28		1.98	0.36	0.15	0.07	0	0.17	
39.0	1.03	1.18	0.23	0.19	2.97		1.69	0.38	0.13	0.07	0	0.16	

Table 6.10: (continued) Absolute differential oscillator strengths for the molecular and dissociative photoionization of CH<sub>3</sub>I from 9 to 59.5 eV.

Photon Energy eV	Differential Oscillator Strength ( $df/dE$ 10 <sup>-2</sup> eV <sup>-1</sup> ) <sup>a</sup>												Ionization Efficiency <sup>b</sup> $\eta_i$
	CH <sub>3</sub> I <sup>+</sup>	CH <sub>2</sub> I <sup>+</sup>	CHI <sup>+</sup>	CI <sup>+</sup>	I <sup>+</sup>	I <sup>2+</sup>	CH <sub>3</sub> <sup>+</sup>	CH <sub>2</sub> <sup>+</sup>	CH <sup>+</sup>	C <sup>+</sup>	H <sub>2</sub> <sup>+</sup>	H <sup>+</sup>	
41.0	0.86	0.90	0.21	0.15	2.48		1.50	0.35	0.12	0.06	0.01	0.16	
43.0	0.82	0.79	0.19	0.15	2.30		1.41	0.38	0.13	0.07	0.02	0.17	
45.0	0.64	0.71	0.17	0.15	2.04		1.24	0.33	0.14	0.08	0.01	0.16	
47.0	0.60	0.55	0.13	0.15	1.86	0	1.11	0.33	0.14	0.06	0.02	0.18	
49.0	0.53	0.52	0.12	0.13	1.74	0	1.03	0.32	0.15	0.06	0.01	0.19	
49.5	0.62	0.52	0.12	0.12	1.84	0.01	1.12	0.32	0.17	0.07	0.02	0.21	
50.5	0.87	0.70	0.24	0.19	2.72	0.03	1.59	0.49	0.27	0.12	0.02	0.32	
51.0	0.74	0.61	0.19	0.16	2.61	0.01	1.45	0.49	0.25	0.11	0.02	0.31	
51.5	0.57	0.40	0.12	0.14	2.48	0.01	1.30	0.42	0.34	0.13	0.02	0.34	
52.5	0.48	0.38	0.12	0.15	2.71	0.03	1.38	0.47	0.36	0.13	0.03	0.41	
53.5	0.52	0.23	0.07	0.09	2.04	0.03	1.05	0.37	0.27	0.10	0.02	0.32	
54.5	0.42	0.36	0.11	0.14	2.03	0.03	1.12	0.39	0.28	0.11	0.02	0.34	
55.5	0.47	0.36	0.13	0.13	1.93	0.04	0.97	0.37	0.29	0.14	0.02	0.44	
56.5	0.50	0.34	0.14	0.14	2.13	0.04	0.98	0.39	0.38	0.18	0.03	0.56	
57.5	0.42	0.28	0.12	0.14	2.16	0.06	0.85	0.39	0.42	0.19	0.04	0.65	
58.5	0.40	0.27	0.10	0.11	2.09	0.09	0.87	0.39	0.47	0.20	0.05	0.77	
59.5	0.39	0.27	0.10	0.11	2.06	0.11	0.93	0.39	0.49	0.20	0.04	0.85	

<sup>a</sup> $\sigma(\text{Mb})=109.75 df/dE$  (eV<sup>-1</sup>).<sup>b</sup>The photoionization efficiency is normalized to unity above 19 eV (see text for details).

Table 6.11: Calculated and measured appearance potentials for the production of positive ions from CH<sub>3</sub>I.

	Process	Appearance Potential (eV)						
		Calc- ulated <sup>a</sup>	Experimental [ref.]					
			This work <sup>b</sup>	[297]	[298]	[299]	[296]	[316]
(1)	CH <sub>3</sub> I <sup>+</sup>	9.538	9.5		9.5		9.6	9.533
(2)	CH <sub>2</sub> I <sup>+</sup> + H		14.0				13.3	
(3)	CHI <sup>+</sup> + H <sub>2</sub>		15.0					
(4)	CHI <sup>+</sup> + 2H							
(5)	CI <sup>+</sup> + H <sub>2</sub> + H		20.0					
(6)	CI <sup>+</sup> + 3H							
(7)	I <sup>+</sup> + CH <sub>3</sub>	12.98	13.5	12.88	12.9		12.9	
(8)	I <sup>+</sup> + CH + H <sub>2</sub>	17.65						
(9)	I <sup>+</sup> + CH <sub>2</sub> + H	17.77						
(10)	I <sup>+</sup> + C + H <sub>2</sub> + H	21.16						
(11)	I <sup>+</sup> + CH + 2H	22.16						
(12)	I <sup>+</sup> + C + 3H	25.68						
(13)	I <sup>2+</sup> + CH <sub>3</sub>		50					
(14)	CH <sub>3</sub> <sup>+</sup> + I <sup>-</sup>	9.132			9.1			
(15)	CH <sub>3</sub> <sup>+</sup> + I	12.28	12.0	12.15	12.2		12.4	12.25
(16)	CH <sub>2</sub> <sup>+</sup> + HI	14.47	16.0			14.6	14.8	
(17)	CH <sub>2</sub> <sup>+</sup> + I + H	17.57				17.7		
(18)	CH <sup>+</sup> + I + H <sub>2</sub>	17.76					21.2	
(19)	CH <sup>+</sup> + HI + H	19.19						
(20)	CH <sup>+</sup> + I + 2H	22.28	23.5					
(21)	C <sup>+</sup> + HI + H <sub>2</sub>	18.80						
(22)	C <sup>+</sup> + I + H <sub>2</sub> + H	19.64						
(23)	C <sup>+</sup> + HI + 2H	23.32						
(24)	C <sup>+</sup> + I + 3H	24.15	25.0				24.9	
(25)	H <sub>2</sub> <sup>+</sup> + CHI							

Table 6.11: (continued) Calculated and measured appearance potentials for the production of positive ions from CH<sub>3</sub>I.

Process	Appearance Potential (eV)					
	Calculated <sup>a</sup>	Experimental [ref.]				
		This work <sup>b</sup>	[297]	[298]	[299]	[296]
(26) H <sub>2</sub> <sup>+</sup> + CI + H						
(27) H <sub>2</sub> <sup>+</sup> + HI + C	22.97					
(28) H <sub>2</sub> <sup>+</sup> + CH + I	22.55					
(29) H <sub>2</sub> <sup>+</sup> + I + C + H	26.06	41				
(30) H <sup>+</sup> + CH <sub>2</sub> I	18.08					
(31) H <sup>+</sup> + CI + H <sub>2</sub>						
(32) H <sup>+</sup> + HI + CH	22.15	22.0				
(33) H <sup>+</sup> + CH <sub>2</sub> + I	20.84					
(34) H <sup>+</sup> + CHI + H						
(35) H <sup>+</sup> + CI + 2H						
(36) H <sup>+</sup> + I + C + H <sub>2</sub>	24.24					
(37) H <sup>+</sup> + HI + C + H	25.66					
(38) H <sup>+</sup> + I + CH + H	25.24					
(39) H <sup>+</sup> + I + C + 2H	28.75					

<sup>a</sup>Values calculated using thermodynamic data for the enthalpy of formation of ions and neutrals (taken from [317]) assuming zero kinetic energy of fragmentation.

<sup>b</sup>±1 eV.

### 6.5.3 Dipole-induced breakdown

The major ions formed by the photoionization of  $\text{CH}_3\text{I}$  below 50 eV are  $\text{CH}_3\text{I}^+$ ,  $\text{CH}_2\text{I}^+$ ,  $\text{I}^+$  and  $\text{CH}_3^+$ . The  $\text{CH}_3\text{I}^+$  ion appears (see figure 6.23) at the ionization threshold of the  $(2e)^{-1}$  state (see table 5.1 on page 112). The HeI PEPICO data for  $\text{CH}_3\text{I}$  reported by Eland *et al.* [288] show clearly that  $\text{CH}_3\text{I}^+$  is the only ion formed from the  $(2e)^{-1}$  electronic state. The  $\text{CH}_3\text{I}^+$  POS curve does not show any higher energy onsets which indicates that it is formed only from the  $(2e)^{-1}$  state. Thus, the  $\text{CH}_3\text{I}^+$  POS curve is equal to the entire  $(2e)^{-1}$  POS curve.

The  $\text{CH}_3^+$  ion first appears at the ionization threshold of the  $(3a_1)^{-1}$  state. Unlike the other methyl halides, the ion pair process,  $\text{CH}_3\text{I} \rightarrow \text{CH}_3^+ + \text{I}^-$ , was not observed in the present photoionization measurements of  $\text{CH}_3\text{I}$  near the  $(2e)^{-1}$  ionization threshold. The PEPICO data of Eland *et al.* [288] indicate that the  $\text{CH}_3^+$  ion is the major product from dissociative photoionization of the  $(3a_1)^{-1}$  state and that it is also formed from the  $(1e)^{-1}$  state. Eland *et al.* [288] reported that a small amount of  $\text{I}^+$  was also formed from photoionization of the  $(3a_1)^{-1}$  state. This is not supported by the present work where the appearance potential of  $\text{I}^+$  was found to be 13.5 eV, which is at the threshold for  $(1e)^{-1}$  ionization and is above the Franck-Condon region of the  $(3a_1)^{-1}$  state. No higher energy onsets are observed in the  $\text{CH}_3^+$  POS curve. From these considerations it can be concluded that  $\text{CH}_3^+$  is the only ion formed from photoionization to the  $(3a_1)^{-1}$  state and that the  $\text{CH}_3^+$  POS curve is equal to the entire  $(3a_1)^{-1}$  POS curve plus some undetermined contribution from the  $(1e)^{-1}$  POS curve.

The  $\text{CH}_2\text{I}^+$ ,  $\text{CHI}^+$ ,  $\text{I}^+$  and  $\text{CH}_2^+$  ions have appearance potentials of 14.0, 15.0, 13.5 and 16.0 eV, respectively, which occur within the Franck-Condon region of the  $(1e)^{-1}$  state. Amongst these four ions the  $\text{CH}_2\text{I}^+$  POS is the only curve that does not show any higher energy onsets. This indicates that  $\text{CH}_2\text{I}^+$  is formed only from photoionization of the  $(1e)^{-1}$  state, thus the shape of the  $\text{CH}_2\text{I}^+$  POS curve can be used as the shape of the  $(1e)^{-1}$  POS

curve to assess the  $(1e)^{-1}$  contributions to  $\text{CH}_2\text{I}^+$ ,  $\text{CHI}^+$ ,  $\text{I}^+$  and  $\text{CH}_2^+$ . Both the  $\text{CHI}^+$  and  $\text{CH}_2^+$  POS curves have one higher energy onset at 20 and 19 eV, respectively. These onsets correspond to the main many-body states of the  $(2a_1)^{-1}$  process. The  $\text{CHI}^+$  and  $\text{CH}_2^+$  POS curves have approximately the same intensity at 25 eV, but the  $\text{CHI}^+$  ion is formed mainly as a result of ionization of the  $(1e)^{-1}$  state while the  $\text{CH}_2^+$  ion is formed largely from the  $(2a_1)^{-1}$  state. For this reason the shape used to represent the  $(2a_1)^{-1}$  POS is obtained from the shape of the  $\text{CH}_2^+$  POS curve after subtracting off the small contribution from the  $(1e)^{-1}$  state (represented by the shape of the  $\text{CH}_2\text{I}^+$  POS curve).

The appearance potentials of the  $\text{CH}^+$ ,  $\text{C}^+$ , and  $\text{H}^+$  ions are 23.5, 25.0, and 22.0 eV respectively, and these all occur in the region of the photoelectron spectrum where the main photoelectron band from the  $(1a_1)^{-1}$  state is observed (see section 6.5.1 above). These ions appear above the Franck-Condon regions of the other electronic ion states, so the  $\text{CH}^+$ ,  $\text{C}^+$ , and  $\text{H}^+$  ions must be formed only from ionization processes corresponding to production of the various  $(1a_1)^{-1}$  many-body states. The shape of the  $(1a_1)^{-1}$  POS is thus obtained from the sum of the  $\text{CH}^+$ ,  $\text{C}^+$ , and  $\text{H}^+$  POS curves.

In summary, the shapes of the electronic state POS curves have been obtained from the molecular and dissociative photoion POS curves as follows: The shape and magnitude of the  $(2e)^{-1}$  state is given by the  $\text{CH}_3\text{I}^+$  POS curve. The shape of the  $(1e)^{-1}$  state is given by the  $\text{CH}_2\text{I}^+$  POS curve and the  $(1a_1)^{-1}$  state by the sum of the  $\text{CH}^+$ ,  $\text{C}^+$  and  $\text{H}^+$  POS curves. By subtracting from the  $\text{CH}_2^+$  POS curve the appropriate contribution from the  $(1e)^{-1}$  state, the shape of the  $(2a_1)^{-1}$  POS curve is obtained. The  $\text{CH}_3^+$  POS curve contains all of the  $(3a_1)^{-1}$  POS along with a contribution from the  $(1e)^{-1}$  state of unknown magnitude.

The  $\text{CI}^+$  ion has an appearance potential of 20.0 eV which is in the many-body state region of the  $(2a_1)^{-1}$  process. A further onset is also observed in the  $\text{CI}^+$  POS curve at  $\sim 26$  eV. This onset, along with a higher energy onset near 25 eV in the  $\text{I}^+$  POS curve, must arise from photoionization of the  $(1a_1)^{-1}$  state which also forms the other small fragment

ions  $\text{CH}^+$ ,  $\text{C}^+$  and  $\text{H}^+$ .

The only other ion detected from valence shell photoionization is  $\text{H}_2^+$  which appears at 41 eV. This likely arises from direct valence shell DPI [308] or from a VVV Auger process (see section 2.5.3). Further discussion on the DPI of  $\text{CH}_3\text{I}$  will be given below.

The various portions (areas) for each of the  $(2e)^{-1}$ ,  $(3a_1)^{-1}$ ,  $(1e)^{-1}$ ,  $(2a_1)^{-1}$  and  $(1a_1)^{-1}$  electronic ion states contributing to the molecular and dissociative ion POSs (as shown in figure 6.23) were summed to provide estimates of the valence shell partial photoionization oscillator strengths for the production of molecular ions in these specific electronic states of  $\text{CH}_3\text{I}^+$ . The unknown magnitude of the  $(1e)^{-1}$  contribution to the  $\text{CH}_3^+$  ion POS necessitates that the  $(3a_1)^{-1}$  and  $(1e)^{-1}$  POSs are reported as the sum  $(3a_1+1e)^{-1}$ . These electronic state partial photoionization oscillator strength estimates, which are shown in figure 6.24 and listed in table 6.12, can be compared with direct measurements obtained using tunable photon energy photoelectron spectroscopy reported by Carlson *et al.* [273], who measured the partial electronic state cross-sections of the three outer valence orbitals of  $\text{CH}_3\text{I}$ . There is excellent agreement between the two sets of data for both the  $(2e)^{-1}$  and the summed  $(3a_1+1e)^{-1}$  states. The largest difference occurs in the  $(2e)^{-1}$  POS measurements reported by Carlson *et al.* [273] at 16 and 17 eV where the POSs are 20 and 30% higher, respectively, than the presently reported values.

The resulting dipole-induced breakdown pattern above 50 eV suggested by the above analysis is summarized in figure 6.25. The  $(3a_1)^{-1}$  and  $(1e)^{-1}$  POSs are reported as the sum  $(3a_1+1e)^{-1}$  because the magnitude of the  $(1e)^{-1}$  contribution to the  $\text{CH}_3^+$  ion POS could not be determined from the dipole ( $e, e+\text{ion}$ ) data. As a result only the relative proportions of the other ions formed from the  $(1e)^{-1}$  were known. In an attempt to address this problem the magnitude of the  $(1e)^{-1}$  POS which forms  $\text{CH}_3^+$  was estimated using the  $(3a_1)^{-1}$  and  $(1e)^{-1}$  POS curves measured using PES by Carlson *et al.* [273]. Based on the magnitude of the measured  $(3a_1)^{-1}$  POS curve [273] it can be determined that the contribution from

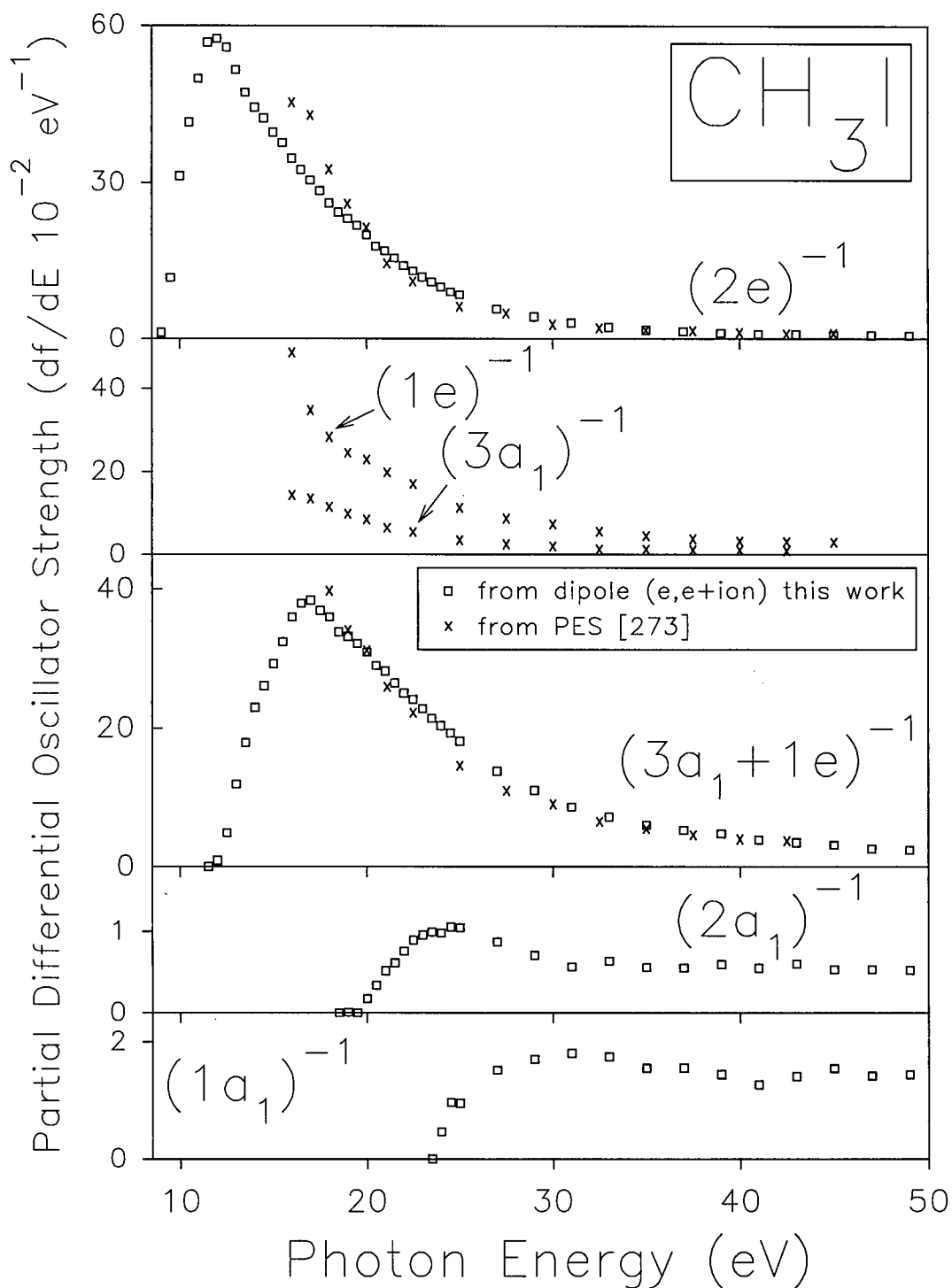


Figure 6.24: Absolute partial photoionization oscillator strengths for production of electronic states of  $\text{CH}_3\text{I}^+$ . Open squares show the estimates from appropriate linear combinations of the present molecular and dissociative photoionization POSs and breakdown scheme (see section 6.5.3). The crosses are the previously published electronic state partial photoionization oscillator strengths of Carlson *et al.* [273].

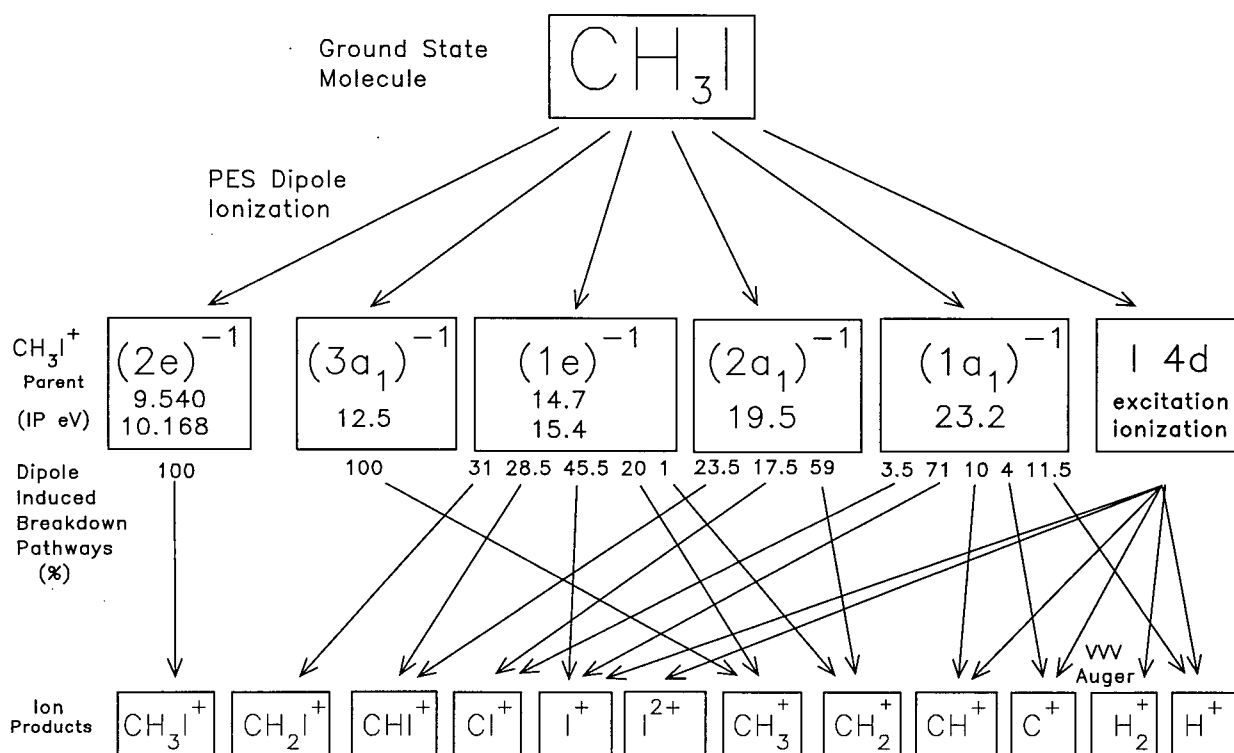


Figure 6.25: Proposed dipole-induced breakdown scheme for the ionic photofragmentation of CH<sub>3</sub>I above  $h\nu = 50$  eV.

ionization of the  $(1e)^{-1}$  state to the CH<sub>3</sub><sup>+</sup> ion is one-fourth the sum of the  $(1e)^{-1}$  contributions to the CH<sub>2</sub>I<sup>+</sup>, CHI<sup>+</sup>, I<sup>+</sup> and CH<sub>2</sub><sup>+</sup> ions. The resulting partition of the  $(1e)^{-1}$  state into the formation of the CH<sub>2</sub>I<sup>+</sup>, CHI<sup>+</sup>, I<sup>+</sup>, CH<sub>3</sub><sup>+</sup> and CH<sub>2</sub><sup>+</sup> ions is shown in figure 6.25.

Using HeII PEPECO spectroscopy, Price and Eland [308] have shown that the threshold for DPI in CH<sub>3</sub>I is at  $\sim 27$  eV. In contrast to the other methyl halides, the double photoionization spectrum of CH<sub>3</sub>I has been studied both in the valence shell [308, 312–314] and in the low energy inner shell [313] regions. The photoionization efficiency, based on the HeII PIPICO data reported by Curtis and Eland [312] of five DPI channels of CH<sub>3</sub>I, is estimated to be 1.09 at 40.83 eV. From the PIPICO data of Dujardin *et al.* [313], who have reported the ratio of the DPI cross-section to the total photoionization cross-section of six DPI channels of CH<sub>3</sub>I from 28 to 62 eV using synchrotron radiation, the photoionization efficiency at 40 eV is determined to be 1.06. Although there is a significant amount of DPI above 30 eV,  $\sim 6$

to 9%, no clear onsets from DPI channels are observed in the presently reported branching ratio or POS curves.

In table 6.13 columns 2 and 3 show the branching ratio and POS measurements, respectively, made in the present work at 41 eV assuming an ionization efficiency of 1.00 (the POSs have also been shown in table 6.10). Based on the ionization efficiency of 1.06 estimated at 40 eV from the data of Dujardin *et al.* [313] and on the relative abundances for twelve of the DPI channels of CH<sub>3</sub>I measured using HeII PEPIPICO spectroscopy by Eland *et al.* [314], the presently reported photoion branching ratios and POSs have been reworked to reflect the distribution of single and double photoionization of CH<sub>3</sub>I. These are presented in columns 4 to 7 in table 6.13. Columns 5 and 7 of table 6.13 show that, while the proportion of the CH<sub>*n*</sub>I<sup>+</sup> POSs from DPI is negligible, about half of the POS of the smaller fragment ions (CH<sub>2</sub><sup>+</sup>, CH<sup>+</sup>, C<sup>+</sup>, H<sub>2</sub><sup>+</sup> and H<sup>+</sup>) arises from the various DPI channels. The main DPI decomposition channels of CH<sub>3</sub>I at 41 eV are CH<sub>*n*</sub><sup>+</sup> + I<sup>+</sup> which were reported [314] to produce 43, 25, 11 and 3.5% of the total DPI products for CH<sub>3</sub><sup>+</sup>, CH<sub>2</sub><sup>+</sup>, CH<sup>+</sup> and C<sup>+</sup>, respectively. Thus ~80% of the I<sup>+</sup> formed at 41 eV is a result of single photoionization and ~20% is the result of the four DPI channels.

The only doubly charged species observed in the present work from photoionization of CH<sub>3</sub>I is I<sup>2+</sup>. This is first detected at 50 eV, in the I 4d excitation region. It was found in the present work that an increased amount of I<sup>+</sup> is formed in the region of the σ\* ← I 4d resonance, which is accompanied by increased yields of the CH<sub>3</sub><sup>+</sup>, CH<sub>2</sub><sup>+</sup>, CH<sup>+</sup> and H<sup>+</sup> ion. This would appear to be the result of a tendency toward breakage of the C–I bond because of excitation to the σ\* (C–I anti-bonding) orbital, which will produce CH<sub>3</sub><sup>+</sup> and I<sup>+</sup> fragment ions, along with significant fragmentation of the CH<sub>3</sub><sup>+</sup> portion. The synchrotron radiation PIPICO data reported by Dujardin *et al.* [313] shows that there is only a slight increase in the amount of DPI at the σ\* ← I 4d resonance and the distribution of DPI amongst the various channels remains virtually unchanged.

Above the  $\sigma^* \leftarrow I\ 4d$  resonance and into the I 4d ionization region the presently reported branching ratios show that the relative amounts of  $CH_nI^+$  and  $CH_3^+$  decrease,  $I^+$  and  $CH_2^+$  are slightly elevated, and  $I^{2+}$ ,  $CH^+$ ,  $C^+$ ,  $H_2^+$  and  $H^+$  increase rapidly, with respect to their valence shell branching ratios below 47 eV. This behaviour is reflected in the PIPICO data reported at 62 eV [313] which show that the relative proportions of  $I^+$  and  $CH_2^+$  formed from DPI remains constant and that large increases occur in the amounts of  $CH^+$ ,  $C^+$ ,  $H_2^+$  and  $H^+$  formed from the various DPI channels. The greatest changes in the distribution of DPI come from a large relative decrease in the  $CH_3^+ + I^+$  channel and a corresponding increase in the  $I^+ + H^+$  channel. The amount of  $I^{2+}$  formed from ionization of  $CH_3I$ , as shown in the presently reported branching ratios and partial oscillator strengths (figures 6.22 and 6.23), remains constant throughout the I 4d excitation region and then rises dramatically at the I 4d ionization threshold and beyond. The presently reported molecular and dissociative photoionization data and the PIPICO data reported by Dujardin *et al.* [313] suggests that ionization from the I 4d will proceed *via* Coulomb explosion of  $CH_3I^{2+}$  ion formed from NVV Auger decay of the  $(I\ 4d)^{-1}$  hole. The Coulomb explosion will result in: 1)  $I^+ + CH_n^+$  (or  $H^+$ ); 2)  $I^{2+} + CH_3$ ; or 3)  $CH_3^{2+} + I$  and further fragmentation of  $CH_3^{2+}$ .

The fragment ions formed as a result of the more abundant DPI channels resulting from I 4d excitation and ionization are indicated in the dipole-induced breakdown scheme shown in figure 6.25.

Table 6.12: Absolute electronic ion state partial photoionization differential oscillator strengths<sup>a</sup> for CH<sub>3</sub>I<sup>+</sup>.

Photon Energy eV	Partial Differential Oscillator Strength $df/dE$ ( $10^{-2}\text{eV}^{-1}$ ) <sup>b</sup>				Photon Energy eV	Partial Differential Oscillator Strength $df/dE$ ( $10^{-2}\text{eV}^{-1}$ ) <sup>b</sup>			
	$(2e)^{-1}$	$(3a_1+1e)^{-1}$	$(2a_1)^{-1}$	$(1a_1)^{-1}$		$(2e)^{-1}$	$(3a_1+1e)^{-1}$	$(2a_1)^{-1}$	$(1a_1)^{-1}$
9.0	1.12				20.5	17.85	29.01	0.34	
9.5	11.65				21.0	16.88	28.21	0.51	
10.0	31.28				21.5	15.46	26.50	0.61	
10.5	41.64				22.0	13.99	25.09	0.76	
11.0	49.94				22.5	12.98	24.13	0.89	
11.5	56.81	0			23.0	11.73	22.81	0.96	
12.0	57.54	0.88			23.5	10.74	21.43	0.99	0
12.5	55.93	4.85			24.0	9.79	20.37	0.99	0.47
13.0	51.60	11.94			24.5	8.88	19.32	1.06	0.96
13.5	47.26	17.94			25.0	8.30	18.13	1.05	0.95
14.0	44.46	22.97			27.0	5.57	13.77	0.87	1.52
14.5	42.44	26.14			29.0	4.13	11.03	0.71	1.70
15.0	39.67	29.26			31.0	2.94	8.65	0.56	1.80
15.5	37.64	32.42			33.0	2.16	7.20	0.64	1.74
16.0	34.65	35.96			35.0	1.62	5.98	0.56	1.55
16.5	32.53	37.95			37.0	1.33	5.25	0.55	1.56
17.0	30.48	38.41			39.0	1.03	4.74	0.59	1.44
17.5	28.46	36.92			41.0	0.86	3.84	0.55	1.27
18.0	26.11	36.02			43.0	0.82	3.47	0.60	1.41
18.5	24.40	33.86			45.0	0.64	3.09	0.53	1.55
19.0	23.17	33.17			47.0	0.60	2.55	0.53	1.42
19.5	21.85	32.20	0		49.0	0.53	2.39	0.52	1.44
20.0	20.04	30.95	0.18						

<sup>a</sup>Estimates obtained from a consideration of the partial oscillator strengths for the molecular and dissociative photoionization of CH<sub>3</sub>I using the dipole induced breakdown scheme derived in section 6.5.3.

See text for details (section 6.5.3).

<sup>b</sup> $\sigma(\text{Mb})=109.75 df/dE$  ( $\text{eV}^{-1}$ ).

Table 6.13: The single and double<sup>a,b</sup> photoionization branching ratios and partial differential oscillator strengths of methyl iodide at 41 eV.

Fragment Ion	Single Photoionization $\eta_i = 1.00$		Single Photoionization $\eta_i = 1.06^a$		Double Photoionization	
	Branching Ratio	POS ( $10^{-2}\text{eV}^{-1}$ ) <sup>c</sup>	Branching Ratio	POS ( $10^{-2}\text{eV}^{-1}$ ) <sup>c</sup>	Branching Ratio <sup>b</sup>	POS <sup>b</sup> ( $10^{-2}\text{eV}^{-1}$ ) <sup>c</sup>
CH <sub>3</sub> I <sup>+</sup>	12.6	0.86	12.6	0.91	0	0
CH <sub>2</sub> I <sup>+</sup>	13.2	0.90	13.1	0.94	0.1	0.01
CHI <sup>+</sup>	3.1	0.21	3.1	0.20	0	0
CI <sup>+</sup>	2.2	0.15	2.1	0.15	0.1	0.005
I <sup>+</sup>	36.5	2.48	31.5	2.27	5.0	0.36
I <sup>2+</sup>	0	0	0	0	0	0
CH <sub>3</sub> <sup>+</sup>	22.1	1.50	19.6	1.41	2.5	0.18
CH <sub>2</sub> <sup>+</sup>	5.1	0.35	3.4	0.25	1.7	0.12
CH <sup>+</sup>	1.8	0.12	1.0	0.07	0.8	0.06
C <sup>+</sup>	0.9	0.06	0.6	0.04	0.3	0.02
H <sub>2</sub> <sup>+</sup>	0.15	0.01	0.09	0.006	0.06	0.004
H <sup>+</sup>	2.3	0.16	1.5	0.11	0.8	0.06
Total	100	6.80	88.6	6.39	11.4	0.82

<sup>a</sup>This estimate of the ionization efficiency was obtained from the PIPICO data reported by Dujardin *et al.* [313].

<sup>b</sup>The estimates of the abundance for each DPI channel were obtained from the PEPICO data of Eland *et al.* [314].

<sup>c</sup> $\sigma(\text{Mb})=109.75 df/dE$  ( $\text{eV}^{-1}$ ).

## Chapter 7

# Photoabsorption and Photoionization of Cyanogen Bromide

### 7.1 Introduction

Cyanogen halides have long been used as model systems to study reaction dynamics, including photodissociation processes in the vacuum ultraviolet (VUV) region [324]. The growing availability of UV and VUV lasers has also further kindled interest in the high-energy photochemistry of these molecules. Cyanogen halides have obvious advantages for dynamics investigations because the resulting CN fragments are formed in electronically excited states, which can readily be studied by their subsequent emission. In this regard Kanda *et al.* [325] have recently pointed out the importance of obtaining improved quantitative information on their VUV photoabsorption spectra, particularly for the high-lying electronic states. Kanda *et al.* [325] have reviewed the BrCN photoabsorption data existing up to 1993.

There have been relatively few studies [244, 325–330] of the valence shell electronic absorption spectra of BrCN at UV and shorter wavelengths and only recently have any detailed absolute valence shell measurements been reported. No photoabsorption spectra have been published for inner-shell excitation processes in BrCN. High resolution UV electronic absorption spectra of ClCN, BrCN, and ICN measured in the 1250 to 2600 Å (4.8 to 9.9 eV) region together with a review of earlier work were published by King and Richardson in 1966 [326]. The second paper published by the same authors [326] in 1966 presented a detailed

analysis and assignment of the discrete structures in the B and C band systems of the three cyanogen halides. While most of the earlier studies reported only relative intensities, the A band oscillator strength for BrCN vapour ( $\lambda_{max} \sim 1990 \text{ \AA}$  or 6.23 eV) was estimated [326] to be  $2.5 \times 10^{-3}$ . It should be noted that the  $\alpha$  band of BrCN reported by King and Richardson [326] was later shown by Felps *et al.* [244] to be anomalous and in fact the  $\alpha$  band is located at significantly shorter wavelengths. King and Richardson [326] also estimated the oscillator strength of the B and C bands to be in the range of  $10^{-1}$  to  $10^{-2}$ , but no specific numerical data values were given for the various transitions.

Following the pioneering work of King and Richardson [326] several further spectral analyses and experimental studies of the electronic spectrum of BrCN have been published [244, 325, 327–330]. Of particular note are the absolute high resolution photoabsorption spectra of ClCN, BrCN, and ICN reported by Felps *et al.* in 1991 [244] in the 4 to 11.8 eV (3100 to 1050  $\text{\AA}$ ) region. In the case of BrCN the spectrum consists of two low energy, weak, and largely featureless continua (the A and  $\alpha$  bands) in the 2600 to 1600  $\text{\AA}$  (4.8 to 7.8 eV) region with more intense discrete structure (the B and C systems) located above 7.8 eV to the limit of the measured data in the vicinity of the LiF cut-off at  $\sim 11.8$  eV. Felps *et al.* [244] provided estimates of the oscillator strength for a number of the discrete excitations. The only other absolute photoabsorption studies of BrCN are the earlier measurements of the B and C bands in the 7.3 to 11.8 eV region reported by West [328] in 1975 (which are shown graphically, but not numerically, in the review of Ashfold *et al.* [324]) and the similar spectra (8.1 to 14.3 eV) recently published by Kanda *et al.* [325]. Although no numerical values of the absolute cross-section (oscillator strength) are given by Kanda *et al.* [325] they state that their values are  $\sim 20\%$  higher than previously reported data [244, 324, 328]. Kanda *et al.* [325] have also studied the emission polarization anisotropy to provide information on the symmetry of the upper electronic states and to aid in the spectral assignments. The detailed study by Felps *et al.* [244] located the correct position of the  $\alpha$  band and otherwise supports

the earlier assignments given by King and Richardson [326] rather than those proposed by Rabalais *et al.* [327]. As was pointed out by Kanda *et al.* [325], the assignment of the extensive valence shell Rydberg structure remains in question because regular Rydberg series cannot be identified. The complexities of assigning the BrCN spectrum, including the problem of Rydberg/valence mixing at lower energies, have also been discussed by Ashfold *et al.* [324].

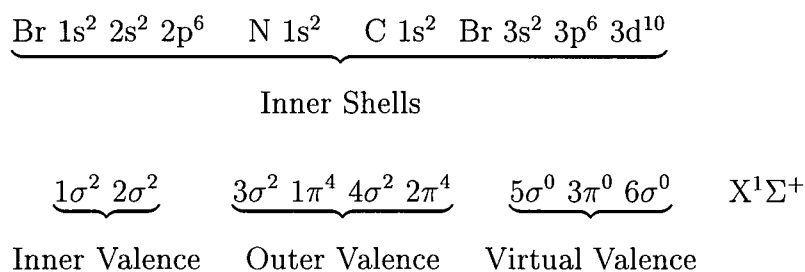
The He I photoelectron spectrum of BrCN has been reported in the literature [331–334] and from these studies the outer valence ionization potentials are well known. To date no experimental investigations of the inner valence ionization of BrCN have been carried out. The only information including the inner valence region of BrCN is the Green's Function calculation of the entire valence shell photoelectron spectrum of BrCN by von Niessen and Cambi [335]. No experimental values for any of the inner-shell (core) IP's of BrCN have been published nor have any oscillator strength calculations been reported for any electronic transitions in BrCN.

In this chapter the absolute photoabsorption oscillator strength spectrum of BrCN, recorded using low resolution ( $\sim 1$  eV) dipole (e,e) spectroscopy from 5 to 451 eV, is reported. In addition, the high resolution absolute photoabsorption spectrum has been recorded in the valence region from 4 to 50 eV (0.05 eV fwhm), in the Br 3d region from 65 to 85 eV (0.1 eV fwhm), and in the C and N 1s regions from 280 to 310 eV (0.1 eV fwhm) and from 390 to 420 eV (0.1 eV fwhm), respectively. The absolute photoabsorption measurements are extended to the molecular and dissociative photoionization channels resulting from photoabsorption in the VUV and soft X-ray regions over the equivalent photon energy range 11.5 to 160 eV, which covers the valence shell and Br 3d regions of excitation and ionization. Using dipole (e,e+ion) spectroscopy the absolute partial differential oscillator strengths for molecular and dissociative photoionization of BrCN have been measured from 11.5 to 160 eV. Furthermore, PIPICO studies of BrCN using synchrotron radiation have been made in order

to investigate the production and decomposition of doubly and triply charged ions arising from valence shell and Br 3d photoabsorption processes.

## 7.2 Electronic Structure

The molecular orbital configuration of the ground electronic state of cyanogen bromide in the independent particle model can be written as:



The vertical ionization potentials (VIPs) of the outer valence orbitals have been determined to be 11.88, 12.07, 13.58, 14.40, and 18.07 eV for the  $2\pi_{\frac{3}{2}}$ ,  $2\pi_{\frac{1}{2}}$ ,  $4\sigma$ ,  $1\pi$ , and  $3\sigma$  orbitals, respectively, by photoelectron spectroscopy (PES) [331, 332]. Green's Function calculations [335] support this ordering. No IP measurements have been reported for the inner valence orbitals of BrCN. Green's Function calculations performed on the entire valence shell region of BrCN by von Niessen and Cambi [335] indicate that very little splitting from electron correlation occurs in the outer valence bands, but that both the  $2\sigma$  and  $1\sigma$  inner-valence bands are severely split by electron correlation effects. The main pole of the  $2\sigma$  band is predicted to be at 28.4 eV carrying 70% of the intensity while the  $1\sigma$  band is split into several significant poles with 7% of the intensity at 25.05 eV and 64% of the intensity occurring from 31.89 to 33.31 eV. To the best of our knowledge no measurements or calculations of the inner-shell (core) IP's of BrCN have been published.

## 7.3 Results and Discussion

### 7.3.1 Low resolution photoabsorption (5 to 451 eV)

The absolute photoabsorption oscillator strength spectrum of cyanogen bromide measured in the present work from 5 to 451 eV using dipole (e,e) spectroscopy at a resolution of 1 eV fwhm is shown in figures 7.1(a) and (b). The corresponding numerical data are given in table 7.1. The wide range low resolution spectrum provides a 'global' view of the valence shell (figure 7.1(a)) and the Br 3d, 3p, and 3s, the C 1s and the N 1s (figure 7.1(b)) oscillator strength distributions in the absolute photoabsorption spectrum. Pre-edge structures resulting from excitation are seen in the valence and inner shell regions. However, the spectral details in the respective valence and inner shell discrete excitation regions are only seen in the higher resolution spectra (see sections 7.3.2 and 7.3.3 below). The positions of the inner shell ionization edges were estimated as described in section 7.3.3 below.

The low threshold ( $\sim 69$  eV) of the Br 3d spectrum results in only a very short valence shell fitting range (41–68 eV) for VTRK sum-rule normalization of the spectrum, thus a much longer (69 eV– $\infty$ ) valence shell extrapolation is required for BrCN than for most other dipole (e,e) studies to date. This situation is therefore ideally suited for normalization using  $S(-2)$ -based methods. Unfortunately no experimental values of the static or dynamic dipole polarizability for BrCN have been published. Thus, the absolute oscillator strength scale had to be established using the valence-shell TRK sum-rule [11] by normalizing the total area under the valence shell Bethe-Born converted electron energy loss spectrum to a total oscillator strength of 16.835. The value corresponds to the 16 valence shell electrons in BrCN plus a small estimated contribution due to Pauli excluded transitions [98, 99]. The area under the valence shell spectrum above 68 eV (the onset of the Br 3d spectrum - see fig 7.7) was estimated by fitting the polynomial given in equation (3.2) to the relative oscillator strength data from 41 to 68 eV and integrating to infinite energy. The best fit

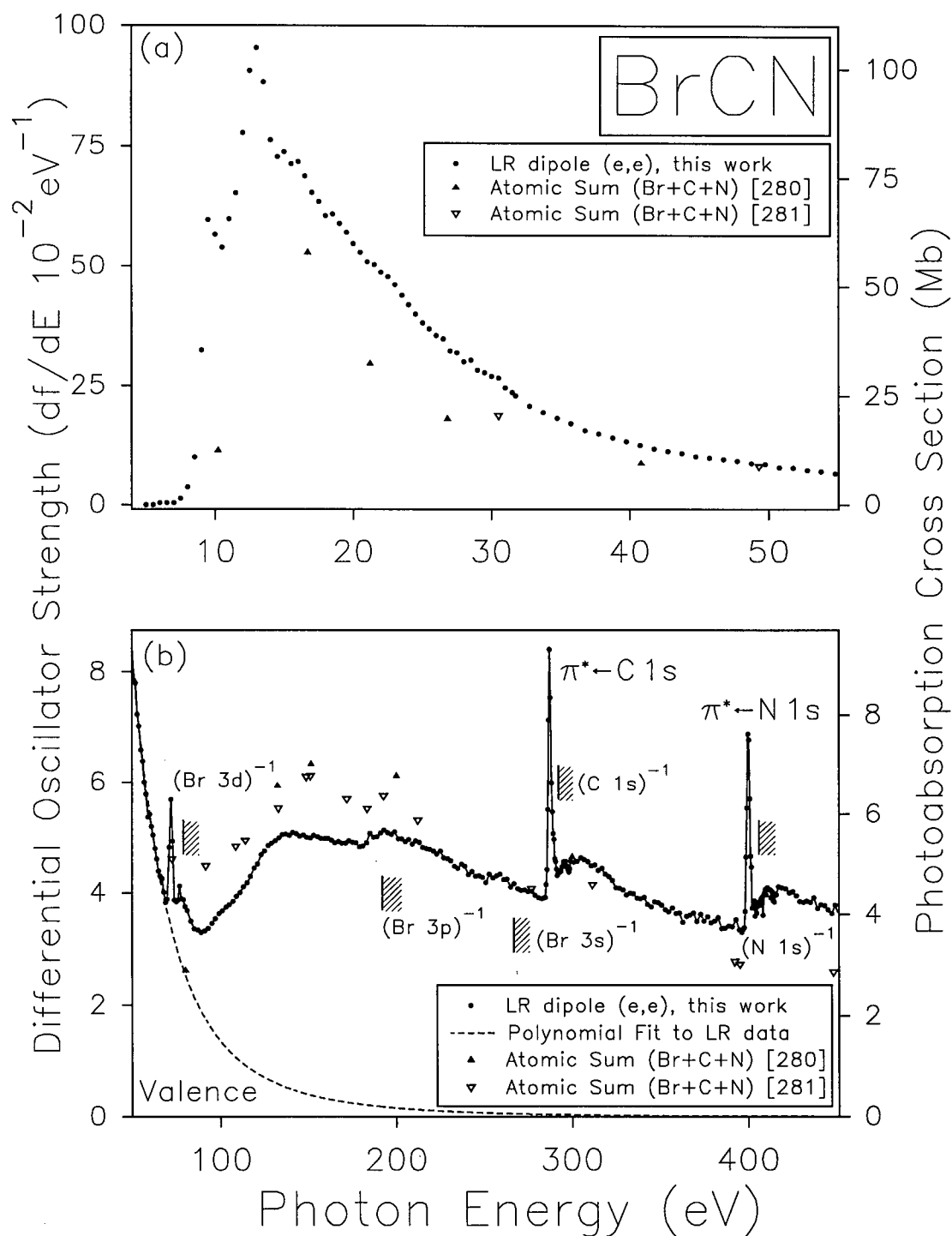


Figure 7.1: Absolute low resolution (1 eV fwhm) photoabsorption oscillator strength (5-451 eV) spectrum of BrCN. (a) The valence shell region from 5 to 55 eV. (b) The high energy inner shell region (50-451 eV). Also shown are previously published theoretical [280] and experimental [281] summed (C + N + Br) atomic oscillator strengths. The dashed line above 68 eV represents the polynomial fit to the valence shell continuum (see text for details).

parameters from equation (3.2) were determined to be  $A = -33.83$  eV,  $B = 2.18 \times 10^4$  eV<sup>2</sup>,  $C = -4.93 \times 10^5$  eV<sup>3</sup>. The area under the fitted polynomial from 68 eV to infinite energy was 7.79% of the total valence shell area. The fitted valence shell polynomial is shown by the dashed line in figure 7.1(b) from 68 to 451 eV.

The  $S(-2)$  sum for cyanogen bromide obtained from the absolute low resolution dipole (e,e) photoabsorption spectrum is 39.15 au. Unfortunately there are no experimental measurements of the dipole polarizability of BrCN with which to compare. However, the experimental value obtained in the present work compares quite favorably with a value of 42.45 au calculated in the present work by the finite field method [176, 180, 336, 337]. Calculations of the total energies were carried out using Hondo [338] at the MP2 level using triply augmented double zeta basis sets, in a fashion similar to the calculations conducted by Archibong and Thakkar [180] on Br<sub>2</sub>. Realizing that the most crucial point in the calculation of the dipole polarizability is the basis set, the choice of basis set was made with the important restriction of keeping it balanced for all atoms [182] and then augmenting it with diffuse functions until a converged dipole polarizability was obtained. The most functional basis set available for Br was the (63311/5311/41) basis set ((14s10p5d)/[5s4p2d]) produced by Ahlrichs [339] which is double zeta quality. Dunning's cc-pvdz double zeta basis sets [340] were used for carbon and nitrogen. To balance the Br basis set an f function was added with an exponent of 0.2780. Successive diffuse functions were added in a geometric progression to augment the basis sets until three functions of s, p, and d-type were added to both the carbon (exponents were s: 0.0638, 0.0255, 0.0102; p: 0.0607, 0.0243, 0.0097; d: 0.2200, 0.0880, 0.0352) and nitrogen (exponents were s: 0.0899, 0.0360, 0.0144; p: 0.0874, 0.0350, 0.0140; d: 0.3268, 0.1307, 0.0523) and three functions of s, p, d and f-type were added to bromine (exponents were s: 0.0520, 0.0208, 0.0083; p: 0.0628, 0.0251, 0.0101; d: 0.2780, 0.1110, 0.0450; f: 0.1110, 0.0450, 0.0178). Convergence was achieved in the dipole polarizability by the triple augmentation level. The calculated dipole polarizability was 60.08 a.u. along the bond axis and 33.63 a.u.

in the perpendicular direction which gives a dipole polarizability of 42.45 a.u. averaged over all directions.

The present photoabsorption oscillator strength measurements are compared with theoretical [280] and experimental [281] atomic oscillator strength sums (C + N + Br) in figures 7.1(a) and (b). As expected the atomic sum provides a poor estimate of the valence shell oscillator strength, particularly in the near threshold region below 40 eV, where molecular effects will be most prominent. Somewhat better agreement is obtained in the more "atomic-like" inner shell continuum regions of the spectrum. Prominent structures in the Br 3d, 3p, 3s, C 1s, and N 1s inner shell excitation and ionization regions are shown in figure 7.1(b). It can be seen that the summed atomic oscillator strengths provide a reasonable prediction of the spectrum in the region above 50 eV except in the Br 3d continuum region from 100 to 200 eV where the atomic sum is 20% too high.

Table 7.1: Absolute differential oscillator strengths for the total photoabsorption of BrCN from 5 to 451 eV.

Photon Energy eV	Oscillator Strength ( $10^{-2}$ eV $^{-1}$ ) <sup>a</sup>	Photon Energy eV	Oscillator Strength ( $10^{-2}$ eV $^{-1}$ )	Photon Energy eV	Oscillator Strength ( $10^{-2}$ eV $^{-1}$ )	Photon Energy eV	Oscillator Strength ( $10^{-2}$ eV $^{-1}$ )
5.00	0.00	23.50	43.77	51.75	7.80	97.00	3.53
5.50	0.00	24.00	41.75	52.75	7.24	99.00	3.63
6.00	0.37	24.50	39.82	53.75	7.02	101.00	3.68
6.50	0.41	25.00	38.01	54.75	6.60	103.00	3.75
7.00	0.43	25.50	36.76	55.75	6.39	105.00	3.79
7.50	1.36	26.00	35.43	56.75	6.00	107.00	3.85
8.00	3.71	26.50	34.79	57.75	5.79	109.00	3.94
8.50	10.09	27.00	32.25	58.75	5.37	111.00	4.00
9.00	32.42	27.50	31.87	59.75	5.42	113.00	4.11
9.50	59.68	28.00	30.00	60.75	5.20	115.00	4.19
10.00	56.66	28.50	30.36	61.75	5.04	117.00	4.30
10.50	53.99	29.00	28.24	62.75	4.79	119.00	4.45
11.00	59.79	29.50	27.74	63.75	4.61	121.00	4.52
11.50	65.28	30.00	26.93	64.75	4.40	123.00	4.69
12.00	77.81	30.50	26.56	65.75	4.30	125.00	4.75
12.50	90.74	31.00	24.50	66.75	4.26	127.00	4.85
13.00	95.49	31.50	23.57	67.75	4.02	129.00	4.89
13.50	88.39	31.75	22.93	68.75	3.83	131.00	4.94
14.00	76.29	32.75	20.77	69.75	3.89	133.00	4.99
14.50	72.75	33.75	19.42	70.75	4.82	135.00	5.04
15.00	73.81	34.75	18.26	71.75	5.69	137.00	5.06
15.50	71.32	35.75	17.11	72.75	4.93	139.00	5.03
16.00	71.78	36.75	15.64	73.75	3.88	141.00	5.09
16.50	68.77	37.75	14.97	74.75	3.84	143.00	5.06
17.00	65.31	38.75	14.10	75.75	3.87	145.00	5.02
17.50	63.45	39.75	13.32	76.75	4.12	147.00	5.04
18.00	60.50	40.75	12.61	77.75	3.89	149.00	5.00
18.50	60.89	41.75	11.84	78.75	3.88	151.00	4.99
19.00	58.87	42.75	11.31	79.75	3.75	153.00	5.03
19.50	57.09	43.75	10.89	81.00	3.69	155.00	5.01
20.00	54.76	44.75	10.17	83.00	3.49	157.00	4.98
20.50	52.94	45.75	9.93	85.00	3.36	159.00	4.98
21.00	50.92	46.75	9.58	87.00	3.33	161.00	4.98
21.50	50.32	47.75	9.24	89.00	3.29	163.00	4.94
22.00	48.61	48.75	8.72	91.00	3.32	165.00	4.90
22.50	47.67	49.75	8.52	93.00	3.37	167.00	4.92
23.00	45.96	50.75	7.85	95.00	3.45	169.00	4.89

Table 7.1: (continued) Absolute differential oscillator strengths for the total photoabsorption of BrCN from 5 to 451 eV.

Photon Energy eV	Oscillator Strength ( $10^{-2} \text{ eV}^{-1}$ ) <sup>a</sup>	Photon Energy eV	Oscillator Strength ( $10^{-2} \text{ eV}^{-1}$ )	Photon Energy eV	Oscillator Strength ( $10^{-2} \text{ eV}^{-1}$ )	Photon Energy eV	Oscillator Strength ( $10^{-2} \text{ eV}^{-1}$ )
171.00	4.89	245.00	4.31	292.75	4.37	347.00	3.84
173.00	4.94	247.00	4.31	293.25	4.40	349.00	3.83
175.00	4.91	249.00	4.28	293.75	4.39	351.00	3.78
177.00	4.90	251.00	4.19	294.25	4.47	353.00	3.70
179.00	4.82	253.00	4.34	294.75	4.49	355.00	3.66
181.00	4.84	255.00	4.27	295.25	4.56	357.00	3.73
183.00	4.90	257.00	4.31	295.75	4.55	359.00	3.64
185.00	5.07	259.00	4.34	296.25	4.57	361.00	3.64
187.00	5.01	261.00	4.24	296.75	4.47	363.00	3.48
189.00	5.01	263.00	4.25	297.25	4.49	365.00	3.58
191.00	5.08	265.00	4.11	297.75	4.42	367.00	3.60
193.00	5.13	267.00	4.17	298.25	4.38	369.00	3.64
195.00	5.09	269.00	4.08	298.75	4.44	371.00	3.49
197.00	5.06	271.00	4.05	299.25	4.57	373.00	3.62
199.00	5.10	273.00	4.06	301.00	4.56	375.00	3.50
201.00	4.97	275.00	4.03	303.00	4.57	377.00	3.57
203.00	4.97	277.00	4.04	305.00	4.63	379.00	3.47
205.00	4.92	279.00	3.96	307.00	4.60	381.00	3.50
207.00	4.96	281.00	3.92	309.00	4.56	383.00	3.56
209.00	4.88	283.00	3.91	311.00	4.49	385.00	3.37
211.00	4.94	284.25	3.91	313.00	4.50	387.00	3.37
213.00	4.91	284.75	3.92	315.00	4.41	389.00	3.41
215.00	4.81	285.25	4.16	317.00	4.45	391.00	3.39
217.00	4.79	285.75	4.42	319.00	4.34	393.00	3.52
219.00	4.78	286.25	5.51	321.00	4.30	395.00	3.34
221.00	4.75	286.75	7.14	323.00	4.23	396.25	3.30
223.00	4.70	287.25	8.41	325.00	4.09	396.75	3.34
225.00	4.75	287.75	7.54	327.00	4.09	397.25	3.36
227.00	4.63	288.25	5.99	329.00	4.06	397.75	3.38
229.00	4.61	288.75	5.47	331.00	3.97	398.25	3.67
231.00	4.58	289.25	5.07	333.00	4.00	398.75	4.64
233.00	4.48	289.75	4.97	335.00	3.99	399.25	5.54
235.00	4.44	290.25	4.61	337.00	3.91	399.75	6.88
237.00	4.52	290.75	4.56	339.00	3.90	400.25	6.78
239.00	4.48	291.25	4.43	341.00	3.92	400.75	5.70
241.00	4.34	291.75	4.32	343.00	3.80	401.25	4.66
243.00	4.38	292.25	4.36	345.00	3.75	401.75	4.47

Table 7.1: (continued) Absolute differential oscillator strengths for the total photoabsorption of BrCN from 5 to 451 eV.

Photon Energy eV	Oscillator Strength ( $10^{-2} \text{ eV}^{-1}$ ) <sup>a</sup>	Photon Energy eV	Oscillator Strength ( $10^{-2} \text{ eV}^{-1}$ )	Photon Energy eV	Oscillator Strength ( $10^{-2} \text{ eV}^{-1}$ )	Photon Energy eV	Oscillator Strength ( $10^{-2} \text{ eV}^{-1}$ )
402.25	3.73	408.25	3.60	414.25	3.86	433.00	3.86
402.75	3.75	408.75	3.97	414.75	3.84	435.00	3.84
403.25	3.86	409.25	4.01	415.25	3.99	437.00	3.92
403.75	3.59	409.75	4.07	415.75	3.97	439.00	3.73
404.25	3.81	410.25	3.97	417.00	4.12	441.00	3.79
404.75	3.64	410.75	4.11	419.00	4.09	443.00	3.78
405.25	3.76	411.25	4.06	421.00	4.08	445.00	3.70
405.75	3.79	411.75	4.07	423.00	4.01	447.00	3.64
406.25	3.84	412.25	4.07	425.00	4.03	449.00	3.79
406.75	3.78	412.75	3.92	427.00	3.95	451.00	3.60
407.25	3.89	413.25	4.04	429.00	3.85		
407.75	3.93	413.75	3.96	431.00	3.84		

<sup>a</sup> $\sigma(\text{Mb})=109.75df/dE(\text{eV}^{-1})$ .

### 7.3.2 High resolution valence shell photoabsorption (4 to 50 eV)

The high-resolution (0.05 eV fwhm) absolute valence shell photoabsorption spectrum of BrCN from 4 to 50 eV is shown in overview in figure 7.2(a). Discrete features can be seen up to  $\sim 17$  eV, i.e. below the IP of the most tightly bound ( $3\sigma$ ) outer valence orbital. At higher energies a smooth continuum monotonically decreases with no evidence of structures preceding the  $2\sigma$  and  $1\sigma$  inner valence [335] ionization regions. The dense discrete structure associated with transitions to virtual-valence and Rydberg orbitals below  $\sim 14$  eV is shown in more detail in figures 7.2(b), 7.3(a) and 7.3(b). The observed features are consistent with those seen in the earlier high resolution direct photoabsorption spectra reported by Felps *et al.* [244], Kanda *et al.* [325], and West [324, 328].

The absolute oscillator strengths obtained from figures 7.2 and 7.3 in selected regions (by either Gaussian fits or integration over selected energy ranges) are shown in table 7.2 and compared with the few earlier published [244, 326] absolute values that are available. The A band, which extends over the 5 to 7 eV region, arises from the lowest energy ( $5\sigma \leftarrow 2\pi$ ) virtual valence transition [244, 326]. The presently determined oscillator strength of  $3.1 \times 10^{-3}$  for this transition is consistent with the earlier estimates of  $2.5 \times 10^{-3}$  [326] and  $2.6 \times 10^{-3}$  [244]. The only numerical estimates of absolute oscillator strengths at higher energies are those reported by Felps *et al.* [244] and a comparison of these with the present values (table 7.2) shows quite good quantitative agreement in the cases of the extremely broad A and  $\alpha$  virtual-valence bands. However, for the much sharper [244, 325] Rydberg structures in the B, C,  $\beta$  and np bands the presently obtained dipole (e,e) values are significantly larger (by as much as a factor of 2 for the B and C bands) than those of the higher resolution direct photoabsorption work of Felps *et al.* [244]. The good agreement for the broad A and  $\alpha$  bands together with the much smaller direct optical values for the sharp Rydberg transitions strongly suggests that line saturation effects (see chapter 1) are causing appreciable errors in the Rydberg

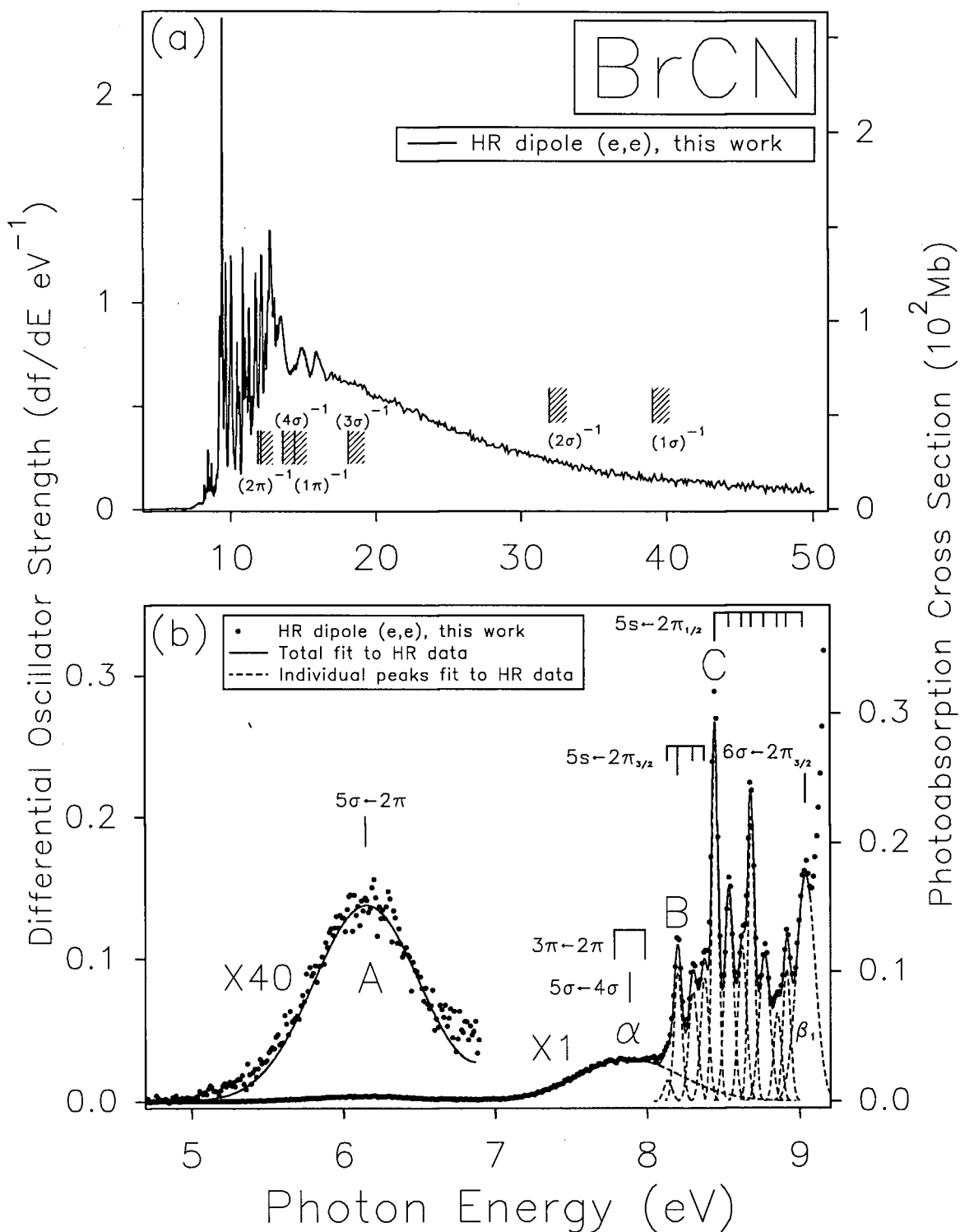


Figure 7.2: Absolute photoabsorption oscillator strength spectrum for the valence shell of BrCN at high resolution (0.05 eV fwhm). (a) Valence shell spectrum from 4 to 51 eV. (b) Expanded view showing the discrete region from 4 to 9.2 eV. Assignments are taken from Felps *et al.* [244] and Kanda *et al.* [325]. Ionization potentials are taken from references [331, 332].

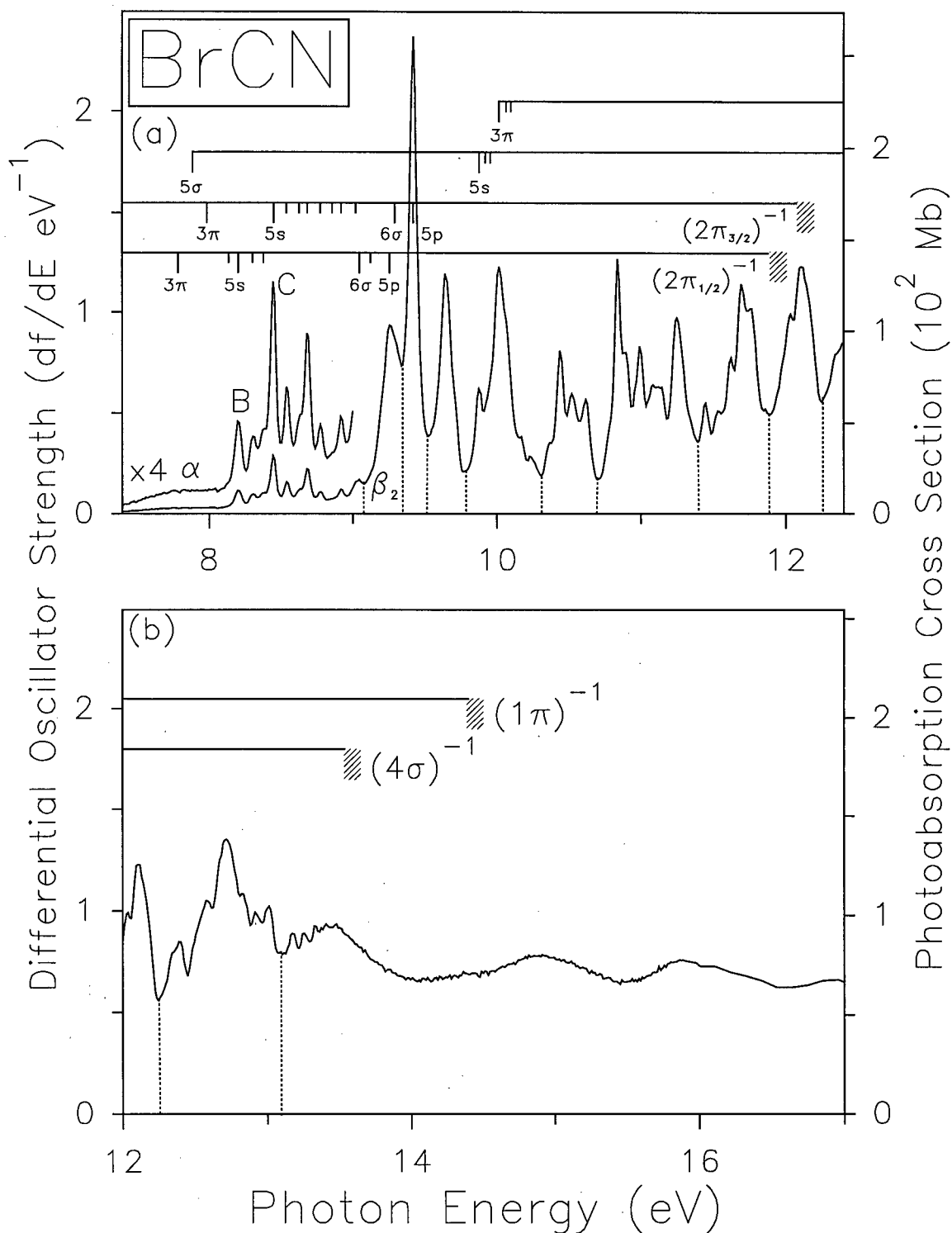


Figure 7.3: Absolute photoabsorption oscillator strength spectrum (7.5-17 eV) for the valence shell of BrCN at high resolution (0.05 eV fwhm). Assignments in the lower energy region (below about 10.5 eV) are taken from the assignments proposed by Felps *et al.* [244] and by Kanda *et al.* [325]. Ionization potentials are taken from references [331, 332]. The dashed lines indicate the integration regions used in table 7.2.

Table 7.2: Absolute oscillator strengths for selected regions of the valence shell photoabsorption spectrum of BrCN.

Main Peak Energy (eV) (Energy Range)	Band System	Oscillator Strength ( $10^{-2}$ )		
		This Work	ref [244]	ref [325]
6.15 (5-7) <sup>a</sup>	A ( $5\sigma \leftarrow 2\pi$ )	0.31	0.26	0.25
7.9 (7-9) <sup>a</sup>	$\alpha$ ( $3\pi \leftarrow 2\pi$ ) ( $5\sigma \leftarrow 4\sigma$ )	2.54	2.5	
8.20 <sup>a</sup>	B (origin) ( $5s \leftarrow 2\pi_{\frac{3}{2}}$ )	0.61	0.45	
8.45 <sup>a</sup>	C (origin) ( $5s \leftarrow 2\pi_{\frac{1}{2}}$ )	1.49	1.10	
(8.14-8.38) <sup>a</sup>	B (bands) ( $5s \leftarrow 2\pi_{\frac{3}{2}}$ )	2.05	0.95	
(8.45-8.91) <sup>a</sup>	C (bands) ( $5s \leftarrow 2\pi_{\frac{1}{2}}$ )	6.41	3.38	
(8.14-8.91) <sup>a</sup>	B + C (bands)	8.46	4.33	
9.04 <sup>a</sup>	$\beta_1$ (bands)	2.65	2.03	
9.26 (9.08-9.34) <sup>b</sup>	$\beta_2$ (bands)	15.06	9.41	
9.43 (9.34-9.52) <sup>b</sup>	intense np Rydberg	20.95	11.1	
(9.52-9.78) <sup>b</sup>		16.31		
(9.78-10.31) <sup>b</sup>		28.75		
(10.31-10.70) <sup>b</sup>		17.85		
(10.70-11.40) <sup>b</sup>		43.93		
(11.40-11.89) <sup>b</sup>		32.93		
(11.89-12.25) <sup>b</sup>		31.06		
(12.25-13.10) <sup>b</sup>		81.35		

<sup>a</sup>Area obtained from fitted gaussian shown on figure 7.2.

<sup>b</sup>Area obtained from integrating spectrum for limits given in column 1 and shown on figure 7.3.

oscillator strengths reported in the photoabsorption work of Felps *et al.* [244].

### 7.3.3 Low and high resolution inner shell photoabsorption

An overview of the low resolution (1 eV fwhm) absolute photoabsorption spectrum of BrCN in the valence, Br 3d, 3p and 3s, C 1s and N 1s regions has already been shown in figure 7.1(b). The inner shell spectral region is shown in more detail in figure 7.4 with the valence shell contribution subtracted (which was determined by the curve fitting procedure described in section 7.3.1). Sharp structures caused by inner shell excitation processes are apparent in the Br 3d, C 1s and N 1s pre-edge regions. In the present section limited range low resolution (1 eV fwhm) as well as more detailed high resolution spectra for each of the Br 3d (0.1 eV fwhm), C 1s and N 1s (0.15 eV fwhm) pre-edge discrete excitation regions are presented. The higher energy C 1s and N 1s spectra will be considered first because of their relative simplicity at the instrumental resolution used. The Br 3d spectra are complicated by both ligand field and spin-orbit splittings which are partially resolved at the experimental resolution of the spectra. As was stated in the introduction, no measurements of inner shell ionization potentials for BrCN have been reported in the literature, which limits the interpretation of the photoabsorption spectrum.

#### 7.3.3.1 C 1s and N 1s spectra

Expanded views of the C 1s and N 1s excitation and ionization regions of the low resolution (1 eV fwhm) absolute oscillator strength spectrum of BrCN are shown in figures 7.5(a) and (b). The positions of the respective ionization edges are estimated (see below). Sharp and relatively intense excitation features resulting from  $3\pi$  ( $\pi^*$ ) excitation from the 1s core orbitals dominate the discrete inner shell spectra. Appreciable oscillator strength contributions remain from the valence and lower energy inner shells as can be seen from the spectral regions preceding and underlying the sharp features (note offset oscillator strength

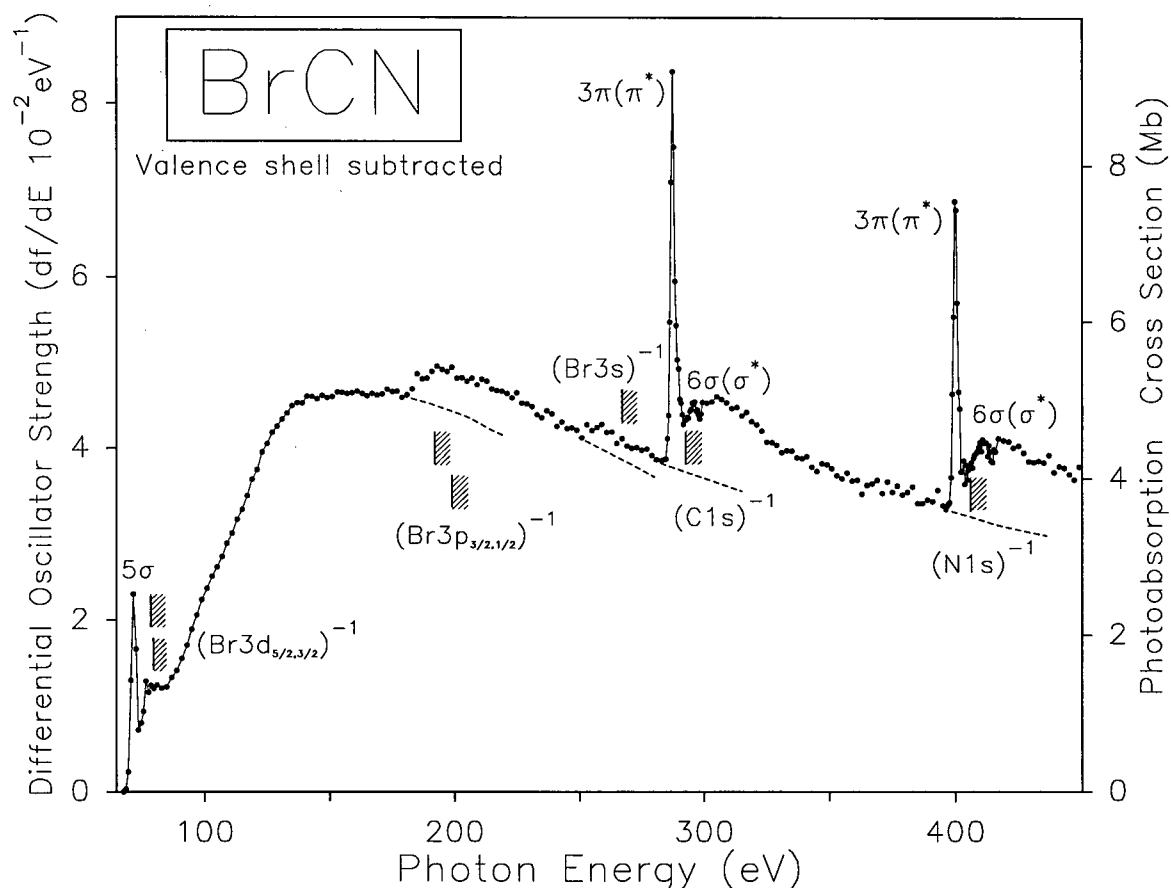


Figure 7.4: Absolute valence shell subtracted photoabsorption oscillator strength spectrum (65-451 eV) of the Br 3d, 3p, 3s, C 1s and N 1s regions of BrCN at low resolution (1 eV fwhm). Note that the underlying valence shell continuum has been subtracted according to the polynomial fit shown in figure 7.1(b).

scales on figures 7.5(a) and (b)). Shake-up transitions (i.e. simultaneous 1s ionization and valence excitation) as well as broad  $6\sigma$  ( $\sigma^*$ ) resonances are apparent in the ionization continua. The C 1s and N 1s spectra of BrCN are remarkably similar to those of CO and N<sub>2</sub> [82, 341] where the shape-resonant enhancement in both the ( $\pi^*$ ) and ( $\sigma^*$ ) channels is well understood [342-344].

High resolution (0.15 eV fwhm) absolute oscillator strength spectra, obtained as explained in section 3.3, are shown in figures 7.6(a) and (b) for the C 1s and N 1s pre-edge regions, respectively. Energy positions, term values and oscillator strengths for the various transitions

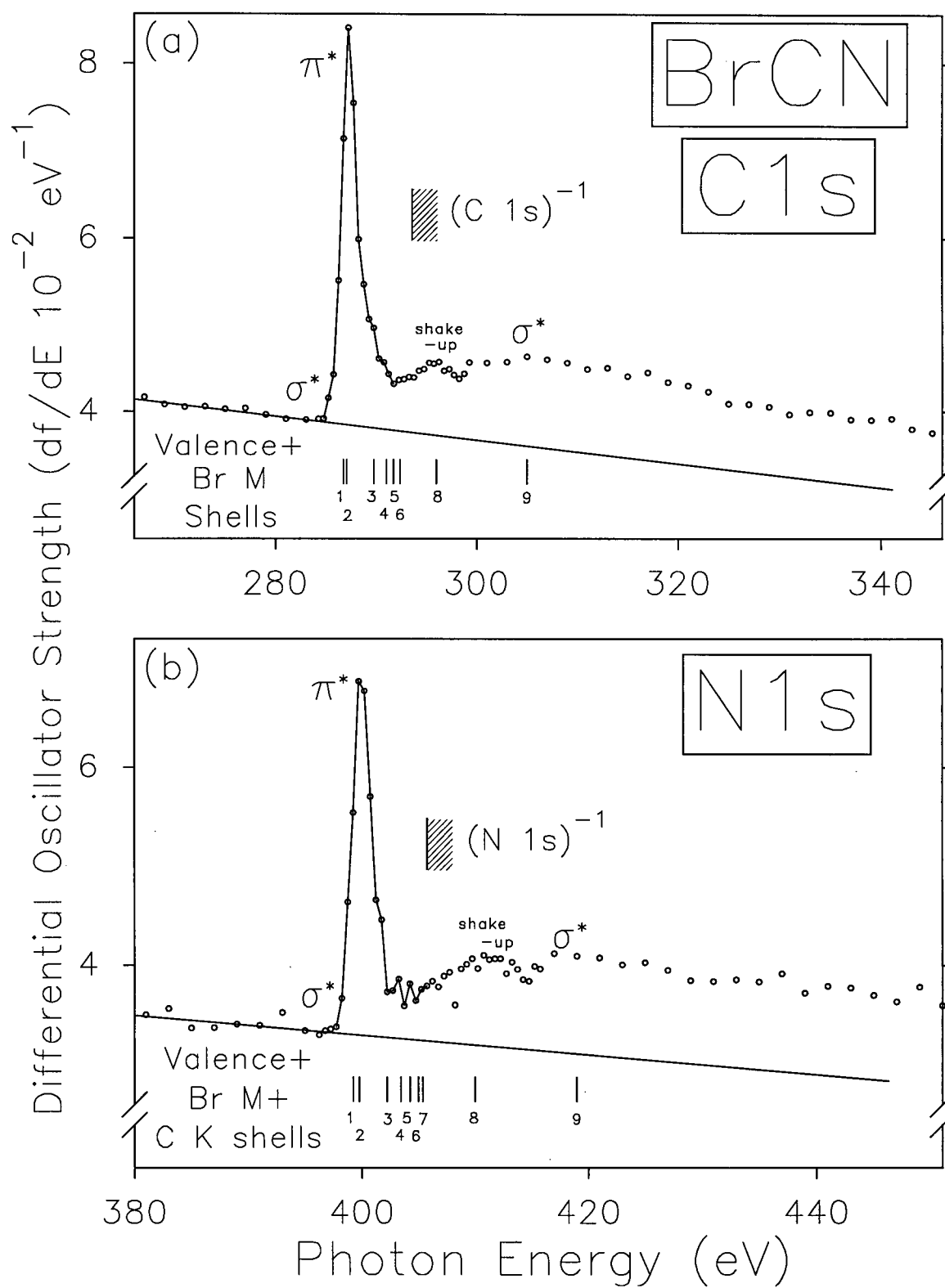


Figure 7.5: Absolute low resolution (1 eV fwhm) photoabsorption oscillator strength spectrum of BrCN. (a) The C 1s spectrum from 266 to 346 eV. (b) The N 1s spectrum from 380 to 451 eV. Note the offset oscillator strength scales.

are given in table 7.3. The large, relatively intense peaks observed at  $\sim 287$  eV and  $\sim 399$  eV in the low resolution spectra (figures 7.5(a) and (b)) are each seen to exhibit a broad shoulder on the low energy side and partially resolved fine structure on the high energy side. Each of these structures in the C 1s and N 1s high resolution spectra can be peak fitted, as shown on figure 7.6, into a broad featureless band at lower energy, which is the  $5\sigma(\sigma^*) \leftarrow 1s$  transition, and a more intense band resulting from the  $3\pi(\pi^*) \leftarrow 1s$  transition which has at least six vibrational ( $v_3$ ) components (spaced by  $\sim 0.25$  eV) associated with it. The spacing of this vibrational progression closely matches the  $v_3$  ground state vibrational mode of BrCN (0.272 eV) and of BrCN<sup>+</sup> (0.229 eV). The  $v_3$  vibrational mode is associated with the C-N stretch [333, 345]. The peak fits shown in figures 7.6(a) and (b) were achieved using a single gaussian peak shape for the  $5\sigma \leftarrow 1s$  transition and a Voigt profile for each of the six vibronic components of the  $3\pi \leftarrow 1s$  transition. This structure is similar to that observed in the  $\pi^*$  excitation in the high resolution inner shell spectra of CO, N<sub>2</sub> [341], and the metal carbonyls [346, 347]. In contrast to the  $3\pi \leftarrow 1s$  transitions, the  $5\sigma \leftarrow 1s$  final states (figure 7.6) show no evidence of vibration structure. Further information on the photoionization decay dynamics of these core excited states could be obtained by electron-ion coincidence [348, 349] and PIPICO [350] experiments. The oscillator strengths for the  $5\sigma \leftarrow 1s/3\pi \leftarrow 1s$  transitions are  $2.88 \times 10^{-2}/4.54 \times 10^{-2}$  and  $2.36 \times 10^{-2}/4.55 \times 10^{-2}$ , for the C 1s and N 1s spectra, respectively. These values are comparable to the more intense valence shell transitions of the B and C bands listed in table 7.2 and are quite large, presumably because of resonant enhancement [342-344].

Weak structures in the regions above the prominent C 1s and N 1s  $5\sigma/3\pi \leftarrow 1s$  resonances in figure 7.6 can be attributed to Rydberg transitions. Since symmetry restrictions will be relaxed in the inner shell spectra [351], both ns and np final states may be expected to contribute. As in the cases of CO, N<sub>2</sub> [82, 341] and other molecules [80, 346, 347, 351, 352] the Rydbergs are not resonantly enhanced. A broad resonance in each continuum (figure 7.5)

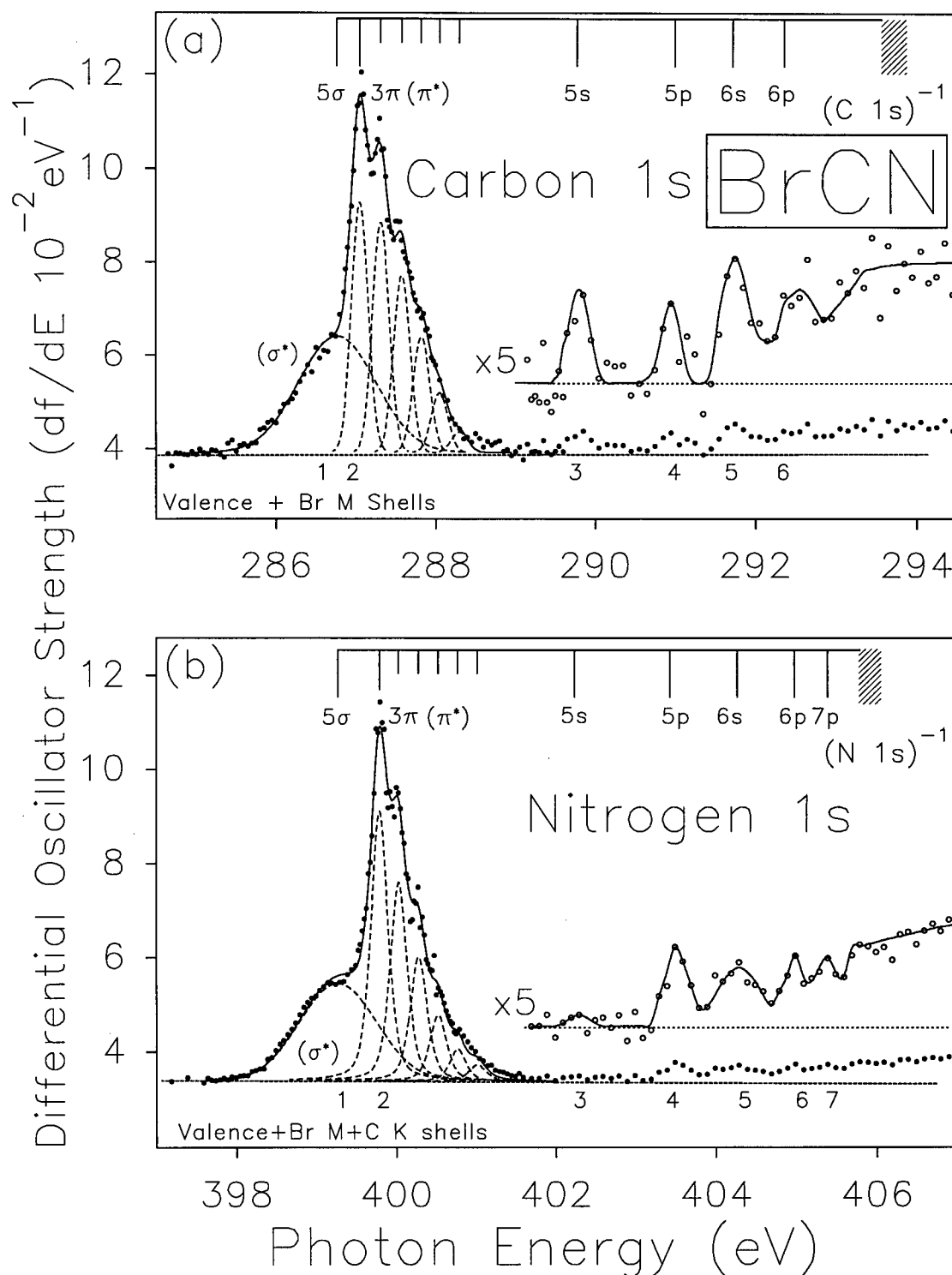


Figure 7.6: Absolute high resolution (0.15 eV fwhm) photoabsorption oscillator strength spectrum of BrCN. (a) The C 1s spectrum from 284.5 to 294.5 eV. (b) The N 1s spectrum from 397 to 407 eV. Dashed lines show the individual peaks fit to the high resolution data. Note the offset oscillator strength scales.

can be attributed to a transition from the respective 1s orbital to the unbound  $6\sigma(\sigma^*)$  virtual valence orbital (see figure 7.5).

Since no experimental core binding energies have been published for BrCN the C 1s and N 1s ionization energies have been calculated with the deMon [353] Density Functional Theory (DFT) programme using the transition state method as reported by Duffy and Chong [354]. Calculated values of the  $(1s)^{-1}$  ionization potentials using DFT for many molecules containing H and the second and third row p-block elements, for which measurements have been made, are typically found [355, 356] to be within a few tenths of an electron volt of the experimental determinations. Given that the experimental XPS measurements themselves have comparable uncertainties the DFT method [355, 356] can be considered to provide reasonably accurate values for inner shell IPs. The calculations [355, 356] were carried out using the Dunning's [357] quintuple zeta valence polarized (cc-pv5z) basis sets with auxiliary fitting functions for all atoms involved. Unfortunately, Dunning basis sets were not available for 4<sup>th</sup> or 5<sup>th</sup> row atoms (e.g bromine and iodine), but a basis set comparable to double zeta quality (63321/5321/41+) [338] was available for Br. To determine the effect that the mixing of basis sets for each individual atom had on the IP calculated, the calculations of Chong [355, 356] were repeated using a quintuple zeta basis set on the atom whose IP was being calculated, while using double zeta quality basis sets on all other atoms in the molecule (each atom was also supplemented with an auxiliary function). These produced excellent calculated IP's for C, N and O  $(1s)^{-1}$ , within 0.05 eV (0.02%) for a sample of 10 simple diatomic and polyatomic molecules. For example, this method produced IPs of 292.13 and 291.62 eV for methyl bromide and methyl iodide (experimental XPS [277] IPs are 292.12 and 291.43 eV, respectively) calculated using the cc-pv5z basis set on the carbon and hydrogen atoms, and using double zeta quality basis sets on bromine and iodine in the respective methyl halides. The C and N 1s IPs for BrCN were calculated using the Dunning cc-pv5z basis sets on the C and N atoms and the double zeta quality (63321/5321/41+) [353] basis set

Table 7.3: Energies, term values, oscillator strengths, and assignments of the C 1s and N 1s spectra of BrCN.

Feature	Carbon K-Shell			Average Term Value (eV)	Nitrogen K-Shell			Assignment
	Energy (eV)	Term Value (eV)	Oscillator Strength ( $10^{-2}$ )		Energy (eV)	Term Value (eV)	Oscillator Strength ( $10^{-2}$ )	
1	286.77	6.80	2.88		399.27	6.52	2.36	$5\sigma$
2	287.05	6.52	1.33		399.79	6.00	1.75	$3\pi$
	287.32		1.22		399.03		1.29	$3\pi v_3^1$
	287.58		0.94		400.28		0.80	$3\pi v_3^2$
	287.82		0.62		400.52		0.42	$3\pi v_3^3$
	288.05		0.32		400.77		0.19	$3\pi v_3^4$
	288.30		0.11		400.01		0.10	$3\pi v_3^5$
3	289.78	3.79		3.7	402.24	3.55		5s
4	291.0	2.57		2.5	403.43	2.36		5p
5	291.72	1.85		1.7	404.27	1.52		6s
6	292.36	1.21		1.0	404.98	0.81		6p
7					405.39	0.4		7p
IP	293.57 <sup>a</sup>				405.79 <sup>a</sup>			$\infty$
8	296				410			shake-up
9	305				419			$\sigma^*$

<sup>a</sup>Value estimated from DFT calculation (see section 7.3.3.1).

on the Br atom. Each atom was also supplemented with an auxiliary function, C (4,4;4,4), N (4,4;4,4) and Br (5,5;5,5), where the meaning of (j,k;m,n) is described elsewhere [358, 359]. The ionization potentials were estimated to be 293.57 eV for the C 1s and 405.79 eV for the N 1s from the DFT calculations. Given the above results, and the fact that quintuple zeta basis sets were used on two of the three atoms in BrCN, the ionization potentials reported here for both the C 1s and the N 1s of BrCN are considered to be accurate to within 0.1 to 0.2 eV.

The calculated C 1s and N 1s IPs for BrCN are shown in table 7.3. These IPs allow approximate term values for the transitions to be determined. The estimated term values and their average values for the C 1s and N 1s Rydberg states are also shown on table 7.3. The short lifetimes of the inner shell excited Rydberg states in the C 1s and N 1s energy regimes preclude observing the  $np\sigma$ / $np\pi$  ligand field splittings at the present energy resolution (0.1 eV fwhm), thus an intermediate  $np$  term value results. It can be seen from table 7.3 that the derived term values for corresponding Rydberg transitions (expected to be the same from transferability considerations [69]) show a systematic shift between the C 1s and N 1s spectra, those for the N 1s spectrum being lower by a few tenths of an eV than those for the C 1s spectrum. These differences likely arise from small errors in the DFT ionization potential calculations. The average (approximate) Rydberg term values of 3.67 (5s), 2.47 (5p), 1.69 (6s) and 1.01 eV (6p) shown in table 7.3 should be transferable (see section 2.5.1) and may therefore be used to assist in the interpretation of both the valence shell and the Br 3d spectra. These are reasonably consistent with the previously reported term values of 3.58–3.72 (5s) and 2.59–2.78 eV (5p) [329], 3.6 (5s) and 2.61–2.80 eV (5p) [324], 2.64–2.80 eV [244] and 2.64 eV (5p) [325]. The approximate Rydberg term values may also be used to provide an estimate of the Br 3d ionization energies of BrCN since no experimental values exist (see section 7.3.3.2 following).

### 7.3.3.2 Br 3d spectrum

Figure 7.7(a) shows the low resolution (1 eV fwhm) absolute photoabsorption spectrum of BrCN from 60 to 280 eV in the Br 3d, 3p and 3s regions. Prominent sharp structures from discrete excitation are visible below the Br 3d edges together with a large, broad continuum resonance ( $\epsilon f \leftarrow 3d$ ) at  $\sim 140$  eV (see section 2.5.2). Further continua and some indication of pre-edge excitation features are visible (see also figure 7.4) in the region of the Br 3p and 3s thresholds. The broad nature of these transitions is likely a result of the very short lifetime of these states, which would likely decay via fast (super) Coster-Kronig type processes to lower continua within the same (sub-) shell. Similar behavior has been observed in the CH<sub>3</sub>Br photoabsorption spectrum in the region of the Br 3p and 3s thresholds (see section 5.5.3). In an attempt to estimate the Br 3p and 3s ionization potentials the following procedure was used. Trends were observed in the behavior of the previously reported Br 3d ionization potentials of C<sub>6</sub>H<sub>5</sub>Br, C<sub>6</sub>H<sub>5</sub>Br and C<sub>2</sub>H<sub>3</sub>Br [277, 279]. These were compared to the Br 3d ionization potential derived in the present work (see below). The trends observed between those molecules and BrCN were then applied to the 3p and 3s ionization potentials of those molecules to estimate the ionization potentials for BrCN. The results were: Br 3p <sub>$\frac{3}{2}, \frac{1}{2}$</sub> , 192 and 199 eV; Br 3s, 276 eV. Note that the oscillator strength scales in figure 7.7 are offset from zero because of the underlying valence shell continuum.

The high resolution (0.1 eV fwhm) Br 3d oscillator strength spectrum from 69 to 82 eV, shown in figure 7.7(b), is rich with structures from transitions to virtual valence and Rydberg orbitals, as well as to the Br 3d <sub>$\frac{5}{2}, \frac{3}{2}$</sub>  continua. The presently measured high resolution oscillator strength spectrum was normalized to the low resolution oscillator strength spectrum in the smooth continuum region at 67 eV where no sharp structure existed. The Br 3d discrete region of the BrCN photoabsorption spectrum is composed of two regions. The region below 76.5 eV is comprised of broad peaks and the region above 76.5 eV is made up of sharp peaks.

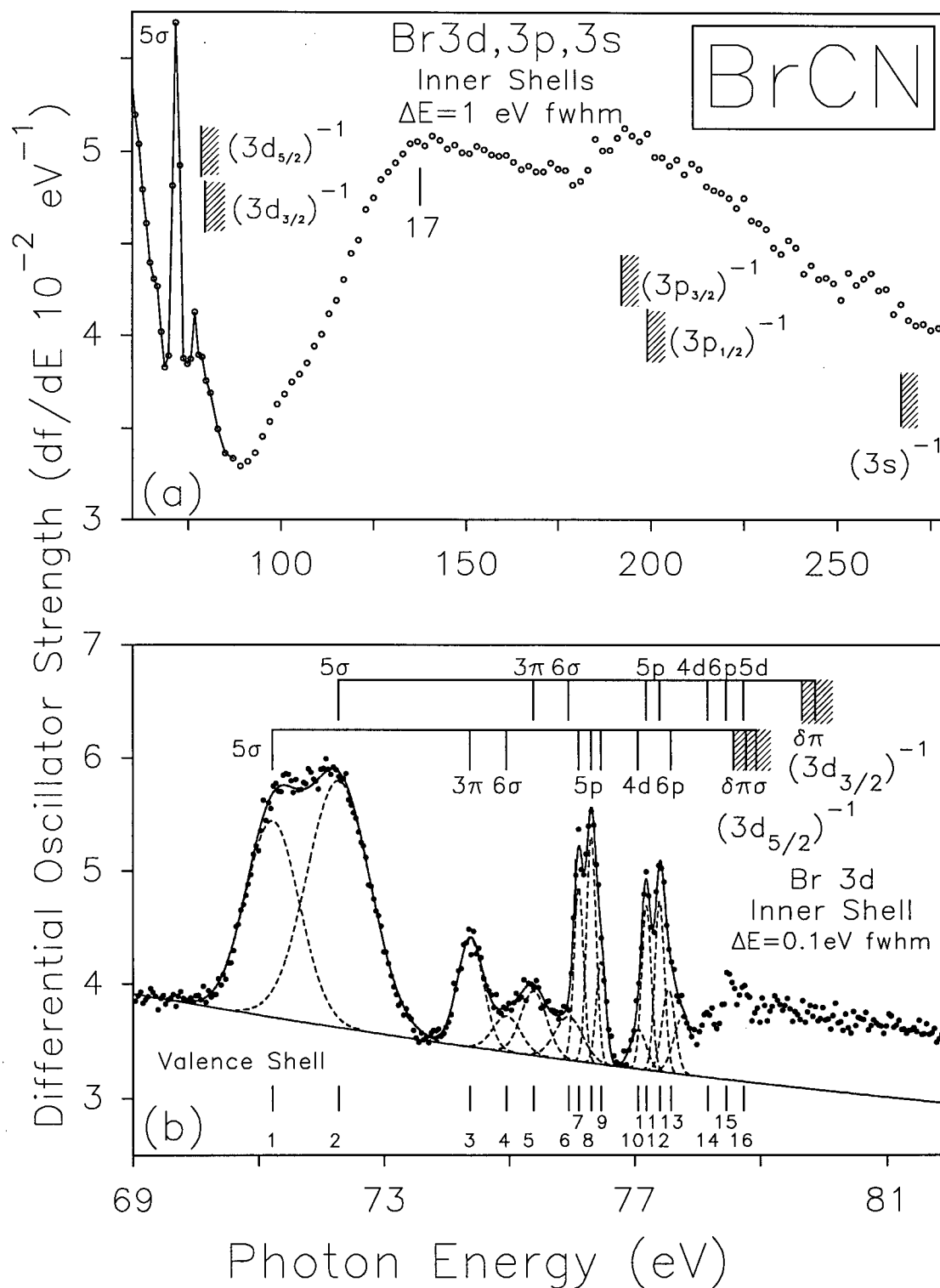


Figure 7.7: Absolute photoabsorption oscillator strength spectrum of BrCN. (a) The low resolution (1 eV fwhm) spectrum in the Br 3d, 3p and 3s regions of BrCN (60-280 eV). (b) The high resolution (0.1 eV fwhm) spectrum in the Br 3d region of BrCN (69-82 eV). Note the offset oscillator strength scales.

The generally broader structures in the Br 3d spectrum below 76.5 eV are assigned to transitions to virtual valence orbitals. Term values for the corresponding transitions in the valence shell are not expected to be transferable, but the term values are expected to be larger (see section 2.5.1). The first band in the Br 3d spectrum, a very intense broad structure centered at 71.75 eV, contains the two spin-orbit components ( $\text{Br } 3d_{\frac{5}{2}, \frac{3}{2}}$ ) of the  $5\sigma \leftarrow \text{Br } 3d$  transition. The next three bands are less intense broad transitions at 74.36, 74.92 and 75.40 eV and are assigned to the virtual valence transitions  $3\pi \leftarrow \text{Br } 3d_{\frac{5}{2}}$ ,  $6\sigma \leftarrow \text{Br } 3d_{\frac{5}{2}}$  and  $3\pi \leftarrow \text{Br } 3d_{\frac{3}{2}}$ , respectively. The final virtual valence transition,  $6\sigma \leftarrow \text{Br } 3d_{\frac{3}{2}}$ , at 76.02 eV, is partially masked by the first of the Rydberg transitions. The second region, which contains the sharp discrete structures in the Br 3d spectrum, is above 76.5 eV and contains transitions to Rydberg orbitals. The dominant Rydberg transitions are expected to be those to the 5p manifolds. Energies, term values, oscillator strengths and tentative assignments are shown in table 7.4.

No XPS measurements or calculations have been reported for the  $\text{Br } 3d_{\frac{5}{2}, \frac{3}{2}}$  ionization potentials. Furthermore the DFT programme [353, 354] used to calculate the C 1s and N 1s IPs in the present work (see section 7.3.3.1) is not equipped to handle fourth row heavy atoms such as Br because of basis set size restrictions. Therefore the positions of the  $\text{Br } 3d_{\frac{5}{2}, \frac{3}{2}}$  IPs shown on figure 7.7 and in table 7.4 have been estimated as follows: First the  $(3d_{\frac{5}{2}})^{-1}$  and  $(3d_{\frac{3}{2}})^{-1}$  spin-orbit split ion states are expected to be further split by ligand field (molecular bonding) effects into  $\delta$ ,  $\pi$  and  $\sigma$  manifolds (due to interactions between the Br  $d_{x^2-y^2}$ ,  $d_{xy}$  and  $d_{z^2}$  orbitals with the CN ligand) and into  $\delta$  and  $\pi$  manifolds (due to interactions with the Br  $d_{xz}$  and  $d_{yz}$  orbitals with the CN ligand), respectively. Such ligand field effects have recently been observed experimentally by Cutler *et al.* in XPS studies of the Br 3d ionization of HBr [283, 360], the I 4d ionization of several iodine containing molecules [278, 361, 362] and the Xe 4d ionization of  $\text{XeF}_x$  ( $x=2,4,6$ ) [363]. Comes *et al.* [364, 365] had earlier reported ligand field effects in the Xe 4d photoabsorption of  $\text{XeF}_2$  and  $\text{XeF}_4$ . In light of the XPS measurements for HBr, Sutherland *et al* [360] and Lui *et al.* [283] have convincingly reinterpreted the 74

to 76 eV region of the Br 3d electron energy loss spectrum (similar to photoabsorption) of HBr [284], ascribing the main features to ligand field splitting of the transitions to the 5p $\pi$  Rydberg orbital rather than the 5p $\sigma$  and 5p $\pi$  molecular symmetry assignments given by Shaw *et al.* [284]. Considerations of the intensities, degeneracies and selection rules, as well as SW-X $\alpha$  calculations, were used to support these re-assignments based on the ligand field splittings [283, 360].

The sharp structure in the 76 to 78 eV region of the Br 3d spectrum of BrCN (figure 7.7(b)) is remarkably similar to that of HBr in the 47 to 76 eV region [284] and thus is also likely to be caused by transitions to the 5p Rydberg orbital. As shown in figure 7.6(b) by the Gaussian curve fit, the broader structure below  $\sim 76$  eV can be ascribed to 3d $_{5/2}$  and 3d $_{3/2}$  transitions to the 5 $\sigma$ , 3 $\pi$  and 6 $\sigma$  virtual valence orbitals. In contrast, the first Rydberg band, between 76 and 77 eV, clearly has two sharp maxima and a weaker shoulder on the high energy side which are well fit by three narrow, equal width, gaussians. These three peaks (features 7, 8 and 9 on figure 7.7(b) and in table 7.4) are assigned to the 5p Rydbergs associated with the 3d $_{5/2}$  ( $\delta$ ,  $\pi$  and  $\sigma$ ), ligand-field split ionization limits. The separations of the peaks 7, 8 and 9 are of similar magnitude to those observed for the  $\delta$ ,  $\pi$  and  $\sigma$  ionization limits of HBr [283, 360]. Similarly two equally narrow peaks (features 11 and 12 on figure 7.7(b)) fitted to the obvious sharp structure in the band just above 77 eV can be ascribed to 5p Rydbergs associated with the 3d $_{3/2}$  ( $\delta$  and  $\pi$ ) ligand-field split ionization limits. The five 3d ionization energies shown on figures 7.4 and 7.7 and in table 7.4 have been estimated by assuming the transferability of the 5p Rydberg term value from the C 1s and N 1s spectra (figure 7.6 and table 7.3). Specifically, an approximate (average) value of 2.47 eV (uncertainty  $\pm 0.2$  eV) was estimated for the 5p term value as detailed in section 7.3.3.1. The oscillator strengths (table 7.4) obtained from the curve fitting (see figure 7.7(b)) for the

various transitions to the 5p Rydberg states result in an intensity ratio

$$\frac{3d_{\frac{5}{2}}(\delta + \pi + \sigma)}{3d_{\frac{3}{2}}(\delta + \pi)} = 1.47$$

which corresponds closely to the expected statistical ratio. Two other broader peaks (features 10 and 13) in the wings of the peak just above 77 eV are tentatively assigned to 4d and 5d Rydberg manifolds. Three higher energy peaks, from transitions to other Rydberg states, can be seen approaching the ionization limits. The various fitted virtual valence and Rydberg peaks in figure 7.7 have equal widths for given spin-orbit split pairs. Note that as expected (compare tables 7.3 and 7.4) the term values for the  $3d_{\frac{5}{2}, \frac{3}{2}}$  transitions to the  $5\sigma$ ,  $3\pi$  and  $6\sigma$  virtual valence orbitals are not transferable from other shells. The  $6\sigma$  peaks in the Br 3d spectrum have term values of  $\sim 3.8$  eV which is very close to the average term value of 3.67 eV found for the 5s Rydbergs in the C 1s and N 1s spectra (see table 7.3). Therefore it is possible that in the Br 3d spectrum the 5s transitions are underlying the peaks ascribed to the transition to the  $6\sigma$  or that Rydberg/valence mixing occurs. Also note that some (apparently unresolved) contributions from the  $\sigma - \pi$  splittings of the 5p Rydberg states are to be expected in the Br 3d spectrum (and also in the valence, C 1s and N 1s spectra). However, such further splittings are likely to be "masked" by broadening of these short-lived, inner shell excited states.

Table 7.4: Energies, term values, oscillator strengths, and assignment of the Br 3d spectrum of BrCN from 65 to 85 eV.

Feature	Photon Energy (eV)	Term Value (eV) <sup>a</sup>		Oscillator Strength (10 <sup>-2</sup> )	Assignment	
		3d <sub>5/2</sub>	3d <sub>3/2</sub>		3d <sub>5/2</sub>	3d <sub>3/2</sub>
1	71.22	7.55 <sup>b</sup>		1.86	$\sigma_{CBr}^*$ (5 $\sigma$ )	
2	72.28		7.48 <sup>c</sup>	2.76		$\sigma_{CBr}^*$ (5 $\sigma$ )
3	74.38	4.39 <sup>b</sup>		0.50	$\pi_{CN}^*$ (3 $\pi$ )	
4	74.96	3.81 <sup>b</sup>		0.17	$\sigma_{CN}^*$ (6 $\sigma$ )	
5	75.40		4.36 <sup>c</sup>	0.28		$\pi_{CN}^*$ (3 $\pi$ )
6	75.95		3.81 <sup>c</sup>	0.21		$\sigma_{CN}^*$ (6 $\sigma$ )
7	76.11	2.47 <sup>d</sup> (2.63)		0.29	5p $\leftarrow$ $\delta$	
8	76.31	2.47 <sup>d</sup> (2.63)		0.38	5p $\leftarrow$ $\pi$	
9	76.47	2.47 <sup>d</sup> (2.63)		0.17	5p $\leftarrow$ $\sigma$	
10	77.06	1.64 <sup>b</sup> (1.12)		0.11	4d	
11	77.19		2.47 <sup>d</sup> (2.63)	0.28		5p $\leftarrow$ $\delta$
12	77.40		2.47 <sup>d</sup> (2.63)	0.29		5p $\leftarrow$ $\pi$
13	77.54	1.12 <sup>b</sup> (2.51)			6p	

Table 7.4: (continued) Energies, term values, oscillator strengths, and assignment of features in the Br 3d spectrum of BrCN from 65 to 85 eV.

Feature	Photon Energy (eV)	Term Value (eV) <sup>a</sup>		Oscillator Strength ( $10^{-2}$ )	Assignment	
		$3d_{5/2}$	$3d_{3/2}$		$3d_{5/2}$	$3d_{3/2}$
14	78.17		1.64 <sup>c</sup> (1.12)			4d
15	78.46		1.34 <sup>c</sup> (2.81)			6p
16	78.74		1.06 <sup>c</sup> (1.42)			5d
IP	78.58				$\delta_{\infty}$	
IP	78.78				$\pi_{\infty}$	
IP	78.94				$\sigma_{\infty}$	
IP	79.66					$\delta_{\infty}$
IP	79.87					$\pi_{\infty}$
17	140					$\epsilon f \leftarrow \text{Br } 3d$

<sup>a</sup>quantum defect values given in parentheses.

<sup>b</sup>with respect to the average ionization potential of 78.77 for the Br  $3d_{5/2}$  manifold.

<sup>c</sup>with respect to the average ionization potential of 79.76 for the Br  $3d_{3/2}$  manifold.

<sup>d</sup>assigned using the term value of 2.47 eV for the 5p Rydberg transitions (see section 7.3.3.1 and table 7.4), determined from the C 1s and N 1s spectra.

Table 7.5: Dipole sums  $S(u)$  and logarithmic dipole sums  $L(u)$  obtained from the absolute photoabsorption oscillator strength spectrum of cyanogen bromide. All values are given in atomic units.

$S(-1)$	$S(-2)$	$S(-3)$	$S(-4)$	$S(-5)$	$S(-6)$	$S(-8)$	$S(-10)$
24.45	39.30	78.43	174.1	416.0	1052	7733	6.765(4)
$L(-1)$	$L(-2)$	$L(-3)$	$L(-4)$	$L(-5)$	$L(-6)$		
-6.356	-24.20	-58.99	-145.5	-375.1	-1002		

### 7.3.4 Dipole sum-rules of cyanogen bromide

The values of the dipole sum-rules  $S(u)$  ( $u=-1, \dots, -6, -8, -10$ ) and logarithmic dipole sum-rules  $L(u)$  ( $u=-1, -2, \dots, -6$ ) obtained from the presently reported absolute oscillator strength spectrum of cyanogen bromide are shown in table 7.5. These values are the first reported dipole sums for cyanogen bromide. The estimated accuracies of the presently reported sums are 5% for  $S(u)$   $u = -2$  to  $-6$  and for  $L(u)$   $u = -2$  to  $-6$ , 10% for  $S(-1)$ , 15% for  $L(-1)$ , 10% for  $S(-8)$ , and 20% for  $S(-10)$ .

To the best of our knowledge no values of the Verdet constant of cyanogen bromide, nor any values of dipole dispersion coefficients involving cyanogen bromide, have been reported in the literature. Values of the normal Verdet constant for BrCN can be obtained for the first time by using equation (4.5) and the dipole sums listed in table 7.5. The values of the  $C_6(A, A)$  and  $C_6(A, B)$  involving cyanogen bromide have been evaluated directly from equation (4.6) using the appropriate absolute photoabsorption spectra. They have also been evaluated from equation (4.9) using the  $S(-2)$  and  $L(-2)$  sums (tables 4.3, 4.4 and 7.5) for all (A,A) and (A,B) combinations involving cyanogen bromide and all of the atoms and molecules discussed in chapter 4. For all combinations equation (4.9) differs by less than 0.5% from those obtained using equation (4.6). For cyanogen bromide, equation (4.9) and the sum-rules of tables 4.3, 4.4 and 5.11 allow estimates of the dispersion coefficients to be obtained for the first time. The accuracy of the dipole-dipole dispersion coefficients,

obtained from dipole (e,e) spectroscopy using equation (4.9) with the S(-2) and L(-2) sums (tables 4.3, 4.4 and 7.5, or those given above using equation (4.6)), is estimated to be better than  $\pm 10\%$ .

### 7.3.5 Molecular and dissociative photoionization

Time-of-flight mass spectra of BrCN were obtained over the equivalent photon energy range 11.5 to 160 eV using dipole (e,e+ion) spectroscopy. Figure 7.8 shows the mass spectrum obtained at 60 eV. The positive ions detected at higher photon energies are BrCN<sup>+</sup>, BrC<sup>+</sup>, Br<sup>+</sup>, BrCN<sup>2+</sup>, Br<sup>2+</sup>, CN<sup>+</sup>, N<sup>+</sup> and C<sup>+</sup> in addition to small amounts of background H<sub>2</sub>O and impurity (CN)<sub>2</sub>. Branching ratios for molecular and dissociative photoionization were determined as the percentage of the total photoionization from integration of the peaks in the background subtracted TOF mass spectra. The yields for bromine containing ions are the summed contributions for the <sup>79</sup>Br and <sup>81</sup>Br isotopes. The branching ratios are presented graphically in figure 7.9 and can be obtained numerically from table 7.6 by dividing the partial oscillator strength for a particular ion by the sum of the partial photoionization oscillator strengths at the energy of interest. While the BrCN<sup>+</sup> molecular ion dominates the breakdown below  $\sim 40$  eV the atomic ions Br<sup>+</sup>, N<sup>+</sup> and C<sup>+</sup> account for  $\sim 70\%$  of the total yield at 100 eV.

The photoionization efficiency curve for BrCN is shown in figure 7.8(b) and given numerically in table 7.6. Relative photoionization efficiency values were determined from the TOF mass spectra by taking the ratio of the total number of electron-ion coincidences to the total number of forward scattered electrons as a function of energy loss. Making the reasonable assumption that the absolute photoionization efficiency is unity at higher photon energies we conclude that the photoionization efficiency is 1 above 21 eV.

Absolute photoionization partial oscillator strengths for the molecular and the disso-

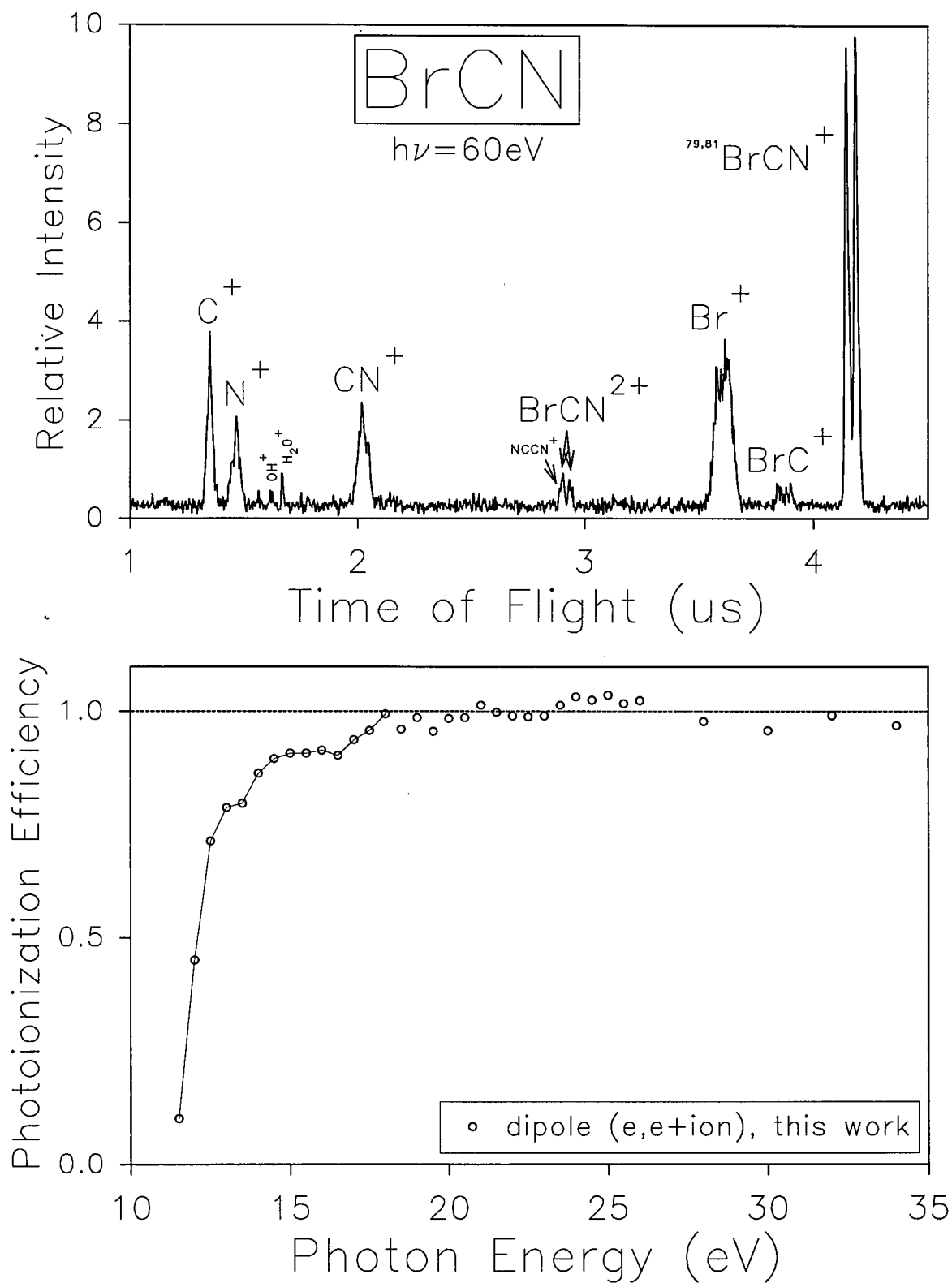


Figure 7.8: (a) TOF mass spectrum of BrCN recorded at an equivalent photon energy of 60 eV. (b) The photoionization efficiency of BrCN from 11.5 to 35 eV.

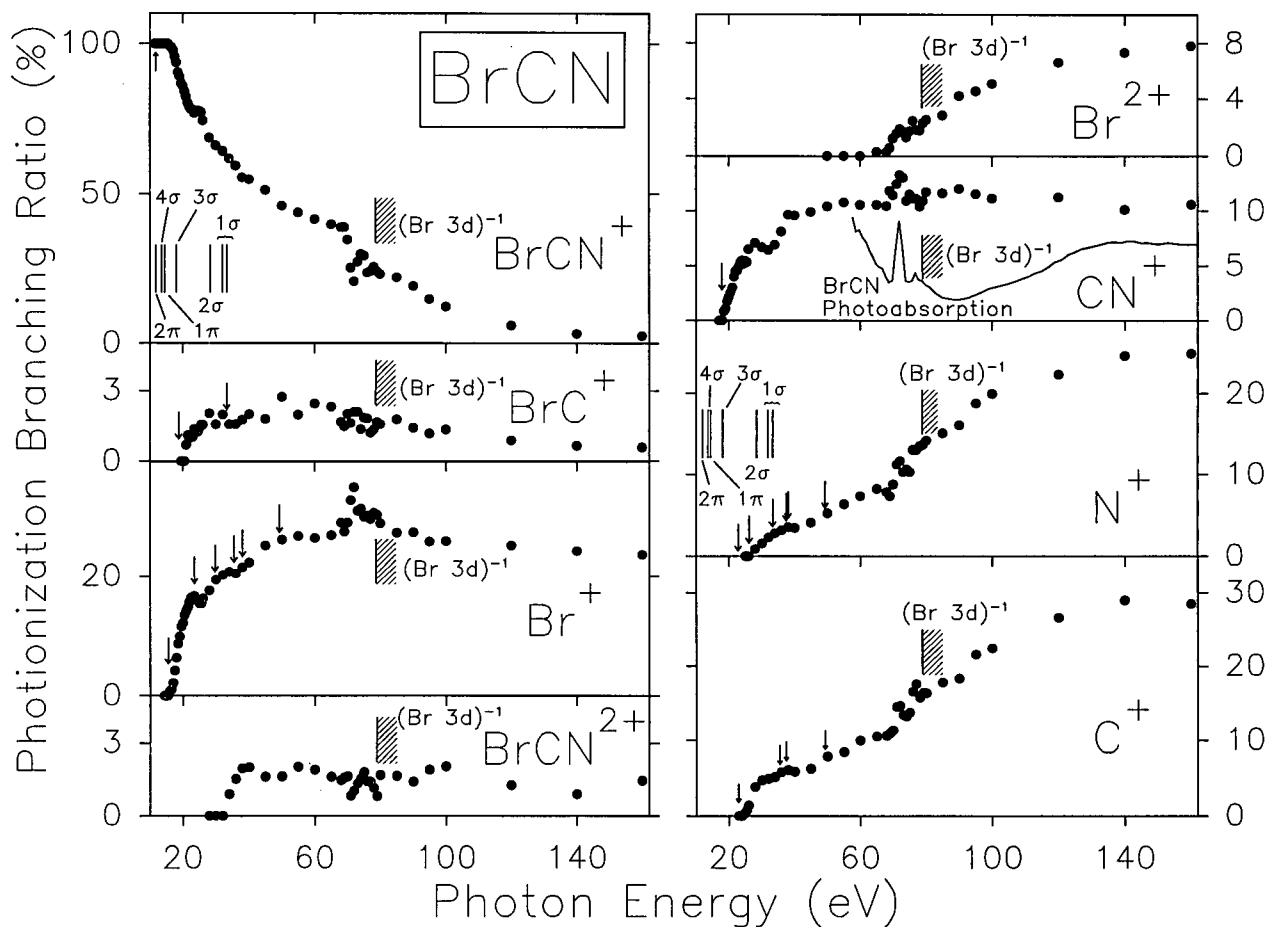


Figure 7.9: Branching ratios for the molecular and dissociative photoionization of BrCN. Vertical arrows represent the calculated thermodynamic appearance potentials [317] of the ions from BrCN (see table 7.7). The outer valence ( $2\pi$ ,  $4\sigma$ ,  $1\pi$  and  $3\sigma$ ) vertical ionization potentials from photoelectron spectroscopy measurements [331, 332] and the calculated [335] positions of the main poles for inner valence ionization are indicated. The position of the Br 3d ionization edge was estimated in section 7.3.3.2.

ciative photoionization channels of BrCN have been obtained at each photon energy from the triple product of the absolute photoabsorption oscillator strength, the photoionization efficiency and the photoion branching ratio. The resulting partial oscillator strengths are shown in figure 7.10 and are given numerically in table 7.6. The presently measured appearance potentials for the ions formed from molecular and dissociative photoionization of BrCN are given in table 7.7 where they are compared with both calculated and previously published [331, 332, 366] appearance potentials. The appearance potentials were calculated from thermodynamic heats of formation [317] assuming zero kinetic energy of fragmentation, so the actual thresholds may be higher.

It is clear that considerable changes in the ionic photofragmentation occur in the region of Br 3d excitation and ionization. Only the molecular ion BrCN<sup>+</sup> is formed below the onset of Br<sup>+</sup> at 16±1 eV. This is in good agreement with the appearance potential for Br<sup>+</sup> of 15.52 eV reported by Dibeler and Liston [366] using PIMS. A consideration of the ionization potentials and Franck-Condon widths determined by high resolution PES [331, 332] indicates that the (2π)<sup>-1</sup> ground ionic states and first two excited ion states ((4σ)<sup>-1</sup> and (1π)<sup>-1</sup>) can only yield BrCN<sup>+</sup>. Since the lowest appearance potential for Br<sup>+</sup> (15.52 eV) is above the upper limit (~14.9 eV) of the (1π)<sup>-1</sup> Franck-Condon region, Br<sup>+</sup> must therefore first be produced by some indirect process such as autoionization rather than by direct dissociative photoionization from an electronic state of BrCN<sup>+</sup>. An examination of the photoabsorption spectrum (see figure 7.2) shows a strong, broad peak above the underlying outer valence continuum centered at ~16 eV. This peak is probably from excited neutral states leading to the 3σ<sup>-1</sup> ionization limit. These excited neutral states of BrCN are evidently responsible for the initial production of Br<sup>+</sup> by dissociative autoionization processes. Above the initial onset for Br<sup>+</sup> at 16 eV the POS rises slowly (figure 7.10) for ~2 eV before rising sharply at ~18 eV because of Br<sup>+</sup> production by direct dissociative photoionization from the 3σ<sup>-1</sup> state of BrCN<sup>+</sup>. The onsets for BrC<sup>+</sup> (21.0±1 eV) and CN<sup>+</sup> (18.5±1 eV) indicate that

these ions are first produced from  $(3\sigma)^{-1}$  ionization. The remaining singly charged ions,  $N^+$  and  $C^+$ , have much higher appearance potentials of  $24.5\pm 1$  and  $28\pm 1$  eV respectively, indicating that these originate from ionization of the inner valence ( $2\sigma$  and  $1\sigma$ ) orbitals. No ionization potential measurements of the  $2\sigma$  and  $1\sigma$  orbitals have been reported in the literature and the only estimates are from the many-body Green's function calculations by von Niessen and Cambi [335], which show extensive breakdown of the independent particle model in the inner valence region. These calculations [335] predict intensity from  $(2\sigma)^{-1}$  many-body states over the 24.66 to 36.03 eV range. The lowest energy  $(2\sigma)^{-1}$  pole is at 24.66 eV, which has a pole strength of 0.041, and the most intense pole (0.70) is at 28.4 eV. These calculations [335] also show  $(1\sigma)^{-1}$  intensity in the 25.05 to 33.31 eV region with the most intense poles occurring at 31.89 and 33.31 eV, having pole strengths of 0.15 and 0.21, respectively. It is therefore clear that  $N^+$  and  $C^+$  must arise from inner valence ( $(2\sigma)^{-1}$  and  $(1\sigma)^{-1}$ ) ionization. Further increases (see the branching ratios in figure 7.9) in the yields of  $Br^+$  at  $\sim 26$  eV in the predicted  $(2\sigma)^{-1}$  energy range and of  $BrC^+$ ,  $Br^+$  and  $CN^+$  at  $\sim 34$  eV in the  $(1\sigma)^{-1}$  range indicate that some contributions to the production of these ions also come from inner valence ionization.

Higher energy onsets in the region of Br 3d excitation to the  $5\sigma$  virtual valence and Rydberg orbitals (see figure 7.7), as well as further significant increases in yield at the Br 3d ionization edges, can be seen in all singly charged ion channels (figure 7.10). These increases are relatively large for  $Br^+$ ,  $CN^+$ ,  $N^+$  and  $C^+$ . It can be seen that the only doubly charged ions are the molecular dication  $BrCN^{2+}$  and the fragment dication  $Br^{2+}$ . The measured appearance potential of  $BrCN^{2+}$  is  $34\pm 2$  eV with further very small increases in the Br 3d excitation and ionization regions. Judging from the appearance potential and energy dependence of  $BrCN^{2+}$ , the stable  $BrCN^{2+}$  ion comes mainly from direct double ionization states involving two electrons from the outer valence orbitals. The  $Br^{2+}$  ion first appears at  $68\pm 2$  eV, at the  $5\sigma(\sigma^*) \leftarrow Br$  3d excitation threshold, with further contributions

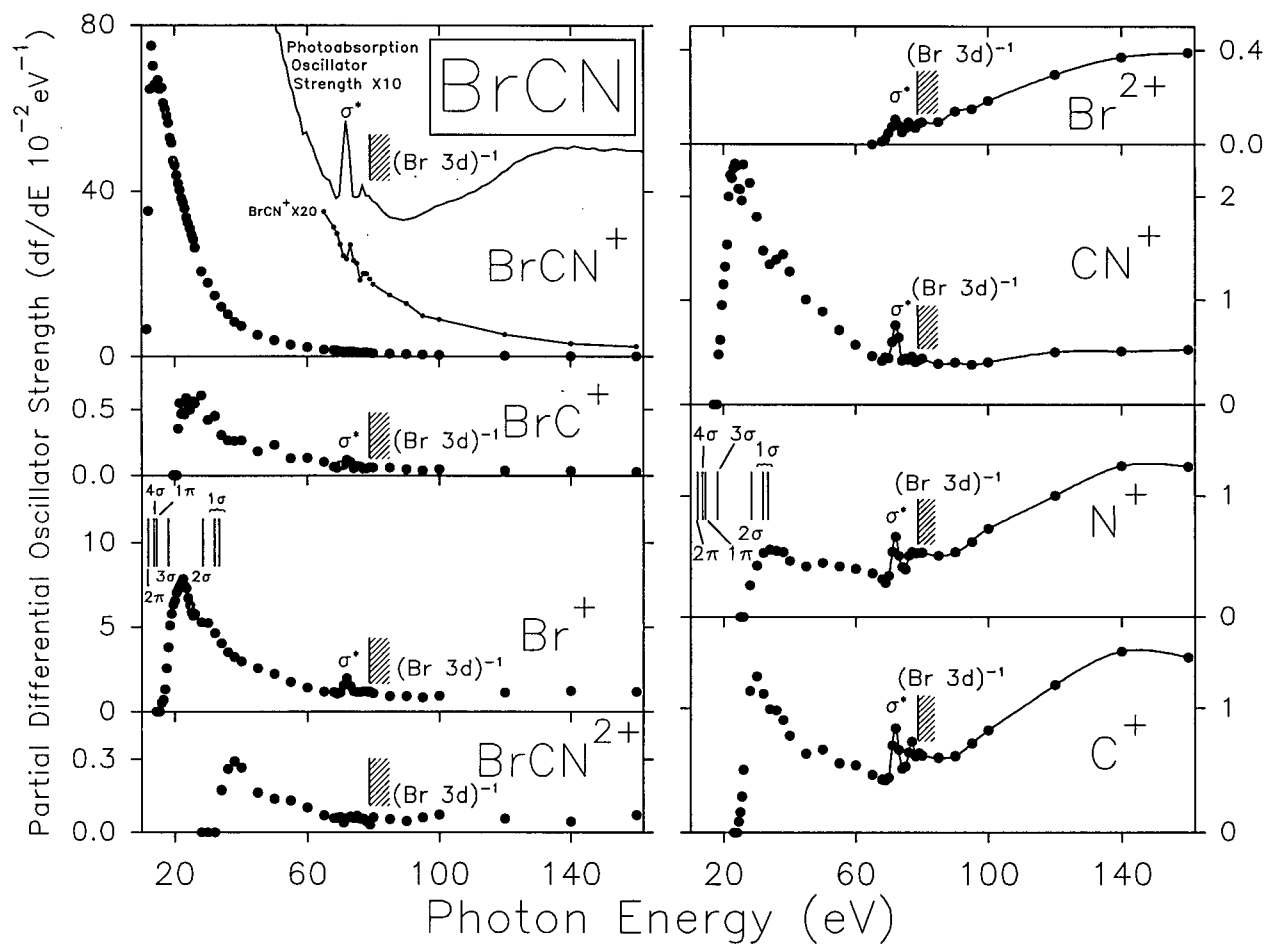


Figure 7.10: Absolute partial photoionization oscillator strengths for the molecular and dissociative photoionization of BrCN. Vertical arrows represent the calculated thermodynamic appearance potentials [317] of the ions from BrCN (see table 7.7). The outer valence ( $2\pi$ ,  $4\sigma$ ,  $1\pi$  and  $3\sigma$ ) vertical ionization potentials from photoelectron spectroscopy measurements [331, 332] and the calculated [335] positions of the main poles for inner valence ionization are indicated. The position of the Br 3d ionization edge was estimated in section 7.3.3.2.

in the Br 3d Rydberg excitation and ionization regions. These observations, together with the (at-most) very small increase in yield of  $\text{BrCN}^{2+}$  in the Br 3d region, indicate that most Auger type processes resulting from 3d vacancies in BrCN result in dissociation (i.e. unstable dications or trications (see also figure 7.13 and section 7.3.6)). The origin of the contributions to  $\text{Br}^{2+}$ ,  $\text{N}^+$  and  $\text{C}^+$  as well as to  $\text{Br}^+$  and  $\text{CN}^+$  in the Br 3d region are further investigated by PIPICO techniques (see section 7.3.6 following). The position of the first onset ( $68 \pm 2$  eV) of  $\text{Br}^{2+}$  indicates that the production of this dication in the Br 3d region must first occur by dissociative resonance Auger emission following the  $5\sigma(\sigma^*) \leftarrow \text{Br } 3d$  excitation process. Such resonance Auger processes and/or autoionization from the Br 3d to  $\sigma^*$  and Rydberg excited states and also the  $(\text{Br } 3d)^{-1}$  ionization continuum are clearly also contributing to all singly charged channels. It can be seen from figure 7.9 that the contribution of the  $\text{BrC}^+$  fragment ion is only about 20% of that of  $\text{CN}^+$ . The significant presence of  $\text{BrC}^+$  is noteworthy since the bond energy for  $\text{C}\equiv\text{N}$  is  $7.738 \pm 0.02$  eV in the neutral molecule [367], which is much stronger than the bond energy of  $2.9 \pm 0.2$  eV for Br-C [368]. Although a simple statistical consideration using these bond energies would predict that the yield of  $\text{BrC}^+$  fragment should be negligible, there clearly is significant breakage of the  $\text{C}\equiv\text{N}$  bond in the ionization of the BrCN molecule.

Table 7.6: Absolute partial differential oscillator strengths for the molecular and dissociative photoionization of BrCN from 11.5 to 160 eV.

Photon Energy eV	Differential Oscillator Strength ( $df/dE$ $10^{-2}eV^{-1}$ ) <sup>a</sup>								Ionization Efficiency <sup>b</sup> $\eta_i$
	BrCN <sup>+</sup>	BrC <sup>+</sup>	Br <sup>+</sup>	BrCN <sup>2+</sup>	Br <sup>2+</sup>	CN <sup>+</sup>	N <sup>+</sup>	C <sup>+</sup>	
11.5	6.54								0.10
12	35.10								0.45
12.5	64.66								0.71
13	75.09								0.79
13.5	70.36								0.80
14	65.78								0.86
14.5	65.08								0.89
15	66.92								0.91
15.5	64.69		0						0.91
16	65.05		0.55						0.91
16.5	61.32		0.70						0.90
17	59.87		1.32						0.94
17.5	58.15		2.57						0.96
18	56.38		3.80			0			0.99
18.5	52.86		5.10			0.48			0.96
19	51.67		5.78			0.62			0.99
19.5	47.27		6.32			0.95			0.96
20	46.19		6.57			1.15			0.98
20.5	43.84	0	7.05			1.32			0.99
21	41.80	0.35	7.23			1.54			1.00 <sup>b</sup>
21.5	40.33	0.55	7.44			2.00			
22	38.30	0.47	7.64			2.21			
22.5	37.17	0.48	7.84			2.18			
23	35.77	0.46	7.45			2.27			
23.5	33.56	0.59	7.30			2.32			
24	32.18	0.54	6.73			2.30		0	
24.5	30.85	0.50	6.31			2.07		0.09	
25	29.36	0.54	5.88			2.07		0.17	
25.5	28.27	0.57	5.67			1.96		0.29	

Table 7.6: (continued) Absolute partial differential oscillator strengths for the molecular and dissociative photoionization of BrCN from 11.5 to 160 eV at 1 eV fwhm.

Photon Energy eV	Differential Oscillator Strength ( $df/dE$ $10^{-2}eV^{-1}$ ) <sup>a</sup>								Ionization Efficiency <sup>b</sup> $\eta_i$
	BrCN <sup>+</sup>	BrC <sup>+</sup>	Br <sup>+</sup>	BrCN <sup>2+</sup>	Br <sup>2+</sup>	CN <sup>+</sup>	N <sup>+</sup>	C <sup>+</sup>	
26	26.30	0.55	5.78			2.31		0.50	
28	20.57	0.61	5.28			2.13	0.26	1.14	
30	17.80	0.42	5.22			1.80	0.43	1.26	
32	14.72	0.45	4.63	0		1.48	0.53	1.12	
34	12.01	0.30	4.03	0.17		1.35	0.56	0.99	
36	10.16	0.27	3.51	0.26		1.39	0.55	0.98	
38	8.32	0.26	3.22	0.29		1.44	0.54	0.90	
40	7.31	0.26	2.96	0.27		1.28	0.46	0.78	
45	5.22	0.18	2.55	0.16		1.01	0.42	0.63	
50	3.93	0.23	2.22	0.14		0.89	0.45	0.67	
55	2.89	0.13	1.76	0.13		0.71	0.42	0.56	
60	2.25	0.13	1.43	0.10		0.57	0.40	0.54	
65	1.75	0.10	1.18	0.07	0	0.46	0.36	0.46	
68	1.56	0.07	1.16	0.06	0.01	0.42	0.31	0.42	
69	1.49	0.06	1.05	0.06	0.02	0.45	0.28	0.42	
70	1.35	0.08	1.12	0.06	0.05	0.44	0.34	0.44	
71	1.22	0.08	1.57	0.04	0.08	0.60	0.54	0.70	
72	1.18	0.12	1.97	0.06	0.11	0.76	0.66	0.83	
73	1.35	0.10	1.52	0.07	0.08	0.64	0.51	0.66	
74	1.16	0.05	1.21	0.06	0.05	0.42	0.41	0.51	
75	1.13	0.07	1.15	0.07	0.07	0.44	0.40	0.53	
76	0.92	0.07	1.16	0.06	0.09	0.43	0.51	0.64	
77	1.00	0.05	1.22	0.06	0.08	0.46	0.54	0.72	
78	1.00	0.05	1.19	0.04	0.07	0.41	0.53	0.61	
79	0.94	0.06	1.17	0.03	0.09	0.42	0.53	0.64	
80	0.87	0.06	1.08	0.06	0.09	0.44	0.53	0.61	
85	0.74	0.06	0.92	0.06	0.10	0.39	0.51	0.60	
90	0.64	0.05	0.91	0.05	0.14	0.40	0.54	0.61	
95	0.49	0.04	0.85	0.06	0.15	0.38	0.62	0.71	

Table 7.6: (continued) Absolute partial differential oscillator strengths for the molecular and dissociative photoionization of BrCN from 11.5 to 160 eV at 1 eV fwhm.

Photon Energy eV	Differential Oscillator Strength ( $df/dE$ $10^{-2}eV^{-1}$ ) <sup>a</sup>								Ionization Efficiency <sup>b</sup> $\eta_i$
	BrCN <sup>+</sup>	BrC <sup>+</sup>	Br <sup>+</sup>	BrCN <sup>2+</sup>	Br <sup>2+</sup>	CN <sup>+</sup>	N <sup>+</sup>	C <sup>+</sup>	
100	0.45	0.05	0.94	0.07	0.19	0.41	0.73	0.82	
120	0.27	0.04	1.13	0.06	0.30	0.50	1.00	1.19	
140	0.16	0.03	1.22	0.05	0.37	0.51	1.25	1.47	
160	0.12	0.03	1.18	0.07	0.39	0.53	1.24	1.42	

<sup>a</sup> $\sigma(\text{Mb})=109.75 df/dE$  ( $eV^{-1}$ ).

<sup>b</sup>The photoionization efficiency is normalized to unity above 21 eV (see text for details)

Table 7.7: Calculated and measured appearance potentials for the production of positive ions from BrCN.

Process	Appearance Potential (eV)			
	Calculated <sup>a</sup>	Experimental		
		This Work (e,e+ion)	This Work PIPICO	[366]
(1) BrCN <sup>+</sup>	11.84	11.5 <sup>b</sup>		11.84 11.88
(2) BrC <sup>+</sup> + N	18.74	21.0 <sup>b</sup>		
(3) BrC <sup>+</sup> + N <sup>+</sup>	33.30		≤40	
(4) Br <sup>+</sup> + CN	15.61	16.0 <sup>b</sup>		15.52
(5) Br <sup>+</sup> + C + N	23.42			
(6) Br <sup>+</sup> + CN <sup>+</sup>	29.72		≤40	
(7) Br <sup>+</sup> + C <sup>+</sup> + N	35.46		≤40	
(8) Br <sup>+</sup> + C + N <sup>+</sup>	37.99		45 <sup>c</sup>	
(9) Br <sup>+</sup> + C <sup>+</sup> + N <sup>+</sup>	49.26			
(10) Br + CN <sup>+</sup>	17.88	18.5 <sup>b</sup>		
(11) BrC + N <sup>+</sup>	22.81			
(12) Br + C + N <sup>+</sup>	26.14	28 <sup>c</sup>		
(13) Br + C <sup>+</sup> + N <sup>+</sup>	37.44			
(14) BrN + C <sup>+</sup>				
(15) Br + C <sup>+</sup> + N	22.87	24.5 <sup>b</sup>		
(16) BrN <sup>+</sup> + C <sup>+</sup>				
(17) BrCN <sup>2+</sup>		34 <sup>c</sup>		
(18) Br <sup>2+</sup> + CN		68 <sup>c</sup>		
(19) Br <sup>2+</sup> + C + N				
(20) Br <sup>2+</sup> + CN <sup>+</sup>			70 <sup>c</sup>	
(21) Br <sup>2+</sup> + C <sup>+</sup> + N			78 <sup>c</sup>	
(22) Br <sup>2+</sup> + C + N <sup>+</sup>			78 <sup>c</sup>	

<sup>a</sup>Values calculated using thermodynamic data for the enthalpy of formation of ions and neutrals (taken from [317]) assuming zero kinetic energy of fragmentation.

<sup>b</sup>±1 eV.

<sup>c</sup>±2 eV.

### 7.3.6 PIPICO spectra and the decomposition of multiply charged ions.

The partial photoionization oscillator strengths (figure 7.10) for  $\text{Br}^{2+}$ ,  $\text{N}^+$  and  $\text{C}^+$  clearly show that there are significant increases in the yields of these ions in the region of Br 3d excitation and ionization (i.e. above  $\sim 70$  eV). Smaller increases also occur in the yields of  $\text{BrCN}^{2+}$ ,  $\text{BrC}^+$ ,  $\text{Br}^+$  and  $\text{CN}^+$ . It is possible that significant contributions to these fragment ions occur from dissociative double and triple photoionization (i.e. from Coulomb explosion of multiply charged ions) at energies below as well as above the Br 3d threshold. These processes have been studied by measurements using PIPICO autocorrelation techniques as described in section 3.5. PIPICO identifies pairs of ions, resulting from Coulomb explosion of multiply charged ions, by their time-of-flight differences. PIPICO measurements were made by Dr. T. Ibuki and Dr. A. Hiraya over the 40 to 130 eV photon energy range using monochromated synchrotron radiation. Typical spectra are shown in figure 7.11(a)–(f) at energies below and above the Br 3d threshold. Figure 7.11(a) shows the PIPICO spectrum in the valence region at 50 eV while figures 7.11(b)–(e) show spectra in the region of Br 3d excitation and ionization. Figure 7.11(f) shows an expanded view of the region of the spectrum at 130 eV involving the lower  $m/e$  pairs of ions.

The PIPICO branching ratios resulting from Coulomb explosion of doubly charged cations are shown in figure 7.12 and are listed as a function of photon energy in table 7.8. Processes leading to the ion pairs  $\text{BrC}^+ + \text{N}^+$ ,  $\text{Br}^+ + \text{CN}^+$ ,  $\text{Br}^+ + \text{N}^+$ ,  $\text{Br}^+ + \text{C}^+$  and  $\text{C}^+ + \text{N}^+$  are observed to occur both in the valence region and also in the Br 3d region above 70 eV. Significant and abrupt changes in the PIPICO branching ratios are observed in the Br 3d region (see figure 7.12(a)) of the photoabsorption spectrum of BrCN (see figure 7.7)) for all channels except for  $\text{Br}^+ + \text{C}^+$  where only a very small increase occurs. The sharpest changes in the PIPICO branching ratios occur above 73 eV. Consideration of the Br 3d photoabsorption

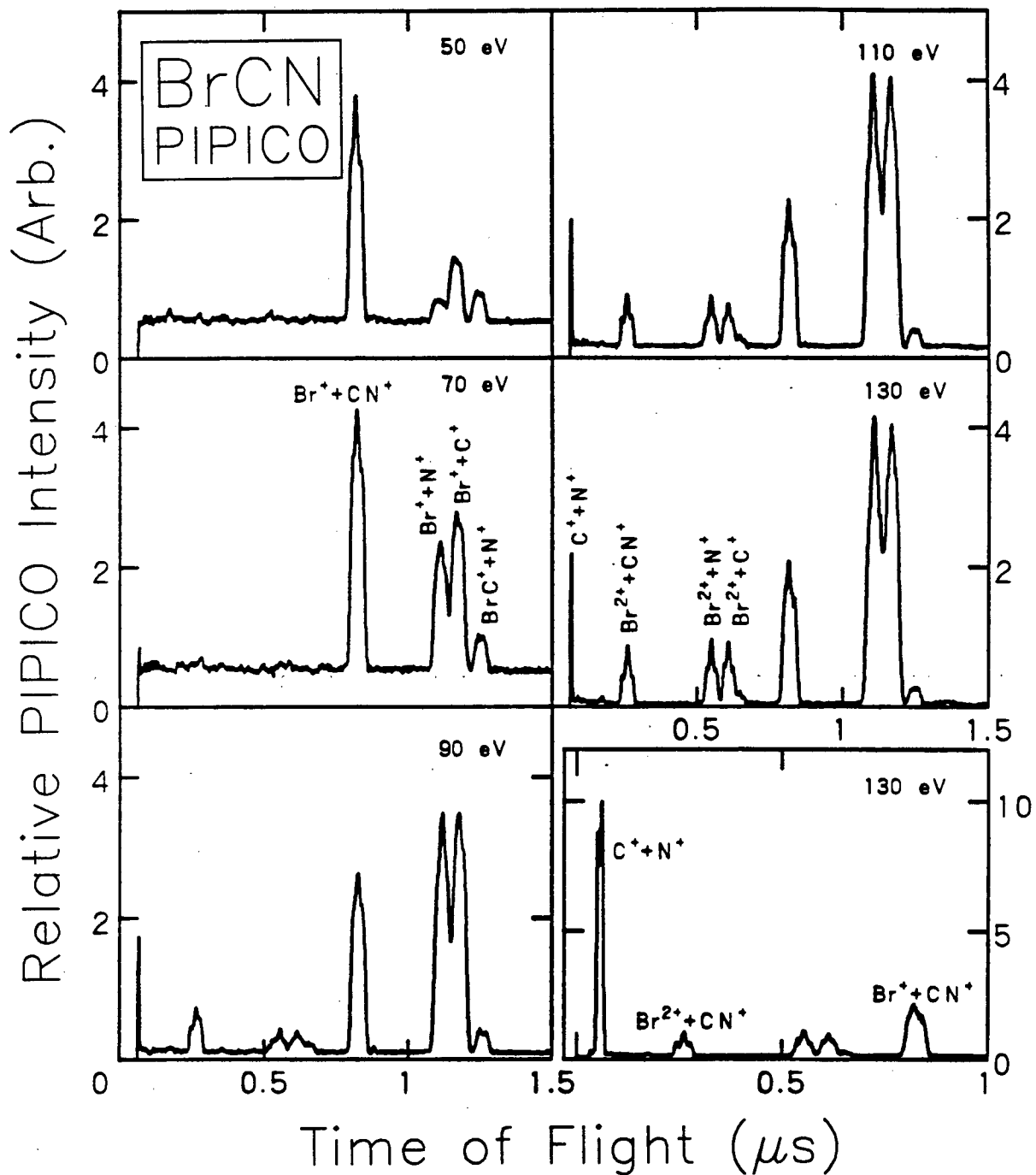


Figure 7.11: PIPICO spectra for double and triple dissociative photoionization of BrCN in the valence and Br 3d regions.

spectrum indicates that this corresponds to the Rydberg excitation and ionization regions with no significant contribution from the  $5\sigma(\sigma^*) \leftarrow \text{Br } 3d$  virtual valence excitation which is the broad band (see figure 7.7)) located between 71 to 73 eV.

The doubly charged molecular dication,  $\text{BrCN}^{2+}$ , is formed as a stable species in the valence and Br 3d regions (see table 7.6 and figures 7.9 and 7.10). An increase in the yield of stable  $\text{BrCN}^{2+}$  is observed in the Br 3d region presumably because of MVV Auger type processes. However, the dication is also in part dissociative with the  $\text{Br}^+ + \text{CN}^+$  pair being dominant below the Br 3d threshold. The  $\text{BrC}^+ + \text{N}^+$  pair accounts for a much smaller fraction of the PIPICO intensity, presumably because of the fact that the  $\text{C}\equiv\text{N}$  triple bond is much stronger than the Br–C single bond. The relative intensities of both of these channels decrease with increasing photon energy and at the Br 3d threshold the branching ratios are approximately halved compared with the situation at 40 eV in the valence shell. The reverse trend is exhibited by the  $\text{Br}^+ + \text{N}^+$ ,  $\text{Br}^+ + \text{C}^+$  and  $\text{C}^+ + \text{N}^+$  channels, which are mainly produced from dissociative double photoionization with the third particle being neutral, although contributions from triple photoionization giving three positive ions cannot be discounted since only two ions are detected by a single stop TAC in the PIPICO autocorrelation mode. The onsets around 40 eV for these three processes are close to the thermochemically estimated values [317] of 35.5 to 38.0 eV. Decomposition into three particles (see figure 7.12) clearly becomes the dominant outgoing channel at the higher energies studied, accounting for 70 to 75% of the PIPICO intensity above 80 eV. As noted above, the  $\text{Br}^+ + \text{N}^+$  and  $\text{C}^+ + \text{N}^+$  channels increase markedly at the onset of the Br 3d Rydberg transitions and at the Br 3d ionization threshold, thus indicating that the creation of a Br 3d core hole favours very extensive “atomization” of the ionized BrCN (into  $\text{Br}^+ + \text{N}^+$  or  $\text{C}^+ + \text{N}^+$ ) *via* an MVV Auger processes. The fact that the  $\text{Br}^+ + \text{C}^+$  channel is little influenced by Br MVV Auger decay is not understood at the present time.

No stable triply charged ions were observed in the presently reported dipole (e,e+ion)

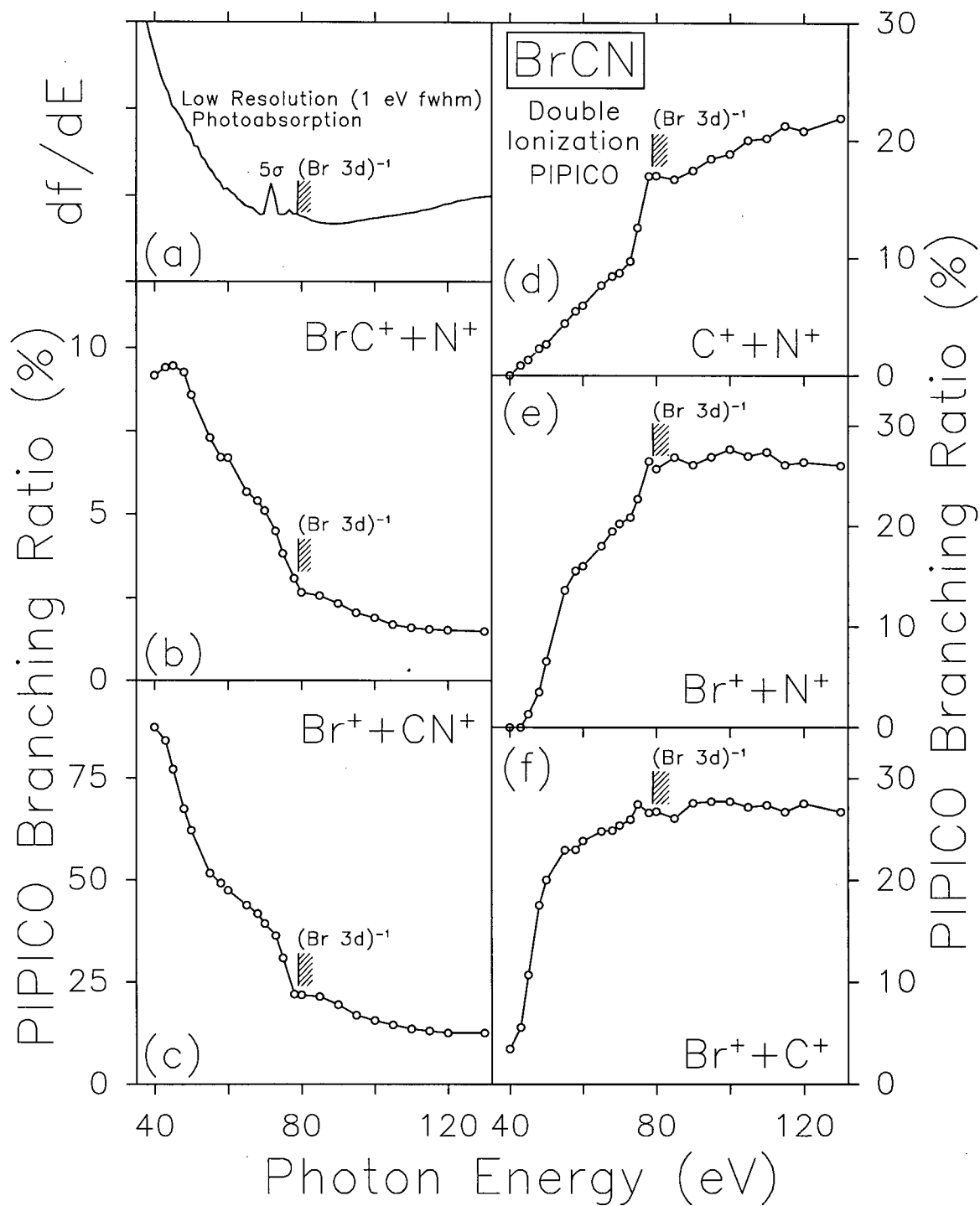


Figure 7.12: PIPICO branching ratios (40–130 eV) for dissociative double photoionization of BrCN (panels b–f). The position of the Br 3d ionization edge was estimated in section 7.3.3.2.

TOF mass spectra. Coulomb explosions of triply charged ions (by Auger decay into singly and doubly charged cations) are observed in the PIPICO branching ratios shown in figure 7.13(b) to (d) for the channels  $\text{Br}^{2+}+\text{CN}^+$ ,  $\text{Br}^{2+}+\text{C}^+$  and  $\text{Br}^{2+}+\text{N}^+$ , respectively. A consideration of the low resolution Br 3d photoabsorption spectrum (figure 7.13(a)) shows that no triple ionization leading to doubly and singly charged ion pairs occurs below the onset of Br 3d excitation. Furthermore, it is clear that  $\text{Br}^{2+}+\text{C}^+$  and  $\text{Br}^{2+}+\text{N}^+$  do not result from the  $5\sigma(\sigma^*) \leftarrow \text{Br}$  3d resonance at 71 eV, but first appear above  $\sim 75$  eV in the Br 3d Rydberg excitation and ionization regions with significant further increases in their branching ratios at  $\sim 90$  eV. In contrast, the initial onset for  $\text{Br}^{2+}+\text{CN}^+$  is between 68 and 70 eV showing that this triple ionization channel results from resonance Auger decay of the  $5\sigma(\sigma^*) \leftarrow \text{Br}$  3d transitions and possibly of the Rydberg excited states. A further sharp increase in the  $\text{Br}^{2+}+\text{CN}^+$  branching ratio occurs in the region of the Br 3d ionization threshold (figure 7.13(d)). Comparing figures 7.12 and 7.13 it can be seen that only  $\sim 12\%$  of the total PIPICO branching ratio intensity at higher energies involves triple ionization processes.

A comparison (see figure 7.13) of the respective initial ( $\sim 68$ ,  $\sim 75$  and  $\sim 75$  eV) and higher energy ( $\sim 80$ ,  $\sim 90$  and  $\sim 90$  eV) onsets in the  $\text{Br}^{2+}+\text{CN}^+$  channel, which does not involve CN triple bond breakage, with the  $\text{Br}^{2+}+\text{C}^+$  and  $\text{Br}^{2+}+\text{N}^+$  channels, which do involve CN bond breakage, shows that the energy differences are similar in magnitude to the neutral  $\text{C}\equiv\text{N}$  bond energy of 7.738 eV [367]. Formation of  $\text{Br}^{2+}+\text{CN}^+$  first occurs at  $\sim 68$  eV, at the Br 3d excitation threshold. This is consistent with triple ionization of BrCN first producing  $\text{Br}^{2+}+\text{CN}^+$  from the  $5\sigma(\sigma^*) \leftarrow \text{Br}$  3d excited state. Production of three particles,  $\text{Br}^{2+}+\text{C}^++\text{N}$  and  $\text{Br}^{2+}+\text{C}+\text{N}^+$ , only commences in the Br 3d Rydberg excitation region, once enough internal energy is available to break the strong CN triple bond. A higher energy onset of  $\text{Br}^{2+}+\text{CN}^+$  occurs at  $\sim 80$  eV, at the  $(\text{Br } 3d)^{-1}$  thresholds. The relative positions of the higher energy onsets in figures 7.13(b), (c) and (d) suggest that separation

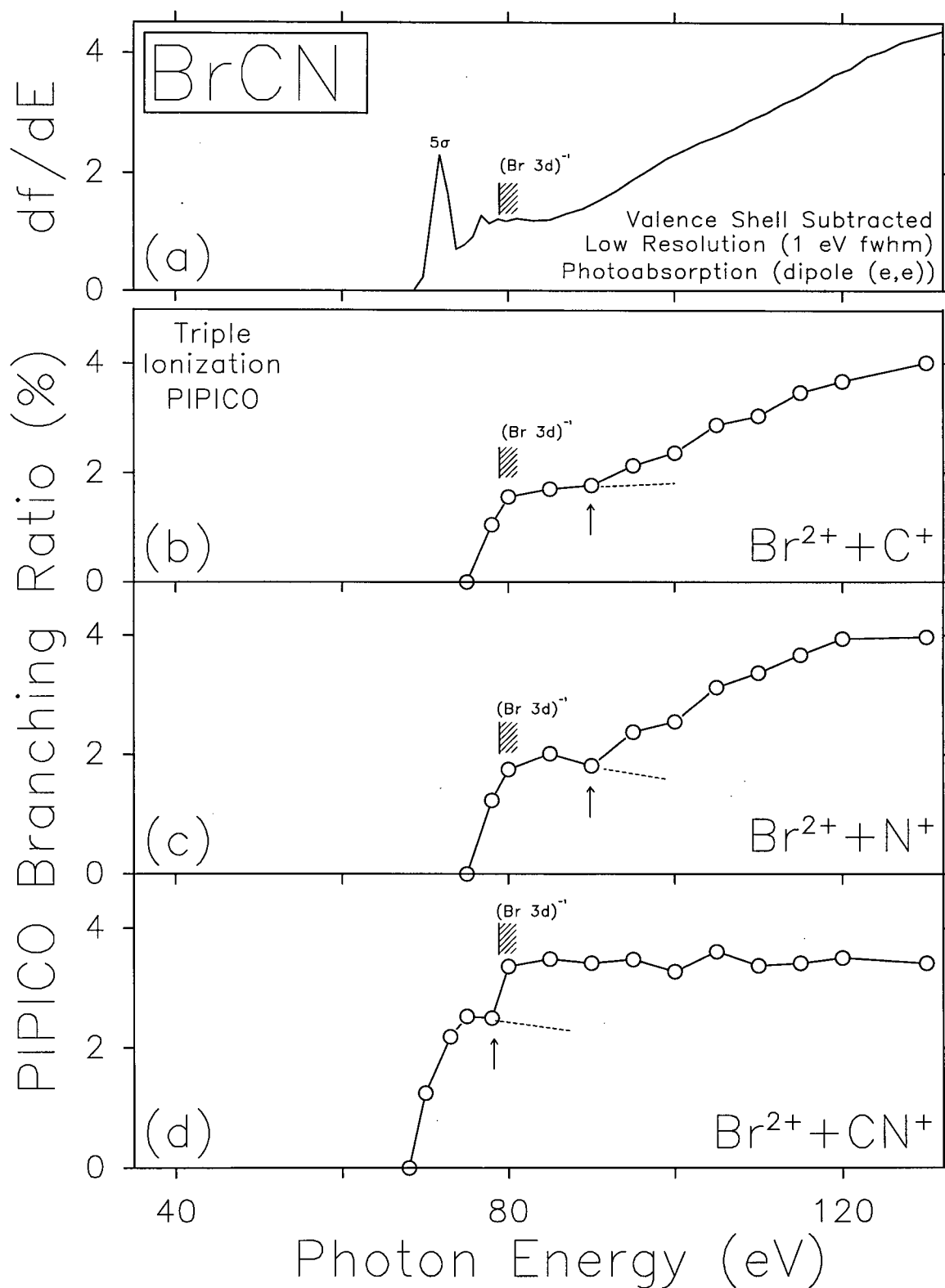


Figure 7.13: PIPICO branching ratios (40–130 eV) for dissociative triple photoionization of BrCN (panels b, c and d). The position of the Br 3d ionization edge was estimated in section 7.3.3.2.

into  $\text{Br}^{2+} + \text{C}^+$  and  $\text{Br}^{2+} + \text{N}^+$  from the Br 3d hole state is delayed until  $\sim 10$  eV above the  $(\text{Br } 3d)^{-1}$  threshold. This difference again corresponds approximately to the energy required to break the CN bond. In summary, both the resonant Auger and the Auger processes initially result in separation of the triply ionized molecule into  $\text{Br}^{2+} + \text{CN}^+$ . Decomposition into three particles  $\text{Br}^+ + \text{C}^+ + \text{N}$  and  $\text{Br}^+ + \text{C} + \text{N}^+$  only occurs when the  $\text{BrCN}^{3+}$  species can obtain enough internal energy to break the  $\text{C}\equiv\text{N}$  bond.

Table 7.8: PIPICO branching ratios for double and triple dissociative photoionization of BrCN from 40 to 130 eV.

Energy(eV)	$\text{Br}^+ + \text{CN}^+$	$\text{BrC}^+ + \text{N}^+$	$\text{Br}^+ + \text{C}^+ + \text{N}$	$\text{Br} + \text{C}^+ + \text{N}^+$	$\text{Br}^+ + \text{C} + \text{N}^+$	$\text{Br}^{2+} + \text{CN}^+$	$\text{Br}^{2+} + \text{C} + \text{N}^+$	$\text{Br}^{2+} + \text{C}^+ + \text{N}$
40	87.36	9.17	3.47	0				
43	84.13	9.41	5.58	0.88	0			
45	77.12	9.46	10.71	1.35	1.34			
48	64.43	9.26	17.54	2.28	3.49			
50	62.17	8.58	20.05	2.67	6.55			
55	51.68	7.30	22.94	4.43	13.65			
58	49.25	6.71	22.97	5.50	15.56			
60	47.48	6.69	23.85	5.95	16.04			
65	43.81	5.67	24.81	7.71	18.01			
68	41.74	4.50	24.89	8.47	19.49	0		
70	39.23	5.10	25.41	8.75	20.26	1.25		
73	36.32	4.48	26.01	9.75	20.90	2.19		
75	30.85	3.82	27.52	12.56	22.71	2.53	0	0
78	22.03	3.07	26.68	17.03	26.46	2.50	1.23	1.05

Table 7.8: (continued) PIPICO branching ratios for double and triple dissociative photoionization of BrCN from 40 to 130 eV.

Energy(eV)	$\text{Br}^+ + \text{CN}^+$	$\text{BrC}^+ + \text{N}^+$	$\text{Br}^+ + \text{C}^+ + \text{N}$	$\text{Br} + \text{C}^+ + \text{N}^+$	$\text{Br}^+ + \text{C} + \text{N}^+$	$\text{Br}^{2+} + \text{CN}^+$	$\text{Br}^{2+} + \text{C} + \text{N}^+$	$\text{Br}^{2+} + \text{C}^+ + \text{N}$
80	20.85	2.65	26.80	17.04	25.72	3.36	1.75	1.56
85	20.42	2.56	26.13	16.76	26.86	3.49	2.01	1.70
90	19.40	2.32	27.64	17.51	26.13	3.42	1.81	1.77
100	15.58	1.88	27.79	18.89	27.65	3.28	2.55	2.37
105	14.45	1.68	27.22	20.05	26.99	3.61	3.13	2.88
110	13.53	1.58	27.44	20.22	27.40	3.38	3.37	3.05
115	12.97	1.53	26.75	21.29	26.10	3.42	3.67	3.47
130	12.51	1.51	27.60	20.84	26.40	3.51	3.94	3.67
130	12.50	1.47	26.74	21.91	26.03	3.41	3.97	4.01

### 7.3.7 Dipole-induced breakdown

An examination of the appearance potentials (table 7.7), the ionization potentials [331, 332, 335] and Franck-Condon widths [331, 332] for the various primary ionization processes of BrCN, together with the shapes and possible higher energy onsets in the photoion partial oscillator strength curves (figure 7.10) indicates that single ionization of the three outermost valence orbitals does not lead to production of any fragment ions. Furthermore,  $C^+$  and  $N^+$  can only be first formed via inner valence ionization ( $2\sigma$  and/or  $1\sigma$ ). Inner valence ( $2\sigma$  and/or  $1\sigma$ ) processes also contribute to the valence shell yields of  $BrC^+$ ,  $Br^+$  and  $CN^+$ .

Unstable doubly charged  $BrCN^{2+}$  ions decompose primarily into  $Br^+ + CN^+$  and  $BrC^+ + N^+$ , with the breakdown pathway involving separation into two atomic ions and one neutral atom only opening up when the exciting photon energy exceeds the thermochemical threshold in the region of 40 eV. The (unstable) triple charged  $BrCN^{3+}$  ion is first generated by resonance double Auger decay following the  $5\sigma(\sigma^*) \leftarrow Br\ 3d$  inner shell excitation process. The resulting  $BrCN^{3+}$  ion rapidly decomposes into the  $Br^{2+} + CN^+$  pair. At the Br 3d ionization potential a second  $Br^{2+} + CN^+$  channel opens. When the primary photon energy is high enough so that the excess energy can break the  $C\equiv N$  bond the doubly dissociative  $Br^{2+} + C^+ + N$  and  $Br^{2+} + C + N^+$  processes occur in the Br 3d Rydberg excitation region and above the Br 3d ionization thresholds.

A joint consideration of the shapes of the photoabsorption spectra (figures 7.1, 7.2 and 7.7), the photoion partial oscillator strengths (figure 7.10) and the PIPICO results (figures 7.11, 7.12 and 7.13) shows that creation of the Br 3d inner-shell excited and ionized states contributes to production of all singly charged fragment ions (figure 7.10) as well as to all dissociative double and dissociative triple ionization processes which result in Coulomb explosion into at least two positively charged fragments.  $Br^{2+}$  arises from Coulomb explosion of unstable triply charged cations formed in dissociative resonance Auger and normal



## Chapter 8

### Concluding Remarks

The electronic excitation and ionization of the methyl halides and BrCN have been studied using dipole electron impact methods to investigate their interaction with UV/VUV and soft X-ray radiation. The present study has provided wide-ranging absolute photoabsorption oscillator strength data for CH<sub>3</sub>F, CH<sub>3</sub>Cl, CH<sub>3</sub>Br, CH<sub>3</sub>I and BrCN at a resolution of 1 eV fwhm. The discrete excitation spectra of these molecule in their valence shell regions and in selected inner shell regions have also been studied at higher resolutions (0.05 to 0.15 eV fwhm) to provide spectral assignment and estimates of transition energies. Where possible oscillator strengths for individual transitions have also been provided.

In addition to providing accurate oscillator strengths, it has been shown that the wide-ranging photoabsorption spectra obtained using dipole (e,e) spectroscopy for 56 atoms and small molecules, including the methyl halides and BrCN, yield dipole sums ( $S(u)$  and  $L(u)$ ) which are highly consistent with experimental and theoretical literature values. It has also been shown that accurate values of molecular and inter-molecular properties, such as the dipole polarizability, normal Verdet constant and  $C_6(A, B)$  interaction coefficients, can be obtained directly from the differential oscillator strength spectra or alternatively from the  $S(u)$  and  $L(u)$  sums. For many systems, the values obtained from the absolute dipole (e,e) photoabsorption spectra are the only values available. Conversely it has been shown that the static and dynamic dipole polarizabilities, the  $S(-2)$  and related sum-rules, can be used for extremely accurate normalization of photoabsorption spectra where appropriate dipole polarizability data are available. This has proven especially useful for molecules containing

heavier atoms where inner shell and other spectral features preclude normalization procedures using the  $S(0)$  or VTRK sum-rules. It should also find application for normalization of synchrotron radiation photoabsorption spectra which thus far are only available over much more limited energy ranges than those obtained using the dipole (e,e) method.

The absolute partial oscillator strengths for molecular and dissociative photoionization of the methyl halides and BrCN, in the valence shells of  $\text{CH}_3\text{F}$  and  $\text{CH}_3\text{Cl}$ , and in the valence shells and low energy inner shells (Br 3d and I 4d) of  $\text{CH}_3\text{Br}$ ,  $\text{CH}_3\text{I}$  and BrCN, have also been reported in the present work. These measurements, along with data from synchrotron radiation PES ( $\text{CH}_3\text{F}$ ,  $\text{CH}_3\text{Cl}$  and  $\text{CH}_3\text{Br}$ ) and PIPICO spectroscopy (BrCN) measurements, have led to a detailed quantitative understanding of the dipole-induced breakdown pathways of the methyl halides and BrCN under the influence of VUV/soft X-ray radiation.

## Bibliography

- [1] J. W. Gallagher, C. E. Brion, J. A. R. Samson, and P.W. Langhoff. *J. Phys. Chem. Ref. Data*, **17** (1988) 9, and references therein.
- [2] M. Guelin. Chemical composition and molecular abundances of molecular clouds. In G. H. F. Dierksen, W. F. Huebner, and P. W. Langhoff, editors, *Molecular Astrophysics*, p 23. D. Reidel Publishing Company, Dordrecht, 1984.
- [3] P. W. Langhoff. Molecular photoionization processes of astrophysical and aeronomical interest. In G. H. F. Dierksen, W. F. Huebner, and P. W. Langhoff, editors, *Molecular Astrophysics*, p 551. D. Reidel Publishing Company, Dordrecht, 1984.
- [4] N. Kaifu. Interstellar molecules. In T. Watanabe, I. Shimamura, M. Shimizu, and Y. Itikawa, editors, *Molecular Process in Space*, p 205. Plenum Press, New York, 1990.
- [5] K. P. Kirby. Molecular photoabsorption processes. In T. W. Hartquist, editor, *Molecular Astrophysics*, p 159. Cambridge University Press, Cambridge, 1990.
- [6] R. D. Hudson. *Rev. Geophys. Space Phys.*, **6** (1971) 305.
- [7] T. Shimazaki. Molecular processes in the upper atmospheres of the earth and other planets. In T. Watanabe, I. Shimamura, M. Shimizu, and Y. Itikawa, editors, *Molecular Process in Space*, p 173. Plenum Press, New York, 1990.
- [8] C. E. Brion and A. Hamnett. *Adv. Chem. Phys.*, **45** (1981) 1.
- [9] C. E. Brion. *Comm. At. Mol. Phys.*, **16** (1985) 249, and references therein.
- [10] T. N. Olney, N. Cann, G. Cooper, and C. E. Brion. *Phys. Rev. A*, (1996) manuscript in preparation.
- [11] G. R. Burton, W. F. Chan, G. Cooper, C. E. Brion, A. Kumar, and W. J. Meath. *Can. J. Chem.*, **71** (1993) 341.
- [12] G. R. Burton, W. F. Chan, G. Cooper, C. E. Brion, A. Kumar, and W. J. Meath. *Can. J. Chem.*, **72** (1994) 529.
- [13] E. Meszaros. *Global and Regional Changes in Atmospheric Composition* (Lewis Publishers, Boca Raton, 1993).
- [14] J. T. Houghton, G. J. Jenkins, and J. J. Ephraums, editors. *Climate Change*. IPCC (Intergovernmental Panel on Climate Change), Cambridge University Press, Cambridge, 1990.
- [15] H. B. Singh, L. J. Salas, H. Shigeishi, and E. Scribner. *Science*, **203** (1979) 899.

- [16] W. L. Chameides and D. D. Davies. *J. Geophys. Res.*, **C 85** (1980) 7383.
- [17] B. J. Finlayson-Pitts and J. N. Pitts. *Atmospheric Chemistry: Fundamentals and Experimental Techniques* (John Wiley & Sons, New York, 1986).
- [18] T. E. Graedel. *Chemical Compounds in the Atmosphere* (Academic Press, New York, 1978).
- [19] R. A. Rasmussen, L. E. Rasmussen, and M. A. K. Khalil. *J. Geophys. Res.*, **85** (1980) 7350.
- [20] D. B. Harper. *Nature*, **315** (1985) 55.
- [21] L. P. Hager. *Science*, **249** (1990) 160.
- [22] V. A. Isidorov. *Organic Chemistry of the Earth's Atmosphere*. Springer-Verlag, Berlin, 1990.
- [23] G. W. Gribble. *J. Nat. Prod.*, **55** (1992) 1353.
- [24] V. D. Karzh. *Atmos. Environ.*, **18** (1984) 2908.
- [25] R. Tokarczyk and R. M. Moore. *Geophys. Res. Letters*, **21** (1994) 285.
- [26] M. B. Hocking. *Modern Chemical Technology and Emission Control* (Springer-Verlag, Berlin, 1985).
- [27] W. F. Chan, G. Cooper, and C. E. Brion. *Phys. Rev. A*, **44** (1991) 186.
- [28] W. F. Chan, G. Cooper, R. N. S. Sodhi, and C. E. Brion. *Chem. Phys.*, **170** (1993) 81.
- [29] W. F. Chan, G. Cooper, and C. E. Brion. *Chem. Phys.*, **168** (1992) 375.
- [30] W. F. Chan, G. Cooper, and C. E. Brion. *Chem. Phys.*, **170** (1993) 123.
- [31] J. A. R. Samson. *Techniques of VUV Spectroscopy* (John Wiley & Sons, New York, 1967).
- [32] W. F. Chan, G. Cooper, K. H. Sze, and C. E. Brion. *J. Phys. B*, **23** (1990) L523.
- [33] H. A. Bethe. *Ann. Phys.*, **5** (1930) 325.
- [34] U. Fano and J. W. Cooper. *Rev. Mod. Phys.*, **40** (1968) 441.
- [35] M. Inokuti. *Rev. Mod. Phys.*, **43** (1971) 297.
- [36] E. N. Lassettre and A. Skeberle. In D. Williams, editor, *Methods of Experimental Physics*, volume 3, p 868. Academic Press, New York, 1974.
- [37] C. E. Brion. *Rad. Research*, **64** (1975) 37.

- [38] E. N. Lassette, A. S. Berman, S. M. Silverman, and M. E. Krasnow. *J. Chem. Phys.*, **40** (1964) 1232.
- [39] E. N. Lassette, M. E. Krasnow, and S. M. Silverman. *J. Chem. Phys.*, **40** (1964) 1242.
- [40] E. N. Lassette, A. Skeberle, M. A. Dillon, and K. J. Ross. *J. Chem. Phys.*, **48** (1968) 5066.
- [41] M. J. Van der Wiel. *Physica*, **49** (1970) 411.
- [42] M. J. Van der Wiel and G. Wiebes. *Physica*, **53** (1971) 225; **54** (1971) 411.
- [43] C. Backx and M. J. Van der Wiel. *J. Phys. B*, **8** (1975) 3020.
- [44] C. Backx, R. R. Tol, G. R. Wight, and M. J. Van der Wiel. *J. Phys. B*, **8** (1975) 2050.
- [45] C. Backx, G. R. Wight, R. R. Tol, and M. J. Van der Wiel. *J. Phys. B*, **8** (1975) 3007.
- [46] W. F. Chan, G. Cooper, X. Guo, and C. E. Brion. *Phys. Rev. A*, **45** (1992) 1420.
- [47] J. D. Jackson. *Classical Electrodynamics*. John Wiley & Sons, New York, 1975.
- [48] Y. Iida, F. Carnovale, S. Daviel, and C. E. Brion. *Chem. Phys.*, **105** (1986) 211.
- [49] G. Cooper, Y. Zheng, G. R. Burton, and C. E. Brion. *Rev. Sci. Instrum.*, **64** (1993) 1140.
- [50] G. R. Burton, G. Cooper, W. F. Chan, and C. E. Brion. *Chem. Phys.*, **167** (1992) 349.
- [51] G. R. Burton, W. F. Chan, G. Cooper, and C. E. Brion. *Chem. Phys.*, **181** (1994) 147.
- [52] K. Siegbahn, C. Nordling, C. Johansson, J. Hedman, P. F. Heden, K. Hamrin, U. Gelius, T. Bergmark, L. O. Werme, R. Manne, and Y. Baer. *ESCA Applied to Free Molecules* (North-Holland, Amsterdam, 1969).
- [53] D.W. Turner, C. Baker, A.D. Baker, and C.R. Brundle. *Molecular Photoelectron Spectroscopy* (wiley-interscience, london, 1970).
- [54] K. Kimura, S. Katsumata, Y. Achiba, T. Yamazaki, and S. Iwata. *Handbook of HeI Photoelectron Spectra of Fundamental Organic Molecules* (japan scientific press, tokyo, 1981).
- [55] J. H. D. Eland. *Photoelectron Spectroscopy 2<sup>nd</sup> Ed.* (Butterworths, London, 1984).
- [56] A. Hamnett, W. Stoll, G. Branton, M. J. van der Wiel, and C. E. Brion. *J. Phys. B*, **9** (1976) 945.
- [57] C. E. Brion, A. Hamnett, G. R. Wight, and M. J. Van der Wiel. *J. Electron Spectry. Relat. Phenom.*, **12** (1977) 323.

- [58] M. G. White, K. T. Leung, and C. E. Brion. *J. Electron Spectry. Relat. Phenom.*, **23** (1981) 127.
- [59] C. E. Brion. In S. Datz, editor, *Physics of Electronic and Atomic Collisions*, p 579. North Holland, Amsterdam, 198284.
- [60] C. E. Brion and J. P. Thomson. *J. Electron Spectry. Relat. Phenom.*, **33** (1984) 301.
- [61] F. Carnovale and C. E. Brion. *Chem. Phys.*, **74** (1983) 253.
- [62] T. Koopmans. *Physica*, **1** (1933) 104.
- [63] D. R. Bates. *Mon. Not. Roy. Astr. Soc.*, **106** (1946) 432.
- [64] S.T. Manson. *Adv. Electron. Electr. Phys.*, **41** (1976) 73.
- [65] H.A Bethe and E.E. Salpeter. *Quantum Mechanics of One- and Two-Electron Atoms* (Springer-Verlag, Berlin, 1957, p. 247).
- [66] W. Heitler. *Quantum Theory of Radiation* (Oxford Univ. Press, London, 1954).
- [67] L. S. Cederbaum. *Theor. Chim. Acta*, **31** (1973) 239.
- [68] L. S. Cederbaum. *J. Phys. B*, **8** (1975) 291.
- [69] M. Robin. *Higher Excited States of Polyatomic Molecules* (Academic Press, New York, 1985).
- [70] R. N. S. Sodhi and C. E. Brion. *J. Electron Spectry. Relat. Phenom.*, **34** (1984) 363.
- [71] A. B. F. Duncan. *Rydberg Series in Atoms and Molecules* (Academic Press, New York, 1971).
- [72] T. N. Olney, T. Ibuki, and C. E. Brion. *Chem. Phys.*, **201** (1995) 505.
- [73] T. N. Olney, T. Ibuki, and C. E. Brion. *Chem. Phys.*, (1996) manuscript in preparation.
- [74] J. Berkowitz. *Photoabsorption, Photoionization and Photoelectron Spectroscopy* (Academic Press, New York, 1979).
- [75] C. Fabre and S. Haroche. In R. F. Stebbings and F. B. Dunning, editors, *Rydberg State of Atoms and Molecules*. Cambridge University Press, London, 1983.
- [76] V. A. Fomichev. *Soviet. Phys. Solid State*, **9** (1968) 2496.
- [77] X. Guo, G. Cooper, W. F. Chan, G. R. Burton, and C. E. Brion. *Chem. Phys.*, **161** (1992) 453; 471.
- [78] V. T. Nefedov. *J. Struct. Chem.*, **11** (1970) 272.
- [79] J. L. Dehmer. *J. Chem. Phys.*, **56** (1972) 4496.

- [80] K. H. Sze and C. E. Brion. *Chem. Phys.*, **140** (1990) 439.
- [81] G. Cooper, W. Zhang, and C. E. Brion. *Can. J. Phys.*, **72** (1994) 1093.
- [82] G. R. Wight, C. E. Brion, and M. J. Van der Wiel. *J. Electron Spectry. Relat. Phenom.*, **1** (1972/1973) 457.
- [83] J. W. Cooper. *Phys. Rev.*, **128** (1962) 681.
- [84] W. F. Chan, G. Cooper, X. Guo, G. R. Burton, and C. E. Brion. *Phys. Rev. A*, **46** (1992) 149.
- [85] S.T. Manson and J. W. Cooper. *Phys. Rev.*, **165** (1968) 126.
- [86] K. Fukui, T. Yonezawa, and H. Shingu. *J. Chem. Phys.*, **20** (1952) 1.
- [87] A.P. Hitchcock, C. E. Brion, and M. J. Van der Wiel. *Chem. Phys.*, **45** (1980) 461.
- [88] L. S. Cederbaum and W. Domcke. *Adv. Chem. Phys.*, **36** (1977) 205.
- [89] W. von Niessen, J. Schirmer, and L. Cederbaum. *Comp. Phys. Reports*, **1** (1984) 57.
- [90] K. Siegbahn, C. Nordling, A. Fahlman, R. Nordberg, , K. Hamrin, J. Hedman, G. Johansson, T. Bergmark, S. Karlsson, I. Lindgren, and B. Lindberg. *ESCA Atomic, Molecular and Solid State Structure Studied by Means of Electron Spectroscopy* (Almqvist and Wiksells, Uppsala, 1967).
- [91] C. E. Brion, D. W. Lindle, P. A. Heimann, T. A. Ferrett, M. N. Piancastelli, and D. A. Shirley. *Chem. Phys. Letters*, **128** (1986) 118.
- [92] I. E. McCarthy and E. Weigold. *Phys. Rept.*, **27C** (1976) 275.
- [93] C. E. Brion. *Int. J. Quantum Chem.*, **29** (1986) 1397.
- [94] A. Minchinton, J. D. P. Cook, E. Weigold, and W. von Niessen. *Chem. Phys.*, **113** (1987) 251.
- [95] A. Minchinton, J. D. P. Cook, E. Weigold, and W. von Niessen. *Chem. Phys.*, **93** (1985) 21.
- [96] M. Inokuti, Y. Itikawa, and J. E. Turner. *Rev. Mod. Phys.*, **50** (1978) 23.
- [97] J. L. Dehmer, M. Inokuti, and R. P. Saxon. *Phys. Rev. A*, **12** (1975) 102.
- [98] J. L. Dehmer, M. Inokuti, and R. P. Saxon. *Phys. Rev. A*, **12** (1975) 102; M. Inokuti. Private communication.
- [99] J. A. Wheeler and J. A. Bearden. *Phys. Rev.*, **46** (1934) 755.
- [100] P. W. Atkins. *Physical Chemistry*, 3<sup>d</sup> ed. (W. H. Freeman and Co., New York, 1986).
- [101] A. D. Buckingham. *Trans. Farad. Soc.*, **52** (1956) 747.

- [102] U. Hohm. *Mol. Phys.*, **74** (1991) 1233.
- [103] U. Hohm and K. Kerl. *Mol. Phys.*, **69** (1990) 803.
- [104] U. Hohm and K. Kerl. *Mol. Phys.*, **69** (1990) 819.
- [105] U. Hohm. *Mol. Phys.*, **81** (1994) 157.
- [106] S. Daviel, C. E. Brion, and A. P. Hitchcock. *Rev. Sci. Instrum.*, **55** (1984) 182.
- [107] W. L. Wiese, M. W. Smith, and B. M. Glenon. *Atomic Transition Probabilities, Vol 1. Hydrogen through Neon NSRDS-NBS. Circular No. 4*, (US GPO, Washington, DC, 1966).
- [108] J. D. Bozek, J. N. Cutler, G. M. Bancroft, L. L. Coatsworth, K. H. Tan, D. S. Yang, and R. G. Cavell. *Chem. Phys. Letters*, **165** (1990) 1.
- [109] G. M. Bancroft D.G.J. Sutherland and K. H. Tan. *J. Chem. Phys.*, **97** (1992) 7918.
- [110] K. H. Tan, G. M. Bancroft, L. L. Coatsworth, and B. W. Yates. *Can. J. Phys.*, **60** (1982) 131.
- [111] L. Karlsson, R. Jardny, L. Mattsson, F. T. Chau, and K. Siegbahn. *Physica Scripta*, **16** (1977) 225.
- [112] T. Masuoka, T. Horigome, and I. Koyano. *Rev. Sci. Instrum.*, **60** (1989) 2179.
- [113] E. Ishiguro, M. Suzui, J. Yamazaki, E. Nakamura, K. Sakai, O. Matsuodu, N. Mizutani, K. Fukui, and M. Wantanabe. *Rev. Sci. Instrum.*, **60** (1989) 2105.
- [114] W. F. Chan, G. Cooper, and C. E. Brion. *Chem. Phys.*, **180** (1994) 77.
- [115] W. F. Chan, G. Cooper, and C. E. Brion. *Chem. Phys.*, **170** (1993) 99.
- [116] N. Cann, T. N. Olney, and C. E. Brion. *Chem. Phys.*, (1996) manuscript in preparation.
- [117] W. F. Chan, G. Cooper, and C. E. Brion. *Chem. Phys.*, **178** (1993) 387.
- [118] C. E. Brion, K. H. Tan, M. J. Van der Wiel, and Ph. E. van der Leeuw. *J. Electron Spectry. Relat. Phenom.*, **17** (1979) 101.
- [119] C. E. Brion, Y. Iida, and J. P. Thomson. *Chem. Phys.*, **101** (1986) 449.
- [120] G. R. Burton, W. F. Chan, G. Cooper, and C. E. Brion. *Chem. Phys.*, **177** (1993) 217.
- [121] W. F. Chan, G. Cooper, and C. E. Brion. *Chem. Phys.*, **170** (1993) 111.
- [122] M. Dyck, G. Cooper, T. N. Olney, and C. E. Brion. *Chem. Phys.*, (1996) manuscripts in preparation.
- [123] W. F. Chan, G. Cooper, and C. E. Brion. *Chem. Phys.*, **178** (1993) 401.

- [124] J. W. Au, G. Cooper, G. R. Burton, T. N. Olney, and C. E. Brion. *Chem. Phys.*, **173** (1993) 209.
- [125] G. Cooper, G. R. Burton, and C. E. Brion. *J. Electron Spectry. Relat. Phenom.*, **73** (1995) 139.
- [126] G. Cooper, T. N. Olney, and C. E. Brion. *Chem. Phys.*, **194** (1995) 175.
- [127] G. Cooper, J. Anderson, and C. E. Brion. *Chem. Phys.*, (1996) in press.
- [128] G. Cooper, J. Anderson, and C. E. Brion. *Chem. Phys.*, (1996) manuscripts in preparation.
- [129] T. N. Olney and C. E. Brion. *Chem. Phys.*, (1996) manuscripts in preparation.
- [130] G. Cooper, G. R. Burton, W. F. Chan, and C. E. Brion. *Chem. Phys.*, **196** (1995) 293.
- [131] E. B. Zarate, G. Cooper, and C. E. Brion. *Chem. Phys.*, **148** (1990) 277; 289.
- [132] J. Au, G. Cooper, and C. E. Brion. *Chem. Phys.*, (1997) manuscripts in preparation.
- [133] J. Au, G. Cooper, and C. E. Brion. *Chem. Phys.*, (1997) manuscripts in preparation.
- [134] G. D. Zeiss, W. J. Meath, J. C. F. MacDonald, and D. J. Dawson. *Can. J. Phys.*, **55** (1977) 2080.
- [135] G. F. Thomas and W. J. Meath. *Mol. Phys.*, **34** (1977) 113.
- [136] B. L. Jhanwar, W. J. Meath, and J. C. F. MacDonald. *Can. J. Phys.*, **59** (1981) 185.
- [137] B. L. Jhanwar and W. J. Meath. *Chem. Phys.*, **67** (1982) 185.
- [138] B. L. Jhanwar, W. J. Meath, and J. C. F. MacDonald. *Can. J. Phys.*, **61** (1983) 1027.
- [139] A. Kumar and W. J. Meath. *Can. J. Chem.*, **63** (1985) 1616.
- [140] A. Kumar and W. J. Meath. *Mol. Phys.*, **75** (1992) 311.
- [141] A. Kumar and W. J. Meath. *Chem. Phys.*, **189** (1994) 467.
- [142] F. E. Cummings. *J. Chem. Phys.*, **63** (1975) 1960.
- [143] M. Inokuti, J. L. Dehmer, T. Baer, and J. D. Hanson. *Phys. Rev. A*, **23** (1981) 95.
- [144] J. Geertsen, J. Oddershede, and J. R. Sabin. *Phys. Rev. A*, **34** (1986) 1104.
- [145] M. J. Packer, S. P. A. Sauer, and J. Oddershede. *J. Chem. Phys.*, **100** (1994) 8969.
- [146] W. M. Kosman and S. Wallace. *J. Chem. Phys.*, **82** (1985) 1385.
- [147] P. W. Langhoff and M. Karplus. *J. Opt. Soc. Am.*, **59** (1969) 863.

- [148] G. Starkschall and R. G. Gordon. *J. Chem. Phys.*, **54** (1971) 663.
- [149] G. A. Parker and R. T. Pack. *J. Chem. Phys.*, **64** (1976) 2010.
- [150] R. T. Pack. *J. Chem. Phys.*, **61** (1974) 2091.
- [151] U. Hohm. *Mol. Phys.*, **78** (1993) 929.
- [152] G. A. Victor and A. Dalgarno. *J. Chem. Phys.*, **50** (1969) 2535.
- [153] P. J. Leonard and J. A. Barker. in *Theoretical Chemistry, Advances and Perspectives.*, **1** (1975) 117.
- [154] D. E. Gerhart. *J. Chem. Phys.*, **62** (1975) 821.
- [155] E. Eggarter. *J. Chem. Phys.*, **62** (1975) 833.
- [156] G. C. Nielson, G. A. Parker, and R. T. Pack. *J. Chem. Phys.*, **64** (1976) 2055.
- [157] G. Cooper, T. Ibuki, and C. E. Brion. *Chem. Phys.*, **140** (1990) 133,147.
- [158] G. Cooper, T. Ibuki, Y. Iida, and C. E. Brion. *Chem. Phys.*, **125** (1988) 307.
- [159] T. Ibuki, G. Cooper, and C. E. Brion. *Chem. Phys.*, **129** (1989) 295.
- [160] G. Cooper, E. B. Zarate, R. K. Jones, and C. E. Brion. *Chem. Phys.*, **150** (1991) 237,251.
- [161] W. Zhang, G. Cooper, T. Ibuki, and C. E. Brion. *Chem. Phys.*, **137** (1989) 391; **151** (1991) 343, 357; **153** (1991) 491.
- [162] E. W. Washburn. *International critical tables*, (McGraw-Hill, New York, Vol 7, pp 2-11, 1930).
- [163] H. A. Stuart. *Landolt-Bornstein, Atom und Molekularphysik*, (Springer-Verlag, Berlin, Vol 1, Part 3, pp 509, 1951).
- [164] A. A. Maryott and F. Buckley. *U.S. National Bureau of Standards Circular No. 537*, (US GPO, Washington, DC, 1953).
- [165] R. R. Teachout and R. T. Pack. *At. Data*, **3** (1971) 196.
- [166] K. J. Miller. *J. Am. Chem. Soc.*, **112** (1990) 8533.
- [167] H. E. Watson and K. L. Ramaswamy. *Proc. Roy. Soc. Lond. A*, **156** (1936) 130,144.
- [168] K. L. Ramaswamy. *Proc. Indian Acad. Sci.*, **A4** (1936) 675.
- [169] U. Hohm and U. Trümper. *Chem. Phys.*, **189** (1994) 443.
- [170] U. Hohm. *Chem. Phys.*, **179** (1994) 533.

- [171] G. Maroulis and A. J. Thakkar. *J. Chem. Phys.*, **88** (1988) 7623.
- [172] G. Maroulis and A. J. Thakkar. *J. Chem. Phys.*, **89** (1988) 7320.
- [173] G. Maroulis and A. J. Thakkar. *Chem. Phys. Letters*, **156** (1989) 87.
- [174] G. Maroulis and A. J. Thakkar. *J. Chem. Phys.*, **93** (1990) 4164.
- [175] G. Maroulis and A. J. Thakkar. *J. Chem. Phys.*, **93** (1990) 652.
- [176] G. Maroulis and A. J. Thakkar. *Mol. Phys.*, **73** (1991) 1235.
- [177] G. Maroulis. *J. Chem. Phys.*, **94** (1991) 1182.
- [178] G. Maroulis. *J. Chem. Phys.*, **97** (1992) 4188.
- [179] G. Maroulis. *Mol. Phys.*, **77** (1992) 1085.
- [180] E. F. Archibong and A. J. Thakkar. *Chem. Phys. Letters*, **201** (1993) 493.
- [181] E. F. Archibong and A. J. Thakkar. *J. Chem. Phys.*, **100** (1994) 7471.
- [182] D. E. Woon and Jr. T. H. Dunning. *J. Chem. Phys.*, **100** (1994) 2975.
- [183] W. Kolos and L. Wolniewicz. *J. Chem. Phys.*, **46** (1967) 1426.
- [184] J. Dougherty and M. A. Spackman. *Mol. Phys.*, **82** (1994) 193.
- [185] S. P. A. Sauer and J. Oddershede. *Intern. J. Quantum Chem.*, **50** (1994) 317.
- [186] A. J. Sadlej. *Theoret. Chim. Acta.*, **79** (1991) 123; **81** (1991) 45; **81** (1992) 339.
- [187] I. Alkorta, H. O. Villar, and J. J. Perez. *J. Phys. Chem.*, **97** (1993) 9113.
- [188] E. Ishiguro, T. Arai, M. Kotani, and M. Mizushima. *J. Phys. Soc. (London)*, **A 213** (1952) 178.
- [189] Y. K. Kang and M. S. Jhon. *Theor. Chim. Acta*, **61** (1982) 41.
- [190] A. C. Newell and R. D. Baird. *J. Appl. Phys.*, **36** (1965) 3751.
- [191] R. H. Orcutt and R. H. Cole. *J. Chem. Phys.*, **46** (1967) 697.
- [192] G. R. Alms, A. K. Burnham, and W. H. Flygare. *J. Chem. Phys.*, **63** (1975) 3321.
- [193] *Landolt-Bornstein. Zahlenwerte und Funktionen*, (Springer, Berlin, Vol 2, Part 8, pp 871, 1962).
- [194] J. Oddershede and E. N. Svendsen. *Chem. Phys.*, **64** (1982) 359.
- [195] E. A. Moelwyn-Hughes. *Physical Chemistry*, 2<sup>nd</sup> ed., (Pergamon Press, Oxford, 1964).
- [196] A. Donaldson and A. D. Caplin. *Phil. Mag. B*, **54** (1986) 27.

- [197] K. F. Luft. *Z. Physik*, **84** (1933) 767.
- [198] K. Kirby and D. L. Cooper. *J. Chem. Phys.*, **90** (1989) 4895.
- [199] C. Cuthbertson and M. Cuthbertson. *Phil. Trans. R. Soc. Lond. A*, **213** (1913) 1.
- [200] O. E. Frivold, O Hassel, and E Hetland. *Physik. Z.*, **39** (1938) 224.
- [201] M. Suto, X. Wang, and L. C. Lee. *J. Chem. Phys.*, **86** (1987) 1152.
- [202] J. A. R. Samson and L. Yin. *J. Opt. Soc. Am. B*, **6** (1989) 2326.
- [203] A. J. Thakkar. *J. Chem. Phys.*, **75** (1981) 4496.
- [204] W. H. Press, S. A. Teukolsky, W. T. Vetterling, and B. P. Flannery. *Numerical Recipes in Fortran*, (Cambridge Press, Cambridge), 1992).
- [205] S. P. A. Sauer, J. Oddershede, and G. H. F. Diercksen. *J. Am. Chem. Soc.*, **42** (1990) 1302.
- [206] R. Serber. *Phys. Rev. A*, **41** (1932) 489.
- [207] H. Becquerel. *C. R. Acad. Sci.*, **125** (1897) 679.
- [208] W. A. Parkinson, S. P. A. Sauer, J. Oddershede, and D. M. Bishop. *J. Chem. Phys.*, **98** (1993) 487.
- [209] E. R. Peck and B. N. Khanna. *J. Opt. Soc. Am.*, **56** (1966) 1059.
- [210] A. Kumar and W. J. Meath. *Theor. Chim. Acta.*, **82** (1992) 131.
- [211] G. C. Maitland, M. Rigby, E. B. Smith, and W. A. Wakeman. *Intermolecular Forces* (Oxford Science Publications, Oxford, 1987).
- [212] A. J. Thakkar, Z-M Hu, C. E. Chuaqui, J. S. Carley, and R. J. LeRoy. *Theor. Chim. Acta*, **82** (1992) 57.
- [213] H. Hettema, P. E. S. Wormer, and A. J. Thakkar. *Mol. Phys.*, **80** (1993) 533.
- [214] H. L. Kramer. *J. Chem. Phys.*, **53** (1970) 2783.
- [215] P. E. S. Wormer and H. Hettema. *J. Chem. Phys.*, **97** (1992) 5592.
- [216] A. J. Thakkar, H. Hettema, and P. E. S. Wormer. *J. Chem. Phys.*, **97** (1992) 3292.
- [217] W. Rijks and P. E. S. Wormer. *J. Chem. Phys.*, **90** (1989) 6507.
- [218] F. Visser, P. E. S. Wormer, and W. P. J. H. Jacobs. *J. Chem. Phys.*, **82** (1985) 3753.
- [219] P. E. S. Wormer, H. Hettema, and A. J. Thakkar. *J. Chem. Phys.*, **98** (1993) 7140.

- [220] H. Hettema, P. E. S. Wormer, P. Jorgensen, H. A.Aa. Jensen, and T. Helgaker. *J. Chem. Phys.*, **100** (1994) 1297.
- [221] A. Kumar and W. J. Meath. *Mol. Phys.*, **54** (1985) 823.
- [222] K. T. Tang, J. M. Norbeck, and P. R. Certain. *J. Chem. Phys.*, **64** (1976) 3063.
- [223] D. M. Bishop and J. Pipin. *Intern. J. Quantum Chem.*, **45** (1993) 349.
- [224] W. Meyer, P. C. Hariharan, and W. Kutzelnigg. *J. Chem. Phys.*, **73** (1980) 1880.
- [225] B. L. Jhanwar and W. J. Meath. *Mol. Phys.*, **41** (1980) 1061.
- [226] G. D. Zeiss and W. J. Meath. *Mol. Phys.*, **33** (1977) 1155.
- [227] W. Rijks, M. van Heeringen, and P. E. S. Wormer. *J. Chem. Phys.*, **90** (1989) 6501.
- [228] G. Cooper, W. Zhang, C. E. Brion, and K. H. Tan. *Chem. Phys.*, **145** (1990) 117.
- [229] R. S. Mulliken. *Phys. Rev.*, **47** (1935) 413.
- [230] W. C. Price. *J. Chem. Phys.*, **4** (1936) 539.
- [231] R. S. Mulliken. *Phys. Rev.*, **61** (1942) 277.
- [232] R. S. Mulliken and E. Teller. *Phys. Rev.*, **61** (42) 283.
- [233] S. Stokes and A. B. F. Duncan. *J. Am. Chem. Soc.*, **80** (1958) 6177.
- [234] L. Edwards and J. W. Raymond. *J. Am. Chem. Soc.*, **91** (1969) 5937.
- [235] P. Sauvageau, R. Gilbert, P. P. Berlow, and C. Sandorfy. *J. Chem. Phys.*, **59** (1972) 762.
- [236] W. R. Harshbarger, M. B. Brown, and E. N. Lassetre. *J. Electron Spectry. Relat. Phenom.*, **1** (1972/73) 319.
- [237] C. Y. R. Wu, L. C. Lee, and D. L. Judge. *J. Chem. Phys.*, **71** (1979) 5221.
- [238] H. Tsubomura, K. Kimura, K. Kaya, J. Tanaka, and S Nagakura. *Bull. Chem. Soc. Japan*, **73** (1964) 417.
- [239] B. R. Russell, L. O. Edwards, and J. W. Raymond. *J. Am. Chem. Soc.*, **95** (1973) 2129.
- [240] J. W. Raymond, L. Edwards, and B. R. Russell. *J. Am. Chem. Soc.*, **96** (1974) 1708.
- [241] P. Hochmann, P. H. Templet, H. t Wang, and S. P. McGlynn. *J. Chem. Phys.*, **62** (1975) 2588.
- [242] S. Felps, P. Hochmann, P. Brint, and S. P. McGlynn. *J. Mol. Spectrosc.*, **59** (1976) 355.

- [243] D. E. Robbins. *Int. Conf. Probl. Relat. Stratos.*, (1976) 255.
- [244] W. S. Felps, K. Rupuik, and S. P. McGlynn. *J. Phys. Chem.*, **95** (1991) 639.
- [245] L. C. Lee and M. Suto. *Chem. Phys.*, **114** (1987) 423.
- [246] J. C. Person and P. P. Nicole. *ANL Radiological Phys. Div. Ann. Rpt.*, **July 1969 - June 1970** (ANL-7760, Pt 1) 97.
- [247] J. C. Person and P. P. Nicole. *J. Chem. Phys.*, **55** (1971) 3390.
- [248] G. C. Causley and B. R. Russell. *J. Chem. Phys.*, **62** (1975) 848.
- [249] R. A. Boschi and D. R. Salahub. *Mol. Phys.*, **24** (1972) 289.
- [250] H. T. Wang, W. S. Felps, G. L. Findley, A. R. P. Rau, and S. P. McGlynn. *J. Chem. Phys.*, **67** (1977) 3940.
- [251] M. A. Baig, J. P. Connerade, J. Dagata, and S. P. McGlynn. *J. Phys. B*, **14** (1981) L25.
- [252] J. A. Dagata, G. L. Findley, S. P. McGlynn, J. P. Connerade, and M. A. Baig. *Phys. Rev. A*, **24** (1981) 2485.
- [253] J. A. Dagata, M. A. Scott, and S. P. McGlynn. *J. Chem. Phys.*, **88** (1988) 9.
- [254] A. Fahr, A. K. Nayak, and M. J. Kurylo. *Chem. Phys.*, **197** (1995) 195.
- [255] G. O'Sullivan. *J. Phys. B*, **15** (1982) L327.
- [256] A. P. Hitchcock and C. E. Brion. *J. Electron Spectry. Relat. Phenom.*, **13** (1978) 193.
- [257] A. P. Hitchcock and C. E. Brion. *J. Electron Spectry. Relat. Phenom.*, **17** (1979) 139.
- [258] M. S. Banna, B. E. Mills, D. W. Davis, and D. A. Shirley. *J. Chem. Phys.*, **61** (1974) 4780.
- [259] M. S. Banna and D. A. Shirley. *Chem. Phys. Letters*, **33** (1975) 441.
- [260] B. P. Pullen, T. A. Carlson, W. E. Moddeman, G. K. Schweitzer, W. E. Bull, and F. A. Grimm. *J. Chem. Phys.*, **53** (1970) 768.
- [261] J. L. Ragle, I. A. Stenhouse, D. C. Frost, and C. A. McDowell. *J. Chem. Phys.*, **53** (1970) 178.
- [262] A. W. Potts, H. J. Lempka, D. G. Streets, and W. C. Price. *Phil. Trans. R. Soc. Lond.*, **A268** (1970) 59.
- [263] C. R. Brundle, M. B. Robin, and H. Basch. *J. Chem. Phys.*, **53** (1970) 2196.
- [264] C. E. Brion, W. B. Stewart, D. S. C. Yee, and P. Crowley. *J. Electron Spectry. Relat. Phenom.*, **23** (1981) 399.

- [265] C. Utsunomiya, T. Kobayashi, and S. Nagakura. *Chem. Soc. Japan*, **53** (1980) 1216.
- [266] U. Heinzmann, B. Osterheld, F. Schäfers, and G. Schönhense. *J. Phys. B Letter*, **14** (1981) L79.
- [267] S. P. Goss, D. C. McGilvery, J. D. Morrison, and D. L. Smith. *J. Chem. Phys.*, **75** (1981) 1820.
- [268] G. Bieri, L. Åsbrink, and W. von Niessen. *J. Electron Spectry. Relat. Phenom.*, **23** (1981) 281.
- [269] W. von Niessen, L. Åsbrink, and G. Bieri. *J. Electron Spectry. Relat. Phenom.*, **26** (1982) 173.
- [270] P. R. Keller, J. W. Taylor, T. A. Carlson, and F. A. Grimm. *Chem. Phys.*, **79** (1983) 269.
- [271] T. A. Carlson, M. O. Krause, F. A. Grimm, P. R. Keller, and J. W. Taylor. *J. Chem. Phys.*, **77** (1982) 5340.
- [272] T. A. Carlson, M. O. Krause, F. A. Grimm, P. R. Keller, and J. W. Taylor. *Chem. Phys. Letters*, **87** (1982) 552.
- [273] T. A. Carlson, A. Fahlman, M. O. Krause, P. R. Keller, J. W. Taylor, T. Whitley, and F. A. Grimm. *J. Chem. Phys.*, **80** (1984) 3521.
- [274] I. Novak, J. M. Benson, and A. W. Potts. *J. Electron Spectry. Relat. Phenom.*, **41** (1986) 225.
- [275] T. D. Thomas. *J. Am. Chem. Soc.*, **92** (1970) 4184.
- [276] W. B. Perry and W. J. Jolly. *Inorg. Chem.*, **13** (1974) 1211.
- [277] W. L. Jolly, K. D. Bomben, and C. J. Eyermann. *At. Data Nucl. Data Tables*, **31** (1984) 433.
- [278] J. N. Cutler, G. M. Bancroft, and K. H. Tan. *J. Chem. Phys.*, **97** (1992) 7932.
- [279] K. H. Sze, C. E. Brion, and A. Katrib. *Chem. Phys.*, **132** (1989) 271.
- [280] J. J. Yeh and I. Lindau. *At. Data Nucl. Data Tables*, **32** (1985) 1.
- [281] B. L. Henke, P. Lee, J. J. Tanaka, R. L. Shimabukuro, and B. K. Fujikawa. *At. Data Nucl. Data Tables*, **27** (1982) 1.
- [282] A. P. Hitchcock and C. E. Brion. *J. Electron Spectry. Relat. Phenom.*, **14** (1978) 417.
- [283] Z. F. Liu, G. M. Bancroft, K. H. Tan, and M. Schachter. *J. Electron Spectry. Relat. Phenom.*, **67** (1994) 299.
- [284] D. A. Shaw, D. Cvejanović, G. C. King, and F. H. Read. *J. Phys. B*, **17** (1984) 1173.

- [285] F. J. Comes, U. Nielsen, and W. H. E. Schwarz. *J. Chem. Phys.*, **58** (1973) 2230.
- [286] R. C. Weast. *CRC Handbook of Chemistry and Physics* (CRC Press Inc., Boca Raton, Florida, 1988).
- [287] R. N. Dixon, J. N. Murrell, and B. Narayan. *Mol. Phys.*, **20** (1971) 611.
- [288] J. H. D. Eland, R. Frey, A. Kuestler, H. Schulte, and B. Brehm. *Intern. J. Mass Spectrom. Ion Processes*, **22** (1976) 155.
- [289] R. Cambi, G. Ciullo, A. Sgamellotti, F. Tarantelli, R. Fantoni, A. Giardini-Guidoni, and A. Sergio. *Chem. Phys. Letters*, **80** (1981) 295.
- [290] S. Katsumata and K. Kimura. *Bull. Chem. Soc. Japan*, **46** (1973) 1342.
- [291] A. M. Semkow, P. Rosmus, H. Brock, and P. Botschwina. *Chem. Phys.*, **40** (1979) 377.
- [292] U. Chandra Singh, P. K. Basu, and C. N. R. Rao. *J. Mol. Structure*, **87** (1982) 19.
- [293] D. Li, J. Zhu, J. Li, and Y. Pan. *Chem. Phys. Letters*, **87** (1982) 463.
- [294] Y. Uehaha, N. Saito, and T. Yonezawa. *Chem. Letters*, **73** (1973) 495.
- [295] G. de Alti, P. Decleva, and A. Sgamellotti. *J. Electron Spectry. Relat. Phenom.*, **12** (1977) 249.
- [296] H. Branson and C. Smith. *J. Am. Chem. Soc.*, **75** (1953) 4133.
- [297] F. P. Lossing, K. U. Ingold, and I. H. S. Henderson. *J. Chem. Phys.*, **22** (1954) 1489.
- [298] S. Tsuda, C. E. Melton, and W. H. Hamill. *J. Chem. Phys.*, **41** (1964) 689.
- [299] S. Tsuda and W. H. Hamill. *J. Chem. Phys.*, **41** (1964) 2713.
- [300] A. J. C. Nicholson. *J. Chem. Phys.*, **43** (1965) 1171.
- [301] J. M. Williams and W. H. Hamill. *J. Chem. Phys.*, **49** (1968) 4467.
- [302] A. S. Werner, B. P. Tsai, and T. Baer. *J. Chem. Phys.*, **60** (1974) 3650.
- [303] R. Locht and J. Momigny. *Intern. J. Mass Spectrom. Ion Processes*, **71** (1986) 141.
- [304] J. Momigny, R. Locht, and G. Caprace. *Intern. J. Mass Spectrom. Ion Processes*, **71** (1986) 159.
- [305] R. Locht, J. Momigny, E. Rühl, and H. Baumgartel. *Chem. Phys.*, **117** (1987) 305.
- [306] T. Masuoka and I. Koyano. *J. Chem. Phys.*, **95** (1991) 1619.
- [307] D. W. Lindle, P. H. Kobrin, C. M. Truesdale, T. A. Ferrett, P. A. Heimann, H. G. Kerkhoff, U. Becker, and D. A. Shirley. *Phys. Rev. A*, **30** (1984) 239.

- [308] S. D. Price and J. H. D. Eland. *J. Electron Spectry. Relat. Phenom.*, **52** (1990) 649.
- [309] I. Nenner, P. Morin, and P. Lablanquie. *Comm. At. Mol. Phys.*, **22** (1988) 51.
- [310] I. Nenner, P. Morin, M. Simon, P. Lablanquie, and G. G. B. de Souza. *Desorption Induced by Electronic Transition "DIET III"*, (R. H. Stulen and M. L. Knotek eds., Springer-Verlag, Vol 13, 1988, p.10).
- [311] I. Nenner, P. Morin, P. Lablanquie, M. Simon, N. Levasseur, and P. Millie. *J. Electron Spectry. Relat. Phenom.*, **52** (1990) 623.
- [312] D. M. Curtis and J. H. D. Eland. *Intern. J. Mass Spectrom. Ion Processes*, **63** (1985) 241.
- [313] G. Dujardin, L. Hellner, D. Winkoun, and M. J. Besnard. *Chem. Phys.*, **105** (1986) 291.
- [314] J. H. D. Eland, F. S. Wort, and R. N. Royds. *J. Electron Spectry. Relat. Phenom.*, **41** (1986) 297.
- [315] S. Suzuki, K. Mitsuke, T. Imamura, and I. Koyano. *J. Chem. Phys.*, **96** (1992) 7500.
- [316] B. P. Tsai, T. Baer, A. S. Werner, and S. F. Lin. *J. Phys. Chem.*, **79** (1975) 570.
- [317] S. G. Lias, J. E. Bartmess, J. F. Liebman, J. L. Holmes, R. D. Levin, and W. G. Mallard. *J. Phys. Chem. Ref. Data*, **17** (1988) 1.
- [318] X. Guo, G. Cooper, W. F. Chan, G. R. Burton, and C. E. Brion. *Chem. Phys.*, **161** (1992) 453.
- [319] X. Guo, G. Cooper, W. F. Chan, G. R. Burton, and C. E. Brion. *Chem. Phys.*, **161** (1992) 471.
- [320] G. Cooper, T. Ibuki, and C. E. Brion. *Chem. Phys.*, **140** (1990) 133.
- [321] M. J. Van der Wiel, W. Stoll, A. Hamnett, and C. E. Brion. *Chem. Phys. Lett.*, **37** (1976) 240.
- [322] P. Baltzer, L. Karlsson, M. Lundqvist, and B. Wannberg. *Rev. Sci. Instrum.*, **64** (1993) 2179.
- [323] A. Minchinton, A. Giardini-Guidoni, E. Weigold, F. P. Larkins, and R. M. Wilson. *J. Electron Spectry. Relat. Phenom.*, **27** (1982) 191.
- [324] M. N. R. Ashfold, M. T. Macpherson, and J. P. Simons. *Top. Curr. Chem.*, **86** (1979) 1.
- [325] K. Kanda, S. Katsumata, T. Nagata, Y. Ozaki, T. Kondow, K. Kuchitsu, A. Hiraya, and K. Shobatake. *Chem. Phys.*, **175** (1993) 399.

- [326] G. W. King and A. W. Richardson. *J. Mol. Spectrosc.*, **21** (1966) 339, 353, and references therein.
- [327] J. W. Rabalais, J. M. McDonald, V. Scherr, and S. P. McGlynn. *Chem. Rev.*, **71** (1971) 73.
- [328] G. A. West. PhD thesis, University of Wisconsin, 1975.
- [329] M. T. Macpherson and J. P. Simons. *J. Chem. Soc. Farad. Trans. II*, **75** (1979) 1572.
- [330] W. S. Felps, G. L. Findley, and S. P. McGlynn. *Chem. Phys. Letters*, **81** (1981) 490.
- [331] E. Heilbronner, V. Hornung, and K. A. Muszkat. *Helv. Chim. Acta.*, **53** (1970) 347.
- [332] R. F. Lake and H. Thompson. *Proc. Roy. Soc. Lond. A*, **317** (1970) 187.
- [333] J. M. Hollas and T. A. Sutherley. *Mol. Phys.*, **22** (1971) 213.
- [334] M. Allan and J. P. Maier. *Chem. Phys. Letters*, **41** (1976) 231.
- [335] W. von Niessen and R. Cambi. *J. Electron Spectry. Relat. Phenom.*, **34** (1984) 291.
- [336] H. D. Cohen and C. C. J. Roothaan. *J. Chem. Phys.*, **43S** (1965) 34.
- [337] A. D. McLean and M. Yoshimine. *J. Chem. Phys.*, **46** (1967) 3682; **47** (1967) 3526.
- [338] M. Dupuis, S. Chin, and A. Marqueq. Chem-station and hondo. In G. L. Malli, editor, *Relativistic and electron correlation effects in molecules and clusters*. NATO ASI Series, Plenum Press, New York, 1992.
- [339] A. Schaefer, H. Horn, and R. Ahlrichs. *J. Chem. Phys.*, **97** (1992) 2571.
- [340] Jr. T. H. Dunning. *J. Chem. Phys.*, **90** (1989) 1007.
- [341] A. P. Hitchcock and C. E. Brion. *J. Electron Spectry. Relat. Phenom.*, **18** (1980) 1.
- [342] J. L. Dehmer and D. Dill. *Phys. Rev. Letters*, **35** (1975) 213.
- [343] J. L. Dehmer and D. Dill. *J. Chem. Phys.*, **65** (1976) 5327.
- [344] T. N. Rescigno and P. W. Langhoff. *Chem. Phys. Letters*, **51** (1977) 65.
- [345] V. K. Wang and J. Overend. *Spectrochim. Acta.*, **29A** (1973) 1623.
- [346] G. Cooper, K. H. Sze, and C. E. Brion. *J. Am. Chem. Soc.*, **111** (1989) 5051.
- [347] G. Cooper, K. H. Sze, and C. E. Brion. *J. Am. Chem. Soc.*, **112** (1990) 4121.
- [348] G. R. Wight, M. J. Van der Wiel, and C. E. Brion. *J. Phys. B*, **9** (1976) 675.
- [349] M. J. Van der Wiel, Th. M. El-Sherbini, and C. E. Brion. *Chem. Phys. Letters*, **7** (1970) 161.

- [350] G. Dujardin, S. Leach, O. Dutuit, P. M. Guyon, and M. Richard-Viard. *Chem. Phys.*, **88** (1984) 339.
- [351] A. P. Hitchcock and C. E. Brion. *Chem. Phys.*, **33** (1978) 55.
- [352] K. H. Sze and C. E. Brion. *Chem. Phys.*, **137** (1989) 353.
- [353] A. St-Amant and D. R. Salahub. *Chem. Phys. Letters*, **169** (1990) 387.
- [354] P. Duffy and D. P. Chong. *Organic Mass Spectry.*, **28** (1993) 321.
- [355] D. P. Chong. *Chem. Phys. Letters*, **232** (1995) 486.
- [356] D. P. Chong. *J. Chem. Phys.*, **103** (1995) 1842.
- [357] R. A. Kendall, Jr. T. H. Dunning, and R. J. Harrison. *J. Chem. Phys.*, **96** (1992) 6796.
- [358] P. Duffy, D. P. Chong, and M. Dupuis. *J. Chem. Phys.*, **102** (1995) 3312.
- [359] D. P. Chong. *Chin. J. Phys.*, **30** (1992) 115.
- [360] D.G.J. Sutherland, Z. F. Lui, G. M. Bancroft, and K. H. Tan. *Nucl. Instrum. Methods Phys. Research, B*, **87** (1994) 183.
- [361] J. N. Cutler, G. M. Bancroft, and K. H. Tan. *J. Phys. B*, **24** (1991) 4897.
- [362] J. N. Cutler, G. M. Bancroft, and D. G. Sutherland. *Phys. Rev. Letters*, **67** (1991) 1531.
- [363] J. N. Cutler, G. M. Bancroft, J. D. Bozek, K. H. Tan, and G. J. Schrobilgen. *J. Am. Chem. Soc.*, **113** (1991) 9125.
- [364] F. J. Comes, R. Haensel, U. Nielsen, and W. H. E. Schwarz. *J. Chem. Phys.*, **58** (1973) 516.
- [365] F. J. Comes, R. Haensel, U. Nielsen, and W. H. E. Schwarz. *J. Chem. Phys.*, **61** (1974) 3581.
- [366] V. H. Dibeler and S. K. Liston. *J. Chem. Phys.*, **47** (1967) 4548.
- [367] Y. Huang, S. A. Barts, and J. B. Halpern. *J. Chem. Phys.*, **96** (1992) 425.
- [368] R. C. West, editor. *CRC Handbook of Chemistry and Physics*. CRC Press, Florida, 1978.